LBL-3530
c.1

RECEIVED
LAWRENCE
BERKELEY LABORATORY

JUN 10 1975

LIBRARY AND
DOCUMENTS SECTION

INORGANIC MATERIALS RESEARCH DIVISION
Annual Report 1974

For Reference

Not to be taken from this room

Lawrence Berkeley Laboratory
University of California Berkeley

LBL-3530 c.1

IMRD

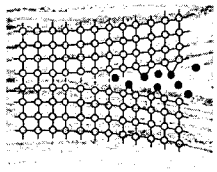

Metallurgical Engineering

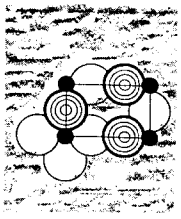

Chemistry

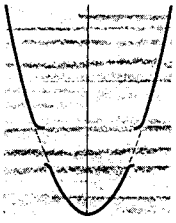

Solid-State Physics

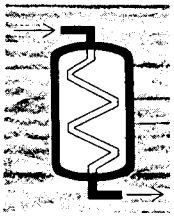

Chemical Engineering

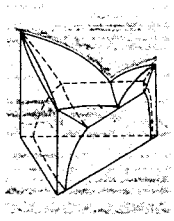

Ceramic Engineering

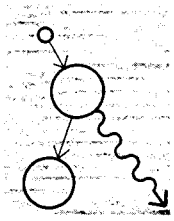

Nuclear Engineering

DISCLAIMER

This document was prepared as an account of work sponsored by the United States Government. While this document is believed to contain correct information, neither the United States Government nor any agency thereof, nor the Regents of the University of California, nor any of their employees, makes any warranty, express or implied, or assumes any legal responsibility for the accuracy, completeness, or usefulness of any information, apparatus, product, or process disclosed, or represents that its use would not infringe privately owned rights. Reference herein to any specific commercial product, process, or service by its trade name, trademark, manufacturer, or otherwise, does not necessarily constitute or imply its endorsement, recommendation, or favoring by the United States Government or any agency thereof, or the Regents of the University of California. The views and opinions of authors expressed herein do not necessarily state or reflect those of the United States Government or any agency thereof or the Regents of the University of California.

LBL-3530
UC-2 General, Miscellaneous,
and Progress Reports
TID-4500-R62

INORGANIC MATERIALS RESEARCH DIVISION
ANNUAL REPORT, 1974

April 1975

Lawrence Berkeley Laboratory
University of California
Berkeley, California

Work done under
U.S. Energy Research and Development Administration
Contract No. W-7405-eng-48

Printed in the United States of America
Available from
National Technical Information Service
U.S. Department of Commerce
5285 Port Royal Road
Springfield, Virginia 22161
Price: Printed Copy $7.60; Microfiche $2.25

INORGANIC MATERIALS RESEARCH DIVISION ANNUAL REPORT, 1974*

Contents

GENERAL INTRODUCTION . . . . . .

I. CHEMISTRY
A. Inorganic Chemistry
William L. Jolly, Principal Investigator
1. X-Ray Photoelectron Spectroscopy 3
2. Boron Hydride and Liquid Ammonia Chemistry 5
3. Germanium Chemistry 6
4. Research Plans for Calendar Year 1975 6
5. 1974 Publications and Reports 6
Robert E. Connick, Principal Investigator
1. Oxygen-17 NMR Studies of the Rate of Water Exchange from Partially Complexed Nickel Ion 8
2. The Exchange Lifetime of Water Molecules in the Second Coordination Sphere of Chromic Ion 8
3. Water Exchange from the First Coordination Sphere of Europous Ion Studied by NMR . 8
4. Computer Modeling of Exchange Reactions 8
5. Studies of Sulfur Dioxide in Aqueous Solutions 8
6. Research Plans for Calendar Year 1975 9
Neil Bartlett, Principal Investigator
1. The Giant Electron Affinity of Platinum Hexafluoride 10
2. Exploitation of O_2^+ Salts 10
3. High Oxidation States of the Heavier Transition Elements and Actinides 11
4. A Novel Tetrafluoride Structure Type and Comments on Magnetic Interactions in Rutile Type Fluoride Structures 11
5. Research Plans for Calendar Year 1975 12
6. 1974 Publication and Reports 12
B. Solid State Chemistry and Physics
Norman E. Phillips, Principal Investigator
1. Heat Capacity of the Kondo-Superconductor (La,Ce)Al_2 14
2. Low-Temperature Heat Capacity of $PrCu_2$ 14
3. Bulk Superconductivity of α-Uranium 16
4. Progress on Very Low Temperature Experiments 17
5. Research Plans for Calendar Year 1975 17
6. 1974 Publications and Reports 18
George Jura, Principal Investigator
1. Infrared Spectra 19
2. Heat Capacity of Bismuth 20
3. Research Plans for Calendar Year 1975 21
4. 1974 Publications and Reports 21
Gabor A. Somorjai, Principal Investigator
1. Low Energy Electron Diffraction (LEED) Studies of Surfaces 22
2. Auger Electron Spectroscopy Studies of Surfaces 23
3. Catalysis by Single Crystal Surfaces 24
4. Molecular Beam Study of the Mechanism of Catalyzed Hydrogen-Deuterium Exchange on Platinum Single Crystal Surfaces 25
5. Coal Conversion Catalysis 26
6. Solar Cell Research 26
7. Research Plans for Calendar Year 1975 28
8. 1974 Publications and Reports 28
Lee F. Donaghey, Principal Investigator
1. Physical and Reactive Sputtering 30
2. Crystallization 30
3. Chemical Vapor Deposition 31
4. Solid-State Electrochemistry 33
5. Research Plans for Calendar Year 1975 33
6. 1974 Publications and Reports 33
C. Electrochemistry
Charles W. Tobias, Principal Investigator
1. Fundamental Studies of Ionic Mass Transport 35
2. Electrolysis at High Current Densities 36
3. Physical Processes in Electrolytic Gas Evaluation 37
4. Electrochemistry in Nonaqueous Solvents 38
5. Research Plans for Calendar Year 1975 39
6. 1974 Publications and Reports 39

Rolf H. Muller, Principal Investigator
1. Optical Studies of Electrochemical Interfaces 40
2. Research Plans for Calendar Year 1975 43
3. 1974 Publications and Reports 44

John Newman, Principal Investigator
1. Potential Distribution in a Corroding Pit 45
2. Mass Transfer to an Eccentric Rotating Disk Electrode 47
3. Coalescence of Droplets in an Electric Field 47
4. Electrical Conductivity and Density Measurements of Concentrated Phosphoric Acid at High Temperature 47
5. Fluid Flow Near the Equator of a Rotating Sphere 48
6. Rotating Ring-Disk Electrodes 48
7. Thermodynamics of Aqueous Solutions Containing One or More Volatile Weak Electrolytes 48
8. Maximum Droplet Growth When Cooling a Saturated Solution 49
9. Double-Layer Capacity Determination of Porous Electrodes 49
10. Porous-Electrode Theory with Battery Applications 49
11. Mass Transfer of Minor Components in a Propagating Crack 49
12. Research Plans for Calendar Year 1975 49
13. 1974 Publications and Reports 49

D. Physical Chemistry

Leo Brewer, Principal Investigator
1. Thermodynamic Properties of Third and Fourth Group Transition Metals with Platinum Group Metals 51
2. Application of the Regular Solution Theory to Metallic Solutions 51
3. Thermodynamic Evaluation and Compilation of Metal Alloy Systems 51
4. The Matrix Spectra of Oxides of Ca and Mg 51
5. Research Plans for Calendar Year 1975 51
6. 1974 Publications and Reports 51

Charles B. Harris, Principal Investigator
1. Coherent Energy Migration in Molecular Solids 52
2. Phosphorescence Microwave Double Resonance Spectroscopy in Ionic Solids and Its Application to Coherent Jahn-Teller States in F Centers of CaO 52
3. Coherence in Electronically Excited Dimers and its Relationship to Excitons in Molecular Crystals 53
4. Application of Optically Detected Spin Locking and Adiabatic Demagnetizagtion to the Investigation of Energy Migration in Molecular Crystals 54
5. Energy Migration in One-Dimensional Solids 55
6. Phonon Interactions in Molecular Crystals and Their Relationships to Coherent Exciton Properties 56
7. Energy Transfer Dynamics in Molecular Solids Using A Tunable Dye Laser 56
8. The Theory of Coherence in Multilevel Systems and Its Application to New Laser Oscillators and Amplifiers 56
9. Picosecond Spectroscopy: Coherence and Vibrational Relaxation in Liquids and Solids 58
10. Energy and Electron Transfer in Photosynthetic Bacterial Systems 58
11. Research Plans for Calender Year 1975 58
12. 1974 Publications and Reports 59

Alexander Pines, Principal Investigator
1. Magnetic Shielding Tensors of Functional Groups 60
2. Effect of Hydrogen-Bonding on Carboxyl Shielding Tensors 62
3. Cross-Polarization Dynamics in Double-Resonance 63
4. Molecular Ordering and Phase Transitions in Liquid Crystals 64
5. Effects of End Chains on Nematic Stability 66
6. Molecular Motion and Order in the Smectic-A Phase 67
7. Rotational Order in the Smectic-C Phase 69
8. Multiple-Pulse Spin Echoes and Molecular Diffusion 72
9. Molecular Motion in Solids 74
10. Research Plans for Calendar Year 1975 76
11. 1974 Publications and Reports 76

Ronald R. Herm, Principal Investigator
1. Spectroscopic and Kinetic Studies of Chemiluminescence from the Reactions of Excited Mercury Atoms (6^3P_1) with Halogen Molecules 78
2. Velocity Dependence of the Cross Section For: $Hg^*(6^3P_2) + NaX \rightarrow HgX + Na^*(3^2P)$ 78
3. Product Velocity and Magnetic Deflection Analysis From Crossed Beams of Li Atoms and Halide or Oxide Molecules 78
4. Atomic and Molecular Scattering in Crossed Beams 79
5. Crossed Beams Observation of Condensation of Br_2 on $(Cl_2)_x$ and $(NH_3)_x$ 79
6. Research Plans for Calendar Year 1975 80
7. 1974 Publications and Reports 80

Harold S. Johnston, Principal Investigator
1. Experimental Studies 81
2. Theoretical Studies 82
3. Research Plans for Calendar Year 1974 83
4. 1974 Publications and Reports 83

Bruce H. Mahan, Principal Investigator
1. Ion-Molecule Collision Phenomena 85
2. Electronic Structure and Chemical Dynamics 85
3. Dynamics of the Reaction of N^+ with H_2 85
4. An Analysis of Direct Ion-Molecule Reactions 86
5. Dynamics of the CO_2^+-H_2 Reaction 86
6. Spectroscopy of Gaseous Ions 86
7. Collinear Collision Chemistry 87
8. Research Plans for Calendar Year 1975 87
9. 1974 Publications and Reports 87

William H. Miller, Principal Investigator
1. Semiclassical Theory of Collisionally Induced Fine-Structure Transition in Fluorine Atoms 88
2. Classical Trajectory Study of Rotational Excitation 89
3. Semiclassical Treatment of Rotational Excitation of Formaldehyde at Very Low Energies 90
4. Quantum Mechanical Transition State Theory for Non-Separable Systems 91
5. Theoretical Treatment of Quenching in $O(^1D) + N_2$ Collisions 92
6. Research Plans for Calendar Year 1975 93
7. 1974 Publications and Reports 93

Rollie J. Myers, Principal Investigator
1. Electron Exchange Interactions Between Hydrated Ions--Results from Paramagnetic Resonance Spectra of Ions in Paramagnetic Lattices 94
2. Electron Spin Relaxation Mechanisms of $Cu(NH_3)_6^{2+}$ in Liquid Ammonia 94
3. Magnetic Resonance Study of Metal-Metal Complexes in Biologically Important Molecules 95
4. Research Plans for Calendar Year 1975 95
5. 1974 Publications and Reports 95

Kenneth S. Pitzer, Principal Investigator
1. Solutions of Electrolytes: Activity and Osmotic Coefficient at High Temperatures and Thermal Properties 96
2. Higher Order Electrostatic Terms in Electrolyte Theory 96
3. Solutions of Electrolytes: Mixed Electrolytes at Room Temperature 97
4. Oxygen-Catalyzed Nuclear-Spin-Species Effects in the Heat Capacity of CH_4 97
5. The Potential Functions for the Anomalous ν_7 Vibrations of PF_5 and VF_5 97
6. Pseudorotation in XeF_6 98
7. Electric Field Deflection of Molecules 99
8. Quantum Chemistry for Heavy Atoms 99
9. Research Plans for Calendar Year 1975 99
10. 1974 Publications and Reports 100

E. Nuclear Science

Donald R. Olander, Principal Investigator
1. Kinetics of the Reaction of Water Vapor on Pyrolytic Graphite by Modulated Molecular Beam Mass Spectrometry 101
2. Molecular Beam Study of the Graphite-Hydrogen Reaction 101
3. Molecular Beam Study of the F_2-UO_2 Reaction 102
4. The Kinetics of Radiolytic Gas Phase Reactions by Modulated Molecular Beam Mass Spectrometry 103
5. Actinide Redistribution Due to Pore Migration in Hypostoichiometric Mixed Oxide Fuel Pins 103
6. Research Plans for Calendar Year 1975 104
7. 1974 Publications and Reports 105

II. METALLURGY

A. Crystal Imperfections

Jack Washburn, Principal Investigator
1. Computer Simulation of Small Dislocation Loops in Field Ion Images of FCC Crystals 109
2. Development of a CdS-Cu_2S Solar Cell with Improved Characteristics 109
3. Boron Precipitates in Ion Implanted Silicon 110
4. Mechanism of Recovery Processes After Phosphorous Implantation in Silicon 110
5. Effect of Surface Layer Composition on Electron Work Function in Ni_4W 111
6. The Preferential Capture of Interstitial Atoms by Dislocations When Both Vacancies and Interstitials are Being Formed at the Same Rate by Radiation Damage 111
7. Mechanism of the Shape Memory Effect in NiTi 112

8. Characterization of Grain Boundaries in Polycrystalline Silicon 112
9. The Mechanism of Interstitial Diffusion in FCC Metals 112
10. Research Plans for Calendar Year 1975 112
11. 1974 Publications and Reports 113

B. Theoretical Metallurgy
J. W. Morris, Jr., Principal Investigator
Introduction 114
1. Phase Stability of Metals and Alloys 114
2. Correlation of Microstructure to Processing 115
3. Correlation of Mechanical Properties to Microstructure 115
4. Alloy Design 119
5. Research Plans for Calendar Year 1975 126
6. 1974 Publications and Reports 127

C. Microstructure, Properties and Alloy Design
Gareth Thomas, Principal Investigator
1. Design of Strong Tough Fe/Mo/C Martensitic Steels and the Effects of Cobalt 129
2. Design of Fe/4Cr/0.4C Martensitic Steels Eliminating Quench Cracking 130
3. Investigation of Heat Treatment for Improved Properties of Low Carbon Fe-0.12%C-0.5%Mn Steels 130
4. Loss of Coherency in Spinodally Decomposed Cu-Ni-Fe Alloys 131
5. Discontinuous Coarsening of Spinodally Decomposed Cu-Ni-Fe Alloys 131
6. Interstitial Order and Embrittlement in Ta-C Alloys 132
7. The Crystallography and Structure of Deformation Induced Epsilon and Alpha Martensite in Fe-Ni-Cr Single Crystals 133

D. Ceramic Alloys Program
Gareth Thomas, Principal Investigator
1. Characterization of Structures in Lithium Ferrite 134
2. Phase Transitions in Lithium Ferrite 135
3. Structure of Non-Stoichiometric TaC 135

E. High Voltage, High Resolution Electron Microscopy
Gareth Thomas, Principal Investigator
1. High Resolution Studies-Ordered Alloys 137
2. High Voltage Studies 140
3. Radiation Damage (200kV-650kV) in Organic Materials (and Devices Measuring Electron Beam Current Densities) 142
4. Theoretical and Experimental Analysis of Crystal Defects with Particular Emphasis to Silicon 143
5. Research Plans for Calendar Year 1975 143
6. 1974 Publications and Reports 144

F. High Strength Materials
Victor F. Zackay and Earl R. Parker, Principal Investigators
Introduction 146
1. An Investigation of Bainite Transformation in Medium Carbon Low Alloy Steels . . . 146
2. Elevated Temperature Properties of Non-Carbon Containing Ferritic Alloys Strengthened by a Laves Phase 147
3. The Design of Alloys with Minimal Swelling Properties on Subjection to Irradiation Damage 149
4. Development of High Strength/High Toughness Fe-Cr-Si-(Mo)-C Steels 149
5. Fracture Toughness in High Strength Fe-Ni-Ti Alloys 150
6. Preparation of Metal-Metal Composite Materials Using a Powder Metallurgy 151
7. Influence of Heat Treatment and Environment on the Fatigue Crack Growth Rates in a Secondary Hardening Steel 152
8. An Investigation of the Bainite Reaction in Se- and Al-Modified Low Alloy High Strength Commercial Steels with Regard to Kinetics of the Transformation and Its Effect on Mechanical Properties 153
9. Thermodynamics of Fe-C-X Alloys 153
10. Characterization of Brittle Crack Initiation in Welded A-36 and A-537 Steels . . . 156
11. The Cryogenic Properties of Fe-Mn and Fe-Mn-Cr Alloys 158
12. Fatigue Crack Propagation Rates in Fe-Ni Alloys 160
13. The Mechanical Properties and Corrosion Resistance of Selected Fe-Mn-Cr Alloys . . 161
14. The Strain Energy of a Disk-Shaped GP Zone 162
15. The Development of Iron-Rich Fe-Zn System 163
16. Quantitative Measurements of Phase Transformation Kinetics in Low Alloy Steels During Programmed Cooling 163
17. The Kinetics of Auto-Tempering in Selected Plain Carbon and Alloy Steels 165
18. Research Plans for Calendar Year 1975 167
19. 1974 Publications and Reports 167

0 0 0 0 4 2 0 7 1 6 4

G. High Field Superconductivity
Milton R. Pickus, Principal Investigator
1. Filamentary Niobium-Tin Wire 169
2. Research Plans for Calendar Year 1975 171

H. Powder Metallurgy
Milton R. Pickus, Principal Investigator
1. Liquid Phase Sintering of High Carbon Alloys in the Iron-Carbon System 172
2. Preliminary Studies of the Rare-Earth Iron Laves Phases Prepared by Powder Metallurgy Techniques 173
3. Morphology Control of Titanium Carbide as a Dispersed Phase in a Type 410 Stainless Steel Matrix 174
4. A Survey of Methods for Coating Powder Particles, with Results of Some Exploratory Experiments 174
5. Research Plans for Calendar Year 1975 175
6. 1974 Publications and Reports 176

I. Advanced Materials
Robert H. Bragg, Principal Investigator
Introduction 177
1. X-Ray Studies of Glassy Carbon 177
2. Kinetic Studies of Ordering in GC 178
3. Electrical Properties of Glassy Carbon 178
4. Electrical Resistivity of Cu-Al_2 Eutectic 179
5. Unidirectional Solidification of Al-Si Eutectic 181
6. Small-Angle Scattering by Glassy Carbon and Pyrolytic Graphite 183
7. Research Plans for Calendar Year 1975 183
8. 1974 Publications and Reports 183

III. CERAMIC SCIENCE

A. High Temperature Reactions
Alan W. Searcy, Principal Investigator
1. Transition State Theory for Vaporization and Condensation 187
2. The Kinetics of Endothermic Decomposition Reactions: I. Steady State Chemical Steps 187
3. The Kinetics of Endothermic Decomposition Reactions: II. The Effects of Pressures of the Gaseous Product 188
4. Effect of Porous Barriers on the Molecular Compositions of Reactive Gas Mixtures 188
5. Application of the Effect of Porous Barriers on Molecular Compositions to Determination of Mass Spectrometer Cross Section 189
6. The Effect of Porous Alumina Barriers on the Rate of Decomposition of Calcium Carbonate 189
7. The Composition of Alkali Chlorates Vapors 189
8. Kinetics of Decomposition of Strontium Sulfate 190
9. The Magnetic Moment of Se_2 190
10. Research Plans for Calendar Year 1975 192
11. 1974 Publications and Reports 192

B. Microstructure and Behavior of Ceramic Materials: Glass and Ceramic-Metal Systems
Joseph A. Pask, Principal Investigator
1. Thermodynamic Considerations of Solid State Sintering 194
2. Kinetics of Intermediate and Final Stages of Sintering 196
3. Polycrystalline Spinel from Powders Prepared by Freeze Drying Technique 196
4. The Silica-Alumina System: Stable and Metastable Equilibria at 1.0 Atmosphere 197
5. Immiscibility and Crystallization Studies in the Silica-Alumina System 197
6. Impact Fracture Behavior of Glass 197
7. High-Temperature Deformation of MgO 199
8. Microstructure Analysis and Stress-Strain Behavior of a Model Refractory System $MgO\text{-}CaO\cdot MgO\cdot SiO_2$ 199
9. High-Temperature Deformation of Polycrystalline Magnesium Oxide 199
10. Effect of Processing on Microstructure and Mechanical Behavior of Magnesium Oxide 200
11. Wetting and Reaction Between Aluminum and Vitreous Silica 200
12. Metal-Glass Interfaces 201
13. Research Plans for Calendar Year 1975 201
14. 1974 Publications and Reports 202

C. Relation of Microstructure of Properties in Ceramics
Richard M. Fulrath, Principal Investigator
Introduction 203
1. Solid State Sintering Studies 203
2. Uniaxial Bend Strength and Fracture Initiation Energy in Glass-Matrix Composites 205
3. Electrical Conductivity in $LiFe_5O_8$ Ceramics 206
4. Physical and Electrical Properties of Controlled Stoichiometry PZT 209
5. A Liquid Phase Densification Technique for the Lead Zirconate Titanate System 211
6. Research Plans for Calendar Year 1975 213
7. 1974 Publications and Reports 213

IV. SOLID STATE PHYSICS
A. Theoretical Solid State Physics
Marvin L. Cohen, Principal Investigator
Introduction 217
1. Electronic Structure of Diamond, Zincblende and Chalcopyrite Semiconductors 217
2. Chain and Layer Materials 218
3. Narrow Gap IV-VI Semiconductors 218
4. Materials, Bonding and Superconductivity 218
5. Electronic Structure of Polytypes and Amorphous Phases of Group IV and III-V Materials 219
6. Surface States on Semiconductors 219
7. Local Fields, Dielectric Functions, Lattice Vibrations 219
8. Research Plans for Calendar Year 1975 219
9. 1974 Publications and Reports 220
B. Far Infrared Properties of Solids
Paul L. Richards, Principal Investigator
1. A Balloon-Based Measurement of the Cosmic Background Radiation 222
2. Far Infrared EPR of $Al_2O_3:Mn^{3+}$ 223
3. Surface Magnetic Resonance in MnF_2 223
4. High Resolution Fourier Transform Spectroscopy of Impurities and Defects in High-Purity Germanium 224
5. Instrumentation for Infrared Spectroscopy 225
6. Infrared Bolometer Detectors 226
7. Infrared Sky Survey 226
8. Far Infrared Spectroscopy of Exciton Droplets 226
9. Millimeters Wave Coherent Detectors 226
10. Research Plans for Calendar Year 1975 227
11. 1974 Publications and Reports 227
C. Superconductivity
John Clarke, Principal Investigator
1. A Low Noise Reliable SQUID Made from Josephson Tunnel Junctions 229
2. Josephson Junction Magnetometer for Use in Geophysics 230
3. A Thin Film Gradiometer 230
4. Nb-Nb Thin Film Josephson Tunnel Junctions 231
5. 1/f Noise 231
6. Low Frequency Noise in Superconducting Thin Films 232
7. Low Frequency Fluctuations in Josephson Junctions 233
8. Superconducting Far Infrared Bolometers 234
9. Determination of BCS Parameter N(0)V in "Normal Metals" 235
10. Research Plans for Calendar Year 1975 235
11. 1974 Publications and Reports 236
D. Experimental Solid State Physics and Quantum Electronics
Y. Ron Shen, Principal Investigator
1. Study of Pretransitional Behavior of Laser-Field Induced Ordering in Isotropic Liquid Crystalline Materials 238
2. Study of Transient Self-Focusing 238
3. Molecular Theory of Orientational Fluctuations and Optical Kerr Effect in the Isotropic Phase of a Liquid Crystal 239
4. Study of Dispersive Raman Modes in Cu_2O By Resonant Raman Scattering 239
5. Effect of Doping on the Resonance Raman Scattering in InSb Near the E_1 Transition 240
6. Resonant Raman Scattering In Se 241
7. Wavelength-Modulation Spectroscopy of Solids 241
8. Luminescence of CdS Under High-Intensity Excitations 242
9. Dispersion of Nonlinear Optical Susceptibilities $\chi^{(2)}(2\omega)$ of GaAs, InAs and InSb 244

10. Nonlinear Optical Effects in Alkali Vapor 244
11. Resonant Raman Scattering in Magnetic Crystals 244
12. Research Plans for Calendar Year 1975 244
13. 1974 Publications and Reports 244

APPENDICES
IMRD STAFF FOR 1974 249
DEGREES AWARDED IN 1974 254
VISITING SCIENTISTS 256
1974 RESEARCH SEMINARS 257

*Preceding Annual Reports: LBL-1400, LBL-2299.

GENERAL INTRODUCTION

Leo Brewer, Division Head
Victor F. Zackay, Associate Head
Rolf H. Muller, Assistant to Division Head

The year 1974 has been one of significance and of transition for the Inorganic Materials Research Division. It has been a significant year in terms of our research accomplishments and of productivity relative to numbers of students graduated with advanced degrees. It has been a year of transition in that fourteen years of sponsorship by the U. S. Atomic Energy (AEC) has ended and a new period begun with the sponsorship of the U. S. Energy Research and Development Administration (ERDA). In the following several pages, a few remarks will be addressed to each of these topics, viz., some highlights will be given of our fourteen years with AEC sponsorship, the efforts of the Division in the past year will be briefly reviewed, and, lastly, several examples of current preparations being made for the transition period will be given.

Some Highlights of the Past

The Staff

The IMRD has been blessed with a loyal, hard working and competent administrative, technical and clerical staff--small in numbers but large in its ability to handle the work load represented by a Division now numbering 326 people. They have effectively and efficiently met the heavy and diverse duties imposed by a student population of nearly two hundred, fifty postdoctoral fellows and a faculty group varying between 30 and 40. A significant measure of the success of IMRD is due to their devotion to the division.

Research

In the past eight years of its existence the research of the Division has resulted in an average of 150 papers, chapters in books, and books each year. In addition, its investigators have several dozen patents to their credit. In the fourteen years since its founding, the Division has been responsible for a total of about 1600 scholarly contributions to refereed journals in the sciences and engineering. In addition, IMRD has sponsored five International Symposia whose proceedings inaugurated a successful technical book series.

Perhaps of even greater significance, the Division's research activities resulted in the sponsorship of over 300 Ph.D's and 200 M.S.'s who have found their respective places in industry, government and education. On the average, about 30% of the doctoral degree students elected to join academic institutions, 25% went to government laboratories, and the remainder (45%) joined the ranks of industry. Sufficient time has now elapsed for many of these students to have established themselves in society. Several of those who have attained positions of responsibility this past year are: J. R. Kane now with ERDA in Washington, D. C., as Acting Deputy Assistant Administrator for Conservation, A. Pasternak, named by Governor Brown to the new Energy and Resources Conservation and Development Commission, and J. Lira-Olivares, named as Director del Instituto de Investigaciones Metalurgicas, Universidad Simon Bolivar, Caracas, Venezuela.

The Past Year

Some representative research highlights, distinguished awards to principal investigators and some current plans being made for a smooth transition to the energy-related mission of ERDA are briefly described in the following section.

Some Research Highlights

A novel tetrafluoride structure type (related to the rutile structure) has been discovered in the tetrafluorides Pb, Pt, Rh, Ir and magnetic studies of the Ir compound have provided insight into the role of F atom bridging in the magnetic coupling between the metal atoms. (N. Bartlett)

Experimental confirmation was obtained that the kinetics of lattice ordering in Glassy Carbon, the model material system representative of hard, nongraphitizing carbons, can be represented by a unique function of time and temperature. (R. Bragg)

A highly reliable and very sensitive Josephson junction magnetometer has been developed utilizing Nb-NbO_x-Pb tunnel junctions. A theory of 1/f noise has been developed that accounts quantitatively for the 1/f noise observed in metal films, superconductors at their transition temperature, and Josephson junctions. (J. Clarke)

Many new developments have resulted from research centered around the electronic structure of solids. The empirical pseudopotential method (EPM) was extended and used to calculate the electronic properties of a variety of materials. Bulk properties; surface states; properties of amorphous materials; chain, layer, ternary and narrow-gap semiconductors; metals; superconductivity; dielectric functions; and lattice vibrations were characteristic subjects of investigation. (M. L. Cohen)

Our study of the distribution and persistence of carbon-14 in the stratosphere (1963-1970) from

nuclear bomb clouds after the 1961-62 tests provided a fairly sharp verification of certain models of stratospheric motion, which had been used to calculate the effect of supersonic transports on ozone. (H. S. Johston)

During the past year our X-ray photoelectron spectroscopic data for a substantial variety of non-transition inorganic molecules have consistently indicated that valence-shell d orbitals play only a minor role in chemical bonding. Our quenched flow reactor for the synthesis of compounds derived from short-lived intermediates has been successfully applied to two syntheses and promises to be useful as a general laboratory technique. We have established the rate law for the $NH_4^+ + BH_4^-$ reaction in liquid ammonia and have demonstrated that $GeH_3CO_2^-$ undergoes a base-catalyzed decomposition to GeO_3^{2-}, and H_2. (W. L. Jolly)

The accumulated research of our project has shown that with electronic state correlation diagrams, it is possible to anticipate the general nature of reaction dynamics, and by using the sequential impulse model of direct reactions, one can make quantitative predictions of product energy and angular distributions and isotope effects for high energy reactions. (B. Mahan)

A more general form of transition state theory for reaction rate constants has been developed which appears to provide an accurate description even at low temperatures where quantum effects are significant. (W. H. Miller).

Concentration profiles in boundary layers on extended electrodes have been derived from interferograms for the first time under consideration of light-deflection in the liquid and reflection from the electrode edge. Turbulence-inducing flow obstacles have been found by interferometry to significantly reduce the thickness of boundary layers under laminar flow over extended distances downstream. (R. H. Muller)

Our investigation of the magnetic interaction between hydrated transition-metal ions has shown that it can be nicely explained by the bonding orbitals of the ions. (R. J. Myers)

The solution to the problem of limiting current mass transfer to a disk electrode rotating on an axis displaced from the center of the electrode was obtained and verified experimentally. The potential distribution in a corroding, hemispherical, metal pit was calculated. A low cost nonpolluting process for recovering copper from ores and scrap metal was developed with Professor Bennion of UCLA. (J. Newman)

The molecular beam study of the graphite-hydrogen reaction has revealed that the free radicals CH and CH_2 are the primary products of this heterogeneous reaction. (D. R. Olander)

Thermodynamic analysis indicated that the change in grain boundary energy has to be taken into account as well as the change in surface energy in determining the driving force for sintering and that the motivation for mass transport is the change of the dihedral angle formed at grain-grain-vapor contacts towards its equilibrium value. (J. A. Pask)

Bulk superconductivity probably occurs in perfect single crystal α-uranium near 0.1°K and does occur at higher temperatures in polycrystals. The values of T_c are not limited by localized spins and the experimentally determined parameters are consistent with a BCS mechanism. Two second-order transitions have been observed in $(LaCe)Al_2$ corresponding to the appearence at T_{c1} and disappearance at a lower temperature, T_{c2} of superconductivity. (N. E. Phillips)

Our success in using our very general equations to fit both the properties of 86 mixed electrolyte systems at room temperature and the properties of NaCl up to 300°C, gives us confidence that these equations will make possible the prediction of both chemical and engineering thermodynamic properties of brines of interest in geothermal energy. (K. S. Pitzer)

A dramatic effect of porous barriers on the molecular compositions of reactive gas mixtures was predicted and the predictions were quantitatively confirmed by demonstrating that barriers that reduce the partial pressure sodium chloride monomers by factors of the order of 100 reduced the partial pressures of the dimer by factors of the order of 10,000 and to values within a factor of two of the predicted values. (A. W. Searcy)

We have shown quantitatively for the first time that transient self-focusing of light can be correctly described by a dynamic trapping model. We have demonstrated that resonant Raman scattering can yield detailed information about phonon structure, electronic structure, and electron-phonon interaction simultaneously which cannot be obtained easily by other methods. (Y. Ron Shen)

Investigation of the hydrogen-deuterium exchange reaction on a series of low and high Miller Index platinum single-crystals has indicated that atomic steps present on the higher index surfaces are necessary for the dissociation and subsequent recombination of hydrogen. Low energy electron diffraction studies of the adsorption of ammonia on the iron (110) crystal face showed that during the dissociation adsorption of the molecule the ordered iron surface becomes completely disordered. (G. A. Somorjai)

A new heat-treatment involving holding in the two-phase ($\alpha+\gamma$) field followed by quenching has been developed which gives a twofold increase in strength. (G. Thomas)

Generalized correlation of limiting rates of electrolysis measured in semi-industrial scale apparatus allows accurate prediction of energy requirements and of distribution of current in channel-flow type electrode configuration. A promising novel scheme has been proposed for the production of hydrogen, involving a combined electrolysis-thermal cycle.

Using a hot stage in the 650kV electron microscope it has been possible to directly and continuously observe the climb of dislocations as they preferentially capture interstitial atoms; since this is the underlying cause of radiation induced swelling of metals the technique will be valuable in giving a more complete understanding of the factors that affect radiation-induced swelling. (J. Washburn)

Largely based on the systematically accumulated evidence and understanding gained over the past dozen years in alloy design, several families of carbon-containing and carbon-free ferrous alloys were developed which can serve as the basis for the synthesis of new alloys for room and elevated temperature service. (E. R. Parker and V. F. Zackay)

Awards and Appointments

The following students and principal investigators either received awards or were elected to distinguished positions.

Neil Bartlett was appointed a member of the advisory panel of the Institute of Materials Research of the National Bureau of Standards. He was also elected an associate member of the J. Stefan Institute, Ljunljane, Yugoslavia and was nominated associate professor of the Faculty of Sciences of the University of Bordeaux, France. He presented a lecture to the Division of Mineral Chemistry at the Annual Meeting of the French Chemical Society in Nancy, France.

Leo Brewer was the William Draper Harkins Lecturer, at the Department of Chemistry, University of Chicago in April 1974. He received the Distinguished Alumni Award the following month from the California Institute of Technology.

Ronald Gronsky and Krishna Seshan received the President's award for the Electron Microscopy Society of America.

Harold S. Johnston was given the American Chemical Society award for Pollution Control.

Charles W. Krause is a NATO Postdoctoral Fellow and is spending one year at the Department of Metallurgy, Oxford University, England.

William H. Miller, a Dreyfuss Teacher Scholar, won the annual prize of the International Academy of Quantum Molecular Science in Paris. He was also made a full professor at UC-Berkeley.

Since January 1973, Rolf H. Muller has been the Co-Chairman of Division 3, Experimental Methods in Electrochemistry, of the International Society of Electrochemistry. He was Host Chairman of the 145th Meeting of that society held in San Francisco in May 1974.

Earl R. Parker was the recipient of the 1974 Western Electric Fund Award from the Pacific Southwest Section of the American Society for Engineering Education for "Excellence in the Instruction of Engineering". He was also elected honorary member of the International Cooperative Fracture Institute of Japan.

Edward L. Quitevis was awarded the Achievement Rewards for Collegiate Scientists Foundation scholarship.

Alexander Pines was presented the Alfred P. Sloan Foundation Basic Research Fellowship. He received an unrestricted grant-in-aid from the Petroleum Research Foundation of the American Chemical Society.

Paul L. Richards received a John Simon Guggenheim Fellowship for the period September 1973 through June 1974.

Robert Ritchie was the recipient of the Miller Research Fellowship.

Krishna Seshan was awarded the first prize at the International Metallographic Exhibit in St. Louis sponsored by the American Society for Metals and the International Metallographic Society. Robert Sinclair and Jan Dutkiewicz received honorable mention at the same meeting.

Gabor A. Somorjai was elected Chairman of the Irvine Solid State Physics Conference on "Chemical Processes at Surfaces". He was also elected Chairman of the Berkeley Symposium on the "Frontiers of Surface Chemistry".

Gareth Thomas was elected President of the Electron Microscopy Society of America for 1975. He will serve as Secretary-General of the International Federation of Electron Microscopy Society for 1974 through 1979.

Charles W. Tobias is President elect of the International Society of Electrochemistry (incorporated in Geneva) and is currently serving as vice-president of that society.

IMRD Review Meeting

The Eighth Annual Review Symposium of the Inorganic Materials Research Division was held January 30 and 31, 1974. The formal reviewers were:

Professor Charles S. Barrett, Department of Chemical Engineering and Metallurgy, University of Denver, Colorado.
Dr. Spencer Bush, Battelle Memorial Institute, Pacific Northwest Laboratory, Richland, Washington.
Professor Lawrence S. Darken, Department of Geosciences, Pennsylvania State University, University Park, Pennsylvania.
Professor Paul H. Emmett, Chemistry Department, Portland State University, Oregon.
Professor Paul Gilles, Chemistry Department, University of Kansas, Lawrence, Kansas.
Professor Norman Nachtrieb, Chemistry Department, University of Chicago, Illinois.
Professor Douglas J. Scalapino, Physics Department, University of California, Santa Barbara, California.

Plans for the Future

In this year of transition, much time and effort

were directed toward planning our research program for the future and a number of important "position" papers on energy-related fields were prepared.

Also, individual principal investigators have studied the impact of their current work as it relates to the mission of ERDA and, in some instances, have initiated entirely new projects. In several projects, new senior personnel have been added who greatly enlarge the capabilities of the Division. One such person is Mr. Alan Levy, a nationally known expert in high temperature (1000°C and above) materials.

Lastly, plans have been completed for a large addition to Building 62. This addition is intended both to relieve the present overcrowded facilities and to allow expansion for new energy-related projects.

0 0 0 0 4 2 0 7 1 6 7

I. Chemistry

A. INORGANIC CHEMISTRY

William L. Jolly, Principal Investigator

I. X-RAY PHOTOELECTRON SPECTROSCOPY

a. X-Ray Photoelectron Spectroscopy of Some Nickel Compounds*

L. O. Pont, A. R. Siedle, M. S. Lazarus, and W. L. Jolly

We have determined the nickel $2p_{3/2}$ binding energies of various nickel complexes, including dicarbollide complexes in which the nickel ostensibly has oxidation states of +3 and +4. The data are presented in Table I.

Table I. Nickel $2p_{3/2}$ Binding Energies

Compound	Ni oxidn. state	E_B, eV
$(1,2\text{-}B_9C_2H_{11})_2NI$	4	857.2
$[1,2\text{-}(CH_3)_2B_9C_2H_9]_2Ni$	4	856.6
$(B_{10}H_{10}CNH_3)_2Ni$	4	856.5
$Rb[(1,7\text{-}B_9C_2H_{11})_2Ni]$	3	855.9
$K[(1,2\text{-}B_9C_2H_{11})_2Ni]$	3	855.6
$K\{[1,2\text{-}(CH_3)_2B_9C_2H_9]_2Ni\}$	3	855.6
$[Ni(H_2O)_4Cl_2]\cdot 2H_2O$	2	857.7
$K_2[Ni(CN)_4]\cdot H_2O$	2	856.6
$K[Ni(gly)_3]$	2	856.5
$KNiIO_6\cdot 0.5H_2O$	2	856.0
$Ni(DMG)_2$	2	855.6
$[Ni(en)_3]S_2O_3$	2	855.6
$(C_5H_5)_3Ni_3(CO)_2$	1	855.0

The binding energies of the dicarbollide complexes of Ni(III) and Ni(IV) are of the same general magnitude as those of the Ni(II) complexes. This is at first sight surprising because of the expected correlation of binding energy with oxidation state. We believe the low binding energies of the dicarbollide complexes are a consequence of the low electronegativities of the donor atoms in these complexes. The nickel-coordinated carbon and boron atoms of the dicarbollide groups donate considerably more electron density to the metal atoms than do the relatively electronegative oxygen and nitrogen atoms in complexes such as $Ni(gly)_3^-$ and $Ni(en)_3^{2+}$. Consequently, the atomic charges of the nickel atoms in the two classes of complexes are not markedly different.

There is a definite increase of about 1 eV in binding energy on going from the Ni(III) dicarbollide complexes to the Ni(IV) dicarbollide complexes. Apparently the increase in positive charge accompanying one-electron oxidation is somewhat localized on the nickel atoms, and there is no need to consider redox reactions of the ligands.

*Abstracted from Inorg. Chem. 13, 483 (1974).

b. Correlation of Core Electron Binding Energies with Charge Distributions for Compounds of Carbon, Silicon, and Germanium*

Winfield B. Perry and William L. Jolly

Core electron binding energies for analogous compounds of carbon, silicon, and germanium have been measured by X-ray photoelectron spectroscopy in the gas phase. A principal aim of the work was to determine whether the valence-shell d orbitals of silicon and germanium are important in determining the charge distributions in compounds of these elements. The chemical shifts have been correlated by the electrostatic potential equation using charge distributions from extended Huckel theory, CNDO/2, and an electronegativity equalization method. The data can be rationalized without any consideration of $p\pi \rightarrow d\pi$ bonding in the silicon and germanium compounds.

*Abstracted from Inorg. Chem. 13, 1211 (1974).

c. Core Electron Binding Energies of Thiazyl Fluoride and Other Sulfur Compounds*

W. L. Jolly, M. S. Lazarus, and O. Glemser

Core electron binding energies were measured for the atoms in NSF_3, SF_5Cl, and S_2Cl_2. These data and similar data from the literature for other sulfur compounds were correlated by the point charge potential method using CHELEQ atomic charges. The results indicate that the bonding in a wide variety of sulfur compounds can be explained using only s and p valence orbitals. The low fluorine 1s bonding energies observed for NSF_3 and OSF_2 are attributed to "no-bond" resonance structures.

*Abstracted from Z. anorg. allg. Chem. 406, 209 (1974).

d. Determination of the Electron Distribution in a Transition Metal Carbene Complex by X-Ray Photoelectron Spectroscopy*

Winfield B. Perry, Theodore F. Schaaf, William L. Jolly, Lee J. Todd, and David L. Cronin

There is a much current interest in the structure and bonding of transition metal carbene complexes.

A carbene complex in which the carbene carbon atom is bonded to a heteroatom with non-bonding electrons, such as LMC(OR)R, may be represented as a resonance hybrid of structures I-III.

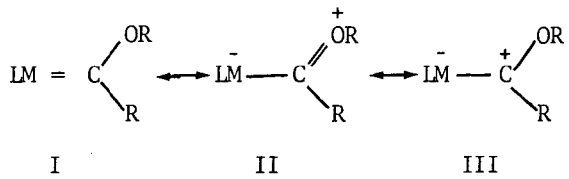

In view of the current interest in the charge distribution in such complexes, we have used X-ray photoelectron spectroscopy to determine the relative importance of the resonance structures in methoxy(methyl)carbenepentacarbonylchromium(0), $(CO)_5CrC(OCH_3)CH_3$. This complex has sufficient volatility at room temperature so that we could study it as a gas and avoid the problems associated with solid-state spectra.

The carbon 1s spectrum is shown in Fig. 1. The only features due to pure core ionization are the peak at 292.37 eV and its low binding energy shoulder. Undoubtedly the main peak is principally due to the five carbonyl carbon atoms. The shoulder and perhaps part of the intensity of the main peak are due to the other three carbon atoms. To provide an objective analysis of this portion of the spectrum, we have resolved the band by a least-squares curve-fitting routine into four peaks with an enforced intensity ratio of 5:1:1:1. This analysis placed the intense peak at 292.37±0.10 eV and the weak peaks at 291.7±0.3, 291.7±0.3, and 290.4±0.3 eV. Although the latter three binding energies are not to be taken very seriously, the analysis does show that the binding energies of the weaker components of this band are lower than that of the intense carbonyl component.

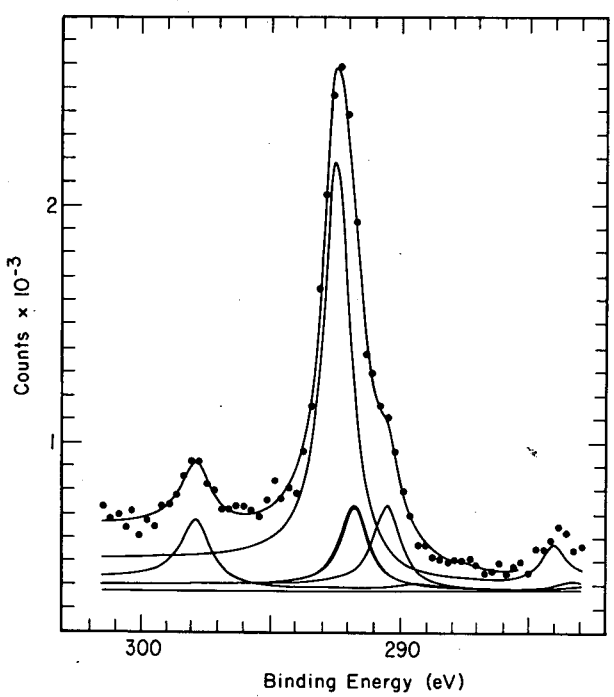

Fig. 1. Carbon 1s spectrum of methoxy(methyl) carbenepentacarbonylchromium(0). The curve through the points is the sum of the computer-resolved curves for individual peaks. Two of the resolved peaks in the shoulder of the main peak are almost superimposed. The weak peak with $E_B \approx 284$ eV is due to the $MgK\alpha_{3,4}$ satellite of the exciting radiation. (XBL 739-1789)

The fact that none of the carbon atoms in the $C(OCH_3)$-CH_3 ligand has a binding energy greater than that of the carbonyl carbon atoms suggests that none of the $C(OCH_3)CH_3$ carbon atoms has a charge more positive than that of the carbonyl carbon atoms. Thus we conclude, contrary to some previous interpretations, that to account satisfactorily for the electron distribution it is necessary to consider significant contributions from all three resonance structures.

*Abstracted from Inorg. Chem. 13, 2038 (1974).

e. Valence Electron Binding Energies of some Silicon Compounds from X-Ray Photoelectron Spectroscopy*

Winfield B. Perry and William L. Jolly

X-Ray photoelectron spectra in the valence electron region were obtained for gaseous SiH_4, SiH_3CH_3, $Si(CH_3)_4$, SiH_3Cl, and SiF_4. The experimental ionization potentials and relative peak intensities are consistent with extended Hückel theory MO calculations. The data can be rationalized without assuming substantial participation of silicon d orbitals in the bonding of these compounds.

*Abstracted from J. of Electron Spectroscopy and Related Phenomena 4, 219 (1974).

f. The Calculation of Atomic Charges by an Electronegativity Equalization Procedure*

William L. Jolly and Winfield B. Perry

In a previous study, an electronegativity equalization procedure for calculating atomic charges of compounds of the first row of the periodic table was calibrated using experimental 1s electron binding energies of carbon, nitrogen, oxygen, and fluorine.[1] We now show that (1) this method can be extended to compounds of elements from the remainder of the periodic table, (2) significant improvement in the core binding energy correlations is achieved by including a relaxation energy term in the potential equation, and (3) compounds for which nonequivalent resonance structures can be written must be specially treated. In this paper we give detailed stepwise instructions for the calculation of atomic charges in molecules for which unambiguous valence bond structures can be written.

*Abstracted from Inorg. Chem. 13, 2686 (1974).

1. W.L. Jolly and W.B. Perry, J. Amer. Chem. Soc. 95, 5442 (1973).

g. The Application of X-Ray Photoelectron Spectroscopy to Inorganic Chemistry (Review)*

William L. Jolly

X-Ray photoelectron spectroscopy (also called ESCA and XPS) involves the determination of the energy distribution of electrons emitted from X-ray-irradiated compounds. In principle all the electrons of a compound, from the atomic cores to the valence levels, can be studied; however, the technique is used principally for the study of core electrons. X-Ray photoelectron spectroscopy has applications in many scientific disciplines, including all the classical branches of chemistry, biochemistry, solid-state chemistry and physics, the study of surface phenomena, and geology. The books by Siegbahn and his coworkers are highly recommended for a general introduction to the field. The several review articles which have been written on this topic have been aimed at audiences of physical chemists or chemical physicists. In this review I have restricted the discussion to matters of interest to inorganic and organometallic chemists, with emphasis on applications to transition metal complexes. The coverage is not intended to be complete; literature data have been cited only as far as necessary to illustrate the important points.

*Abstracted from Coord. Chem. Revs. 13, 47 (1974).

2. BORON HYDRIDE AND LIQUID AMMONIA CHEMISTRY

a. Chemical Syntheses with a Quenched Flow Reactor. Hydroxytrihydroborate and Peroxynitrite*

Janice W. Reed, Hansel H. Ho, and William L. Jolly

The technique of mixing two streams of reactant solutions in a reaction tube with downstream injection of a solution containing a quenching reagent has been used for studying the kinetics of fast reactions but does not seem to have been applied to laboratory synthesis. The method is ideal for a synthesis involving the formation of an intermediate species which (1) must be prepared under conditions such that its half-life is in the range between a millisecond and several seconds and (2) can be stabilized by rapid reaction with a quenching reagent. We now report the successful use of this method for preparing solutions of two different compounds in high yield, sodium hydroxytrihydroborate and sodium peroxynitrite. Each synthesis involves the formation of an unstable intermediate species which is stabilized by deprotonation with hydroxide ion.

The apparatus consists of a Lucite rod bored to a depth of 10 cm with a 3-mm hole. Two 1.5-mm holes for the introduction of the reactants enter from the side of the rod, joining the 3-mm tube tangentially at its inner end. A third 1.5-mm hole, for the quenching solution, enters the tube at a point 5 cm from the two reactant holes. The holes are connected to glass tubes on the outside of the rod; these are connected through glass and Teflon needle valves to siphon tubes inserted into three separate bottles. The bottles can be simultaneously pressurized with nitrogen gas at a regulated pressure from a cylinder. The reaction tube is mounted vertically, and the quenched product is collected in a beaker placed beneath the open end of the tube.

The borohydride ion reacts very rapidly with strong acid to form H_2OBH_3. This species hydrolyzes with a half-life of about 20 msec at 0°, but it can be deprotonated to form the relatively stable BH_3OH^- ion, which has a half-life of several hours at room temperature. Thus, it seemed reasonable to attempt the synthesis of BH_3OH^- using the quenched flow reactor with aqueous solutions initially at 0° and with a reaction time (time between the initial mixing of H^+ and BH_4^- and the quenching with OH^-) of the order of 20 msec or less. Relatively high yields, as high as 94%, were obtained for reaction times of 10-21 msec; the yield dropped off for a reaction time of 26 msec.

The reaction of nitrous acid with hydrogen peroxide in acidic solution yields peroxynitrous acid.

$$HNO_2 + H_2O_2 \rightarrow HOONO + H_2O$$

This acid decomposes to nitric acid with a half-time of 7 sec at 0°, but the conjugate base, peroxynitrite ion, is relatively stable in alkaline solutions. The literature procedure for the synthesis of peroxynitrite involves the mixing of an acidic peroxide solution with a nitrite solution, immediately followed by treatment with excess base. Yields of 45-50% have been reported. We have carried out this synthesis with our quenched flow reactor, using equal flow rates of the solutions at 0°, and have obtained yields as high as 82%.

*Abstracted from the J. Am. Chem. Soc. 96, 1248 (1974).

b. The Chemistry of Borane-Ammine, BH_3NH_3

Thomas S. Briggs and William L. Jolly

The reaction of the ammonium ion, NH_4^+, with the borohydride ion, BH_4^-, in liquid ammonia has been studied in a thermostated reactor using a high pressure differential mercury manometer for measuring the evolved hydrogen as a function of time.

$$NH_4^+ + BH_4^- \rightarrow H_2 + NH_3BH_3$$

The reaction is first-order in NH_4^+ and in BH_4^-, and rate constants determined at 25, 30, 35, 40, and 45° yield an activation energy of 38.5 kcal/mol. This reaction in liquid ammonia shows promise as a useful synthetic method for NH_3BH_3. Heating

NH_3BH_3 in an NH_3 atmosphere produces an unstable, volatile substance which has not yet been identified.

3. GERMANIUM CHEMISTRY

a. The Synthesis and Characterization of Methyl 2-Germaacetate and Ethyl 2-Germaacetate*

Kenneth A. Strom and William L. Jolly

The chemical properties of an ester of a carboxylic acid are markedly changed by replacing the α carbon atom of the acid by a silicon or germanium atom. Although esters of the type R_3GeCO_2R' and R_3SiCO_2R' have been studied, no studies of the corresponding unsubstituted esters, in which R=H, have been carried out. To further our understanding of these compounds and their reactions, we have prepared the methyl and ethyl esters of 2-germaacetic acid, GeH_3CO_2H, by reaction of the appropriate trialkyloxonium fluoroborates with potassium 2-germaacetate. We have investigated their thermal decomposition reactions and their acid- and base-catalyzed hydrolyses.

*Abstracted from Organomet. Chem. 69, 201 (1974).

b. The Decomposition of Aqueous 2-Germaacetate Solutions

Duck Yang and William Jolly

We have found that alkaline solutions of $KGeH_3CO_2$ decompose by two different reactions:

$$GeH_3CO_2^- + OH^- \rightarrow GeH_4 + CO_3^{2-}$$

$$GeH_3CO_2^- + H_2O + 3OH^- \rightarrow 4H_2 + GeO_3^{2-} + CO_3^{2-}$$

The first reaction is first-order in $GeH_3CO_2^-$ and has an activation energy of 31 kcal/mol. The second reaction is probably first-order in both $GeH_3CO_2^-$ and OH^- and becomes the predominate process in strongly alkaline solutions (pH > 14). The second reaction involves the formation of a soluble intermediate species which has not yet been characterized.

4. RESEARCH PLANS FOR CALENDAR YEAR 1975

William L. Jolly

a. X-Ray Photoelectron Spectroscopy

The following projects are nearing completion, and the results will soon be ready for publication: (i) a study of charge distributions in tetracovalent compounds of nitrogen and phosphorus, and (ii) a study of binding energies in isoelectronic compounds to evaluate the importance of hyperconjugation.

We plan to study the binding energies of a wide variety of compounds of tin and vanadium to test our ability to predict chemical shifts. We shall investigate the possibility of calculating atomic charges directly from binding energy data, using estimated relaxation energies.

b. Boron Hydride and Liquid Ammonia Chemistry

We have demonstrated that BH_3OH^- reduces ethyl benzoate (whereas BH_4^- will not). We plan to obtain quantitative data for this reaction and to optimize the conditions. Other reactions in which BH_3OH^- is superior to BH_4^- will be sought and studied.

The effect of ionic strength on the rate constant of the $NH_4^+ + BH_4^-$ reaction in ammonia will be investigated. The kinetics of the decomposition of NH_3BH_3 to H_2 and $(NH_2BH_2)_x$ will be studied. We shall attempt to characterize the volatile product formed in the pyrolysis of NH_3BH_3 in an ammonia atmosphere.

c. Germanium Chemistry

The kinetics of the base-catalyzed decomposition of the 2-germaacetate ion (to give germanate and hydrogen) will be studied, and the unstable intermediate species involved in that reaction will be characterized. Eventually we plan to study the kinetics of the acid-catalyzed decarbonylation of $GeH_3CO_2^-$, in which CO is evolved.

5. 1974 PUBLICATIONS AND REPORTS

William L. Jolly and Associates

Journals

1. W. L. Jolly, M. S. Lazarus, and O. Glemser, Core Electron Binding Energies of Thiazyl Fluoride and Other Sulfur Compounds, Z. anorg. allg. Chem. 406, 209 (1974) (LBL-2503).

2. W. L. Jolly, The Application of X-Ray Photoelectron Spectroscopy to Inorganic Chemistry, Coord. Chem. Reviews 13, 47 (1974) (LBL-1878).

3. L. O. Pont, A. R. Siedle, M. S. Lazarus, and W. L. Jolly, X-Ray Photoelectron Spectroscopy of Some Nickel Compounds, Inorg. Chem. 13, 484 (1974) (LBL-1897).

4. J. W. Reed, H. H. Ho, and W. L. Jolly, Chemical Syntheses with a Quenched Flow Reactor. Hydroxytrihydroborate and Peroxynitrite, J. Am. Chem. Soc. 96, 1248 (1974) (LBL-2206).

*5. W. B. Perry, T. F. Schaaf, W. L. Jolly, L. J. Todd, and D. L. Cronin, Determination of the Electron Distribution in a Transition Metal Carbene Complex by X-Ray Photoelectron Spectroscopy, Inorg. Chem. 13, 2038 (1974) (LBL-2237).

6. W. B. Perry and W. L. Jolly, Correlation of Core Electron Binding Energies with Charge Distributions for Compounds of Carbon, Silicon, and Germanium, Inorg. Chem. 13, 1211 (1974) (LBL-2238).

7. W. B. Perry and W. L. Jolly, Valence Electron Binding Energies of Some Silicon Compounds from X-Ray Photoelectron Spectroscopy, J. of Electron Spectros. and Related Phenomena 4, 219 (1974) (LBL-2562).

*8. W. L. Jolly and W. B. Perry, Calculation of Atomic Charges by an Electronegativity Equalization Procedure, Inorg. Chem. 13, 2686 (1974) (LBL-2565).

9. K. A. Strom and W. L. Jolly, The Synthesis and Characterization of Methyl 2-Germaacetate and Ethyl 2-Germaacetate, J. Organomet. Chem. 69, 201 (1974) (LBL-2223).

Papers presented

1. W. L. Jolly, Atomic Charges and X-Ray Photoelectron Spectroscopy, Univ. of Calif., San Diego, Jan. 25, 1974.

2. W. L. Jolly, X-Ray Photoelectron Spectroscopy, five talks given at A.C.S. local sections in Missoula, Mont., Bozeman, Mont., Idaho Falls, Ida., Provo, Utah, and Salt Lake City, Utah, April 15-19, 1974.

3. W. L. Jolly, Inorganic Applications of X-Ray Photoelectron Spectroscopy, talks given at the Inorganic Institutes of the University of Würnburg and the University of Frankfurt, Germany, Aug. 1974.

4. W. L. Jolly, Empirical Calculations in ESCA, Gordon Research Conference on X-Ray Photoelectron Spectroscopy, Wolfeboro, N. H., July 15-19, 1974.

5. W. L. Jolly, The Distribution of Electrons in Gaseous Coordination Compounds from X-Ray Photoelectron Spectroscopy, 16th Intl. Conference on Coordination Chemistry, Dublin, Ireland, Aug. 19-24, 1974.

6. W. L. Jolly, Molecular Charge Distribution from X-Ray Photoelectron Spectroscopy, Symposium on the Chemical Bond at the Regional A.C.S. Meeting, San Francisco, Calif., Oct. 1974.

7. W. L. Jolly, Applications of X-Ray Photoelectron Spectroscopy to Inorganic Systems, Symposium on Photoelectron Spectroscopy at the Regional A.C.S. Meeting, Houston, Tex., Dec. 9-11, 1974.

LBL reports

1. Winfield Blount Perry, Electronic Structure in Small Inorganic Molecules: Some Results Obtained from X-Ray Photoelectron Spectroscopy, (Ph.D. thesis), LBL-3133, Oct. 1974.

2. S. C. Avanzino, W. L. Jolly, M. S. Lazarus, W. B. Perry, R. R. Rietz, and T. F. Schaaf, d Orbitals and Hyperconjugation. An X-Ray Photoelectron Spectroscopic Study of Some Isoelectronic Compounds, LBL-3502, Oct. 1974.

3. W. B. Perry and W. L. Jolly, The Calculation of Atomic Charges by an Electronegativity Equalization Procedure: A Description of Program CHELEQ, LBL-3520, Nov. 1974.

4. W. B. Perry, T. F. Schaaf, and W. L. Jolly, An X-Ray Photoelectron Spectroscopic Study of Charge Distributions in Tetracovalent Compounds of Nitrogen and Phosphorus, LBL-3517, Nov. 1974 (submitted to J. Am. Chem. Soc.).

*Supported in part by N.S.F. Grant GP-41661X.

Robert E. Connick, Principal Investigator

1. OXYGEN-17 NMR STUDIES OF THE RATE OF WATER EXCHANGE FROM PARTIALLY COMPLEXED NICKEL ION

Thomas V. Rowland

The two different rates of water exchange from the nonequivalent sites on the nickel iminodiacetate (IDA) complex have been measured over the temperature range of 0°C to 140°C, and a least-squares fit of the data has been completed. The NMR spectrometer has been modified, increasing field stability through the use of an external NMR lock system, and the bulk water chemical shift of the nickel IDA complex has also been measured as a function of temperature. The shift data, which depend upon the same parameters as the line broadening, will be fitted simultaneously with the line broadening data in order to determine better the water exchange rates. Also an investigation using the totally complexed nickel bis-IDA ion has been completed, providing a rough determination of the amount of water exchange at the position normally occupied by the carboxylate arms of the IDA, as well as a measure of the fraction of the time the arms are not coordinated to the nickel ion.

2. THE EXCHANGE LIFETIME OF WATER MOLECULES IN THE SECOND COORDINATION SPHERE OF CHROMIC ION

William L. Earl

The transverse relaxation times of the bulk ^{17}O in aqueous solutions of Cr(III) have been measured from the linewidth of the ^{17}O NMR absorption signal. The longitudinal relaxation times of the same solutions have been measured by power saturation of the absorption. Preliminary measurements of the longitudinal relaxation, made by pulsed NMR techniques, are in good agreement with the saturation data. Analysis of the relaxation times indicates that the lifetime of water in the second coordination sphere is 3×10^{-10} sec. Chemical shift measurements have been made on the Cr(III) solutions, and the relaxation times of Al(III) solutions have been measured. From these data most of the parameters of the NMR relaxation mechanisms in Cr(III) solutions will be obtained.

3. WATER EXCHANGE FROM THE FIRST COORDINATION SPHERE OF EUROPOUS ION STUDIED BY NMR

Thomas H. Norris*

Work is just starting on the measurement of the lifetime of water molecules in the first coordination sphere of europous ion in aqueous solution, using oxygen-17 as the water "tracer". It is not yet certain that the measurements will be successful, but the corresponding study on iso-electronic Gd^{3+} gives encouragement. Potentially the results are of great interest because Eu^{2+} would be the largest divalent metal ion yet measured; the exchange should be extremely rapid.

*On sabbatical leave from Oregon State University.

4. COMPUTER MODELING OF EXCHANGE REACTIONS

Robert E. Connick*

The rate of exchange of solvent molecules in the first coordination sphere of metal ions with bulk solvent molecules has been studied extensively by nuclear magnetic resonance. To probe the detailed movements in such reactions we are attempting to simulate these systems with the computer calculation of a hard sphere (metal ion) which attracts 89 larger, hard spheres (solvent) by a charge-dipole force law (inverse cube). Working in two dimensions and using an 18 step potential function, results have been obtained for several activation energies. For "high" activation energies the exchange appears to occur exclusively by an expansion of the normal coordination number of 4 to 5; there is probably a barely stable intermediate of coordination number 5. We do not know yet whether this behavior arises from the finite number of steps in the potential well or would be present for a continuous potential. The computer calculations were made by constraining one particle of the system to a distance from the "metal ion" corresponding approximately to that of the activated complex, letting the system equilibrate for a time, and then suddenly releasing the constrained particle. On following the system forward and backward in time, exchange occurred if the constrained particle settled into the first coordination sphere in one case and did not in the other. Starting the system in a configuration near that of the activated complex was necessary because at "high" activation energies the low probability of exchange makes necessary too much computer time to see even a single event.

*With B. J. Adler of Lawrence Livermore Laboratory.

5. STUDIES OF SULFUR DIOXIDE IN AQUEOUS SOLUTIONS

Robert E. Connick

Sulfur dioxide occurs as a pollutant in the exhaust gas from coal and oil combustion. Currently it is being removed primarily by scrubbing these gases with various aqueous solutions. The solutions do not behave as expected for SO_2, HSO_3^-,

and $SO_3^{=}$, presumably because a variety of other species is being formed. These chemical changes are not understood nor have the species been identified. I would like to have a post-doctoral fellow undertake a study of these systems, but do not currently have the funding to do so.

6. RESEARCH PLANS FOR CALENDAR YEAR 1975

Robert E. Connick

The research by Rowland in Paper 1 has established the exchange behavior of water molecules on the nickel-IDA complexes and also has given information on the lability of the acetate arms. An attempt will be made by K. Klotter to obtain one further intimate detail of the dynamic behavior of these nickel complexes by measuring the lifetime for exchange of the bound carboxylate oxygen of the acetate arms with the unbound carboxylate oxygen. The experiment will be tried with oxygen-17 enriched IDA by observing the resonance of the unbound oxygens. By variation of the temperature, the increased broadening from exchange should be observable if it falls within an accessible temperature region. With the completion of this work we should have an unusually detailed picture of the dynamics of these interesting metal complexes.

The research described in Paper 2 should be completed during the first half of 1975. If time permits, the rate of water exchange of second coordination sphere water with bulk water will be studied for some partially complexed Cr(III) species.

It is anticipated that the measurements reported in Paper 3 will be concluded by summer 1975. The data will provide a stringent test of the correlation of rate with charge divided by radius cubed, developed by Neely and Connick for such reactions.

The calculations made with Alder (Paper 4) will be extended to three dimensions and with a potential function more nearly approximating a continuous curve. We are very interested in observing the dependence of the rate and mechanism on the radius ratio of "metal ion" to solvent. The effect of the shape of the potential function will be investigated as well as the activation energy. If time and computer capability permit, we would like to make the model conform more closely to real solvent systems, or at least to investigate the sensitivity of the results to solvent-solvent interactions. While the model is extremely crude, it is hoped that the general characteristics of such exchange reactions will be deduced. A knowledge of these characteristics would have wide applicability to the great variety of such reactions that occur in chemical processes, including biological processes. Hopefully increased understanding will lead ultimately to better prediction and control of such rates of reaction.

The project on studies of sulfur dioxide in aqueous solutions (Paper 5) was stimulated by a conversation with Professor C. B. Meyer at the University of Washington. We submitted a joint proposal for a collaborative effort on July 19, 1974 which was not funded. Should resources be obtained to support a postdoctoral fellow, I will maintain close contact with whatever work Professor Meyer is able to undertake at Washington.

Neil Bartlett, Principal Investigator

1. THE GIANT ELECTRON AFFINITY OF PLATINUM HEXAFLUORIDE*

Neil Bartlett and Kevin Leary

The heat of formation of the salt $O_2^+PtF_6^-$ was determined by direct interaction of O_2^+ and PtF_6 gases in a calorimeter designed and constructed by Dr. Barberi at the Centre d'Etudes Nucléaires. The mean $\Delta Hf°$ from ten independent experiments was -59 kcal mole^{-1} with an uncertainty estimated to be less than 1 kcal mole^{-1}. Higher precision is eventually anticipated but for our present purposes this value is sufficient. It indicates that the enthalpy for the process $PtF_{6(g)} + e \rightarrow PtF_{6(g)}^-$ (i.e. the ΔH term for the electron affinity) must be $-\{281(I,O_2) - U(O_2^+PtF_6^-) + 59\}$ kcal mole^{-1}. The most exothermic value we can reasonably allow for $U(O_2^+PtF_6^-)$, the lattice energy of that salt, is -130 kcal mole^{-1}, which indicates that the electron affinity of PtF_6 has a value of at least 210 kcal mole^{-1} (9.3 eV). This is more that 2-1/2 times that of the F atom (80 kcal) and approximately twice that of WF_6. Indeed a recent measurement of $E(WF_6)$ by Compton and Cooper[1] sets this affinity at 104.5 kcal mole^{-1}. The electron affinity increase across the third series hexafluorides thus agrees well with the previous estimate by Bartlett,[2] made on a chemical basis. Evidently there is an increase of ~1 eV for each unit increase in nuclear charge of the central atom from WF_6 to PtF_6. The ionization potential for AuF_6 should therefore be ~10.3 eV.

*This work done in collaboration with Paul Barberi of the Centre d'Etudes Nucléaires, Saclay, France.

1. C. D. Cooper and R. N. Compton, American Physical Society Meeting, Atlanta, Georgia, Dec. 5-7, 1974.
2. N. Bartlett, Angewante Chemie (Int. Ed) 7, 433 (1968).

2. EXPLOITATION OF O_2^+ SALTS

Thomas J. Richardson and Neil Bartlett

a. Salts Containing Aromatic Cations

The use of O_2^+ salts in the generation of aromatic cations[1] was further explored. Although direct synthesis of perfluoro naphthalene cation did not occur, it proved possible to prepare the $C_{10}F_8^+$ salt by metathesis from the $C_6F_6^+$ salt:

$$C_{10}F_8 + C_6F_6^+AsF_6^- \rightarrow C_{10}F_8^+AsF_6^- + C_6F_6$$

$$(C_6F_6^+AsF_6^- \text{ from } O_2^+AsF_6^- + C_6F_6 \rightarrow C_6F_6^+AsF_6^- + O_2)^1$$

The perfluoro naphthalene salt is a dark green solid which is much more stable thermally than its C_6F_6 relative (and has been kept in a sealed vessel for several weeks at ambient temperature). The crystal structure of $C_{10}F_8^+AsF_6^-$ appears to be simple but it is presently unknown whether or not the positive charge is localized on one ring of the aromatic.

Interaction of $C_6F_6^+AsF_6^-$ with benzene suggests that it may be possible to make $C_6H_6^+AsF_6^-$. Much pyrolysis of the starting salt occurs in the rather energetic reaction (with the production of C_6F_6, C_6F_8 and AsF_5). Nevertheless, a low yield of a dark blue solid, which could be $C_6H_6^+AsF_6^-$, is obtained.

b. Interaction of O_2^+ with Cl_2

The salt $O_2^+AsF_6^-$ combines with dry liquid chlorine at -40° to generate a purple solid without liberation of oxygen. The tensimetric data are somewhat uncertain but they indicate a 1:1 adduct. The solid is paramagnetic and the esr spectrum (g=1.999) is not that of $O_2^+AsF_6^-$. Removal of the chlorine under vacuum at temperatures approaching ambient, restores high mole fractions of the dioxygenyl salt. Moreover, decomposition slowly occurs at ambient temperature but infrared spectra of the decomposition product have not yet yielded evidence of chlorine fluorides--chlorine, oxygen and AsF_5 are certainly among the decomposition products. It appears probable that the Cl_2 molecule forms a sideways attachment to the O_2^+ ion, the bonding involving donation of an anti-bonding π pair of electrons on the Cl_2 molecule to the vacant antibonding π orbital of the O_2^+.

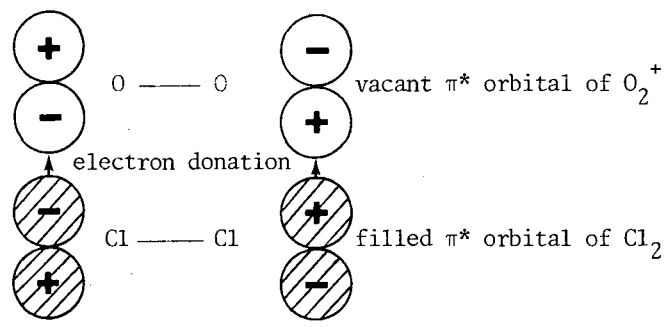

A possible bonding situation for $(O_2\ Cl_2)^+$

This would be a novel bonding situation.

A dramatic finding in the course of this work was evidence for the existence of the O_2F radical molecule at ambient temperature. All previous work on this molecule has been carried out at 77°K or lower and it has been widely assumed that decomposition to O_2 and F_2 readily occurred. Infrared spectra of the solid Cl_2, $O_2^+Sb_2F_{11}^-$ salt between AgCl plates in a KelF-bodied cell confirmed the visual impression that interaction quickly occurred between the window material and the solid

under inspection. A very simple sharp line spectrum with bands at 3060,ms; 1530,s; and 590 cm^{-1},ms, was seen however. This agrees closely with that reported[2] from matrix isolation spectrometry for O_2F: 1494,ms; 584 cm^{-1},s. Evidently O_2F is kinetically stable in KelF vessels. It now appears certain that the efficient synthesis of $O_2^+AsF_6^-$ from $O_2 + F_2 + AsF_5$ is facilitated by the long lived O_2F species and not, as previously conjectured,[3] by virtue of an AsF_6 radical.

1. T. J. Richardson and N. Bartlett, J. Chem. Soc., Chem. Commun. 427 (1974).
2. A. Arkell, J. Amer. Chem. Soc. 87, 4057 (1965).
3. K. O. Christe, R. D. Wilson, A. E. Axworthy, Inorg. Chem. 12, 2478 (1973).

3. HIGH OXIDATION STATES OF THE HEAVIER TRANSITION ELEMENTS AND ACTINIDES

Kevin Leary, Lionel Graham, Raymond D. Peacock and Neil Bartlett

a. Utilization of Noble-Gas Fluorides in Oxidation

Although KrF_2 is the most powerfully oxidizing of the noble-gas fluorides and is the reagent of choice for the most difficult oxidizing tasks, we have explored XeF_2 first because of its relative ease of preparation and handling.

Following upon the work of Zemva and Bartlett in which liquid XeF_2 was shown to be an oxidizer of Pd(III) to Pd(IV) and Pt(IV) to Pt(V), milder conditions for these oxidations and for the disproportionation of Xe(II) to Xe(IV) have been sought. It now appears that acid catalysis of the oxidations by XeF_2 may be achieved by working in anhydrous-hydrogen fluoride. The effect of this catalysis is indicated by the interaction of XeF_2 with UF_4. Although the two fluorides interact smoothly with liberation of some xenon to yield a grey-green solid (probably $XeF^+UF_6^-$) at temperatures close to ambient, no UF_6 is found. On addition of HF there is rapid evolution of xenon and UF_6 is found quantitatively at room temperature.

An attempt to prepare $NpOF_5$ by oxidation of $NpOF_4$ with KrF_2 failed.

b. The Preparation of $NpOF_4$ and its Structural Characterization*

$NpOF_4$ was prepared by the controlled addition of water to NpF_6 ($NpF_6+H_2O \rightarrow NpOF_4+2HF$). The brown solid gave a sharp-line Debye-Scherrer X-ray powder photograph which proved to be almost identical to that of UOF_4, the structure of which was recently reported by Paine, Ryan and Asprey.[1] The unit cell is trigonal, R 3 m, with the following parameters: a_0=13.17±0.02, c_0=5.70±0.02Å.

*This work done in collaboration with N. Edelstein of the Nuclear Chemistry Division, LBL.

1. R. G. Paine, R. R. Ryan and L. B. Asprey, Abstracts Am. Cryst. Assoc. 2, series 2, 55 (1974).

4. A NOVEL TETRAFLUORIDE STRUCTURE TYPE AND COMMENTS ON MAGNETIC INTERACTIONS IN RUTILE TYPE FLUORIDE STRUCTURES

Neil Bartlett and Alain Tressaud*

The tetrafluorides of Rh, Ir, Pd and Pt have been shown to be isostructural and to possess a structure which is related to that of rutile in which half of the metal atom sites are vacant in an ordered arrangement. The new structure type is represented in the Fig. 1, where it is compared with that of rutile.

The new structure is of interest for two reasons.

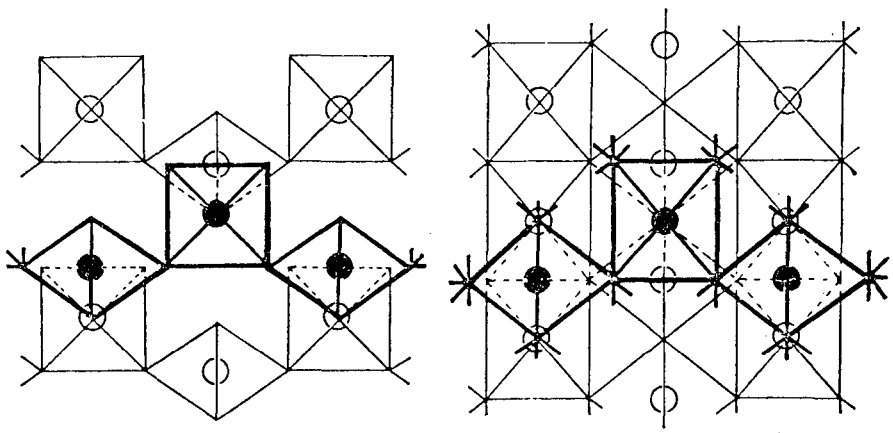

(a) (b)

Fig. 1. Linkage of MF_6 octahedra in the structure types IrF_4 (a) and rutile (b). (XBL 751-5629)

Firstly, it shows that the M-F-M linkages for these tetrafluorides have essentially the same angle as in the other fluorides of these elements--irrespective of oxidation state. Thus, typically, in RhF_3, RhF_4 and RhF_5 the bridging angles are in each case close to 130°. Secondly, the magnetic behavior of IrF_4 (a d^5_{t2g} system) appears to be of antiferromagnetic type (Fig. 2). The M-F-M bridging at 135° is to be associated with this antiferromagnetism. In rutile it has been suspected for some time that the magnetic interactions of metal atoms with one another, within the edgeshaved-chains of octahedra (M-F-M 100°) were in effect zero and that the observed antiferromagnetism was to be associated with that between chain linkages, which are characterized by M-F-M bridging angles close to 130°. Our findings are nicely in harmony with these views and suggest that correlation of the bridging angles with magnetic properties be further explored.

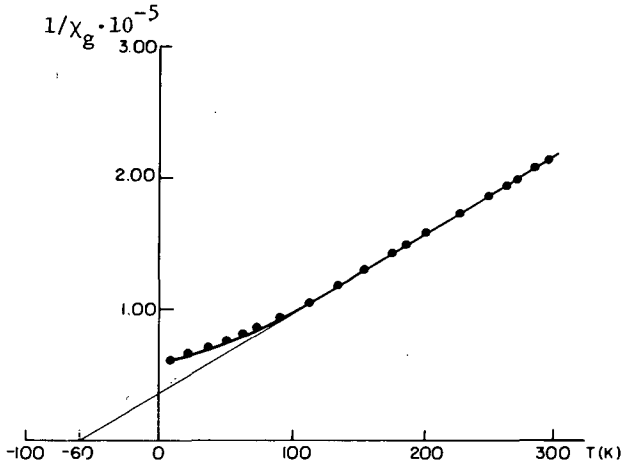

Fig. 2. Dependence of the reciprocal of the magnetic susceptibility of IrF_4 upon absolute temperature. (XBL 744-5987)

*Work done in part at Laboratoire de Chimie Minérale et Structurale, Université de Bordeaux, France.

5. RESEARCH PLANS FOR CALENDAR YEAR 1975

Neil Bartlett

Electrolysis of fluoromelts. A number of fluoride, oxyfluoride and oxide unit-charged species have stable (at least kinetically stable) uncharged relatives, e.g. NO^+, NO; NO_2^+, $NO_2(N_2O_4)$; SO_3F^-, SO_3F, $(S_2O_6F_2)$; WF_6, WF_6^-; $OsOF_5$; and RuF_6^-, RuF_6. Efforts will be made to interconvert these or similar pairs by oxidation-reduction at electrodes. Since the neutral nontransition element derivatives are stable radicals (NO, NO_2, SO_3F) it is possible that the redox processes for these could be very facile. Successful electroconversions of this kind will not only offer synthetic routes to novel species such as AuF_6 (which offers the possibility of argon fixation as $ArF^+AuF_6^-$), $NpOF_5$ and ClO_4, but would also provide an opportunity to evaluate such systems (particularly SO_3F^-/SO_3F) as fuel cell or battery components. A major practical aspect of this program is the search for and evaluation of suitable electrode and container materials. For the former, graphite and mixed valence fluorides will be explored. Fluorinated ceramics and perfluorocarbon polymers will be tried for the latter.

Actinide compounds. The preparation of UF_5X species, where X=Cl, Br, SO_3F, CF_3, OSF_5 and SF_5 will be attempted and their spectroscopic, other structural and chemical properties determined. The effect of the bulky, electronegative, SO_3F, CF_3 and SF_5 groups upon the kinetic stability of the hexacoordinate uranium (VI) atom is a particular point of interest.

Our successful synthesis of $NpOF_4$ leads us to suppose that $NpOF_5^-$ will be preparable. We will attempt to displace $NpOF_5$ from the anion with PtF_6 or by cation-anion annihilation (e.g. $KrF^+ + NpOF_5^- \rightarrow NpOF_5 + Kr + 1/2\ F_2$). The vibrational and other structural properties of $NpOF_5$, compared with the anion and the related NpF_6 and UOF_5^- species, would provide further indications of which orbitals are used by the heavier actinide elements in high oxidation states.

The fixation of krypton. We will continue to attempt to fix argon as a salt of the cation ArF^+ (the synthesis of AuF_6 is tied to this attempt). Such a species would surely fix krypton spontaneously: $ArF^+ + Kr \rightarrow Ar + KrF^+$. Irradiation of KrF_2 in a fluorine matrix will also be carried out since there are theoretical grounds for supposing that KrF_4 may be a bound molecule. Substitution of the F ligands of KrF_2 by other electronegative groups will also be tried.

Further studies of O_2^+ salts and the characterization of O_2F. The O_2^+, Cl_2 adduct will be further studied in order to establish the nature of the bonding. An effort will also be made to generate O_2F in macroscopic quantities directly from the elements and to establish its kinetic stability at ordinary temperatures. Work on the production and characterization of $C_6H_6^+$ and other aromatic salts will also continue. Encapsulation of O_2^+ in crown ethers will be attempted in order to facilitate solution of the salts in less polar solvents.

6. 1974 PUBLICATIONS AND REPORTS

Neil Bartlett and Associates

Journals and books

1. Kevin Leary, Allan Zalkin, and Neil Bartlett, Crystal Structure of $Xe_2F_{11}^+AuF_6^-$ and the Raman Spectrum of $Xe_2F_{11}^+$, Inorg. Chem. 13, 775 (1974) (LBL-1426).

2. N. Bartlett, B. G. DeBoer, F. J. Hollander, F. O. Sladky, D. H. Templeton and A. Zalkin, crystal Structures of $[Xe_2F_3^+][AsF_6^-]$ and $[XeF_5^+][AsF_6^-]$, Inorg. Chem. 13, 780 (1974)(LBL-1170).

3. T. J. Richardson and N. Bartlett, Salts of the Hexafluorobenzene Cation, $C_6F_6^+$, J. Chem. Soc., Chem. Commun., 1974, p. 427 (LBL-2593).

*4. T. X. Carroll, R. W. Shaw, Jr., T. D. Thomas, C. Kindle, and N. Bartlett, Electron Distribution in the Xenon Fluorides and Xenon Oxide Tetrafluoride by ESCA and Evidence for "Orbital Independence" in the Xenon-Fluorine Bonding, J. Am. Chem. Soc. 96, 1989 (1974)(LBL-3153).

*5. N. Bartlett and A. Tressaud, Sur un nouveau type structural de tetrafluorures d'éléments de transition: synthèse, étude cristallographique et magnétique de IrF_4, Compties Rendues Acad. Science (Paris), 278C, 1501 (1974).

6. C. J. Adams, Acceptor Properties of Iodine Heptafluoride: Octafluoroperiodate (VII), Inorg. Nucl. Chem. Lett. 10, 831 (1974) (LBL-3704).

Invited lectures

1. "Structure et liaison chimiques des composés de gaz rares." Societé Chimique de France, Section of the West, Nantes, Friday March 8, 1974.

2. Invited lecture of the physical chemistry and mineral chemistry division of the French Chemical Society at the Annual General Assembly in Nancy, May 29-31, 1974. Lecture title: "A chemistry of high oxidation states: salts of rare-gas cations, O_2^+ and $C_6F_6^+$."

3. Seminar of the Laboratory of Mineral Chemistry at the University of Grenoble, Tuesday April 9, 1974. "Structural and Magnetic Relationships of the Fluorides of Palladium."

4. "A chemistry of high oxidation states: salts of rare-gas cations, O_2^+ and $C_6F_6^+$," to the Bordeaux section of the French Chemical Society, April 16, 1974.

5. Inorganic Chemistry Seminar, The University of Oxford, June 25, 1974: "A Chemistry of High Oxidation States."

6. "Noble-gas Compounds" in the symposium on "Aspects of the Chemical Bond" at the 1974 Pacific Conference on Chemistry and Spectroscopy, Oct. 16-18, San Francisco, California.

7. Departmental seminar of the Chemistry Dept., The University of Wyoming, Laramie, Wyoming, Nov. 5, 1974, entitled "Noble-gas Compounds."

8. 5th European Symposium on Fluorine Chemistry, Aviemore, Scotland, September 16-20, 1974. Two papers:
   a) "Salts of the Hexafluorobenzene Cation, and Related Chemistry"
   b) "A New MF_4 Structure Type (M=Ir, Rh, Pd, Pt)"

LBL reports

1. Neil Bartlett and Alain Tressaud, The New MF_4 Structure Type (M=Ir, Rh, Pd, Pt), LBL-2717 Abstract, April 1974 (for presentation at The Chemistry Society 5th Symposium on Fluorine Chemistry, Sept. 16-20, 1974 at Aviemore, England.

2. T. J. Richardson and Neil Bartlett, Salts of the Hexafluorobenzene Cation, $C_6F_6^+$, and Related Chemistry, LBL-2718 Abstract, April 1974 (ibid.)

3. P. R. Rao, Alain Tressaud and Neil Bartlett, The Tetrafluorides of Iridium, Rhodium and Palladium, LBL-2714, March 1974 (submitted to the Herbert H. Hyman Memorial Issue of the Journal of Inorganic and Nuclear Chemistry).

4. Thomas Jay Richardson, Perfluoroaromatic Cations and Related Studies, (Ph.D. Thesis) LBL-3183, December 1974.

---

*Supported by the Laboratorie de Chimie Minerale Structurale of the Univ. of Bordeaux.

B. SOLID STATE CHEMISTRY AND PHYSICS

Norman E. Phillips, Principal Investigator

1. HEAT CAPACITY OF THE KONDO-SUPERCONDUCTOR (La,Ce)Al_2

Samuel D. Bader, William E. Fogle and Norman E. Phillips

The heat capacities of several dilute solutions of $CeAl_2$ in $LaAl_2$ were described in the 1973 IMRD report. These measurements showed that in the normal state the solutions were spin 1/2 Kondo systems and displayed the competition between the two types of ordering (spin compensation of the Kondo type and Cooper pair formation) in the superconducting state. The measurements on the most dilute sample have been extended to lower temperatures, and an additional intermediate concentration sample has been studied. In addition, further analysis of the data on the 0.64 at.% sample has shown evidence for the lower transition (back to the normal state).

The zero-field and 0.5 kOe heat capacities for the 0.640 at.% Ce sample are shown on an expanded scale and compared with the magnetically determined transitions in Fig. 1. In Fig. 1(b), ΔC represents the heat capacity relative to a smooth reference curve that was chosen to approximate the zero-field normal-state heat capacity. To that approximation, the 0.5 kOe points represent the field dependence of the normal-state heat capacity and the zero-field points represent $C_s - C_n(H=0)$. The precision of the data in the region 0.3 to 0.5K is relatively poor because this is the region of overlap of two separate sets of measurements. Nevertheless, both the zero-field and 0.5 kOe data show a peak or shoulder in this region. The fact that it occurs in both fields shows that it reflects a systematic error (e.g., an error in the temperature scale or an irregularity in the reference curve) and that it has no significance for $C_s - C_n(H=0)$. Relative to the 0.5 kOe data, however, there are two well-defined peaks in the zero-field data. They occur in the outer regions of the magnetically determined transitions [see Fig. 1(a)] but, given the breadth of the transitions and the different nature of the two measurements, the agreement in temperature is quite reasonable. The anomaly at T_{c1} has a shape consistent with a slightly broadened second-order transition. It is similar to that observed by Steglich and Armbrüster[1] who have shown that its size is consistent with a bulk superconducting transition. In Fig. 1(b) a similar anomaly appears just below T_{c2}, and the negative values of $C_s - C_n(H=0)$ required by the equality of the free energies at T_{c1} occur at intermediate temperatures. The shapes of the anomaly at T_{c2} and of $C_s - C_n(H=0)$ at intermediate temperatures depend on the assumptions made in deriving $C_n(H=0)$, but the existence of the anomaly is clear in any precise comparison of the zero-field and 0.5 kOe data. The anomaly at T_{c2} appears to be smaller than that at T_{c1}, but that would be quite reasonable in view of the lower temperature, and we believe it is evidence for a bulk second-order transition.

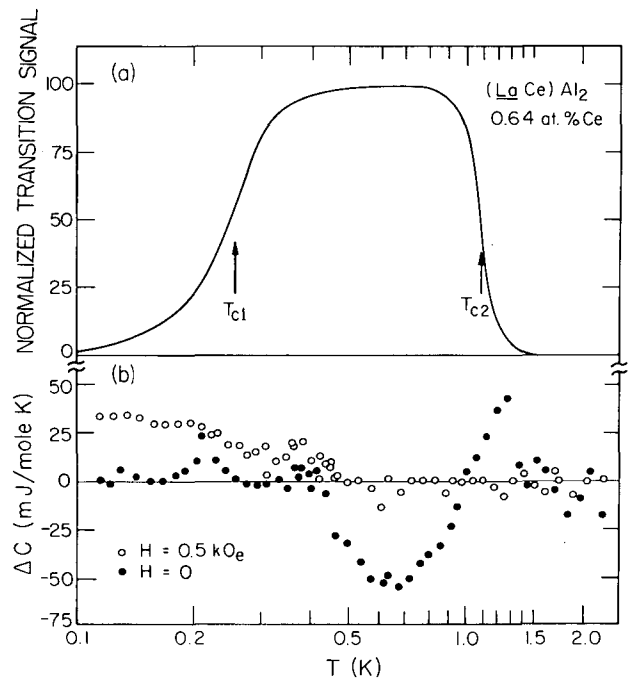

Fig. 1. (a) Magnetically determined transitions in the 0.640 at.% Ce sample. (b) Zero-field and 0.5 kOe heat capacity data, relative to a common reference curve (XBL 748-6956)

1. F. Steglich and H. Armbrüster, to be published.

2. LOW-TEMPERATURE HEAT CAPACITY OF $PrCu_2$*

Marilyn Wun and Norman E. Phillips

Andres et al.[1], on the basis of susceptability and heat capacity measurements, have reported cooperative nuclear ordering in $PrCu_2$. Since their measurements showed several unusual features, we have repeated them, and have also made some measurements in magnetic fields.

Our results for the heat capacity between 0.3 and 10 K are shown in Fig. 1. To provide a rough estimate of the lattice and electronic heat capacities, we have also shown the heat capacity of $LaCu_2$. (The structures of $LaCu_2$ and $PrCu_2$ differ,[2] but are related by a small distortion,[3] and the density of $LaCu_2$ is approximately 10% lower[2] than that of $PrCu_2$). The 7 K anomaly is

somewhat higher and sharper than reported by Andres et al.[1] and, as shown in Fig. 1, it is much sharper than a two-level Schottky anomaly. The shape of the anomaly shows that it cannot be produced by fixed crystal-field levels as suggested by Andres et al.[1], but suggests instead that it arises from a cooperative transition. Similar anomalies have been observed, for example, in $TmAsO_4$[4] and $TmVO_4$[5], and attributed to Jahn-Teller distortions. In each of these cases the data are accurately reproduced by a molecular field calculation. In the present case, the transition is somewhat broadened, possibly by strains and inhomogeneities, and we have introduced a gaussian distribution of critical temperatures into the calculation to account for this. The solid curve in Fig. 1 represents a molecular field calculation for the case of two levels that are degenerate (or nearly degenerate) at high temperatures, but with the degeneracy lifted by a Jahn-Teller distortion. The mean critical temperature is 7.5 K and the half width in critical temperature is 0.35 K. Figure 1 shows that there must be an additional contribution to the heat capacity at temperatures near 8 K and above, and our data at higher temperatures suggests that it persists to above 20 K. A third crystal-field state that produces a Schottky anomaly with a peak near 12 or 13 K would give a contribution of the correct magnitude. Thus, although we have not made a detailed calculation, it seems probable that the crystal-field heat capacity between 1 and 20 K is the sum of that associated with a Jahn-Teller distortion involving the two lowest states, which have a separation $\Delta/k \ll 7K$ at $T \gtrsim 7K$ and $\Delta_o/k = 15K$ at OK, and that arising from a third state near 25 K.

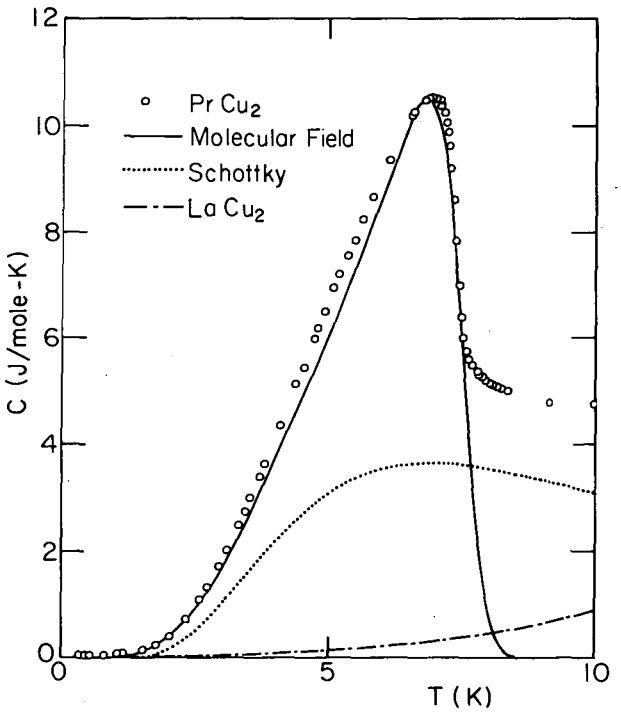

Fig. 1. The zero-field heat capacity of $PrCu_2$ between 0.3 and 10 K. (XBL 749-7270A)

Our heat capacity results below 1 K are shown in Fig. 2. The zero-field results are similar to those of Andres et al.[1], but they are lower in magnitude--only 60% as great at 0.1 K--and show a weaker temperature dependence--only the few points below 80 mK increase as rapidly as T^{-2}. For $0.3 \leq T \leq 0.6$ and $0 \leq H \leq 20$ kOe, our results are represented by $C = 0.029\ T + (0.003 + 7.94 \times 10^{-5} H^2)\ T^{-2}$ J/mole K, where H is the field in kOe. In this region it is reasonable to associate the field-dependent term with a hyperfine-enhanced nuclear contribution,

$$C = R\ [(I + 1)\ /\ 3I][(1 + K\ \mu H/k\ T]^2.$$

This gives $1 + K = 29 \pm 1$ for the Knight shift. This value is in good agreement with that obtained by Andres et al.[1], $1 + K = 32 \pm 10$, from an analysis of the susceptibility.

In summary, our interpretation of the crystal-field heat capacity differs from that given in Ref. 1, but is consistent with a singlet ground state for the Pr^{+3} ions at $T \leq 7K$. Our value for $1 + K$ agrees with that derived from susceptibility measurements to within the uncertainty of that value. Our measurements show no indication of a cooperative nuclear ordering, but they do not extend to the temperature of the susceptibility maximum.

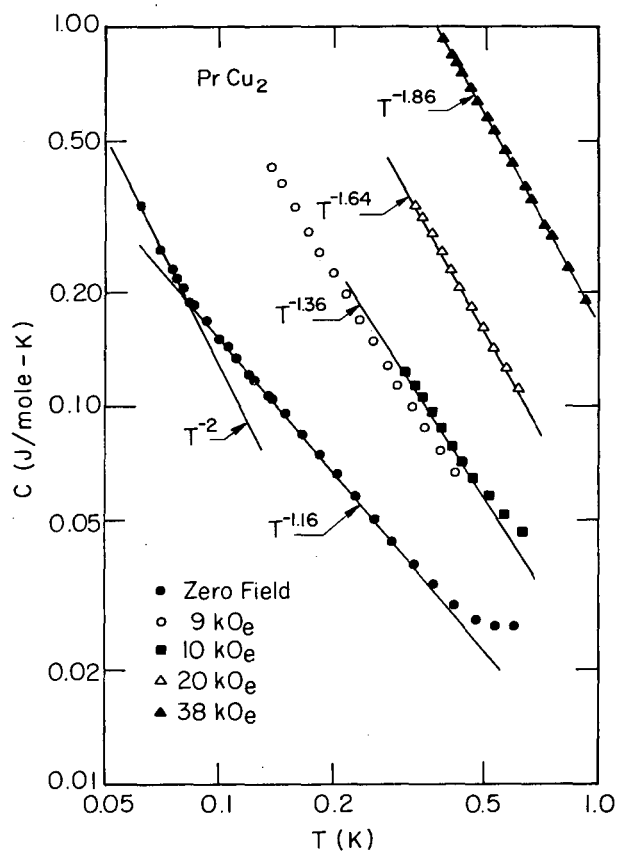

Fig. 2. The heat capacity of $PrCu_2$ at temperature below 1 K. (XBL 749-7266)

*We are indebted to G. P. Schwarz for his active collaboration in the early stages of this work.

1. K. Andres, E. Bucher, J. P. Maita and A. S. Cooper, Phys. Rev. Letters 28, 1652 (1972).
2. A. R. Storm and K. E. Benson, Acta. Cryst. 16, 701 (1962).
3. Allen C. Larson and Don T. Cromer, Acta. Cryst. 14, 73 (1961).
4. J. H. Colwell and B. W. Mangum, Solid State Commun. 11, 83 (1972).
5. A. H. Cooke, S. J. Swithenby and M. R. Wells, Solid State Commun. 10, 265 (1972).

3. BULK SUPERCONDUCTIVITY OF α-URANIUM

Samuel D. Bader and Norman E. Phillips.

Magnetic measurements have consistently shown the occurrence of superconductivity in α-U at zero pressure, with T_c ranging from about 0.2K for single crystals [1,2], to above 1K in some high purity polycrystals.[3] Calorimetric studies have so far failed to substantiate the existence of superconductivity at zero pressure, but at 10 kbar they are in agreement with magnetic, measurements in showing that α-U is a bulk superconductor with a T_c of approximately 2K.[4] Thus, α-U is one of the most strongly pressure-enhanced superconductor known, although the precise degree of the enhancement is uncertain because of the uncertainty in the zero-pressure T_c. The heat capacity measurements reported here were undertaken to clarify the nature of superconductivity in α-U at zero pressure.

Five samples were studied. Sample Ia was a large grained polycrystal that was later swaged to produce Sample Ib which had a striated, cold worked structure. Samples IIa and IIb were parts of a sample that had been studied earlier[4] and had been given different surface treatments. Sample III was a single crystal.

The normal-state data were analyzed to obtain the nuclear heat capacity $C_N = fAT^{-2}$, where f is the mole fraction of ^{235}U, and the normal-state electronic heat capacity, $C_{NS} = \gamma T$. The results are shown in Table I. The zero-field electronic heat capacity (and some additional data) are shown in Figs. 1-4. They have been fitted to BCS transitions broadened by a Gaussian distribution of T_c values as represented by the solid curves in Figs. 1-3. The average T_c, $\bar{T}_c$, the half width of the distribution, δT_c, and the fraction of the sample exhibiting superconductivity at 0K, X_s, are also given in Table I. For Samples Ia, IIa and IIb, there is clear evidence for bulk superconductivity with T_c = 0.27K. For Sample Ib, the transition is much broader, and the uncertainty is the parameters in such that this sample may also be essentially entirely superconducting at 0K. For Sample III, the zero-field heat capacity increases rapidly with decreasing temperature at the lowest temperatures, but a number of factors conspired to prevent the extension of the measurements to lower temperatures.

It is evident that strains have an unusually marked effect in broadening the transition and shifting it to higher temperatures. Strains also increase the value of γ. The two effects are

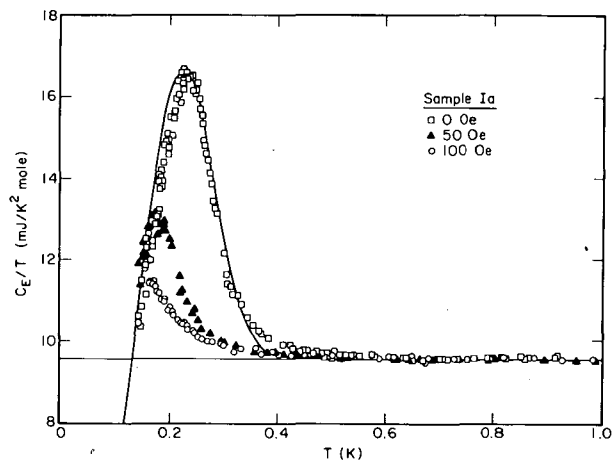

Fig. 1. The electronic heat capacity of Sample Ia. The horizontal line represents the γ-value. The curve represents a BCS heat capacity anomaly broadened by a Gaussian distribution of transition temperature, with $\bar{T}_c$ = 0.27 K and δT_c = 0.05 K. (XBL 7312-7125)

TABLE I. Calorimetrically determined properties of α-U.

Sample	A (mJ-K/mole^{235}U)	γ (mJ/K^{2}mole)	Onset T_c (K)	T_c (K)	δT_c (K)	X_s
Ia	- -	9.59	0.4	0.27	0.05	1.0
Ib	- -	9.86	1.0	0.20	0.35	0.7
IIa	10.3	9.82	0.7	0.27	0.20	0.9
IIb	10.7	9.90				
III	11.4	9.14	(0.25)	- -	- -	- -

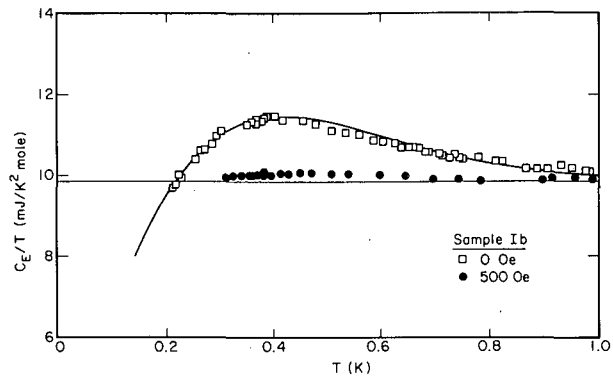

Fig. 2. The electronic heat capacity of Sample Ib. The horizontal line represents the γ-value. The curve represents a BCS heat capacity anomaly broadened by a Gaussian distribution of transition temperatures, with $\bar{T}_c$ = 0.2 K and δT_c = 0.35 K. (XBL 7312-7124)

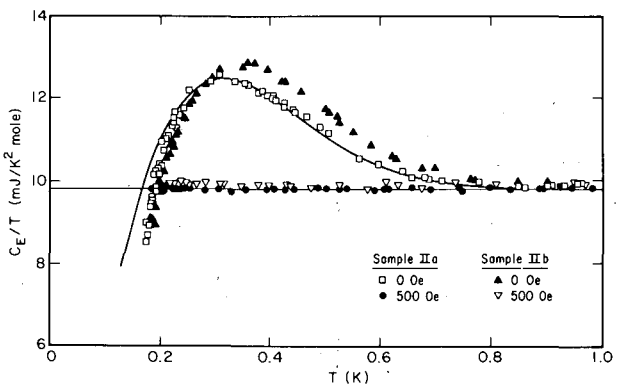

Fig. 3. The electronic heat capacity of Samples IIa and Sample IIb. The horizontal line represents BCS heat capacity anomaly broadened by a Gaussian distribution of transition temperatures, with $\bar{T}_c$ = 0.27 K and δT_c = 0.2 K. (XBL 7312-7129)

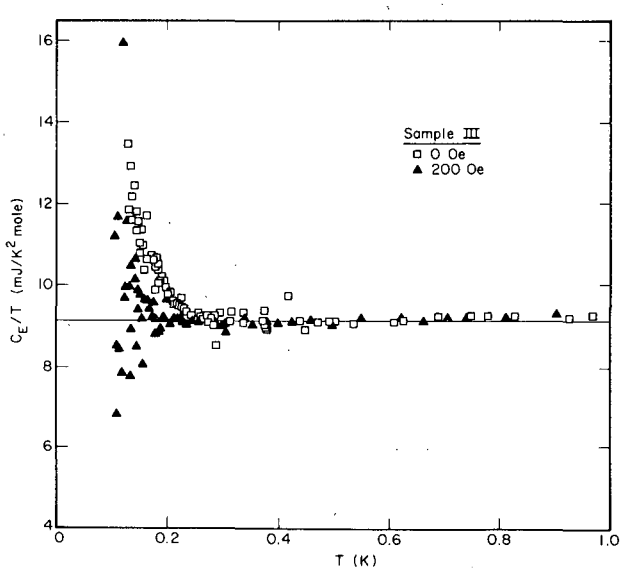

Fig. 4. The electronic heat capacity of Sample III. The horizontal line represents the γ-value. (XBL 7312-7130)

consistent with a strongly strain-dependent electron-phonon interaction and a constant effective coulomb repulsion. The T_c for strain-free α-uranium is not determined accurately, but the partial transition observed in Sample III and comparison with Samples Ia, IIa and IIb suggest that it is of the order of 0.1K. The fact that the 10kbar transitions and the strain-broadened low-pressure transitions can all be represented by BCS heat capacity functions shows that localized magnetic moments are not involved in determining the pressure dependence of T_c.

1. T. H. Geballe et al., Science 152, 755 (1966).
2. C. Palmy and E. S. Fisher, Solid State Comm. 8, 653 (1970).
3. E. S. Fisher, T. H. Geballe and J. M. Schreyer, J. Appl. Phys. 39, 4478 (1968).
4. J. C. Ho, N. E. Phillips and T. F. Smith, Phys. Rev. Lett. 17, 694 (1966).

4. PROGRESS ON VERY LOW TEMPERATURE EXPERIMENTS

Erwin W. Hornung, Gary E. Brodale and N. E. Phillips

Several improvements in the dilution refrigerator have considerably increased its cooling power. The most important of these was a redesign of the still to reduce the circulation of ^{4}He. Using only one discrete exchanger the refrigerator produces a limiting temperature of 26 mK.

The equipment for γ-ray anisotropy thermometry has been set up, tested and put into use. The experiments to data have used ^{60}Co in a single-crystal Co host.

Several experiments have been carried out to obtain data for the design of an intermediate temperature (5 to 20 mK) adiabatic demagnetization stage. These were based on a CMN-epoxy-copper wire construction. The results are encouraging from the point of view of equilibrium times and reversibility--it appears that a very close approximation to reversible behavior can be obtained--but the properties of the CMN were modified by the epoxy and the lowest temperatures attained were only 30 mK.

5. RESEARCH PLANS FOR CALENDAR YEAR 1975

Norman E. Phillips

A calorimeter for measurements to about 20 mK is being built. It will use a dilution refrigerator for cooling and a "SQUID" - based nuclear susceptibility thermometer for temperature measurements. The nuclear susceptibility thermometer will be calibrated against CMN and a γ-ray anisotropy thermometer. This system will be used to study dilute magnetic alloys and in particular the ordering of magnetic impurities in superconducting hosts and the density of states in

superconductors containing magnetic impurities. The results will give detailed information about pair-breaking mechanisms in superconductors.

Modifications to the apparatus for low-temperature heat capacity measurements on He will be continued. The most important component not yet completed is the value for closing the sample cell. The first measurements to be undertaken in this apparatus will be on liquid ^{4}He. At this time most experimental evidence on the low-energy excitation spectrum in liquid ^{4}He agrees with our original calorimetric evidence for negative phonon dispersion, but there is still great uncertainty about the magnitude and even the form of the second and higher terms in the dispersion relation. New heat capacity measurements to 0.1 K or slightly below will put firmer limits on the possible phonon dispersion curve.

The work on the very low temperature apparatus will take several directions. New, large-capacity discrete exchanges are being added to the dilution refrigerator in the expectation that temperatures near 15 mK can be attained. At the same time, an intermediate temperature adiabatic demagnetization stage will be designed that should be capable of providing a starting temperature for a second demagnetization of 5 to 10 mK. Several related experiments will be undertaken in this apparatus:

(1) Measurements of the Kapitza resistance between ^{3}He and metals containing magnetic impurities will be made to identify systems in which the magnetic impurities are effective in heat transfer. These experiments will also employ a nuclear susceptibility thermometer, calibrated against a γ-ray anisotropy thermometer, as the working thermometer. The results will be important in designing apparatus to cool ^{3}He into the region in which the newly-discovered superfluid phases exist, since the most promising method of reaching these temperatures requires nuclear cooling in metals, and the thermal contact to the ^{3}He is severely limited by the Kapitza resistance. (2) As a by-product of these experiments the powdered CMN temperature scale will be compared with nuclear susceptibility and γ-ray anisotropy experiments. Although this temperature scale appears to be reasonably well established, additional confirmation would be useful. (3) Some preliminary experiments on nuclear cooling to obtain temperatures in the region below 1 mK will be undertaken.

6. 1974 PUBLICATIONS AND REPORTS

Norman E. Phillips and Associates

Journals

1. M. P. Mathur, M. Ashkin, J. K. Hulm, C. K. Jones, M. M. Conway, N. E. Phillips, H. E. Simon and B. B. Triplett, Specific Heat of SnTe between 0.06 and 30 K Under Strong Magnetic Field. Low-Temperature Physics - LT13, Plenum Publishing Corp., New York, 1974, Vol. 2, p. 601 (LBL-1137).

2. M. M. Conway and Norman E. Phillips, Low-Temperature Heat Capacity of α- and β-Cerium, ibid., p. 629. (LBL-1138)

LBL reports

1. Samuel David Bader, Some Calorimetric Investigations of the Role of f-Electrons in Superconductivity and Magnetism, Ph.D. thesis, LBL-2297, Jan. 1974.

2. S. D. Bader and N. E. Phillips, M. B. Maple and C. A. Luengo, Heat Capacity of the Superconducting-Kondo System $(LaCe)Al_2$, LBL-2744, May 1974.

3. Marilyn Wun, Calorimetric Studies of Singlet Ground State Systems, M.S. thesis, LBL-3177, Sept. 1974.

4. Marilyn Wun and N. E. Phillips, Low-Temperature Specific Heat of Apiezon-N Grease, LBL-3185, Oct. 1974 (to be published in Cryogenics).

5. Marilyn Wun and Norman E. Phillips, Low Temperature Heat Capacity of $PrCu_2$, LBL-3184, Sept. 1974.

George Jura, Principal Investigator

1. INFRARED SPECTRA

Raymond F. Glienna and George Jura

The infrared spectra of dichlorobenzene and tetrachlorobenzene were determined to a pressure of 30 kbars at room temperature. Similar experiments were performed on the out-of-plane vibration of the alkaline earth carbonates.

a. Alkaline Earth Carbonates

The shifts in the frequencies of the mode under investigation for the different carbonates are shown in Fig. 1.

The interesting feature of this particular mode is the fact that Decius has suggested a volume relationship with the frequency. That is, in principle, his theory would permit the determination of the compressibility from the spectral data.

Madelung and Fuchs measured the average compressibilities for the above minerals on powdered samples and found that the compressibility increased with the size of the cation and ranged from 1.5×10^{-6} bar^{-1}. From our measurements and the application of the theory of Decius, we find values ranging from 3×10^{-6} to 6.6×10^{-6} bar^{-1}.

The agreement is really considerably better than appears by the direct comparison of the numbers. First, only the nearest neighbor approximation has been made for the computation of the interaction potential of the dipole moments of the carbonates; and secondly, the resolution of the infrared instrument available to us had a resolution, on the order of 1 cm^{-1}, which is really too poor since the calculation involves the differences in the frequencies, and these differences are small.

An increase in the accuracy of the instrumentation and the refinement of the theory are both indicated by the present results. The results obtained in these experiments are sufficiently encouraging to warrant further work.

b. Dichloro and Tetrachlorobenzene

The spectra of these two molecules were measured to a pressure of 30 $kbar^{-1}$. Davydov splitting was observed for both molecules. This permitted the calculation of the repulsive interaction potential. Fermi resonance was observed in tetrachlorobenzene. Typical of the frequency shifts in both molecules is shown in Fig. 2. The separation of the Fermi resonance components near 1450 cm^{-1} in tetrachlorobenzene is shown in Fig. 3. The Davydov splitting of the 1394 cm^{-1} band is shown in Fig. 4.

The results show that dichlorobenzene behaves as a two-dimensional solid, while tetrachlorobenzene acts as a one-dimensional solid. The structures behave analogously to those of graphite and antimony respectively.

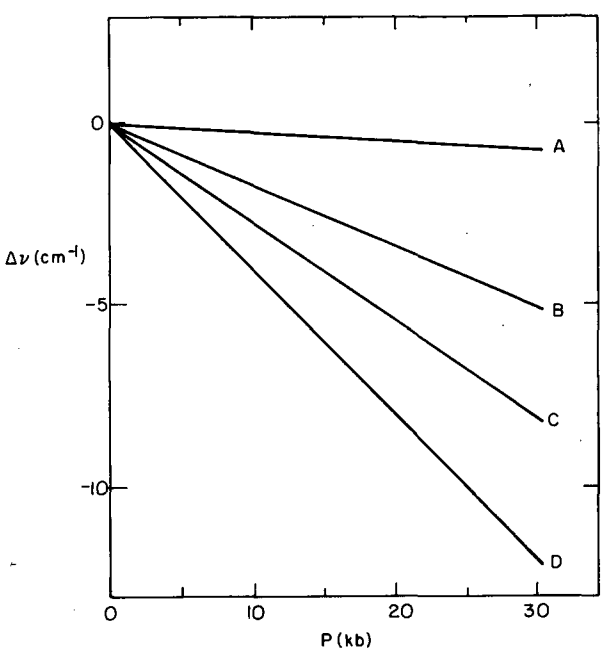

Fig. 1. Shift of out-of-plane bending frequencies with pressure for some alkaline earth carbonates.

A - Calcite
B - Strontianite
C - Witherite
D - Aragonite

(XBL 748-7092)

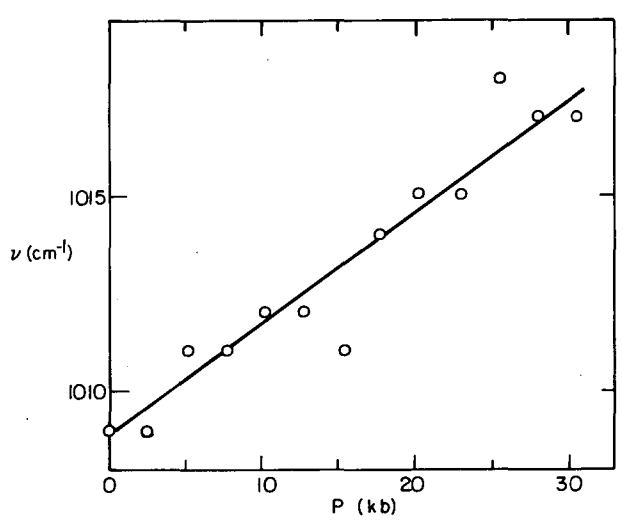

Fig. 2. DCB, B_{1u} vibration. (XBL 748-7082)

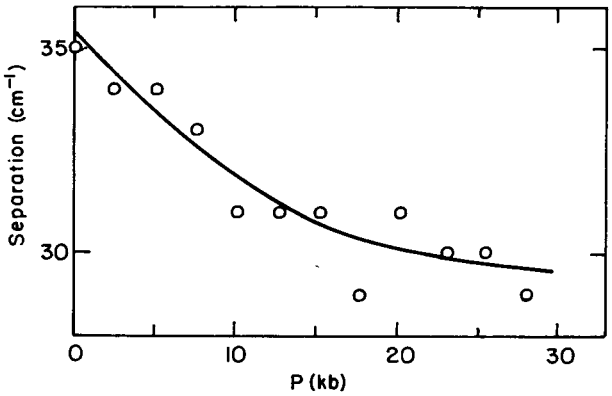

Fig. 3. Separation of Fermi resonance components near 1450 cm^{-1} in TCB. (XBL 748-7087)

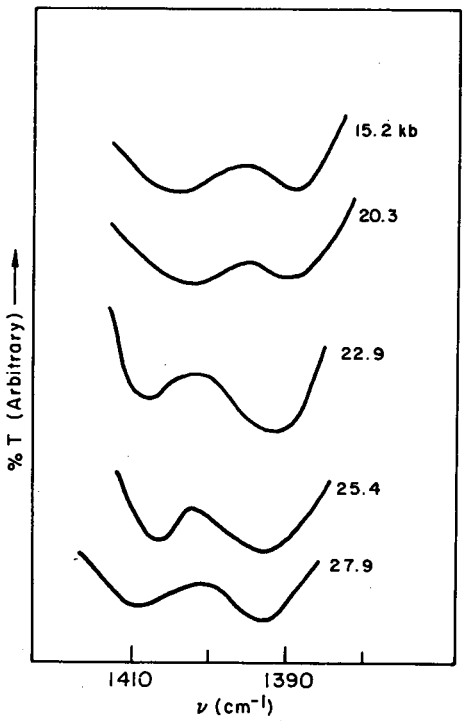

Fig. 4. Davydov splitting of 1394 cm^{-1} absorption of DCB at various pressures. (XBL 748-7080)

2. HEAT CAPACITY OF BISMUTH

Berado Jurado and George Jura

The microsecond pulse method for the determination of the heat capacity of metals was refined and finally perfected. The results of a given pulse are fed into an averager of some sorts, a scope or computer. In this manner voltage vs. time results are obtained that are superior to those obtained heretofore on an oscilloscope. The treatment of the data was given in last year's annual report. Most important, it has been possible to determine the time during which it is permissible to consider the temperature of the ambient to be constant. This depends upon the ability to determine dE/dt. The ambient can be considered to be constant as long as the time derivative of the voltage drop is a linear function of the voltage drop across the sample. An actual test is illustrated in Fig. 1, at a pressure of 50 $kbars^{-1}$ and room temperature.

The temperature behavior of the metal was known to be complex. Early studies have been made in phase 1 by Clarke and the senior investigator. This is the region where the solid behaves as a semiconductor. Figure 2 shows what are temperature reisitance values at a single pressure in the three different phases. Only the resistance in phase 5 behaves like most normal metals. The value of dE/dT, the temperature coefficient of resistance, is important to us since this term appears explicitly in the heat capacity evaluation.

Figures 1 and 2 show the heat capacity results

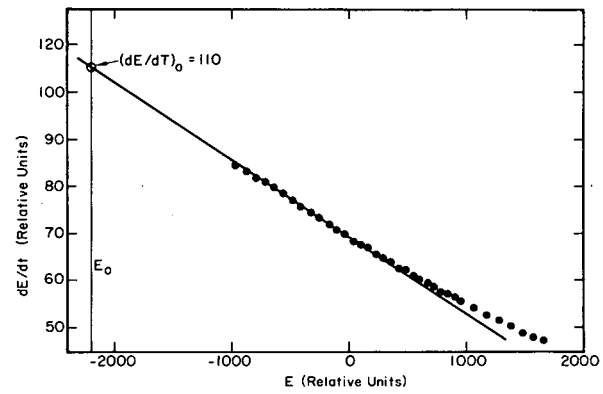

Fig. 1. dE/dt vs. E for bismuth at 50 Kbar (phase III). (XBL 747-6851)

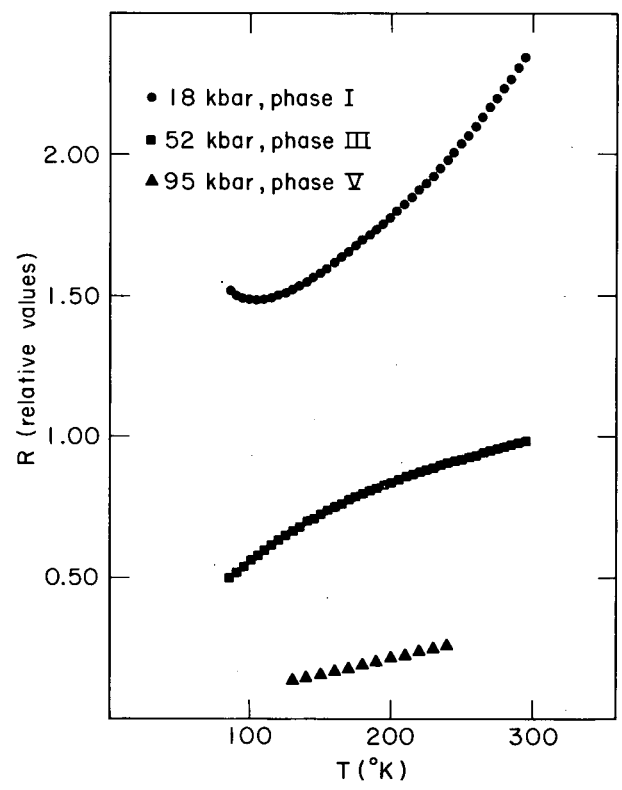

Fig. 2. The resistance of bismuth vs. temperature and pressure. (XBL 748-4066)

at room temperature as a function of pressure as obtained using two different pulse detectors, and the results of Dzhavadov. Two isobars were obtained; one in phase three, the other in phase 5. For comparison, the results at one atmosphere are also shown. The behavior under pressure is markedly different in the two phases and from the results at one atmosphere.

More work is necessary to elucidate the final results. More isobars, and isotherms at lower pressures.

3. RESEARCH PLANS FOR CALENDAR YEAR 1975

George Jura

The plans for the coming year are quite ambitious. Permanent improvement of the present equipment so that we can use Professor Meyers PDP 8 computer as a detector and averager. The arrangement will be such that the work can be done by one man rather than the two now required when the computer is used.

We intend to finish the work on bismuth. When this is finished, we expect to do all of ytterbium, through the semiconducting phase and the final metallic phase. We also hope to do cesium; all phases through 50 kbars. At the same time, we plan to extend the measurement of the heat-leak constant to the degree that we can use longer pulses to directly measure the heats of transitions of polymorphs.

4. 1974 PUBLICATIONS AND REPORTS

George Jura and Associates

Journal

1. Che-Kuang Wu and George Jura, High Pressure Effects on the Intensity of Infrared Spectra of Molecular Crystals, Spectrochimica Acta, 30A, 797 (1974).

LBL reports

1. Tang-Hua Chen, Microsecond Pulse Techniques for Heat Capacity Measurement, Ph.D. thesis, LBL-2574, May 1974.

2. Raymond Fredric Glienna, Infrared Properties of Solids Under High Pressure: Chlorinated Benzenes and Inorganic Carbonates, (Ph.D. thesis), LBL-3169, Sept. 1974.

3. Berado Jurado, The Heat Capacity of Bismuth as a Function of Pressure and Temperature, (Ph.D. thesis), LBL-3162, Sept. 1974.

Gabor A. Somorjai, Principal Investigator

1. LOW ENERGY ELECTRON DIFFRACTION (LEED) STUDIES OF SURFACES

a. LEED Studies of Napthalene and Ice Crystal Surfaces at Low Temperature

Lawrence E. Firment and Gabor A. Somorjai

Surface structure determination by LEED can be readily carried out for clean metals, semiconductors, and for adsorbed monolayers of gases. As first step toward the application of LEED to a different and important class of material, molecular crystals, LEED studies have been carried out on thick films of molecular solids adsorbed and grown on a platinum single-crystal substrate.

The systems studied were naphthalene and water deposited at low temperatures (100-200°K) on a Pt(111) single crystal face. The physical properties of these two dissimilar molecules are well documented. The Pt(111) surface was chosen as a substrate because earlier work[1] has shown organic materials form ordered monolayers relatively easily on thin crystal face.

Both naphthalene and water are found to grow in a manner that produce ordered surfaces. The nature of the naphthalene diffraction pattern depends upon the degree of order of the first layer of naphthalene on the metal. Grown on an ordered first layer, the pattern consists of diffraction spots indicating the presence of an ordered (001) naphthalene surface structure; grown on a disordered monolayer, the pattern is a series of rings which are indicative of rotational disorder. Water grows giving an apparent $(\sqrt{3} \times \sqrt{3})$ R30° pattern, indicating it grows as ordered hexagonal sheets parallel to and in good registry with the Pt substrate.

Studies of these systems continue, with the goal of better defining the growth conditions, the thickness of the deposited layer, electron beam damage and surface changing effects. Similar studies will then be initiated of molecules of different types, of different intermolecular binding and of different crystal structures. With this information, generalizations may be made about the structure and molecular arrangement at the surface of a molecular solid.

---

1. John L. Gland, Ph.D. thesis, LBL-1816.

b. LEED Studies of Iron Crystal Surfaces and of Chemisorption of Gases

Clifford A. Megerle and Gabor A. Somorjai

A series of LEED Auger studies were carried out on clean iron single crystal surfaces. LEED intensities for the (00), (10), ($\bar{1}$1), (11), (20), and the (02) diffracted beams from the Fe(111) surface were measured. These experimental intensities will be compared to calculated intensities for this surface in order to determine the surface structure.

The intensities of LEED beams diffracted from single-crystal surfaces depend upon the mean vibrational amplitude of the atoms from which the incident electrons are scattered. The temperature dependence of the (00) beam intensities from the Fe(111) surface at various beam voltages were measured. Extrapolation of this data to zero incident energy has permitted the calculation of a surface Debye temperature of 165°K for this surface.

The surface structure and chemistry of the clean Fe(110) surface has been studied using LEED and Auger. Nitrogen, hydrogen, acetylene and ammonia were found not to adsorb on this surface at a pressure of 10^{-7} torr to an extent greater than 1/100 of a monolayer. Carbon monoxide was seen to adsorb to a very limited extent, but did not order on the surface. A series of adsorption experiments on this surface at 10^{-5} torr at various temperatures between 25°C and 600°C are being carried out. Nitrogen was found not to adsorb at this higher pressure at any of the temperatures studied.

c. Surface Crystallography of the Clean (111) Crystal Face of Platinum and of Adsorbed Acetylene on Platinum.

Peter C. Stair, Larry L. Kesmodel and Gabor A. Somorjai

The focus of this work is the development of a surface crystallography using low-energy electron diffraction (LEED) to determine the surface atomic structure of clean and adsorbed overlayer systems. In experimental work, a new rapid and accurate method for the measurement of LEED beam intensities has been developed and used to measure the beam intensities from the platinum (111) crystal face. The technique involves photographing the fluorescent screen (diffraction pattern) using a fast film of suitable sensitivity to obtain all the diffraction beam intensities simultaneously. The diffraction beam intensity can be measured over a range of three orders of magnitude. Photographs are machine developed for uniformity and calibrated for point-by-point conversion from digitalized optical density to intensity. This is followed by computer analysis of the integrated intensities and background correction. The intensities measured photographically have been shown to be in excellent agreement with those measured by the much slower, conventional spot photometer method.

In theoretical work, the LEED intensities from the clean (111) face of platinum have been calculated using a T-Matrix multiple-scattering theory with corrections for lattice vibrations. Calculated intensities have been compared with our experimental results for specular and non-specular beams at several angles of incidence for electron energies ≤ 100 eV. The calculations predict peak positions accurately and adequately describe the shapes and relative intensities of primary and secondary features in the experimental intensity profiles. Analysis of the data indicates that the spacing of the topmost atomic layer is the same as the bulk value to within 5% (or approximately 0.1Å).

The above techniques, both experimental and theoretical, are being extended to determine the bonding sites and bonding lengths of acetylene adsorbed on a Pt(111) surface in an ordered, low-coverage structure. Preliminary data has been obtained for the overlayer system and detailed calculations have been made.

d. LEED Studies of the Structure and Stability of Stepped Platinum Surfaces

Donald W. Blakely and Gabor A. Somorjai

The stability of both atomically clean and covered platinum single crystal surfaces has been determined by LEED. On atomically clean platinum surfaces monatomic heights steps are stable for most crystal orientations below the melting point. Very rough surfaces with orientations far from the 3 low index poles are unstable with increasing temperature and small facets of low index planes 5 to 50 nm wide form. When the platinum surfaces are covered with a monatomic layer of carbon, the stable terrace width is usually 4 nm for orientations greater than 6.5° from the low index poles.

e. Calculation of the Structure and Charge Density of Stepped Surfaces

Yvonne Tsang, Larry L. Kesmodel, Leo M. Falicov and Gabor A. Somorjai

When a crystal surface is cleaned, one expects relaxations of the surface atoms to new equilibrium positions different from bulk equilibrium structure. A knowledge of the actual positions of atoms in a stepped surface may be useful in the understanding of the catalytic properties of stepped platinum surfaces. The equilibrium structure of a stepped surface is determined by minimizing step surface energy as a function of surface atom positions. To study crystal structure, we have chosen the stepped surface corresponding to Miller indices (11,0,1) of Ar, a rare gas solid and NaCl, an alkali halide.

In Ar, we used the Lennard-Jones potential in the surface energy minimizing procedure, we found that the energy is minimized if every surface atom moves inward by about .01 (9/2), a being the Ar lattice constant. The corresponding lowering of surface energy is negligible (.1% of the indisplaced stepped surface energy).

In the case of NaCl, we have included 1) Madelung (coulomb) energy, 2) Short range repulsive energy and 3) Polarization energy in the calculation of stepped surface energies as a function of ion displacements. We found that the most important contribution to surface ion displacements arises from polarization effect. This accounts for the negligibly small atom displacements in Ar. Our preliminary results indicate that the Na^+ ions can move inward by as much as .08 (9/2), a is again the lattice constant; whereas the Cl^- surface ions generally move outward. Figure 1 shows the ion displacements in the stepped surface. The results in Fig. 1 are based on the assumption that ion displacements are small so that the relevant physical quantities such as the electric field on the surface ions and their dipole moments remain at the unperturbed values of the undisplaced step. The relatively large displacements obtained indicate a need for a more self-consistent calculation, which is currently in progress.

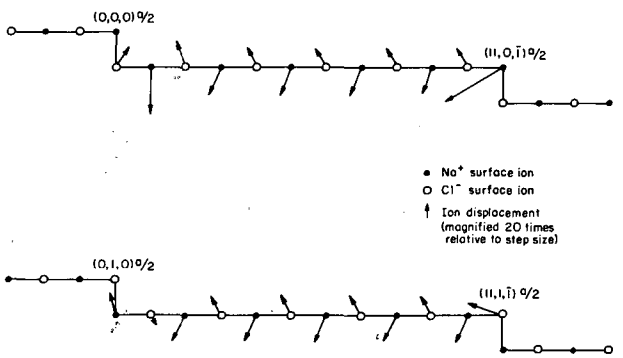

Fig. 1. Ion displacements on NaCl stepped surfaces. (XBL 7412-7683)

Calculations of the electronic charge density and the electrostatic potential for a single model of a stepped metal surface are being carried out. The results indicate that the electrostatic potential has a local minimum in the region of the step which is on the order of 0.5 eV below that of the bulk. This would imply that atoms in the sites corresponding to a step geometry would experience a different electrostatic potential than atoms in the bulk and this would in turn cause a rearrangement of electronic charge. The magnitude of this effect depends on the density of states near the Fermi level as well as the details of the electrostatic potential in the region of the step.

2. AUGER ELECTRON SPECTROSCOPY STUDIES OF SURFACES

a. The Surface Composition of Binary Alloys

Steven Overbury and Gabor A. Somorjai

The thermodynamics of a metal alloy surface predicts that the component with the lowest

surface tension will be present in the top atomic layers in excess of that component's composition in the bulk of the solid.[1,2] Throughout this last year Auger electron spectroscopy has been used as a tool to study this effect in the binary alloy system Au-Ag. The Au-Ag alloy is a non-ideal solution which forms no compounds and has no long-range ordering, but which has a heat of solution which is larger than the surface tension difference between Au and Ag. We have found that this large heat of mixing appears to be quite important in determining the surface composition, so that the surface segregation of Ag does not seem to occur to the extent predicted for an ideal solution. The measured temperature independence of the surface composition tends to support this argument. We have also obtained useful information regarding the effects of sputtering on the alloy surface and the times necessary for return of the composition of the sputtered surface to equilibrium.

Having completed the Au-Ag system studies, we will soon continue on other alloy systems. Alloy systems of great interest are those which form very well ordered crystals, such as Au-Cu, since surface effects may interrupt the bulk ordering at the interface. Alloy systems of low mutual solubility, such as Au-W, which is interesting catalytically and as a contact in devices, might be studied as films since there may be surface phases formed.

---

1. S. Berglund and G. A. Somorjai, J. Chem. Phys. 59, 5537 (1973).
2. S. H. Overbury, P. A. Bertrand and G. A. Somorjai, Chemical Reviews, (to be published).

3. CATALYSIS BY SINGLE CRYSTAL SURFACES

a. The Reactivity of Stepped Platinum Surfaces in the Catalysis of Hydrocarbon Reactions at Low Pressures

Donald W. Blakely and G. A. Somorjai

The rates of catalytic hydrocarbon reactions on various platinum stepped single crystal surfaces (high Miller index) have been measured. The rate of cyclohexane dehydrogenation to benzene has been found independent of surface orientation, while the hydrogenation to cyclohexane varies greatly with surface orientation. The rates of both reactions are commonly considered surface structure independent from studies on dispersed industrial catalysts.

The isomerization and hydrogenolysis of n-heptane have also been studied. The rates of these reactions on the various stepped platinum surfaces were not much different from each other. However, the product distributions may vary widely from crystal face to crystal face. Heat treatment of the stepped surfaces in oxygen above 1,000°C markedly affects the product distribution in these hydrocarbon reactions.

b. Catalysis on Platinum Single Crystal Surfaces at High Pressures

Richard K. Herz, Eugene Petersen and G. A. Somorjai

The sensitivity of platinum catalyzed reaction rates to various crystal faces is being studied at total reactant pressures ranging from atmospheric pressure to 10^{-5} torr. The rate of dehydrocyclization of cyclopropane to propane on a Pt(111) crystal face was determined to be equal to the rate on a stepped Pt 6(111)×(100) crystal face. This reaction appears to be insensitive to the surface crystallography of the platinum catalyst. A reaction which is dependent upon the crystal surface structure is the dehydrocyclization of n-heptane to toluene at low (10^{-5} to 10^{-4} torr) pressures. This reaction is being studied at atmospheric pressures on single platinum crystals. The crystals are cleaned in a UHV system equipped with an Auger electron spectrometer, then isolated from the main system by a movable cup which encloses the crystal. Reactant gases are circulated past the crystal and analyzed by gas chromatography. Using a flame ionization detector both the reactant and the products (toluene) are readily detectable.

c. The Reactivity of Au-Pt and Au-Ir Alloys in Hydrocarbon Reactions

David Hagen and Gabor A. Somorjai

The bulk electronic properties of a metal can be substantially altered by alloying a second metal with it. For example, alloying a transition metal whose d-band is only partially occupied with one whose d-band is full (e.g. Au) may yield a material with an intermediate d-band occupancy. Although little work has been done to determine the electronic density of states in the d-band of such alloys, it seems likely from, for example, the Engel-Brewer correlation that such d-band filling would occur in practice. Thus, it may be possible to produce an alloy out of such materials that would be similar in its electronic properties to platinum and display similar catalytic behavior. It is this possibility that is being investigated in the present program.

The procedure followed is to place the metal in an ultra-high vacuum environment and to clean it so that Auger electron spectroscopy gives a spectrum characteristic of the pure material. If the metal is to be alloyed with gold, the latter is evaporated on the sample in monolayer amounts and annealed in ultra-high vacuum to give the desired surface composition as determined by Auger. The reactant gases are introduced to a total pressure in the 10^{-4} torr range and the sample is heated to the desired temperature which is generally about 300°C. The product gases are then observed with the aid of a mass spectrometer. The initial rate at which the products are being formed at the reactant temperature is taken as indicative of the catalytic activity.

Hydrogenolysis of propane, cyclopropane, n-heptane, iso-butane, and neo-pentane generally yield only methane as a hydrogenolysis product under the experimental conditions described above.

The exceptions are that ethane is seen in addition to methane for propane hydrogenolysis having a maximum initial rate, expressed as molecules of product formed per incident reactant hydrocarbon molecule, on a 10% Au-90% Pt surface. Secondly, propane is seen in addition to methane for cyclopropane hydrogenolysis. These results are in contrast to work done at high pressures where a more-or-less even distribution of C_n reaction products are seen. The rate of hydrogenolysis on platinum decreases very rapidly with increasing gold coverage, that is, tenfold for a 10% gold coverage. Hydrogenolysis to methane was found to poison relatively slowly as compared to isomerization and dehydrocyclization. The time for poisoning was typically about ten minutes. The initial hydrogenolysis rate for methane production was roughly the same for all hydrocarbons studied except for propane where it was nearly 4 times larger with a rate of 2×10^{-4} methane molecules produced per incident propane molecule. As function of temperature, the initial hydrogenolysis rate goes through a maximum in the range 270-300°C for all hydrocarbons studied. Finally, the inital hydrogenolysis rate increases as a function of hydrogen to hydrocarbon ratio.

Isomerization of iso-butane to n-butane and the reverse reaction were found to have an initial rate greater on pure platinum than either hydrogenolysis or dehydrocyclization and were found to poison rapidly in only a few minutes. The isomerization rate behaves similarly to hydrogenolysis as a function of temperature where it reaches a maximum at about 300°C. The isomerization rate decreases approximately linearly with gold coverage in contrast to the very rapid decrease observed with hydrogenolysis. No isomerization of neopentane to either iso-pentane or n-pentane was detected. The isomerization rates go through a maximum, as a function of hydrogen to hydrocarbon ratio, at a ratio of 5:1 as compared to the uniform increase for hydrogenolysis. Finally, the ratio of the initial rate of isomerization to that of hydrogenolysis has a maximum as a function of gold coverage at a coverage of about 25% gold.

Dehydrocyclization of n-heptane to toluene was found to poison in less than a minute at the reaction temperature and had a maximum initial rate about three orders of magnitude less than isomerization and hydrogenolysis. No strong temperature dependence for dehydrocyclization was found in the range 350-450°C. Dehydrocyclization rates decrease approximately linearly with increasing gold coverage, as with isomerization.

d. The Interaction of Oxygen and Hydrogen with Thorium Crystal Surfaces

Thomas N. Taylor, Carlos A. Colmenares and Gabor A. Somorjai

An ultra-high vacuum system has been assembled at the Lawrence Livermore Laboratory for the study of the chemisorption and surface reactions of gases (primarily oxygen and hydrogen) on both polycrystalline and single crystal thorium. The surface interactions are monitored via low energy electron diffraction (LEED), Auger electron spectroscopy (AES), and change in work function measurements. In addition, high resolution AES may be done using a cylindrical mirror analyzer system located at the same Livermore facility.

Detailed information on the Auger spectrum of thorium and its surface impurities has been obtained. These data have enabled assignment of Auger transition levels to the thorium peaks in the spectrum. LEED examination during exposure of Th(100) to $\sim10^{-8}$ torr of oxygen reveals the growth of an "out of registry" oxide layer. Change in work function measurements during a similar oxygen exposure showed an initial rapid decrease in work function ($\Delta\phi\sim-0.5$eV) prior to a much slower increase until saturation.

Additional information will be obtained on Th(111) and (110) using the above techniques. Preparations are under way for measurements on water vapor adsorption. Further studies are planned which examine the effect that graphitized carbon films have on oxide formation.

4. MOLECULAR BEAM STUDY OF THE MECHANISM OF CATALYZED HYDROGEN-DEUTERIUM EXCHANGE ON PLATINUM SINGLE CRYSTAL SURFACES

a. The H_2-D_2 Exchange Reaction or Stepped Platinum Surfaces

Steven L. Bernasek and Gabor A. Somorjai

The hydrogen-deuterium exchange reaction was studied by molecular beam scattering on low and high Miller index crystal faces of platinum in the surface temperature range of 300-1300°K. Under the condition of the experiments which put strict limitation on the residence time of the detected molecules, the reaction product, HD, was readily detectable from the high Miller index, stepped surfaces (integrated reaction probability, defined as total desorbed HD flex divided by D_2 flux, is $\sim10^{-1}$) while HD formation was below the limit of detectability on the Pt(111) low Miller index surface (reaction probability $<10^{-5}$). Atomic steps at the platinum surface must play a controlling role in dissociating the diatomic molecules. The exchange reaction is first-order in D_2 beam pressure and half-order in H_2 background pressure. This observation indicates that an atom-molecule reaction or possibly an atom-atom reaction is the rate-limiting step in the exchange. The absence of beam kinetic energy dependence of the rate indicates that the molecular adsorption does not require activation energy. The surface is able to store a sufficiently large concentration of atoms which react with the molecules by a two branch mechanism. At lower temperatures (<600°K) the rate constant for the exchange is $k_1 = (2\pm1)\times10^5 \exp(-4.5\pm.5 \text{ kcal/RT}) \text{ sec}^{-1}$. The rate determining step appears to be the diffusion of the D_2 molecule on the surface to a step site where HD is formed via a three-center (atom-molecule) reaction, or via a two-center (atom-atom) reaction subsequent to D_2 dissociation at the step. At higher temperatures (>600°K) the reaction between an adsorbed H atom and an incident D_2 gas molecule competes with the low temperature branch.

The rate constant for this branch is $k_2=(1\pm2)\times10^2 \exp(-0.6\pm.3 \text{ kcal/RT}) \text{ sec}^{-1}$. The catalyst action of the platinum surface for the exchange reaction is due to its ability to adsorb and dissociate hydrogen molecules with low activation energy and to store atomic hydrogen on the surface thereby converting the gas phase molecule-molecule reaction to an atom-molecule or atom-atom reaction of low activation energy.

b. Small Molecule Reactions on Stepped Single Crystal Platinum Surfaces

Steven L. Bernasek and Gabor A. Somorjai

Ultrahigh vacuum molecular beam techniques coupled with LEED and Auger Electron Spectroscopy are particularly well suited to the study of surface chemical reactions because of the ability to assess the effect of the surface conditions on the reaction probability. Investigation of the hydrogen-deuterium exchange reaction on a series of low and high Miller Index platinum single crystals has indicated that the steps present on the high index surfaces are necessary for the dissociation and subsequent recombination of hydrogen. We have undertaken a systematic study of a series of small molecule reactions on these stepped surfaces to determine the reaction probability on stepped platinum surfaces. Reactions involving dissociation of H_2, D_2, O_2, OH, NH, and CH bonds proceed on the stepped surfaces with much higher reaction probabilities than reactions requiring dissociation of N_2 or CO bonds. All of the reactions studied resulted in cosine product angular distributions except for the formation of CO_2, which exhibited a distribution more peaked at the normal to the surface.

c. Molecular Beam Studies of Hydrogen Atom Recombination on Metal Surfaces

Rebecca Johnson, Wigbert J. Siekhaus and Gabor A. Somorjai

A tungsten thermal dissociation source of hydrogen atoms has been constructed to study the recombination and exothermic surface reactions of hydrogen atoms with adsorbed species. Our main area of interest lies in the energy exchange of the "hot" reaction products with the surface; specifically in the kinetic energy of the products leaving the surface.

An apparatus has been designed and is presently being built for this investigation. A cross correlation chopper will be used to modulate the reaction product signal to the mass spectrometer. This technique provides better resolution than the conventional variable speed chopper as well as more information per experiment, i.e. one obtains the amplitude and phase of a number of frequency components of the signal rather than just the phase and amplitude for a particular frequency. With this apparatus we should be able to measure the kinetic energy of scattered products and their angular distribution.

The first system that will be studied is the recombination of hydrogen atoms on tungsten. Since this reaction is highly exothermic it should be possible to observe translationally excited products, if they form as a result of the surface reaction.

5. COAL CONVERSION CATALYSIS

Donald W. Blakely and Gabor A. Somorjai

A project has been set up to study the catalyzed surface reactions leading to the liquification of coal by metal ligand catalysts. A high ash, bonded coal was studied by Auger Electron Spectroscopy and XPS. All the elements present in the bulk coal (C, N, O, Al, Ai, Si, S, Ca, Fe) were detectable within the top 10Å to 20Å of the surface with much higher concentration on fractured surfaces than on polished surfaces. With these techniques the chemical bonding changes during catalysis may be monitored. As a first step in this program synthetic coals will be studied. These are pure highly aromatic hydrocarbon polymers similar to ordinary plastics. They will be studied for surface crystallinity, electronic conductance and low energy electron damage as well as catalytic depolymerization.

6. SOLAR CELL RESEARCH

Wigbert J. Siekhaus and Gabor A. Somorjai

Photovoltaic conversion of sunlight into electricity in solar cells is feasible but presently uneconomical. Efficient and stable solar cells are manufactured today from high-purity silicon single crystals sliced into thin (0.3 mm) rectangular wafers of approximately 10 cm^2 area ($\sim2\times10^{-2}$ watt average output). Five thousand of these cells must be interconnected to provide 1 kW. Our research is aimed at developing a polycrystalline silicon solar cell with suitable electrical properties that will make photovoltaic energy conversion economical. 1) We are studying the various methods to deposit thin layers of solar cell material with sufficient crystallinity over a large area (m^2). The catalysis of condensation and recrystallization of silicon doped with suitable impurities is investigated to produce the thin silicon layers at low temperatures.
2) Electron spectroscopy low energy electron diffraction and electron microscopy are utilized to investigate the surface and grain boundary structure of the thin films and their effect on the electrical properties. We have dedicated to this solar cell research: an ultrahigh vacuum system equipped with LEED, a high-resolution electron spectrometer, an ion sputtering gun, and a device to break materials under ultrahigh vacuum conditions; a high-vacuum system with three electron-beam gun evaporators modified for silicon deposition work; and electronic instrumentation to measure electrical properties of solar cell films produced in the laboratory. The following experiments are planned or being performed in the laboratory.

a. Identification of Impurities Segregated on Grain Boundaries and Their Effect on Electronic Surface States

Wigbert J. Siekhaus, Jim Crump, Tom Kaminska and Gabor A. Somorjai

The review by Monch[1] and more recent work by Rowe and Ibach[2] show clearly that the large concentration of surface states which are traps and recombination centers for photoelectrons can be filled or decreased by orders of magnitude by exposure to various adsorbates. Polycrystalline samples of electronic and metallurgical grade silicon (either before or after they have been diffused to form pn junctions) are being broken along grain boundaries under ultrahigh vacuum conditions. Impurities on the grain boundaries are being identified (qualitatively and quantitatively) using Auger electron spectroscopy. Single-crystal silicon samples with low-Miller-index surfaces will be exposed under ultrahigh vacuum conditions to various adsorbed impurities. The effect of impurities on surface states will be studied using high resolution electron loss spectroscopy and photoelectron spectroscopy.

The physical structure of the surface will, through its effect on bonding, influence surface states as well as the concentration of impurities.

To study one aspect of this problem on a wall controlled system, a LEED-Auger study of the Si(111) surface has been undertaken with the aim of gathering information on the reconstructed surface giving a (7×7) LEED pattern.

This surface reconstruction has been seen by many observers using samples which cover a wide range of doping levels. We have found that at background pressures between $5 \cdot 10^{-10}$ and $5 \cdot 10^{-9}$ the reconstruction proceeds rapidly above 700°C, producing a well-defined diffraction pattern.

Analysis of the (00) beam intensity versus voltage curves for both unreconstructed and reconstructed surfaces has shown distinctive and contrasting features. So far the comparison of the (1×1) and (7×7) intensity versus voltage curves has been restricted to the 50-150 volt region, because at higher energies the pattern for the (1×1) surface is poorly resolved. For the (7×7) surface; the study is easily extended to 300 volts.

A comparison of the temperature dependence of the various intensity maxima of diffraction beams from the (1×1) and the (7×7) structure is underway. The aim here is to obtain reliable data showing whether surface reconstruction causes a measurable change in the surface Debye-Waller factor, and hence, by the harmonic oscillator model, a change in the mean square displacement of top layer atoms in the direction normal to the surface.

b. Deposition and Characterization of Silicon Films for Solar Cell Use

Chin-An Chang, Tom Kaminska and Wigbert J. Siekhaus

1. Catalysis of Crystallization. Production of Si polycrystalline thin films can be achieved using techniques such as chemical vapor deposition (CVD), evaporation, sputtering, etc. The CVD method will be the main technique used in this laboratory for the near future. For the epitaxial growth of Si films using the CVD technique, silane gas, SiH_4, has been widely used. SiH_4 decomposes on a heated substrate at ~1100°C and silicon is deposited. The substrate temperature necessary for the thermal decomposition of silane can be significantly lowered by a codeposition of silane with another gas, diborane, B_2H_6. The lowest temperatures of decomposition that were achieved were 300-600°C.[3] The Si thin films produced this way, however, have very low photovoltaic efficiencies because of their polycrystalline structure. To improve the film qualities, we plane to combine CVD with the ultrathin alloy zone-crystallization (UTAZC) technique.[4] In the UTAZC technique an extremely thin alloy layer is deposited on the substrate prior to sublimation or evaporation of Si. The grain size of the Si film thus deposited was found to increase to 300μ, compared with the usual 5-μ size achieved at a substrate temperature of 1100°C. The combined use of the CVD and UTAZC techniques could therefore produce single crystal-like Si films at lower substrate temperatures. This would allow the use of all as the substrate material for a good electrical contact with the Si films deposited.

To investigate the use of a thin aluminum layer as a catalyst for crystallization, silicon thin films were vacuum deposited onto fused quartz at 600°C with a prior coating of an ultrathin aluminum layer (ca 500 Å).[5] As a result, significant increase in crystallinity was observed, using x-ray diffraction as well as transmission electron microscopy.

Systematic studies will be carried out to find the best catalyst for lower temperature CVD of silane, and the best alloy film for the UTAZC purpose. Also, cheaper starting material such as $SiCl_4$ will be tested for CVC of Si. The Si films produced will be characterized by electrical measurements (resistivity, photoconductivity, carrier mobility and lifetime) by their grain structure and surface properties. Pichaud and Drechsler[6] have shown increased surface self-diffusion and surface recrystallization of tungsten under the influence of adsorbed nickel. If such a surface alloy can be maintained during deposition of silicon, large grain silicon films can be formed at a temperature low compared with the conventional recrystallization temperature; i.e., the adsorbed species acts as a crystallization catalyst.

In the planned experiment the surface recrystallization temperature will be measured as a function of the adsorbed element. Elements will be chosen that have low bulk solubility in silicon. LEED will be used to define the recrystallization temperature.

2. Auger Analysis of the Interaction of Allotropic Forms of Carbon with Silicon during High Temperature Si Thin Film Deposition on Graphite. An important problem in thin film solar cells is the interaction between the substrate and

the thin film. Carbon has been suggested as a suitable substrate for silicon solar cells; we have investigated therefore the carbon-silicon film interaction.[7]

Silicon films (2000-3000 Å thick) were vacuum deposited onto various allotropic forms of carbon (graphitic, amorphous, glass-like) at 1150°C to test the possibility of using carbon as a substrate in thin film silicon solar cells. The distribution of silicon and carbon in the carbon-silicon interface was studied using Auger spectroscopic depth profiling. The results showed that, for all substrates, carbon diffused deeply into silicon films, and for all substrates except glassy carbon, silicon also diffused deeply into carbon. In both cases, silicon carbide is formed. Several methods to build diffusion barriers were tested. A diffusion mechanism is proposed according to which silicon atoms first form a carbide layer with the surface carbon atoms, followed by breaking up of the carbon lattice and diffusion of silicon through the carbide layers into the carbon substrates. This mechanism is shown to explain very well the dependence of the measured silicon and carbon contents on the structures of the carbon substrates used for depositions.

Since Auger analysis combined with argon sputtering is used as the principal tool in our investigation we want to study the effect of sputtering on the concentration profile. As a first step, the fate of the ions implanted during sputtering is studied theoretically as a function of the relative removal probability and the diffusion coefficient.[8]

A theoretical solution has been given for the time dependent concentration of implanted ions (assumptions: constant diffusion coefficient in the range of penetration, $(d(x) = \delta(x-x_0)$, $c(x=0,t)=0)$ together with general proof that the number of bombarding ions contained in a target at saturation is increased if the ions diffuse throughout the target, unless $c(o,t)=0$.

This solution has been used to determine the concentration profile and the total number of imbedded atoms at saturation as a function of a parameter p(relative removal probability) and the diffusion constant $D_0(x)$. Measurements will show whether diffusion during sputtering is an important problem.

---

1. Winfried Mönch, On the Physics of Clean Silicon Surfaces, XIII Advances in Solid State Physics, Pergamon Press, March 1973.
2. J. E. Rowe and H. Ibach, Phys. Rev. Letters 31, 2 (1973).
3. L. H. Hall and K. M. Koliwad, J. Electrochem. Soc. 120, 1438 (1973); F. C. Eversteyn and B. H. Put, ibid. 120, 106 (1973); and references therein.
4. J. D. Filby and S. Nielsen, J. Electrochem. Soc. 112, 957 (1965).
5. Chin-An Chang, Wigbert J. Siekhaus, Thomas Kaminska and Donald Tai-Chan Huo, Enhanced Crystallinity of Silicon Film Deposited at Low Temperature, LBL-3165, September 1974.
6. M. Pichaud, Surface Sci. 36(3), 813-16 (1973).
7. Chin-An Chang and Wigbert J. Siekhaus, Auger Analysis of the Allotropic Forms of Carbon with Silicon During High Temperature Thin Film Deposition, LBL-3186, September 1974.
8. Wigbert J. Siekhaus, The Effect of Diffusion and Relative Removal Probability on the Total Number and on The Concentration Profile of Ion's Imbedded into a Target During Sputtering, LBL-3205, September 1974.

7. RESEARCH PLANS FOR CALENDAR YEAR 1975

Gabor A. Somorjai

Ultraviolet photoemission study of coal will be initiated to study the surface composition and its changes during chemical reactions at low pressures.

The recombination of H atoms on metal surfaces and the energy distribution of the product molecules will be studied.

Electron spectroscopy will be employed to investigate impurity segregation at the surface and at the grain boundaries of polycrystalline silicon.

The ammonia synthesis reaction on iron crystal surfaces will be studied.

8. 1974 PUBLICATIONS AND REPORTS

Gabor A. Somorjai and Associates

Journals

1. Kenneth Baron, D. W. Blakely and G. A. Somorjai, Low Energy Electron Diffraction Studies of the Surface Structures of Adsorbed Hydrocarbons (n-Heptane, Toluene, Benzene, Ethylene and Cyclohexane) on Stepped (High Miller Index) Platinum Surfaces, Surface Science 41, 45 (1974) (LBL-1813).

2. J. L. Gland and G. A. Somorjai, Low Energy Electron Diffraction and Work Function Change Studies of the Adsorption of Substituted Aromatic Molecules on the (111) and (100) Crystal Faces of Platinum, Surface Science 41, 387 (1974) (LBL-1815).

3. G. A. Somorjai, Abstract: Correlation Between the Catalytic Activity and the Surface Structure of Platinum Crystals, J. Vac. Sci. Technol. 11, 250 (1974) (LBL-2208 Abs.).

4. S. L. Bernasek and G. A. Somorjai, Molecular Beam Scattering from Clean and Carbon Monoxide Covered Platinum (111) Crystal Surfaces, J. Chem. Phys. 60, 4552 (1974) (LBL-2511).

5. D. R. Kahn, E. E. Petersen and G. A. Somorjai, The Hydrogenolysis of Cyclopropane on a Platinum Stepped Single Crystal at Atmospheric Pressure, J. of Catalysis 34, 291 (1974) (LBL-2586).

6. S. B. Brumbach and G. A. Somorjai, The Interaction of Molecular Beams with Surfaces, Critical Reviews in Solid State Sciences, 429 (1974) (LBL-2212) (Chemical Rubber Company).

7. F. J. Szalkowski and G. A. Somorjai, Characteristic Energy Loss Spectra of Vanadium and of V_2O_3, Phys. Rev. B. 9, 3369 (1974) (LBL-

8. F. J. Szalkowski and G. A. Somorjai, Auger Electron Spectroscopic Investigations of Chemical Shifts in Some Vanadium Compounds, J. Chem. Phys. 61, 2064 (1974) (LBL-

9. G. A. Somorjai, "Surface Chemistry", in Solid State Chemistry and Physics Vol. 2, (ed. P. F. Weller, Marcel Dekker, Inc., 1974) p. 667.

10. Chin-An Chang, Empirical Calculations of the Force Constant, Dissociation Energies and Bond Lengths of Diatomic Molecules, LBL-2252, High Temp. Sci. 6, 276 (1974).

LBL reports

1. M. S. Chesters, Jean Paul Deville and G. A. Somorjai, Characterization of Adsorbed Hydrocarbons by Chemical Shifts in Auger Electron Spectra, presented at International Symposium on Characterization of Adsorbed Species in Catalytic Reactions, June 17-19, 1974, University of Ottawa, Canada, LBL-2548 Abs. Jan. 1974.

2. G. A. Somorjai and S. L. Bernasek, Molecular Beam Scattering from Solid Surfaces, Chapter in Progress in Surface Science, Sidney G. Davison, ed., Pergamon Press, LBL-2591, March 1974.

3. S. H. Overbury, P. A. Bertrand and G. A. Somorjai, The Surface Composition of Binary Systems. Prediction of Surface Phase Diagrams of Solid Solutions, LBL-2746, May 1974 (chapter in Chemical Review, Harold Hart, ed.).

4. J. L. Gland, K. Baron and G. A. Somorjai, Low-Energy Electron Diffraction, Work Function Charge and Mass Spectrometric Studies of Chemisorption and Dehydrogenation of Cyclohexane, Cyclohexene, and 1,3-Cyclohexadiene on the Pt(111) Surface, LBL-2768, May 1974.

5. G. A. Somorjai, The Mechanism of Hydrocarbon Catalysis of Platinum Crystal Surfaces, LBL-3126, August 1974, presented at Battelle Conference on Physical Basis for Heterogeneous Catalysis to be held at Astaad, Switzerland, Sept. 2-6 1974.

6. P. C. Stair, T. J. Kaminska, L. L. Kesmodel and G. A. Somorjai, A New Rapid and Accurate Method to Measure Low-Energy Electron Diffraction Beam Intensities. The Intensities for the Clean Pt(111) Crystal Face, LBL-3149, Aug. 1974.

7. L. L. Kesmodel and G. A. Somorjai, Structure Determination of the Pt(111) Crystal Face by Low-Energy Electron Diffraction, LBL-3148, Aug. 1974.

8. G. A. Somorjai and L. L. Kesmodel, The Structure of Solid Surface, LBL-3135, Aug. 1974.

9. Chin-An Chang, Wigbert J. Siekhaus, Thomas Kaminska and Donald Tai-Chan Huo, Enhanced Crystallinity of Silicon Film Deposited at Low Temperature, LBL-3165, Sept. 1974.

10. S. L. Bernasek and G. A. Somorjai, Molecular Beam Study of the Mechanism of Catalyzed Hydrogen-Deuterium Exchange of Platinum Single Crystal Surfaces, LBL-3115, Oct. 1974.

11. G. A. Somorjai and M. A. Chesters, The Structure of Surfaces, LBL-3187, Oct. 1974.

12. G. A. Somorjai, The Structure and Thermodynamics of Clean Surfaces - Principles Chapter in Treatise on "Solid State Chemistry". ed. N. B. Hannay (1974).

13. S. L. Bernasek and G. A. Somorjai, Small Molecule Reactions on Stepped Single Crystal Platinum Surfaces, Proc. of Surf. Sci. Conf., Rolle, Mo. (1974 to be published) LBL-2759, Aug. 1974.

14. L. E. Firment and G. A. Somorjai, Low Energy Electron Diffraction (LEED) Studies of Molecular Crystals: The Surface Structures of Vapor Grown Ice and Naphthalene, LBL-3558, Dec. 1974.

Lee F. Donaghey, Principal Investigator

1. PHYSICAL AND REACTIVE SPUTTERING

a. Computer Simulation of Sputtering*

P. V. Mundkur and L. F. Donaghey

The sputtering yield from monocrystalline targets by impacting ions was studied by a computer simulation model.

The sputtering of monocrystalline copper by neon was studied to elucidate the dependence of the sputter yield on the form of the potential function describing the interaction between an incident neon ion and the copper target. Results of the simulation indicate that the variation of the sputtering yield with incident ion energy is dominated by the nature of the Ne^+-Cu interatomic potential function, and that the overall sputter rate correlates well with the theory of Magnuson.[1]

Data on the sputtering of single crystal copper was used to extract information about the potential function for Cu-Cu interactions in the energy regions over which the sputtering data was available. The Ne^+-Cu and Cu-Cu interaction potentials were so derived that the variation of the sputtering ratio for the three Cu crystal faces (111), (100) and (110) matched experimental data. In addition, the Cu-Cu interatomic potential was adjusted so that repulsive force contributions matched the experimental elastic moduli of copper. The derived potentials differed significantly from the Gibson-2 potential which has been used for Cu-Cu interactions in all previous sputter simulations. The above method for backing out information on interatomic potentials could prove useful in obtaining information on potenital functions at energies where information has thus far been lacking.

A computer simulation model was applied to calculate the sputter ratio of (100) Cu by 10 keV Ne^+ ions at incidence angles from 20° to 50° from the surface normal in the (110) plane. The calculation results show maxima and minima in the sputter ratio at incident angles which are in relative agreement with the experimental data of Onderdelinden. A submaximum in sputter yield was obtained near the 45° minimum. The peak was larger for Ne^+ sputtering than for Ar^+ sputtering of copper.

The use of computer simulation techniques offers opportunity to study the sputtering mechanisms in detail, and to gain fundamental understanding that can be applied to circumstances for which experimental data is not yet available.

*Abstracted from LBL-3172.

1. G. D. Magnuson and C. E. Carlston, J. Appl. Phys. 34, 3267 (1963).

b. Reactive Sputtering of Titanium Oxides*

Kenneth G. Geraghty and Lee F. Donaghey

Reactively sputter deposited titanium dioxide has potential application as a corrosion and wear resistant coating in coal gasification reactors and in hot-press environments. The sputter deposition of titanium oxides was studied by reactively sputtering titanium in an oxygen-argon rf plasma with oxygen mole fractions in the range 0 to 0.15 and bias voltages in the range of 1 to 2 kV. Deposited titanium oxide films formed at various plasma oxygen compositions were characterized for density, deposition rate, electron diffraction characteristics and uv, visible and ir absorbance. The deposition rates of the amorphous films varied from 1 to 10 Å/sec, with a sharp transition occurring at a critical mole fraction of oxygen in the plasma equal to 0.007. A similar trend was noted for other film properties.

The effect of target oxidation on deposition parameters was concurrently investigated, and transient and steady-state behavior of the reactive sputter process were correlated with film properties. The critical oxygen mole fraction in the plasma necessary for the initiation of target oxidation was found to be independent of pressure. The sputtering rate reached a maximum at an oxygen mole fraction 0.002. When an oxide of finite thickness was formed on the target at high oxygen mole fraction the sputtering rate was significantly reduced.

Models for target oxidation based on a transient logarithmic growth law and an exponential dependence of the overall sputtering rate on oxide thickness are explored. From the model it is shown that a finite, steady-state target oxide thickness required that y exceed a critical value. The experimentally observed critical threshold for target oxidation is a consequence of the competing oxidation and sputter etching processes, and of the higher sputter yield of the metal as compared to that of the oxides. The application of titanium oxide films for protective coating was explored.

*Abstracted from LBL-2788.

2. CRYSTALLIZATION

a. Liquid Phase Epitaxial Crystal Growth from Solution*

Pei-shiun Chen and Lee F. Donaghey

Thermochemical properties of solvent systems

are important in solution crystal growth processes. Together with forced convection the solvent properties influence the perfection and yield of single crystals. In this study, the fluid flow conditions produced by axial rotation and the properties of PbO-BaO-B_2O_3 solvents were studied to determine optimum conditions for the solution crystal growth of rare-earth garnets by the Czochralski method and by liquid phase epitaxy on axially rotating substrates.

Fluid flow patterns were studied with time-lapse photography using the dye-tracer method for flow delineation. Simulation of solution crystal growth and Czochralski crystal growth revealed that the convection currents induced by crystal rotation in a stationary and slowly co-rotating crucible provided for best mixing conditions at the crystallization interface. The boundary layer beneath the crystal became more uniform and thinner as the crystal rotation rate increased. The dimensions of the crystal boundary-layer cell and overall mixing rates were reduced by counterrotation of the crucible. The overall convective mixing rate was lowest for co-rotation of the crystal and crucible with comparable angular velocities.

The mixed solvent system $PbO_x(BaO \cdot B_2O_3)_{1-x}$ was investigated theoretically and experimentally for conditions allowing congruent saturation of rare-earth magnetic garnets and efficient liquid phase epitaxial growth. High quality $Eu_1Er_2Ga_{0.7}Fe_{4.3}O_{12}$ films were obtained from solvents containing 10 mole % garnet oxides and 26 mole % PbO.

*Abstracted from LBL-2284.

3. CHEMICAL VAPOR DEPOSITION

a. Vapor Phase Etching Kinetics of GaAs*

Ronald H. Bissinger and Lee F. Donaghey

Surface preparation by vapor phase etching prior to successful chemical vapor deposition of epitaxial compound layers is of significant industrial importance for electronic device processing. For electronic applications of gallium arsenide in electroluminescence and photovoltaic devices, it is necessary to devise vapor phase etching processes which produce a smooth, damage-free surface. Although the thermal etching of (111) GaAs has been studied previously,[1] the thermal etching and chemical vapor etching of the more industrially important (100) GaAs surface has not been previously studied.

Thermal vaporization of (100) GaAs was studied in the temperature range from 900 to 1050°K. Two surface reaction kinetic regimes were found from an Arrhedius plot of the free evaporation rate. At temperatures above 1000°K the apparent activation enthalpy of vaporization was 72.0 kcal/mole, while at lower temperatures the apparent activation enthalpy was 14.0 kcal/mole. The activation enthalpy for the high temperature regime agrees closely with that for (111) GaAs, but the overall vaporization rate was larger by a factor of ~ 8.

Vapor phase etching of (100) GaAs in HCl-H_2 mixtures was found to have a reaction order of near unity, and to yield an apparent activation energy of zero with respect to HCl. For the overall reaction

$$GaAs_{(s)} + HCl_{(v)} \rightarrow GaCl_{(v)} + 1/2\ H_{2\ (v)} + 1/4\ As_4$$

the etching reaction rate could be approximated by the expression

$$r_{HCl} = (9.4\times10^{-6})(p_{HCl})^{1.11}$$

where r_{HCl} has units of mg-cm^{-2}-sec^{-1} and p_{HCl} has units of μmHg and is valid for $930° < T < 980°K$ and $0 < p_{HCl} < 135$ μmHg. A mechanism is proposed in which the rate limiting step is the absorption of molecular HCl on ledge sites of the GaAs surface. The addition of H_2 to the vapor phase hindered the HCl etching reaction with GaAs by shifting the dissociated HCl adsorption equilibrium and reducing the absorbed Cl concentration. The rate limiting step proposed is then the reaction between absorbed Cl and Ga.

*Abstracted from LBL-2783

1. C. Lou, Ph.D. thesis, LBL-19685, 1970.

b. Modeling of a Vertical Cylinder Reactor for Chemical Vapor Deposition of Silicon

Charles W. Manke and Lee F. Donaghey

The barrel, or vertical cylinder, chemical vapor deposition reactor has significant potential for scale-up of the industrial processing of integrated circuits and solar cells. Recently several designs of vertical cylinder reactors have been introduced into commercial use, yet little experimental results of operating characteristics or analysis of optimum design for enhancing deposition rate uniformity has yet appeared in the literature.[1] In this study the vertical cylinder reactor is studied by numerical simulation and analytical methods to determine design characteristics yielding optimum deposition uniformity of silicon from SiH_4 and chlorosilanes. The effect of process variables such as inlet flow rate distribution and reactor design variables such as susceptor tilt angle are studied with respect to deposition rate non-uniformity and deposition yield. Results of analytical studies will be compared with recently completed experimental measurements obtained using a commercial model reactor.

A numerical simulation of the reactor is under development utilizing methods developed by Spalding for solution of transport equations for simultaneous mass, heat and momentum.[2] The method is based on a six-node finite difference calculation, and on a marching integration, allowing for spatial variations in transport coefficients.

Parallel analytical solutions for the deposition rate distribution are based on fully-developed laminar flow within the reactor. This study should provide a basis for the design of large scale vertical cylinder reactors for chemical vapor deposition of silicon.

---

1. E. Fujii, H. Nakamura, K. Haruna and Y. Koga, J. Electrochem. Soc. 119, 1106 (1972).
2. D. B. Spalding, "A General Computer Program for Two-Dimensional Boundary Layer Problems," Dept. of Mech. Eng., Imperial College, London, Sept. 1973.

c. Vapor-Solid Equilibria of Compound Semiconductor Diffusion Systems

Steven R. Styer and Lee F. Donaghey

Vapor-solid phase equilibria of compound semiconductor diffusion systems is under study using atomic absorption spectroscopy to measure the composition of the vapor phase. Currently there is limited information available for the design of high temperature diffusion systems for controlling the group IIB impurity distribution in compound semiconductors, and few non-destructive methods for monitoring such processes. Optical absorption spectroscopy is currently being studied for the measurement of phase equilibria and for use in controlling diffusion systems for introducing Zn or Cd into group III arsenides and phosphides.

A high temperature optical system has been constructed for the experimental measurement of optical density as a function of temperature and spectral wavelength. The system uses a Heath EU 700 monochrometer and deuterium lamp for measurements over the 2000 to 4000 Å range. Measurement of optical density is facilitated with a solid-state electrometer amplifier and logarithmic current amplifier. Vapor pressures in T-shaped, two zone experimental cells are measured by comparing optical density measured at different wavelengths and temperatures with the optical densities of samples with known vapor pressures.

Current investigations are directed in particular to systems involving GaAs, GaP, As, P, Zn and Cd. Optical densities of the pure components have been obtained. Systems currently under study include Ga-As-Zn, Ga-As-Cd, Ga-P-Zn and Ga-P-Cd. The results will provide vapor phase equilibria for use in designing closed-tube and open-tube diffusion systems. The methods developed will have general applicability to diffusion processes involving other semiconducting materials.

d. Heteroepitaxial Growth of GaAs for Solar Cell Application

Alice L. Lin and Lee F. Donaghey

The growing demand for electrical energy and the increasing shortage of the commonly used materials (such as petroleum, fossil fuels and natural gas) for electric power generation have aroused the interest for the development and production of solar cells. Wysocki and Rappaport[1] have calculated the maximum efficiency attainable for photovoltaic conversion of solar to electrical energy for different materials at different temperatures. Their result shows that materials with energy gaps in the vicinity of 1.5 eV at room temperature promise to have the highest possible efficiency. Hence GaAs, with room temperature band gap of 1.43 eV, is one of the most promising materials for solar cells. Besides its high efficiency, GaAs solar cells also have some other attractive properties: negligible environmental degradation. Its efficiency is relatively insensitive to temperature as compared to the narrower band gap materials, such as Si.

The disadvantage of using GaAs solar cells for terrestrial applications is the high production cost. One major reason for the current high cost is that presently available GaAs solar cells are fabricated on the expensive GaAs single crystal substrate. Hence finding a suitable low cost substrate on which to grow GaAs thin films is the most important means with which to obtain stable, high efficiency and yet low cost GaAs solar cells.

In recent years, the development of high speed surface acoustic wave device technology offers the great achievement of heteroepitaxial growth of GaAs on insulator substrates, such as sapphire and spinel.[2,3] However, heteroexpitaxial growth of GaAs on metal or other cheaper glasses has seldom been studied yet. The purpose of this study is to develop high efficiency GaAs solar cells on alternate, low cost substrate. The film will be grown by a chemical vapor deposition process involving the decomposition of trimethyl gallium and arsine in an H_2 atmosphere. This method has two advantages: First, it requires only one hot temperature zone for deposition. And secondly, it is free of any halide. Consequently it greatly reduces the possible etchback[4] and resulting impurity concentration. Growth of GaAs thin films on different substrates such as metals (Mo, W, etc.) and glasses will be investigated systematically. The grown films will be examined with respect to crystal growth (nucleation and growth rate), crystal morphology (orientation, dislocation, grain size and their relations to the film thickness) and electrical properties (carrier concentration, mobility, lifetime and imperfection levels). Photovoltaic devices will be fabricated for solar conversion by a Schottky barrier approach. I-V characteristics, short circuit current, open circuit voltage, solar efficiency, capacitance and spectral response of the device will then be studied.

---

1. J. J. Wysocki and P. Rappaport, J. Appl. Phys. 32, 371 (1960).
2. A. C. Thorsen and H. M. Manasevit, J. Appl. Phys. 42, 2519 (1971).
3. C. C. Wang, F. C. Dougherty, P. J. Zanaucchi, and S. H. McFarlane III, J. Electrochem. Soc. 121, 571 (1972).
4. Ronald H. Bissinger, Vapor Phase Etching Kinetics of GaAs, M.S. thesis, LBL-2783, June 1974.

e. Phase Equilibria and Kinetics for the Chemical Vapor Deposition of $GaP_{1-x}N_x$.

Carlos Figueroa and Lee F. Donaghey

Isoelectronic substitutional defects play a significant role in increasing the opto-electronic energy conversion efficiency in indirect band gap semiconductors. The controlled addition of nitrogen to gallium phosphide has allowed the fabrication of green-light emitting diodes with the highest quantum efficiency so far reported.[1] The nitrogen occupies phosphorus substitutional sites in the lattice and provides a powerful radiative transition at an energy close to that of the indirect band gap. Optimum performance of GaP in electroluminescence devices requires a high concentration of isoelectronic traps.

Recent studies of the chemical vapor deposition of $GaP_{1-x}N_x$ have shown an anomalously high solubility of nitrogen, obtained by imposing a large excess partial pressure of ammonia during epitaxial growth.[2] In the present study, an analysis of the chemical vapor deposition process has shown that the epitaxial growth process is kinetically limited by the decomposition of ammonia and that excess GaN should precipitate in the $GaP_{1-x}N_x$ solid solution. This analysis has provided a means for predicting the rate kinetics for epitaxial growth, and indicates that the published estimates of GaN solubility in GaP[3] are too low by a factor of 3. The analytical results obtained by numerical simulation will be utilized in experimental studies of gas-solid reaction kinetics in the Ga-N-P-Cl-H system. This study should provide a basis for efficient chemical vapor deposition of nitrogen-substituted gallium phosphide.

---

1. R. A. Logan, H. G. White and W. Wiegmann, Appl. Phys. Letters 13, 139 (1968).
2. G. B. Stringfellow, M. E. Weiner and R. A. Burmeister, to be published.
3. G. B. Stringfellow, J. Electrochem. Soc. 119, 1780 (1972).

4. SOLID-STATE ELECTROCHEMISTRY

a. Solid-State Electrochemical Studies of Compound Semiconductors

Timothy J. Anderson and Lee F. Donaghey

Compound semiconductors of the group IIIB and V elements are known to offer significant advantages over elemental semiconductors in opto-electronic applications. Electroluminescence devices, injection lasers and photovoltaic cells fabricated for III-V compounds have shown exceptionally high quantum and overall efficiencies for electro-optical energy conversion. Large scale, economic application of these materials, and optimization of opto-electronic devices through solid solution formation require accurate determinations of phase equilibria and thermodynamic properties for use in optimizing the materials and device fabrication processes.

This research project concerns the measurement of thermodynamic properties of III-V compounds and solid solutions by means of solid-state electrochemical methods utilizing CaF_2 as a solid electrolyte. Previous work by Samokhval and Vetcher have shown that CaF_2 can be used in solid-state electrochemical studies to temperatures as low as 720°K.[1] Currently, the free energy of formation of GaSb is under study utilizing electrodes of $Ga_{(\ell)}$, GaF_3 and GaSb, Sb, GaF_3. Also under study are the range of applicability of solid-state electrochemical methods to III-V compound solid solutions, and the compatibility of materials for high-temperature galvanic cells.

---

1. V. V. Samokhval and A. A. Vetcher, Zh. Fiz. Khim. 42, 644 (1968).

5. RESEARCH PLANS FOR CALENDAR YEAR 1975

Lee F. Donaghey

Reactive sputtering of titanium carbide, and of phases in the Ti-C-O system will be studied toward developing corrosion and wear resistant coatings for coal gasification reactors. An rf diode sputtering system will be used with a polycrystalline Ti target. Phases deposited will be characterized by electrical, optical and diffraction methods.

The chemical transport crystal growth of uranium compounds will be studied to determine optimum conditions and growth rates of single crystals by chemical transport. A diffusion-controlled model for transport will be studied by computer simulation, utilizing recently determined thermodynamic data, and vapor pressures that will be measured by optical absorption spectroscopy.

The properties of polycrystalline GaAs solar cells will be studied in relation to growth conditions and substrate properties. Hetero-epitaxial relationships to metallic and glassy substrates will be studied by diffraction techniques.

6. 1974 PUBLICATIONS AND REPORTS

Lee F. Donaghey and Associates

Journals

1. L. F. Donaghey and Raymond Pong, Oxygen Transfer Kinetics Between Ga-Ga_2O_3 Electrodes and the Solid Electrolyte Calcia-Stabilized Zirconia, J. Electrochem. Soc. 121, 506 (1974) (LBL-1892).

2. Lee F. Donaghey, A Course in Electronic Materials: Process Technology of Solid-State Materials and Devices, Chem. Engr. Ed. Fall 1974, p. 164 (LBL-3106).

3. L. F. Donaghey and S. A. Shaikh, Tank-Mixing Methods for producing Time-Varying Reactive Gas Mixtures, J. Crystal Growth, 26, 69 (1974) (LBL-2298).

Papers presented

1. L. F. Donaghey, Superalloys: New Materials for Dentistry, Chicago Dental Society 109th Midwinter Meeting, Chicago, Ill., February 8-9, 1974.

2. T. T. Shih and L. F. Donaghey, Applications of Velocity-Selective Freeze-Pushing to the Separation and Characterization of Airborne Solid Particulate Matter in Air Pollution Samples, 1974 National AICHE Meeting, Tulsa, Oklahoma, March 13, 1974.

3. L. F. Donaghey, Welcoming Remarks and Introduction, 2nd Annual Electronic Materials Symposium, Palo Alto, California, March 21, 1974.

4. L. F. Donaghey, Solid State Electrochemical Methods for Thermodynamic Studies of III-V Compound Semiconductor Alloys, Abstract 143, 145th Meeting of the Electrochemical Society, San Francisco, California, May 13, 1974.

5. S. A. Shaikh, H. K. Chou and L. F. Donaghey, Vapor Phase Etching of GaAs in HCl-AsH_3-H_2, Abstract 151, 145th Meeting of the Electrochemical Society, San Francisco, California, May 14, 1974.

6. L. F. Donaghey, Crystal Growth on Rotating Surfaces: Hydrodynamics Fluid Flow, and Solvent Selection for LPE Growth of Garnet Films, Northern California Crystal Growers Meeting, Palo Alto, California, October 30, 1974.

LBL reports

1. Ronald Henry Bissinger, Vapor Phase Etching Kinetics of GaAs, (M.S. thesis), LBL-2783, June 1974.

2. Kenneth George Geraghty, Reactive Sputtering of Titanium Oxides: Target Oxidation Phenomena and Thin Film Characterization, (M.S. thesis), LBL-2788, Sept. 1974.

3. Pei-shiun Chen, Fluid Flow Patterns and Solvent Selection for Liquid Phase Epitaxial Crystal Growth on Rotating Crystals, (M.S. Thesis), LBL-2284, Dec. 1974.

4. Pravin Vasudeva Mundkur, Computer Simulation of Sputtering, (M.S. thesis), LBL-3172, Dec. 1974.

C. ELECTROCHEMISTRY

Charles W. Tobias, Principal Investigator

1. FUNDAMENTAL STUDIES OF IONIC MASS TRANSPORT

a. Distribution of Mass Transport Rates Along Parallel Plane Electrodes in Forced Convection

Uziel Landau and Charles W. Tobias

The distribution of ionic mass transport rates along a segmented electrode embedded in the wall of a flow channel has been measured by the limiting current technique.[1] Copper was electrodeposited from acidified copper sulfate solutions; local transport rates were determined from segmental currents recorded simultaneously at nine different locations along the electrode. Flow rates and transport properties of the solutions were varied over the ranges:

$$400 < Re < 125{,}000 \ ,$$

$$1200 < Sc < 25{,}100 \ .$$

In the laminar flow region ($400 \leq Re \leq 2500$), in agreement with the Levegue equation, local transport rates are correlated by:

$$Sh_x = 1.247 \left[Re \ Sc \ \frac{d_h}{x} \right]^{0.331}$$

Data in the turbulent region shown in Fig. 1, and measured locally at the downstream end of the mass transport section are best represented by two separate correlations: For $2800 < Re < 12{,}000$

$$Sh_L = 0.0129 \ Re^{0.872} \ Sc^{0.333}$$

and for fully developed turbulent flow,

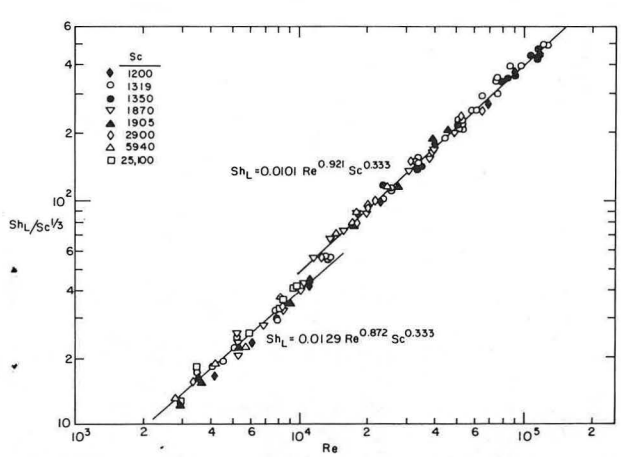

Fig. 1. Fully developed mass transfer rates in the turbulent regime. (XBL 744-6011)

$$12{,}000 < Re < 125{,}000$$

$$Sh_L = 0.0101 \ Re^{0.921} \ Sc^{0.333} \ .$$

These results indicate that the decay of turbulent eddies near a solid wall is proportional to the cube of their distance from it. The exponent on the Re number points towards a Stanton number dependence on $\sqrt{f}$, as suggested by Levich, rather than towards linear dependence, as implied by the Chilton-Colburn analogy.

The local transport rates in the entrance region of the mass transport section are proportional to the inverse cube root of the distance from the leading edge as predicted by theory. In the ranges of Re and Sc numbers investigated, the length of the entrance region x_e is shown to be independent of Sc:

$$(x_e/d_n) = a \cdot Re^b \ .$$

Observations were made on the effect of flow on the morphology of the deposit for flat electrodes and for deposition on and around single protrusions. Preferential deposition was observed on protrusions which were small with respect to the boundary layer thickness. Larger protrusions resulted in wake-shaped deposits, the size and form of which depended on the flow rate and the geometry of the protruding element.

---

1. Uziel Landau and Charles W. Tobias, Flow Circuit for Ionic Mass Transfer Studies at High Flow Rates, IMRD Annual Report for 1970, UCRL-20500, April 1971, p. 39.

b. The Effect of Flow of Electrolyte on Surface Morphology in the Electrodeposition of Metals

Eric J. Carlson and Charles W. Tobias

The influence of solution side transport on the development of morphology of electrodeposited metal near surface imperfections was observed using roughness analysis, optical-scanning and electromicroscopy, and coulometric analysis of current distribution.[1] The effects of size and shape of protruding imperfections (hemispheres and cylinders) were interpreted at various current/limiting current ratios and Reynolds number (see Fig. 1).

In turbulent bulk flow ($20{,}000 < Re < 50{,}000$) past a planar electrode, distinct wakes appear in the copper deposit around protrusions when $H > 100$ microns and $i/i_L > 0.9$. The average current density within the wake is roughly twice that outside the wake.

The formation of rough deposit in the wake is attributed to a combination of: 1) increased mass transfer rate per unit area, and 2) three-

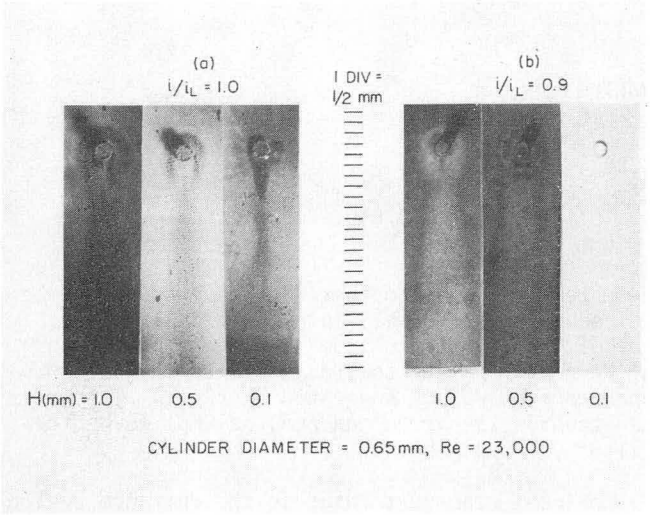

Fig. 1. The effect of the fraction of the limiting current (i/i_L) and cylinder height on the form of the wake for a 0.65 mm diameter wire. (XBB 748-5448)

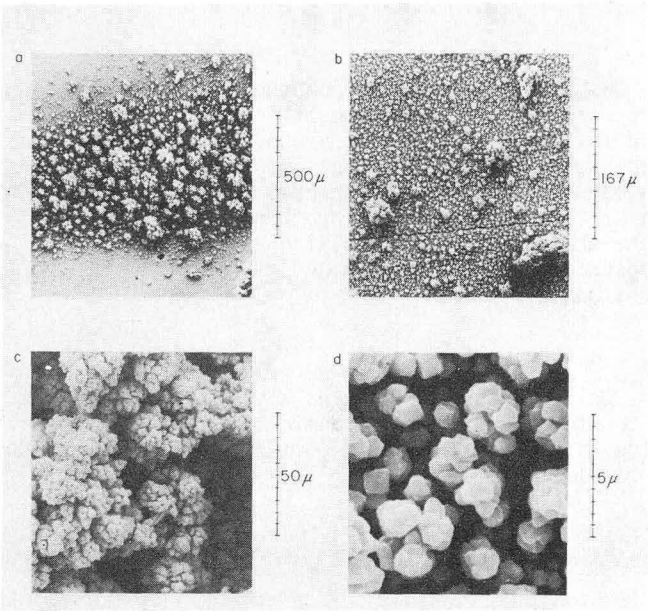

Fig. 2. Porosity of the deposit in- and outside the wake. (Re 628,000, $\langle i \rangle$ = 10.8 mA/cm^2, $\langle C/cm^2 \rangle$ = 13.0, η = -350 mV)

a) Deposit in the tip of the wake.
b) Deposit outside the wake.
c) Deposit in the center of the far-wake.
d) Deposit outside the wake. (XBB 7410-6946)

dimensional growth of the surface roughness elements within the wake as a result of the thinner boundary layer. Figure 2 illustrates the cluster growth within the wake (three-dimensional growth) and the columnar growth outside (one-dimensional).

---

1. Eric J. Carlson, Uziel Landau, and Charles W. Tobias, The Effect of Electrolyte on Surface Morphology in the Electrodeposition of Metals, IMRD Annual Report for 1973, LBL-2299, 1973, p. 36.

2. ELECTROLYSIS AT HIGH CURRENT DENSITIES

a. Periodic Phenomena During High Current Density Anodic Dissolution of Copper

John F. Cooper, Rolf H. Muller, and Charles W. Tobias

Results of an experimental study of anode potential oscillations observed during copper dissolution have been interpreted, and a model for the oscillations has been proposed.

The anode potential oscillations (10-30 V amplitude) occur during the galvanostatic dissolution of copper in chlorate electrolyte at current densities from 0.3 to 150 A/cm^2. Frequency increases over this range from 10^{-3} to 10^3 Hz. Frequency and amplitude are only weakly dependent on mass transport conditions (Re=200-10,000 in channel flow), on electrolyte pH (1.4-11), and on electrolyte temperature (4-80°C). The rise and fall of anode potential reflects alternate growth and destruction of an adherent cuprous oxide surface film.

During growth of the surface film, current flows predominantly by the migration of cations through the film. The observed relation (Fig. 1) between mean field strength (E) and current density (I) may be expressed by the equation

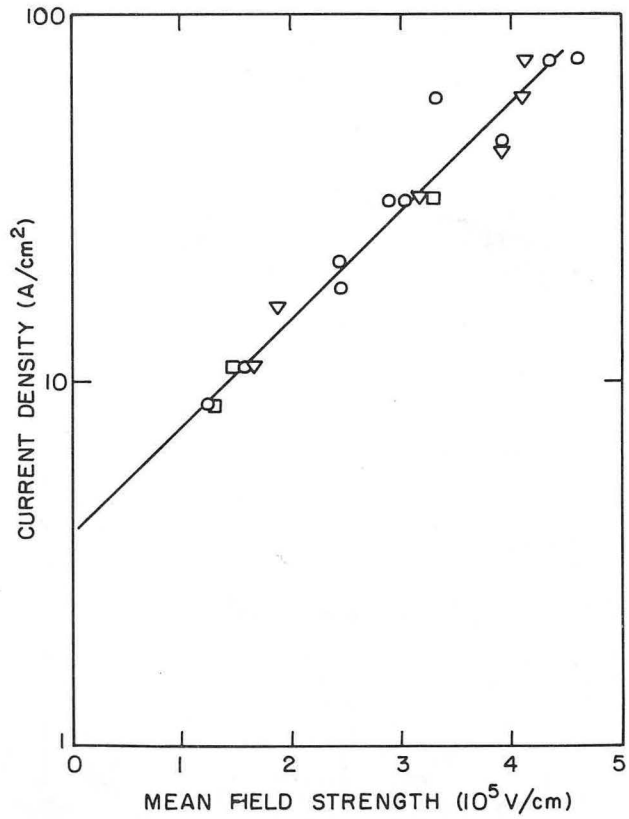

Fig. 1. Logarithmic dependence of current on mean field strength for transpassive films formed during copper dissolution. Cu/2F $NaClO_3$; stagnation point flow system; ○, Re=700; □, Re=1300; △, Re=1450. (XBL 749-7142)

$$I = A \exp (BE) ,$$

where A and B are empirical constants. This relation may be derived from the theory of high field ionic conduction in a crystalline matrix, which has been found applicable to a variety of anodic oxide films.[1] The value of B derived from Fig. 1, 6.8×10^{-6} V/cm, is close to that determined for the transpassive films associated with the electropolishing of copper (7.8×10^{-6} V/cm)[2].

The breakdown of potential is believed to result from a field-dependent electronic insulator-to-conductor transition in the transpassive film. Such transitions have been observed with dried specimens of the transpassive films produced during dissolution. The introduction of parallel paths of high electronic conductivity in the film lowers the mean field strength below the level necessary to sustain ionic current and, therefore, film growth and repair. Electronic current flows until the bulk of the layer has been dissolved or undermined by direct (active) dissolution of the copper substrate. Film growth is then restored, and the cycle begins anew.

---

1. M. J. Dignam, Mechanisms of Ionic Transport through Oxide Films, in The Anodic Behavior of Metals and Semiconductors--Oxides and Oxide Films, Vol. 1, edited by J. Diggle (Marcel Dekker, New York, 1972) Chap. 2.
2. K. Kojima, A Study of the Mechanism of the Electropolishing of Copper (Ph.D. thesis, University of California, Berkeley), LBL-140, Feb. 1972.

b. Current Distribution in Electrochemical Machining

James B. Riggs, Rolf H. Muller, and Charles W. Tobias

In the present state of electrochemical machining (ECM) technology an empirical "trial and error" procedure is required for the design of the tool piece (cathode) shape which will yield the desired metal removal in the workpiece. Based upon previous work[1,2] on high-rate anodic dissolution a mathematical model for ECM is being developed which will determine the proper tool piece geometry. This model is based upon a numerical solution of Laplace's equation with electrode overpotentials which are modeled as functions of temperature, electrolyte concentration, and electrolyte gas content.

As a starting point for the development of this model, several nonsteady-state current distribution problems have been solved:

a) The development of the profile of a "stopped off" copper electrode as anodic dissolution progresses under primary distribution (i.e. current independent overpotential) as well as when linear overpotential is imposed.

b) As a first attack on the "surface memory" problem the progressive dissolution of a copper anode of sinusoidal shape has been subjected to analysis. Here a planar cathode is advanced toward the anode during dissolution while the applied potential is maintained constant. The inter-electrode distance progressively decreases to an equilibrium gap, while the amplitude of the wave shape of the anode diminishes. Figure 1 shows the change of anode profile with time; evaluation of the amount of copper removed simply requires use of the appropriate value of current at each time step.

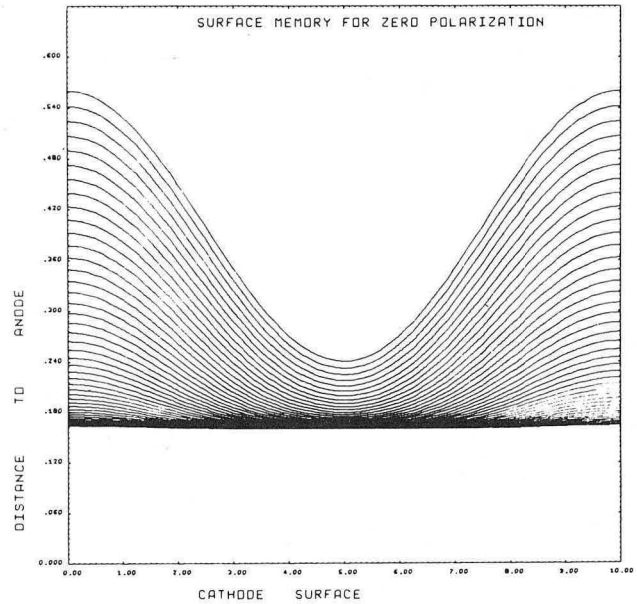

Fig. 1. Progressive leveling of initial sinusoidal copper surface upon anodic dissolution. Anode is advanced toward parallel planar cathode. Applied constant voltage, 100 V; conductivity, 0.1 Ω^{-1} cm^{-1}; equilibrium gap, 0.16 cm. (XBL 749-1511)

---

1. Raul E. Acosta, Transport Processes in High Rate Electrolysis (Ph.D. thesis, University of California, Berkeley), LBL-2242, May 1974.
2. R. N. Fleck, D. N. Hanson, and C. W. Tobias, Numerical Evaluation of Current Distribution in Electrochemical Systems, UCRL-11612, Sept. 1964.

3. PHYSICAL PROCESSES IN ELECTROLYTIC GAS EVALUATION

a. Physical Processes in Electrolytic Gas Evolution

Ronald A. Putt and Charles W. Tobias

Nucleation site and frequency, bubble growth, residence time, size distribution and coalescence are being studied in the electrolytic generation of hydrogen on nickel surface over a range of current densities of practical interest.[1,2]

In 1 M KOH on a horizontal nickel cathode facing upward the average bubble size, after separation, ranges from 135 microns at 820 mA/cm^2 to 200 microns at 3.3 A/cm^2 and the size distribution is

Gaussian. As a result of longer residence time in the supersaturated region near the electrode, from a vertically mounted cathode the corresponding average diameters are 185 and 245 microns, respectively. Further, as shown in Fig. 1, at high current densities bubble coalescence leads to significant departure from Gaussian size distribution.

The ohmic voltage loss in the electrolyte depends both on the average volume fraction and on the spatial distribution of the gas phase. Therefore, the residence time on the surface and the velocity of rise, both size dependent, affect the energy efficiency of electrolytic hydrogen generators.

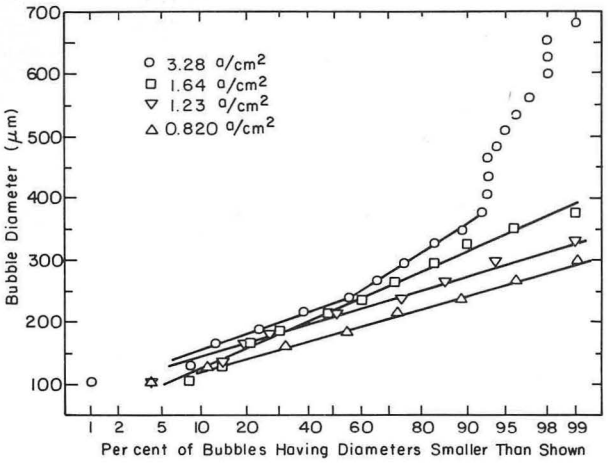

Fig. 1. Hydrogen bubble size distribution from a vertical nickel cathode in 1 M KOH.
(XBL 751-5499)

1. J. P. Glas and J. W. Westwater, Measurement of the Growth of Electrolytic Bubbles, Int. J. Heat Mass Transfer 7, 1427 (1964).
2. C. K. Bon, Supersaturation at Gas Evolving Electrodes (M.S. thesis) UCRL-19612, Sept. 1970.

4. ELECTROCHEMISTRY IN NONAQUEOUS SOLVENTS

a. Studies on the Practical Feasibility of the Electroreduction of Potassium

Oscar Chacon, Henry Law, and Charles W. Tobias

Potassium metal has been obtained in gram quantities by cathodic deposition at room temperature from 0.5-1.0 M solutions of KPF_6 or $KAlCl_4$ in propylene carbonate. Good quality deposits have been obtained from carefully purified electrolytes over periods of up to 150 hours and at current densities up to 30 mA/cm^2. Using a pair of potassium electrodes, cyclic deposition-dissolution was conducted over 150 hours without any evidence of deterioration of the solvent, or change in the character of the metal deposited (see Fig. 1).[1]

The electrolyte purification procedure required for these excellent results, however, is still very tedious and so far developed only for small (100-200 cc) batches. The practical feasibility of a process for the production of potassium according to the scheme proposed earlier[2] will depend, on the one hand, whether an economical method for electrolyte preparation can be devised, on the other, whether the solvent remains unattacked over practical (i.e., many months) electrolysis cycle periods.

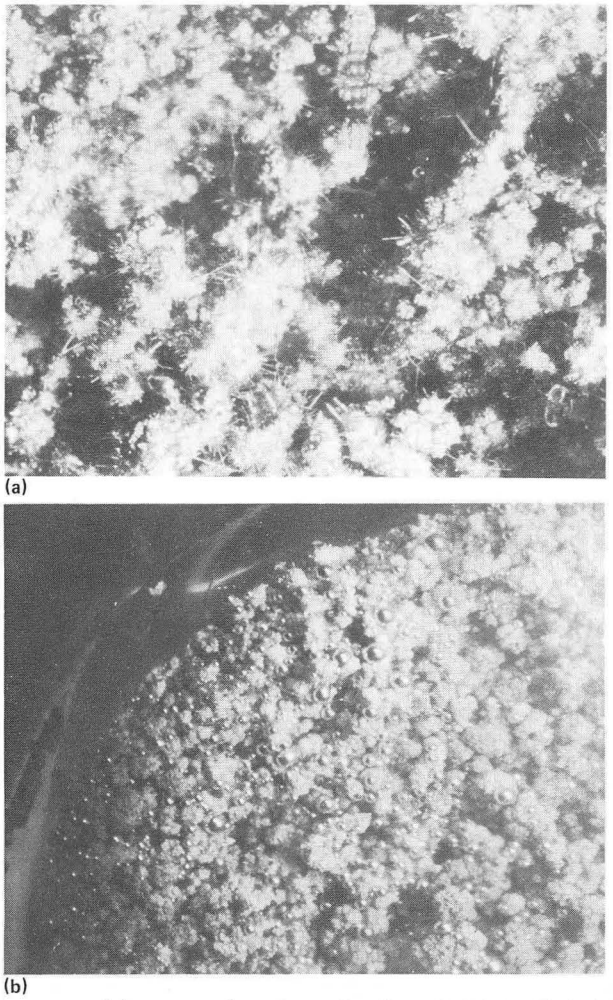

Fig. 1. (a) Potassium deposit from $KAlCl_4$ (0.5m) solution in PC. Current density: 1m A/cm^2. Temperature: 25°C. Duration of electrolysis: 65 hours. Magnification: X20.
(b) Potassium deposit from $KAlCl_4$ (0.5m) solution in PC. Current density: 1m A/cm^2. Temperature: 25°C. Duration of electrolysis: 160 hours. Magnification: X20. (XBB 7410-7180)

1. Oscar Chacon, Cathodic Reduction of Potassium in Propylene Carbonate Electrolytes (M.S. thesis, University of California, Berkeley), LBL-3542, Nov. 1974.
2. Charles W. Tobias and Jacob Jorne, Method of Production of Alkali Metals and their Alloys, U.S. Patent No. 3,791,945.

5. RESEARCH PLANS FOR CALENDAR YEAR 1975

Charles W. Tobias

Research on charge and mass-transfer processes which have a decisive role in determining the energy efficiency and capital cost in electrolysis and galvanic cells will include: a) elucidation of the role of electrolyte convection and of electric field on the morphology of metal phase formed by electrodeposition, b) experimental and theoretical study of the dynamics of growth (deposition) and recession (dissolution) of metal surfaces under conditions characteristic of practical applications in forming and shaping and in galvanic cells. Experimental techniques to be used include sectioned electrodes in a large-scale flow loop for the measurement of local current distribution, interferometry (see project under R.H. Muller) for the direct observation of boundary layers, and scanning electron microscopy and microphotography for the analysis of surface morphology. Realistic modeling of progress of surface changes will be pursued by computer implemented solution of the Laplace equation.

Study of physical processes involved in the electrolytic generation of gases aimed at improving energy efficiency will include: a) determination of bubble size distribution, frequency of coalescence, and surface coverage, and b) the measurement of effective resistance of gas-electrolyte emulsion as a function of distance from the electrode surface. Attempts will be made for the measurement of concentration fields around gas bubbles by interferometry.

Exploration of the practical feasibility of the newly proposed hydrogen generation scheme by combined electrolysis-thermal cycle will concentrate on the investigation of overpotential behavior of selected lower/higher oxide couples, which may be regenerated by thermal decomposition. It is an essential criterion for any further work on this proposed scheme to demonstrate fast kinetics of the positive electrode; only then will there be sufficient incentive to proceed to the investigation of the thermal decomposition loop.

To further the practical feasibility of ambient temperature processes for the recovery of alkali metals by electro-reduction, a) the propylene carbonate electrolyte preparation and purification procedures will be revised to achieve consistency and adaptability for large scale use, and b) current and energy efficiency measurements on potassium reduction, and development of practical design considerations, will also be initiated.

6. 1974 PUBLICATIONS AND REPORTS

Charles W. Tobias and Associates

Journals and patent

1. Jacob Jorne and Charles W. Tobias, Electrode Kinetics of the Alkali Metals in $AlCl_3$-Propylene Carbonate Solution, J. Electrochem. Soc. 121 (8) 994 (1974) (LBL-1111 Rev. 1).

2. Charles W. Tobias and Jacob Jorne, Method of Production of Alkali Metals and their Alloys, U.S. Patent No. 3,791,945, assigned to AEC.

3. Jacob Jorne and Charles W. Tobias, Conductance Studies of the Alkali Metal Chlorides in $AlCl_3$-Propylene Carbonate Solution, J. Phys. Chem. 78 (24) 2521 (1974) (LBL-1111 Rev. 2).

4. Jacob Jorne and Charles W. Tobias, Thermodynamics of Ion Solvation of the Alkali Metal Chlorides in $AlCl_3$-Propylene Carbonate Solution, J. Phys. Chem. 78 (25) 2576 (1974) (LBL-1111 Rev. 3).

LBL reports

1. Jacob Jorne and Charles W. Tobias, Thermodynamic Properties of the Alkali Metals in $AlCl_3$-Propylene Carbonate Solution, LBL-1111 Rev. 4, Aug. 1974 (submitted to J. Phys. Chem.).

2. Raul Acosta, Transport Processes in High Rate Electrolysis, (Ph.D. thesis), LBL-2242, May 1974.

3. Oscar Antonio Chacon, Cathodic Reduction of Potassium in Propylene Carbonate Electrolytes (M.S. thesis) LBL-3542, Nov. 1974.

4. Eric J. Carlson, Electrodeposition Around Protruding Surface Imperfections in Turbulent Flow (M.S. thesis), LBL-3175, Dec. 1974.

5. Frank R. McLarnon, Interferometry of Electrochemical Mass Transfer Boundary Layers (Ph.D. thesis), LBL-3500, Dec. 1974.

6. Frank R. McLarnon, Rolf H. Muller, and Charles W. Tobias, Surface Reflection Effects in Interferometry, LBL-3140, Dec. 1974.

7. Frank R. McLarnon, Rolf H. Muller, and Charles W. Tobias, Derivation of One-Dimensional Refractive-Index Profiles from Interferograms, LBL-3141, Dec. 1974.

8. Frank R. McLarnon, Rolf H. Muller and Charles W. Tobias, Interferometric Study of Transient Diffusion Layers, LBL-3550, Dec. 1974.

Papers presented and invited lectures

1. Charles W. Tobias, Current Distribution and Transport in Parallel Plane Electrode Structures, special opening lecture, 25th meeting of the International Society of Electrochemistry, Sept. 22-27, 1974, Brighton, Great Britain.

2. Frank R. McLarnon, Rolf H. Muller, and Charles W. Tobias, Light Deflection Errors in the Interferometry of Electrochemical Mass Transfer Boundary Layers, 145th meeting of the Electrochemical Society, May 12-17, 1974, San Francisco, Ca.

Rolf H. Muller, Principal Investigator

1. OPTICAL STUDIES OF ELECTROCHEMICAL INTERFACES

a. Interferometry of Electrochemical Mass Transfer Boundary Layers

Frank R. McLarnon, Rolf H. Muller and Charles W. Tobias

Electrolytic mass transfer boundary layers have been characterized by optical interferometry. Such layers are responsible for the limited output of most electrochemical reactors and a detailed understanding of boundary layers is essential for the design of electrochemical processes for the conversion and storage of energy or the preparation of chemicals and metals.

A traveling, doubly-emitting laser interferometer[1] has been employed to study the development of convective mass transport boundary layers associated with cathodic deposition of Cu onto horizontal electrodes from 0.1 M $CuSO_4$ in a flow channel of 1×2.54 cm cross-section. The experimental interferograms (fringe patterns) were converted to $CuSO_4$ concentration profiles by a computational analysis that has been developed previously[2] to take light-deflection due to refractive-index gradients as well as reflection from the electrode edge into account.

Laminar boundary layers have been investigated for two electrode orientations: cathode facing up and cathode facing down. At the downward-facing cathode, the mass transfer process is dominated by forced convection alone because a lower density liquid region (depleted electrolyte) is flowing above a higher density liquid (bulk electrolyte). The effect of electrolyte flow velocity on boundary layer thickness is illustrated by the experimental interferograms in Fig. 1. An increase in the electrolyte flow rate reduces the boundary layer thickness markedly. However, the pressure drop associated with the higher flow rate, that results in higher pumping costs, can outweigh the advantage of the resulting higher current density.[3]

The steady-state boundary layer thicknesses and interfacial concentrations derived from the interferograms of the downward-facing cathode show good agreement with those predicted by the heat transfer correlation of Norris and Streid.[4] (Fig. 2, solid line) At the upward-facing cathode, the mass-transfer process is greatly accelerated by the superposition of natural convection on the forced convection flow field. (Fig. 2, dashed curves) This effect becomes visible after an induction period of about 20 sec. The location downstream from the cathode leading edge where the onset of natural convection effects is apparent has been correlated with a critical Rayleigh Number.

An alternate method of thinning the boundary layer consists in placing small obstacles on or near the electrode surface to promote local turbulence in an otherwise laminar stream. The experimental interferograms in Fig. 3 illustrate the boundary layer thinning caused by local turbulence at Re=1500 downstream of a triangular prism attached to the cathode surface. 1.5 cm downstream from the obstacle, the Nernst boundary layer thickness is reduced from 0.25 to 0.08 mm. Bulk turbulent flow of Re=2790 would be required to accomplish the same thinning. 12.5 cm from the obstacle, the original boundary layer is restored.

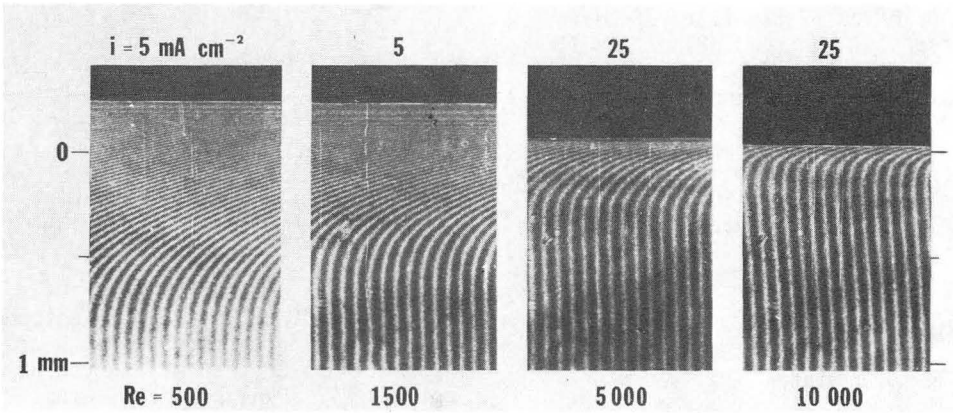

Fig. 1. Experimental interferograms showing the effect of electrolyte flow velocity (Re=500 to 10,000; 3.5 to 70 cm/s) on steady-state boundary layer thicknesses for pure forced convection 50 cm downstream from leading edge. Current densities 5 and 25 mA/cm^2. Ordinate: distance from true (undistorted) location of cathode surface. (XBB 748-5798)

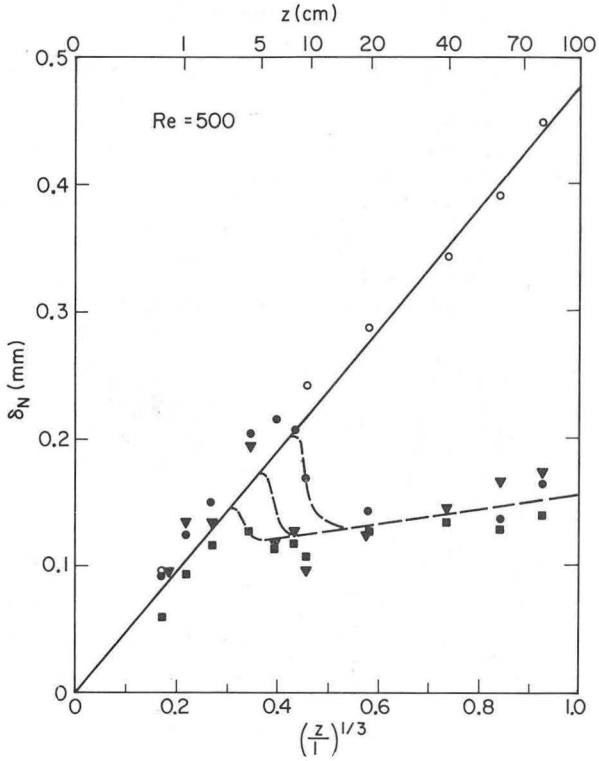

Fig. 2. Variation of Nernst boundary layer thickness δ_N with distance z from leading edge at Re=500 (3.5 cm/sec) derived from experimental interferograms. Effect of natural convection (L=100 cm, length of electrode). Open symbols, ____, absence of natural convection (cathode facing down). Solid line, Norris and Streid correlation.[4] Filled symbols, - - -, presence of natural convection (cathode facing up). ○● i = 2.0, ▼i = 3.8, ■ i = 6.1 mA/cm^2.

(XBL 7411-8224)

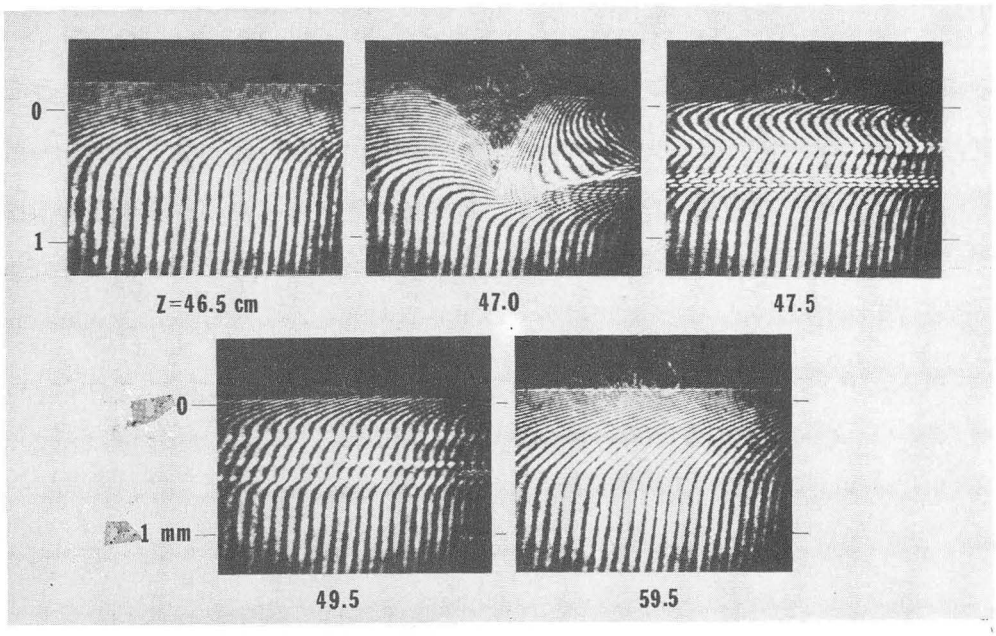

Fig. 3. Experimental interferrograms of the effect of a 0.76 mm high prismatic turbulance inducer of triangular cross-section on the boundary layer, shown 0.5 cm upstream of the obstacle, at the obstacle and 0.5, 2.5, 12.5 cm downstream of it. Electrolyte flow from left to right. (XBB 7411-8126)

---

1. K. W. Beach, R. H. Muller and C. W. Tobias, Rev. Sci. Instr. 40, 1248 (1969).
2. F. R. McLarnon, R. H. Muller and C. W. Tobias, IMRD Annual Report for 1973, LBL-2299, p. 42.
3. R. E. Acosta, R. H. Muller and C. W. Tobias, IMRD Annual Report for 1972, LBL-1400, p. 39.
4. R. H. Norris and D. D. Streid, Trans, ASME 62, 525 (1940).

b. Ellipsometry of Surface Layers

Craig G. Smith and Rolf H. Muller

The unique capabilities of our fast, automatic ellipsometer[1] has made in situ optical observation of electrochemically produced surface layers on metals possible during their formation (growth

rates up to about 2.5 μ per second). In contrast to the conventional ellipsometry of static or slowly-changing films, transport processes occur at significant rates under these growth conditions and the question arises, what the effect of the resulting boundary layers on the ellipsometric measurement is.[2] In addition, we are interested in whether ellipsometry could be used for measuring mass transport boundary layers that are too thin (<30μ) for quantitative observation by interferometry.

Calculations of the ellipsometric phase parameter, Δ, for copper deposition-boundary layers of parabolic and linear concentration profiles are given in Fig. 1. Over the thickness range of typical electrochemical boundary layers (1 to 100μ; e.g., 23μ for Re=22,000[3]) the ellipsometer has been found to be sensitive to the concentration difference across the boundary layer but not to its thickness. Also, the precise functionality of the concentration profile does not seem to greatly affect the ellipsometer measurement: results for a linear profile (dashed curve) differ only slightly from those for a parabolic profile (solid curves) in the lower thickness range and agree exactly for larger thicknesses (triangles). The computations have also shown that, for purposes of ellipsometry, boundary layers are not well represented by a homogeneous liquid layer of properties intermediate between the limits of an inhomogeneous layer.

An experimental test has confirmed the above computations, deposition of Cu from 0.1 M $CuSO_4$ at 16.7 mA/cm^2 at Re=990 resulted in a measured change in Δ of 1.00°, while a value of 1.02° would have corresponded to the expected average surface concentration of 0.044 M. Further tests are in progress. The principal difficulty in their conduct arises from a roughening of the electrode surface due to the metal deposition.

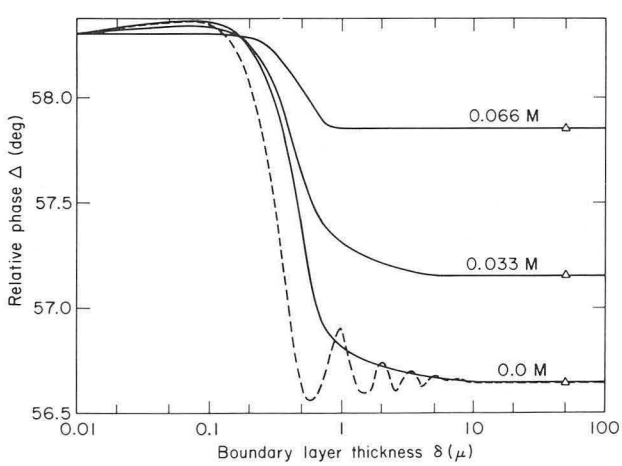

Fig. 1. Effect of mass transport boundary layers of thickness δ, resulting from the deposition of Cu from 0.1 M aqueous $CuSO_4$, on the ellipsometric parameter Δ. Interfacial concentration indicated along curves. —— parabolic concentration profiles, ----, Δ linear concentration profiles. Refractive index of substrate 0.93-2.39 i.
(XBL 751-2001)

In an extension of a previous study,[4] the anodic film formed during the dissolution of copper in sodium chlorate that is believed to be responsible for electrical oscillations of large amplitude, has been investigated. The optical properties of such films has been found to be strongly affected by the current density of dissolution and, to a lesser extent, by the flow rate of the electrolyte. The measurements cannot be explained by the formation of one or two homogeneous layers of different porosity but can be interpreted by the assumption of an inhomogenous layer with porosity varying continuously in the direction normal to the surface. Independent evidence for this model is being sought.

---

1. H. J. Mathieu, D. E. McClure and R. H. Muller, Rev. Sci. Instrum. 45, 789 (1974).
2. R. H. Muller, Principles of Ellipsometry in Advances in Electrochemistry and Electrochemical Engineering, Vol. 9, R. H. Muller, ed. Wiley-Interscience, New York, 1973, p. 167.
3. R. E. Acosta, Transport Processes in High Rate Electrolysis, Ph. D. Thesis, Dept. Chem. Engr. U. C. Berkeley, LBL-2242, May 1974.
4. H. J. Mathieu and R. H. Muller, Anodic Behavior of Copper in Aqueous Solutions Determined with a Self-Nulling Automatic Ellipsometer, LBL-2520 (1973).

c. Optical Interference in Thin Electrolyte Films

Michael L. Sand and Rolf H. Muller

Thin electrolyte films on metal substrates are of importance in many electrochemical reactions that involve solid, liquid and gaseous phases, such as fuel cell reactions, gas evolution and corrosion processes. In order to quantitatively determine film thicknesses from interference colors, polarized light with a specific angle of incidence on the specimen should be used. This way well-defined phase and amplitude changes occur in reflection.[1] An optimum angle of incidence has been defined at which the visibility of monochromatic interference fringes is one. As shown in Fig. 1, this angle can be different for p and s polarization and depends greatly on the optical constants of the substrate. Optimum interference conditions for white light should produce the most saturated interference colors. Colorimetric computations, based on the CIE system, have shown that the optimum angle of incidence based on color saturation agrees with the monochromatic value for substrates of low reflectance and is a few degrees smaller for substrates of high reflectance, where color saturation is lower.

For the practical thin film observation by interference colors, it is of interest how far one can deviate from optimum conditions for valid interpretations. To establish these limits, our generalized charts of interference colors[2] are being re-examined for use in liquid-film experiments.

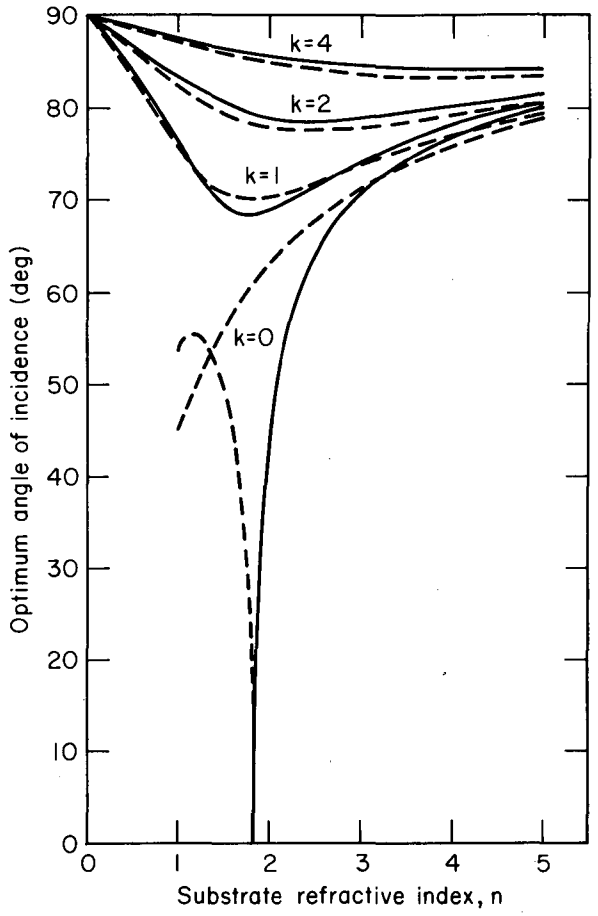

Fig. 1. Computed optimum angle of incidence for observation of monochromatic light-interference (fringe visibility = 1) in an aqueous thin film (refractive index = 1.35) on substrates of optical constants n-ik. ——— s-polarization, - - - p-polarization. (XBL 751-2000)

---

1. C. R. Brown, Interferometry of Solid Thin Films (M.S. Thesis), LBL-2264, December 1973.
2. J. H. Turney, Profiles of Supermenscus Electrolyte Films on Partially Submerged Gas Electrodes (M.S. Thesis), LBL-171, August 1971.

d. Laser Velocimetry

Calvin T. Chew and Rolf H. Muller

Combined forced and natural convection has been shown previously[1] to increase mass transport at electrodes significantly, thereby, offering increased output for electrochemical reactors. Although our recent interferometric observations (see Sec. 1a) confirm the large effect of natural convection on the interfacial concentration field, the flow fields in the boundary layer region are not positively established.

To provide direct evidence of such three-dimensional flow fields, a confocal backscatter laser velocimeter[2] that is capable of operating both in the reference and the differential mode has been built. In the reference mode[3] the Doppler frequency provides a measurement of the velocity component parallel to the optical axis, while in the differential mode[4] the velocity component normal to the optical axis is measured. The sign of the velocity components can be identified by modulation of the incident light. Thus, the average three-dimensional velocity over a microscopic volume[5] in the fluid can be determined.

Tests of the equipment have revealed the need for a better electronic spectrum analyzer. The effect of light-deflection due to the refractive-index gradients on spatial resolution is being analyzed by theoretical means developed in our work on interferometry.

---

1. R. G. Hickman, Ph. D. Thesis, Department of Chemical Engineering, University of California, Berkeley, December 1963.
2. K. L. Orloff and E. G. Logan, Appl. Opt. 12, 2477 (1973).
3. E. R. Pike, D. A. Jackson, P. J. Bourke and D. I. Page, J. Sci. Instrum. (J. Phys. E.) 1, 727 (1968).
4. C. M. Penney, Appl. Phys. Lett. 16, 167 (1970).
5. O. Lanz, C. C. Johnson and S. Morikawa, Appl. Opt. 10, 884 (1971).

2. RESEARCH PLANS FOR CALENDAR YEAR 1975

Rolf H. Muller

Turbulent boundary layers, induced by flow-obstacles under conditions of laminar flow, will be investigated for the purpose of defining optimum size, shape and spacing of obstacles for achieving increased transport rates with the least possible increase in flow resistance.

Theoretical expectations on the ellipsometry of mass transfer boundary layers will be tested experimentally and the effect of such layers on the ellipsometry of solid thin films during their formation will be analyzed. Independent evidence for porosity profiles for surface layers, inferred from ellipsometry, will be sought.

Surface forces responsible for the formation of thin electrolyte films on metals will be investigated.

Electrolyte velocity distributions in boundary layers under superimposed forced and natural convection and the onset of turbulent flow will be determined by laser velocimetry. The effect of light-deflection on the measurements will be considered.

Experimental tests of the theoretically expected reproduction of cathode shapes in high-rate anodic metal dissolution will be initiated (see section by C. W. Tobias).

3. 1974 PUBLICATIONS AND REPORTS

Rolf H. Muller and Associates

Journals and books

1. H. J. Mathieu, D. E. McClure and R. H. Muller, Fast Self-Compensating Ellipsometer, Rev. Sci. Instrum. 45, 798 (1974) (LBL-2256 Rev.).

2. R. H. Muller and H. J. Mathieu, Performance Tests for Automatic Ellipsometers, Appl. Optics 13, 2222 (1974 (LBL-1857 Rev.).

*3. H. J. Mathieu, K. K. Reinhartz and H. Rickert, The Mechanism of the Electrochemical Degradation of Cu_2S-CdS Solar Cells, Conference Record (9th IEEE Photovoltaic Specialists Conf., IEEE, New York) p. 93.

*Supported by Deutsche Forschungsgemeinschaft.

Paper presented

1. F. R. McLarnon, R. H. Muller and C. W. Tobias, Light-Deflection Errors in the Interferometry of Electrochemical Mass Transfer Boundary Layers, Electrochemical Society, San Francisco, May 17, 1974.

Reports

1. F. R. McLarnon, R. H. Muller and C. W. Tobias, Light-Deflection Errors in the Interferometry of Electrochemical Mass Transport Boundary Layers, LBL-2240 Rev., Aug. 1974.

2. W. T. Giba and R. H. Muller, Mechanical Components for Automatic Ellipsometer, LBL-2505, May 1974.

3. R. E. Acosta, Transport Processes in High-Rate Electrolysis, Ph. D. Thesis, LBL-2242, May 1974.

4. F. R. McLarnon, R. H. Muller and C. W. Tobias, Surface Reflection Effects in Interferometry, LBL-3140, Dec. 1974.

5. F. R. McLarnon, R. H. Muller and C. W. Tobias, Derivation of One-Dimensional Refractive-Index Profiles from Interferograms, LBL-3141, Dec. 1974.

6. F. R. McLarnon, R. H. Muller and C. W. Tobias, Interferometric Study of Transient Diffusion Layers, LBL-3550, Dec. 1974.

7. F. R. McLarnon, Interferometry of Electrochemical Mass Transfer Boundary Layers (Ph. D, Thesis), LBL-3500, Dec. 1974.

John Newman, Principal Investigator

1. POTENTIAL DISTRIBUTION IN A CORRODING PIT

John Newman, Donald N. Hanson, and K. Vetter

The occurrence of hemispherical corroding pits in metal surfaces has been known for many years, and qualitative explanations have been given to explain the phenomenon in terms of passivation at the uncorroded flat surface. However, the quantitative solution of potential distribution in such a system, which would be necessary for a test of experimental data, has not been made. The problem is complicated by the discontinuity in surface flux at the edge of the pit. The flux normal to the surface inside the pit can be assumed constant over the whole surface since the pit remains hemispherical during corrosion. However, at the pit edge the normal flux if abruptly reduced to zero, and the planar surface acts essentially as an insulator.

a. Problem Formulation and Solution

Figure 1 shows a cross-sectional view of the hemispherical pit embedded in a planar surface. The potential distribution in the pit and in the surrounding infinite electrolyte can be obtained from a numerical solution of Laplace's equation in spherical coordinates with appropriate boundary conditions. If symmetry about the axis is assumed, the problem is reduced to a problem in two coordinates, θ and r,

$$2r \frac{\partial\phi}{\partial r} + r^2 \frac{\partial^2\phi}{\partial r^2} + \cot\theta \frac{\partial\phi}{\partial\theta} + \frac{\partial^2\phi}{\partial\theta^2} = 0. \qquad (1)$$

At $\theta=0$ and $\theta=\pi$, the boundary condition $\partial\phi/\partial\theta = 0$ leads to

$$2r \frac{\partial\phi}{\partial r} + r^2 \frac{\partial^2\phi}{\partial r^2} + 2 \frac{\partial^2\phi}{\partial\theta^2} = 0 . \qquad (2)$$

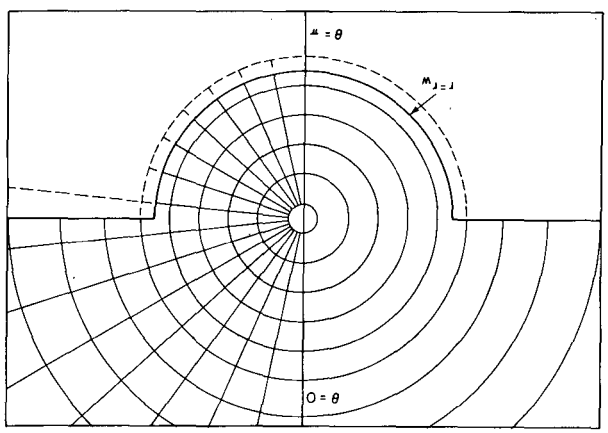

Fig. 1. Pit geometry showing grid for finite difference calculations. (XBL 752-5872)

The remaining boundary conditions are as follows: The potential approaches zero as r approaches infinity for all points outside the pit; the planar surface acts as an insulator, and the normal component of the current density is zero; at the pit surface the normal component of the current density is constant.

The problem was first normalized by dividing all radial distances by the radius of the pit, r_W, so that the dimensionless distance r^* becomes

$$r^* = \frac{r}{r_W} .$$

The problem was further normalized by utilizing a dimensionless potential $\phi^*=\kappa\phi/r_W i_W$ so that the radial dimensionless field at the pit wall is equal to unity

$$\left.\frac{\partial\phi^*}{\partial r^*}\right|_W = 1 .$$

Equations (1) and (2) are unchanged in form by the normalization, and ϕ^* and r^* may be directly substituted.

Consideration of the difficulties inherent in placing a mesh point at the pit lip led to the adoption of the unusual set of meshes illustrated by Fig. 1. The intervals chosen for both the θ-coordinate and r^*-coordinate were such that no point fell on the pit lip. This was accomplished by using an odd number of $\Delta\theta$ intervals and placing the first radial position from the center at a value of r^* equal to one half of the chosen Δr^*. With these selections no mesh points lie on either the pit surface or on the planar surface.

Since the potentials near the pit surface are of most interest, mesh intervals were chosen to yield approximately square meshes at the pit surface. To satisfy the criterion $r^* = r_W^*\Delta\theta = \Delta\theta$, the number of angular divisions was taken as 3 times (as an approximation of π) the number of radial divisions inside the pit. The crudest grid used in this work utilized 5 radial divisions inside the pit and 15 angular divisions. This grid is shown in Fig. 1.

In order to match the boundary condition at large radii, it was assumed that at a radius of 10 r_W^* the potential was constant, with no angular dependence. However, use of the same Δr^* outside the pit as that chosen inside the pit would thus have required nine times as many mesh intervals outside the pit as inside. Large amounts of computer time would have been required for solution of potentials in the region outside the pit where potentials change relatively slowly with radius. In order to avoid this problem, Eqs. (1) and (2) were recast in terms of $\ln r^*$ instead of

r^*, and outside the pit the radii considered were separated by a constant $\Delta \ell n r^*$. Many fewer points are thus required to extend the calculation to large r^*. Figure 1 shows the increasing radial interval outside the pit.

To avoid matching at the boundary between the two blocks of potentials, the inner block with a radial mesh interval of Δr^* and the outer block with a radial mesh interval of $\Delta \ell n r^*$, the value of $\Delta \ell n r^*$ was chosen so that the potentials at the extremes of one radial mesh interval would be correct in both coordinate systems. The radial interval which spanned the pit wall radius was arbitrarily chosen for this purpose. If r_p^* and r_m^* represent the radii immediately above and below r_w^* then

$$\Delta r^* = r_p^* - r_m^*$$

$$\Delta \ell n r^* = \ell n r_p^* - \ell n r_m^* \quad .$$

Thus the two potential blocks overlapped across the interval $r_p^* - r_m^*$, and calculation proceeded smoothly from one block to the other.

The potential at the outer radial boundary, R^* was calculated from the assumption that at R^* the potential was independent of θ and hence the current density was also independent of θ. For this to apply at all radii greater than R^*, the necessary dimensionless potential is

$$\phi_{R^*}^* = \frac{1}{R^*} \quad .$$

Calculations were made with three different numbers of mesh intervals, proceeding from a coarse grid to a highly refined grid. Optimum over-relaxation factors were developed from each of the first two grids in order to speed the calculations at the next finer grid. The grid systems were related by a factor of three in each case. Doubling the number of mesh intervals is a common technique, but in this case it was necessary to use tripling in order to preserve the odd number of angular mesh intervals. The most refined grid consisted of 45 radial intervals inside the pit plus an additional 108 logarithmic intervals outside the pit together with 135 angular intervals.

Because of the unusual mesh system, several special finite-difference equations were used. All equations were of order h^2 accuracy or better. Convergence of the calculation was taken to be a movement of less than 10^{-8} in any dimensionless potential.

b. Results

The results of the solution for the potential map were interpolated to determine equipotential lines. Fields and local fluxes were calculated and integrated to provide flux lines. The results of these calculations are shown in Fig. 2 where equipotentials of ϕ^* are plotted, together with flux curves enclosing values of normalized total current.

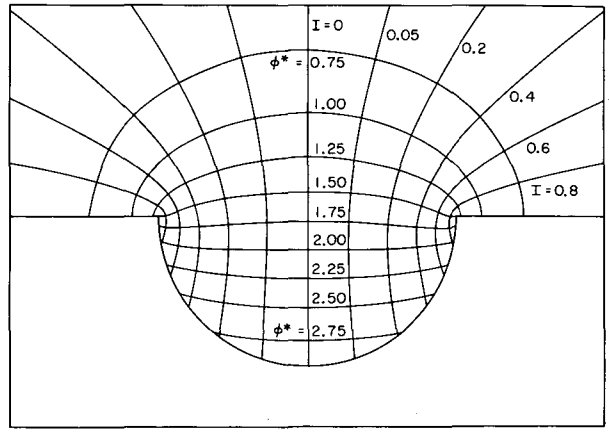

Fig. 2. Normalized equipotentials and flux curves for a corroding pit with uniform current density in the pit and zero current density on the surrounding planar surface. Flux lines show enclosed current divided by total current.
(XBL 752-5871)

It is apparent that the expected pattern of flux lines has been found. The flux lines gather sharply toward the pit edge and turn abruptly just outside the mouth of the pit.

Figure 3 shows values of dimensionless potential along various lines. The potential along the pit surface has been plotted against distance along

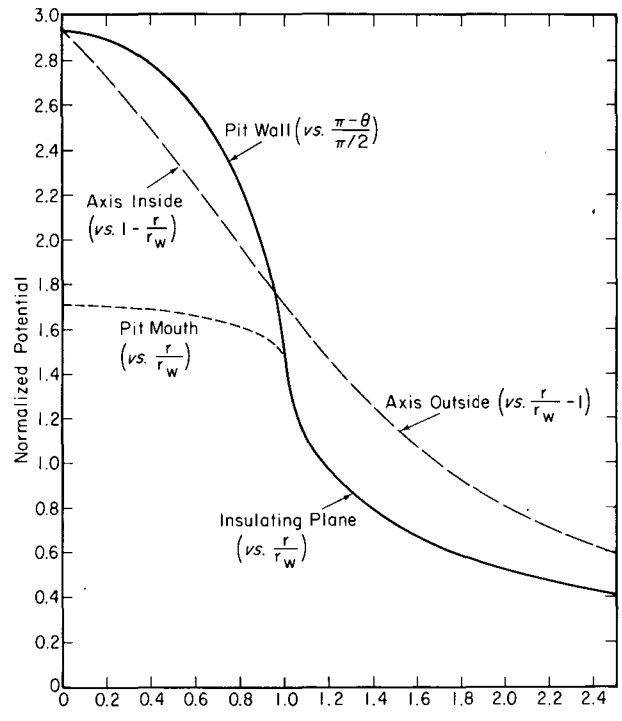

Fig. 3. Normalized potential on pit surface, on the plane, and along the pit axis.
(XBL 752-5870)

the surface, starting at the bottom of the pit, and is seen to flow smoothly into the potential along the flat surface outside the pit. The slope near the pit edge is very high, perhaps infinite, as expected.

The most important values of the dimensionless potential in interpreting corrosion measurements are those at the bottom of the pit and the pit edge. The values found in this work are, respectively, 2.929 and 1.434.

The growth of hemispherical pits would appear to require a discontinuous drop in the curve of current vs potential at the point of passivation. Otherwise, the small potential differences involved with typical pitting conditions would lead to pits with severely rounded edges.

2. MASS TRANSFER TO AN ECCENTRIC ROTATING DISK ELECTRODE

Charles M. Mohr and John Newman

The problem of limiting-current mass transfer to a disk electrode rotating about an axis displaced from the center of the electrode is of interest in electroanalytical chemistry and in the experimental determination of diffusion coefficients for electroactive species. Prior analyses[1,2] are inappropriate for the small eccentricities that would result from slight machining errors (in manufacture) or bearing looseness (in operation) of such electrodes. A model based on a diffusion layer approximation has been developed and solved numerically[3] for small and moderate eccentricities, and an asymptotic form valid for large eccentricities has also been derived. The results have been tested by an experimental study of the deposition of copper on eccentric copper rotating disk electrodes, and the data so gathered support very well the conclusions of the analysis. A somewhat surprising conclusion that is supported by the experimental results, is that the mass transfer rate is unaffected until the eccentricity exceeds approximately 2/3 of the electrode radius.

---

1. M. Bardin and W. Dikusar, Elektrokhimiya 6, 1147 (1970).
2. D. T. Chin and M. Litt, J. Electrochem. Soc. 119, 1338 (1972).
3. C. Mohr and J. Newman, LBL Report 2719 (April, 1974).

3. COALESCENCE OF DROPLETS IN AN ELECTRIC FIELD

Charles M. Mohr, John Newman, and Richard D. Newman

The motion of neighboring droplets under the influence of an electric field has an important effect upon the rate of coalescence of these drops. Since some researchers have indicated that the field enhances coagulation,[1] and, for sufficient field strengths, coagulation is instantaneous for a certain (small) separation of the drops, it seems profitable to study the relative motion of the drops at larger separation which results from application of the electric field. In order to simplify this problem, the drops are taken to be conducting, neutrally buoyant, and spherical in shape, and the electric field is assumed to be parallel to the line of centers of the two drops of interest (the continuous fluid phase is non-conducting). For this geometry, the field perturbation due to the presence of the drops has been solved by Jeffrey,[2] and the hydrodynamic flow for a similar case (but with solid spheres rather than drops) has been treated by Brenner. Following Brenner[3] the equations for creeping motion were solved via a numerical technique to yield a dimensionless approach velocity as a function of separation, force of attraction, and viscosities of the two media. Combining this with the results of the electrostatic problem gives the approach velocity as a function of field strength, the viscosities, and separation. The analysis is expected to apply in those cases where the velocity of approach of the droplets is rate-determining and difficulty is anticipated for very small separations, at which the drops may become distorted from their spherical shape due to pressure effects. For large separations, an asymptotic form has been developed that agrees well with the numerical calculations.

---

1. A. H. Brown and C. Hanson, Chem. Eng. Sci. 23, 841 (1968).
2. G. B. Jeffrey, Proc. Royal Soc. London 109, (1912).
3. H. Brenner, Chem. Eng. Sci. 16, 242 (1961).

4. ELECTRICAL CONDUCTIVITY AND DENSITY MEASUREMENTS OF CONCENTRATED PHOSPHORIC ACID AT HIGH TEMPERATURE

Peter E. Pierini and John Newman

The acid fuel cell is being actively developed to level peak power production requirements on conventional rotating power producing machinery. The natural advantages offered by fuel cells include a higher theoretical efficiency and a relative insensitivity to load fluctuations. H_3PO_4 appears to be the electrolyte that will be used in commercial fuel cells of the next decade. Great numbers of fuel cells are tentatively planned for load leveling. All design parameters should be optimized since even a small improvement would result in large scale energy conservation. Data[1,2] exist, covering the temperature range of 18°C to 170°C with concentrations varying from 10 wt.% to 100 wt.%. Current design trends indicate that an extension of the data would be useful in formulating the most efficient device. Extrapolation of existing data is uncertain since a similar electrolyte, H_2SO_4, shows two maxima

in conductivities over similar concentration ranges.[3]

---

1. D. I. MacDonald and J. R. Boyack, J. of Chem. and Engineering Data 14, No. 3, 380-384 (1969).
2. Monsanto Technical Bulletin 1-239, "Industry Guide to the Profitable Use of Monsanto Phosphoric Acid."
3. J. E. Kunzler and W. F. Giauque, J. Amer. Chem. Soc. 74, 804-806 (1952).

5. FLUID FLOW NEAR THE EQUATOR OF A ROTATING SPHERE

Peter E. Pierini and John Newman

The hydrodynamic boundary layers on a rotating sphere begin with an influx of fluid at the poles and then flow around the sphere towards the equator. The boundary layers collide at the equator, separate from the surface and form a radial swirling jet. Bowden and Lord[1] have published excellent photographs of this phenomenon. Boundary layer computations have been carried out by Banks[2] and Manohar.[3] Banks[2] unsuccessfully tried to match the boundary layer solution to an inviscid flow proposed by Stewartson.[4] Presently, effort is being devoted to identifying the regions in which the classic assumptions of hydrodynamics can be properly applied. These regions blend asymptotically with one another and will be used to match the colliding boundary layers with the radial swirling jet. However, the problem of solving the full Navier-Stokes equations, though only in a small region, seems unavoidable.

---

1. F. P. Bowden and R. G. Lord, Proc. Roy. Soc. A, 271, 143-153 (1963).
2. W. H. H. Banks, Quart. J. Mech. Appl. Math. 18, No. 4, 443 (1965).
3. R. Manohar, Z. Angew. Math. Phys. 18, 320 (1967).
4. K. Stewartson, Boundary Layer Research, p. 59, I.V.T.A.M. Symposium (1957).

6. ROTATING RING-DISK ELECTRODES

Peter E. Pierini and John Newman

Rotating ring-disk electrodes are now being used more frequently in research applications. Data have been taken for a ferro-ferri cyanide redox reaction.[1] The limiting current was computed and measured with excellent agreement. However, data were present for operating conditions below the limiting current, but no computations were attempted. We are presently making these computations utilizing methods presented in Newman[2] for potential distribution and mass transfer which have not yet had such a test of validity. The redox kinetic expression[3] is being used and we will obtain parameters for the ferro-ferri cyanide reaction which are not presently available. Finally an explanation of anomalous limiting currents measured on the ring with the disk operating at a net zero current will be made.

---

1. W. H. Smyrl and J. Newman, J. Electrochem. Soc. 119, 212 (1972).
2. J. Newman, The Fundamental Principles of Current Distribution and Mass Transport in Electrochemical Cells, in Electroanalytical Chemistry, Vol. 6, edited by Allen J. Bard (Marcel Dekker, New York, 1973), 187.
3. J. Newman, Electrochemical Systems (Prentice-Hall, Englewood Cliffs, N.J., 1973), 432 pp.

7. THERMODYNAMICS OF AQUEOUS SOLUTIONS CONTAINING ONE OR MORE VOLATILE WEAK ELECTROLYTES*

Thomas J. Edwards, John Newman and John M. Prausnitz

A thermodynamic framework has been formulated[1] for predicting equilibrium vapor-liquid compositions for dilute aqueous solutions of one or more volatile weak electrolytes. The electrolytes examined are ammonia, carbon dioxide, hydrogen sulfide, sulfur dioxide, and hydrogen cyanide over the temperature range 0-100°C and for liquid-phase concentrations covering four orders of magnitude, from 10^{-4} to 1 molal (moles per 1000 gms of water).

Binary parameters are obtained from reduction of experimental data for single-solute solutions. Additional parameters required for descriptions of multisolute systems are estimated from correlations. These parameters, coupled with chemical equilibria and reasonable simplifying assumptions, are used to predict multicomponent vapor-liquid equilibria.

Restrictions of relative amounts of solutes are not imposed on this analysis. At a fixed temperature, either liquid-phase or vapor-phase compositions may be calculated if the composition of the other phase is known.

Although the framework has no adjustable parameters for multisolute systems, predicted equilibria of the NH_3-H_2S-H_2O and the NH_3-CO_2-H_2O systems are in satisfactory agreement with experiment.

---

*Funded by American Petroleum Institute (Refining Division), and the National Science Foundation.

1. Thomas J. Edwards, John Newman, and J. M. Prausnitz, AIChE J. in press.

8. MAXIMUM DROPLET GROWTH WHEN COOLING A SATURATED SOLUTION*

Hugo A. Massaldi, John Newman, and C. Judson King

The maximum size of a droplet or spherical solid particle which grows from an initially saturated, homogeneous binary solution as the temperature decreases is predicted through an approximate, closed solution valid for solutes of moderate solubility (up to 1%).[1] The dimensionless radius-time relationship is presented for various levels of the parameters, which involve the activation energy for the temperature dependence of the diffusivity, the heat of solution, and the initial and final temperatures of the system. The decrease of diffusivity with time is shown to hinder the growth process, offsetting the simultaneous increase in driving force.

*Partially supported by Consejo Nacional de Investigaciones Cientificas y Tecnicas de la Republica Argentina.

1. Hugo A. Massaldi, John Newman, and C. Judson King, "Maximum Droplet Growth when Cooling a Saturated Solution," to be published in Chemical Engineering Science.

9. DOUBLE-LAYER CAPACITY DETERMINATION OF POROUS ELECTRODES*

William Tiedemann and John Newman

A method is presented[1] for evaluating double-layer charging of porous electrodes. The maximum in the curve of $i\sqrt{t}$ vs. $\sqrt{t}$ lends itself readily to experimental evaluation. Values of the double-layer capacity determined for the Pb and PbO_2 electrodes in sulfuric acid are in agreement with those reported in the literature.

*Supported by Globe-Union, Inc., Milwaukee, Wisconsin 53201

1. William Tiedemann and John Newman, Double-Layer Capacity Determination of Porous Electrodes, Journal of the Electrochemical Society, 122, 70-74 (1975).

10. POROUS-ELECTRODE THEORY WITH BATTERY APPLICATIONS

John Newman and William Tiedemann

Developments in the theory of flooded porous electrodes are reviewed[1] with regard to simulation of primary and secondary batteries, adsorption of ions and double-layer charging, and flow-through electrochemical reactors.

1. John Newman and William Tiedemann, Porous-electrode Theory with Battery Applications, AIChE Journal 21, 25-41 (1975).

11. MASS TRANSFER OF MINOR COMPONENTS IN A PROPAGATING CRACK

William H. Smyrl and John Newman

The mass transfer of a dilute species in a liquid in a propagating crack is treated.[1] The analysis includes the effect of convective flow of the liquid. The results of the calculations show that the crack tip is devoid of the minor species, and that the mass flux of this component is also negligible in this region. Therefore, minor components could not behave as "critical" species in such systems. Calculation of the flux distribution allowed the determination of the potential distribution in the crack.

1. William H. Smyrl and John Newman, J. Electrochem. Soc. 121, 1000-1007 (1974).

12. RESEARCH PLANS FOR CALENDAR YEAR 1975

John Newman

Mass transfer for turbulent flow between rotating concentric cylinders separated by a very thin gap will be measured using the ferri-ferro cyanide redox reaction in an attempt to improve upon existing correlations for such systems. Measurements of mass transfer rates to a rotating disk in transitional flow will be continued. Mass transfer computations for a rotating ring-disk in a ferro-ferri cyanide system will be continued. The electrical conductivity of phosphoric acid solutions in the range from 95 to 110% H_3PO_4 and 190-200°C will be measured. Computations for the coupled potentials and resistances of a ring-disk system will be completed. Work on the influence of design specifications on the optimum configuration of batteries will be begun. Experimental organic electrosynthesis utilizing flow-through porous electrodes will be initiated.

13. 1974 PUBLICATIONS AND REPORTS

John Newman and Associates

Journals and patent

1. J. Newman and W. H. Smyrl, Fluid Flow in a Propagating Crack, Metallurgical Transactions 5, 469 (1974) (LBL-824).

2. K. Nişancioğlu and J. Newman, Transient Convective Diffusion to a Disk Electrode, J. Electroanal. Chem. 50, 23 (1974) (LBL-1881).

3. K. Nişancioğlu and J. Newman, Current Distribution on a Rotating Sphere below the Limiting Current, J. Electrochem. Soc. 121, 241 (1974) (LBL-1837).

4. R. V. Homsy and J. Newman, An Asymptotic Solution for the Warburg Impedance of a Rotating Disk Electrode, J. Electrochem. Soc. 121, 521 (1974) (LBL-2209).

5. K. Nişancioğlu and J. Newman, The Short-Time Response of a Disk Electrode, J. Electrochem. Soc. 121, 523 (1974) (LBL-1896).

6. D. N. Bennion and J. Newman, Method and Apparatus for the Electrochemical Removal of Metal Ions, United States Patent 3,804,733, April 16, 1974.

7. W. H. Smyrl and J. Newman, Mass Transfer of Minor Components in a Propagating Crack, J. Electrochem. Soc. 121, 1000 (1974) (LBL-2596).

8. J. Newman, Mass Transport and Potential Distribution in the Geometries of Localized Corrosion. B. F. Brown, J. Kruger and R. W. Staehle, eds. Localized Corrosion, (Houston: National Association of Corrosion Engineers, 1974) pp. 45-61, (LBL-408).

9. R. V. Homsy and J. Newman, Current Distribution on a Plane below a Rotating Disk, J. Electrochem. Soc. 121, 1448 (1974) (LBL-1887).

Papers presented

1. J. Newman, Non-Uniform Current Distribution and its Significance in the Interpretation of Electrochemical Phenomenon, invited lecture at the Gordon Research Conference on Electrochemistry held in Santa Barbara, Calif., Jan. 7-11, 1974.

2. W. H. Symrl (Speaker) and J. Newman, Studies of Plating Corrosion, Symposium on Interfacial Phenomena in Electrochemical Energy Converter Systems at the Washington meeting of the American Institute of Chemical Engineers, Dec. 1-5, 1974.

3. W. Tiedemann (Speaker) and J. Newman, Double-Layer Capacity Determination of Porous Electrodes, Symposium on Interfacial Phenomena in Electrochemical Energy Converter Systems at the Washington meeting of the American Institute of Chemical Engineers, Dec. 1-5, 1974.

4. Thomas J. Edwards, J. Newman and J. M. Prausnitz, Thermodynamics of Aqueous Solutions Containing One or More Volatile Weak Electrolytes, Symposium on Solution Thermodynamics, with Emphasis on Systems at High Temperatures and Pressures, at the Washington meeting of the American Institute of Chemical Engineers, Dec. 1-5, 1974.

LBL reports

1. R. V. Homsy, Mass Transfer to a Plane below a Rotating Disk (Ph.D. thesis), LBL-2291, March 1974.

2. R. V. Homsy and J. Newman, Mass Transfer to a Plane below a Rotating Disk: Experimental, LBL-2720, April 1974.

3. C. M. Mohr, Jr. and J. Newman, Mass Transfer to an Eccentric Rotating Disk Electrode, LBL-2719, May 1974.

4. D. T. Scalise and J. Newman, An Improved Solution to the Classical Near-Wake Boundary-Layer Problem, LBL-1430, Feb. 1974.

5. W. Tiedemann and J. Newman, Porous-electrode Theory with Battery Applications, LBL-3117, Aug. 1974.

Translations

1. A. Winsel, Contributions to the Knowledge of the Current Distribution in Porous Electrodes, Zeitschrift für Elektrochemie 66, 287-304 (1962), translated by John Newman, UCRL-Trans-1495, Feb. 1973.

2. J. Euler and W. Nonnenmacher, Current Distribution in Porous Electrodes, Electrochimica Acta 2, 268-286 (1960), translated by John Newman, UCRL-Trans-1513, March 1974.

3. A. Winsel, Research Technique of Porous Electrodes, Chemie-Ing.- Techn. 43, 191-195 (1971), translated by Joe Miksis, UCRL-Trans-1519, Dec. 1974.

D. PHYSICAL CHEMISTRY

Leo Brewer, Principal Investigator

1. THERMODYNAMIC PROPERTIES OF THIRD AND FOURTH GROUP TRANSITION METALS WITH PLATINUM GROUP METALS

Gary B. Bullard

Studies are continuing to establish the variation of the Gibbs energy with concentration for solid solutions of the strongly interacting third and fourth group transition metals such as Zr and Nb and the platinum group metals. It is hoped that these results will allow improvement of bonding models based on utilization of low-energy bonding orbitals. A high-temperature-solid-electrolyte cell has been constructed using a ZrO_2-CaO electrolyte. Alloys of Ta with Pd are presently under study.

2. APPLICATION OF THE REGULAR SOLUTION THEORY TO METALLIC SOLUTIONS

John P. Stiga and Robert H. Lamoreaux

Calculations for the lanthanide and actinide metals indicate that the proper cohesive energy to use for calculation of thermodynamic properties of metal alloys through use of the regular solution theory is the bonding energy of the valence state. Values of the valence state bonding energies have been tabulated for all the elements; these values are being used for calculation of phase diagrams. Excess entropies are being estimated from the relation to excess volume and internal pressure difference.

3. THERMODYNAMIC EVALUATION AND COMPILATION OF METAL ALLOY SYSTEMS

Leo Brewer and Ralph R. Hultgren

A bibliography of publications on the thermodynamics of metallic binary and ternary systems is being maintained. Compilations are in progress for the thermodynamic properties of molybdenum and its compounds*, the thermodynamic properties of alloy systems of the lanthanide and actinide elements, and the solubilities of intermetallic compounds in iron.

*Partially supported by the International Atomic Energy Agency

4. THE MATRIX SPECTRA OF OXIDES OF Ca AND Mg*

Walter D. Duley, John Ling-Fai Wang, and Lester Andrews

A multitude of species are formed when Ca or Mg are deposited together with N_2O, O, O_2, and O_3 in rare gas or nitrogen matrices at liquid hydrogen temperatures.

Experiments are in progress to attempt to unambiguously identify these species.

*Supported in part by N.S.F.

5. RESEARCH PLANS FOR CALENDAR YEAR 1975

Leo Brewer

It is expected that the matrix isolation studies will elucidate the oxide species of Mg and Ca and the program will be terminated this year. The high-temperature-solid-electrolyte cell work will be extended to ThO_2-Y_2O_3 electrolyte cells that will allow measurements with more strongly reducing alloys. The application of regular solution theory to metallic alloys will be extended and applied to the calculation of thermodynamic data and phase diagrams for systems which lack experimental data. It is hoped that the rate of compilation effort will be accelerated as these results will be of considerably value in application of new materials to development of new energy processes.

6. 1974 PUBLICATIONS AND REPORTS

Leo Brewer and Associates

Journals

1. L. Brewer, Prediction of Transition Metal Phase Diagrams, J. Nucl. Mat. 51, 2 (1974) (LBL-2234).

2. L. Brewer, Consequences of Partial Delocalization of D-Electron Orbitals in Transition Metals, Review Chimie Minerale 11, 616 (1974) (LBL-3102).

3. L. Brewer, The Importance of Accelerating Thermodynamic Compilation Endeavors, CODATA (Committee on Data for Science and Technology) Newsletter 13, 6 (1974) (LBL-2774 excerpt).

LBL Reports

1. Leo Brewer, The Relevance of Thermodynamics to National Energy Problems, presented at conference of Thermodynamics and National Energy Problems, Warrenton, Virginia, June 10, 1974 (LBL-2774).

2. Beat Meyer, The Structures of Elemental Sulfur, chapter in Advances in Inorganic Chemistry and Radiochemistry, edited by J. H. Emeleus, LBL-3163, September 1974.

Charles B. Harris, Principal Investigator

1. COHERENT ENERGY MIGRATION IN MOLECULAR SOLIDS*

Charles B. Harris

A series of experiments and their associated theoretical interpretations have been developed in order to investigate coherent migration of electronic energy in molecular solids at low temperatures within the context of three general considerations important in almost all transport problems. These are:

(1) What explicit physical principles in solids are responsible for energy migration evolving from a collective coherent wavepacket-type propagation to a Stochastic-Markoffian random walk process?

(2) What are the interrelationships between coherence, incoherence, kinetic descriptions or statistical models for describing transport?

(3) What features in energy migration give rise to non-Boltzmann distribution functions and what interactions are responsible for a system evolving in time or under influence of some external variant, such as temperature, to a Boltzmann description?

To these ends, we have experimentally elucidated and determined qualitatively and quantitatively some important features associated with the form and functionality of coherence. These include the wavepacket group velocities, $V_g(k)$; the wavepacket coherence times, $\tau(k)$, and the coherence length, $\ell(k)$, in the coherent limit, the random walk limit and where possible in the intermediate region.

In addition, we have determined experimentally what features are responsible for a system evolving towards Boltzmann equilibria and what are the interrelationships between $V_g(k)$, $\tau(k)$, $\ell(k)$, the creation of delocalized wavepackets from localized states and kinetic or statistical models for nonequilibrium distribution functions. Knowledge of these three parameters as a function of temperature bandwidth, and the structural form of the crystal, such as the average number of molecules per exciton chain has provided considerable insight into the physical basis for coherent migration and the physical principles responsible for transport evolving from a coherent wavepacket-type propagation to Stochastic-Markoffian random walk processes in time or under some external variance such as temperature.

The systems which have been investigated and which form the basis for the experimental investigations are "one-dimensional" molecular solids having, as their lowest excited states, delocalized triplet bands and localized triplet "molecular" states. Many of the experiments have utilized zerofield optically detected magnetic resonance in excited triplet states and heat pulse techniques. The emphasis has been the use of optically detected electron spin echoes, spin locking, and adiabatic demagnetization or "ordering" of the excited triplet spin ensemble to elucidate the dynamics of triplet Frenkel exciton migration.

*Partially supported by NSF

2. PHOSPHORESCENCE MICROWAVE DOUBLE RESONANCE SPECTROSCOPY IN IONIC SOLIDS AND ITS APPLICATION TO COHERENT JAHN-TELLER STATES IN F CENTERS OF CaO

Charles B. Harris

Phosphorescence microwave double resonance spectroscopy (PMDR) is a technique which has allowed much of the kinetic information regarding the populating routes and decay channels of electronic excited state energy into triplet states to be obtained easily and routinely in molecular solids. PMDR monitors the individual vibronic bands in emission and measures the quantitative changes induced in the emission by a microwave field resonant with the zerofield splittings. Because of the sensitivity of photon detection, it is capable of measuring properties on as few as 10^4 excited states depending upon the details of the radiative channels being monitored.

Although many properties of ionic solids are different from molecular solids, the basic features of excited F centers are similar to excited triplet states, particularly in zero-field. If one considers the F center oxygen vacancies in CaO, there is a one-to-one correlation of the individual spin sublevels of the F center in zerofield with $^3B_{1u}$ molecular excited triplet states. In D_{4h}, the F center can be established as a $^3B_{1u}$ (σ,σ^*) state when the X axis of the zerofield tensor is defined along the C_4 symmetry axis of the center. Many excited triplet states in molecular crystals have been unequivocally established through PMDR in $^3B_{1u}$ (π,π^*) states. We expect, therefore, that the dynamics of populating and depopulating excited centers can be elucidated in ionic solids as simply and easily as in triplet states in molecular solids. Moreover, PMDR has been recently used to establish coherence in excited triplet excitons and spins in molecular solids, and one might expect the same could be accomplished in ionic and semiconducting crystals having accessible triplet states. Indeed, in the past year we have (a) demonstrated zerofield PMDR in ionic solids, specifically in F centers of CaO, (b) illustrated how the methods can be used to extract the Jahn-Teller splittings from the zero-phonon origin in CaO, and finally, (c) determined

a minimum coherence time for the Jahn-Teller split states and shed some light on how the coherence is lost, and its relationship to the dynamic Jahn-Teller effect. A schematic diagram is given in Fig. 1 to illustrate the principles and the data is presented in Fig. 2.

The results from these experiments can be understood as follows. Two zerofield transitions, hereafter labeled ω_1 and ω_2, are seen at 1675.5 and 1696.7 MHz, respectively [cf. Fig. 2(a)].

PMDR IN COHERENT JAHN-TELLER SPLIT F-CENTERS

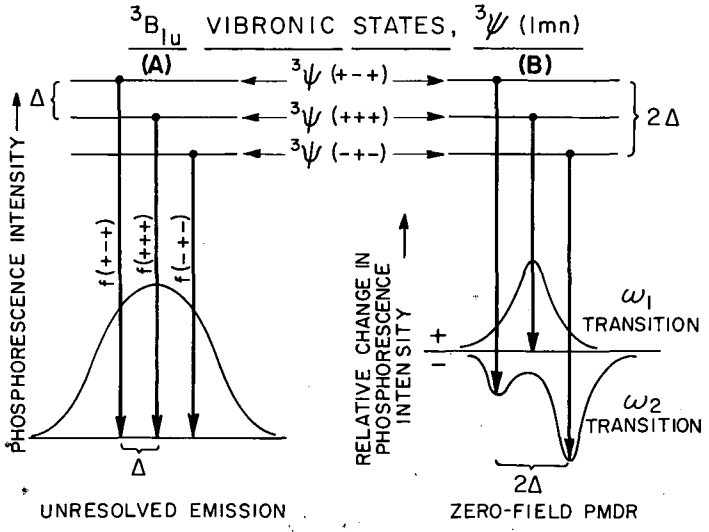

Fig. 1. Schematic diagram of the principles used to elucidate the dynamic Jahn-Teller effect using PMDR. (XBL 745-6276)

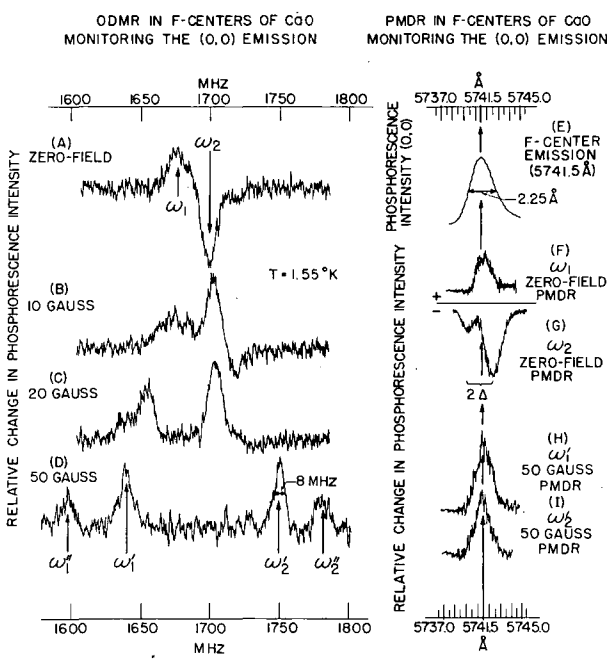

Fig. 2. ODMR and PMDR spectra of F centers in CaO (XBL 745-6275)

The PMDR spectrum of ω_1 [2(f)] yields a spectrum where the maximum in the phosphorescence emission is coincident with the maximum in the PMDR spectrum. On the other hand, the PMDR spectrum of ω_2 [2(g)] yields two peaks symmetrically split from ω_1 by about 4.2±0.2 cm^{-1}. Moreover, the microwave-induced change in phosphorescence increases for ω_1 and decreases for ω_2 indicating a difference in the populating and decay rates for the three stationary Jahn-Teller states. In the zerofield ODMR spectrum [2(a)] the difference between the zerofield splitting in the $^3\psi(+++)$ and $^3\psi(^{+-+}_{-+-})$ states is 21 MHZ because of selective spin-orbit coupling contributions to the zerofield splittings. The difference in their respective optical PMDR spectra amounts to 2.1±0.1 cm^{-1}. This means that the tunnel splitting is Δ=2.1±0.1 cm^{-1}.

The fact that all three splittings are resolved in the PMDR spectrum [2(f), 2(g)] means that the Jahn-Teller states are coherent in zerofield. A minimum coherence time can be established from exchange theory which states that intermediate exchange is given by the condition $(\omega_2-\omega_1)\tau \sim 1$. The coherence time, τ, in CaO is therefore longer than 5×10^{-8} sec. Thus, coherence persists in the Jahn-Teller states in zerofield at least 6×10 times longer than that associated with the stochastic "random" incoherent limit, which is given by $(2\Delta)^{-1}$ sec.

3. COHERENCE IN ELECTRONICALLY EXCITED DIMERS AND ITS RELATIONSHIP TO EXCITONS IN MOLECULAR CRYSTALS*

Ahmed H. Zewail and Charles B. Harris

The growing interest in studying energy transport in insulators is evidence of the many interesting questions which pertain to this problem. A large effort was devoted to establish whether or not the energy migration is coherent or incoherent. In the coherent description of energy migration excitons are described by a group velocity, and hence the individual k states are characterized by a coherence length and a coherence time. The magnitude of the coherence length is determined by the nature of scattering centers in crystals. Moreover, the propagation of the exciton is determined by many radiative and non-radiative processes such as trapping, surface quenching, exciton-exciton interactions and exciton-phonon coupling. The extent to which this coupling alters the stationary and non-stationary properties of the band depends on the nature of the matrix elements which connect the exciton and phonon states. It is therefore important to establish the dimensionality of the interactions as well as the scattering cross-sections.

A dimer is a two-molecular chain and therefore must have a direct relationship to the parent infinite-molecule chain (exciton). Hence, the physics governing the scattering processes and the anisotropy of the interactions are interrelated. Recently we have shown that low-temperature electron spin resonance in zero field is a suitable

probe for studying the dynamics of energy transfer in dimer and exciton states. The magnetic properties of translationally equivalent and translationally inequivalent dimers in their triplet states were shown to depend on the magnitude of the resonance interactions, the local symmetry of the dimer and the coupling between the spin and orbital angular momentum in the crystal site. Further, the microwave absorption and dispersion in dimers are directly related to the microwave absorption and dispersion of triplet Frenkel excitons, as illustrated in Figs. 1 and 2. Hence the dimensionality of the interactions can be established from the zerofield EPR spectra. Also the magnetic spectra give the cross-section for the exciton-phonon coupling which in turn determines the limit of spin exchange (slow, intermediate and fast) and the statistics governing the scattering processes. Coherence in the excited states of dimers and excitons was established from these experiments. In crystals of 1,2,4,5-tetrachlorobenzene at low temperatures, the coherence time is proven to be 10^5 times that of the stochastic limit, implying a persistence of correlation among the members of the ensemble for times very much longer than the energy exchange time.

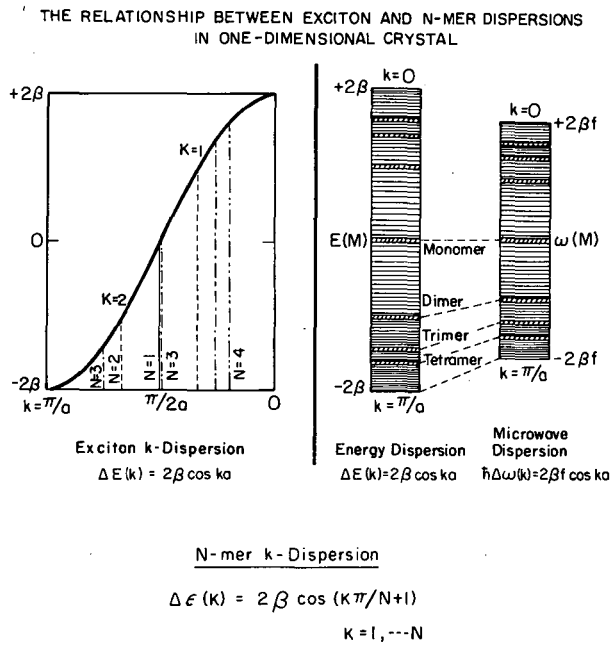

Fig. 1. The relationship between exciton and N-mer dispersions for one-dimensional systems. The figure on the left gives the k dispersion (cosine curve) for the exciton while the vertical lines give the energy position of the N-mers. The rest of the k states are not shown for the sake of clarity. The position of the monomer at the center of the band is only true if there is no host polarization or hyperfine effects. The schematic on the right-hand side of the figure gives both the energy and microwave dispersions for the different states of the different clusters. The position of the k=0 level is arbitrarily chosen. The figure clearly shows that there is a one-to-one correspondence between the optical and microwave dispersions.
(XBL 747-6804)

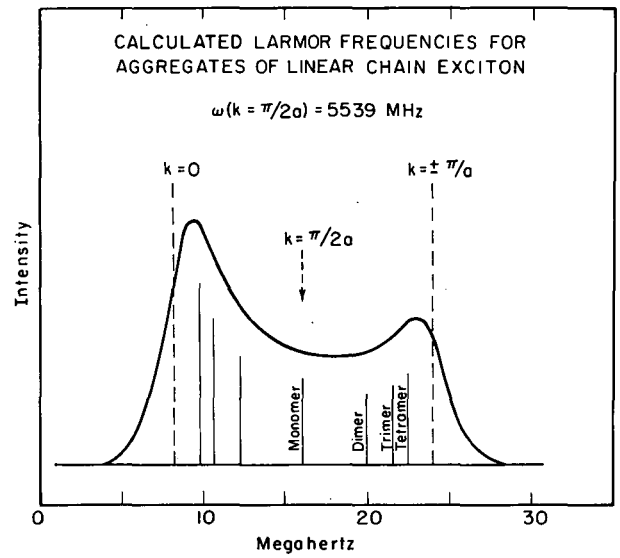

Fig. 2. Calculated Larmor frequencies for aggregates of one-dimensional systems. The continuous double-humped curve is the exciton band-to-band transition, calculated for a Boltzmann distribution amongst the k states and $\omega(k=\pi/2a)$ = 5539 MHz. The vertical lines represent the relative positions of the N-mer resonance transitions. The intensity distribution among the N-mer states is not calculated and only drawn this way to follow the exciton line shape.
(XBL 747-6805)

*Partially supported by NSF

4. APPLICATION OF OPTICALLY DETECTED SPIN LOCKING AND ADIABATIC DEMAGNETIZATION TO THE INVESTIGATION OF ENERGY MIGRATION IN MOLECULAR CRYSTALS*

Henry C. Brenner, John C. Brock and Charles B. Harris

Recently we have employed two different pulsed optically detected electron spin resonance techniques to investigate the processes involved when an excitation in a localized "trap" state is promoted to the exciton band and becomes mobile. This process is known to be an important mechanism for energy transfer in molecular crystals and is intimately related to the question of whether or not statistical models can be used to describe the relative populations of various energy states in solids. We have employed the technique of optically detected spin locking to measure the dynamics of phonon-assisted promotion of excitations to states isoenergetic with the exciton band, and have combined this information with results obtained from optically detected adiabatic demagnetization in the rotating frame to acquire information on the

relative number of promotion events resulting in mobile excitons leading to trap-to-trap energy transfer. A temperature dependence study of this "quantum yield" for mobile excitons upon promotion from localized states has shown that exciton-phonon scattering can drastically alter the efficiency of the detrapping-migration-retrapping process, even at very low temperatures. The dependence of this energy transfer process on the density of exciton states is currently being investigated. The initial results are given in Figs. 1 and 2.

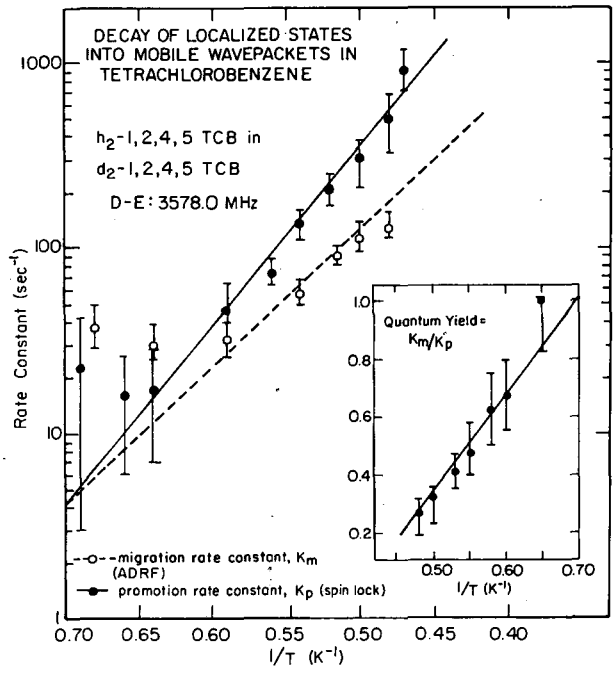

Fig. 1. Experimentally measured values of the rate constants for promotion of h_2-TCB localized trap states in d_2-TCB to the d_2-TCB exciton band (solid circles), and for h_2-TCB trap-to-trap migration (open circles). The rate constants K_p and K_m were measured versus temperature by means of optically detected spin locking and adiabatic demagnetization in the rotating frame, respectively. (XBL 745-6410)

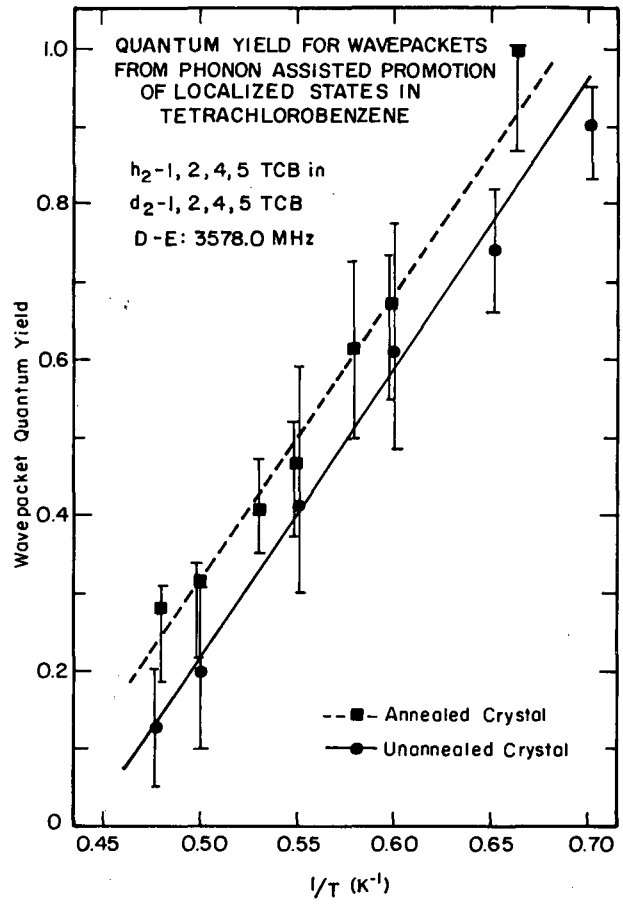

Fig. 2. Quantum yield for h_2-TCB trap-to-trap migration in d_2-TCB. The quantum yield given by the ratio of the migration rate constant to the promotion rate constant represents the fraction of trap spins which migrate to other traps after promotion to the exciton band. (XBL 745-6409)

*Partially supported by NSF

5. ENERGY MIGRATION IN ONE-DIMENSIONAL SOLIDS*

Mark T. Lewellyn, John C. Brock, Ahmed H. Zewail and Charles B. Harris

Details of trap-to-trap energy transfer in isotopically mixed crystals of 1,2,4,5-tetrachlorobenzene have been studied using a variety of techniques including pulsed coherence experiments and steady state luminescence studies. These experimental tools were utilized to investigate the affects of temperature and trap concentration on excitation transfer between monoprotonated (hd) and perprotonated (h_2) traps in perdeuterated TCB host crystals. Optically detected spin locking experiments yielded kinetic information on the absolute promotion rates of excited state population out of the h_2 traps to higher energy hd traps and host d_2 states. Adiabatic demagnetization in the rotating frame experiments were also performed to determine the effects of trap concentration on loss of order from the h_2 states. The experiments allow one to extract a complete picture of the different routes important in energy transfer in crystals representing one-dimensional systems.

*Partially supported by NSF

6. PHONON INTERACTIONS IN MOLECULAR CRYSTALS AND THEIR RELATIONSHIPS TO COHERENT EXCITON PROPERTIES

Alan R. Burns, Marc E. Tarrasch and Charles B. Harris

The temperature dependence of such processes as detrapping and trap-to-trap migrations in molecular crystals has been associated with phonon-exciton interactions. In order to elucidate some of the details of the phonon interactions in exciton dynamics, we are applying the technique of heat pulses. Short-duration current pulses in thin-film resistors deposited on quartz substrates have been shown to generate a wide band of high-frequency phonons which will propagate through a crystal in thermal contact with the resistive film. So far, we have been able to demonstrate thermal modulation of the relative populations of the excited triplet state sublevels with the application of heat pulses.

Experiments are now under way where we apply heat pulses to a spin-locked ensemble of excited triplet states. From these experiments we can obtain information regarding the dependence of relaxation processes in traps on the phonon distribution and a measure of the importance of higher order phonon scattering events.

In addition, we are exploring the use of superconducting junctions to produce a narrow band of high energy phonons, so that we may make detailed phonon frequency measurements up to the Debye cutoff.

7. ENERGY TRANSFER DYNAMICS IN MOLECULAR SOLIDS USING A TUNABLE DYE LASER

Robert M. Shelby, Ahmed H. Zewail and Charles B. Harris

The study of dynamical processes such as excitonic energy migration, phonon-assisted promotion of localized trap states, exciton-phonon interaction, exciton-exciton annihilation, interaction between trap states, and other aspects of energy transfer has been broadened in our laboratories through the use of a nitrogen-laser-pumped narrow line tunable dye laser. It is possible, using this laser, to directly populate a selected guest or host triplet state level. Then, in the simplest of these experiments, one monitors the time evolution of the phosphorescence emission to obtain information related to the presence and relative importance of existing decay channels, the extent of exciton-phonon and exciton-exciton interactions, etc.

We are currently applying these techniques to the study of energy migration in the model systems, 1,2,4,5-tetrachlorobenzene and 1,4-dibromonaphthalene, which are examples of narrow band and wide band one-dimensional exciton systems, respectively. Additional experiments utilizing a combination of high-resolution laser excitation and microwave pumping are in preparation.

8. THE THEORY OF COHERENCE IN MULTILEVEL SYSTEMS AND ITS APPLICATION TO NEW LASER OSCILLATORS AND AMPLIFIERS*

William G. Breiland, Michael D. Fayer and Charles B. Harris

By treating an excited triplet state as a coherent driven two-level system that is in contact with a "population reservoir," as illustrated in Fig. 1, a complete, closed form theoretical development has been obtained that includes the effects of spin-spin relaxation, both in the Bloch and modified Redfield forms, spin-lattice relaxation, and spontaneous emission. The formalism was extended to the case involving coherent driving fields in the optical frequency region. In addition to providing a sound basis for quantitative applications of experiments involving excited state spin coherence, the development has revealed that a substantial amount of spin coherence can be maintained for essentially indefinite periods of time, despite the fact that relaxation and excited state decay processes are continually destroying the coherent state. This condition may be achieved by applying an off-resonance high power field to the system; the combination of incoherent feeding and coherent driving field serve to maintain the coherent component in the presence of decay

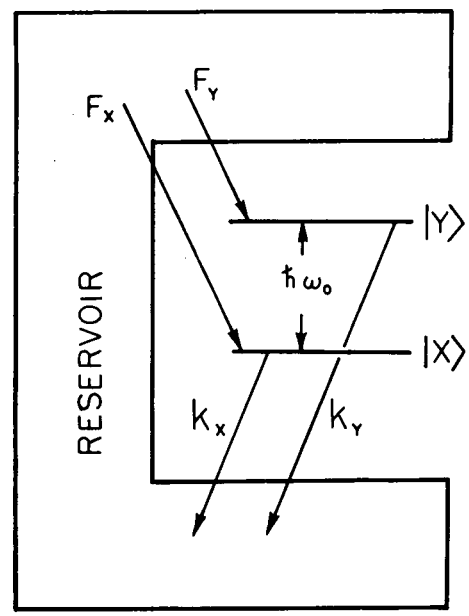

Fig. 1. Pictorial description of the model system presented in the discussion. F_Y and F_X are constant feeding rates, whereas k_Y and k_X are decay rates. (XBL 751-5623)

mechanisms, as illustrated in Fig. 2. An experimental verification of the long-term coherent state was made using two independent methods, wherein it was demonstrated that the coherent component was maintained for a time corresponding to 57 lifetimes of the excited triplet state without any observable loss in magnitude. The results of these experiments are presented in Figs. 3 and 4. Although applications of this technique in the microwave region of the spectrum are somewhat limited, it should prove very much more useful for optical frequencies, for then the coherent component is a macroscopic oscillating dipole that results in a superradiant state. These results predict that a novel method for maintaining and controlling a supperradiant state by use of a driving field and incoherent feeding would be possible.

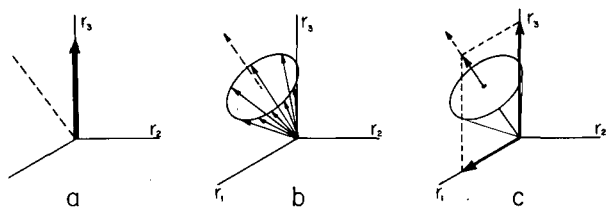

Fig. 2. (a) Initial population difference vector (heavy arrow) will precess about the effective field direction (dashed arrow in r_1-r_3 plane). (b) Feeding and dephasing processes produce a cone of vectors about the effective field direction. (c) Vector sum of the cone yields a vector aligned along the effective field direction and having a coherent component. (XBL 751-5624)

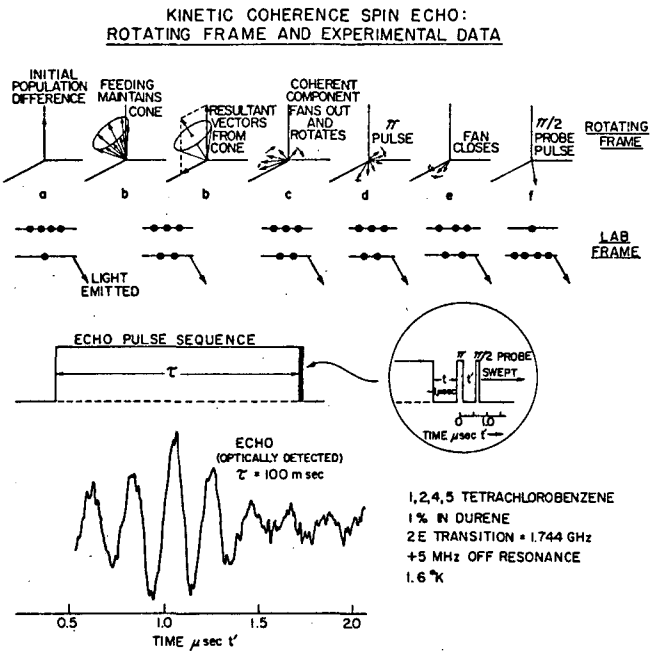

Fig. 3. "Kinetic Coherence" in an electron spin system detected by the spin echo technique. (XBL 745-6282)

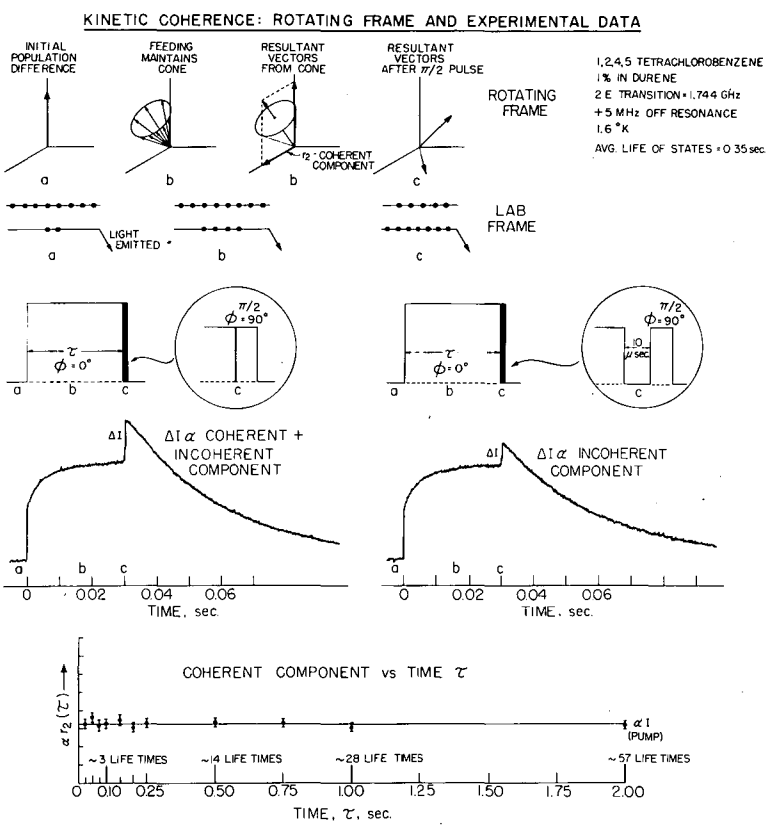

Fig. 4. "Kinetic Coherence" vs. time in an electron spin system. (XBL 745-6284)

*Partially supported by NSF

9. PICOSECOND SPECTROSCOPY: COHERENCE AND VIBRATIONAL RELAXATION IN LIQUIDS AND SOLIDS

Robert M. Shelby and Charles B. Harris

The study of many aspects of energy transfer, in particular those related to radiationless transitions or involving vibrational energy transfer and relaxation, is complicated by the extremely short (10^{-9} - 10^{-12} sec) time scales involved. The technique of picosecond laser spectroscopy, although presenting considerable instrumental difficulties, circumvents the poorer time resolution of more conventional techniques through the use of mode-locked lasers as sources of ultra-short pulses of high intensity, coherent light. These pulses are used to excite the system, and then to spectroscopically monitor the state of the system at some time following excitation, thus reflecting the time evolution of the system in the interim.

Specifically, it has been shown in other laboratories that it is possible to produce coherent vibrational excitation of organic molecules in the liquid phase using the phenomenon of stimulated Raman scattering. The decay of both the coherence and the vibrationally excited population itself can then be monitored via the intensity of the coherent and incoherent anti-Stokes scattering, respectively, of probing pulses of light. We have constructed a mode-locked Nd-glass laser, and using pulse selection and laser amplification techniques, are extending these studies with two basic goals in mind. First, the study of vibrational energy relaxation and loss of coherence in liquids should lead to further insight into the mechanisms and pathways responsible for the decays. Secondly, we are extending these methods of investigation to the study of vibrational energy transfer in solids.

10. ENERGY AND ELECTRON TRANSFER IN PHOTOSYNTHETIC BACTERIAL SYSTEMS*

Robert M. Shelby, Kenneth Sauer and Charles B. Harris

A mode-locked ruby laser has been used to probe absorbance changes associated with the primary processes of photosynthesis on a time scale ranging from 20 picoseconds to several nanoseconds. Preliminary results from a recent experiment designed to probe for absorbance changes at 793 nm in reaction centers from the photosynthetic bacterium Rps. spheroides indicate that there may be a bleaching of P800 at 0.5 nanosecond after excitation with 793 nm light.

*Collaborative with Prof. Kenneth Sauer, LBL-Biodynamics

11. RESEARCH PLANS FOR CALENDAR YEAR 1975

Charles B. Harris

(A) Phosphorescence Spectroscopy and Optically Detected Magnetic Resonance of Aromatic Hydrocarbons Adsorbed on Catalytic Metal Surfaces

The recent advances in phosphorescence double resonance spectroscopy (PMDR) made in these and other laboratories have provided a great deal of new information about excited states in the bulk crystal as well as in dilute guest-host mixtures. The sensitivity of this method allows one to examine details of the excited state which have previously been inaccessible. We plan to apply these methods to investigate the nature of monolayers of organic molecules in excited states on the surface of a clean metal or semiconductor. Because of the sensitivity of the techniques, we expect to be able to measure coverages as low as 0.01%. The studies will also be correlated with the existing surface and structural data through LEED and Auger Electron Spectroscopy. The investigation will start with the (111) and (100) surfaces of platinum and the platinum High Miller index faces, characterized by stepped surfaces, and then will be extended to other transition metal, alloy and organic surfaces.

The need for additional techniques to study surface phenomena is self-evident. Apart from complementing the additional techniques, these new studies should provide a great deal of experimental data that has not been obtainable heretofore. Additionally, these methods should provide the first experimental information about the radiative and non-radiative decay of excited states when the molecules are adsorbed as monolayers on surfaces. There is significant theoretical interest on this subject at the present time, yet virtually no experimental information is available to assess the importance of various channels.

(B) Dynamics of Energy Transfer in Solids

The study of dynamical processes such as energy transfer in molecular crystals will be extended using the techniques of laser spectroscopy. In particular, a nitrogen-pumped tunable dye laser will be used to populate specific energies of localized and delocalized states, and the techniques developed in 1974 will be hybridized with high-resolution laser techniques to study directly additional properties of excited triplet states and exciton bands, including bimolecular exciton-exciton annihilation.

(C) Phonon Interactions in Solids

The specifics of phonon interactions in molecular excited states will be investigated, utilizing the new optical detection techniques developed in this laboratory. Electron spin relaxation rates in excited triplet states will be monitored with optically detected microwave pulse techniques while the molecular crystal is subjected to controlled heat pulses.

The specifics of phonon interaction in the

molecular crystal will be mapped by varying the phonon distribution of the heat pulse. This will be accomplished by varying the voltage and the electrical pulse duration applied to the resistive element of the heater. The resistive elements are being fabricated by metal evaporation onto a quartz substrate on which the crystal is placed.

In addition, laser techniques will be employed to investigate the coherence of phonon states in solids, particularly the q=0 wavevector states.

(D) Picosecond Laser Technology

Additional techniques in picosecond laser technology and their application to coherent phenomena will be extended to solids.

12. 1974 PUBLICATIONS AND REPORTS

Charles B. Harris and Associates

Journals

1. M. D. Fayer and C. B. Harris, Coherent Energy Migration in Solids. I. Band-Trap Equilibria at Boltzmann and Non-Boltzmann Temperatures, Phys. Rev. B 9, 748 (1974) (LBL-1808).

2. C. B. Harris, Phosphorescence-Microwave-Double-Resonance in Exciton States of Molecular Crystals and Coherent States of Triplet Spin Ensembles, Pure and Appl. Chem. 37, 73 (1974) (LBL-1845).

3. H. C. Brenner, J. C. Brock and C. B. Harris, The Use of an "Ordered" Electron Spin State As A Probe In Molecular Spectroscopy: Optically Detected Adiabatic Demagnetization in Excited Triplet States in Zero Field, Chem. Phys. Letters 60, 4448 (1974) (LBL-2293).

4. C. B. Harris and M. D. Fayer, Coherent Energy Migration in Solids. II. Spin-Resonance Absorption in Coherent-Wave-Packet States and the Effects of Phonon-Exciton Scattering, Phys. Rev. B 10, 1784 (1974) (LBL-2210).

5. C. B. Harris, M. Glasbeek and E. B. Hensley, Phosphorescence Microwave Double Resonance Spectroscopy in Ionic Solids and Its Application to Coherent Jahn-Teller States in F Centers of CaO, Phys. Rev. Letters 33, 537 (1974) (LBL-2740).

6. A. H. Zewail and C. B. Harris, Coherence in Electronically Excited Dimers. The Observation of Coherent Dimers and Its Relationship to Coherent Excitons, Chem. Phys. Letters 28, 8 (1974) (LBL-2733).

7. C. B. Harris, The Radiationless Decay of Localized States into Delocalized Band States in Solids, Radiationless Processes, Schliersee, Germany (1974).

8. A. H. Zewail, Triplet Exciton Band Structure of Crystalline Phenazine. Chem. Phys. Lett. 29, 630 (1974) (LBL-2794 Rev.).

9. M. D. Fayer and C. B. Harris, The Decay of Localized States into Delocalized Band States. Theory and Preliminary Experimental Investigations Using Optically Detected Electron Spin Coherence, Chem. Phys. Lett. 25, 149 (1974) (LBL-2550).

Invited lectures

1. University of Arizona, Colloquium in Solid State Sciences, Tempe, Arizona, January 1974.

2. Harvard-MIT Colloquium in Physical Chemistry, Cambridge, Massachusetts, May 1974.

3. University of Illinois at Chicago Circle, Department of Chemistry, Chicago, Illinois, May 1974.

4. University of Amsterdam, Departments of Chemistry and Physics, Amsterdam, The Netherlands, June 1974.

5. University of Groningen, Department of Chemistry, Groningen, The Netherlands, June 1974.

6. 2nd International Conference on Radiationless Processes, Schliersee, Germany, September 1974.

LBL reports

1. Michael David Fayer, Coherence in Excited Triplet States of Molecular Crystals, (Ph.D. thesis) LBL-2708, May 1974.

2. A. H. Zewail and C. B. Harris, Coherence in Electronically Excited Dimers. III. The Observation of Coherence in Dimers Using Optically Detected Electron Spin Resonance In Zero Field and its Relationship to Coherence in One Dimensional Excitons, LBL-3139, Aug. 1974.

3. A. H. Zewail and C. B. Harris, Coherence in Electronically Excited Dimers. II. Theory and its Relationship to Exciton Dynamics. LBL-2734, Aug. 1974.

4. A. H. Zewail, Coherence in the Excited States of Multidimensional Systems: Dimer and Exciton Dynamics in Crystalline Phenazine, LBL-3521, Dec. 1974.

5. W. G. Breiland, H. C. Brenner and C. B. Harris, Coherence in Multilevel Systems. I. The Optical Detection of Coherence in Excited States and Its Application to Phosphorescent Triplet States in Zero Field, Sept. 1974 (LBL-2739).

6. W. G. Breiland, M. D. Fayer and C. B. Harris, Coherence in Multilevel Systems. II. Description of a Multilevel System as Two Levels in Contact with a Population Reservoir. Dec. 1974 (LBL-3111).

Alexander Pines, Principal Investigator

1. MAGNETIC SHIELDING TENSORS OF FUNCTIONAL GROUPS

Alexander Pines and James J. Chang

We have continued our work on the determination of magnetic shielding tensors for ^{13}C nuclei in single crystals, and have looked at various functional groups, examining the characteristic behavior in relation to environment in the crystal, molecular structure and hydrogen-bonding, etc. From these studies a general picture has begun to emerge and the data have been extremely useful in structural and dynamical studies of various phases of chemical materials--solids, liquid crystals, adsorbed phases, etc.

As an example of these magnetic properties we show some results on crystals of ammonium hydrogen malonate:

$$HOOC\text{--}CH_2\text{--}COO\ (NH_4) \qquad (1)$$

This was found to be an excellent candidate for our continuing work, for several reasons:

(a) Large single crystals could be grown.

(b) There are only six magnetically inequivalent carbon sites in the unit cell.

(c) There are two functional groups of interest, carboxyl and methylene.

(d) The crystal structure necessary for orientation of the tensor was determined in a parallel study by Chapuis, Zalkin and Templeton of the Nuclear Chemistry Division.

(e) Proton T_1 is short due to the orientationally mobile ammonium groups combined with spin diffusion.

A particularly interesting feature of the present study is the fact that one oxygen of each carboxyl group is strongly hydrogen bonded while the other is not, yielding different CO bond lengths. This has a marked effect on the chemical shielding tensor and produces an orientation quite different from that of the more symmetrical carboxyl groups studied previously.

Single crystals of ammonium hydrogen malonate were grown by slow evaporation from aqueous solution. A suitable crystal was cut and mounted in a machined Kel-F cube whose edges defined the xyz axis system for determination of the tensors. Spectra were obtained with rotation of the crystal about crystal cube xyz axes and analyzed as before to obtain six tensors for the four orientationally inequivalent carboxyl and two methylene groups in the unit cell.

The crystal structure of ammonium hydrogen malonate has space group C2/c with eight molecules per unit cell. The orientation of the xyz axis system with respect to the orthogonal abc* crystal system was determined by means of X-ray precession techniques.

The unit cell of ammonium hydrogen malonate contains four orientationally inequivalent molecules, two pairs related by a center of symmetry. The two inequivalent molecules are shown in Fig. 1 with a projected view down the b axis. Thus, in a general orientation six lines are expected in the ^{13}C nmr spectrum, four from the carboxyl groups and two from the methylene groups. Six or less lines were indeed observed and followed for the three rotational experiments.

The orientation of the principal axes of the tensors with respect to the crystallographic abc* axes is presented in Table 1 as direction cosines. The principal values are discussed in the next section. The primed tensors are related to the unprimed tensors by a rotation about the b axis and are therefore assigned to different molecules. This symmetry requirement reduces the number of possible assignments to eight. Of the eight remaining possibilities only one assignment is consistent with the requirements that (a) the tensors should be related to the local molecular environment in the same way and (b) the most shielded element of the tensor should lie along the perpendicular to the plane formed by the carboxyl group. The orientation of the principal tensor axes with respect to molecular bond directions with this assignment is shown in Table II. The bond notation employs the numbering of Fig. 1. The other two principal axes of the carboxyl tensor are in the plane of the carboxyl group. However, unlike previous cases where σ_{11} bisect the OCO angle, this axis is rotated in the plane such that σ_{22} comes closer to the shorter of the CO bonds. This situation is depicted

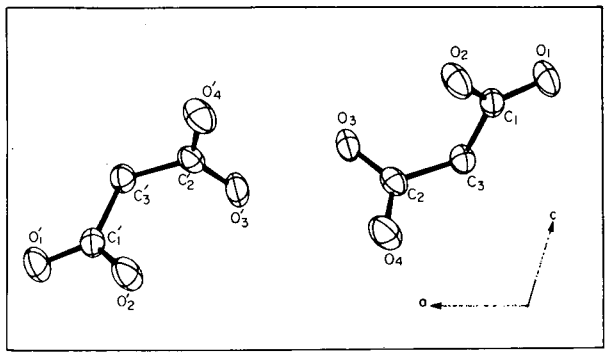

Fig. 1. ORTEP plot of two inequivalent molecules in ammonium hydrogen malonate. The atom numbering is that used in the tensor designation in the text and in the tables. The prime and unprimed atoms are related by a twofold symmetry axis. The C_1 and C'_1 carboxyl groups are in the (C-C-C) planes while the other carboxyl groups are perpendicular to the plane. (XBL 749-1498)

Table I. Direction Cosines of Tensor Principal Axes Relative to Crystallographic Axes.

	Tensor 1			Tensor 1'		
a	.0956	.9265	-.3639	-.0329	-.9099	.4135
b	.6701	.2105	.7718	.7335	.2591	.6283
c*	.7362	-.3119	-.6007	-.6789	.3239	.6589
	Tensor 2			**Tensor 2'**		
a	.9843	-.1499	-.0939	-.9966	.0805	.0186
b	-.1717	-.6816	-.7112	-.0658	-.6379	-.7673
c*	.0426	.7161	-.6967	-.0500	-.7659	.6410
	Tensor 3			**Tensor 3'**		
a	-.1391	-.4423	.8860	.0080	.4236	-.9058
b	-.9595	.2815	-.0101	-.9956	.0875	.0321
c*	-.2450	-.8515	-.4635	.0929	.9016	.4224

Table II. Orientation of Principal Axes of ^{13}C Shielding Tensors Relative to Molecular Bond Directions[a]

	Tensor 1			Tensor 1'		
	σ_{11}	σ_{22}	σ_{33}	σ_{11}	σ_{22}	σ_{33}
$C_3 \rightarrow C_1$[b]	25.2	115.1	88.3	23.9	113.7	92.6
$\perp (C_1OO)$[c]	93.2	91.1	3.4	87.3	88.4	3.2
$\parallel (C_1OO)$[d]	65.0	25.2	87.6	66.4	23.8	92.5
	Tensor 2			**Tensor 2'**		
$C_3 \rightarrow C_2$	27.8	117.8	92.0	24.0	113.9	89.4
$\perp (C_2OO)$	86.0	87.1	5.0	90.9	90.9	1.3
$\parallel (C_2OO)$	62.5	28.0	94.5	66.1	23.9	88.8
	Tensor 3			**Tensor 3'**		
$C_3\ C_1$	131.55	111.91	130.45	127.26	121.51	126.89
$C_3\ C_2$	104.3	97.58	16.25	99.88	97.90	12.70
$\perp (C_1C_3C_2)$	119.12	29.12	90.29	130.50	40.50	90.40

[a]errors in angles are ± 3°

[b]$C_i \rightarrow C_j$ is along the C_i-C_j bond bisecting the OC_jO bond angle.

[c]perpendicular to the carboxyl plane.

[d]perpendicular to the above two directions.

schematically in Fig. 2. As shown in the X-ray work, one of the oxygens of each carboxyl group is strongly hydrogen bonded to a hydrogen bridge atom between two molecules. The two CO bonds are therefore close to being pure double (C=O) and single (C-O) bonds. Thus there is no local C_{2v} symmetry axis bisecting the OCO angle as in benzoic acid and thus no requirement for σ_{11} or σ_{22} to be in any specific direction. *The rotation away from the ideal symmetry case is thus a reflection of the hydrogen bonding.* We have found this in other cases too, and have also noticed a correlation between the magnitude of σ_{22} and the rotation angle of the axes in the plane.

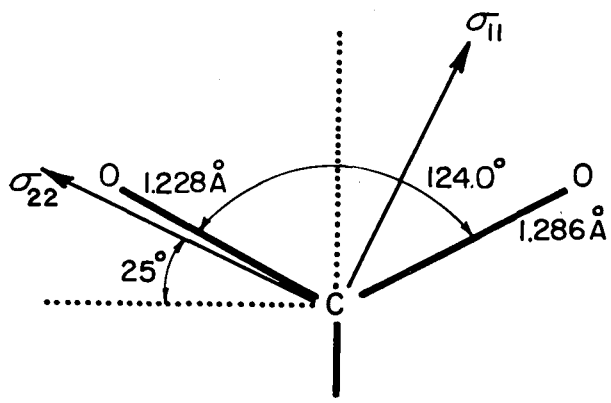

Fig. 2. Orientation of principal axes of ^{13}C chemical shielding tensor for carboxyl groups in ammonium hydrogen malonate. The most shielded element σ_{33} is perpendicular to the carboxyl plane while the other two axes are oriented as shown. (XBL 748-7108a)

The orientation of the methylene tensors with respect to the methylene group geometry also appears in Table II as tensors 3 and 3'. The tensor is found to have the most shielded element in the plane defined by the 3 carbons. The malonate molecule is in a configuration such that one of the carboxyl group planes is in the same plane as the molecular (CCC) skeleton plane and the plane of the other carboxyl group is perpendicular to the C-C-C plane. The most shielded element of the tensor is oriented 14.5° away from the CC bond which is adjacent to the out of plane carboxyl group.

In our carbon-13 liquid crystal work, we have noticed that in the isotropic-nematic transitions, the lines from side chain methylene carbons shift upfield. Since the nematic ordering involves an arrangement of the aliphatic side chains parallel to the magnetic field, this means that the most shielded element of the methylene tensor is more or less "along the chain". This is in agreement with the orientation of the malonate methylene tensor described above. It is clear that a detailed study of these tensors and a characterization of relationships between structure and tensor orientation will yield valuable information for the application of nmr to structure and dynamics of chemical systems.

2. EFFECT OF HYDROGEN-BONDING ON CARBOXYL SHIELDING TENSORS

Alexander Pines and James J. Chang

An important use of the nuclear magnetic shielding properties which we have determined is the elucidation of local microscopic structure in solids. In this section we illustrate this with some work showing a correlation between distortion in the orientation of shielding tensors for the carboxyl group (^{13}COO) and asymmetry in hydrogen bonding. Theoretical calculations explaining the behavior are under way and together with the results should be invaluable in understanding the effects of intermolecular forces on electronic structure.

Figure 1 shows how a large number of carboxylic acids and salts pack in the solid--they dimerize through double hydrogen-bonding. Concentrating on the ^{13}C nucleus, we see that if the two hydrogen bonds were equivalent we would have local C_{2v} symmetry at the nucleus, imposing an orientation of the shielding tensor conforming to this symmetry, i.e. σ_{11} bisecting the OCO angle, σ_{33} perpendicular to the carboxyl plane. As the hydrogen-bonding becomes unsymmetrical, yielding unequal CO bond lengths, the symmetry is destroyed and we can say nothing a priori about the orientation of σ_{11}.

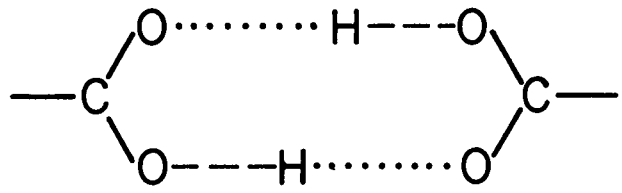

Fig. 1. Hydrogen-bonding in solid carboxylic acids. (XBL 751-5549)

We have determined tensors in a number of materials to see these effects and Table I summarizes some of the results. From X-ray data it is seen that the higher angles in the right hand column correspond to higher distortions in the COO symmetry, so indeed the tensor is a valuable diagnostic tool for local structural determination. Another striking fact is the sensitivity of the magnitude of σ_{22} to the distortions, whereas the other elements are relatively insensitive. This behavior is not yet understood fully and work is continuing to elucidate these effects.

Table I. $^{13}COO^-$ Shielding Tensors

Compound	σ_{11}	σ_{22}	σ_{33}	$<(\sigma_{33},\perp)^a$	$<(\sigma_{11},C\text{-}C)^b$
alanine	-116±2	-56±2	19±2	3±4	10±4
malonic acid	-114±2	-48±2	23±4	0±2[c]	32±2
ammonium hydrogen malonate	-113±2	-46±3	26±2	3±3	25±3
ammonium tartrate	-111±3	-62±4	22±2	7±3	4±3
benzoic acid	-103±4	-60±4	25±4	4±2	0±3

[a]angle between σ_{33} and perpendicular to $^{13}COO^-$ plane.

[b]angle between σ_{11} and C-C direction bisecting CO bonds.

[c]imposed on tensor, not by X-ray orientation.

3. CROSS-POLARIZATION DYNAMICS IN DOUBLE-RESONANCE

Alexander Pines and Thomas W. Shattuck

Energy transfer in spin systems is induced by the interaction of time-dependent nuclear magnetic moments. This interaction, for example, allows the exchange of spin energy between the protons and carbon-13 nuclei in an organic solid. The magnetic dipole interaction causes a modulation of the magnetic field at a particular ^{13}C nucleus. This fluctuating field induces transitions between the ^{13}C Zeeman levels causing the energy transfer, and can be characterized by a correlation time τ_c. This can be thought of as the average time during which the magnetic field at a ^{13}C nucleus stays constant. The correlation time can be rigorously calculated knowing the structure of the solid of interest. It can also be measured experimentally. This has been accomplished in our laboratory for polycrystalline adamantane.

The general characteristics of the energy exchange are expressed by the correlation function of fluctuations in unlike spin coupling. The spectrum of the fluctuations, the strength of the fluctuation at a particular frequency, which is related to the Fourier transform of the fluctuations, is given by:

$$T_{IS}^{-1}(\omega_1) = \langle \omega_{IS}^2 \rangle \tau_c \exp(-\omega_1 \tau_c) \qquad (1)$$

I,S depict the ^1H and ^{13}C nuclear spins, $T_{IS}^{-1}(\omega)$ is the rate of energy exchange, which measures the strength of the fluctuation at frequency ω_1, τ_c is the correlation time and $\langle \omega_{IS} \rangle$ is a constant given by the structure of the solid, related to the second moment of the S resonance. These calculations are of great interest since (a) they are useful structural tools, (b) they will permit the design of optimal high sensitivity techniques for detection of rare isotopes, (c) they provide good models for statistical mechanical theories of spin behavior.

The transfer of nuclear spin energy from ^1H to ^{13}C for our experiments on adamantane is depicted in Fig. 1. The ^1H spins were adiabatically

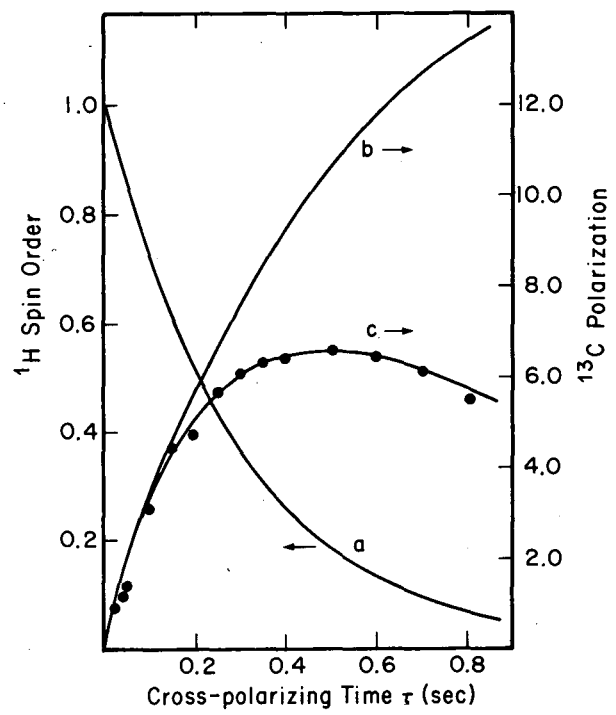

Fig. 1. Growth of ^{13}C magnetization after coupling to ^1H spins. The circles are experimental data. Curve a shows the loss of proton spin order due to spin-lattice relaxation of the dipolar reservoir. Curve b shows the predicted growth of the ^{13}C magnetization with no ^1H spin-lattice relaxation and curve c is the combined predicted behavior. From these data the best value for $T_{IS}^{-1}(\omega_1)$ are extracted. In this case, H_1 the rotating ^{13}C field was 11 Gauss. (XBL 7314-7170)

demagnetized in the rotating frame and then coupled to the ^{13}C spins in the rotating frame by an oscillating magnetic field at the ^{13}C frequency as in the experiments of McArthur et al. on ^{43}Ca-^{19}F. The nuclear spin energy then transfers from the ^{1}H to ^{13}C spins and $M(\tau)$ in Fig. 1 is the time dependence of the ^{13}C magnetization. The decrease for long τ is due to loss of energy between the spins and the lattice, spin-lattice relaxation. From this graph, one value $T_{IS}(\omega_1)$ in (1) is extracted, where ω_1 is given by:

$$\omega_1 = \gamma H_1 \tag{2}$$

and H_1 is the strength of the applied ^{13}C oscillating field in the rotating frame. Such experiments were done for various values of ω_1 and from (1) a value of τ_c extracted, yielding

$$\tau_c = 140 \pm 20 \ \mu\text{sec} \tag{3}$$

Theoretically, τ_c is given in terms of lattice sums as:

$$\frac{1}{\tau_c^2} = \frac{1}{36} S(S+1)\gamma^4\hbar^2 \frac{M_1M_2 - M_4}{M_1} \tag{4}$$

where

$$M_1 = \sum_i [P_2(\cos\theta_i)]^2 r_i^{-6} \tag{5}$$

$$M_2 = \sum_{ij} [P_2(\cos\theta_{ij})]^2 r_{ij}^{-6} \tag{6}$$

$$M_4 = \sum_{i<j} P_2(\cos\theta_{ij})\, P_2(\cos\theta_i)\, P_2(\cos\theta_j)(r_{ij}\, r_i r_j)^{-3} \tag{7}$$

The variables r_i, r_{ij}, θ_i, θ_{ij} are related only to the lattice structure and are shown in Fig. 2. These sums have been performed on a computer for the face-centered-cubic structure of adamantane for a lattice containing 1000 molecules. The calculation is a priori and rigorous with no adjustable parameters.

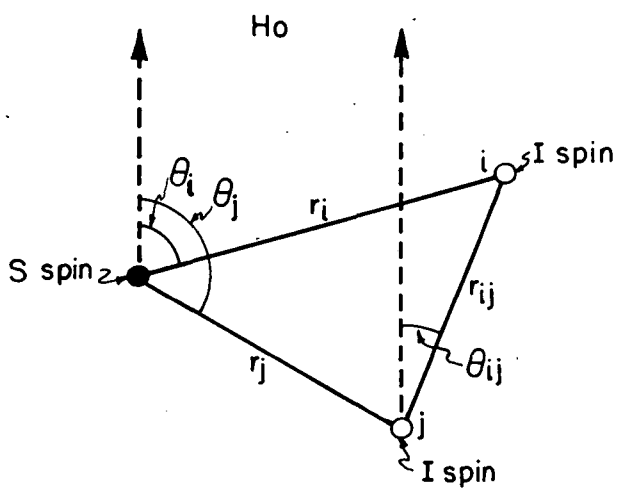

Fig. 2. Lattice variables for interacting spins. (XBL 752-5722)

The average value of τ_c calculated for a polycrystalline sample from these data is τ_c = 122 μsec which is reasonable agreement with the experimental value in (3). These data have been found invaluable in spin-decoupling studies currently in progress in our laboratory.

4. MOLECULAR ORDERING AND PHASE TRANSITIONS IN LIQUID CRYSTALS

Alexander Pines, Stuart A. Allison, and James J. Chang

Although nuclear magnetic resonance (nmr) has featured prominently in the study of liquid crystals, its application has not been straight forward. The reason for this is readily appreciated: the molecules comprising liquid crystal systems are normally long, rod-like in character. In isotropic liquid phase rapid molecular reorientation takes place and thus averages to zero the direct magnetic dipolar couplings between nuclear spins. In the liquid crystalline phase, motion about the long axes is rapid, but the axes (the molecular directors) are aligned preferentially along the magnetic field and reorientation is inhibited. This leads to complicated, normally intractably broadened nmr spectra. Some of the common liquid crystal phases are depicted in Fig. 1.

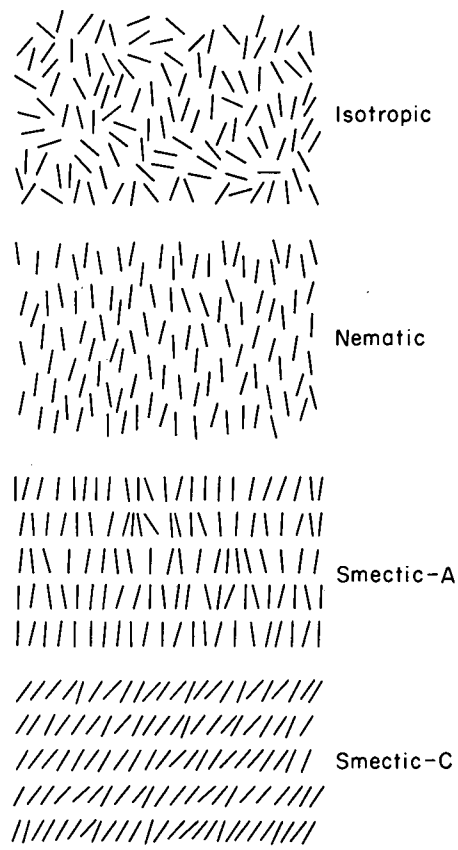

Fig. 1. Schematic description of the high temperature liquid crystal phases. (XBL 748-7063)

Here, we show the observation of ^{13}C nmr spectra in the isotropic, nematic and solid phases of p-methoxy benzylidene p'-n-butylaniline (MBBA), Fig. 2. This work provides the first high resolution ^{13}C nmr study of the phase transitions in a liquid cyrstal and opens the way for a detailed study of structure and dynamics in liquid crystals on a microscopic scale. The advantages of observing ^{13}C derive from the absence of ^{13}C-^{13}C dipolar splittings due to its low natural isotopic abundance (~ 1%), the large range of chemical shifts and thus sensitivity to molecular ordering, and the dominant dependence of the ^{13}C spectra and spin relaxation times upon local intramolecular effects. The study of liquid crystals is extremely important for several reasons: (a) They serve as models for phase transitions and critical phenomena, e.g. superconductivity (b) they provide well defined orienting environments (c) technological importance in displays, non-linear optical devices, etc. and (d) models for biological membranes.

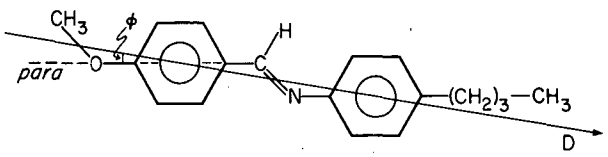

Fig. 2. p-methoxybenzylidene-N-butylaniline (MBBA). (XBL 752-5832)

Figure 3 depicts the ^{13}C line positions over a wide temperature range in MBBA. The six sets of points below 18° were taken with temperature decreasing from the nematic phase; above this temperature, points were taken both with temperature increasing and with temperature decreasing, giving similar behavior. From our results a number of conclusions can be drawn:

1. In the nematic phase only one line is observed from each pair of ortho carbon positions. This demonstrates unequivocally that the benzene rings reorient rapidly about their para axes.

2. The single line at 75 ppm is due to the O-CH_3 group and changes only by 1.5 ppm from the isotropic phase to the nematic phase at 10°C. This indicates that the angle between the O-CH_3 axis and the molecular axis (D) is close to 54.7°, the 'magic angle'. In p-azoxy dianisole (PAA) we have observed similar behavior and have found $\sigma_{\parallel}-\sigma_{\perp}$ ~ 60 ppm for the O-CH_3 group in the solid.

3. Since the molecules reorient rapidly about D, each ^{13}C tensor $\underset{\sim}{\sigma}$ yields a motionally averaged tensor $\bar{\underset{\sim}{\sigma}}$ with components $\bar{\sigma}_{\parallel}$ along D and $\bar{\sigma}_{\perp}$ perpendicular to D. The chemical shifts from the isotropic to nematic phase are given by:

$$\Delta\sigma = \frac{2}{3} S \, (\bar{\sigma}_{\parallel} - \bar{\sigma}_{\perp}) \qquad (1)$$

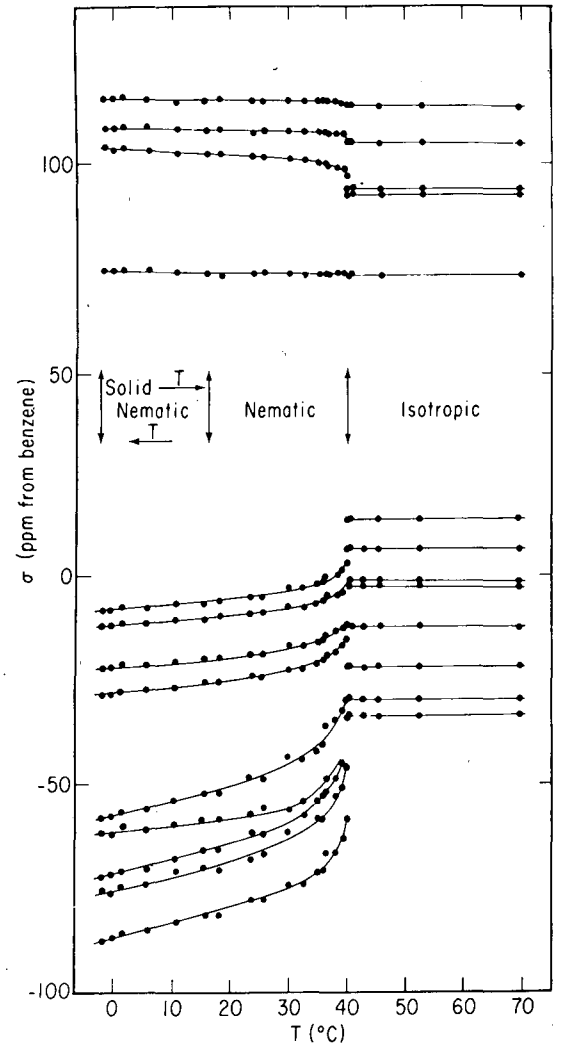

Fig. 3. Dependence of ^{13}C line positions in MBBA on temperature. The points below 18°C were taken with temperature decreasing from the nematic phase, since the lines are broad in the solid. (XBL 743-5843a)

where S is the order parameter. We have used average data for $\underset{\sim}{\sigma}$ from studies of model aromatic solids, taking σ_{11} = -98, σ_{22} = -13, σ_{33} = 108 ppm to calculate values of S from the data in Fig. 3 and equation. We estimate, for example, S = 0.58 at 10°C in the nematic phase and S = 0.29 just below the clearing point (40.6°), with a consistency of ± 0.03 between the different sets of ^{13}C nuclei. To compare our results with previous work, Fig. 4 shows relative values of S calculated from the ^{13}C shifts and normalized (N) to the value of Lee et al. at T_C-T = 2°. A full determination of the tensors $\underset{\sim}{\sigma}$ from solid state work will yield precise values of S and molecular conformation parameters and such work is under way in our laboratory.

4. In the nematic phase, cross-polarization between the ^{1}H and ^{13}C spins is efficient and most of the spectra were obtained using this technique. Unlike the case of solids, this

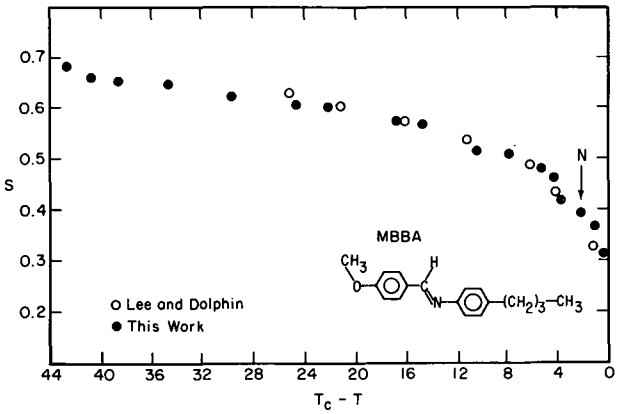

Fig. 4. Temperature dependence of order parameter from our work compared with Lee et al. normalized to 0.39 at T_c-T = 2°C. (XBL 744-6036)

probably proceeds by an intramolecular transfer since translational diffusion is rapid. The advantage of this approach over normal Fourier-transform nmr are enhanced signal/noise and the possibility of studying order fluctuations through cross-polarization dynamics.

5. EFFECTS OF END CHAINS ON NEMATIC STABILITY

Alexander Pines, David J. Ruben, and Stuart A. Allison

Although molecular end chains are known to have perceptible and important effects on the properties of liquid crystals, until recently, theories of the liquid crystal phase have not included their effects explicitly. Rather, their influence was taken into account indirectly by assuming simply that they 'take up space' and thus affect the average interaction between essentially rigid molecules. Marvelja has recently presented a theory which accounts specifically for the effects of the end chains on the anisotropic interactions between the molecules. This theory provides good agreement with experimental data on isotropic-nematic transition temperatures and entropies, and explains for the first time the "even-odd" effect in these quantities along a homologous series. A quantity of prime concern in the structure of the nematic phase is the degree of orientational molecular ordering, described by nematic order parameter:

$$S = \langle P_2(\cos\theta) \rangle \qquad (1)$$

where θ is the angle between the long molecular axis and the nematic director. A striking prediction of the theory is that S should depend significantly on the end chains and should also exhibit the even-odd effect in a homologous series. Here we present the results of measurements of the order parameter for a homologous series of nematic liquid crystals at the isotropic-nematic transitions and lower in the nematic phase. These data provide the first convincing manifestation of the effects of chains on microscopic ordering, the even-odd effect for the ordering near the transitions, and a reliable basis for the quantitative examination of microscopic theories of liquid crystal phases. In addition, we present some conclusions regarding conformational motion of the liquid crystal molecules and ^{14}N spin relaxation in the nematic phase.

The liquid crystal series is that of Fig. 1, p-alkoxyazozybenzenes, with n + 1 from 1 to 7.

In order to extract quantitative values of the order parameters for comparison with theory, we make the assumptions that the aromatic $\underset{\sim}{g}$ tensors remain the same and that the geometry of the aromatic region of the molecules is similar throughout the homologous series. The values of σ for the low field lines obtained by our techniques can then be used to calculate relative values for S. Such values at the isotropic-nematic transitions and 5°C below are shown in Fig. 2, normalized to 0.43, the Maier-Saupe value for n + 1 = 1. The values at the transition temperatures were obtained in a separate set of experiments with spectra displaying two sets of lines from the isotropic and nematic phases in

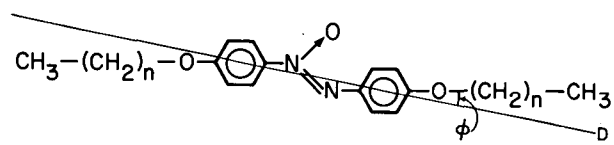

Fig. 1. p-Alkoxyazoxybenzenes, series I.D represents the long molecular axis and ϕ is the angle between this axis and the benzene 'para' axes. (XBL 746-1058A)

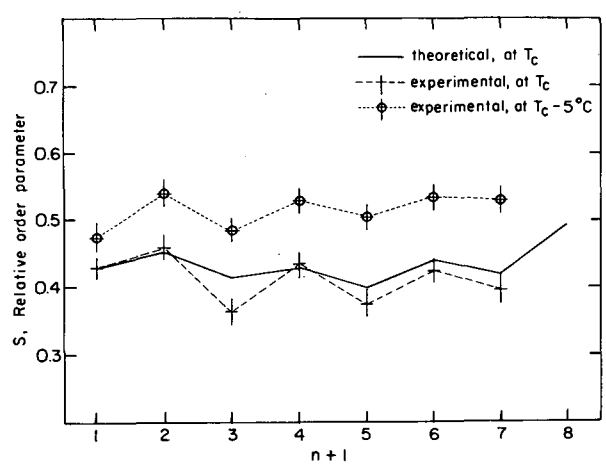

Fig. 2. Relative order parameters calculated from the aromatic chemical shifts at T_c (normalized to 0.43 for n + 1 = 1) and 5°C below T_c in the nematic phase. The vertical bars depict the typical range of values from the different aromatic lines. The theoretical data are taken from the mean field calculation of Marčelja. (XBL 747-6740)

equilibrium. Also shown are the transition values calculated in a mean field approximation by Marvelja. Although these are not expected to be accurate in a mean field theory near the transitions, the correspondence in general trend and in the even-odd effect is quite remarkable.

Finally, it is interesting to comment on some aspects of conformational motion and spin relaxation which can be studied by our technique:

1. Molecular reorientation about the long axes is certainly rapid, but there is a question of conformational rigidity. In particular, are the benzene rings fixed or do they rotate rapidly about the para axes? If the rings are fixed for the series I which we have studied, then in the nematic phase we expect a chemical shift difference $\Delta\sigma$ for the two carbon positions ortho to the N=N linkage given by:

$$\Delta\sigma \approx 1.73 \cdot S \cdot \sin\phi \cos\phi \, (\sigma_{22} - \sigma_{11}) \qquad (2)$$

We find $\Delta\sigma \approx 12$ ppm which is clearly within the limits of our resolution. Since no such additional splittings occur in the nematic phase, we conclude that the benzene rings rotate or flip about the para axes at a rate greater than 1 kHz for the whole series throughout the nematic ranges.

2. A striking observation from the spectra in Fig. 2 is that one set of lines appears to disappear consistently for the whole series in the isotropic-nematic transitions. These are the lines assigned to ^{13}C nuclei bonded to the N=N group and thus coupled to ^{14}N nuclei. A possible explanation for this effect is the combination of ^{13}C-^{14}N magnetic dipolar coupling and ^{14}N spin relaxation by fluctuating electric field gradients. The threefold splitting in ^{13}C lines expected from the coupling is ~ 1 kHz and thus ^{14}N spin relaxation with $T_1 \sim 1$ ms would cause a severe broadening of the ^{13}C lines making the resonance essentially unobservable. Much slower or more rapid ^{14}N spin relaxation would yield three or one sharp lines respectively. ^{14}N spin relaxation has been measured in the isotropic phase of PAA, and it would be interesting to check our contention directly in the nematic phases.

6. MOLECULAR MOTION AND ORDER IN THE SMECTIC-A PHASE

Alexander Pines and Stuart A. Allison

In the previous section we discussed nematic liquid crystals which are characterized only by orientational order. Below the nematic phase, one sometimes finds a smectic phase in which there is translational order. In the case of the smectic-A phase this translational order takes the form of a layering with the long molecular axes perpendicular to the layers as shown in Fig. 1 of Sec. 4. Thus, the system looks like a stacking of two-dimensional liquids and there are two questions of importance:

(a) What are the microscopic conformation and ordering in these phases?

(b) With what facility do molecules diffuse in the layers and between the layers?

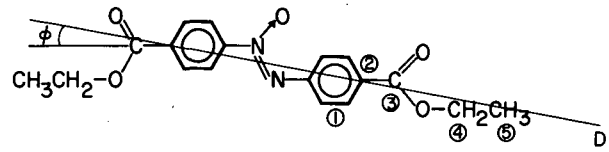

Fig. 1. Di-ethylazoxybenzoate (DEAB) molecule. The long molecular axis is denoted D and the angle between this axis and the benzene 'para' axis is ϕ. 1 refers to the 'ortho' carbons, 2, 2' to the 'para' carbons. The numbering is symmetrical on both sides of the molecule. (XBL 749-7315)

Here we deal with (a) and in a later section we treat in general the problem of diffusion in ordered phases.

One sample we have worked on is di-ethyl azoxybenzoate, shown in Fig. 1. This exhibits a direct isotropic-smectic-A transition, bypassing the nematic phase.

A. Spectrum in Smectic-A Phase

As the temperature is lowered from the isotropic phase, a transition into the smectic-A phase occurs, exhibiting long-range orientational order about a smectic-A director, in this case along the magnetic field, as well as a layered structure. In the case of the smectic-A phase we consider three types of orientational motion: (a) rapid reorientation about the long molecular axis (Fig. 1) (b) fluctuations of the long axis about the smectic-A director, the local average direction of the axis by angle $\theta'(t)$ (c) internal conformational motion.

Looking at the molecular structure of DEAB in Fig. 1, and the qualitative directional properties of σ we can predict that in the isotropic smectic-A transition, with the molecular axes aligning on the average along the magnetic field, the aromatic lines should appear at lower field and the aliphatic side chain lines at higher field. The properties of $\underline{\sigma}$ for the carboxyl group are similar to those of the aromatic, namely σ_{33} perpendicular to the π-nodel plane, so the carboxyl line should also shift downfield. *These qualitative predictions are indeed borne out.* This behavior is similar to that observed for nematic phases.

B. Sample-Rotation in Smectic-A Phase

Consider a liquid crystal sample aligned in a magnetic field, by cooling from the isotropic phase. In nematic liquid crystals it is known that if the direction of the magnetic field is changed suddenly, the molecules rapidly realign with the field. The smectic phases on the other hand, are characterized by large values of the twist elastic constant due to the requirement that planes be maintained, and thus this realignment cannot occur. This behavior of the sample on

rotation of a smectic-A phase in a magnetic field is depicted in Fig. 2. Here, we show the effects of sample rotation on the high resolution ^{13}C nmr spectra, indicating that the line positions are sensitive to the reorientation and should provide a tool for local structural and dynamical studies in the smectic phases.

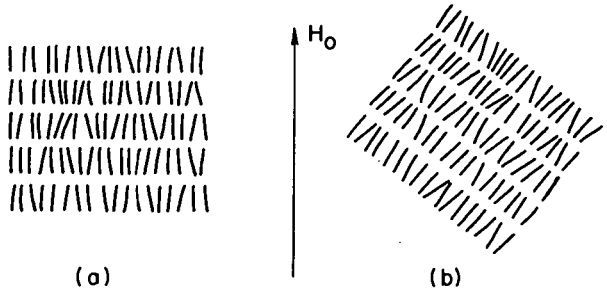

Fig. 2. Schematic description of behavior of smectic-A phase under rotation of the sample. In (a), the sample is cooled into the smectic-A phase and aligns along the magnetic field. In (b), with sample rotation, the layer structure is preserved and the director rotates away from the field. (XBL 748-4010)

Figure 3 shows ^{13}C nmr spectra in the smectic-A phase as the sample is rotated about an axis perpendicular to the magnetic field. The sample was first heated to the isotropic phase in the magnetic field, then cooled into the smectic-A phase, producing an aligned sample, as in

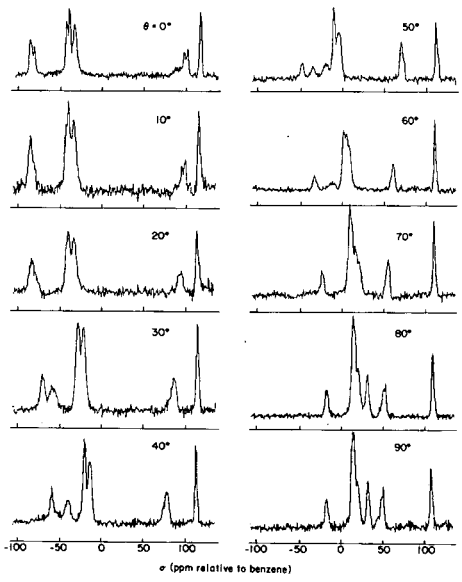

Fig. 3. ^{13}C nmr spectra in the smectic-A phase of DEAB at 114°C at various sample orientations with proton decoupling. The rotation axis is perpendicular to the magnetic field. Note the apparence of a new line at $\theta = 50°C$. (XBL 746-6587)

Fig. 2(a). The sample rotation then reorients the layers as in Fig. 2(b), and as seen from Fig. 3, the line positions are sensitive to this reorientation. The equation describing the orientation dependence of the shifts is:

$$\sigma = \sigma_i + \frac{2}{3} S P_2 (\cos\theta) (\bar{\sigma}_{\parallel} - \bar{\sigma}_{\perp}) \qquad (1)$$

where θ is the angle of sample rotation, i.e., the angle between the director and the magnetic field.

The behavior of the spectra is fitted quantitatively to Eq. (1) in Fig. 4 using σ_i, $S\cdot(\bar{\sigma}_{\parallel} - \bar{\sigma}_{\perp})$ as two parameters. Thus, the behavior is exactly in accord with a well aligned sample, maintaining its orientation and layering undistorted on sample rotation, and with the molecules rotating rapidly about their long axes.

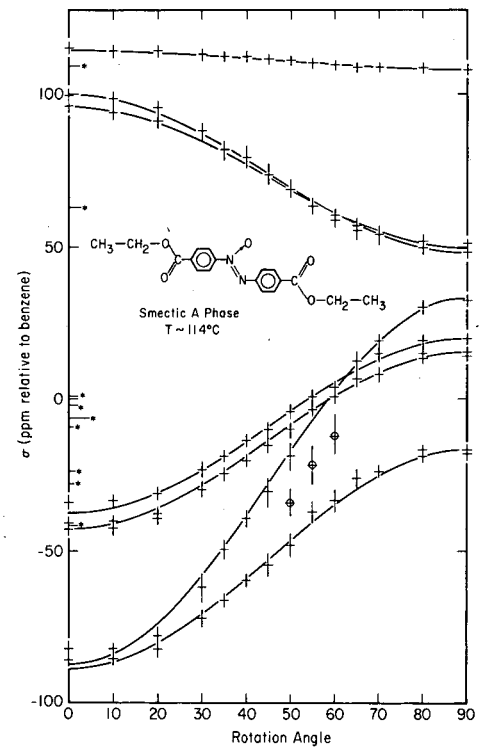

Fig. 4. Dependence of ^{13}C chemical shift on orientation (see Fig. 4) in the smectic-A phase of DEAB. The solid lines are fits using Eq. (1). The lines with asterisks on the left depict the isotropic positions σ_i from Fig. 2. Note that they correspond quite well to the average shifts on rotation $\bar{\sigma} = 1/3\ \bar{\sigma}_{\parallel} + 2/3\ \bar{\sigma}_{\perp}$. The experimental points with circles at θ=50°, 55° and 60° are thought to be from carbons 2' (Fig. 1) with broadening by ^{14}N dipolar coupling. (XBL 746-6597)

C. Temperature-Dependence

The temperature dependence of the ^{13}C lines in the isotropic and smectic-A phases of DEAB is

shown in Fig. 5. In the isotropic phase, as expected, the chemical shift is independent of temperature. However, *the data show that this is also true in the smectic-A phase.* Looking at Eq. (1), we see that this implies for the order parameter:

$$S = \text{const} \qquad (2)$$

in the smectic-A phase, which is very different from the behavior in nematics and in other smectic phases. This indicates that care must be taken in extrapolating from the behavior of probe solutes to the liquid crystal sample itself.

The order parameter is very high in the smectic-A phase, considerably higher than in the nematics we have studied, and the next section attempts a quantitative discussion of this point.

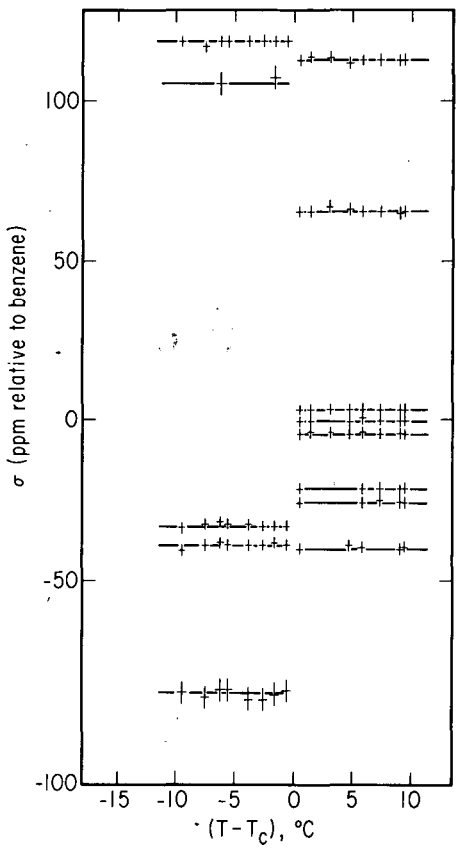

Fig. 5. Temperature dependence of ^{13}C chemical shifts in DEAB. Note the abrupt first order change at T_C=122°C, and the independence on T in the smectic-A phase, corresponding to a more or less constant order parameter. (XBL 748-6929)

D. Order in the Smectic-A Phase

In this section we present a semiquantitative evaluation of the order parameters S in the smectic-A phase. To calculate $\bar{\underset{\sim}{\sigma}}$ the motionally averaged tensor, we define two sets of axes:

(1,2,3) - principal axes of $\underset{\sim}{\sigma}$, with the convention $\sigma_{11} \leq \sigma_{22} \leq \sigma_{33}$.

(x,y,z) - molecular axes, with z along the long molecular axis D, x perpendicular to the molecular plane, y completing a right handed system.

Defining a transformation from (1,2,3) to (x,y,z) in terms of Euler angles (α,β,γ), we obtain a transformed tensor which is then averaged about the z axis corresponding to rapid molecular representation about this axis. This yields for $\bar{\underset{\sim}{\sigma}}$ an axially symmetric tensor with:

$$\bar{\sigma}_{\parallel} = \cos^2\alpha \sin^2\beta\, \sigma_{11} + \sin^2\alpha \sin^2\beta\, \sigma_{22} + \cos^2\beta\, \sigma_{33}$$

$$\bar{\sigma}_{\perp} = \frac{1}{2}(1-\cos^2\alpha \sin^2\beta)\sigma_{11} + \frac{1}{2}(1-\sin^2\alpha \sin^2\beta)\sigma_{22} + \frac{1}{2}\sin^2\beta\, \sigma_{33} \qquad (3)$$

The observed shifts $\Delta\sigma = \sigma - \sigma_i$ can then be used to yield S. The results for these calculations are shown in Table I. The value for angle ϕ (Fig. 1) was taken as 10°. *The $\underset{\sim}{\sigma}$ tensors for each carbon characterized by values of* $(\sigma_{11},\sigma_{22},\sigma_{33},\alpha,\beta,\gamma)$ *were taken from model studies of aromatic carboxyl and methylene groups and the known X-ray crystal structure of DEAB.* The methyl group was not included since its directional shielding properties are not well characterized. For carbons 1, 3, 4, two conformations were considered with two sets of (α,β,γ) shown in the table.

These values, averaged over the conformational motion, are reported as 'averaged' in the table and are the ones used to calculate the order parameters from Eq. (1). A reasonable summary of these figures is:

$$S = 0.9 \pm 0.1 \qquad (4)$$

i.e. almost perfect order, as in the solid, but with facile translational diffusion.

7. ROTATIONAL ORDER IN THE SMECTIC-C PHASE

Alexander Pines, Stuart A. Allison and Alfred Höhener

One of the possible low-temperature liquid crystal phases is the smectic-C. From X-ray studies, it is known that this derives from the smectic-A by a tilt of the molecules in the layers. The microscopic molecular structure of this phase is still a controversial question and is of great importance since it can teach us about the nature of the molecular forces which cause the condensation into the various phases. A microscopic theory due to McMillan proposes that the mechanism for the tilting is derived from interactions between electric dipoles on the molecules as

Table I. Shielding Tensors and Order Parameter for Carbon Nuclei in Smectic-A DEAB.

Carbon[a]	σ_{11}[b]	σ_{22}	σ_{33}	α[c]	β	γ	$\bar{\sigma}_{\parallel}$[c,d]	$\bar{\sigma}_{\perp}$	$\bar{\sigma}_{\parallel}-\bar{\sigma}_{\perp}$[e]	$\Delta\sigma_{obs}$[f]	S (order parameter)
2	- 98	-13	108	100°	90°	90°	- 95	46	-141	-81	0.9
				40°	90°	90°	- 48	23			
1	- 98	-13	108						- 52	-39	1.1
				-20°	90°	90°	- 23	10			
				90°	3°	0°	120	59			
4	53	65	121						59	33	0.8
				90°	-17°	0°	118	61			
				67°	90°	90°	-121	-19			
3	-138	-31	9						- 77	-48	0.9
				47°	90°	90°	- 88	-36			

[a]From numbering in Fig. 1.

[b]From model single crystal work; see text. The values are in ppm relative to an external reference of liquid benzene.

[c]Where two values appear, they refer to the two conformations.

[d]Calculated from Eq. (3).

[e]Average of two conformations.

[f]$\Delta\sigma_{obs} = \sigma - \sigma_i = \frac{2}{3} S(\bar{\sigma}_{\parallel} - \bar{\sigma}_{\perp})$ from Eq. (1).

[g]This clearly means the anisotropy $\bar{\sigma}_{\parallel} - \bar{\sigma}_{\perp}$ taken is too small.

shown in Fig. 1. This would require that the molecules freeze in their rotation about the long axes, unlike the smectic-A and it is this phenomena which experimentalists have been attempting to investigate by several means.

We present here some of our calculations and experiments on the smectic-C phase and present structural evidence which conflicts with some of the proposals from other laboratories. First, we calculate the expected behavior of spectra for any observable which derives from a second rank tensor for some reasonable models of the smectic-C phase. The effect of magnetic fields when the sample is reoriented is calculated and differs dramatically for that in the smectic-A phase.

Consider a sample in a magnetic field cooled into the smectic-C phase. The tilting induces a phase depicted schematically in Fig. 2a. Since the azimuthal angle of the plane normal about the

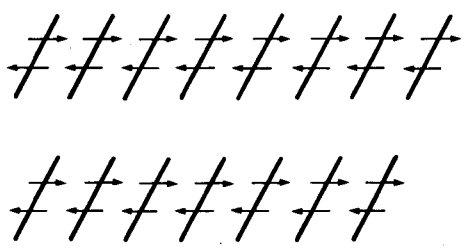

Fig. 1. Electric dipole forces between molecules causing smectic-C molecular tilt according to microscopic theory of McMillan. (XBL 751-5436)

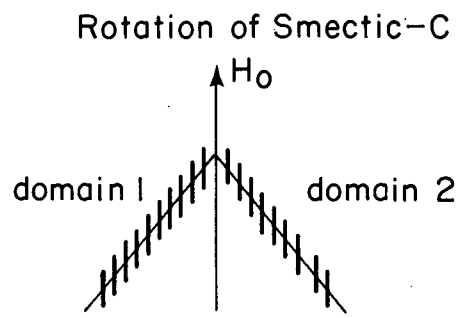

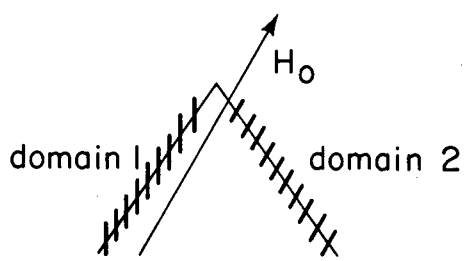

Fig. 2. Behavior of domains in smectic-C phase upon rotation of sample in high magnetic field. (XBL 751-5494)

magnetic field is arbitrary the sample can break into domains, two of which are shown in the figure. The Hamiltonian for our tensor observable $\underset{\approx}{Q}$ is given by:

$$\mathcal{H} = \sum_{m} (-1)^m F_{2m} T_{2-m} + \frac{1}{3} \mathrm{Tr}\underset{\approx}{Q}\, T_{\infty} \qquad (1)$$

We consider the case of a quadrupole tensor. *The observed quantity for (a) is the quadrupole splitting which we call* $\langle \Delta Q \rangle$. What we would like to calculate is $\langle \Delta Q \rangle$ for the average over molecular motion and orientation in the smectic-C phase.

We define three coordinate transformations:

A. principal axes of $\underset{\approx}{Q}$ → molecular symmetry axes [Ω_F]

B. molecular axes → liquid symmetry axes [Ω] (2)

C. liquid crystal symmetry axes → laboratory axes [Ω_H]

Ω are the Euler angles (α,β,γ) of the transformations. For the first calculation we have assumed $\Omega_H = 0$, i.e., an unrotated sample. Using these in Eq. (1) we have

$$\mathcal{H} = \sum_{m,n,k} (-1)^m D^{(2)}_{nm}(\Omega)\, D^{(2)}_{kn}(\Omega_F)\, F_{2k}\, T_{2-m} \qquad (3)$$

where now F_{2k} are in the principal axis system of $\underset{\approx}{Q}$ and T_{2m} are in the laboratory magnet system. $D^{(2)}$ are elements of the Wigner rotation matrices. If the magnetic field is high, then we can neglect all terms in Eq. (3) which do not commute with I_z, the nonsecular terms, yielding together with (1):

$$\mathcal{H} = \frac{eQ}{4} \left[\sum_{n,k} D^{(2)}_{no}(\Omega)\, D^{(2)}_{kn}(\Omega_F)\, F_{2k} \right] (3I_z^2 - I^2) \qquad (4)$$

Now since the molecule fluctuates, Ω is time dependent and we must average over the fluctuation giving the final observable:

$$\langle \Delta Q \rangle = \frac{3eQ}{2\gamma\hbar} \sum_{n,k} \langle D_{no}(\Omega) \rangle\, D^{(2)}_{kn}(\Omega_F)\, F_{2k} \qquad (5)$$

The $\langle D_{no}(\Omega) \rangle$ are the order parameters given as usual by:

$$\langle D_{no}(\Omega) \rangle = \int D_{no}(\Omega)\, P(\Omega)\, d\Omega \qquad (6)$$

where $P(\Omega)$ is the orientational distribution function for the molecules, given in terms of the molecular potential $V(\Omega)$ by:

$$P(\Omega) = \frac{\exp(-V(\Omega))}{\int \exp(-V(\Omega))\, d\Omega} \qquad (7)$$

McMillan's model of the smectic-C phase is a mean field one in which:

$$V(\Omega) = -V_1 \cos^2\beta - V_2 \cos\phi \qquad (8)$$

where $\cos\phi = \cos\alpha \cos\beta \cos\gamma - \sin\alpha \sin\gamma$ and $(\alpha,\beta,\gamma) \equiv \Omega$. The first term in (8) represents the normal nematic quadrupolar interaction with a mean spontaneous quadrupolar field V_1 along the z axis, and the second term is the electric-dipole interaction with a mean spontaneous electric field V_2 along the x axis. If $V_2 = 0$, we find that the only nonzero term in (6) is $\langle D_{20} \rangle$ with, $\langle D_{20} \rangle = S$, i.e. the normal single nematic parameter.

For $V_2 \neq 0$, the calculation yields:

$$\begin{aligned} \langle \Delta Q \rangle = \frac{3e^2Qq}{4\gamma\hbar} \Big[& S(3\cos^2\beta_F - 1) \\ & + \langle \cos^2\alpha \rangle (1-S)(1-\cos^2\beta_F) \Big] \\ & + \eta\sqrt{\tfrac{3}{2}} \cos^2\alpha_F \Big[S \sin^2\beta_F \\ & + \tfrac{1}{3} \langle \cos^2\alpha \rangle (1-S)(2-\sin^2\beta_F) \Big] \end{aligned} \qquad (9)$$

So the additional order parameter which appears is $\langle \cos^2\alpha \rangle$ describing the freezing in of motion about the long molecular axes. *Thus we now have a bridge between the interesting quantity* $V(\Omega)$, *the molecular potential, and the observable* $\langle \Delta Q \rangle$.

Figure 2b shows the expected behavior of domains, which we assume conform to the requirement that the magnetic anisotropy energy:

$$E_m = -\underset{\sim}{H}\, \underset{\approx}{\chi}\, \underset{\sim}{H} \qquad (10)$$

is minimized with the molecules maintaining a constant tilt angle with respect to the smectic layers as shown in Fig. 3.

Molecules reorient with fixed tilt angle to minimize magnetic energy

$$E = -\underset{\sim}{H}\, \underset{\approx}{\chi}\, \underset{\sim}{H}$$

Fig. 3. Interaction of smectic-C domain with magnetic field. (XBL 751-5493)

The observed spectrum will be a superposition from all domains and Fig. 4 shows our computed spectra with no rotational order of the molecules for orientation of the sample perpendicular to the z axis. The smectic tilt angle was taken to be 45°. The form of the spectra is extremely sensitive to $\langle \cos^2\alpha \rangle$ and thus $P(\Omega)$ and we are currently performing experiments to determine the potentials and molecular motion in the smectic-C phase. Our preliminary findings are that even in the smectic-C phase there is free rotation about the long axes and that the ordering cannot be transverse electric dipole in nature, and is more likely repulsive in nature.

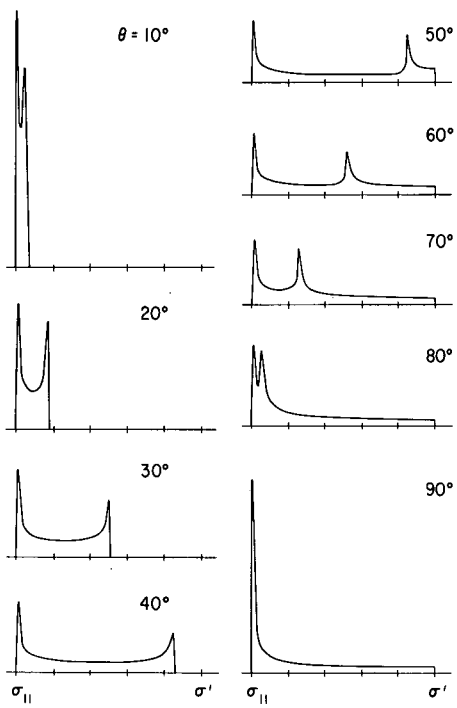

Fig. 4. Illustrative computed spectra for smectic-C phase at various orientations of sample in magnetic field with theory in text. The spectra are very sensitive to fluctuations and rotational molecular order (XBL 7412-7671)

8. MULTIPLE-PULSE SPIN ECHOES AND MOLECULAR DIFFUSION

Alexander Pines, Thomas W. Shattuck and David J. Ruben

The method of spin echoes has been extremely useful in increasing diffusion constants for isotropic fluids. We are engaged in extending this to more ordered systems such as adsorbed phases, liquid crystals, solids, etc. In these cases, it will be possible to measure anisotropies in the diffusion, which are extremely difficult if not impossible to measure by other methods.

The approach is technically quite complicated since it involves a combination of high power rf and video field gradient pulses as shown in Fig. 1. If the refocusing pulse is at time τ, the strength of the field gradient $G(t)$, and the *diffusion constant in the direction of the gradient* D, then it can be shown that the amplitude of the echo at time 2τ compared to that at 0 is given by:

$$\ln\left[\frac{M(2\tau)}{M(0)}\right] = -\gamma^2 D\left[\int_0^{2\tau} \tilde{G}^2(t)dt - 4\tilde{G}(\tau)\int_\tau^{2\tau} \tilde{G}(t)dt + 4\tilde{G}(\tau)\tau\right] \quad (1)$$

where

$$G(t) = \int_0^\tau G(t')\,dt' \quad (2)$$

In the case that $G(t) = G_0$, a constant, i.e., the classical method applied to fluids, we see:

$$\ln\left[\frac{M(2\tau)}{M(0)}\right] = -\frac{2}{3}\gamma^2 D G_0^2 \tau^3 \quad (3)$$

the result of Carr and Purcell. In our case, for reasons we cannot go into here, the gradient is applied in pulses as in Fig. 1 and if the duty cycle for the pulses is δ with amplitude G_0, then for N pulses we find:

$$\ln\left[\frac{M(2\tau)}{M(0)}\right] = -\frac{2}{3}\gamma^2 D G_0^2 \delta^2\tau^3\left(1 + \frac{1-\delta}{2N^2}\right) \quad (4)$$

This has been applied as a check to the diffusion of liquid water at room temperature.

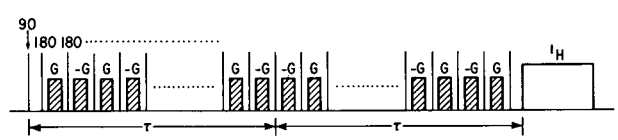

Fig. 1. Pulse sequence used for measurement of diffusion. The 180 pulses induce decoupling of the spin to maintain spin coherence. The G pulses indicate field gradients induced by direct currents. The spin echo is observed during the region marked 'H and from the magnitude of this echo for various values of and directions of G, the diffusion tensor can be determined. (XBL 748-6933)

Figure 2a shows the decay of water magnetization in water using the above pulse sequence with no field gradient applied, showing the normal decay due to spin relaxation. The effect of a gradient, i.e. non-zero G_0 is shown in Fig. 2b--the magnetization now decays rapidly and reappears in the form of a spontaneous echo.

If Eq. (4) holds, then we expect a linear dependence of $\ln M(2\tau)$ on G_0^2, the latter being varied by the pulsed current flowing through

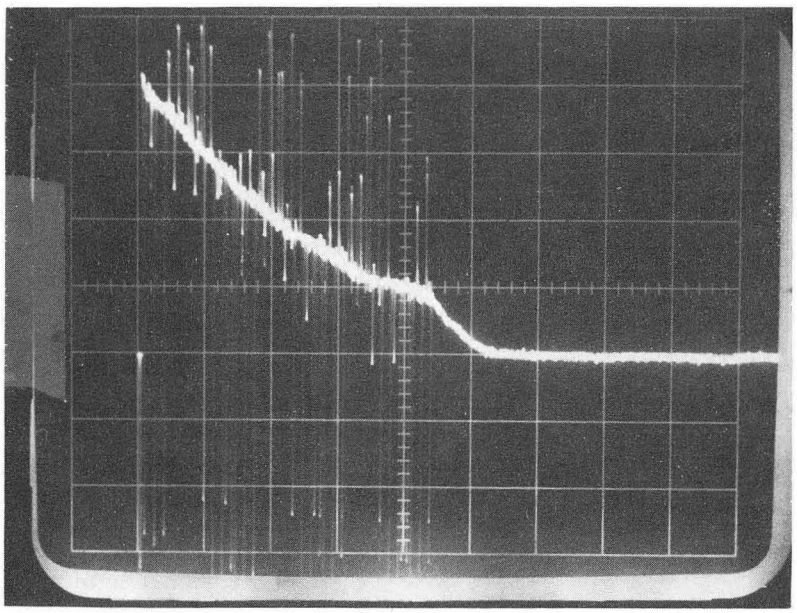

(a)

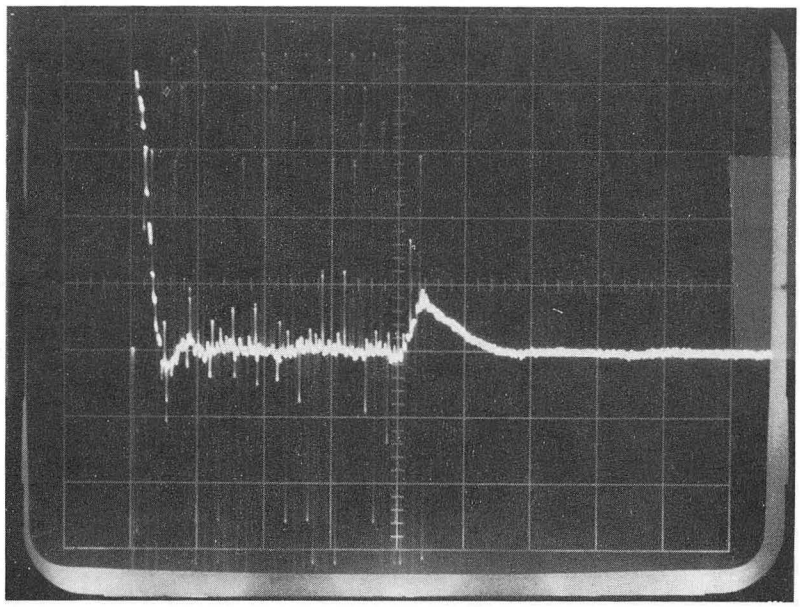

(b)

Fig. 2. (a) Oscilloscope trace showing decay of ^1H magnetization in paramagnetically doped water at room temperature with pulse sequence of Fig. 1 and G=0. The decay is due to normal spin-lattice relaxation. (XBB 7412-7054)

(b) Same as Fig. (a) but with $G \neq 0$. Note now that the magnetization decays rapidly but is refocused as an echo with no loss of coherence even with the large number of pulses. (XBB 7412-7053)

quadrupole gradient coils (0-20 amps). Figure 3 shows such a plot from which a diffusion constant

$$D = 1.8\times10^{-5}\ cm^2/sec$$

is extracted, in good agreement with previous values. Work on applying this to anisotropic diffusion in smectic phases to see the effect of the layered structures is currently under way in our laboratory.

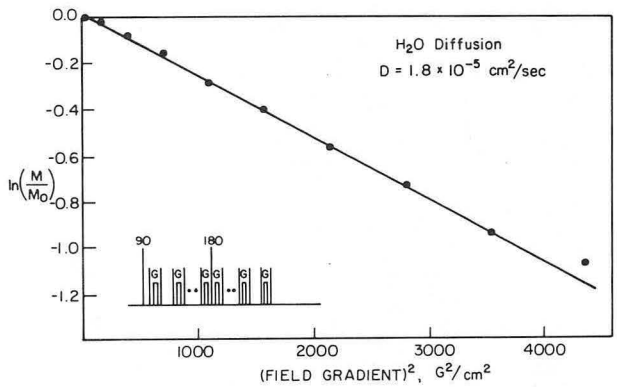

Fig. 3. Dependence of spin echo on field gradient yielding self diffusion constant.
(XBL 751-5605)

9. MOLECULAR MOTION IN SOLIDS

Alexander Pines, David E. Wemmer and David J. Ruben

A perennial and difficult question in the study of molecular solids has been that of the mode of molecular motion. In particular, one expects the potential binding rotational motion in the solid state to differ substantially from that in liquid or gaseous environments. Thus, rotational diffusion is usually assumed for fluids whereas transitions between discrete potential minima are more likely in a solid. Clearly, it is not simple to investigate experimentally the mode of motion in the solid since most observable properties are likely to differ very little between the different cases of motion.

To take a particular example, how would one tell what the mode of molecular reorientation is for the solid phases of benzene, a molecule which possesses a six-fold axis of symmetry. It is known that in solid benzene (above ~ 40 K) the molecules are indeed rotating about the six-fold axes at a rate in excess of several kHz, yielding an average of various spectral parameters which fall in this frequency range. But the mode of motion, and the magnitude of the potentials are questions of great interest, in particular for the study of conformational motion and stability of systems of chemical interest.

One set of properties that differentiates between modes of motion are the time-correlation functions:

$$G_{\ell m}(\tau) = \langle T_{\ell m}(o)\ T_{\ell -m}(\tau) \rangle \qquad (1)$$

where $T_{\ell m}$ are components of spherical tensors of rank ℓ, which are related to our normal observables, e.g., dipole moment (ℓ=1), quadrupole moment (ℓ=2), magnetic shielding tensor (ℓ=2), etc., and $\langle\ \rangle$ denotes an ensemble average. Although magnetic resonance is normally a powerful microscopic tool, the $G_{\ell m}(\tau)$ in (1) cannot normally be extracted in full from experiments, and only a small number of points can be provided by relaxation studies. Thus, even though the different modes of motion yield different $G_{\ell m}(\tau)$, it has not been possible to use magnetic resonance to resolve this, and other approaches such as Raman scattering for direct measurement of (1) are even more difficult.

Alexander and coworkers in Israel and Spiess and coworkers in Germany have recently predicted that it should be possible to distinguish between modes of motion by direct observation of anisotropic spectral parameters in powdered samples. Let us take an example of the magnetic shielding tensor $\underset{\approx}{\sigma}$ for the aromatic nuclei in hexamethylbenzene. This has a six-fold axis like benzene but is easier to handle experimentally. Using expansion techniques, developed in collaboration with Freed at Cornell University, Alexander et al. have calculated the lineshapes for two extreme modes of motion: (a) the molecule jumps between discrete sites corresponding to the minima in a six-fold potential, (b) random jumps between all sites about the six-fold axis. In the region where the rate of rotations is of the order of the magnetic shielding anisotropy, they predict a striking difference in powder lineshapes. No experiments were done on this system before our contribution since the observation of such effects are beyond the technical capabilities of most laboratories.

We show here some direct calculations which we have done on the above system, together with experimental results. Our calculations are 'exact' in the sense that they represent a direct computer solution of the equations of motion, and they do indeed bear out the elegant asymptotic calculations of Alexander et al. Figure 1 indicates the basis of the problem. The powder

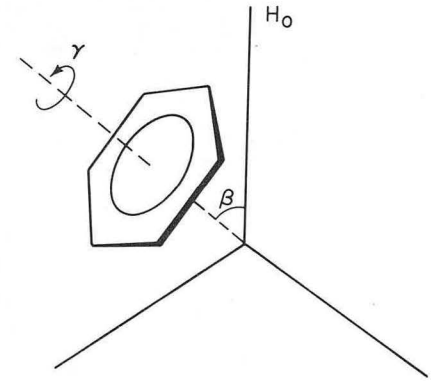

Fig. 1. Orientation of rotating molecules in powder sample. (XBL 751-5546)

sample consists of molecules at all orientations in space, namely, an isotropic distribution in angles (β,γ) in the figure. These molecules reorient about their six-fold axes. Let us denote by σ the observed parameter of the tensor $\underset{\approx}{\sigma}$, i.e., the chemical shift, and by $I_m(\sigma)$ the spectrum of a molecule with orientation Ω in space. Then the observed powder spectrum $I(\sigma)$ is given by:

$$I(\sigma) = \int I_m(\sigma)\ P(\Omega)\ d\Omega \qquad (2)$$

where $P(\Omega)$ is the orientational probability distribution function and $I_m(\sigma)$ is clearly a function of Ω. To calculate $I_m(\sigma)$ we assume the molecule reorients by discrete jumps between sites in a symmetrical n-fold potential. It can then be shown that $I_m(\sigma)$ is given by:

$$I_m(\sigma) \propto \cdot\mathrm{Real}\left\{\sum_{j=1}^{n}\ \sum_{k=1}^{n} A_{jk}^{-1}\right\} \qquad (3)$$

A_{jk}^{-1} are the elements of a matrix $\underset{\approx}{A}^{-1}$ which is the inverse of a relaxation matrix $\underset{\approx}{A}$, with

$$A_{jk} = \tau_{jk}^{-1}\ ,\quad j\neq k$$

$$A_{jj} = i(\sigma-\sigma_j) \sum_{k=1}^{n} \tau_{jk} - T_2^{-1} \qquad (4)$$

The parameters that appear in this matrix are:

τ_{jk}^{-1} : probability of transition from site j to k.

σ_j : the observed shift for site j

T_2^{-1} : natural homogeneous linewidth for σ.

The only missing ingredient then is the dependence of σ on Ω which is straightforward since $\underset{\approx}{\sigma}$ transforms as a second rank tensor. Since we work in high magnetic field, the observable σ is the zero order component of the spherical tensor, i.e., that corresponding to T_{20}.

We have solved the lineshape Eq. (3) for the two cases n=6 and n=24. The first corresponds to the case of a discrete six-fold potential whereas the latter already approximates well the lineshapes for the case of continuous rotational diffusion. For simplicity, all τ_{jk}^{-1} were taken equal to τ^{-1} which is then used as the single parameter to correlate with the experimental dependence of lineshape on temperature.

Figure 2 shows theoretical spectra calculated in this way for various values of τ in the two cases. The case n=24 is on the left. Only the left edge of the powder calculations are shown. Values for σ_{11}, σ_{22} and σ_{33} were taken from measurements at low temperature, and the angles

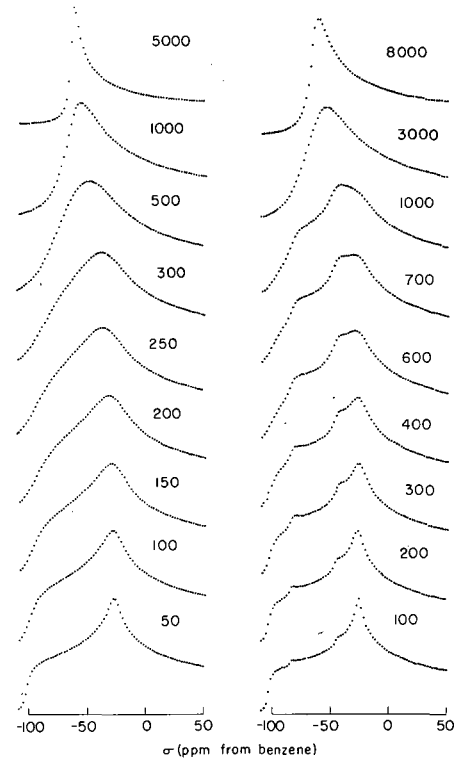

Fig. 2. Calculated powder spectra for benzene jumps. Leftside: in a 24-fold potential approximating continuous rotation. Details of the calculation appear in the text. Note the smooth transition of the lineshape from the low to the high jump rate regimes. The numbers next to the spectra are the transition probabilities τ-1 between the 24 sites in Hz. Rightside: same for a 6-fold potential. Note the peculiar side-band features which appear in this case.
(XBL 752-5720A)

Ω in (5) were determined by assuming that the symmetry of $\underset{\approx}{\sigma}$ is the same as the local molecular symmetry at the nucleus. Note the smooth transition from spectra in the low temperature (low τ^{-1}) require where the molecules are rigid to the high temperature (high τ^{-1}) case where they rotate rapidly about their six-fold axes.

In striking contrast to this, the right side of Fig. 2 shows the calculated spectra for the case n=6. Here, instead of a smooth, featureless transition, structure is seen which is quite characteristic of the symmetry of the potential. The experimental results for polycrystalline hexamethylbenzene are shown in Fig. 3, and we believe that they conform more closely to the case of six-fold discrete jumps in Fig. 2. Thus, this technique appears to provide a sensitive way of determining details of molecular motion. We are currently in the process of calculating the magnitude of the hindering potential from these results and are also extending the work to other molecular solids and potentials.

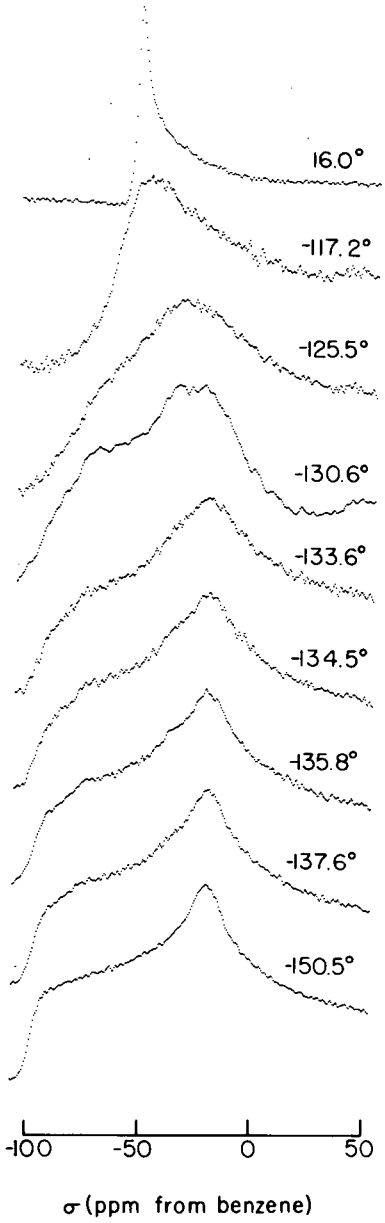

Fig. 3. Left side of experimental spectra for aromatic ^{13}C nuclei in polycrystalline hexamethylbenzene. The spectra appear to conform more closely to the discrete 6-fold case. (XBL 752-5779)

10. RESEARCH PLANS FOR CALENDAR YEAR 1975

Alexander Pines

1. Application of carbon and deuterium nuclei to the elucidation of structure and dynamics in liquid crystals. A new spectrometer (high field-180 MHz for protons) is now operational in our laboratory and increases substantially the resolution and sensitivity in these experiments.

2. Measure anisotropic molecular diffusion in the anisotropic environments of adsorbed phases and liquid crystals. Correlate with structural and environmental parameters.

3. Elucidate modes of molecular motion for molecular solids and correlate to intermolecular potentials.

4. Extend microscopic theory of smectic liquid crystals to include coupling between order parameters.

5. Continue development of techniques for using nuclear spin to influence chemical reactions.

11. 1974 PUBLICATIONS AND REPORTS

A. Pines and Associates

Journals and Abstracts

1. A. Pines and J. S. Waugh, Dipolar Spin Temperature in a Periodically Perturbed Nuclear Spin System, Phys. Lett. A., 47 337 (1974) (LBL-2515).

2. A. Pines and J. S. Waugh, Quasi-Equilibrium in a Perturbed Nuclear Spin System, presented at the 1974 American Physical Society Meeting, Philadelphia, Pa., Bull. Am. Phys. Soc., 19, 251 (1974) (LBL-2512 Abs.)

3. J. J. Chang, R. G. Griffin and A. Pines, Chemical Shielding Tensor of ^{13}C in a Carboxyl Group, J. Chem. Phys. 60, 2561 (1974) (LBL-2513).

4. A. Pines, J. J. Chang and R. G. Griffin, High Resolution ^{13}C NMR in Solid Ammonium Tartrate, presented at the 1974 American Physical Society Meeting, Philadelphia, Pa., Bull. Am. Phys. Soc., 19, 349 (1974) (LBL-2509 Abs.)

5. A. Pines and T. W. Shattuck, Carbon-13-Proton Cross-Polarization Dynamics in Nuclear Magnetic Double Resonance, presented at the 1974 American Physical Society Meeting, Philadelphia, Pa., Bull. Am. Phys. Soc., 19, 351 (1974) (LBL-2508 Abs.).

6. A. Pines and T. W. Shattuck, Carbon-13-Proton NMR Cross-Polarization Times in Solid Adamantane, J. Chem. Phys., 61, 1255 (1974) (LBL-2545).

7. T. Merrick, S. Smiriga and A. Pines, A Simple Data Aqu. System for Proton-Enhanced Nuclear Induction Spectroscopy, J. Mag. Res., 14, 270 (1974) (LBL-2546).

8. A. Pines and E. Abramson, Chemical Shielding Tensors of ^{13}C in Dimethyl Oxalate, J. Chem. Phys., 60, 5130 (1974) (LBL-2522).

9. A. Pines and J. J. Chang and R. G. Griffin, Carbon-13 NMR in Solid Ammonium Tartrate, J. Chem. Phys., 61, 1021 (1974) (LBL-2700).

10. A. Pines and J. J. Chang, Study of the Isotropic-Nematic-Solid Transitions in a Liquid Crystal by Carbon-13-Proton Double Resonance, Phys. Rev. A, 10, 946 (1974) (LBL-2716).

11. A. Pines and J. J. Chang, The Effect of Phase Transitions on ^{13}C NMR Spectra in p-Azoxydianisole, A Nematic Liquid Crystal, J. Am. Chem. Soc., 96, 5590 (1974) (LBL-2742).

12. A. Pines and R. G. Griffin, Chemical Shielding Tensors of ^{13}C in Oxalates, presented at the 1974 APS Meeting, Washington, D.C., Bull. Am. Phys. Soc., 19, 486 (1974) (LBL-2564 Abs.).

13. A. Pines, Book Review of "Advances in Magnetic Resonance", (Vol. 6, Academic, N.Y.), J. Am. Chem. Soc., 96, 6538 (1974).

14. A. Pines, D. J. Ruben and S. Allison, Molecular Ordering and Even-Odd Effect in a Homologous Series of Nematic Liquid Crystals, Phys. Rev. Lett., 33, 1002 (1974) (LBL-3118).

Presentations

1. A. Pines, Carbon-13 NMR Spectra and Spin Echoes in Solids, 15th Experimental NMR Conference, Raleigh, North Carolina, April 1974, invited talk, LBL-2589, March 1974.

2. A. Pines, Nuclear Magnetic Resonance Studies of Liquid Crystals, International Summer School on Liquid Crystals, Portoroz, Yugoslavia, June 1974, invited lecturer.

3. A. Pines, ^{13}C NMR Studies of Phase Transitions and Motion in a Smectic Liquid Crystal, LBL-2736 Abs., April 1974, presented at Pacific Conference on Chemistry and Spectroscopy, San Francisco, Calif., Oct. 15-18, 1974.

4. A. Pines and J. J. Chang, ^{13}C NMR Studies of the Nematic-Isotropic Phase Transition in Liquid Crystals, LBL-2737 Abs., April 1974, ibid.

LBL reports

1. J. J. Chang, R. G. Griffin and A. Pines, Carbon-13 Chemical Shielding Tensors in Ammonium Hydrogen Malonate, LBL-3518, Nov. 1974.

2. J. J. Chang, A. Pines, J. J. Fripiat and H. A. Resing, Qualitative Analysis of Chemisorbed Molecular Species via ^{13}C NMR, to be published. LBL-3721, Oct. 1974.

3. A. Pines, Carbon-13 NMR in Liquid Crystals, 18th Ampere Congress, Nottingham, England, Sept. 1974. LBL-2763 Abs., May 1974.

4. A. Pines and J. J. Chang, Carbon-13 Chemical Shielding Tensor of $^{13}COO^-$ in Single Crystal L-Alanine, 18th Ampere Congress, Nottingham, England, Sept. 1974. LBL-2766 Abs., May 1974.

Ronald R. Herm, Principal Investigator

1. SPECTROSCOPIC AND KINETIC STUDIES OF CHEMILUMINESCENCE FROM THE REACTIONS OF EXCITED MERCURY ATOMS (6^3P_1) WITH HALOGEN MOLECULES

Lara A. Gundel and Ronald R. Herm

We have completed our studies of the mercurous halide $HgX(B^2\Sigma^+ \rightarrow X^2\Sigma^+)$ electronic chemiluminescence which is produced by 2537Å irradiation of a vapor mixture of Hg atoms and halogen molecules. Kinetics studies indicate that this chemiluminescence is due to the bimolecular reaction:

$$Hg(6^3P_1) + xy(^1\Sigma_g^+) \rightarrow HgX(B^2\Sigma^+) + y(^2P). \qquad (1)$$

An approximate Franck-Condon (FC) factor analysis of the HgCl chemiluminescence accompanying the $Hg(6^3P_1) + Cl_2$ reaction indicated that the HgCl $(B^2\Sigma^+)$ has maximum population in the 14th vibrational level and that the average fraction of the epothermicity of R_{xn} (1) appearing as $HgCl(B^2\Sigma^+)$ vibration is ~50%. Auxilliary experiments with He buffer gas produced a thermal $HgCl(B^2\Sigma^+)$ vibrational distribution, thereby substantiating this FC factor analysis. Thus, the energy partitioning produced by R_{xn} (1) resembles the reactions of ground state alkali atoms with halogen molecules.

2. VELOCITY DEPENDENCE OF THE CROSS SECTION FOR: $Hg^*(6^3P_2) + NaX \rightarrow HgX + Na^*(3^2P)$

Lambert C.-H. Loh and Ronald R. Herm

By measuring the 5890Å ($3^2P \rightarrow 3^2S$) Na fluorescence produced by crossing a beam of metastable Hg atoms (6^3P_2) with a velocity selected beam of NaBr or NaI (NaX), we have determined the dependence on relative collision speed (g) of the total cross section (Q_R) for the reaction

$$Hg^*(6^2P_2) + NaX \rightarrow HgX + Na^*(3^2P) \ .$$

Figure 1 shows that Q_R decreases very rapidly with increasing g for NaBr; similar behavior was also found for NaI.

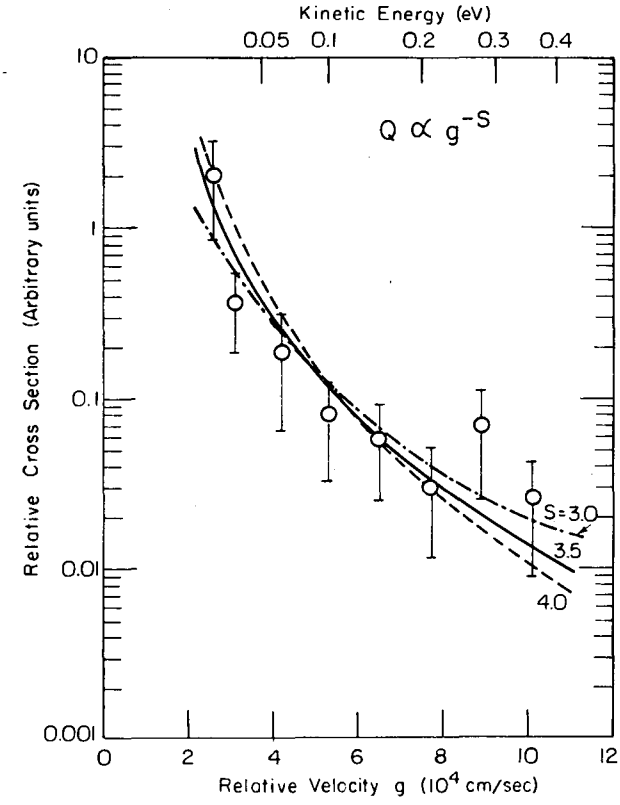

Fig. 1. Velocity dependence of the total cross section (arbitrary units) for production of $Na^*(3^2P)$ fluorescence in reaction of $Hg^*(6^3P_2)$ with NaBr. Error bars show standard deviations of individual data points from the mean. Curves show fits to the data obtained by convoluting trial functions of the form $Q_R \propto g^{-S}$ over the beam speed distributions. (XBL 7312-7116)

3. PRODUCT VELOCITY AND MAGNETIC DEFLECTION ANALYSIS FROM CROSSED BEAMS OF Li ATOMS AND HALIDE OR OXIDE MOLECULES

Charlotte M. Sholeen and Ronald R. Herm

In previous IMRD Annual Reports, we have reported progress on an on-going crossed beams study of Li atom reactions wherein a slotted-disk velocity selector is employed to analyze the product signal. These studies are considerably more difficult than crossed beam studies of heavier alkali reactions because magnetic deflection analysis of the scattered signal must be employed to distinguish nonreactive scattering of paramagnetic Li atoms from reactive scattering of Li containing products. Over the past year, however, we have finally managed to collect excellent data on the reactions of Li atoms with Br_2, Cl_2, NO_2, CH_3NO_2, CCl_4, CH_3I, PCl_3, and $SnCl_4$. Computer analysis of this data which is currently in progress should yield center-of-mass maps for the reactive scattering in each of these systems. In the meantime, the data also permit the following qualitative observations.

a. In agreement with observations on the heavier alkali reactions, the product recoil speed distribution from Li + $SnCl_4$ is bimodal (at some angles), suggesting two product channels (presumably LiCl + $SnCl_3$ and $LiCl \cdot SnCl_2$+Cl).

b. The ground state of LiO is $^2\pi$ and an excited $^2\Sigma$ state is also energetically possible from the $Li+NO_2$ reaction. The $^2\Sigma$ state (which might, however, radiate to the $^2\pi$ level before detection) would be paramagnetic, and the magnetic response of the $^2\pi$ level would be dependent on the intermolecular angular momenta coupling. Careful measurements of the magnetic deflection patterns, however, indicated that the LiO product behaved exclusively as a diamagnetic species.

c. Calculations have suggested a binding energy for LiF_2 (relative to LiF+F) large enough to make the $Li+SF_6 \rightarrow LiF_2 + SF_4$ reaction energetically possible. Accordingly, we conducted a careful magnetic deflection analysis study of the scattering of Li from SF_6, but failed to observe a paramagnetic species with the LiF_2 mass.

4. ATOMIC AND MOLECULAR SCATTERING IN CROSSED BEAMS

Richard Behrens, Jr., Andrew Freedman, Timothy P. Parr, and Ronald R. Herm

Several types of exploratory studies have been performed on the new "universal detector" crossed-molecular beam apparatus (described in previous IMRD Annual Reports). We have measured the elastic scattering of Ar from CH_4 and NH_3, and analysis of this data is in progress.

We have also searched for possible facile bimolecular exchange reactions between two stable molecules. We have failed to observe such behavior in crossed nozzles of $BBr_3 + BCl_3$ and NO_2 + HI or PCl_3. However, we have observed the reaction:

$$MI_2 + XY \rightarrow MIY + XI$$

where XY = Cl_2 or HCl. Here M refers to Mg, Sr, or Ba, and we observe a strong trend in reactivity in this series with $Q_R(Ba) > Q_R(Sr) \gg Q_R(Mg)$. We have measured the product recoil energy distribution for the Ba reaction and are currently analyzing the data to generate center-of-mass maps of the reactive scattering. Our prime motivation in initiating this study was to search for the exchange process:

$$MI_2 + Cl_2 \rightarrow MCl_2 + I_2 \quad .$$

Unfortunately, however, we have failed to obtain any evidence that it takes place.

5. CROSSED BEAMS OBSERVATION OF CONDENSATION OF Br_2 ON $(Cl_2)_x$ AND $(NH_3)_x$

Richard Behrens, Jr., Andrew Freedman, Timothy P. Parr, and Ronald R. Herm

While attempting to exploit dimerization in a nozzle expansion to conduct crossed-beams studies of recombination reactions (e.g., HCl + $(NH_3)_2 \rightarrow NH_4Cl + NH_3$), we have instead observed a new type of phenomenon, condensation on larger clusters, B_x, in the beam. Our observations to date provide little quantitative insight into the phenomenon because of uncertainties regarding fragmentation of such clusters upon ionization. Nevertheless, we wish to describe them briefly because they suggest that it may be possible to study the kinetics of condensation on such clusters as well as modes of decomposition of energized clusters by means of the crossed beams technique.

As the nozzle source pressure (both Cl_2 and NH_3 have been studied) is raised so as to increase the dimer concentration in the beam,[1] mass spectrometer signals corresponding to higher polymer ions, B_x^+, invariably appear as well. The apparent beam cluster distribution, $I(B_x^+)$, decreases rapidly with increasing x; in the absence of knowledge of fragmentation behavior, however, it is not possible to characterize the time distribution in size of the neutral clusters. Nevertheless, these higher clusters appear to dominate the "reactive scattering". For $Br_2 + (C)_2)_x$, for example, mass peaks[2] in the scattered signal have been observed at $BrCl^+$, $Br_2Cl_2^+$, $Br_2Cl_4^+$, $Br_2Cl_6^+$, $Br_2Cl_8^+$, and $Br_2Cl_{10}^+$. The angular distributions of each of these peak within a few degrees of the Cl_2 beam, although the higher mass peaks fall off more steeply with increasing LAB angle, Θ. They appear only for $\Theta > 0$, however, indicating that this is not some artifact due to "beam interference" in the detector. A similar effect has been observed for $Br_2 + (NH_3)_x$. Here, we have measured angular distributions of $BrNH_3^+$, $Br_2NH_3^+$, $Br_2(NH_3)_2^+$, $Br_2(NH_3)_3^+$, and $Br_2(NH_3)_5^+$ which peak at $\Theta \sim 6°$. Figure 1 presents a velocity diagram summarizing

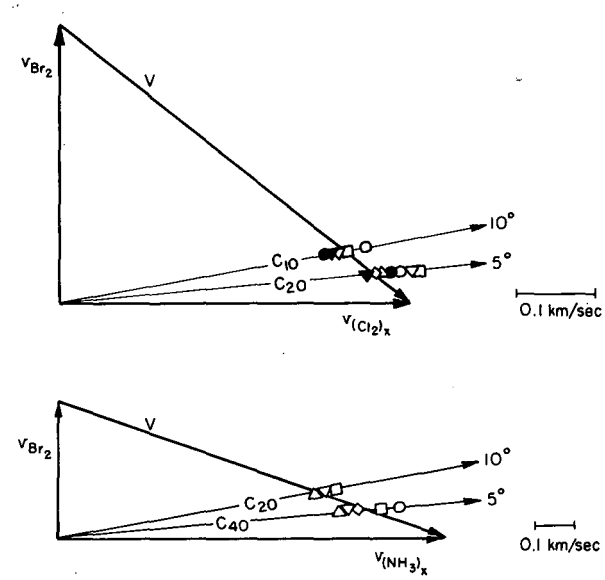

Fig. 1. Velocity Velector diagrams for 90° intersection of beams of Br_2 and $(Cl_2)_x$ or $(NH_3)_x$; note different scales on the two diagrams. Data points show measured most probable recoil speeds of: ○ - $BrCl^+$ and $BrNH_3^+$ signals; □ - $Br_2Cl_2^+$ and $Br_2NH_3^+$; △ - $Br_2Cl_4^+$ and $Br_2(NH_3)_2^+$; ▽ - $Br_2Cl_6^+$ and $Br_2(NH_3)_3^+$; ◇ - $Br_2Cl_8^+$ and $Br_2(NH_3)_5^+$. Darkened data symbols refer to results of a different apparatus pump-down. Solid lines at Θ = +5° and +10° also refer to the centroid direction, C_x, for $Br_z + B_x$ collision. (XBL 7412-7673)

results of time-of-flight (TOF) measurements the these systems. Although the TOF distributions of the scattered species sometimes appear broader than that of the main beams, Fig. 1 illustrates that the most probable LAB recoil speeds of these species concentrate about the relative velocity vector. This suggests that they are formed via

$$Br_2 + B_x \rightarrow Br_2B_x^*$$

where the $Br_2B_x^*$ energized cluster may be stabilized by the "boiling off" of a few particles with low recoil energies so that the resultant cluster tends to recoil in the LAB along the centroid velocity vector.

---

1. Experimental parameters which determine the cluster distributions are not well understood. For example, D.L. King, D.A. Dixon, and D.R. Herschbach, J. Am. Chem. Soc. 96, 3328 (1974) managed to exhibit formation of higher clusters so as to study $Br_2 + (Cl_2)_2 \rightarrow 2BrCl + Cl_2$.
2. Br_2 was chosen simply as a convenient, heavy probe particle.

6. RESEARCH PLANS FOR CALENDAR YEAR 1975

Ronald R. Herm

This program will be transferred to the Ames Laboratory-USAEC in January, 1975. Thereafter, IMRD's commitment to this program will be phased out with the final publication of the projects described earlier.

7. 1974 PUBLICATIONS AND REPORTS

Ronald R. Herm and Associates

Journals

1. B. L. Earl and R. R. Herm, Photodissociation of NaBr, NaI, and KI Vapors and Collisional Quenching of $Na^*(3^2P)$, $K^*(4^2P)$, and $K^*(5^2P)$ by Foreign Gases, J. Chem. Phys. 60, 4568 (1974) (LBL-2500).

LBL reports

1. Lambert C.-H. Loh, Molecular Beam Studies of Electronic Energy Transfer Processes with Metastable Mercury Atoms (Ph.D. thesis), LBL-2253, Jan. 1974.

2. Lambert C.-H. Loh, Charlotte M. Sholeen, Ronald R. Herm and David D. Parrish, Sensitized Fluorescence in Crossed Atomic Beams: $Hg^*(6^3P_{0,2}) + Tl(6^2P_{3/2})$, LBL-3156, Dec. 1974.

Harold S. Johnston, Principal Investigator

I. EXPERIMENTAL STUDIES*

a. Reactivity of Hydroxyl Radicals as a Function of Vibrational Energy State

Gerald Streit

By reacting hydrogen atoms with ozone at low pressure in a large tank,

$$H + O_3 \rightarrow (HO(v \leqslant 9) + O_2$$

hydroxyl radicals are produced in excited vibrational energy levels, up to v=9. The presence of vibrationally excited hydroxyl radicals was followed by overtone vibrational emission in the visible range of the spectrum. All states from v=4 to v=9 could be monitored in this way. Rate constants were obtained as a function of vibrational energy of the hydroxyl radical for ozone destruction

$$HO(v) + O_3 \rightarrow HOO + O_2$$

or

$$\rightarrow H + O_2 + O_2 \ .$$

Rate constants were obtained for vibrational deactivation

$$HO(v') + M \rightarrow HO(v) + M \ .$$

b. Photolysis of the Nitrate Free Radical (NO_3)

Richard Graham

For radiation with wavelengths from 580 to about 700 nm, it is energetically possible to photolyze the nitrate free radical to nitric oxide and oxygen:

$$NO_3 + h\nu(580\text{-}700 \text{ nm}) \rightarrow NO + O_2(^1\Sigma) \ . \qquad (1)$$

Below 580 nm, another path is energetically possible

$$NO_3 + h\nu(< 580 \text{ nm}) \rightarrow NO_2 + O \qquad (2)$$

which produces nitrogen dioxide and an oxygen atom. Although the work is not yet completed, it appears that the quantum yield to produce nitric oxide is low, less than 0.1, perhaps very much less than 0.1. Radiation above 580 nm appears not to dissociate NO_3. Radiation below 580 nm does dissociate NO_3, and the products appear to be NO_2 + O.

c. Rate of Formation of Nitrous Acid from NO, NO_2, and H_2O

Brian Nordstrom

The rate of the reaction

$$NO + NO_2 + H_2O \rightarrow 2\ HNO_2$$

was studied in an all-silica cell, and the rate was compared with that previously observed here (Soon-Ky Neoh) in a cell composed of stainless steel and silica. The rate in the partly stainless steel system was over 100 times faster than that in the silica cell. This reaction appears to be strongly catalyzed by metal surfaces.

d. Photolysis of Nitrous Acid Vapor

Edward Quitevis

By adding carbon monoxide to a system containing nitrous acid (in equilibrium with NO, NO_2, and H_2O), it was shown that hydroxyl radicals are produced by radiation between 300 to 400 nm

$$HNO_2 + h\nu(300\text{-}400 \text{ nm}) \rightarrow HO + NO$$

$$HO + CO \rightarrow CO_2 + H \ .$$

Carbon dioxide was removed and measured by a mass spectrometer. The system is very complicated and a full analysis of the data was not possible. However, it appears that the quantum yield for formation of hydroxyl radicals is approximately one.

e. Development of Ground-Based Method to Monitor Stratospheric Nitrogen Dioxide

Peter Connell

A. W. Brewer and coworkers (Nature, 246, 129, 1973) have used a spectroscopic method, based on differential absorption of visible light, to measure the concentration of nitrogen dioxide in the stratosphere. Their method appears to be very promising, but the first results appear to be incorrect in some respects. Brewer observed changes of sunlight at three closely spaced wavelengths. We are using an optical multichannel analyzer to observe 100 to 500 channels simultaneously. By thus overdetermining the parameters needed, we hope to discover and eliminate systematic errors in the method. A matter of especial interest is to follow the diurnal variations of NO_2. At sunset virtually all stratospheric nitric oxide is rapidly (minutes) converted to nitrogen dioxide

$$NO + O_3 \rightarrow NO_2 + O_2$$

During the night about half the nitrogen dioxide is converted to dinitrogen pentoxide

$$NO_2 + O_3 \rightarrow NO_3 + O_2$$

$$NO_2 + NO_3 \overset{M}{\rightarrow} N_2O_5$$

During the next day N_2O_5 is photolyzed to the lower oxides of nitrogen (NO, NO_2, NO_3).

2. THEORETICAL STUDIES

a. Calculation of the potential Energy Surface for Ne plus H_2

John Birks and H. F. Schaefer

A quantum-mechanical study was made of the potential energy surface for neon and two hydrogen atoms. Complete results were obtained for linear Ne-H-H, and results were also obtained for 90° angles of approach. Intermediate angles of approach were found by interpolation. Classical mechanical trajectory calculations were carried out for potentially dissociative collisions of neon and hydrogen.

b. Model Calculations of Stratospheric Ozone

Gary Whitten and Harold S. Johnston

The "method of instantaneous rates" was extended to see if the random experimental error in five observed quantities (solar intensity above the atmosphere, cross sections for absorption of radiation by oxygen and by ozone, rate constants for the reaction: $O + O_2 + M \rightarrow O_3 + M$, $O + O_3 \rightarrow O_2 + O_2$) could account for the appearance that ozone is formed from sunlight five times faster than it is destroyed by the reaction, $O + O_3 \rightarrow O_2 + O_2$). If one takes on observed global distribution of ozone and temperature, the observed intensity of radiation above the stratosphere, the instantaneous rate of ozone formation and destruction can be calculated for the world, on the basis of a fairly fine grid of atmospheric volume elements. This calculation was repeated 200 times with random assignments of error to each of the five experimental data. The Monte Carlo distribution of ozone imbalances shows that it is extremely improbable that random experimental error is the source of the ozone imbalance (natural oxides of nitrogen destroy about 70% of the natural ozone, and this accounts for the apparent discrepancy).

c. Calibration of Models of Stratospheric Motion by Means of Observed Carbon-14 Data

Harold S. Johnston, David Kattenhorn, and and Gary Whitten

There are (at least) nine different models of average, one-dimensional, vertical, eddy transport in the stratosphere. These models were obtained from a number of consideration (measured heat fluxes, particulate radioactive fall-out ozone distribution, methane distribution, and guesses). They predict widely different residence times for SST exhaust gases deposited in the stratosphere. There are extensive data for every three months from 1955 to 1967 and some more data in 1970-71 for the distribution of excess carbon-14 from the atmospheric nuclear bomb $^{14}CO_2$ were not used to construct the 9 theories of atmospheric motion in the first place, and thus it is a true test of the theories to assign one $^{14}CO_2$ distribution as initial condition and to let the theory calculate later distributions. This procedure was carried out. Three out of the 9 models gave a very poor description of the distribution and persistence of excess carbon-14. Three out of the nine gave faily good predictions of the general shapes of the carbon-14 distribution between January 1963 and November 1970. One model gave remarkably good qualitative and quantitative agreement. This exercise was useful in narrowing down the spread in assumed models of atomospheric motion. The shape and magnitude of the vertical diffusion parameter is determined very sensitively by the ^{14}C data.

d. The Oxides of Nitrogen with Respect to Urban Smog, Supersonic Transports, and Global Methane

Edward Quitevis and Harold S. Johnston

A given set of 23 species, 36 reactions, and appropriate photolyses were used to predict the effect of NO_x on ozone from the ground to the top of the stratosphere. Methane and ozone at naturally obserbed concentrations were included. The photochemical model shows that NO_x, CH_4, and H_2O form ozone by a smog mechanism near the ground, and destroy ozone by catalytic cycles in the stratosphere. At 45° latitude the crossover point between ozone formation and destruction by NO_x occurs at 13 km. The formation of ozone in the tropsphere and destruction of ozone in the stratosphere by NO_x, CH_4, and H_2O are natural consequences of the differences in solar radiation fields, temperature, and ambient ozone as a function of elevation.

e. Reviews of Experimental and Theoretical Results Concerning Ozone Reduction by Oxides of Nitrogen, Chlorine Oxides, etc.

Harold S. Johnston

During 1974 there has been a flood of results from the many projects of the Climatic Impact Assessment Program, concerning stratospheric composition, projections of future sizes of SST fleets, model calculations of the effect of NO_x on stratospheric ozone, and biological consequences of artificially reduced ozone. In a series of public lectures and review articles, these new findings have been organized, brought together with older data, and presented to the scientific public. The present concensus is that very large ozone reductions would occur as a result of (1) an all out nuclear war, (2) SST fleets of the sizes projected by DOT for the period 2000-2025 AD, unless NO_x emission are reduced by a factor of at least 100, (3) chlorofluorocarbons of the aerosol spray industry continues to expand at its recent rate of growth for another 10 to 20 years. The

readily projected upper bound ozone reduction is well over a factor of two reduction for each of these hazards. The expected effect from current rates of usage of chlorofluorocarbons or for a few hundred Concorde-like SSTs is a matter of 5 percent global ozone reduction and 10 percent increase in biologically damaging ultraviolet radiation.

f. Interpretation of the Effect of Metal Surfaces on Lockheed's Smog-Chamber Data

Peter Connell

The Lockheed Company (Sunnyvale, California) has carried out a series of studies of the effect of surfaces (glass, teflon, aluminum, stainless steel) on smog chamber results. They used a relatively simple chemical system, propylene, air, water vapor, and nitric oxide as reactants. They found that the smog reaction occurred much faster in a stainless steel chamber than with the other materials. A partial explanation is that stainless steel catalyzes the formation of nitrous acid from NO, NO_2, and H_2O; and the photolysis of nitrous acid produces hydroxyl radicals, which are known to be extremely active initiators of the smog-formation reaction.

g. Atmospheric Reactions of Chlorine-Containing Species

Robert T. Watson

A critical review was made of the chemical kinetic data for reactions of chlorine, chlorine atoms, chlorine oxides, hydrogen chloride, and related compounds. This study included a review of the photochemical data for these compounds.

*Acknowledgement: The subjects, 1a,b,c,d,e; 2b,c,d,e,f,g, were supported in part by the U.S. Department of Transportation, Climatic Impact Assessment Program.

3. RESEARCH PLANS FOR CALENDAR YEAR 1974

Harold S. Johnston

We plan to complete studies of the photolysis of NO_3 and to review and summarize the data for the N_2O_5 family of reactions.

A matter of considerable emphasis is to complete development of the method of observing stratospheric NO_2 (and also tropospheric) by differential absorption spectrometry.

We believe that new developments in the molecular modulation method gives us a good chance to measure the rate constant of the very elusive reaction, $HO + HOO \rightarrow H_2O + O_2$. These new developments will be pushed in order to study other radical-radical reactions.

We plan to keep up with the new results on stratospheric pollution by NO_x, ClO_x, or other, as the results come in.

4. 1974 PUBLICATIONS AND REPORTS

Harold S. Johnston and Associates

Journals and books

1. H. S. Johnston, Catalytic Reduction of Stratospheric Ozone by Nitrogen Oxides, chapter in Advances in Environmental Science and Technology, Vol. 4, edited by James N. Pitts, Jr. and Robert L. Metcalf (John Wiley & Sons, Inc., 1974) p. 264 (LBL-1180).

2. H. S. Johnston, Photochemistry in the Stratosphere--with Applications to Supersonic Transports, Acta Astronautica 1, 135 (1974) (LBL-2217).

3. H. S. Johnston, Shih-Ger Chang, and Gary Whitten, Photolysis of Nitric Acid Vapor, J. Phys. Chem. 78, 1 (1974) (LBL-1865).

4. H. S. Johnston and Richard Graham, Photochemistry of NO_x and HNO_x Compounds, Canadian Journal of Chemistry 52, 1415 (1974) (LBL-2249).

5. R. A. Graham and H. S. Johnston, Kinetics of the Gas-Phase Reaction Between Ozone and Nitrogen Dioxide, J. Chem. Phys. 60, 4628 (1974) (LBL-2561).

6. H. S. Johnston, Supersonic Aircraft and the Ozone Layer, Environment and Change 2, 339 (1974).

7. H. S. Johnston, Pollution of the Stratosphere, Environmental Conservation 1(3) (1974).

Presented papers

1. H. S. Johnston, Pollution of the Stratosphere, Sigma Xi Lecture, Sonoma State University, April 23, 1974.

2. H. S. Johnston, Photochemistry in the Stratosphere, Portland State University, May 8, 1974.

3. H. S. Johnston, Pollution of the Stratosphere, Colorado State University, May 14, 1974.

4. John Birks, Chemiluminescence of Iodine Monofluoride, 167th National Meeting of the American Chemical Society, March 31 - April 5, 1974.

5. Gary Whitten, Rate Constant Evaluations Using a New Computer Modeling Scheme, American Chemical Society Meeting, March 31 - April 5, 1974.

6. R. A. Graham, Kinetics of the Gas Reaction Between Ozone and Nitrogen Dioxide at Low Temperatures, American Chemical Society Meeting, March 31 - April 5, 1974.

7. Douglas Martin and John Girman, The Quantum Yield of $O(^1D)$ in the Photolysis of Ozone Near 310 nm, American Chemical Society Meeting, March 31 - April 5, 1974.

8. R. T. Watson, A Study of the Br $(^2P_{3/2})$ + OClO Reaction System at 298°K, Using Molecular Beam Mass Spectrometry, American Chemical Society Meeting, March 31 - April 5, 1974.

9. Gerald E. Streit, The Quenching of Vibrationally Excited HO and the Reaction of HO(v) with O_3, American Chemical Society Meeting, March 31 - April 5, 1974.

10. H. S. Johnston, Frontiers in Chemistry Lecture, Wayne State University, Detroit, Michigan; June 3, 1974.

11. H. S. Johnston and Edward Quitevis, The Oxides of Nitrogen with Respect to Urban Smog, Supersonic Transports, and Global Methane, 5th International Congress of Radiation Research, July 14-20, 1974 Seattle, Washington.

12. H. S. Johnston, Photochemistry in the Stratosphere, National Center for Atmospheric Research, Boulder, Colorado, August 20, 1974.

13. H. S. Johnston and G. Whitten, Chemical Reactions in the Atmosphere as Studied by the Method of Instantaneous Rates, CODATA Meeting, Warrenton, Virginia, September 26, 1974.

14. H. S. Johnston, Pollution of the Stratosphere, University of California, Los Angeles, October 22, 1974.

15. Peter Connell, Interpretation of Chamber Design Effects, Bi-Annual Smog Chamber Researcher's Meeting, Research Triangle Park, North Carolina, October 23-24, 1974.

16. H. S. Johnston, Pollution of the Stratosphere, Symposium at Los Alamos Scientific Research Lab, Los Alamos, New Mexico, November 24-26, 1974.

17. H. S. Johnston, Use of Carbon-14 Data to Calibrate Models of Stratospheric Ozone Depletion by Supersonic Transports, Numerical Data Advisory Board Meeting, Washington, D.C., December 3-4, 1974.

LBL reports

1. H. S. Johnston, Annual Report to the Climatic Impact Assessment Program, June 1974 (compiled Sept. 1974).

2. R. T. Watson, Rate Constants of ClO_x of Atmospheric Interest, LBL-2745, May 1974.

3. Gerald Edward Streit, Hydroxyl Radical Kinetics: Reaction with Ozone and Vibrational Quenching, LBL-2795 (Ph. D. thesis) Aug. 1974.

4. Harold S. Johnston, Chemical Reactions in the Atmosphere, LBL-2779 Abstract, June 1974, presented at a CODATA Meeting, Warrington, Virginia, Sept. 16-18, 1974.

5. Harold S. Johnston and Edward Quitevis, The Oxides of Nitrogen with Respect to Urban Smog, Supersonic Transports, and Global Methane, LBL-3509, July 1974 presented at the 5th International Congress of Radiation Research, Seattle, Wash., July 14-20, 1974.

6. John Birks, Theory of the Dissociation of Diatomic Molecules and a Study of the Emission Spectra of IF (Ph. D. thesis) LBL-2743, Nov. 1974.

7. H. S. Johnston, D. Kattenhorn and G. Whitten, Use of Carbon-14 Data to Calibrate Models of Stratospheric Ozone Depletion by Supersonic Transports, LBL-3548, (submitted to Journal of Geophysical Research) Dec. 1974.

Bruce H. Mahan, Principal Investigator

1. ION-MOLECULE COLLISION PHENOMENA*

Bruce H. Mahan

This review article deals with recent developments in the study of elastic, inelastic, and reactive ion-molecule scattering phenomena. The topics discussed were chosen on the basis that they contribute directly to the general understanding of the dynamics of chemical reactions. Some of the important results which impinge on plasma and radiation chemistry are the following.

In the realm of elastic scattering, angular distributions have been used to determine the dissociation energies of such species as HeH^+ and He_2^+. Inelastic scattering experiments have yielded the first angular cross sections for vibrational excitation and collisional dissociation of a number of small molecules including H_2. One of the more significant studies has provided detailed cross sections for the vibrational excitation of H_2 by H^+. Reactive scattering experiments have made substantial contributions to our understanding of the connection between chemical reactivity and electronic structure. Specific experiments of this type from the author's laboratory include investigations of the C^+-H_2, N^+-H_2, and O^+-H_2 systems, which may be important impurity reactions in controlled fusion reactors.

*Abstracted from a paper to appear in the MTP International Review of Science (Series II, Vol 9, Chemical Kinetics, Butterworths, 1975).

2. ELECTRONIC STRUCTURE AND CHEMICAL DYNAMICS*

Bruce H. Mahan

This article describes how, by using the known electronic properties of reactants, products, and intermediates, much of the chemical behavior and detailed dynamics in simple systems can be rationalized or predicted. The emphasis is on the use of electronic state correlation diagrams, as illuminated by molecular orbital correlations, to deduce the qualitative nature of potential energy surfaces. By this technique it is possible to decide whether or not a given electronic state of the products can be reached adiabatically by collision of ground state reactants. Moreover, it is possible to decide which of the potential energy surfaces available have deep wells which allow the formation of long-lived collision intermediates, or high barriers which require substantial initial kinetic energy to promote reaction. The correlation diagram method is particularly successful in explaining the dynamics of the reactions (or the reason for no reaction) of H_2 with C^+, N^+, O^+, Ne^+ and He^+. In all cases except the last, these collision processes have been examined experimentally in the author's laboratory.

*Abstracted from an article to appear in Accounts of Chemical Research, and LBL-3525.

3. DYNAMICS OF THE REACTION OF N^+ WITH H_2*

James A. Fair and Bruce H. Mahan

The reaction $N^+(H_2,H)NH^+$ has been investigated in the range of initial relative energies from 0.79 to 2.8 eV, thereby extending work done previously in this laboratory[1] at higher initial energies. Despite the deep potential energy well (6 eV) associated with the symmetric NH_2^+ ion, we find that the reaction proceeds by a direct or short-lived interaction mechanism at initial relative energies as low as 2 eV. This apparently anomalous behavior can be explained in terms of the electronic state correlation diagram for the system, Fig. 1.

On the right side of the diagram we see that the ground state reactants $N^+(^3P) + H_2(^1\Sigma)$ correlate via a collinear complex to the lowest states of NH^+ by potential surfaces that are expected to be flat, or to have only very shallow depressions. Thus formation of NH^+ by a short lived direct interaction is possible at all initial relative energies. From the left side of the diagram,

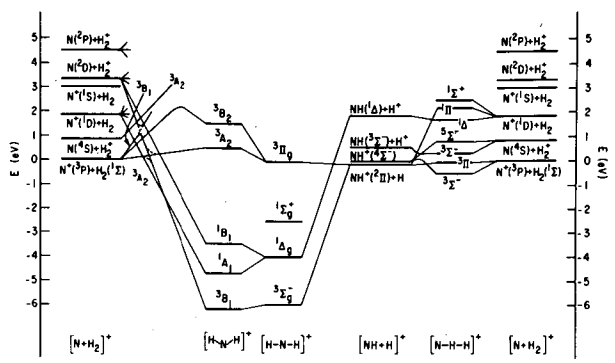

Fig. 1. An electronic state correlation diagram for the low lying surfaces of the N^+-H_2 system. At the far right, a collinear approach of N^+ to N_2 is assumed. At the far left, N^+ approaches H_2 along the perpendicular bisector of the molecule. Surface crossings that are avoided in C_{2v} symmetry are indicated by straight dashed lines. Surface crossings that become avoided in C_s symmetry are indicated by curved dashed lines. (XBL 7410-7487)

we see that as $N^+(^3P)$ approaches H_2 perpendicularly, it may proceed to products on the nearly flat $^3A_2$ surface. If it does this, the reaction mechanism will again be of the direct type. However, this $^3A_2$ state crosses the $^3B_1$ surface which leads to the ground state potential well of symmetric NH_2^+. While this surface crossing is allowed for C_{2v} (isosceles triangle) conformations, it is forbidden for distorted conformations, since in this case both surfaces have $^3A''$ symmetry. Thus at very low velocities reactants will move adiabatically on the lower $^3A''$ surface and reach the potential well. A long-lived collision complex will be expected, and is observed. At slightly higher energies, the system can be expected to behave nonadiabatically, and jump from the lower to the upper (flat) $^3A''$ surface. The result will be reaction by a direct mechanism, as is observed experimentally above 1 eV relative energy. Thus it is the transition probability between electronic states that controls the reaction dynamics, not simply the depth of the potential well.

*Abstracted from a paper to appear in J. Chem. Phys. and LBL 3501.

1. E. A. Gislason, B. H. Mahan, C. W. Tsao, and A. S. Werner, J. Chem. Phys. 54, 3897 (1971).

4. AN ANALYSIS OF DIRECT ION-MOLECULE REACTIONS*

Bruce H. Mahan

One of the major goals of the study of molecular collision phenomena is to learn how to analyze and predict the cross sections and dynamics of elementary reactions without engaging in extensive numerical calculations. This is of particular importance in ion-molecule chemistry, where often the reaction dynamics are affected by more than one potential energy surface. In such cases, a near exact calculation to find the potential energy surfaces followed by a detailed treatment of the reaction dynamics could be very expensive. In order to avoid these difficulties, we have developed the sequential impulse model of direct reactions. This model uses the most basic properties of potential surfaces to predict the important features of the reaction product energy and angular distributions.

In the sequential impulse model, the reaction A(BC,C)AB is pictured as resulting from a sequence of two impulsive elastic scattering processes: A hits B, B hits C. Reaction occurs if after the impulse sequence, the relative energy of A and B is less than the bond dissociations energy. With this model it is possible to understand several features of reactive scattering that have been observed experimentally. Among these are: the prevalence of the spectator stripping process; the loss of product intensity at small scattering angles in the high energy regime; the propensity for small angle scattering of H abstracted from HD; and the simultaneous large angle scattering of the deuterated product. The model shows how geometric factors and product stabilization control the total reaction cross section. All calculations with the model can be made with an electronic hand calculator, so the prediction and analysis of reaction phenomena is rapid and inexpensive.

*Abstracted from a paper presented at the NATO Institute on Ion-Molecule Reactions, Biarritz, France, 1974, and LBL-3155. To be published in book form by Plenum Press, 1975.

5. DYNAMICS OF THE CO_2^+-H_2 REACTION

Bruce H. Mahan and Peter J. Schubart

We have measured the energy and angular distributions of several of the products of CO_2^+-H_2 collisions over the laboratory energy range from 25 to 250 eV. The distributions of the DCO_2^+ product reflected a large component of reaction by direct interaction even at low energies. At relative energies above 10 eV, there was significant intensity loss due to product dissociation.

The HCO^+ distributions displayed the symmetric shape associated with long-lived complex formation when the initial relative energy was low. At the higher initial energies, this symmetry was lost, and HCO^+ was formed by a direct interaction mechanism. Nonreactively scattered CO_2^+ showed broad energy distributions even at low initial relative energy. This constitutes important evidence for the formation of a relatively long-lived $CO_2H_2^+$ collision complex at low relative energies.

The distributions of CO^+ and O^+ showed that these products are formed by an impulsive dissociation mechanism. The intensity of OH^+ was always quite small, and no H_2O^+ was detected at any energy. The experimental results were compared with predictions based on molecular orbital correlation diagrams, and reasonable qualitative agreement was found.

*Abstracted from a manuscript to be submitted to the J. Chem. Phys., and LBL-3154.

6. SPECTROSCOPY OF GASEOUS IONS

Bruce H. Mahan and Ralph Terkowitz

We are completing construction of an apparatus designed to obtain the electronic spectra of gaseous ions by a laser induced fluorescence method. Ions that are trapped mass selectively in an inhomogeneous radio frequency field are irradiated with the light from a pulsed tunable dye laser, and the fluorescence induced is detected with a photomultiplier. The apparatus can be operated at a resolution sufficient to obtain rotationally resolved spectra of small

ions. Hence the method should provide valuable information on the geometric structure and electronic and vibrational energy levels of polyatomic ions.

7. COLLINEAR COLLISION CHEMISTRY

Bruce H. Mahan

It is shown that by using a simple model for the potential energy surface of reactive and nonreactive systems, it is possible to understand how such factors as mass distribution and attractive forces, potential wells and barriers influence the nature of collisions and the distribution of energy in reaction products. This work is primarily pedagogical, but contains several insights that should be more widely understood by research workers.

*Abstracted from J. Chem. Ed. 51, 308,377 (1974), and LBL-2537 and LBL-2538.

8. RESEARCH PLANS FOR CALENDAR YEAR 1975

Bruce H. Mahan

Our immediate plans are to continue to establish the connection between electronic structure and chemical reactivity by studying reactions in which the electron spin conservation rule may be violated. Systems in which this may occur include the $C\ell^+(H_2,H)HC\ell^+$ reaction, currently under study, and the $S^+(H_2,H)HS^+$ reaction. An understanding of the spin-conservation rule is essential to the successful prediction of cross sections for product formation and excited state production in several reactions of interest in connection with hydrogen plasma contamination. In addition, experiments with multiple charged ions like N^{++} and O^{++} will be attempted, in order to assess the role these play in plasma energy loss processes.

The apparatus for the study of laser induced fluorescence of gaseous ions will be completed, and experiments of this type begun. Emphasis will be on obtaining spectra of simple ions like CH_2^+, NH_2^+, and H_2O^+ so that significant comparisons with the prediction of ab initio calculations can be made.

The sequential impulse model for direct reactions will be developed further, with the emphasis on improving the realism of the interaction potentials involved. The aim is to improve the accuracy of the predictions of the total reaction cross sections as a function of energy.

9. 1974 PUBLICATIONS AND REPORTS

Bruce H. Mahan and Associates

Journals and books

1. Bruce H. Mahan, Collinear Collision Chemistry I. A Simple Model for Inelastic and Reactive Collision Dynamics, J. Chem. Education 51, 308 (1974) (LBL-2537).

2. Bruce H. Mahan, Collinear Collision Chemistry II. Energy Disposition in Reactive Collisions, J. Chem. Education 51, 377 (1974) (LBL-2538).

3. William L. Dimpfl and Bruce H. Mahan, Large Angle Inelastic Scattering of Na^+ by D_2, J. Chem. Phys. 60, 3238 (1974) (LBL-2530).

4. W. R. Gentry, Yuan-tseh Lee, and Bruce H. Mahan, Erratum: Charge Transfer between Positive Alkali Ions and Atoms, [J. Chem. Phys. 49, 1758 (1968)] JCP 61, 1606 (1974).

5. Bruce H. Mahan, Activated Complex Theory of Bimolecular Reactions, J. Chem. Education 51, 709 (1974) (LBL-2735).

Papers presented

1. B. H. Mahan, "An Analysis of Direct Ion-Molecule Reactions", Proceedings of the NATO Institute on Ion-Molecule Reactions, Biarritz, France, June 24 - July 7, 1974.

2. B. H. Mahan, "Electronic Structure and Ion-Molecule Reaction Dynamics", Santa Cruz Conference on the Dynamics of Chemical Reactions, Santa Cruz, Calif., July 29-August 2, 1974.

LBL reports

1. Bruce H. Mahan, An Analysis of Direct Ion-Molecule Reactions, LBL-3155, August 1974 (to appear in the Proceedings of the NATO Institute on Ion-Molecule Reactions 1974, Biarritz, France, June 24-July 1, 1974.

2. Bruce H. Mahan, Microscopic Reversibility and Detailed Balance, LBL-3197, October 1974, submitted to J. Chem. Education.

3. J. A. Fair and B. H. Mahan, Dynamics of the Reaction of N^+ with H_2 II. Reactive Scattering at Relative Energies below 3 eV, LBL-3501, October 1974 (submitted to J. Chem. Phys.).

4. James Alan Fair, An Apparatus for Investigating Low Energy Ion-Molecule Reactions and its Application to the Reactive Scattering of N^+ by H_2, LBL-3178 (Ph.D. thesis) November 1974.

5. Peter J. Schubart, Ion Molecule Reactions: Correlation Time-of-Flight Ion Spectroscopy and the CO_2^+-H_2 System, LBL-3154 (Ph.D. thesis) October 1974.

6. Bruce H. Mahan, Electronic Structure and Chemical Dynamics, LBL-3525, Nov. 1974, (to appear in Accounts of Chemical Research).

William H. Miller, Principal Investigator

1. SEMICLASSICAL THEORY OF COLLISIONALLY INDUCED FINE-STRUCTURE TRANSITION IN FLUORINE ATOMS*†

Richard K. Preston, Christine S. Sloane, and William H. Miller

As a general rule electronic transitions in low energy atomic and molecular collisions take place locally, i.e., only at certain critical configurations of the nuclei. The best known example of this is the case that two potential curves cross, and here the Landau-Zener approximation allows one to compute the transition probability.

Miller and George[1] have proposed a more general kind of semiclassical approximation for describing electronic transitions in low energy atomic and molecular collisions which also applies to the case that the potential curves do not cross, or have an "avoided crossing". Thus, suppose that the difference of the two adiabatic potential curves has the form

$$\Delta V(r) = \Delta + Ae^{-\lambda r} , \qquad (1)$$

where Δ, A and λ are constants. Here there is no avoided crossing, and one might think that no semiclassical approximation is possible. In terms of the Miller-George theory, however, one notes that the two curves do cross at a complex value of r; i.e., the equation

$$\Delta V(r) = 0 \qquad (2)$$

has the root

$$r_c = \frac{1}{\lambda} \ln (A/\Delta) + i \frac{\pi}{\lambda} . \qquad (3)$$

The transition between the two adiabatic potential curves is then described by classical trajectories that go through this complex crossing point.

Calculations have been carried out for the excitation of the $3/2 \rightarrow 1/2$ fine structure transition in fluorine atom by collision with Xe and H^+:

$$F(^2P_{3/2}) + Xe,H^+ \rightarrow F(^2P_{1/2}) + Xe,H^+ . \qquad (4)$$

The primary interest in this process is that it is a simple prototype for the system $F + H_2$ in which fine structure transitions could have a significant effect on the reaction

$$F + H_2 \rightarrow HF + H . \qquad (5)$$

Figures 1 and 2 show the results for excitation by Xe atoms. The cross section is seen to be quite small until the translational energy is about 10 times the threshold energy for the transition. Figure 3 shows the result for excitation by H^+, and the solid points show the results of quantum mechanical calculations[2] for this process. Agreement between the semiclassical and quantum mechanical values seems to be reasonably good, thus lending confidence to the semiclassical theory.

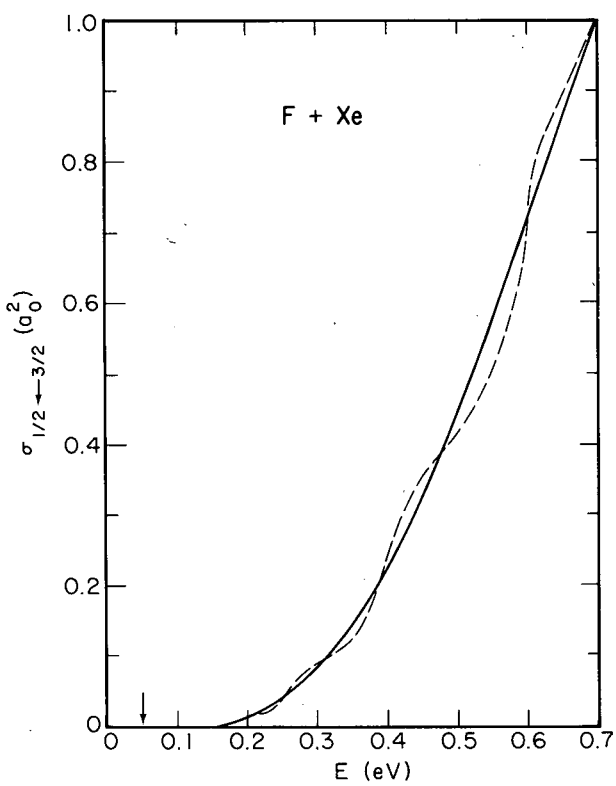

Fig. 1. The cross section for Xe + $F(^2P_{3/2}) \rightarrow$ Xe + $F(^2P_{1/2})$ as a function of initial translational energy; the arrow indicates the threshold of the transition. The solid curve is the semiclassical result which omits interference and tunneling, and the dashed curve the result of the complete semiclassical calculation.
(XBL 741-5409)

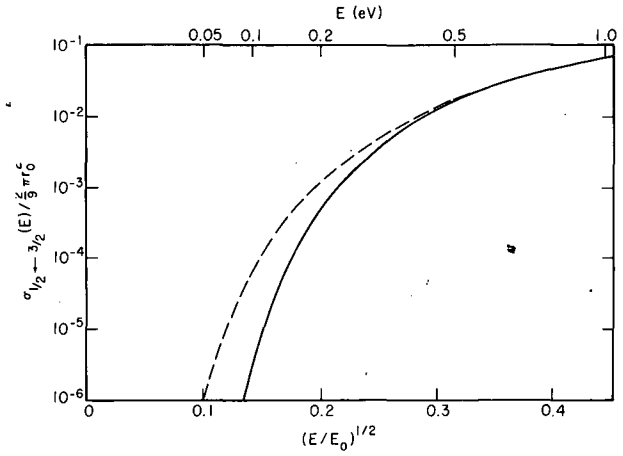

Fig. 2. The solid line is the same quantity as in Fig. 1, but with more detail of the energy region near threshold. The dashed line is an approximation to it which is seen to fail at very low energies. (XBL 742-5609)

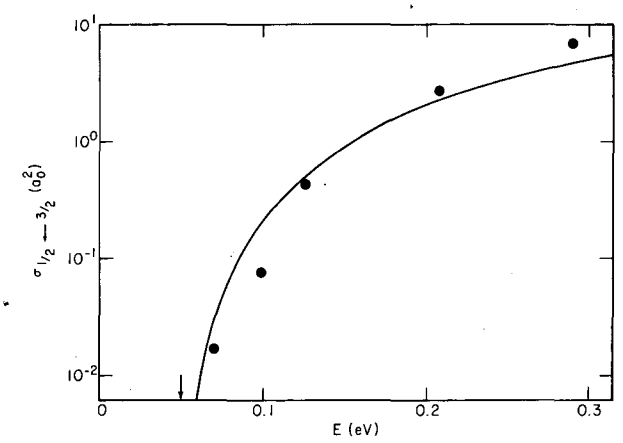

Fig. 3. The cross section for $H^+ + F(^2P_{3/2}) \rightarrow H^+ + F(^2P_{1/2})$ as a function of initial translational energy; the arrow indicates the threshold for the transition. The points are the quantum mechanical values of Ref. 2. (XBL 742-5611)

*Abstracted from J. Chem. Phys. 60, 4961 (1974).

†Supported in part by the National Science Foundation.

1. W. H. Miller and T. F. George, J. Chem. Phys. 56, 5637 (1972).
2. F. H. Mies, Phys. Rev. A 7, 942, 957 (1973).

2. CLASSICAL TRAJECTORY STUDY OF ROTATIONAL EXCITATION*†

Stuart D. Augustin and William H. Miller

Rotational excitation in molecular collisions is typically a strong, "classically allowed" process and can thus be treated reasonably accurately by classical mechanics. The most accurate classical treatment, of course, is a numerical classical trajectory calculation, and it is important to compare such calculations whenever possible with accurate quantum mechanical calculations to test their level of accuracy.

Figure 1 shows such a comparison for the $0 \rightarrow 2$ rotational excitation of H_2 by He,

$$He + H_2(j=0) \rightarrow He + H_2(j=2) \quad , \qquad (1)$$

which is probably the most severe test for classical mechanics since this is an unusually weak transition. Nevertheless, the agreement is seen to be reasonably good.

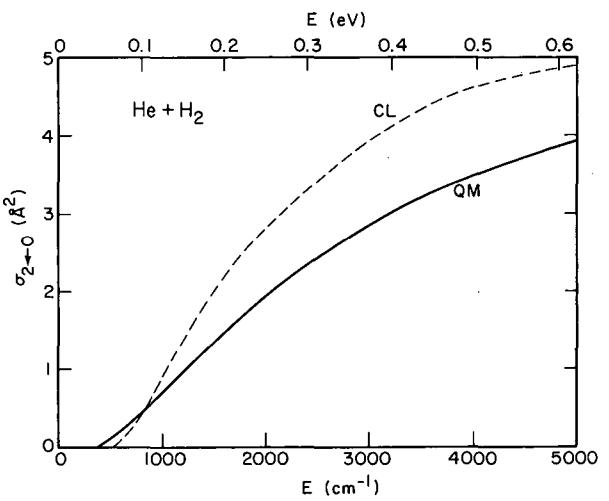

Fig. 1. The cross section for the $0 \rightarrow 2$ rotational excitation of H_2 by He as a function of initial translational energy. The solid curve shows the accurate quantum mechanical calculations of Green (S. Green, private communication), and the dashed curve the classical trajectory results. (XBL 745-6334)

Figure 2 shows similar results for rotational excitation of CO by He

$$He + CO(j=0) \rightarrow He + CO(j=1,2,3,4) \quad , \qquad (2)$$

and the agreement is also seen to be reasonably good here. The primary source for disagreement here is that the purely classical treatment omits an interference effect which is seen more clearly in Fig. 3. This may be thought of as the remnant of a $\Delta j = 0,2,4,\ldots$ selection rule that would exist if CO were homonuclear. To describe this effect a theory is needed which incorporates quantum mechanical interference.

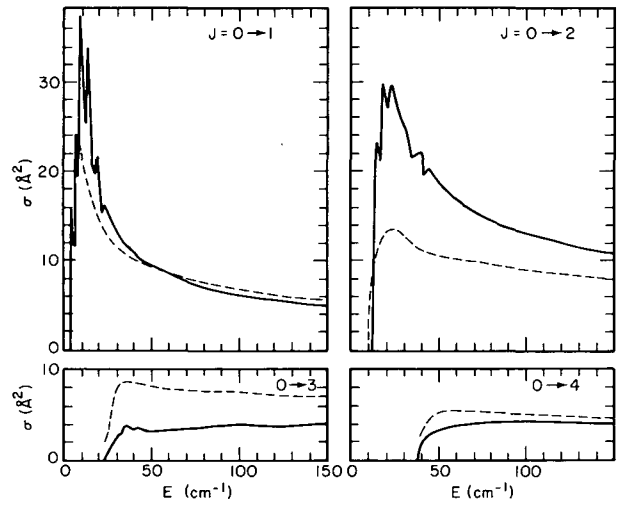

Fig. 2. The cross section for the 0 → j, j=1-4, rotational excitation of CO by He, as a function of initial translational energy. The solid curve is the accurate quantum mechanical result of Green and Thaddeus (S. Green, and P. Thaddeus, to be published), and the dashed curve the results of the classical trajectory calculation. (XBL 745-6290)

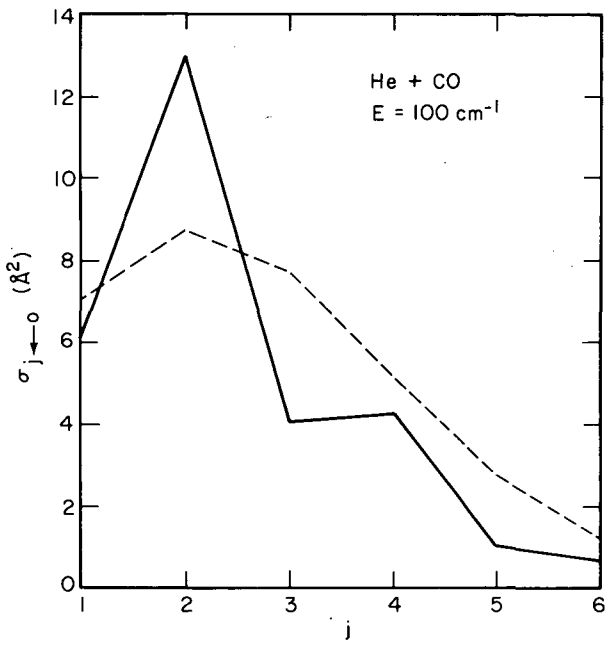

Fig. 3. The same quantity as in Fig. 2 (solid line = quantum, dashed line = classical) but shown as a function of final rotational quantum number j for a given initial translational energy E = 100 cm^{-1}. (XBL 745-6291)

*Abstracted from Chem. Phys. Letters 28, 149 (1974).

†Supported in part by the National Science Foundation.

3. SEMICLASSICAL TREATMENT OF ROTATIONAL EXCITATION OF FORMALDEHYDE AT VERY LOW ENERGIES*†

Stuart D. Augustin and William H. Miller

The $1_{11} \rightarrow 1_{10}$ transition of formaldehyde is seen in absorption against the 2.7°K cosmic background radiation in cool interstellar dust clouds, indicating that the lower state (1_{11}) has a population greater than would be expected if the system were in equilibrium with the background radiation.[1,2] Townes and Cheung[3] have noted that since the 2_{12} state spontaneously decays (via a dipole-allowed transition) to the 1_{11} state, while the 2_{11} state spontaneously decays to the 1_{10} state, collisional excitation which favors the 2_{12} over the 2_{11} state could produce the observed "cooling" (i.e., enhancement of the population of the 1_{11} state). They further argue[3] that since the 2_{12} state corresponds to the rotational angular momentum being predominantly about the axis perpendicular to the plane of the molecule, collisional excitation of formaldehyde from a j=1 state to a j=2 state should indeed be preferentially to the 2_{12} state.

To test the Townes-Cheung mechanism, classical and semiclassical calculations were carried out for rotational excitation of formaldehyde from j=1 to j=2 states by H_2 (which was taken to be spherical). Figure 1 shows the results of these

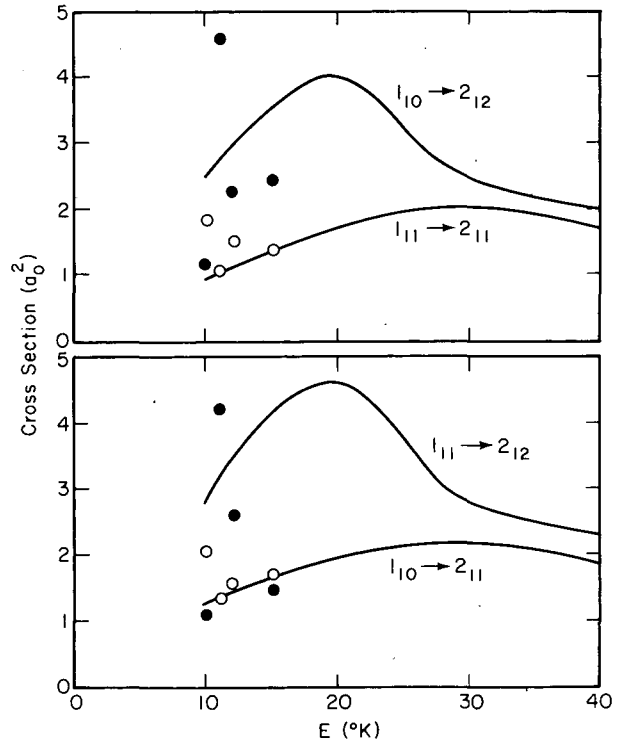

Fig. 1. Cross sections for the indicated rotational excitations in H_2 + H_2CO collisions as a function of initial relative translational energy. The solid lines are the results for the Monte Carlo classical trajectory calculations and the points are the semiclassical values. The energetic threshold for all four transitions is ~ 7°K. (XBL 745-6395)

calculations at these very low collision energies; the average translational energy is thought to be in the range 10-20°K. Since the cross sections for excitation to the 2_{12} state are larger than that to the 2_{11} state, the basic idea of the Townes-Cheung mechanism is supported by these calculations. Figure 2 shows the ratio of population of the 1_{10} state to that of the 1_{11} state which is predicted by these cross sections. This result is in quite good agreement with the observations, for the $1_{11} \rightarrow 1_{10}$ absorption is interpreted[1-3] to give a population ratio between 1.1 and 1.2.

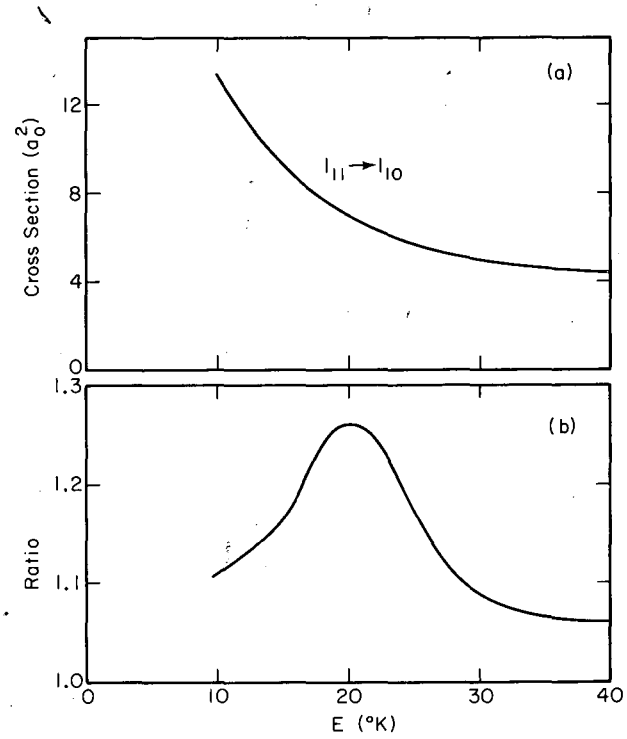

Fig. 2. Part b of this figure shows the ratio of population of Ne 1_{10} state to that of the 1_{11} state as a function of translational energy. (XBL 745-6396)

*Abstracted from J. Chem. Phys. 61, 3155 (1974).

†Supported in part by the National Science Foundation.

1. P. Palmer, B. Zuckerman, D. Buhl, and L. E. Snyder, Astrophys. J. 156, L147 (1969).
2. N. J. Evans, G. Morris, T. Sato, and B. Zuckerman, in preparation.
3. C. H. Townes and A. C. Cheung, Astrophys. J. 157, L103 (1969).

4. QUANTUM MECHANICAL TRANSITION STATE THEORY FOR NON-SEPARABLE SYSTEMS*†

William H. Miller

Classical trajectory calculations do not correctly describe the threshold region for chemical reactions with activation energy; i.e., quantum effects (e.g. tunneling) are significant in this region. The fundamental assumption of transition state theory, however--namely, that all flux through a specially chosen dividing surface is reactive flux--is expected to be valid for the threshold region. Conventional transition state theory is not satisfactory, though, because it assumes separability of motion along a reaction coordinate, and this is now known to be a poor approximation for the threshold region. What is needed is a way of implementing the fundamental assumption of transition state theory quantum mechanically but without incorporating the separability approximation.

Such a theory has been proposed.[1] Starting with the exact expression from quantum scattering theory for the rate constant, a sequence of formal manipulations gives it in the form

$$k_{b\leftarrow a} = \mathrm{tr}(e^{-\beta H} FP)/\mathrm{tr}(e^{-\beta H_a}) , \qquad (1)$$

where a and b denote reactants and products, respectively, H is the total Hamiltonian, F is a flux operator, and P a projection operator which contains all the dynamics; P projects onto all states which have evolved in the infinite past from the reactant region of configuration space. It is then easy to see how to inject the fundamental assumption of transition state theory, namely by the replacement

$$P \rightarrow h(p_s) , \qquad (2)$$

where p_s is the momentum operator normal to the dividing surface and h is the usual step function

$$h(x) = \begin{cases} 1, & x > 0 \\ 0, & x < 0 \end{cases} ; \qquad (3)$$

i.e., the transition state approximation assumes that positive momentum at the dividing surface implies evolution in the infinite past from reactants.

The first preliminary results of this theory are shown in Fig. 1 for the collinear $H + H_2$ reaction. The upper line is the exact rate constant computed as the Boltzmann average of quantum scattering results,[2] and the points are the preliminary values of the present theory. The lower line is the result of conventional transition state theory (with the conventional one-dimensional tunneling correction). One sees that even this preliminary version of the theory has gone a long way toward correcting the deficiencies of conventional transition state theory.

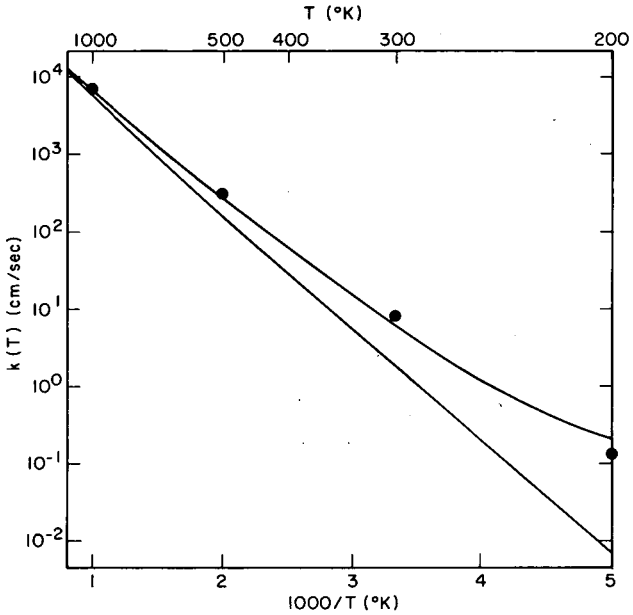

Fig. 1. Rate constant for the collinear $H + H_2 \rightarrow H_2 + H$ reaction as a function of temperature. Upper line is the quantum scattering result of Reference 2, and the lower line the results of conventional transition state theory. The dots give the result of the present quantum mechanical transition state theory. (XBL 7411-7555)

*Abstracted from J. Chem. Phys. 61, 1823 (1974).

†Supported in part by the National Science Foundation.

1. W. H. Miller, J. Chem. Phys. 61, 1823 (1974).
2. D. G. Truhlar and A. Kuppermann, Chem. Phys. Letters 9, 269 (1971).

5. THEORETICAL TREATMENT OF QUENCHING IN $O(^1D) + N_2$ COLLISIONS*

George E. Zahr, Richard K. Preston and William H. Miller

Classical trajectory calculations have been carried out for the quenching of $O(^1D)$ by N_2

$$O(^1D) + N_2 \rightarrow O(^3P) + N_2 \quad , \qquad (1)$$

and it is seen that this process goes by way of a collision complex at thermal energies. This is primarily due to the fact that there is a strongly attractive interaction between $O(^1D) + N_2$, and the initial collision between them leads to enough rotational and vibrational excitation of N_2 to "trap" the pair in the attractive well; Fig. 1 depicts this mechanism schematically. Once a collision complex is formed, even the weak spin-orbit coupling can induce a transition from the $O(^1D)$-N_2 to $O(^3P)$-N_2 electronic state. A

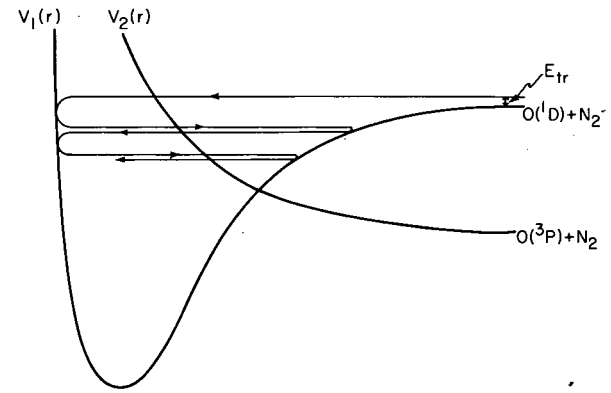

Fig. 1. A sketch of the lowest singlet, $V_1(r)$, and a typical triplet, $V_2(r)$, potential curve for the O - N_2 system. The arrow depicts a thermal energy collision of $O(^1D)$ and N_2 which results in sufficient rotational/vibrational excitation of N_2 (occurring predominantly at the inner classical turning point) to form a collision complex. (XBL 749-7224)

statistical model is introduced to describe the decay of the collision complex. The cross section for quenching at thermal (0.03 eV) collision energy is calculated to be ~ 30Å^2, in good agreement with experimental values. About 20% of the exoergicity of the reaction goes into vibrational excitation of N_2. Figure 2 shows the vibrational energy distribution of N_2 at three different initial translational energies; these distributions are seen to be qualitatively Boltzmann-like.

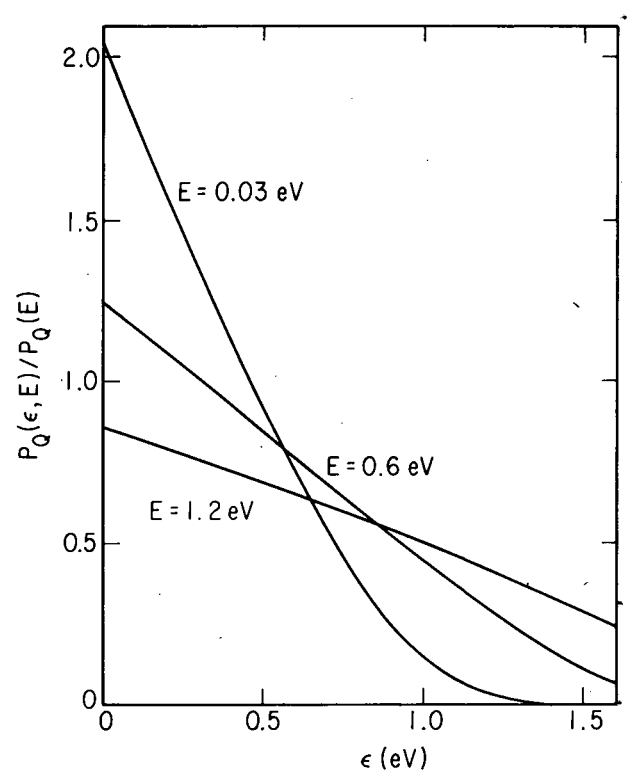

Fig. 2. The distribution of vibrational energy ϵ in the product N_2 molecule at three different initial collision energies E. (XBL 7410-7380)

*Supported in part by the National Science Foundation.

6. RESEARCH PLANS FOR CALENDAR YEAR 1975

William H. Miller

There are several projects planned which have to do with the generalized transition state theory described in paragraph IV above. Three dimensional calculations for $D + H_2 \rightarrow DH + H$ are planned since experimental rate constants down to 167°K have been accurately measured for this reaction. There are several different versions of the theory which need to be explored, and in particular, a semiclassical model which allows dynamical corrections to the "fundamental assumption" of transition state theory to be incorporated.

Over the last few years we have studied several examples of Penning ionization,

$$He^* + A \rightarrow He + A^+ + e^- \quad (1)$$

$$\rightarrow HeA^+ + e^- , \quad (2)$$

where A is an atom. If A is a diatomic molecule, then in addition to reactions (1) and (2), one may have "reactive ionization",

$$He^* + AB \rightarrow HeA^+ + B + e^- , \quad (3)$$

and dissociation ionization,

$$He^* + AB \rightarrow He + A^+ + B + e^- . \quad (4)$$

We plan to study these processes in considerable detail, perhaps the specific system being $He^* + H_2$. The relevant potential energy surfaces and autoionization rates will be computed, and then the dynamics will be described by classical trajectory methods, thereby obtaining the cross sections for reactions (1) through (4) as well as the energy distribution of the ionized electron.

Classical trajectory calculations provide the most generally useful way of determining the internal distribution of products in an exothermic reaction. Plans are to look at ways of obtaining this information from a potential energy surface without a full trajectory calculation. In particular, the idea is to look at the structure of the Liouville operator--the classical propagator--to see if its properties contain this information in any simple way. We already know how to do this in a crude manner, and it is hoped that refinements can make the description more quantitative.

7. 1974 PUBLICATIONS AND REPORTS

William H. Miller and Associates

Journals

*1. W. H. Miller, "Classical-Limit Quantum Mechanics and the Theory of Molecular Collisions", Adv. Chem. Phys., 25, 69 (1974).

2. R. K. Preston, C. Sloane and W. H. Miller, Semiclassical Theory of Collisionally Induced Fine-Structure Transitions in Fluorine Atoms, J. Chem. Phys., 60, 4961 (1974) (LBL-2578).

3. S. M. Hornstein and W. H. Miller, Modified Classical S-Matrix for Tunneling in the Collinear $H + H_2$ Reaction, J. Chem. Phys., 61 745 (1974) (LBL-2595).

4. S. D. Augustin and W. H. Miller, Semiclassical Treatment of Atom-Asymmetric Rotor Collisions; Rotational Excitation of Formaldehyde at Low Energies, J. Chem. Phys., 61, 3155 (1974) (LBL-2778)

5. W. H. Miller, Quantum Mechanical Transition State Theory and a New Semiclassical Model for Reaction Rate Constants, J. Chem. Phys. 61, 1823 (1974) (LBL-2729).

6. S. D. Augustin and W. H. Miller, Classical Trajectory Study of Rotational Excitation in Low Energy He - CO and He - H_2 Collisions, Chem. Phys. Lett. 28, 149 (1974) (LBL-2760).

7. A. W. Raczkowski and W. H. Miller, Classical S-Matrix Calculation for Vibrationally Inelastic Transitions in Three-Dimensional Collisions of Li^+ with H_2, J. Chem. Phys. 61 5413 (1974) (LBL-3171).

†8. R. I. Masel, R. P. Merrill and W. H. Miller, Semiclassical Trajectory Calculations of Helium Scattering from W(112), Sur. Sci. 46, 681 (1974).

Papers presented

1. W. H. Miller, "Semiclassical Methods in Reactive and Non-Reactive Collisions", S.R.C. Atlas Symposium: Quantum Chemistry--The State of the Art, St. Catherine's College, Oxford, England, April 8-10, 1974.

2. W. H. Miller, "Theory of Atomic and Molecular Collisions" (a series of ten lectures), Bielefeld University, West Germany, June 17-28, 1974.

3. W. H. Miller, "Theories of Reactive Scattering", Conference on the Dynamics of Molecular Collisions, University of California at Santa Cruz, July 19-August 2, 1974.

LBL reports

1. G. E. Zahr, R. K. Preston and W. H. Miller, "Theoretical Treatment of Quenching in $O(^1D) + N_2$ Collisions", LBL-3192, Sept. 1974.

2. S. Chapman, S. M. Hornstein and W. H. Miller, "Accuracy of Transition State Theory for the Threshold of Chemical Reactions with Activation Energy: Collinear and Three-Dimensional $H + H_2$", LBL-3504, Oct. 1974.

3. W. H. Miller, "Semiclassical Limit of Quantum Mechanical Transition State Theory for Non-Separable Systems", LBL-3541, Nov. 1974.

4. Stuart Dudley Augustin, Semiclassical Methods and Their Application to Problems in Collision Theory, LBL-3143 (Ph. D. thesis) Sept. 1974.

*Supported by NSF.

†Supported by AF-OSR and NSF.

Rollie J. Myers, Principal Investigator

1. ELECTRON EXCHANGE INTERACTIONS BETWEEN HYDRATED IONS--RESULTS FROM PARAMAGNETIC RESONANCE SPECTRA OF IONS IN PARAMAGNETIC LATTICES

Michael R. St. John and Rollie J. Myers

The theoretical study of the interpretation of EPR spectra of paramagnetic impurities in paramagnetic hosts has continued. Two methods of attack have been developed. The first utilizes the molecular field approach discussed previously.[1] The second approach is a slight modification of a perturbation method used by Hutchings, et al.[2] The Hamiltonian employed is that for a cluster of magnetic ions, impurity ion plus host neighbors. When host wavefunctions are known, matrix elements of the host ions may be evaluated leaving a Hamiltonian containing only impurity spins. The result is an impurity spin Hamiltonian with modified g and D values.

Application of the theories to the interpretation of g-value shifts has been successful for ions which have small orbital moments, e.g. Cu^{2+}, Mn^{2+}, V^{2+}, with both theories giving essentially the same result. The interpretations of ions possessing large orbital moments, like Co^{2+}, have been less successful, and further work is required. The effects of the ion interactions on the zero-field splittings also needs additional study.

Experimentally, a crystal of α-$NiSO_4 \cdot 6H_2O$ doped with V^{2+} was prepared, and its spectra observed. The results obtained verified the trend seen for Cu^{2+}, Co^{2+}, and Mn^{2+} that the impurity e_g orbitals participate in a ferromagnetic interaction with the lattice and t_{2g} orbitals in an antiferromagnetic interactions.

Verification of the theory in other host lattices would also be valuable, and some other lattices are being investigated.

Table I. Summary of pair interactions

Pair	Interaction	$-2J(cm^{-1})$	Impurity Spin
Cu^{2+}-Ni^{2+}	ferro	0.144	e_g
Co^{2+}-Ni^{2+}	slightly ferro ?	-	$(t_{2g})\ (e_g)^2$
Mn^{2+}-Ni^{2+}	very small	~ 0	$(t_{2g})^3(e_g)^2$
V^{2+}-Ni^{2+}	antiferro	-0.06	$(t_{2g})^3$

1. Annual Report 1973
2. M.T. Hutchings, C.G. Windsor, and W.P. Wolf, Phys. Rev., 148, 444 (1966).

2. ELECTRON SPIN RELAXATION MECHANISMS OF $Cu(NH_3)_6^{2+}$ IN LIQUID AMMONIA

Richard C. Wilson and Rollie J. Myers

We have previously reported preliminary observations of the relaxation of $Cu(NH_3)_6^{2+}$ in liquid ammonia.[1] Further line width work on this system has been done to determine the relaxation mechanisms. While our preliminary measurements did indicate that electron spin-rotation interaction was important, the low temperature (and high viscosity) region showed some deviation.

If we include the regular anisotropic tumbling mechanism[2] to the fit the result is shown in Fig. 1. One can see from this figure that the experimental points are well fit by the sum of both theories. This fit is particularly impressive since the same radius seems to be satisfactory for both tumbling and spin-rotation.

If we attempt to apply the same theory to the nuclear spin dependent linewidth terms, we do not obtain good agreement. There seems to be required a contribution of the spin-rotation to these nuclear dependent terms. Such an effect was postulated by Nyberg[3] to be possible in systems where spin-rotation interaction is large. No previous experimental evidence for such an effect has been reported. Further experiments at a different frequency are being conducted to verify

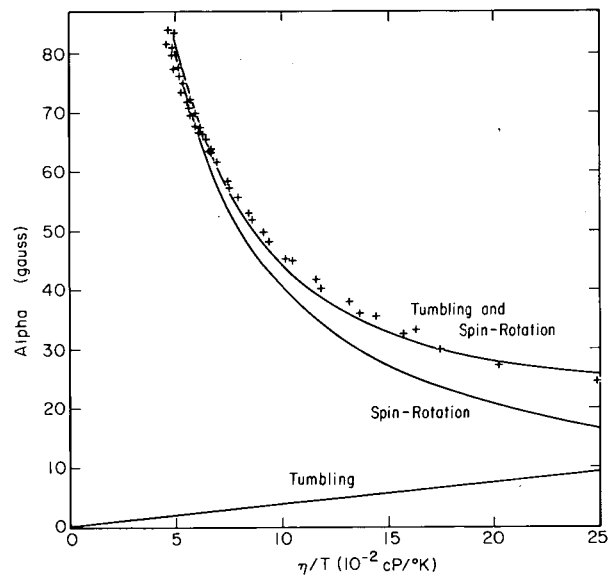

Fig. 1. Experimental values of the nuclear spin independent linewidth of $Cu(NH_3)_6^{2+}$ in liquid ammonia are plotted as a function of viscosity divided by absolute temperature. The theoretical contributions to the linewidth from spin-rotation and tumbling are summed and are shown to agree well with experiment. (XBL 751-5545)

whether this mechanism is involved.

1. R.C. Wilson and R.J. Myers, 1973 IMRD Annual Report, LBL-2299.
2. R. Wilson and D. Kivelson, J. Chem. Phys. 44, 154 (1966).
3. G. Nyberg, Mol. Phys. 12, 69 (1967).

3. MAGNETIC RESONANCE STUDY OF METAL-METAL COMPLEXES IN BIOLOGICALLY IMPORTANT MOLECULES

Duane L. Lindner and Rollie J. Myers

We have been using electron paramagnetic resonance spectroscopy to study the coordination and magnetic interactions of transition-metal ions in several proteins and their analogs.

We have been primarily interested in the protein ferritin, which stores iron in the form of a microcrystal of composition $8FeOOH \cdot FeO(OPO_3H_2)$. This microcrystal has an analog in the hydrolysates of Fe(III) salts in aqueous solution. In both systems the iron atoms are strongly anti-ferromagnetically coupled and both exhibit a strong resonance due to a phenomenon known as superparamagnetism. Several different models of the crystal structure of these microcrystals have been proposed. We have attempted to dope paramagnetic impurity ions coordiantion in them. So far we have been unable to observe spectra from any such probes.

EPR spectra of ferritin also show the presence of an Fe(III) site of rhombic coordination geometry. This site apparently is involved in the catalytic oxidation and reduction of iron. Since such a site has been postulated, but is not observed by other methods, we hope to study its properties by observing the EPR spectra of iron as well as other paramagnetic ions bound to the site. However, such a study on the native protein is inhibited by the relaxation effects of the magnetic moment of the iron oxyhydroxide microcrystal. Recently, we have isolated pure, active protein which does not contain the microcrystal and can now begin the study of the site.

We are also studying iron dimers linked by oxygen or hydroxide bridging groups. These dimers exhibit antiferromagnetic exchange. Several such compounds have been prepared. EPR of thermally excited states of these dimers should give information on the parameters of the spin Hamiltonian for these systems. Eventually, we hope to use this information in the study of hemerythrin, an oxygen carrying protein found in invertebrates, and which is believed to contain pairs of iron atoms which bind oxygen in a method analogous to those in the system we are now studying.

4. RESEARCH PLANS FOR CALENDAR YEAR 1975

Rollie J. Myers

The major part of our research is presently directed to a study of transition metal systems which have interacting sites for paramagnetic ions. Such systems include paramagnetic ions which are doped into paramagnetic lattices and complexes which contain two or more such intersecting ions. While our major research tool is electron paramagnetic resonance spectroscopy we also use nuclear resonance and magnetic susceptibilities.

Complexes containing interacting paramagnetic ions are important as catalysts both for industrial and for biological processes. By combining more than one transition metal ion in a single complex, it is possible to produce quite specific catalytic functions.

One phase of our work is to study ions such as Cu^{2+}, Mn^{2+} and V^{2+} doped into lattices containing Ni^{2+}, Fe^{2+} or Cr^{2+}. The EPR spectra of the doped ions is sensitive to the electron exchange interaction with the host. Most of our previous work was done with $NiSO_4 \cdot 6H_2O$ as a host, but we plan to utilize other host lattices.

Our work on Cu^{2+} doped apoferritin will continue. We will also work on some model compounds containing pairs or clusters of interacting ions.

We also plan to continue studies of electron spin relaxation both in solutions and in solids. Particular attention will be paid to Cu^{2+} and Ti^{3+}. Some work will also be done utilizing the dynamic nuclear polarization technique developed for a study of electron spin relaxation in solution.

5. 1974 PUBLICATIONS AND REPORTS

Rollie J. Myers and Associates

Journals

1. C. D. LeCroix, R. F. Curl, P. M. McKinney and R. J. Myers, Microwave Spectrum of Silyl Methyl Ether, J. Mol. Spec. 53, 250 (1974) (LBL-2590).

2. D. C. McCain and R. J. Myers, Dynamic Nuclear Polarization as a Means of Determining Electronic Spin-Lattice Relaxation Times in Aqueous Solutions of Cr^{3+}, Cu^{2+}, and Gd^{3+}, J. Mol. Phys. 28, 1109 (1974) (LBL-2751).

Presented paper

1. M. R. St. John and R. J. Myers, Molecular Field Interactions and g-Value Shifts for Transition Metal Ions in Paramagnetic Host Lattices, presented at the 18th Ampere Congress, Nottingham, England, Sept. 1974. (LBL-2755 Abs.)

LBL reports

1. Thomas Michael Hynes, Proton and Electron Spin Relaxation in Aqueous Solutions of Nickel (II) and Cobalt (II) Ions, (Ph.D. thesis) LBL-2248, May 1974.

Kenneth S. Pitzer, Principal Investigator

1. SOLUTIONS OF ELECTROLYTES: ACTIVITY AND OSMOTIC COEFFICIENT AT HIGH TEMPERATURES AND THERMAL PROPERTIES

Leonard F. Silvester and Kenneth S. Pitzer

Theoretical modeling of aqueous solutions with particular emphasis on compositions and temperatures of geothermal interest is continuing for such thermodynamic parameters as (1) activity and osmotic coefficients, (2) heats of solution and dilution, (3) heat capacities, and (4) apparent molal volumes.

The available osmotic and activity coefficient data for NaCℓ(aq) solutions from 0-300°C has been fit successfully at fixed temperatures by the equations

$$\phi - 1 = -\frac{|Z_M Z_X| A_\phi I^{1/2}}{1+bI^{1/2}} + m\left(\frac{2\nu_M\nu_X}{\nu}\right)\left(\beta_{MX}^{(0)} + \beta_{MX}^{(1)} e^{-\alpha I^{1/2}}\right) \tag{1}$$

$$+ m^2\left(\frac{2(\nu_M\nu_X)^{3/2}}{\nu}\right) C_{MX}^{\phi}$$

$$\ln\gamma_\pm = -|Z_M Z_X| A_\phi \left[\frac{I^{1/2}}{1+bI^{1/2}} + \frac{2}{b}\ln(1+bI^{1/2})\right]$$

$$+ m\left(\frac{2\nu_M\nu_X}{\nu}\right)\left[2\beta_{MX}^{(0)} + 2\beta_{MX}^{(1)}\left(1-(1+I^{1/2}-\frac{\alpha I}{2})e^{-\alpha I^{1/2}}\right)\right]$$

$$+ m^2\left(2\frac{(\nu_M\nu_X)^{3/2}}{\nu}\right)\left(\frac{3}{2}C_{MX}^{\phi}\right) \tag{2}$$

where $\beta^{(0)}$, $\beta^{(1)}$, and C^ϕ are temperature dependent experimentally determined parameters particular to a given salt, while α and b are temperature independent parameters which are fixed for a large class of salts. Various functional forms for the temperature and pressure dependence of $\beta^{(0)}$, $\beta^{(1)}$, and C^ϕ are currently being investigated.

From Eqs. (1) and (2) the relative apparent molal heat content, ϕ_L, is given as

$$\phi_L = \frac{\nu}{2}|Z_M Z_X| \frac{A_H}{3}\left(\frac{2}{b}\right)\ln(1+bI^{1/2})$$

$$- m(2RT^2\nu_M\nu_X)\left[\left(\frac{\partial\beta_{MX}^{(0)}}{\partial T}\right)_p\right.$$

$$\left. + \frac{2}{\alpha^2 I}\left(1-(1+\alpha I^{1/2})e^{-\alpha I^{1/2}}\right)\left(\frac{\partial\beta_{MX}^{(1)}}{\partial T}\right)_p\right]$$

$$- m^2\left(RT^2(\nu_M\nu_X)^{3/2}\right)\left(\frac{\partial C_{MX}^{\phi}}{\partial T}\right) . \tag{3}$$

Heat of dilution and heat of solution data for over one-hundred different salts at 25°C have been successfully fit to Eq. (3). In addition, modeling of the essential thermodynamic and electrostatic properties of water used for calculating various Debye-Hückel parameters found in these equations has been completed for the temperature and pressure range of 0-700°C and 0-1 kbar.

There are relatively extensive experimental data on systems involving singly and doubly charged ions but few measurements on ions with higher charge. Hence, in addition to the theoretical efforts, an experimental program aimed at understanding the behavior of aqueous solutions containing high-charged species has been undertaken. Preliminary experiments indicate the salts $La_4(Fe(CN)_6)_3$ and $Ca_2Fe(CN)_6$ are suitable for cells similar to La(ION)|$La_4(Fe(CN)_6)_3$(aq)|$Ag_4Fe(CN)_6$(s)|Ag(s) where La(ION) is a lanthanium ion-specific electrode. The data from these cells will be analyzed in terms of "higher order" limiting laws and to aid in picking appropriate theoretical models for dealing with electrolytes that undergo association in solution.

This program is also supported by the AEC through the Geothermal Energy Project at the Lawrence Berkeley Laboratory.

2. HIGHER ORDER ELECTROSTATIC TERMS IN ELECTROLYTE THEORY

Kenneth S. Pitzer

Various theoretical studies have yielded purely electrostatic terms of higher order than those giving the Debye-Hückel limiting law, but these effects have not been positively related to experimental results for the activity or osmotic coefficient. In the case of unsymmetrical mixing, the theory was extended beyond the higher-order limiting law term to yield a closed-expression for all of the purely electrostatic effects in addition

to the Debye-Hückel term. The addition of this function to our earlier equations for mixed electrolytes eliminated a large disagreement for the $HCl-AlCl_3$ system and improved the accuracy of agreement for $HCl-BaCl_2$ and other examples of unsymmetrical mixing. The data for various systems were evaluated on this basis.

The other higher-order limiting laws were also examined, but their effects were not found to be significant in relationship to existing activity or osmotic coefficient data.

3. SOLUTIONS OF ELECTROLYTES: MIXED ELECTROLYTES AT ROOM TEMPERATURE

Kenneth S. Pitzer and Janice J. Kim

An equation has been developed with the guidance of recent statistical theories of electrolytes which is designed for convenient and accurate representation and prediction of the thermodynamic properties of aqueous electrolytes including mixtures with any number of components. Previous papers have given the theoretical background and the evaluation of parameters for pure electrolytes of various charge types. The equation is here applied to a wide variety of mixed aqueous electrolytes at room temperature and at ionic strengths up to 6M in many cases and occasionally even higher. The first objective is the prediction of properties of mixed electrolytes using only the parameters for pure electrolytes; on this basis standard deviations in $\ln\gamma$ or ϕ for 69 sets of mixtures are less than 0.01 in 36 cases and above 0.05 in only seven cases all involving Cs^+ or OH^-. A second objective is the determination of parameters giving the differences in short-range interaction of ions of the same sign where these differ significantly from zero. As expected, these difference terms, while always small, are relatively most important for singly-charged ions (and especially for OH^- and Cs^+) and less important for ions of higher charge. The equations, including difference terms where known from binary mixtures with a common ion, were finally tested on 17 sets of mixtures involving four or more ions without any further adjustment of parameters. The standard deviation is less than 0.01 in all cases and is 0.003 or less in 11 cases. Thus these equations appear to yield accurate predictions of properties of mixed aqueous electrolytes.

4. OXYGEN-CATALYZED NUCLEAR-SPIN-SPECIES EFFECTS IN THE HEAT CAPACITY OF CH_4

Gerald J. Vogt and Kenneth S. Pitzer

Due to weak magnetic coupling between the nuclear spins of CH_4 and the bulk lattice, studies on the equilibrium properties of solid CH_4 are practically impossible for temperatures less than 8°K. However, by doping the CH_4 lattice with paramagnetic O_2 the rate of interconversion among the nuclear spin states and the spin-lattice coupling are sufficiently increased to allow heat capacity measurements by the heat-pulse method. From these measurements analysis of the nonlattice contribution will hopefully provide some understanding on the extent of nuclear interconversion and on the thermal properties of phase II ($T < 20.48$°K) in CH_4.

A series of experiments on CH_4-O_2 mixtures ($[O_2] \leq 1$ mole %) have recently been completed and only a rather preliminary study of these results has been made. Above 8°K our results agree generally with those published by Colwell, et al.[1] and others, although there appear to be some quantitative differences.

Published heat capacity data for CH_4 do not extend below 5°K; however, in our experiments data for the CH_4-O_2 mixtures have been taken down to 0.4°K. Below 4°K the heat capacity of the O_2-doped samples shows two more anomalies, both reaching a maximum of 1 cal/deg-mole at approximately 1°K and 0.6°K, respectively. These effects are too large to be accounted for by the oxygen impurity (see results of Burford and Graham[2]) and must relate primarily to solid CH_4. Their detailed explanation awaits further work.

---

1. J. H. Colwell, E. K. Gill and J. A. Morrison, J. Chem. Phys. 39, 635 (1963).
2. J. C. Burford and G. M. Graham, J. Chem. Phys. 49, 763 (1968).

5. THE POTENTIAL FUNCTIONS FOR THE ANOMALOUS ν_7 VIBRATIONS OF PF_5 AND VF_5

Lawrence S. Bernstein, Janice J. Kim, and Kenneth S. Pitzer

Trigonal bipyramidal molecules of the MF_5 type have been of interest because they have relatively low barriers to axial-equatorial fluorine interchange. This tendency to fluorine interchange produces a marked anisotropy in the ν_7 vibration (equatorial bend) which is the predominant contributor, at small coordinate displacements, to the interchange pathways. We have determined that a potential of the form

$$V(\rho,\phi) = 1/2\ a\rho^2 - b\cos(3\phi)\ \rho^3 + c\rho^4 \qquad (1)$$

is an adequate representation of the ν_7 potential and also provides an approximate representation of the axial-equatorial interchange potential for large coordinate displacements where a substantial amount of axial bend is mixed in with the equatorial bend. ρ and ϕ are the polarcoordinate transformations of the symmetry coordinates S_{7x}, S_{7y} and a, b, and c are potential constants which may be estimated by electronic and structural properties of the molecule. The interaction between the axial and equatorial bending coordinates is described by a pseudo-Jahn-Teller effect coupling the D_{3h} ground-electronic state to higher states via these symmetry coordinates.

The energy levels for the ν_7 equatorial bending motion of PF_5 have been calculated using this potential and are found to be in excellent agreement with the observed transitions. The potential constants may be approximated by a model which relates a, b and c to the curvature of the potential, K_o, and the value of the ρ coordinate at the saddle point of symmetry C_{4v} between adjacent D_{3h} configurations. These initial estimates for a, b and c were refined to reproduce the $0 \rightarrow 1$ (175 cm^{-1}) and the two $1 \rightarrow 2$ (178 cm^{-1}, 164 cm^{-1}) observed transitions for PF_5. The final values were determined to be a=0.09080 mdyn/Å b=0.03 mdyn/$Å^2$, and c=0.007 mdyn/$Å^3$, in good agreement with model estimates of 0.089, 0.028, and 0.0045 respectively. Using the refined constants with no additional adjustments, additional transitions were calculated which agreed remarkably well with the observed fine structure pattern about the ν_7 fundamental. The observed and computed frequencies for PF_5 are summarized in Table I.

In addition, our model estimates the barrier to axial equatorial interchange for PF_5 to be

$$E(C_{4v}) = 1371 \text{ cm}^{-1} \text{ (3.92 kcal/mole)}. \qquad (2)$$

Recent calculations have shown that the above potential may also be used to accurately describe the equatorial bending motion of VF_5. Using the refined constants a=0.03406 mdyn/Å, b=0.012 mdyn/$Å^2$, c=0.00484 mdyn/$Å^3$, the energy levels were computed and compared with the observed transitions. The results are shown in Table II. The barrier height for VF_5 was calculated to be 629 cm^{-1} (1.98 kcal/mole).

Table I. Observed, computed frequencies (cm^{-1}) for PF_5 and assignments for Q branches in ν_7 region.

Transition	Species	ν_{calc}	ν_{obs}
$0 \rightarrow 1$	$A_1' \rightarrow E'$	175.0	175
$1 \rightarrow 2$	$E' \rightarrow E'$	177.9	178
	$E' \rightarrow A_1'$	164.6	164
$2 \rightarrow 3$	$E' \rightarrow E'$	154.7	159 (w)
	$A_1' \rightarrow E'$	168.0	167
	$E' \rightarrow A_1'$	178.4[a]	
	$E' \rightarrow A_1'$	182.0	180 Sh
	$A_1' \rightarrow A_1'$	191.7	191 Sh
	$A_1' \rightarrow A_1'$	195.3	194

[a]This feature is undoubtedly obscured by the more intense transitions at 178 cm^{-1}.

Table II. Observed, computed frequencies (cm^{-1}) for VF_5 and assignments for Q branches in ν_7 region.

Transition	Species	ν_{calc}	ν_{obs}
$0 \rightarrow 1$	$A_1' \rightarrow E'$	105.8	
$1 \rightarrow 2$	$E' \rightarrow E'$	109.5	109.4
	$E' \rightarrow A_1$	97.9	98.1
$2 \rightarrow 3$	$A_1' \rightarrow E'$	103.2	103.6
	$E' \rightarrow E'$	91.6	91.9
	$E' \rightarrow A_1'$	110.9	
	$E' \rightarrow A_1'$	114.1	
$3 \rightarrow 4$	$E' \rightarrow A_1'$	99.3	
	$E' \rightarrow E'$	106.6	
	$A_1' \rightarrow E'$	84.1	85.8
	$A_1' \rightarrow E'$	87.3	
	$A_1' \rightarrow E'$	113.5	
	$A_1' \rightarrow E'$	116.7	

6. PSEUDOROTATION IN XeF_6

Lawrence S. Bernstein and Kenneth S. Pitzer

After more than a decade a reasonably clear picture of the unusual noble gas compound XeF_6, has been established. This work, and the recent crystal-field model of Wang and Lohr,[1] provide strong support for a pseudo-Jahn-Teller effect as the basis for the unusual properties of XeF_6.

Within the pseudo-Jahn-Teller formalism we have derived a potential of the form

$$V(R,\theta,\phi) = -aR^2 + bR^4 - cR^4[\sin^4\theta\left[\frac{\sin^2 2\phi}{4} - 1\right] + \sin^2\theta]$$

where R, θ, ϕ are spherical coordinates which describe the large amplitude motions in t_{1u} coordinate space. The constants a, b, and c were refined from a wide body of experimental information: (1) electron diffraction of gaseous XeF_6; (2) Raman and infrared spectra in the gas phase and in inert matrices at liquid helium temperatures; (3) ultraviolet spectra; (4) heat capacity measurements; and (5) electric field deflection work. We were able to establish the following ranges for the potential parameters a, b, and c.

$$a \approx 0.087 \quad \text{mdyn/Å}$$

$$0.064 \leqslant b \leqslant 0.084 \quad \text{mdyn/Å}^3$$

$$0.02 \leqslant c \leqslant 0.08 \quad \text{mdyn/Å}^3$$

This range of potential constants represents XeF_6 as a hindered pseudorotator. With this form of the XeF_6 potential there is an analogy between this motion and a diatomic molecule rotating in an octahedral field.

---

1. S. Y. Wang and L. L. Lohr, Jr., J. Chem. Phys. 60, 3901 (1974).

7. ELECTRIC FIELD DEFLECTION OF MOLECULES

Lawrence S. Bernstein and Kenneth S. Pitzer

The deflection of molecular beams in an inhomogeneous electric field provides in many cases a very sensitive method for determining electrical polarity. For a normally rigid, symmetric-top, dipolar molecule, such as $XeOF_4$, dipole moments as low as 0.03D can be detected by this method. However, if the molecule possesses one or more degrees of internal freedom which can readily undergo large amplitude displacements, the sensitivity of this method to electrical polarity is greatly reduced. We have derived expressions for molecules with several types of large amplitude motions in this type of experiment. This list includes: (1) MX_3 - one dimensional inversion; (2) MX_7 - two dimensional pseudorotation; and (3) XeF_6 - three dimensional pseudorotation.

The lower limit of detectability for an ammonia-like molecule, MX_3, is given by the inequality

$$\frac{\mu^2}{\Delta} > 0.01\ D^2/(cm^{-1})$$

where μ is an effective dipole moment and Δ is the separation of inversion doublets.

Similar expressions resulted for the two and three dimensional pseudorotators. However, the derivations of these expressions took into full account the entire range of closely spaced pseudorotational states, whereas in typical MX_3 systems only a single pair of inversion doublets needs consideration.

For the MX_7 molecules it was determined that threshold dipoles of 0.4D for IF_7 and 0.5D for ReF_7 would be needed for detection.

The behavior of XeF_6 was evaluated for both a free pseudorotation and also for a hindered pseudorotation. In the free pseudorotating limit a dipole moment as large as 1.2D was determined to be the threshold of detectability. However, for the restricted pseudorotation the threshold dipole varied from 0.2D for the high angular barrier limit to 0.6D for a low angular barrier case. These limits are large enough to eliminate the apparent contradiction between the absence of detection of XeF_6 in these experiments and other results indicating a polar distortion.

8. QUANTUM CHEMISTRY FOR HEAVY ATOMS

Yoon S. Lee and Kenneth S. Pitzer

This program is in an exploratory stage. Large relativistic effects introduce new features to the quantum mechanical treatment of the chemical behavior of heavy atoms and we aim to develop methods appropriate to those conditions.

An initial step is the evaluation of the relative magnitude of the effects (1) of relativity and (2) of the introduction of the 4f shell of 14 electrons in departure of chemical properties of elements such as Tl, Pb, and Bi from the pattern established by lighter elements in the same groups.

9. RESEARCH PLANS FOR CALENDAR YEAR 1975

Kenneth S. Pitzer

Extension of the electrolyte program to temperatures other than 25°C and to the related properties of enthalpy and heat capacity, which was initiated in 1974, should be completed in 1975 for pure electrolytes. We will then turn to mixed electrolytes and to pressure effects. Particular attention is being given to the range of conditions and components important for geothermal brines and partial support is received via the geothermal energy project at Lawrence Berkeley Laboratory. We have considerable confidence that both the chemical and the engineering thermodynamics of these brines will be predictable to the needed accuracy.

Efforts will be made to extend the general theoretical approach which has been successful for thermodynamic properties to transport properties such as conductance. Either Monte Carlo or molecular dynamics calculations will be needed at the initial stage and these are being discussed with Dr. Alder of Lawrence Livermore Laboratory.

The work on nuclear spin conversion effects in solid methane is nearing completion, but some additional measurements are required. Also we must study the thermal effects of the small concentration of oxygen added as a spin conversion catalyst; it may be possible to predict these effects theoretically, but it is also possible that experiments may be required. Theoretical interpretation of the newly-discovered anomalies near 1°K will be undertaken.

Work will continue in the general area of anomalous or special effects in the structures and properties of compounds of heavy elements. As an example of relativistic quantum chemistry, we are planning calculations related to the electronic state and spectra of the Bi^+ ion and other anomalous species in that part of the periodic table. Progress in this area should improve the prospect of correct prediction of the properties of still heavier elements whose production is now being explored by others.

10. 1974 PUBLICATIONS AND REPORTS

Kenneth S. Pitzer and Associates

Journals and books

1. Kenneth S. Pitzer and Guillermo Mayorga, Thermodynamics of Electrolytes. III. Activity and Osmotic Coefficients for 2-2 Electrolytes, J. Solution Chemistry, 3, 539 (1974) (LBL-2282).

2. Kenneth S. Pitzer and Janice J. Kim, Thermodynamics of Electrolytes. IV. Activity and Osmotic Coefficients for Mixed Electrolytes, J. Am. Chem. Soc. 96, 5701 (1974)(LBL-2713).

LBL reports

1. Lawrence S. Bernstein Large Amplitude Motion in Molecules, LBL-2701 (Ph.D. thesis), May 1974.

2. Kenneth S. Pitzer, Thermodynamics of Electrolytes. V. Effects of Higher Order Electrostatic Terms, LBL-3105, July 1974 (submitted to J. Solution Chem.)

3. Lawrence S. Bernstein, A New Look at an Old Problem: Inversion in $MX_3(C_{3v})$ Molecules, LBL-3514, November 1974 (submitted to Journal of Chemical Physics).

4. Lawrence S. Bernstein and Kenneth S. Pitzer, Electric Field Deflection of Molecules with Large Amplitude Motions, LBL-3526, November 1974 (submitted to Journal of Chemical Physics).

E. NUCLEAR SCIENCE

Donald R. Olander, Principal Investigator

1. KINETICS OF THE REACTION OF WATER VAPOR ON PYROLYTIC GRAPHITE BY MODULATED MOLECULAR BEAM MASS SPECTROMETRY

Rajarama T. Acharya, Alan Z. Ullman, and Donald R. Olander

This H_2O-graphite study was conducted in two parts. The first part consisted of the study of the isotope exchange reaction of a continuous beam of D_2O and a modulated beam of H_2O on the basal and prismatic surfaces of pyrolytic graphite. The exchange product HDO was detected and measured in the target temperature range of 300 to 1800°K. The observed HDO reaction product vector (i.e., signal amplitude and phase shift) was typical of the double diffusional mechanism.[1] The slowest step in this process is the diffusion of water into the grains via the grain boundaries. In order to account for fine structure in the observed phase lags, the double diffusional model has been extended to include the finite thickness of both the target and the grains. The isotope exchange reaction on both basal and prismatic surfaces follows the above mechanism and the best fit values of the parametric constants have been determined. In addition, precise measurement of the phase shift of the scattered H_2O signal compared to a neon reference has led to a value of 0.15 for the sticking probability of H_2O on graphite.

The second part of the investigation consisted of the study of the reaction of water vapor in the temperature range of 1500 to 2400°K on both the basal and prismatic orientations of the graphite surface. At high temperatures the reaction products H_2, CO, and CO_2 were observed. Only the CO signal was sufficiently large to provide information on the reaction mechanism. The apparent reaction probability for CO was between one and two orders of magnitude lower than that of HDO. However, the data indicated show that the reaction product CO also undergoes a diffusional process very similar to the previous one. The mechanism of the H_2O-graphite reaction is summarized in Fig. 1. Gaseous water vapor adsorbs on the graphite surface with a probability of 15% per collision. The adsorbed H_2O simultaneously undergoes solution/diffusion in the bulk solid (as indicated by the pairs of arrows in the figure) and surface reaction. The latter consists of two branches; the most likely surface reaction of adsorbed H_2O is simple desorption, but a small fraction reacts with the carbon substrate to produce CO and H_2. The CO reaction product is also subject to solution/diffusion in competition with desorption. The H_2 product, however, appears to be released immediately from the surface.

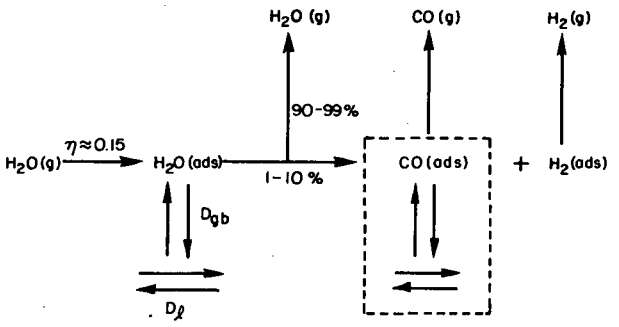

Fig. 1. The mechanism of the water vapor graphite reaction. (XBL 743-5680)

---

1. D. R. Olander, R. Jones, J. A. Schwartz, and W. J. Siekhaus, J. Chem. Phys. 57, 421 (1972).

2. MOLECULAR BEAM STUDY OF THE GRAPHITE-HYDROGEN REACTION

Mehdi Balooch and Donald R. Olander

The reaction of hydrogen with graphite is under investigation using the techniques of modulated molecular beams coupled with mass spectrometric identification of reaction products. The reaction probability of molecular hydrogen with pyrolytic graphite is below the sensitivity limit of our apparatus (minimum detectable reaction probability $< 10^{-5}$). Consequently, we are investigating the reaction of hydrogen atoms with the graphite surface. Figure 1 shows the high-temperature furnace for producing a beam of atomic hydrogen. A tungsten tube (0.37 cm, 0.25 mm thick wall, 7 cm in length) is held firmly at one end by a water-cooled copper block. The tungsten tube is closed off at the other end and a 1-mm-diameter effusion orifice is spark-cut into the

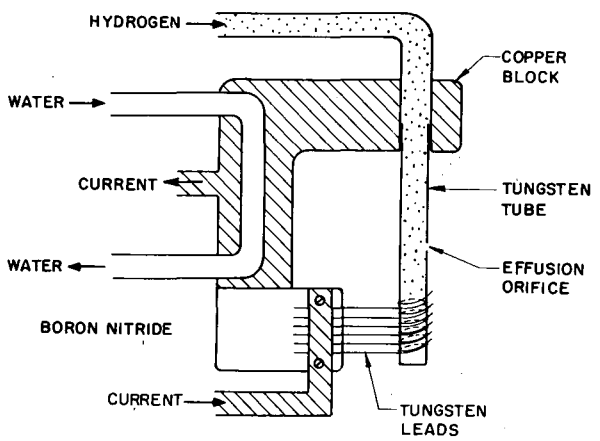

Fig. 1. Atomic Hydrogen Beam Source. (XBL 751-5500)

wall at about the midplane. The tube is heated resistively by current entering through six tungsten leads (0.76 mm diameter) which are wound around and spring-loaded to the bottom of the tungsten tube. In this way, no significant bending moment is applied to the tungsten tube, which is essentially free-hanging. When heated, the tube expands axially by sliding down through the spiral of tungsten wire leads. The resistance of the tungsten tube is higher than that of the tungsten leads, so that the maximum temperature occurs near the midplane of the tube where the orifice is located. The temperature is quite uniform along most of the tube length. The maximum usable temperature is ~2500°K, which is achieved for 150 amps of current and 0.75KW of power. Heat loss is minimized by two cylindrical radiation shields around the tungsten tube.

The strongest atomic hydrogen beam which can be handled by the diffusion pump is obtained with a total source pressure of 6 torr. From equilibrium calculations, the pressure of atomic hydrogen in the source tube should be ~1.5 torr and the flux of atomic hydrogen on the target should be ~8.5×10^{16} atoms/cm^2-sec. This flux is equivalent to an isotropic gas of atomic hydrogen at 5×10^{-4} torr and 2500°K. The calculated ratio of the atomic and molecular hydrogen signals from the mass spectrometer is ~0.17. The H_2 contaminant in the beam has no effect on the reaction; it simply scatters from the surface as would a rare gas.

Preliminary results from the atomic hydrogen-graphite prism plane reaction indicate that methane (CH_4) is the predominant product at the surface temperatures below 1000°K. This reaction product disappears at temperatures above 1200°K. At very high temperatures (>~2200°K) C_2H_2 is produced by the surface reaction.

3. MOLECULAR BEAM STUDY OF THE F_2-UO_2 REACTION

Albert Machiels and Donald R. Olander

The molecular beam apparatus shown in Fig. 1 has been built for the study of heterogeneous reactions which cannot be investigated by the older equipment used in Sections 1 and 2. The new apparatus differs from the old one in three principal ways: First, the target mount in the new device is horizontal, so that fragile solid (or liquid) targets can be studied; second, the liquid helium cryopump on the new apparatus permits production of molecular beams of reactive gases, which cannot be handled by diffusion pumps; third, the electron multiplier is offset from direct line-of-flight view of the ionizer to reduce noise from photons and excited neutral atoms produced by electron bombardment but not eliminated in the quadrupole structure.

The apparatus is being used to study the kinetics of the fluorination of uranium dioxide. The overall reaction:

$$UO_2(s) + 3F_2(s) \rightarrow UF_6(g) + O_2(g)$$

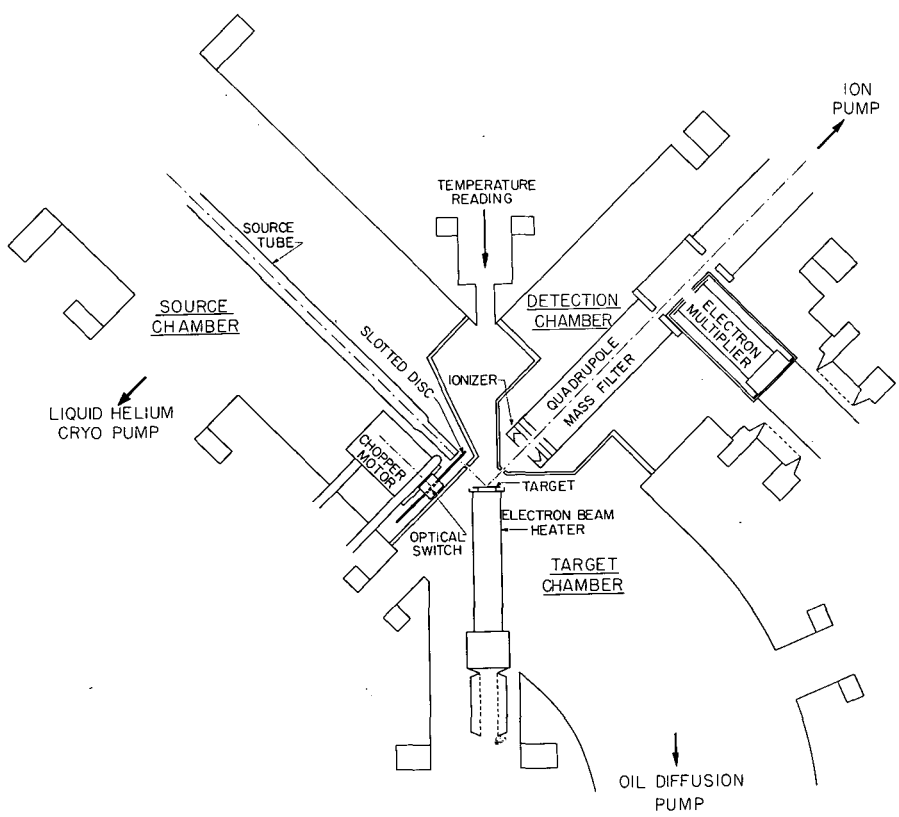

Fig. 1. Molecular beam apparatus for the UO_2-F_2 reaction. (XBL 751-5501)

is of importance in the nuclear fuel cycle; it forms an integral part of the volatility method of fuel reprocessing and it is the means by which newly mined and recycled uranium is prepared for isotopic enrichment in the gaseous diffusion plants.

Preliminary experiments have included the measurement of the mass spectrometer cracking pattern of what was expected to be the major reaction product (i.e., UF_6). As with many other large inorganic vapor molecules, the parent peak in the UF_6 cracking pattern is quite small. For our quadrupole mass spectrometer, the relative abundances of the ions were found to be: UF_6^+ = 1%, UF_5^+ = 100%, UF_4^+ = 23%, UF_3^+ = 23%, UF_2^+ = 25%, UF^+ = 15%, and U^+ = 6%.

As a result of reactive scattering of fluorine on single-crystal wafers of UO_2, a large reaction product signal is observed at a mass number of ~295. This species could either be UF_3^+ (mass 295) or possibly UOF_2^+ (mass 292). Positive identification of the reaction product is expected following investigation of the fragmentation pattern of UF_4 and repetition of the reaction experiments at higher mass spectrometer resolution. In any case, it is quite clear that the predominant reaction product is not the expected UF_6 species. In conventional kinetic experiments, the primary heterogeneous reaction apparently produces a less highly fluorinated product which is sufficiently volatile to escape from the surface. Further fluorination to produce UF_6 takes place in the gas phase, not on the surface.

4. THE KINETICS OF RADIOLYTIC GAS PHASE REACTIONS BY MODULATED MOLECULAR BEAM MASS SPECTROMETRY

Valerie Kruger and Donald R. Olander

An experimental system was developed to enable on-line mass spectrometric analysis of gas phase radiolysis flow systems, and was applied to observation of the oxygen radiolysis system in particular. In this experimental system, energy from a beam of 1-MeV protons is deposited in the oxygen as it flows through a fast-flow reaction tube. A molecular beam source samples the flow gas, and the resulting molecular beam is then modulated and analyzed with a quadrupole mass spectrometer.

Experimentally determined quantities are the concentrations of atomic oxygen, molecular oxygen, and ozone as functions of reaction time, system pressure, and total absorbed dose. Operating parameters were in the following ranges:

System pressure:	[1.5-4.0] Torr
Irradiation time:	[0.2-0.3] sec
Total energy deposited:	[0.5-15] 10^{12} MeV/cm^3
Dose Rate:	[0.2-20] 10^{20} MeV/g·sec.

Observed concentrations of the radiolysis products atomic oxygen and ozone were of the order:

Atomic oxygen:	[5-40] 10^{12} atoms/cm^3
Ozone:	[3-20] 10^{13} molecules/cm^3

The ozone levels observed are substantially higher than those predicted by pre-existing chemical models, and the discrepancies cannot be explained in terms of increased g-values (atoms produced per unit energy deposited) or of systematic errors in the measurement.

A modification to the chemical model is proposed, in which an excited vibrational state O_2^* is postulated as a precursor to ozone via the reaction:

$$O_2^* + O_2 \rightarrow O_3 + O$$

Calculations including this modification indicate that agreement with the data is improved, although neither the agreement nor the explanation can be considered complete. It is concluded that further investigation of the low-pressure behavior in the oxygen radiolysis system is indicated, particularly with regard to the role of excited species in the chemical mechanism.

5. ACTINIDE REDISTRIBUTION DUE TO PORE MIGRATION IN HYPOSTOICHIOMETRIC MIXED OXIDE FUEL PINS

Sergio Guarro and Donald R. Olander

Actinide redistribution caused by the migration of porosity up the temperature gradient in a mixed oxide fuel pin occurs because moving disk-shaped pores become enriched in the less volatile of the two heavy-metal components of the mixed oxide (usually plutonium) by preferential evaporation of the more volatile species across the pore. The variation of the Pu/U ratio behind and ahead of a pore moving up the temperature gradient in hypostoichiometric mixed oxide [$(U,Pu)O_{2-x}$] is shown in Fig. 1. Because of the depletion of uranium on the hot front face of the pore (the volatility of UO_3 and UO_2 is greater than that of PuO_2 and PuO), the solid becomes enriched in plutonium. Solid state diffusion permits the concentration perturbation on the hot face to extend into the solid ahead of the moving pore. As a result, a "bow wave" of excess plutonium precedes the pore as it travels up the temperature gradient towards the central void. In order to satisfy conservation of plutonium along the path of the pore, a plutonium-deficient spike is generated at the initial position of the pore. The plutonium missing from this "start-up spike" is contained primarily in the plutonium-rich distribution preceding the migrating pore. However, the excess plutonium in the bow wave changes during migration for two reasons: (1) the pore moves into regions of increasing temperature and (2) at a fixed position, the ambient temperature gradually diminishes due to restructuring and central void formation. These two effects alter the plutonium

fraction in the columnar grain formed between the initial pore locations, and result in the "trail" behind the pore in Fig. 1.

These elementary redistribution events of single pores are then combined to determine the gross redistribution in the fuel. For typical LMFBR fuel operating conditions, calculated redistribution due to pore migration is orders of magnitude smaller than that observed in irradiated pins. If actinide redistribution by vapor transport is to be the predominant mechanism in mixed oxide fuels, it must proceed via radial cracks along the temperature gradient rather than by moving closed porosity. If radial cracks are not present, only true thermal diffusion (the Soret effect) remains to explain the plutonium enrichment of the centerline of irradiated fuel pins.

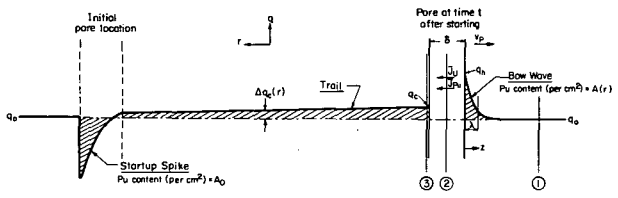

Fig. 1. Plutonium redistribution due to motion of a pore. (XBL 7410-7419)

6. RESEARCH PLANS FOR CALENDAR YEAR 1975

Donald R. Olander

The research proposed for 1975 consists of fundamental studies of high-temperature materials which are important to the general field of energy production. Most of the work concerns fission or fusion reactor materials, but coal gasification studies are also contemplated.

Approximately 50% of our effort will be devoted to the molecular beam apparatus developed for the purpose of investigating heterogeneous chemical kinetics on a microscopic scale. The older molecular beam apparatus will be utilized to investigate the reaction of graphite and atomic hydrogen. The encouraging preliminary results obtained in 1974 will be explored in greater detail in order to develop a sound mechanistic understanding of this technologically significant reaction.

The development of a strong atomic hydrogen beams source for this apparatus makes it possible to begin studying gas-solid interaction phenomena of importance to the CTR. Atomic hydrogen is the major chemically reactive constituent of a thermonuclear plasma, and the reactions of this species with the structural components of the reactor are of great concern. As a start to this program, we plan to study the reaction of H with insulating materials (e.g., Al_2O_3 or Y_2O_3) to determine the extent of the reduction of the ceramic and the concommitant production of water vapor, which contaminates the plasma.

The new molecular beam apparatus will be committed to completion of the UO_2-F_2 reaction for most of the year. The diffusion coefficient of oxygen ions in $UO_{2\pm x}$ will begin.

High-temperature phenomena which are important in the materials performance of the oxide fuel of fission reactors are to be investigated experimentally. A furnace capable of generating a steep temperature gradient (~5000°K/cm) in ceramic specimens at a peak temperature of ~3000°K is under development. When completed, this apparatus will be useful for studying a wide variety of phenomena which occur in the thermal gradient of nuclear reactor fuel pins. The processes include migration of fission products, the heavy metals U and Pu, oxygen, and bubbles and pores in the fuel. We have chosen to study thermal gradient migration of small particles of metal in UO_2. The metal powder simulates the small precipitate particles of noble-metal fission products observed in irradiated oxide fuels. The extent of motion of the particles, after several days in the temperature gradient, will be measured by successive vaporization of small amounts of the UO_2 matrix and microscopic counting of the exposed particles. The results will be compared to the predictions of the surface diffusion model proposed for this type of migration.

One of the most important physical properties of oxide fuels needed for safety analyses of nuclear reactors is the vapor pressure of the fuel. We plan to utilize the laser pulsing apparatus to determine if the vapor pressure of UO_2 can be measured at temperatures beyond the reach of conventional methods. The method is based upon detection of the vaporization pulse with a mass spectrometer following bombardment of the target with a giant laser pulse. If the equilibrium theory of Langmuir vaporization is applicable to the rapid transient, the vapor pressure can be deduced from knowledge of the temperature transient and the mass spectrometer response to the vapor pulse.

Time and personnel permitting, the laser pulsing apparatus will be used to study the reactions of carbon with O_2 and H_2O under the very rapid surface temperature transient produced by the laser. We are interested in comparing the chemical kinetics obtained in the transient situation with the kinetics which have already been determined from steady state reaction in the molecular beam apparatus.

Finally, if personnel are available, the gas phase radiolysis utilizing the 1-MeV van de Graaff accelerator will be used to investigate the radiolytic water gas shift reaction, $CO + H_2O \rightleftharpoons H_2 + CO_2$. This reaction is of technological importance in the corrosion resistance of the graphite core of the High Temperature Gas Cooled Reactor (HTGR).

7. 1974 PUBLICATIONS AND REPORTS

Donald R. Olander and Associates

Journals

1. H. C. Tsai and D. R. Olander, The Viscosity of Liquid Cesium up to 1600°C, High Temp. Sci. 6, 142 (1974) (LBL-2201).

2. A. Ullman, R. Acharya and D. R. Olander, Thermal Accommodation Coefficients of Inert Gases on Stainless Steel and UO_2, J. Nucl. Mat. 51, 277 (1974) (LBL-2533).

3. D. R. Olander, Reply to "Comments on Papers by Olander Regarding Actinide Redistribution in Mixed-Oxide Fuels" by R. O. Meyer, J. Nucl. Mat. 52, 329 (1974) (LBL-3119).

Invited talks

1. D. R. Olander, "Molecular Beam Studies of the Reactions of Graphite with Oxygen and Water Vapor," Symposium on Molecular Processes at Solid Surfaces, American Chemical Society National Meeting, Los Angeles, April 1, 1974.

2. D. R. Olander, "Heterogeneous Chemical Kinetics Using Modulated Molecular Beams," Gordon Research Conference on High-Temperature Chemistry, Andover, New Hampshire, July 22-26, 1974.

LBL reports

1. R. Yang and D. R. Olander, Diffusion of Lanthanum in Molten Uranium, LBL-2534, Jan. 1974.

2. R. A. Olstad and D. R. Olander, Evaporation of Solids by Laser Pulses, Part I - Iron, LBL-3167, Aug. 1974 (J. Appl. Phys.).

3. R. A. Olstad and D. R. Olander, Evaporation of Solids by Laser Pulses, Part II - Zirconium Hydride, LBL-3168, Aug. 1974 (J. Appl. Phys.).

4. Valerie Ruth Petersen Kruger, The Kinetics of Radiolytic Gas Phase Reactions by Modulated Molecular Beam Mass Spectrometry (Ph. D. Thesis), LBL-2727.

5. S. Guarro and D. R. Olander, Antioxide Redistribution Due to Migration in Hypostoichiometric Mixed Oxide Fuel Pins, LBL-3196, Oct. 1974.

0 0 0 0 4 2 0 / 2 1 9

II. Metallurgy

A. CRYSTAL IMPREFECTIONS

Jack Washburn, Principal Investigator

1. COMPUTER SIMULATION OF SMALL DISLOCATION LOOPS IN FIELD ION IMAGES OF FCC CRYSTALS

Kaj G. Stolt and Jack Washburn

It is shown that small dislocation loops 30Å or less in diameter cause field ion image contrast while wholly inside the tip. During a field evaporation sequence that brings the loop successively closer to the surface characteristic, changes in the contrast occur which make it possible to clearly distinguish between vacancy type and interstitial type loops. The results show that unambiguous interpretation of image contrast observed in a single photograph is not possible for small loops. The contrast effects for small loops are in many cases rather slight distortions of the image rings which for a single photograph could occur for other reasons such as tip asymmetry or the presence of impurities. For this reason an entire field evaporation sequence is essential. It is pointed out that only sessile loops can be observed in the FIM, since the stresses associated with the electric field will remove glissile loops from the specimen.

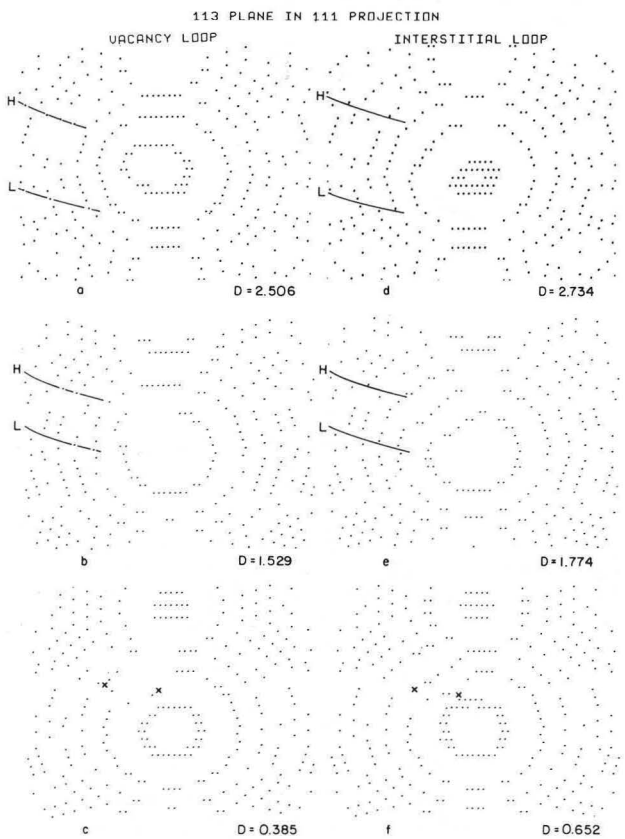

Fig. 1. Predicted FIM image distortions for small interstitial and vacancy loops lying just under (a, b and d, e) and intersecting, (c and f) the surface. (XBL 748-6864)

Figure 1 shows three rather widely separated stages of simulated field evaporation sequences for a vacancy and an interstitial loop respectively. L is the trace of the plane of the loop in the surface and H is the position where the normal to the loop through its center cuts through the surface.

The conclusions have been based on a large number of computer plots with loops in various positions.

2. DEVELOPMENT OF A CdS-Cu_2S SOLAR CELL WITH IMPROVED CHARACTERISTICS

Terry M. Peterson and Jack Washburn

The CdS-Cu_xS heterojunction solar cell is currently one of the most promising for terrestrial power generation at a competitive cost per kilowatt hour. However, there are serious problems concerning life time. It undergoes degradation due to diffusion of copper into CdS during operation. These problems may or may not turn out to have practical solutions.

Our calculations have suggested that one of the factors that probably contributes to the degradation is the gradual change in lattice constant of Cu_xS as Cu diffuses into the CdS. This leads to an increasingly dense network of misfit dislocations at the partially coherent interface between Cu_xS and CdS. The dislocations act as recombination centers and thus cause a decrease in the number of carriers that successfully pass through the junction.

Our experiments are aimed at discovery of a heterojunction cell for which more perfect coherence (fewer misfit dislocations) is possible and for which the diffusion problem can be minimized.

The operation of the cuprous sulfide/cadmium sulfide solar cell has been studied theoretically by means of calculations of response characteristics based on an extension of a current model of such junctions which assumes the photo-current is due (almost entirely) to absorption in the cuprous sulfide. Our extension to this model emphasizes the role of interfacial dislocation networks accompanying phase changes both during cell fabrication and during subsequent degradation while in operation. Comparison of these calculations with published experimental data suggests that the extended model can account for previously unexplained features of cuprous sulfide/cadmium sulfide cell behavior.[1] These results

have prompted an investigation of the characteristics of a cuprous sulfide cell made with a solid solution of zinc sulfide and cadmium sulfide ($Zn_{1-y}Cd_yS$) used in place of CdS.

A study of the $Zn_{1-y}Cd_yS$ cell is now in progress. Preliminary activities in this study include the fabrication of several cuprous sulfide/zinc sulfide cells made from single crystal ZnS doped with excess zinc, and some experimentation to determine a practical method for obtaining high conductivity $Zn_{1-y}Cd_yS$ crystals.

Also underway, are further theoretical calculations whose aim is to explain the appearance of certain non-linear photo-response characteristics in some cuprous sulfide/cadmium sulfide junctions in terms of a recently proposed band structure for the cuprous sulfides and the previously mentioned model.

---

1. See LBL-2281.

3. BORON PRECIPITATES IN ION IMPLANTED SILICON

Wei-Ku Wu and Jack Washburn

Long rod-like defects are observed in ion implanted silicon when boron is present either as a prior dopant addition or as the implanted species. For many years these rods have been described variously as precipitates, lines of point defects, dislocation dipoles, or elongated dislocation loops. The diffraction contrast from the defects has been difficult to interpret unambiguously because of their very narrow spacing.

Our recent work indicates that they have the characteristics of narrow extrinsic dipoles or elongated dislocation loops and that there are two different types along each of the six ⟨110⟩ directions. The two different types have recently been very clearly distinguished by annealing experiments in which the same area of a foil is repeatedly observed by transmission electron microscopy with intermediate holding at a temperature which causes shrinkage of the rod defects, Fig. 1. From the temperature dependence of the shrinkage rate an activation energy of 3.5±.1 eV has been determined for one type of rod. These shrink from the ends at a conveniently measurable rate at about 800°C. This value of the activation energy suggests that the rate controlling process is boron diffusion. The second type shrinks much more slowly at this temperature. The rate of shrinkage probably depends on the rate of silicon self diffusion.

Another factor which has been found to influence the shrinkage rate is the distance between the end of a rod and another defect such as a dislocation loop. It appears that these loops may act as vacancy sources or as sinks for boron. Other interesting observations have also been made. During shrinkage rods have been observed to rotate off ⟨110⟩ and lie along ⟨112⟩ and sometimes to change their diffraction contrast characteristics

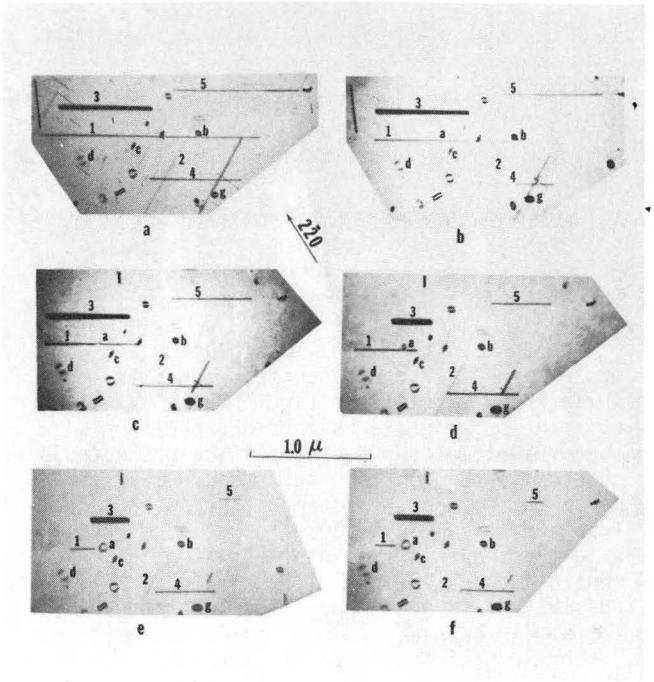

Fig. 1. Showing the shrinkage of long linear defects. Type Ā linear defects, e.g. 1, 2, 4, and 5, shrink faster than Type A, e.g. 3, in this temperature range. It is noted that a new dislocation loop a is nucleated when defect 1 is shrinking. Small faulted dislocation loops, e.g. b and g grow a bit while Type Ā defects are shrinking. Figures a-d are annealed at 802°C for 25 min successively. Figure e is annealed at 802°C for 50 min and Fig. f is annealed at 750°C for 70 min. (XBB 7411-7744)

as if they had converted from one burgers vector to another. These interesting observations are the subject of continuing experimental work.

4. MECHANISM OF RECOVERY PROCESSES AFTER PHOSPHOROUS IMPLANTATION IN SILICON

Krishna Seshan and Jack Washburn

There has been considerable confusion in the literature as to the nature of small loops and rod defects that appear on low temperature annealing of room temperature phosphorous implanted silicon. There is evidence for some replacement of silicon on the fault by a smaller atom such as boron, phosphorous or oxygen which leads to the displacement a/x ⟨111⟩ rather than a/3 ⟨111⟩. Because of the small size of these defects interpretation of the diffraction contrast is difficult. Some new experimental work on electron diffraction contrast from small defects has been a necessary part of this investigation. Through use of weak beam techniques, it has now been possible to show clearly that most of the small loops are faulted and lie on {111} planes with burgers vector a/x ⟨111⟩. It seems likely that the contradictory results

that have been obtained by various investigators have been caused by the presence of different impurities or dopant elements. The internal stresses associated with certain solute elements probably are responsible for the appearance of perfect, rather than faulted loops in some cases.

Experiments still in progress suggest that the interstitial loops form from break-up of small clusters of interstitial atoms that have formed during room temperature ion implantation or in the early stages of annealing below 600°C.

A model has been developed to explain the electron microscope observations and changes in electrical characteristics that occur after phosphorous implantation to a dose that is below that necessary to form a continuous amorphous layer.

5. EFFECT OF SURFACE LAYER COMPOSITION ON ELECTRON WORK FUNCTION IN Ni_4W

Joaquin Lira-Olivares and Jack Washburn

Many related experiments have been reported by others in the past. Typically work function measurements have been made before and after evaporation of enough atoms onto a tungsten surface to constitute a monolayer of another species. A severe weakness in almost all of these experiments is the fact that the actual surface geometry is unknown.

We have used a combination of field-ion microscopy and field emission microscopy to make relative work function measurements on well characterized surfaces. In particular we have studied the effect of the composition of the outermost layer of a superlattice plane of the compound Ni_4W. By field evaporation, layer by layer, the surface is alternately Ni and W. For this well characterized case it has been found that the work function does not depend only on the composition of the outermost layer.

6. THE PREFERENTIAL CAPTURE OF INTERSTITIAL ATOMS BY DISLOCATIONS WHEN BOTH VACANCIES AND INTERSTITIALS ARE BEING FORMED AT THE SAME RATE BY RADIATION DAMAGE

Thomas H. Kosel and Jack Washburn

Preferential drift of interstitials to dislocations is the underlying cause for void growth during high fluency radiation damage. If dislocations did not preferentially attract interstitials, voids could not grow and radiation induced swelling could not occur.

Almost all of the experiments on void growth and swelling have been done at accelerated rates. This is necessary to get measurable swelling rates or void growth rates in an experiment that takes minutes or days rather than months or years. We believe that it is important to extend "swelling" experiments to lower defect production rates closer to those that will exist in a fusion reactor inner shell or in the fuel cladding in a liquid metal fast breeder reactor. This can be done if the dislocation climb rates are measured directly rather than void growth rates or swelling rates.

In a first attempt to demonstrate the usefulness of this technique we are studying dislocation climb rates in a series of copper alloys of varying stacking fault energy during electron irradiation in the high voltage electron microscope. The same area is photographed repeatedly with intermediate electron irradiation at a known elevated temperature. The aim of the first set of experiments is to find out whether or not wide splitting of the dislocations in a low stacking fault energy alloy has a significant effect on preferential capture of interstitials.

Figure 1 shows a typical series of pictures of the same area from which climb rates are measured. In the Cu-Al alloys which have been studied, the interstitial loops are always perfect, they have 1/2 ⟨110⟩ burgers vectors, and are oriented near the pure edge orientation. Climbing dislocations tend to remain on {111} planes. Therefore, edge loops are rhombus shaped and dislocations near screw orientation develop into helical dislocations that are segmented so that the glide cylinder has {111} surfaces. Preliminary measurements suggest that dislocations near pure edge orientation climb at the same rate as those near screw orientation. This suggests that a pure screw dislocation can not preferentially capture interstitials and feed them by pipe diffusion to the climbing edge segments.

The fact that the climbing dislocations tend to remain on {111} suggests that they remain dissociated and that jog pair nucleation is the slowest step in the climb process.

This research has been partially funded through a grant from the General Electric Company.

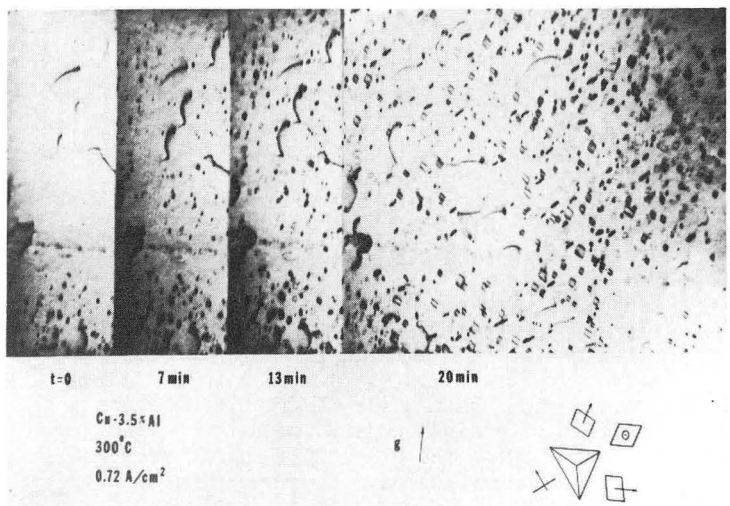

Fig. 1. Growth of interstitial loops and climb of dislocations near screw orientation during elevated temperature electron bombardment of -Cu-3.5% Al in the beam of the 650 kv electron microscope. (XBB 753-1742)

7. MECHANISM OF THE SHAPE MEMORY EFFECT IN NiTi

Hani Mohammed and Jack Washburn

Support through the National Science Foundation has recently been obtained by the Lawrence Berkeley Laboratory for further development of a low temperature heat engine using NiTi as the working substance. When deformed at room temperature by up to 6% strain and then heated by only 40 to 50°F above room temperature the NiTi returns to its original shape with great force. This permits mechanical work to be extracted. An engine of this type has been running at LBL long enough so that the working elements have been through more than 10^7 cycles with no sign of irreversible changes or fatigue cracking.

Considerable experimental work has been done on this material particularly by F. E. Wang at Naval Ordinance Laboratory, White Oak, Maryland. However, electron diffraction studies of the high and low temperature phases and transmission electron microscopy results on the morphology of the diffusionless transformation and memory effect are extremely limited. Much of the previous work is contradictory or done on poorly characterized material.

It is the aim of our research to clearly establish the crystal structures of the low and high temperature phases and to identify the mechanism of the low temperature plastic deformation and of its complete recovery on heating.

It is also an important purpose to try to establish whether or not any irreversible changes in structure have occurred in elements of NiTi that have been subjected to 10^7 or more work cycles.

8. CHARACTERIZATION OF GRAIN BOUNDARIES IN POLYCRYSTALLINE SILICON

Tai-Chan D. Huo and Jack Washburn

This research is just starting. It is motivated by the hope that silicon solar cells can make a contribution to the power needs of the future and a realization that this is probably not likely with single crystal silicon cut from large crystals. Cells using thin film polycrystalline silicon probably represent the best hope for achieving low enough cost with a silicon cell.

We will study segregation of various dopant elements at the grain boundaries of silicon by attempting to achieve intergranular fracture of polycrystalline samples in vacuum in the Auger spectrograph and combine the results of this analysis of grain boundary composition with measurements of the electrical characteristics of the boundary region. The long-range aim is to see if the presence of certain elements in the boundary can have an important effect on its ability to act as a recombination center for majority and minority carriers.

This work is being carried out in cooperation with Professor Somorjai's group.

9. THE MECHANISM OF INTERSTITIAL DIFFUSION IN FCC METALS

Robert M. Drosd and Jack Washburn

Cu-7.5%Al alloys and Cu-3%Si alloys are being irradiated in the high voltage electron microscope at accelerating voltages above and below that necessary to displace copper atoms directly to form a stable Frenkel pair. It has been observed that interstitials and vacancies are still produced in the Cu-Al solid solution, because of displacement of the aluminum atoms, at an accelerating voltage 100 volts below the threshold voltage necessary for direct displacement of copper.

One object of the experiments is to determine whether or not the asymmetric Cu-Al or Cu-Si split interstitial is more or less stable than the ordinary Cu-Cu split interstitial. If either of the former are more stable and therefore have a life time of more than one diffusion jump, then the immediate vicinity of the interstitial dislocation loops that are observed to grow during electron irradiation should be richer in Al or Si than the average composition regardless of accelerating voltage. If a migrating split interstitial tends to avoid Al or Si atoms then the immediate vicinity of a growing interstitial should be less rich in Si or Al than the average. Because Al is a larger atom than Cu and Si is a smaller atom there may be strain contrast effects strong enough to detect these changes in local composition.

If the composition of the growing interstitial loops is always exactly the same as the average regardless of accelerating voltage the experiments will constitute experimental verification of the interstitially mechanism of diffusion.

10. RESEARCH PLANS FOR CALENDAR YEAR 1975

Jack Washburn

a. Radiation Damage Research

The mechanism of climb of dislocations caused by the preferential capture of interstitial atoms during elevated temperature radiation damage in the beam of the 650 kV electron microscope will be investigated with particular emphasis on the effect of stacking fault energy and the dissociation of 1/2 ⟨110⟩ and 1/3 ⟨111⟩ dislocations into partials. Climb rate for dislocations in edge orientation will be compared to that for dislocations near screw orientation. These climb measurements are to be undertaken under the same temperature and displacement rate conditions that cause void growth and irradiation induced swelling. The purpose is to improve understanding of the basic cause of radiation induced swelling which is preferential capture of interstitial atoms by dislocations.

b. Solar Energy Materials

i) The most immediate application of solar energy will be for heating and cooling of buildings. Particularly for cooling, it is advantageous to be able to collect solar energy at a temperature close to 100°C for operation of absorption refrigeration systems. At this temperature a spectrally selective surface, (one that is a good absorber for visible and near infrared but acts like a mirror for infrared wavelength) becomes highly desirable. Existing surfaces having this property have disadvantages; either they are too expensive, or are degraded by water vapor. A type of spectrally selective surface that has not been sufficiently well investigated is one that depends for its selectivity on fine scale roughness. Sharp peaks and crevices of a size of about 10^{-4} cm are required. It is planned to study possible techniques for producing nickel surfaces with this scale of roughness. Nickel is a good reflector for infrared and can be easily electroplated on steel and copper substrates.

ii) Photovoltaic solar cells would become an attractive source of electric power if their cost could be reduced by at least a factor of 100. If silicon cells are ever produced at a low enough cost they will probably have to be polycrystalline or ribbon grown single crystals. Research is in progress aimed at better characterization of grain boundaries in silicon. Particularly it is intended to study segregation of various impurities and dopant elements to grain boundaries using Auger spectroscopy.

The currently most promising heterojunction cell is Cu_x-S-CdS. It suffers degradation during use due to copper diffusion into the CdS. An attempt is being made to decrease the rate of degradation by substituting a mixed crystal of $(CdS)_y+(ZnS)_{1-y}$ for the CdS.

c. Ion Implantation in Silicon

Defects produced by post-implantation annealing have been characterized and related to changes in electrical characteristics. It has been shown that observation of a silicon specimen on the hot stage of the 650 kV electron microscope is a very useful technique because large numbers of displaced silicon atoms can be produced by the electron beam at any desired temperature so that their interaction with various dopant elements can be studied. This technique will be used for further study of the mechanism of precipitation of boron and silicon interstitials.

11. 1974 PUBLICATIONS AND REPORTS

Jack Washburn and Associates

Journals

1. W. Wu, L.-J. Chen, J. Washburn and G. Thomas, Indexing of Diffracting Planes Using the Kikuchi Pattern, J. Appl. Phys. 45, 563 (1974) (LBL-1811).

2. Wei-Kuo Wu and Jack Washburn, Identification of Interstitial- and Vacancy-Type Dislocation Loops in Ion-Implanted Silicon, J. Appl. Phys. 45, 1085 (1974) (LBL-1812).

3. T. Peterson and J. Washburn, On the Nature of the Long-Term Degradation of Cadmium Sulfide Solar Cells, Phys. Stat. Sol. (a) 22, 721 (1974) (LBL-2281).

4. L. J. Chen and K. Seshan, High Resolution Imaging in Bright and Dark Field at High Voltages, 32nd Annual Processing of the Electron Microscopy Society of American, St. Louis, Missouri, 1974 (edited by C. J. Arceneaux) (LBL-2712).

5. K. Seshan, Non-Conventional Electron Microscopy in Small Defect Characterization, ibid (LBL-2585).

6. K. Seshan and J. Washburn, The Nature and Habit Planes of Defects in P^+ Ion-Implanted Silicon Phys. Stat. Solidi, 26, 345 (1974) (LBL-2761).

LBL reports

1. Thorvald Astrup, On the Annealing of Stacking-Fault Tetrahedra and Frank Dislocation Loops in Silver, Ph.D. thesis, LBL-1172, May 1974.

2. Joaquin Lira-Olivares, A Study of Electron Current Intensities Emitted from the Superlattice Planes of an Ordered Alloy, Ph.D. thesis, LBL-2265, May 1974.

3. Jon Roberts, Memory Filaments in Amorphous As-Te-I Semiconductors, M. S. thesis, LBL-1463, Dec. 1974.

B. THEORETICAL METALLURGY

J. W. Morris, Jr., Principal Investigator

Introduction. The overall objective of this research program is to advance the theory of alloy design. The problem of designing an engineering alloy may be subdivided into four parts: (1) estimation of the thermodynamic properties of an alloy of given composition; (2) prediction of the microstructure resulting from a specified treatment of an alloy of given thermodynamic and kinetic properties; (3) prediction of the engineering properties of an alloy of given microstructure; (4) synthesis of this information in the selection of alloy composition and processing.

1. PHASE STABILITY OF METALS AND ALLOYS

Charles W. Krause and J. W. Morris, Jr.

In previous research[1] we used a simple model of a metallic alloy to compare the relative cohesive energies of selected metallic crystal structures as a function of the conduction electron to atom ratio A. Continuing this inquiry we adapted the same approach to model lattice vibrations in metallic alloys and probed the mechanical stability of the close-packed crystal structures.

The model begins from the observation (by Harrison) that to second-order perturbation the cohesive energy of a simple metal may be written

$$E = E_0 + E_1 + \sum_{ij} V(r_{ij}) \qquad (1)$$

where the zero- and first-order terms depend on the nature of the atom and on the atomic volume. The structural contribution to the cohesive energy appears first in the second-order term, which is expressible as a sum of two-body interactions in real space. The potential $V(r_{ij})$ depends on the precise pseudopotential assumed, but has the asymptotic form

$$V(r) \rightarrow V_0 \frac{\cos(2k_F r)}{(2k_F r)^3} \qquad (2)$$

valid for large values of $k_F r$, where V_0 is a function of structure-independent parameters from pseudopotential theory and k_F is the Fermi wavenumber. We obtain a simple tractable model by approximating $V(r_{ij})$ by its asymptotic form. The structural contribution to the cohesive energy may then be written as the dimensionless sum

$$\varepsilon_{ST} = E_{ST}/V_0 = \sum_{ij} v(r_{ij}) \qquad (3)$$

where v(r) is the "Friedel potential"

$$v(r) = \cos(2k_F r)/(2k_F r)^3 . \qquad (4)$$

For given crystal structure the energy ε_{ST} depends only on the electron-atom ratio (Z). The model may be generalized to treat alloys by simply using the mean value of Z for the alloy, a step which implicitly involves the assumption of a random solution and the use of the virtual crystal model.

Equation (3) may be used to estimate the energy change on an arbitrary rearrangement of atoms at constant atomic volume. In previous work we compared the cohesive energies of a selected set of common crystal structures as a function of Z. Similarly, by letting the displacement of atoms be infinitesimal and periodic Eq. (3) may be used to construct model phonon dispersion curves as a function of Z. This procedure yields the elastic constants for deformation at constant volume and illustrates the mechanical instabilities which limit the range of stability of crystal structures.

We have specifically computed the dispersion relations for transverse phonons propagating perpendicular to the close-packed planes of the face centered cubic and hexagonal close packed structures. These cases are particularly simple since the associated lattice deformation is a rigid shear of close-packed planes. The equations of motion may be written in one dimension with the planes taken to interact according to a slight modification of the Blandin-Friedel-Saada interplanar form of the Friedel potential. As the electron to atom ratio Z is varied the resulting dispersion relations exhibit the two common types of lattice mechanical instability: elastic instability, which appears as an imaginary frequency in the long wavelength limit, and other instabilities of the "soft-mode" type, which are characterized by the imaginary frequency of a short wavelength vibration while the long wavelength vibrations, and hence the elastic constants, remain well behaved. In either case the unstable oscillation will grow in amplitude, demonstrating the instability of the reference structure with respect to an alternate structure which differs through a continuous distortion.

Some results of these computations are summarized and compared to those obtained in earlier work in Fig. 1. Plot 2A shows the regions of relative preference of the FCC and HCP structures as determined through direct computation of structural energy, ignoring possible instability of the lattice. Plot 2B shows the region over which the HCP and FCC structures are stable with respect to the formation of a stacking fault. Plot 2C shows the values of Z over which the FCC and HCP structures are stable

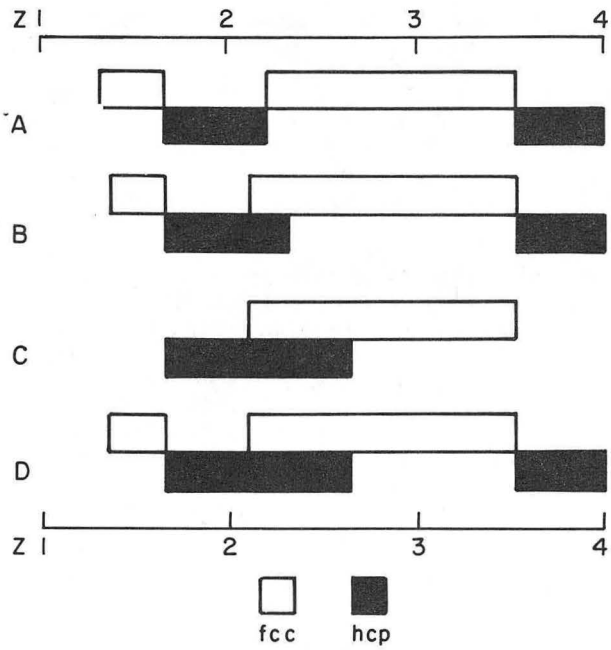

Fig. 1. Ranges of electron to atom ratio Z over which various stability criteria are satisfied for the FCC and HCP structures:

A) Relative cohesive energy at 0°K
B) Stability against faulting
C) Real phonon frequency
D) Positive elastic constants.

(XBL 7410-7455)

with respect to transverse vibration of the close-packed planes. Plot 2D shows the regions of elastic stability of the FCC and HCP lattices.

---

1. C. W. Krause and J. W. Morris, Jr., Acta Met. 22, 767 (1974).

2. CORRELATION OF MICROSTRUCTURE TO PROCESSING

Kenton L. Hanson, Kim P. Walker, and J. W. Morris, Jr.

Alloy processing usually depends on the control of solid state reactions to achieve a desired microstructure. The processing times and conditions are chosen to control both the extent of transformation and the morphological features of the change of phase, since these two factors together determine the ultimate microstructure. In engineering practice the choice of processing conditions is empirical; there are now virtually no solved problems on the evolution of microstructure during processing.

A related problem of equal importance is the characterization of microstructure from opaque metallographic sections. One would like to identify the salient geometric features of a microstructure and to be able to specify these through reasonably straightforward metallographic observations.

To attack these problems we began a program of research involving the direct computer simulation and characterization of microstructures generated by nucleation and growth processes in the solid state. The generation of microstructure involves two processes: the nucleation and growth to impingement of individual grains and the coarsening or relaxation of the microstructure during subsequent annealing. The first of these processes is particularly simple when the transformation goes to completion in a one-component system and when the growth rate of nucleated grains is assumed to be constant and isotropic. The resulting microstructure is the classic Johnson-Mehl microstructure, some of whose topological properties are known from previous theoretical work.

Our initial research objective is to complete a geometric characterization of the Johnson-Mehl microstructure. To accomplish this we required a computer code capable of generating example microstructures efficiently, with sufficient flexibility to survey the physically relevant ranges of nucleation and growth parameters and with sufficient resolution to allow a full treatment of geometric properties. The code was completed during the past year. It allows the use of pre-specified nucleation and growth parameters, heterogeneous nucleation sites, and simultaneous treatment of competing nucleation processes. The code will then plot a planar section of the microstructure on a pre-selected plane on a 1024×1024 element grid and compute geometric properties. Three-dimensional features can be studied through successive sectioning of the microstructure. Research using this code is in progress.

3. CORRELATION OF MECHANICAL PROPERTIES TO MICROSTRUCTURE

Plastic Deformation of Idealized Crystals

Kenton L. Hanson, Sabri Altintas, and J. W. Morris, Jr.

The achievement of a microstructure-based theory of the mechanical behavior of engineering alloys remains one of the central objectives of basic research in metallurgy. Its engineering importance is two-fold. First, a predictive theory of mechanical behavior is needed to provide a firm basis for materials selection and engineering design with real materials. Second, an interpretive theory of mechanical behavior is needed to guide metallurgical research in the design of new alloys. The complexity of the mechanical behavior of real materials suggests that accurate, detailed theories will be slow in coming (as they have been). On the other hand, the evident potential engineering benefit to be derived from successful research would certainly seem to justify a sustained, systematic effort.

Our research under this program has focused on what appears to be the simplest realistic problem in the dislocation theory of plasticity: the deformation of a crystal through the planar glide of non-interacting dislocations. The dislocations are idealized as flexible, extensible strings of constant tension. The crystal is assumed to contain microstructural features which are idealized as randomly-distributed point barriers to dislocation glide. The deformation rate of the crystal is to be determined as a function of the applied stress, the temperature, and the nature and density of the point barriers. Our technical approach to this problem has been to use computer models to directly simulate dislocation glide under precisely controlled conditions and to use the results to guide the development of predictive theories.

The problem may be set up as follows.[1] Consider a crystal plane which is the glide plane of a dislocation. Let it contain a random distribution of microstructural barriers which are represented[2] as point obstacles to dislocation glide. The array is described by the statement that its points are randomly distributed and by a characteristic length

$$\ell_s = a^{1/2} \tag{1}$$

where a is the mean area per point. A dislocation in this plane is modeled as a flexible, extensible string of constant line tension, Γ, and Burgers' vector of magnitude b, taken to lie in the plane. The resolved shear stress, τ, impelling glide of this dislocation may be conveniently written in dimensionless form

$$\tau^* = \tau \ell_s b/2\Gamma \tag{2}$$

Let the dislocation, under the applied stress τ^*, encounter a configuration of point obstacles denoted by (i). Between two adjacent obstacles the dislocation will take the form of a circular arc of dimensionless radius $R^*(= 1/2\tau^*)$. If the distance between any two adjacent obstacles along (i) exceeds $2R^*$ or if the dislocation line anywhere intersects itself, then the configuration (i) is transparent to the dislocation and will be mechanically by-passed. If (i) is not transparent, its mechanical stability is governed by the strength of the dislocation-obstacle interaction.

At the $k^{\underline{th}}$ obstacle on (i) the dislocation line forms the asymptotic angle ψ_i^k $(0 \leqslant \psi_i^k \leqslant \pi)$. The force, F_i^k, that the dislocation exerts on the $k^{\underline{th}}$ obstacle is, in dimensionless form,

$$\beta_i^k = F_i^k/2\Gamma = \cos(\tfrac{1}{2}\psi_i^k) \tag{3}$$

The mechanical strength of the obstacle is measured by the dimensionless parameter β_c (or angle ψ_c) and corresponds to the maximum force the obstacle can sustain without being cut or locally by-passed. A non-transparent line configuration of obstacles constitutes a mechanically stable barrier to the glide of a dislocation under stress τ^* if $\beta_i^k < \beta_c$ for all obstacles k on i, hence if $\beta_i < \beta_c$ where β_i is the maximum of the β_i^k. The smallest stress τ^* at which $\beta_i > \beta_c$ for all configurations within the array (i.e., $\beta_1 > \beta_c$, where β_1 is the minimum of the β_i) is the critical resolved shear stress, τ_c^*. When $\tau^* < \tau_c^*$ the dislocation will encounter at least one stable configuration within the array, and can glide only with the help of thermal activation.

Our investigation of this problem began with a study of the statistics of thermally activated glide through an array of like obstacles.[1] We found that statistical theorems could be used to substantially simplify the computational effort required in a simulation of thermally activated glide and to give a precise statistical definition to the glide velocity obtained. In particular, if the glide velocity is defined in dimensionless form as the area swept by the dislocation per unit time divided by the edge length of the array, then its expected value $\langle v^* \rangle$ may be written as a function of three variables

$$\langle v^* \rangle = f(\tau^*, \beta_c, T^*) \tag{4}$$

where T^* is a dimensionless temperature. High- and low-temperature limits were identified which reduce the theoretical problem to the computation of characteristics of particular dominant configurations found in glide: the most stable, or "strength-determining" configuration in the case of low-temperature glide, and the "random" configuration in the case of high-temperature glide. This research also identified a significant theoretical problem which had been less apparent in earlier work: at intermediate temperatures, the glide path, or sequence of configurations assumed during glide, becomes a statistical function of temperature. It deviates from the well-defined low-temperature path in ways difficult to account for theoretically, which may cause a significant deviation from the simple Arrhenius behavior often assumed in treating the thermal effect on glide.

The statistical results were used in a systematic study of thermally activated glide at low temperature,[3] assuming an array of like obstacles and a dislocation-obstacle interaction of simple step form. The central results obtained were three: (i) Studying the glide velocity as a function of temperature, stress and obstacle strength, we found that low temperature approximations could be used to represent the data over a wide range of conditions. Since these approximations obey relatively simple equations, they may easily be used to assess the effect of the operational variables on the qualitative features of glide. (ii) Behavior in low-temperature glide is strongly influenced by the characteristics of the most stable configuration encountered during glide. These most stable configurations depend on applied stress, but are identically the configurations which determine the critical resolved shear stress as a function of obstacle strength. Detailed examination of these configurations showed that while their strengths were reasonably approximated by a simple model which

had been suggested by Friedel, their other pertinent characteristics (shape, distribution of forces, distribution of segment lengths) were not. This discrepancy is significant, since the distribution of forces is important to the kinetics of low-temperature glide and since the mean segment length is a parameter often used in attempts to fit experimental data to the point obstacle model. (iii) Simulation of crystal deformation using a model constructed by "stacking" slip planes showed features in interesting correspondence with the deformation of real crystals. At very low temperature slip concentrated on well-defined slip planes. As temperature was raised deformation became more uniform, appearing homogeneous at high temperature.

Given this background, four research tasks were completed during 1974:

1. Theory of the strength-determining configuration in an array of like obstacles. As computer simulation has shown, both the critical resolved shear stress for athermal dislocation glide through an array of point obstacles and the velocity of thermally activated glide at low temperature are determined by the properties of the most stable obstacle configuration encountered. In a random array, this configuration is known to be a unique function of the applied stress (τ^*). In the current literature its properties are frequently approximated by extrapolating a simple, high temperature model due to Friedel, in which the configuration is approximated by a straight line of equi-spaced points. Assuming that τ^* is small, this model yields the three relations

$$\beta_1 = (\tau^*)^{2/3} \tag{5}$$

$$\langle \ell^* \rangle = (\tau^*)^{-1/3} \tag{6}$$

$$\rho_1(\beta,\tau^*) = \delta(\beta - \beta_1) \tag{7}$$

for the strength (β_1), the mean segment length $\langle \ell^* \rangle$, and the distribution of forces ($\rho_1(\beta,\tau^*)$) along the most stable configuration. Direct computer simulation[3] has shown that while Eq. (5) is a good approximation for small τ^*, Eqs. (6) and (7) are not. We hence sought a more accurate theory.

We found[4] that it is possible to use a variant of the "extinction theorem" of branching processes in probability theory to establish a "limiting" obstacle configuration. This configuration has the property that it is necessarily more stable than the most stable configuration which may be encountered in glide through an array of arbitrarily large size at a given value of τ^*. Hence it places a definite lower bound on the function $\beta_1(\tau^*)$. Moreover, this limiting configuration represents the empirical strength-determining configuration remarkably well for $\tau^* \lesssim 0.5$, a range exceeding that which parallels theoretical work (by Bacon, Kocks, and Scattergood of the Argonne Laboratory) and argues that this limitation is physically realistic. The fit between theory and computer simulation experiment is illustrated in Figs. 1-3. The theoretical curves are obtained through the simultaneous solution of integral equations. However, when τ^* is small they yield the simple relations

$$\beta_1 = 1.083(\tau^*)^{2/3} \tag{8}$$

$$\langle \ell^* \rangle = 0.734(\tau^*)^{-1/3} \tag{9}$$

$$\rho(\beta,\tau^*) = (0.79\beta_1)^{-1}[(\beta/\beta_1) + 0.34]^2 \tag{10}$$

which may be compared to the Friedel Eqs. (5)-(7).

2. The critical resolved shear stress for glide through a random mixture of distinct obstacle types. Plastic deformation in real solids generally involves dislocation glide over planes containing obstacles of several distinct types. Even when glide occurs in a crystal hardened by a single solute species the nature of the dislocation-solute interaction is such that effectively two distinct obstacle types are present. The presence of multiple obstacle types complicates the simulation or theoretical treatment of thermally activated dislocation glide. Prior computer simulation studies have treated only the special case of two obstacle types over a limited range of relative concentration and properties. Aside from occasional speculations in the literature, there is no prior theoretical work on the behavior of a dislocation in glide through an array of multiple obstacle types. A micromechanical theory of the deformation of real crystal nonetheless requires a solution to this problem.

By generalizing the statistical approach used to establish the limiting configuration for glide through a random array of like obstacles, we

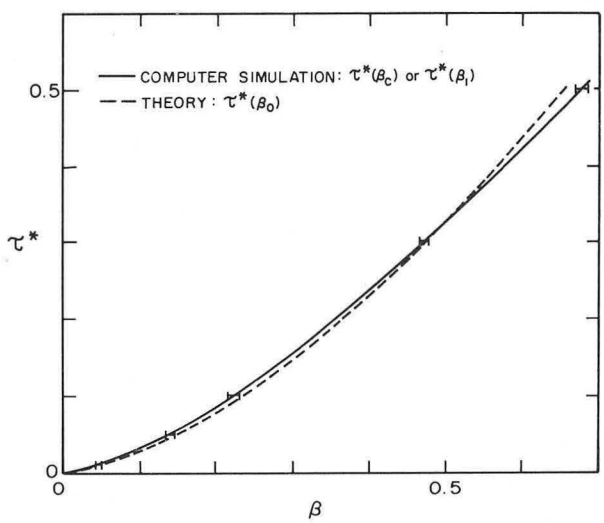

Fig. 1. The limiting stress $\tau_0(\beta_0)$ compared to the function $\tau^*(\beta_1)$ obtained by direct computer simulation of glide through arrays of 10^4 obstacles. The bars include the values of the maximum force (β_1) in the most stable configuration encountered in glide through each of ten arrays of 10^4 points at each value of the stress τ^* for which a data bar is shown. (XBL 748-6942)

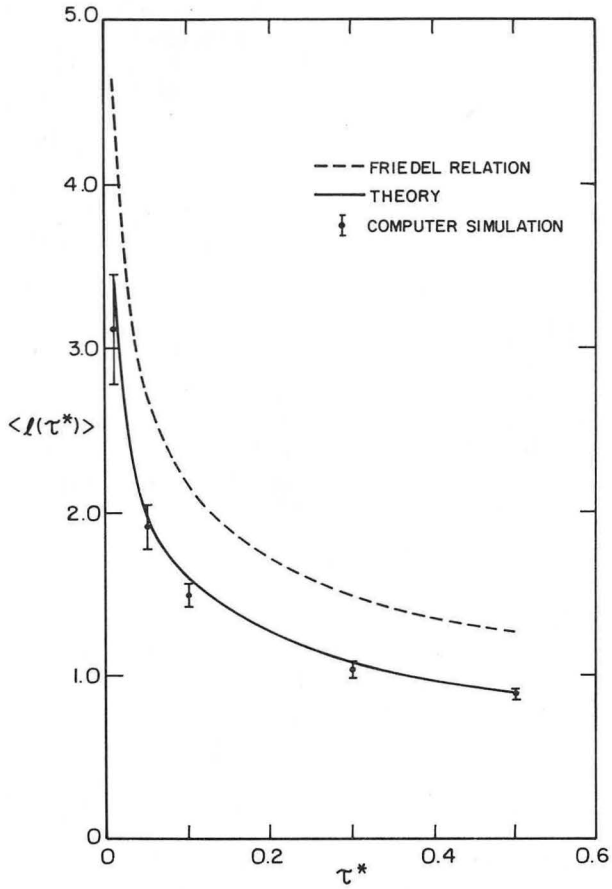

Fig. 2. The mean segment length $\langle \ell(\tau^*) \rangle$ in the limiting configuration compared to that predicted by the Friedel relation (Eq. 6) and that determined by direct computer simulation of glide through arrays of 10^4 points. The data bars include the mean segment length in the most stable configuration in each of ten arrays of 10^4 points at each value of the stress for which a data bar is shown. (XBL 748-6944)

found[5] that it is possible to establish an equivalent solution for the most stable configuration encountered in glide through a random array of point obstacles of arbitrary properties. The solution again requires the simultaneous treatment of integral equations, but yields results in good agreement with those obtained through computer simulation. The significance of the solution is that it allows an analytic approximation of the critical resolved shear stress for glide through an array of obstacles of arbitrary types, gives an estimate of the properties (e.g., fraction of obstacles of a given type, mean segment length, distribution of forces) along the configuration which determines the critical resolved shear stress, and may be easily generalized to predict the velocity of thermally activated glide at low temperature.

3. Simulation of glide through arbitrarily large obstacle arrays. The available computer simulation codes for dislocation glide have been practically limited to arrays containing 10^4 obstacle points or less. This limitation has been a severe restriction on the simulation of glide through arrays of weak obstacles (corresponding, for example, to solute atoms) or of arrays of mixed obstacles in which the concentration of obstacle types is significantly different. To overcome this problem we have written a code[6] which permits the tractable simulation of glide through arrays of 10^6 points or more. Several distinct data-handling features contribute to the ability of this code to handle very large obstacle arrays efficiently. The most important are the statistical generation of the array as the dislocation moves and the use of grid numbering schemes with a random number generator to insure that a minimal subarea of the array is generated at any given time and that this subarea is found in a fully reproducible manner.

4. Simulation of plastic deformation in an idealized crystal. In earlier work[3] we reported

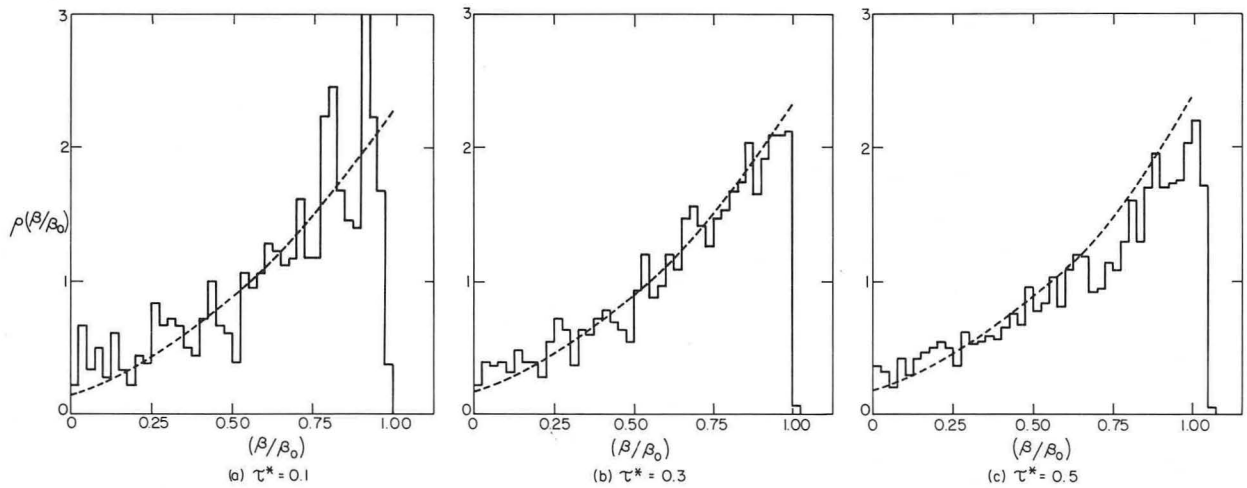

Fig. 3. The distribution of forces in the limiting configuration compared to histograms obtained through direct computer simulation of glide through arrays of 10^4 points. The limiting forces (β_0) are: $\beta_0 = 0.2322$ at $\tau^* = 0.1$, $\beta_0 = 0.4751$ at $\tau^* = 0.3$, $\beta_0 = 0.6526$ at $\tau^* = 0.5$. (XBL 748-6943)

preliminary results on the deformation of an idealized crystal at constant strain rate. The crystal was assumed to deform through planar glide of dislocations over well-defined slip planes, which were assumed to contain obstacles to glide and dislocation sources such that the time average density of dislocations per plane was constant. The results were interesting in that the crystal not only showed the anticipated trend of flow stress with temperature but also exhibited a characteristic shift in the morphology of deformation with temperature: low temperature deformation concentrated on well-defined slip planes which became less pronounced as the temperature was raised.

To continue exploration of this behavior we simulated[7] the plastic deformation of an ideal crystal made up of a stacking of slip planes containing randomly dispersed obstacles having roughly the properties expected of small dispersion or precipitate particles. Each slip plane was assumed to contain active sources of dislocations leading to a constant density of non-interacting dislocations in the plane. We then modeled deformation as a function of temperature and applied stress, determining the strain rate and the morphological characteristics of slip.

Figure 4 illustrates the deformation of an idealized crystal made up of ten parallel glide planes containing a uniform distribution of non-interacting dislocations and a Poisson distribution of 10^3 obstacles having strength $\beta_c = 0.6$ and an interaction function of simple step form. The figure shows the morphology of slip as a function of dimensionless temperature $T^*(= kT/2\Gamma d$, where d is the effective width of the obstacle) after a total tensile strain of 20% at constant strain rate. The deformation is quite heterogeneous at low temperature, but rapidly becomes uniform as T^* is raised. The simulation also allowed a study of the strain rate as a function of applied stress, and of the variation of flow stress with strain rate and temperature.

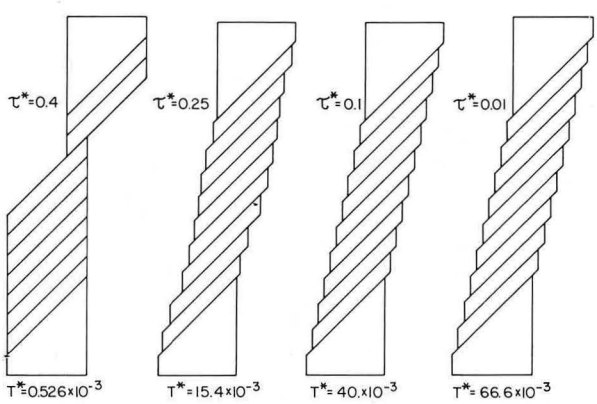

Fig. 4. Illustration of slip morphology with temperature at constant strain rate ($\ln \langle \tilde{\nu}^* \rangle = -10$). (XBL 7410-7499)

---

1. J. W. Morris, Jr., and D. H. Klahn, J. Appl. Phys 44, 4882 (1973).

2. J. W. Morris, Jr., and C. K. Syn, J. Appl. Phys. 45, 961 (1974).
3. J. W. Morris, Jr., and D. H. Klahn, J. Appl. Phys. 45, 2027 (1974).
4. K. Hanson and J. W. Morris, Jr., LBL-3160 (in press, J. Appl. Phys.).
5. K. Hanson and J. W. Morris, Jr., LBL-3432 (in press, J. Appl. Phys.).
6. K. Hanson, Ph.D. research.
7. S. Altintas, K. Hanson and J. W. Morris, Jr., LBL-3508 (in press, J. Eng. Mat. & Tech.).

4. ALLOY DESIGN

a. The Design of Tough Ferritic Cryogenic Steels*

Sungho Jin, Sun-Keun Hwang, Sheree H. Wen, Bradley W. Whitaker and J. W. Morris, Jr.

The need for major engineering advances in the production, transport, and storage of useful energy has brought about an increasing interest in the potential of cryogenic systems. Relevant current problems include the safe transport and storage of liquified gases and the design of advanced engines, power generation facilities, and coal conversion devices utilizing superconducting magnets cooled in liquid helium. Progress in solving these problems will require significant improvements in engineering materials as well as in systems design.

The research reported here has focused on one potential materials need: strong, tough alloy steels which retain good properties to 4°K, the ambient temperature of a cooled superconducting magnet. The initial problem which had to be overcome in this research was the "ductile-brittle transition" behavior common to ferritic steels (steels having a matrix based on the ferrite, or body-centered-cubic crystal structure of iron).

As is well known, materials having a body-centered-cubic (bcc) crystal structure show an appreciable increase in strength when tested at low temperature. This "thermal component" of the yield strength of bcc alloys makes ferritic steels particularly attractive for cryogenic use; one may easily make alloys which become very strong at cryogenic service temperatures. However, as the strength of a ferritic alloy increases on cooling the alloy also tends to become brittle, often through a dramatic loss of toughness over a rather narrow temperature range which defines the "ductile-brittle transition temperature" (T_B). This low temperature embrittlement severely restricts the use of ferritic alloys in cryogenic systems. If metallurgical techniques can be employed to overcome low temperature embrittlement in ferritic steels or to suppress T_B to well below service temperatures then it becomes possible to design steels having exceptional combinations of cryogenic strength and toughness.

The technical approach we have followed in this research is to select compositions and processing techniques based on the Fe-Ni alloy system to establish a microstructure conducive to cryogenic

toughness at high strength. The microstructural criteria are three: first, the alloy substructure should be a ductile, dislocated martensite favorable to deformation; second, the grains should be fine and non-aligned; and third, unwanted species which may segregate to embrittle grain boundaries or pin dislocations should be eliminated or gettered into innocuous precipitates.

The central result of our previous year's work on this program was the development of a thermal cycling procedure to grain refine an Fe-12Ni-0.25Ti alloy which appeared to meet all other design criteria. The result[1,2] was an alloy showing a unique combination of strength and toughness at liquid nitrogen temperature (77°K) and outstanding impact toughness to liquid helium temperature (4°K). During the past year we sought to document its fracture toughness at 4°K, which required the development of new techniques to carry out fracture toughness tests in liquid helium. We further sought to improve the alloy from the point of view of properties, economics of composition, or ease of processing, and to utilize basic microstructural studies to gain new insight into the sources of its behavior. Specific research tasks included the following:

1) Development of an inexpensive technique for fracture toughness testing in liquid helium

Sungho Jin, Sun-Keun Hwang and J. W. Morris, Jr.

A simple method of fracture toughness testing at liquid helium temperature was devised to avoid the need for an elaborate cryostat.[3] The technique is based on a modification of the "lucite box" technique we had previously devised for Charpy impact testing in liquid helium.[4] A compact tension fracture toughness specimen is covered with grooved styrofoam and wrapped with cellophane tape. The insulated specimen is then inserted into a rectangular lucite box. The box is provided with two ovular holes for the pins which pass through the specimen and the grips of the MTS machine, a polyethylene inlet pipe through which liquid helium is fed to bathe the specimen during testing, a small hole through which a thermocouple and protection tube are passed to monitor specimen temperature, and a rectangular hole through which a clip-in strain gauge is installed. This last opening also serves as an exit for the liquid and evaporated helium.

Figure 1 illustrates the testing procedure. The specimen is bathed with liquid helium continuously during testing. The specimen temperature is monitored with a thermocouple inserted to the center of the sample near the pre-induced fatigue crack and insulated from the liquid helium. At a helium gas pressure of 6 psi, a specimen temperature of 5-6°K is obtained less than 3-4 minutes after the transfer of liquid helium is begun. This steady-state temperature is maintained as long as helium transfer is continued. Liquid helium consumption is 5-7 liters for each fracture toughness test. The lucite box remains intact during the test, but is sacrificed

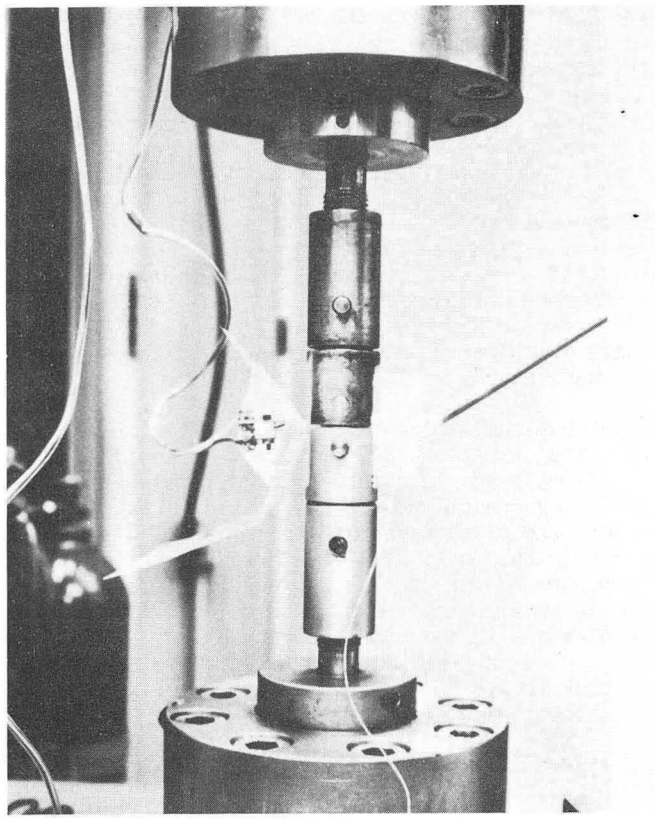

Fig. 1. Illustration of technique for fracture toughness testing at liquid helium temperature. The insulated specimen, liquid helium transfer line, clip-in displacement gauge, and thermocouple are properly arranged. (XBB 745-3043)

to break the specimen for subsequent fractography.

A similar technique may be used to conduct dynamic tear tests at liquid helium temperature. Such tests were conducted on candidate cryogenic alloys by invitation at the Naval Research Laboratories in May, 1974.

2) Comparative mechanical testing of cryogenic alloys

Sungho Jin, Sun-Keun Hwang and J. W. Morris, Jr.

The testing technique described above was combined with other cryogenic testing techniques to establish the cryogenic mechanical properties of the ultrafine grained Fe-12Ni-0.25Ti alloy and to compare these to the properties of other cryogenic alloys.[5,6]

Thermal cycling to ultrafine grain size is accomplished through alternate anneals in the austenite (γ) and two-phase ($\alpha+\gamma$) stability fields.[2] After four cycles a final structure (2B) is obtained which has mean grain diameter near 1 μm (ASTM #17).

The tensile, Charpy impact, and fracture toughness properties of the grain refined alloy

Table I. Cryogenic Tensile and Impact Properties

	Alloy	Y.S.* ksi	U.T.S. ksi	Elong. pct.	R.A. pct.	Charpy Energy ft-lb
77°K	Fe-12Ni-0.25Ti (2B)	149	154	26.8	72.1	115
	9-Ni steel	146	172	29.6	66.8	92
	304 stainless	81	235	47.3	65.6	128
4.2°K	Fe-12Ni-0.25Ti (2B)	195	219	19.3	69.8	99
	9-Ni steel	208	231	21.2	59.1	75
	304 stainless	105	270	41.6	52.7	130

*At 77°K, 0.2 percent offset yield strengths were taken. At 4.2°K, the first discontinuous yield points were used.

Table II. Fracture Toughness at Cryogenic Temperatures

	K_{IC} at 77°K ksi$\sqrt{in.}$	K_{IC} at 6°K ksi$\sqrt{in.}$
9-Ni steel	168*	73 (valid K_{IC})
Fe-12Ni-0.25Ti (2B)	307*	232*
304 stainless	213*	168*

*Values calculated using Equivalent Energy concept.

†Compact tension fracture toughness specimens of 0.7 in. thickness were tested in accordance with ASTM specification.

(structure 2B) at 77°K (liquid nitrogen temperature) and at 4-6°K (near liquid helium temperatures) are summarized in Tables I and II. The data are compared to those obtained with the Fe-12Ni-0.25Ti alloy before grain refining (structure 1A) and to those of two commercial cryogenic steels: 9Ni steel, an Fe-9Ni-1Mn-0.1C ferritic steel with an addition of retained austenite for cryogenic toughness, and 304 stainless steel, an Fe-18Cr-8Ni austenitic alloy. As can be seen from the tables the grain refined Fe-12Ni-0.25Ti alloy combines the high yield strength of the 9Ni steel (~200 ksi at 4°K) with a fracture toughness (~230 ksi$\sqrt{in.}$) in excess of that of the relatively soft 304 stainless steel. The post-test fracture toughness specimens at 77°K and 6°K are shown in Fig. 2. Scanning electron fractographs of the specimens tested in liquid helium are shown in Fig. 3. The extraordinary ductility of the 2B structure is visually apparent.

3) The introduction and influence of retained austenite in fine-grained Fe-12Ni-0.25Ti

Sun-Keun Hwang, Sungho Jin, and J. W. Morris, Jr.

The development of a retained austenite phase in ferritic steels has been the subject of a significant body of research in recent years. The motivation for this research comes from two sources: fundamental interest in the phase transformation behavior and the possibly beneficial effect of retained austenite on subsequent mechanical properties. With respect to mechanical properties, a significant lowering of the ductile-brittle transition temperature has been observed in low-nickel cryogenic steels, and several researchers have suggested a beneficial effect of retained austenite on the fracture toughness of a variety of steels. For these reasons we hoped that the introduction of a controlled distribution of retained austenite might have a beneficial

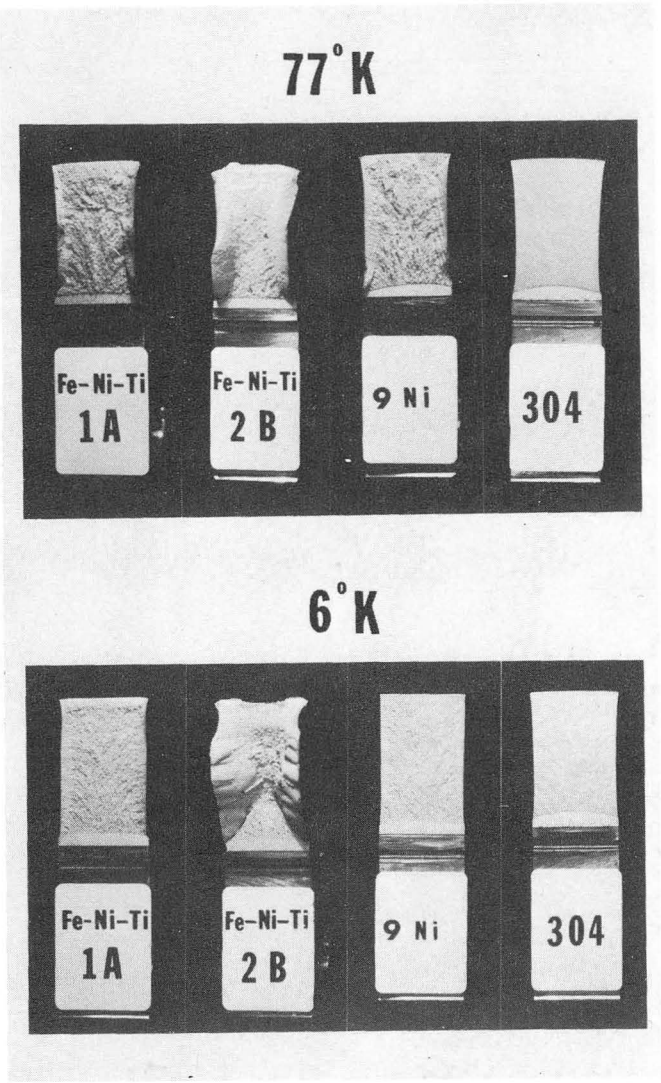

Fig. 2. Post-test compact tension fracture toughness specimens. (a) at 77°K, (b) at 6°K. (XBB 745-3045)

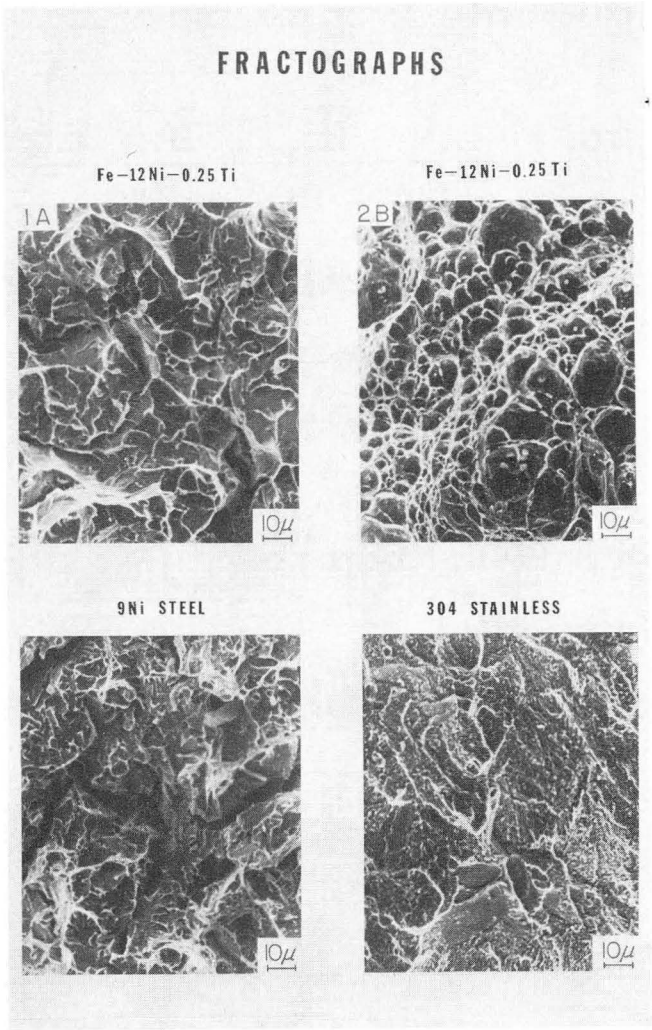

Fig. 3. Scanning electron fractographs taken from the fracture surfaces of the compact tension specimens tested at 6°K. (XBB 745-2982)

effect on the cryogenic properties of the fine-grained Fe-12Ni-0.25Ti cryogenic alloy, and began research to learn to control the amount and distribution of retained austenite. The results are reported by Hwang.[7]

The alloys used in this investigation were grain-refined through the alternate thermal cycling treatment. As grain refined, the alloy has a typical martensite lath structure with a high density of dislocations. No austenite is detectable by X-ray or TEM techniques.

Retained austenite was introduced into the grain-refined structure by reheating in the lower part of the two-phase ($\alpha+\gamma$) region, at temperatures 475-600°C. Transmission electron microscopy revealed that the austenite formed preferentially as small islands at two types of sites: as elongated particles along martensite lath boundaries and as more globular particles associated with Ni_3Ti precipitates in the microstructure. While it has long been speculated that the Ni_3Ti precipitates might catalyze austenite reversion, this is apparently the first clear evidence.

The retained austenite treatment influenced low temperature mechanical properties, including the tensile properties, Charpy impact toughness, and the fracture toughness. The change in yield strength was small, and consisted of a slight increase on low temperature aging and a slight decrease as the reheat temperature was raised. These changes may well be influenced by a change in the precipitate distribution as well as by the austenite.

The Charpy impact toughness at cryogenic temperature was markedly increased by the presence of retained austenite; an increment ranging from 30 to 40 ft-lbs at 4°K was obtained. However, the equivalent K_{IC} value measured at 77°K is

apparently unaffected by the presence of retained austenite (Table III). There is, in fact, some evidence for a deleterious effect of the austenite since the reheated samples show an unstable crack propagation which is not observed in the ferritic material. The discrepancy between these fracture tests might be indicative of a strong strain rate effect. However, increasing the strain rate in K_{IC} tests at 77°K by a factor of 10^3 gave no change in the comparative fracture toughness values. It would appear that in this case also the Charpy impact test gives an inexact ranking of the relative toughness of cryogenic alloys.

Table III. Fracture toughness at 77°K (Fe-12Ni-0.25Ti)

C.H.S.: 1.3 cm×10^{-3}/sec units; ksi$\sqrt{in}$.

H.T.	Equivalent K_{IC} From E.E.	From J-Int.
G.R.	298	300
G.R.+450°C/20 h/WC	230	232
G.R.+475°C/2 h/WC	258	258
G.R.+550°C/2 h/WC	300	304
G.R.+550°C/60 h/WC	280	281
G.R.+600°C/2 h/WC	274	274

C.H.S.: 1.3 cm/sec

H.T.	K_{IC} From E.E.	From J-Int.
G.R.	154	255
G.R.+550°C/2 h/IBQ	162	242
G.R.+550°C/2 h/AC	157	248

E.E.: Equivalent energy approach
J-Int.: J-Integral approach
C.H.S.: Cross Head Speed

4) The design of an 8Ni cryogenic alloy

Sungho Jin, Sun-Keun Hwang and J. W. Morris, Jr.

Economic considerations make it highly desirable to duplicate the properties obtained with the Fe-12Ni-0.25Ti alloy using alloys of lower nickel content. To accomplish this two problems must be overcome. First, the ductile-brittle transition temperature tends to increase as the Ni content is lowered. Hence one must anticipate a higher transition temperature (T_B) if Ni content is decreased with a given grain size, and must be prepared to utilize other techniques to restore low temperature toughness. Second, as nickel content decreases in an Fe-Ni alloy the phase transformation temperatures rise, a trend due principally to the increase in the equilibrium transformation temperatures shown in the schematic phase diagram. As the transformation temperatures rise the heat treating temperatures needed for grain refinement by thermal cycling increase, grain growth becomes more significant, and the grain refinement process is less efficient. Hence an ultrafine grain size is more difficult to achieve.

To overcome these problems we are investigating simultaneous modifications in alloy composition and processing. Initial success has been obtained with an alloy of nominal composition Fe-8Ni-2Mn-0.25Ti. The addition of manganese principally serves to lower the transformation temperatures in the alloy and permit grain refinement through thermal cycling, though there are experimental indications that the manganese may contribute a decrease in T_B. A further depression in T_B is accomplished by introducing a controlled distribution of retained austenite (γ). While, as pointed out above, retained austenite apparently does not improve the fracture toughness of these steels when tested above T_B, it appears to be quite useful in suppressing T_B to cryogenic temperatures. Results are reported by Jin, Hwang, and Morris, LBL-3576.

The processing sequence for the Fe-8Ni-2Mn-0.25Ti alloy is shown schematically in Fig. 4. The first step is an annealing treatment to remove the deformation strain introduced during the previous forging process. The next four steps (1A-2B) are a grain refinement sequence, essentially identical to that used for the 12Ni alloy. The final step incorporates a distribution of retained austenite, principally in the grain boundaries. Approximately 5% in volume of retained austenite was found in the structure 2BR by the X-ray diffraction analysis. The resulting microstructure is fine grained, though the grains appear slightly larger and slightly less uniform than was the case for the 12Ni alloy. The form and distribution of retained austenite are

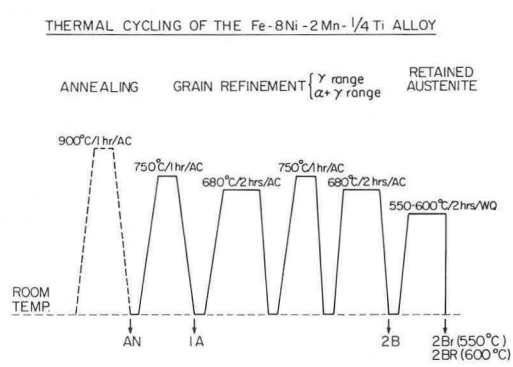

Fig. 4. Thermal cycling procedure for grain refinement and introduction of austenite in an Fe-8Ni-2Mn-0.25Ti alloy. (XBL 7410-7449)

illustrated in the electron micrograph of Fig. 5, which also reveals the substructure of matrix grains.

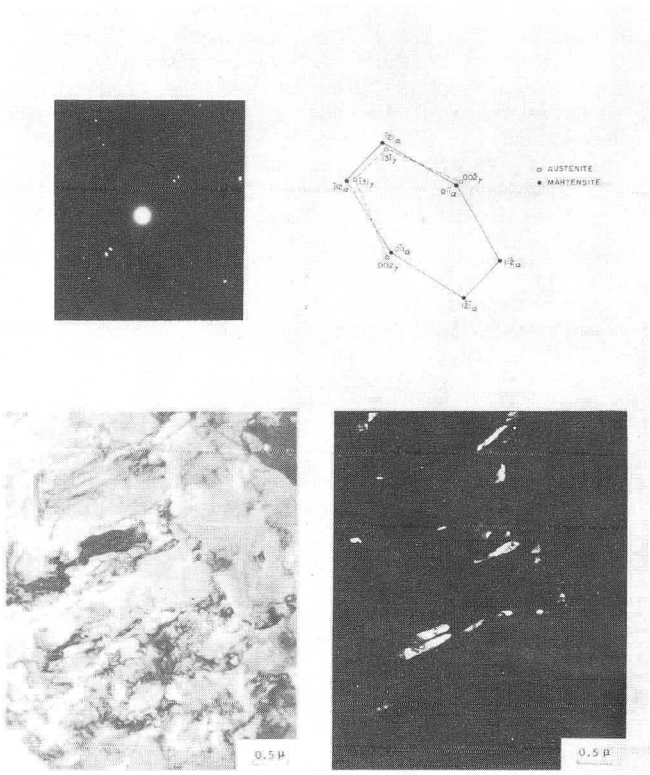

Fig. 5 Transmission electron micrographs of a heat treated Fe-8Ni-2Mn-0.25Ti alloy. (a) Bright field image showing substructure. (b) Dark field image from the $(200)_\gamma$ reflection. The bright areas in the dark field image are properly oriented austenite grains. (XBB 7411-7592)

The tensile properties, the grain size, and the amount of retained austenite of the Fe-8Ni-2Mn-0.25Ti alloy are included in Table IV.

Table IV. Tensile Properties at -196°C

	Y.S.* ksi	T.S. ksi	Elong. %	R.A. %	Grain Size μm	Retained Austenite vol.%
AN	131	149	22.5	44.9	38	0
1A	134	151	26.6	62.4	12	0
2B	137	157	28.5	69.2	1.5	0
2Br	135	146	34.7	73.0	1.5	~5
2BR	124	148	36.0	75.1	1.5	~5

*0.2% offset yield strength.

The variation of T_B with processing is illustrated in Fig. 6. As is apparent from the figure, the alloy retains outstanding impact toughness to liquid helium temperature. The grain refinement process suppresses T_B, as measured by the Charpy impact energy, from +44°C to -118°C. The addition of retained austenite further suppresses T_B to below liquid helium temperature. Cryogenic fracture toughness tests on this alloy are currently in progress.

5) The role of nickel in the structure of martensite

Sheree H. Wen and J. W. Morris, Jr.

The beneficial effect of nickel on the properties of steel is one of the central facts of engineering metallurgy. Virtually every high

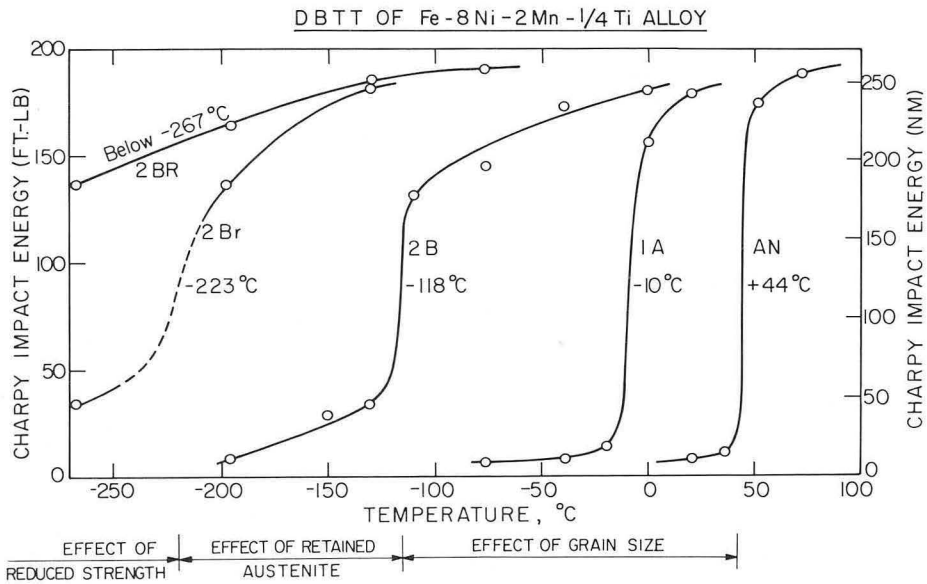

Fig. 6. Effect of microstructural changes on the impact energy transition in an Fe-8Ni-2Mn-0.15Ti alloy. (XBL 7410-7450)

strength, high toughness steel now available for engineering use contains a substantial nickel concentration (9-25% by weight) which seems to be essential to its engineering properties. On the other hand, the fundamental sources of the nickel contribution remain obscure. Current speculations include the effect of nickel on the native resistance of the crystal lattice to dislocation motion, its effect on the chemical potential of interstitial impurities, and its influence on the substructure of martensite in steel. The resolution of this fundamental question has economic as well as scientific importance. Engineering progress has created a need for alloy steels superior to any now available, whose design will almost certainly require the metallurgical exploitation of nickel alloying. At the same time the cost and scarcity of nickel make it imperative that acceptable substitutes be found for use in more conventional steels.

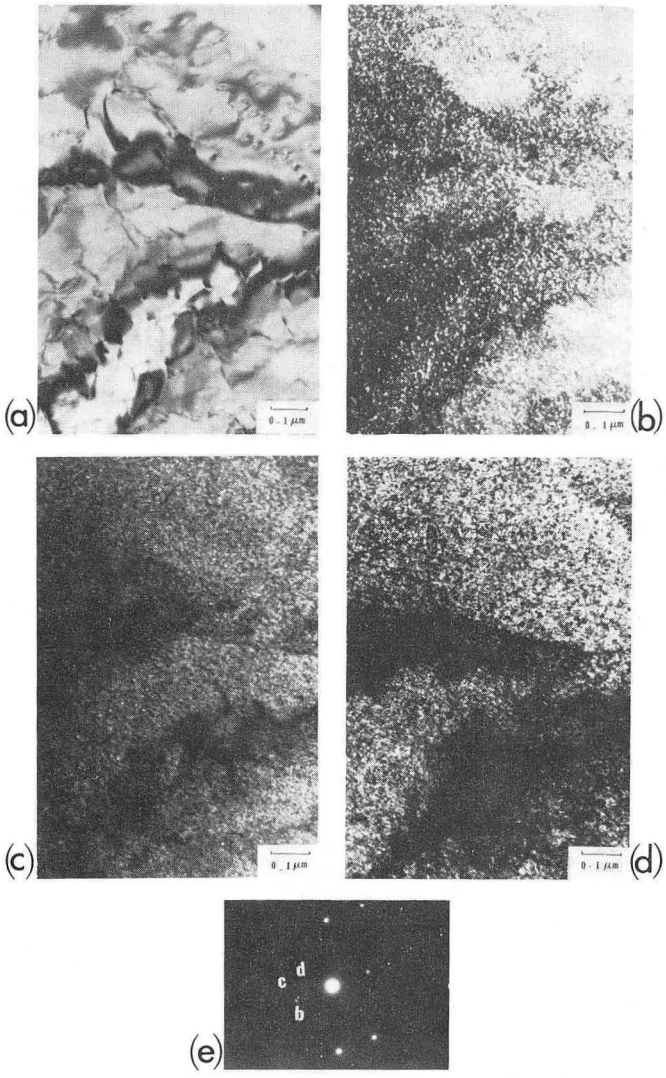

Fig. 7. (a) The bright field micrograph of an ordered area. (b) The corresponding dark field micrograph with intermediate aperatures on b which include (110) matrix diffraction and possibly one orientation variant of the ordered phase. (c) The dark field image of the weak super lattice deflection which was indicated by c. (d) The dark field image of the super lattice deflection which was indicated by d. (e) The electron diffraction pattern with beam on [113] matrix orientation. (XBB 751-560)

Our fundamental research on this problem has concentrated on the role of nickel in determining the substructure and morphology of martensite, with particular emphasis on the 8-12%Ni steels which we are using for cryogenic alloys. The research involves a detailed transmission electron microscope study of the evolution of the martensite and its substructure during thermal processing.

The fascinating initial result of this research has been the identification of a significant fine-scale ordering in Fe-12Ni and Fe-12Ni-0.25Ti alloys of a type which does not seem to have been previously detected in ferritic steels. The evidence for this ordering is shown in Fig. 7, which shows a bright- and dark-field survey of an ordered region in the lattice. The upper left-hand image is a bright-field image, showing the interior of a grain of dislocated martensite. The upper-right hand picture is a dark-field image from a BCC diffraction spot, including possibly one orientation variant of the ordered phase. The larger bright regions which speckle the micrograph are presumedly the BCC phase. The lower two micrographs are dark field images taken from the weak superlattice spots which are hardly visible in the diffraction pattern at the bottom. They show an ordered phase which appears to consist of acicular microdomains less than 50Å in size.

An unambiguous crystallographic identification of the ordered phase is difficult to obtain, given the small size of the domains and the possible presence of several orientation variants. Crystallographic studies are now in progress.

*Also supported by the Office of Naval Research under Contract N0014-69-A-1062, NR031-762.

1. S. Jin, J.W. Morris, V.F. Zackay, Adv. in Cryogenic Engr. 19, 379 (1974).
2. S. Jin, J.W. Morris and V.F. Zackay, LBL-2539.
3. S. Jin, S.K. Hwang and J.W. Morris, LBL-3109.
4. S. Jin, W.A. Horwood, J.W. Morris and V.F. Zackay, Adv. in Cryogenic Engr. 19, 373 (1974).
5. S. Jin, S.K. Hwang and J.W. Morris, LBL-3164.
6. S. Jin, B.W. Whitaker, J.W. Morris and V.F. Zackay, LBL-2756.
7. S. K. Hwang, LBL-3503.

b. Improvement in Fracture Toughness by Phase Transformation of the Precipitate-Embedded Matrix*

Sungho Jin, Der-Hung Huang, and J. W. Morris, Jr.

As an initial effort to obtain a high strength steel with very high toughness (Y.S. ≈ 200 ksi, K_{IC} ≈ 200 ksi$\sqrt{in.}$), the austenitic and martensitic phase transformation of precipitation-hardened maraging steel was utilized. The 250 grade

commercial maraging steel (Table I) was re-annealed at 850°C for 2 h and was given the following treatments.

I. Maraged 580°C/5 hrs + rapidly austenized in a salt bath (765°C for 2.5 min) and water cooled.
+ maraged again 380°C/3 h/AC.

II. Maraged 550°C/5 h + rapidly austenized in a salt bath (750°C for 2.5 min) and water cooled.
+ maraged again 380°C/3 h/AC.

Table I. Chemical Composition

Fe	Ni	Co	Mo	Ti	Al	C	S	P
Bal.	18.17	7.66	4.93	0.44	0.05	0.025	0.005	0.008

The precipitates in the 250 grade maraging steel are known to be mostly Ni_3Mo with some Ni_3Ti intermetallic compounds. When the martensite matrix with these precipitates is to phase transformation to austenite and subsequent transformation back to martensite, one or several of the following changes are expected to occur:

1. The presence of precipitates could slow down the movement of martensite-austenite interface during the M→A or A→M transformation resulting in a refined microstructure.

2. During the initial maraging treatment at relatively high temperatures (550~580°C for 5 h), the defect density (dislocations, vacancies) tends to decrease. Also many of the available dislocations are pinned by precipitates (as is well known, precipitates nucleate and grow at dislocations on maraging). By the additional M→A and A→M transformations of the aged matrix, the overall dislocation density will be restored to that of fresh dislocated martensite (and possibly even higher) with ample unpinned mobile dislocations.

3. Precipitates may serve as sources of interaction and multiplication of dislocations during the phase transformations.

The change of material hardness on heat treatments described previously is given in Table II.

Table II. Change of Hardness (R_C) in 1 in. Thick Maraging Steel Specimen

	Maraged	Rapidly austenized and cooled	Additional maraging
I	42	39	44
II	45	40	46

It can be seen from Table II that the rapid austenization does not sacrifice the aged strength very much. The additional maraging treatment was given to achieve the required yield strength of ~200 ksi.

Fracture toughness testing was conducted in an MTS machine with 1 in. thick compact tension specimens. The results are compared with other heat treatments of the same alloy in Fig. 1. Strength-toughness combinations of Y.S. ≈ 200 ksi with $K_{IC} \approx 161$ ksi$\sqrt{in.}$, and Y.S. ≈ 2.3 ksi with $K_{IC} \approx 134$ ksi$\sqrt{in.}$ were obtained. While there are only limited numbers of data points, these values are clearly superior to other heat treatments given to the same material as can be seen in Fig. 1. Rearrangement of heat treating processes is under way to achieve higher strength and toughness without an additional aging treatment.

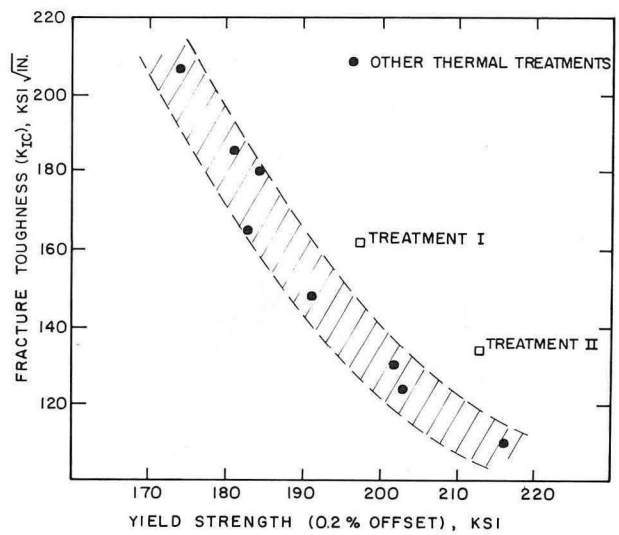

Fig. 1. Plane strain fracture toughness v.s. yield strength of the treated maraging steel. (XBL 751-5604)

*Also supported by the Air Force Materials Laboratory under Contract F33615-73-C-5100.

5. RESEARCH PLANS FOR CALENDAR YEAR 1975

J. W. Morris, Jr.

1. We plan to continue computer simulation studied on the microstructures obtained through solid state phase transformations in simple systems. The specific research objective for the coming year will be the full characterization of the Johnson-Mehl microstructure.

2. We plan to continue theoretical and computer simulation studies on the plastic deformation of idealized crystals. We specifically hope to complete a theoretical solution of

the problem of thermally activated dislocation glide through arrays of point obstacles. Given our prior research, such a solution can be obtained if we can theoretically predict the properties of the obstacle configuration encountered in glide along the "minimum-angle" path.

3. We plan to initiate research on the mechanical equation of state of simple solids.

4. We plan to continue research in the design of cryogenic alloys. During the coming year, we hope to design ferritic alloys having outstanding cryogenic properties with lower nickel content and to develop austenitic alloys based on the substitution of Mn for nickel.

5. We plan to continue research toward high strength, high toughness alloys for room temperature use, initially by exploiting the reaustenitizing treatments which appear successful in raising the toughness of maraging steels.

6. We plan to continue basic research on the role of nickel in the morphology of martensite. Our research will specifically concentrate on the nature and consequences of the recently-discovered Fe-Ni ordering reactions.

6. 1974 PUBLICATIONS AND REPORTS

John W. Morris, Jr. and Associates

Journals

1. S. Jin, W. A. Horwood, J. W. Morris, Jr., and V. F. Zackay, A Simple Method for Charpy Impact Testing Below 6°K, Advances in Cryogenic Engineering, K. D. Timmerhaus, Ed., Vol. 19, Plenum Press, New York, pp. 373-378 (1974) (LBL-1483).

2. S. Jin, J. W. Morris, Jr. and V. F. Zackay, An Iron-Nickel-Titanium Alloy with Outstanding Toughness at Cryogenic Temperature, in Advances in Cryogenic Engineering, K. D. Timmerhaus, Ed., Vol. 19, Plenum Press, New York, pp. 379-384 (1974) (LBL-1484).

3. V. F. Zackay, E. R. Parker, J. W. Morris, Jr. and G. Thomas, The Application of Materials Science to the Design of Engineering Alloys, Materials Science and Engineering 16, 201 (1974) (LBL-2261).

4. J. W. Morris, Jr. and Dale H. Klahn, Thermally Activated Dislocation Glide Through a Random Array of Point Obstacles: Computer Simulation, J. Appl. Phys. 45 (5), 2027 (1974) (LBL-2276 Rev.).

5. C. W. Krause and J. W. Morris, Jr., On the Relative Energies of Simple Metallic Structures Acta Met. 22, 767 (1974 (LBL-2214).

6. J. W. Morris, Jr. and C. K. Syn, Point-Obstacle Representation of the Dislocation-Obstacle Interaction, J. Appl. Phys. 45 (2), 961 (1974) (LBL-2211).

7. Kenton Hanson and J. W. Morris, Jr., Thermally Activated Dislocation Glide through a Random Array of Point Obstacles, Bull. Am. Phys. Soc. 19, 672 (1974) (LBL-3703 Abs.).

Presented papers

1. Sungho Jin, B. Whitaker, J. W. Morris, Jr., and V. F. Zackay, Cryogenic Toughness Through Microstructure Control in a Ferritic Fe-Ni-Ti Alloy, ASTM Symposium on the Properties of Materials for Liquified Natural Gas Tankage, Boston, May, 1974.

2. Sungho Jin and J. W. Morris, Jr., Cryogenic Fracture Toughness of Fe-Ni-Ti Alloys Grain-Refined Through Thermal Cycling, The Metallurgical Society Spring Meeting, Pittsburgh, May 1974.

3. Sungho Jin and J. W. Morris, Jr., Techniques for Cryogenic Toughness Testing, TMS/ASM Materials Science Symposium, Detroit, Nov. 1974.

4. S. K. Hwang, Sungho Jin and J. W. Morris, Jr., The Effect of Retained Austenite on the Cryogenic Toughness Properties of Fe-Ni-Ti Alloys, TMS/ASM Materials Science Symposium, Detroit, Nov. 1974.

5. K. L. Hanson and J. W. Morris, Jr., Limiting Properties of the Strength-Determining Configuration in Dislocation Glide Through a Random Array of Point Obstacles, The Metallurgical Society Spring Meeting, Pittsburgh, May 1974.

6. J. W. Morris, Jr. and F. Hamzeh, Symmetry Relations in Steady-State Diffusion, TMS Spring Meeting, Pittsburgh, May 1974.

7. K. L. Hanson and J. W. Morris, Jr., Thermally-Activated Dislocation Glide Through a Random Array of Point Obstacles, Am. Phys. Soc., June Meeting, Salt Lake City, June 1974.

8. M. J. Schanfein, M. J. Yokota, V. F. Zackay, E. R. Parker and J. W. Morris, Jr., The Cryogenic Properties of Fe-Mn and Fe-Mn-Cr Alloys, ASTM Symposium on Properties of Materials for Liquified Natural Gas Tankage, Boston, May 1974.

9. K. L. Hanson and J. W. Morris, Jr., The Critical Resolved Shear Stress for Dislocation Glide Through an Array of Unlike Obstacles, TMS/ASM Fall Meeting, Detroit, Nov. 1974.

LBL reports

1. Dionysios I. Grivas, Steady State Creep in Pb-Sn Eutectic Alloys, (M.S. thesis) LBL-2547, Jan. 1974.

2. Sungho Jin, Enhancement of Cryogenic Fracture Toughness Through Microstructural Control in a Ferritic Fe-12Ni-0.25Ti Alloy System, (Ph.D. thesis) LBL-2789, June 1974.

3. Charles W. Krause, The Effect of a Long Range Interatomic Potential on the Stability of Crystal Lattices, (Ph.D. thesis), LBL-3151, Sept. 1974.

4. S. Jin, S. K. Hwang and J. W. Morris, Jr., Comparative Fracture Toughness Testing of Cryogenic Alloys at Liquid Helium Temperature,

LBL-3164, Aug. 1974, Metallurgical Transactions, in press and ONR Tech. Report #5.

5. K. Hanson and J. W. Morris, Jr., A Limiting Configuration Glide Through a Random Array of Point Obstacles, LBL-3160, Aug. 1974 (to be published in Journal of Applied Physics).

6. C. W. Krause and J. W. Morris, Jr., On the Determinants of the Stability of Metallic Phases, LBL-3139, Oct. 1974 (submitted to Scripta Metallurgica).

7. C. K. Syn, A. Ahmadieh and J. W. Morris, Jr., Elastic Solute-Dislocation Interaction in an Anisotropic HCP Crystal, LBL-3198, Nov. 1974 (Philosophical Magazine, in press).

8. C. W. Krause and J. W. Morris, Jr., Lattice Vibration and Mechanical Stability in an Idealized Alloy, LBL-3199, Oct. 1974, (submitted to Acta Metallurgica).

9. S. Altintas, K. Hanson and J. W. Morris, Jr., Computer Simulation of Plastic Deformation Through Glide in an Idealized Crystal, LBL-3508 Oct. 1974 (J. Eng. Materials and Technology, in press).

10. Sun-Keun Hwang, The Effect of Retained Austenite on the Cryogenic Mechanical Properties in Fine-Grained Fe-12Ni-0.25Ti Alloy, (M.S. thesis), LBL-3503, Dec. 1974

11. J. W. Morris, Jr. and Sungho Jin, The Design of Tough Ferritic Cryogenic Steels, LBL-3527, Dec. 1974 (to be published in Trans. ASME).

12. Kenton Hanson and J. W. Morris, Jr., Estimation of the Critical Resolved Shear Stress for Dislocation Glide Through a Random Mixture of Distinct Obstacles, LBL-3532, Nov. 1974 (J. Applied Physics, in press).

13. M. J. Schanfein, M. J. Yokota, V. F. Zackay, E. R. Parker and J. W. Morris, Jr., The Cryogenic Porperties of Fe-Mn and Fe-Mn-Cr Alloys, LBL-2764 (The Properties of Materials for LNG Tankage, ASTM, in press).

14. Sungho Jin, B. Whitaker, J. W. Morris, Jr. and V. F. Zackay, Cryogenic Toughness Through Microstructure Control in a Ferritic Fe-Ni-Ti Alloy, LBL-2756, June 1974 (The Properties of Materials for LNG Tankage, ASTM, in press).

C. MICROSTRUCTURE' PROPERTIES AND ALLOY DESIGN

Gareth Thomas, Principal Investigator

Structural Steels: Alloy Design

The main emphasis of this program is the development of experimental structural steels having superior tensile and toughness properties and which can be obtained as economically as possible. Thus mechanical processing is presently excluded from processing sequences. The fundamental principles of this program were detailed in last year's annual report (LBL-2299) and the first five abstracts describe the new results achieved since that report. The other abstracts describe fundamental work concerned with phase transformations and the development of microstructures, beneficial and deleterious.

1. DESIGN OF STRONG TOUGH Fe/Mo/C MARTENSITIC STEELS AND THE EFFECTS OF COBALT*

Robert A. Clark and Gareth Thomas

The microstructures and mechanical properties of a series of vacuum melted Fe/(2-4)Mo/(0.2-0.4)C steels with and without cobalt have been investigated in the as-quenched fully martensitic condition and after quenching and tempering for one hour at 673°K(400°C) and 873°K(600°C); austenitizing was done at 1473°K(1200°C) in argon. The mechanical properties are summarized in Fig. 1. Very good strength and toughness properties were obtained with the Fe/2Mo/0.4C alloy in the as-quenched martensitic condition and this is attributed mainly to the absence of internal twinning. The properties of this alloy compare favorably to those of commercial steels as shown in Fig. 2. The slightly inferior toughness properties compared to Fe/Cr/C steels is attributed to the absence of interlath retained austenite (Fig. 3).

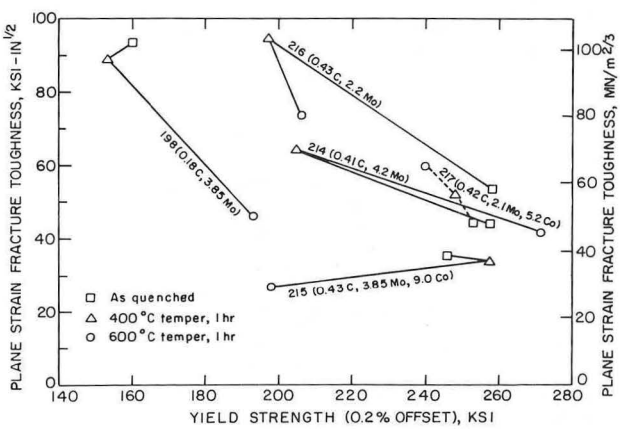

Fig. 1. Room temperature plane-strain fracture toughness vs tensile yield strength for each of the tempering conditions. (XBL 732-5719A)

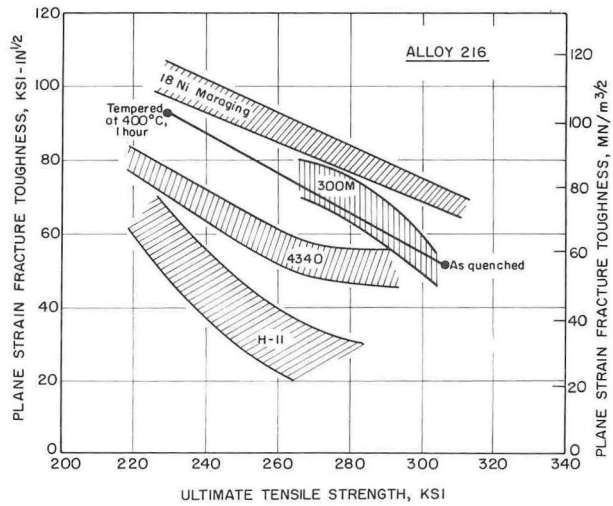

Fig. 2. Comparison of ultimate tensile strength and plane strain fracture toughness of alloy 216 with the strength and toughness properties of several ultrahigh-strength commercial steels. (XBL 732-5717A)

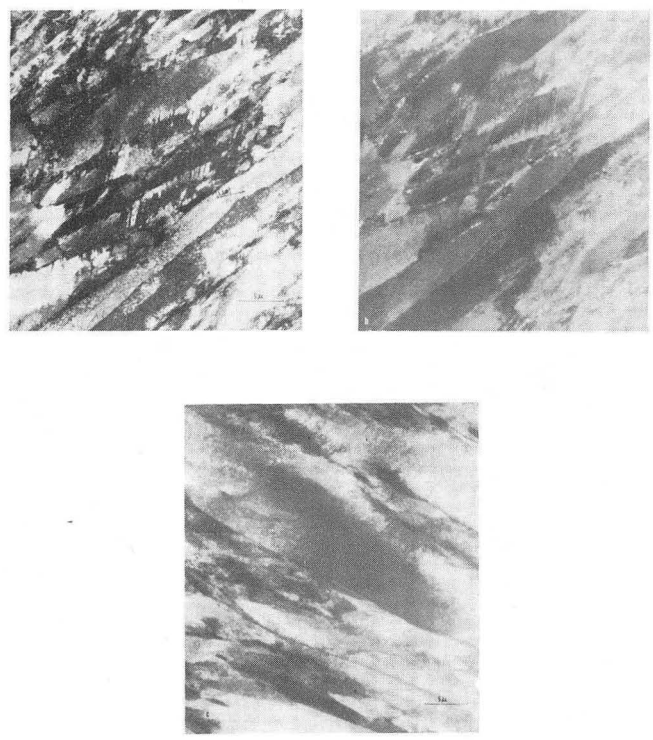

Fig. 3(a). Typical as-quenched microstructures of 0.4C alloys. Alloy 214: Bright fields (a) and (c); Dark field of carbide spot (b). (XBB 736-3521)

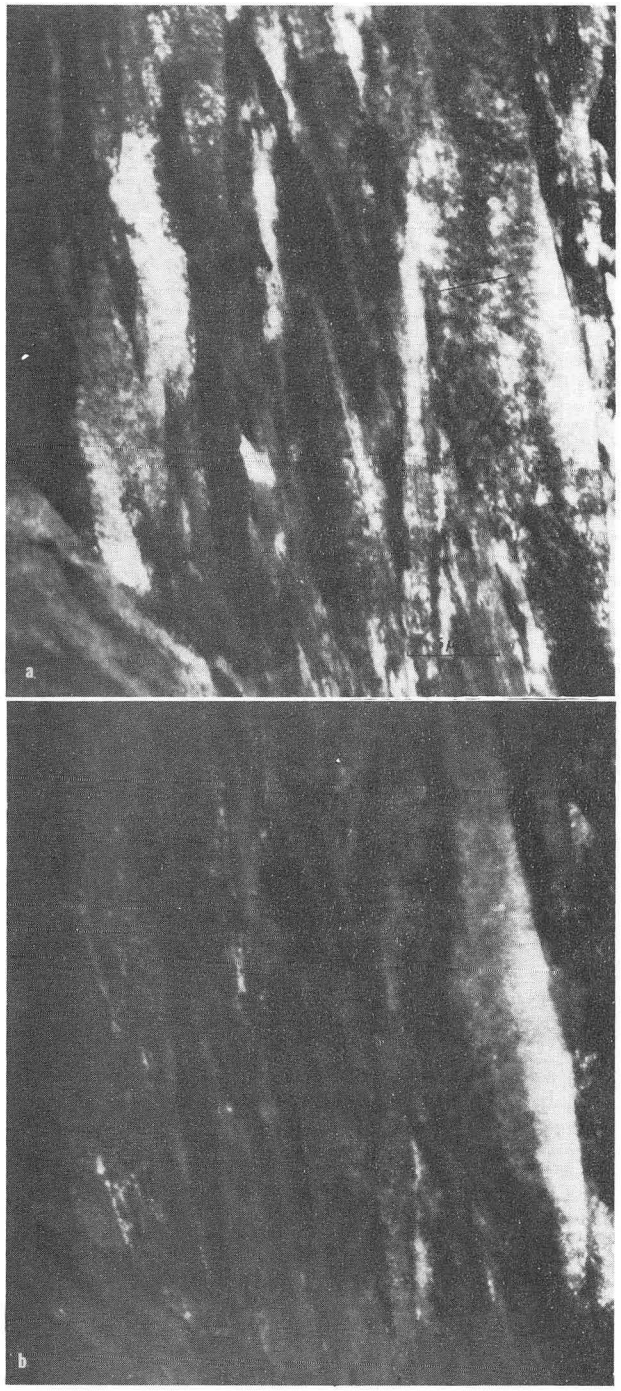

Fig. 3(b). Bright field (a) and dark field showing typical Fe_3C distribution (b) in as-quenched alloy 216. (XBB 736-3522)

The two 0.4% carbon steels having low Mo contents had approximately one-half the amount of transformation twinning associated with the two 0.4% carbon steels having high Mo contents. The plane strain fracture toughness of the steels with less twinning was markedly superior to the toughness of the steels with similar alloy chemistry which had more heavily twinned microstructures. Experiments showed that additions of Co to a given Fe/Mo/C steel raised M_s but did not decrease twinning nor improve toughness. Molybdenum carbide particles were found in all specimens tempered at 673°K(400°C). The Fe/Mo/C system exhibits secondary hardening after tempering at 873°K(600°C). The precipitate is probably Mo_2C. This secondary hardening is associated with a reduction in toughness. Additions of Co to Fe/Mo/C steels inhibited or eliminated the secondary hardening effect normally observed. Toughness, however, did not improve and in fact decreased with Co additions (Fig. 1).

*LBL-2504, Met. Trans., (in press).

2. DESIGN OF Fe/4Cr/0.4C MARTENSITIC STEELS ELIMINATING QUENCH CRACKING

B. V. Narasimha Rao*

Inter-granular cracking in the as-quenched structures of vacuum melted Fe/4Cr/0.4C steel has been investigated in terms of the heat treatment conditions. It has been shown that the amount of carbon in solution and the martensite packet size are the two most important factors influencing cracking tendency. Multiple heat-treatments have been designed in order to take advantage of higher austenitizing temperature and fine austenite grain size. Relatively good mechanical properties have been obtained after these treatments, e.g. tensile strengths in excess of 300,000 psi at Charpy Impact Energies of 10 ft lbs. The conventionally heat treated steel has no toughness as it is full of quench-cracks, so these new heat treatments offer great potential for high carbon steels.

*B.V.N. Rao, M.S. thesis. Submitted to Material Science and Engineering.

3. INVESTIGATION OF HEAT TREATMENTS FOR IMPROVED PROPERTIES OF LOW CARBON Fe-0.12%C-0.5%Mn STEELS

Jayoung Koo*

A new process of thermal cycling has been studied in order to improve the tensile property of commercially available steels which are currently of interest in several areas, e.g. transportation, especially the automobile industry. The composition is basically Fe-0.12%C-0.5%Mn.

The thermal cycling consisting of alternate annealing in the γ and two phase ($\alpha + \gamma$) range with intermediate iced brine quenching has been utilized so as to obtain desirable microstructures which directly influence the mechanical properties. In this heat treatment, the major contribution to the strength of the partially austenitized steel is obtained by the martensitic transformation of the carbon-enriched austenite. In addition, grain refinement ($0.5\mu \sim 3\mu$) of proeutectoid ferrite is achieved.

The tensile properties resulting from this heat treatment were compared with those from conventional methods. The results suggest that the heat

treatments arrived at in this research ideally combine the beneficial effects of finer prior austenite grain size, retained asutenite, martensite, ultrafine subgrain size of proeutectoid ferrite, and fine distribution of carbides.

*M.S. Thesis, LBL-3587.

4. LOSS OF COHERENCY IN SPINODALLY DECOMPOSED Cu-NiFe ALLOYS[1]

Ronald J. Livak* and Gareth Thomas

Coarsening of the spinodal microstructure in copper-nickel-iron alloys has been studied in detail using transmission electron microscopy. Loss of coherency in this lamellar microstructure occurs by the capture of slip dislocations and subsequent multiplication at the interphase interfaces. An example of the structure is shown in Fig. 1. Based on the observations, it is proposed that the multiplication process providing the misfit-accommodating dislocation loops proceeds by the spiraling of the captured dislocations around the platelets by climb, similarly to the formation of helical dislocations. This process is illustrated in Fig. 2. Because the Burgers vector of the captured dislocation is inclined at 45° to the {100} interface, diffusion controlled rotation of the initial {100} coherent interface toward the {100} plane containing $\bar{b}$ occurs in order to lower the interfacial energy. This rotation of the semicoherent interfaces results in a change of the initial platelet morphology to a microstructure containing rod-shaped and more equiaxed particles.

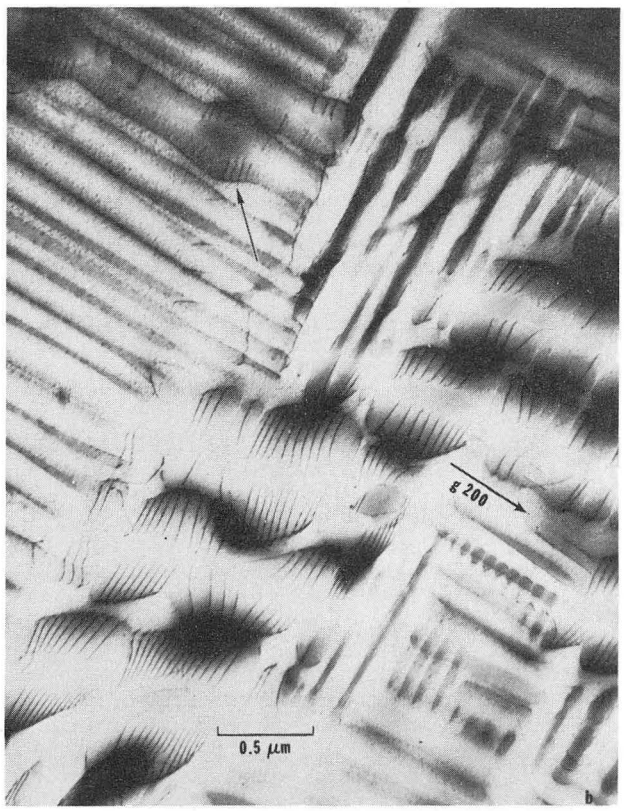

Fig. 1. Bright field micrograph showing some particles losing coherency. Note rotation of semi-coherent interface in the upper left corner. Electron beam parallel to [011] zone axis. (XBB 729-4742)

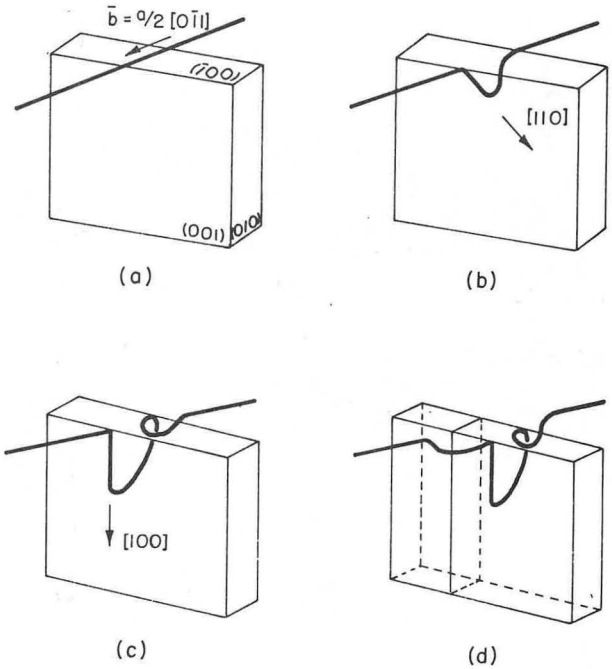

Fig. 2. Proposed mechanism for the spiraling of a captured slip dislocation around a coherent platelet to form misfit-accommodating dislocation loops. (XBL 729-6904)

*Present address: Precision Foundries, Oakland, California

1. R. J. Livak and G. Thomas, Acta Met. 22, 589 (1974).

5. DISCONTINUOUS COARSENING OF SPINODALLY DECOMPOSED Cu-Ni-Fe ALLOYS

Ronald D. Gronsky* and Gareth Thomas

The coarsening behavior of two Cu-Ni-Fe alloys has been found to include a discontinuous reaction which originates at large misorientation grain boundaries. By providing high diffusivity paths, these boundaries promote enhanced growth of the matrix spinodal product which they border

(see Fig. 1). After sufficient aging time, select boundary segments migrate, and in the role of reaction fronts, leave behind large irregularly shaped particles in a cellular morphology. The driving force for the grain boundary reaction is the reduction in overall interphase interfacial energy; hence it is appropriately a "discontinuous coarsening" reaction.

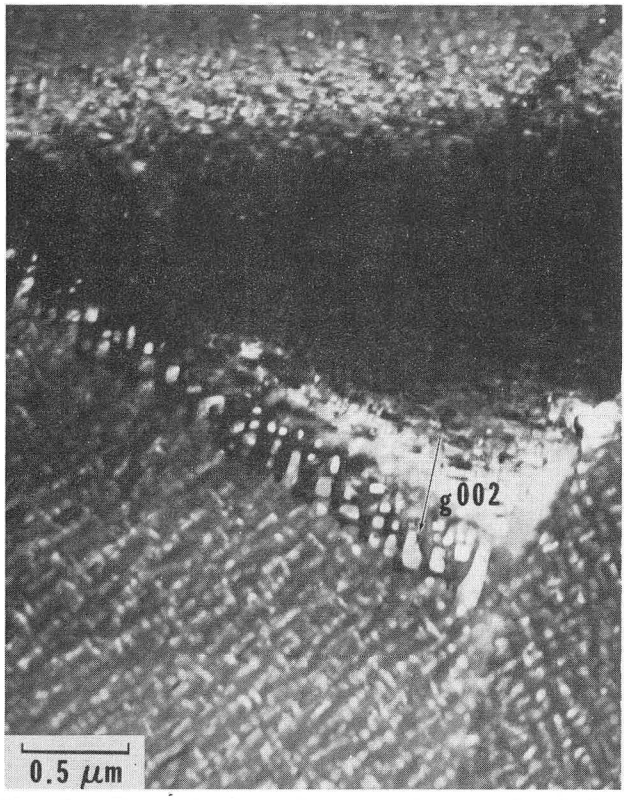

Fig. 1. Transmission electron micrograph of the asymmetrical alloy aged 10 hrs. at 654°C showing enhanced growth in the boundary vicinity (λ≈1150Å) compared to that of the matrix (λ≈400Å). Bright field, [110] zone. (XBB 743-1799)

Although the rate of boundary migration initially suggests grain boundary diffusion control, it decreases progressively with aging time leading to additional coarsening within the cellular constituent. As shown in Fig. 2, the effective interparticle spacing (λ_2) of the semi-coherent boundary-fed particles varies as:

$$\lambda_2 = k_2 t^{0.7} ,$$

compared to that (λ_1) of the semi-coherent matrix product,

$$\lambda_1 = k_1 t^{0.34} .$$

In both cases, the rate of coarsening is greater in the alloy of asymmetrical composition than in the symmetrical alloy.

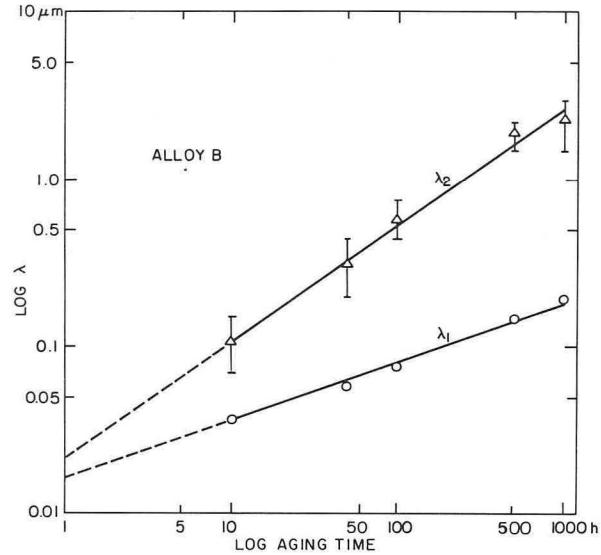

Fig. 2. Plot of the interparticle spacing of the matrix (λ_1) and boundary (λ_2) particles as a function of aging time at 654°C for the asymmetrical alloy. (XBL 747-6729)

This coarsening process at grain boundaries results in microstructures which lead to intergranular embrittlement. These fracture properties are currently being investigated.

*M.S. Thesis, LBL-3134 (Acta Met., in press 1975).

6. INTERSTITIAL ORDER AND EMBRITTLEMENT IN Ta-C ALLOYS*

P. Rao[1] and Gareth Thomas

The effects of carbon on the structure and mechanical properties of tantalum at 77°K, 196°K and 300°K have been investigated. The alloys contained 0.76, 1.27, 1.53 and 2.05 at %C as determined by He-3 activation analysis.

Interstitial ordering was observed in all alloys with the formation and growth of aligned particles in ⟨110⟩ causing tweed contrast in electron micrographs (Fig. 1). Analyses of electron diffraction patterns indicated that the fully developed single phase structure which is attained in Ta 1.53 and 2 at %C corresponds to a tetragonal or orthorhombic ordered lattice of composition $Ta_{64}C$ or $Ta_{32}C$. A model to explain these structures based on carbon fluctuations on specific {110} Ta planes is suggested. The alloys become completely brittle and cleave along {110} when the ordered structure is fully developed i.e. when the carbon content is 1.53 at % or more (Fig. 2). It is suggested that this embrittlement results from the severe elastic strains which arise due to ordering such that the restrictions on the elastic compliances can no longer be maintained.

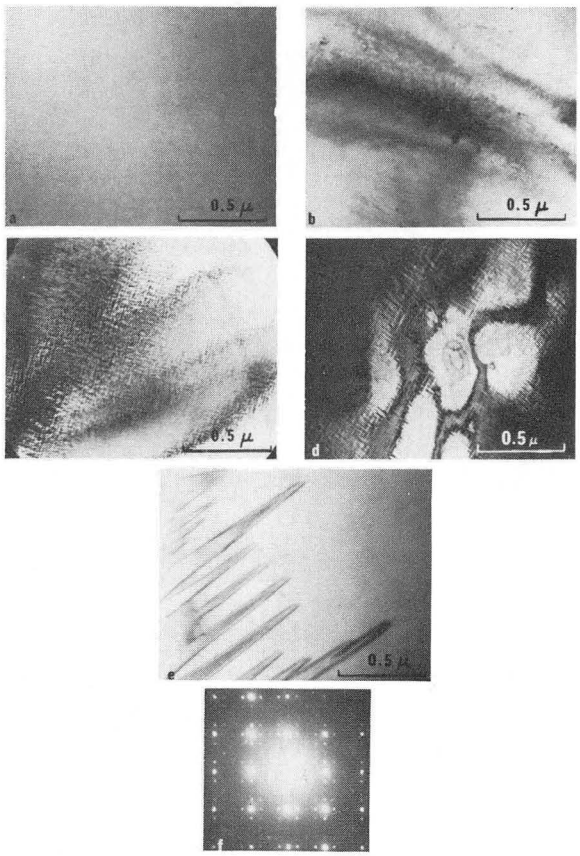

Fig. 1. Bright field electron micrographs of various stages of the interstitial ordering transformation:
(a) Pure tantalum
(b) Ta-0.76 at %C showing contrast due to fine fluctuations in carbon composition.
(c) Ta-1.27 at %C showing the formation of "ordered" particles which align themselves along the ⟨110⟩ directions.
(d) Ta-1.53 at %C showing growth along ⟨110⟩ till impingement.
(e) Ta-2.05 at %C showing the formation of highly ordered regions separated by coherent antiphase domain boundaries. (XBB 6911-7115)

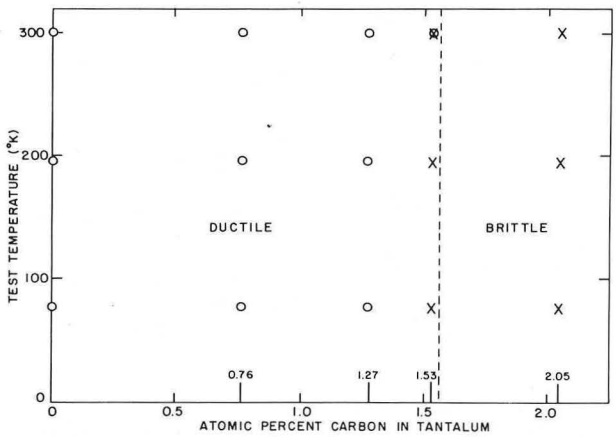

Fig. 2. Summary of ductile-brittle behavior of tantalum-carbon alloys containing up to 2.05 at %C in a plot of test temperature (°K) vs. atomic percent carbon in tantalum. (XBL 6910-5962)

*LBL-2570, Acta Met., in press.

1. Present address: General Electric Company, Corporate Research and Development, Schenectady, New York 12301.

7. THE CRYSTALLOGRAPHY AND STRUCTURE OF DEFORMATION INDUCED EPSILON AND ALPHA MARTENSITE IN Fe-Ni-Cr SINGLE CRYSTALS

Glen A. Stone*

A comprehensive study of the crystallography and structure of deformation induced ε and α martensite (from austenite) in a low stacking fault energy Fe-15wt%Ni-15wt%Cr alloy has been completed. The martensite needle axis, magnitude of the shape change and direction of the shape change have been measured. When these results were compared to the Acton-Bevis two shear phenomenological theory, using two slip shears, the following result was obtained for the habit plane normal (assuming the long axis of the needles lie in the habit plane and the habit plane is perpendicular to the slip plane),

$\vec{h} = \langle 0.333, 0.812, 0.479 \rangle_\gamma$ Experimental

$\vec{h} = \langle 0.341, 0.812, 0.475 \rangle_\gamma$ Theoretical

for the direction of the shape change vector,

$\vec{u} = \langle 0.822, 0.129, 0.555 \rangle_\gamma$ Experimental

$\vec{u} = \langle 0.825, 0.158, 0.542 \rangle_\gamma$ Theoretical

and for the magnitude of the shape change experimental values varied between 0.21 to 0.30 and theoretical values varied between 0.25 to 0.39.

The magnitude of the critical resolved shear stress (CRSS) on possible α martensite habit planes controls which variants of the habit that can form. Measurements of the habits present in deformed single crystals agree well with the CRSS model of Patel and Cohen. The variants of the Kurdjumov-Sachs (KS) orientation relation present for α martensite were always the variants that contained both the active slip planes and slip directions. These results demonstrate that the K-S variants that are present also depend on the CRSS.

The sequence of transformations in the temperature range studied are $\gamma \rightleftharpoons \varepsilon$ and $\gamma \rightarrow \alpha$. The $\varepsilon \rightarrow \alpha$ transformation was not observed. The ease of these transformations above Es_γ and Ms_γ depends on the magnitude of the CRSS on potential habits. The $\gamma \rightarrow \varepsilon$ transformation is believed always to occur first. The $\varepsilon \rightarrow \gamma$ (reversion) occurs at large plastic strains after a significant amount of α martensite has formed. In addition to the ε - α interface formed by ε sheets parallel to $\{111\}_\gamma$ planes, ε martensite surrounding the entire α martensite needle has been observed. This situation is formed during accommodation deformation of the austenite adjacent to the growing α martensite needle.

*Ph.D. thesis LBL-1800.

D. CERAMIC ALLOYS PROGRAM

Gareth Thomas, Principal Investigator

The need for more in-depth structure-property correlations and "alloy" design applications for ceramic systems has now been well documented (e.g. the N.A.S. report "Materials and Man's Needs", 1974).

A small program was started in 1969 on the microstructures and phase transformations in certain ferrites and minerals and very recently a study has been done on non-stoichiometric TaC. The future plans call for two major efforts viz:

1. Studies of phase transformations in ferrites and the correlation of microstructure with magnetic properties especially coercive force. The aim will be to design ceramic alloys of high coercive force for applications such as permanent magnets (e.g. in electric motors, computers).

2. Studies of microstructure and mechanical properties of refractory ceramics, particularly carbides (TaC, SiC) and nitrides of desirable crystal structure (cubic) and the influence of environment on structure and properties (e.g. surface stoichiometry).

Abstracts of our research progress follows:

1. CHARACTERIZATION OF STRUCTURES IN LITHIUM FERRITE

Omer O. Van der Biest* and Gareth Thomas

A theoretical and experimental study of cation stacking faults in the spinel structure has been completed. From geometric and energetic arguments it has been shown that for a 1/4 ⟨110⟩ cation fault, the plane perpendicular to the displacement vector (viz {110}) will have the lowest surface free energy in a stoichiometric spinel.[1] In the nonstoichiometric case, deviation from this orientation may occur. As reported previously,[2] faults of type {110} 1/4 ⟨110⟩ were found in flux grown lithium ferrite single crystals, using high voltage electron microscopy.

At 750°C an order-disorder reaction takes place in lithium ferrite. The space group symmetry is lowered from Fd3m (spinel structure) to $P4_132$ or $P4_332$. The ordered structure can exist in two enantiomorphous forms (Fig. 1).

Simple electron microscopy techniques have been developed[3] which allow one to detect the presence of two enantiomorphous forms of a structure within an apparent single crystal. The first method consists of a characterization of the interface between the two enantiomorphs. In the second method advantage is taken of violations in Friedel's law which can occur in non-centrosymmetrical crystals. These techniques have

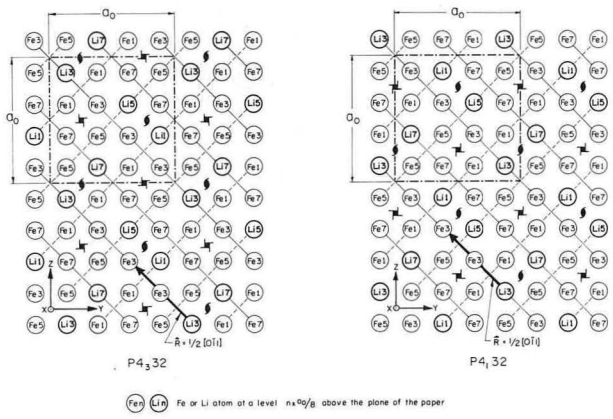

Fig. 1. Projection of the octahedral sites in lithium ferrospinel on the (100) planes, showing the two enantiomorphs. The unit cell indicated in the conventional is for the $P4_332$ space group It is indicated how the octahedral sites are aligned in ⟨011⟩ direction with one Li ion followed by three Fe ions. (XBL 745-6281)

been illustrated by an analysis of the domain structure in ordered $LiFe_5O_8$. Consistent results were obtained with both methods. The first method yields a more complete description of the domain structures.

Ordered lithium-ferrite contains boundaries of three different types (Fig. 2): (1) ordinary anti-phase boundaries, occurring within one enantiomorph, characterized by a displacement vector $\bar{R} = 1/2 \langle 110 \rangle$, (2) inversion boundaries characterized by an inversion operation, (3) boundaries described by an inversion and a translation. The contrast to be expected from each of these has been calculated. Each of these boundaries can be unambiguously identified by

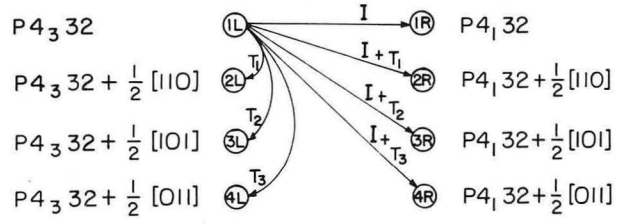

Fig. 2. Schematic representation of the seven different boundaries in ordered lithium ferrite. Eight different ordered arrangements are possible, four within each space group and the nature of the boundary between them is indicated (T=translation, I=inversion). (XBL 738-1636B)

contrast experiments in the microscope (Fig. 3). It has also been found that cation stacking faults can serve as a boundary between right and left-handed structures. In the ordered structure cation stacking faults can change character from {110} 1/4 ⟨110⟩ type to {110} 1/4 ⟨$\bar{1}$12⟩ type.

Future Research Plans

1. "In situ" observation of the ordering reaction in lithium ferrite.
2. Phase transformations in lithium ferrite at high temperatures.
3. Microstructural studies in commercial ferrites (nickel ferrite, pure and aluminum doped, magnesium-manganese ferrites).

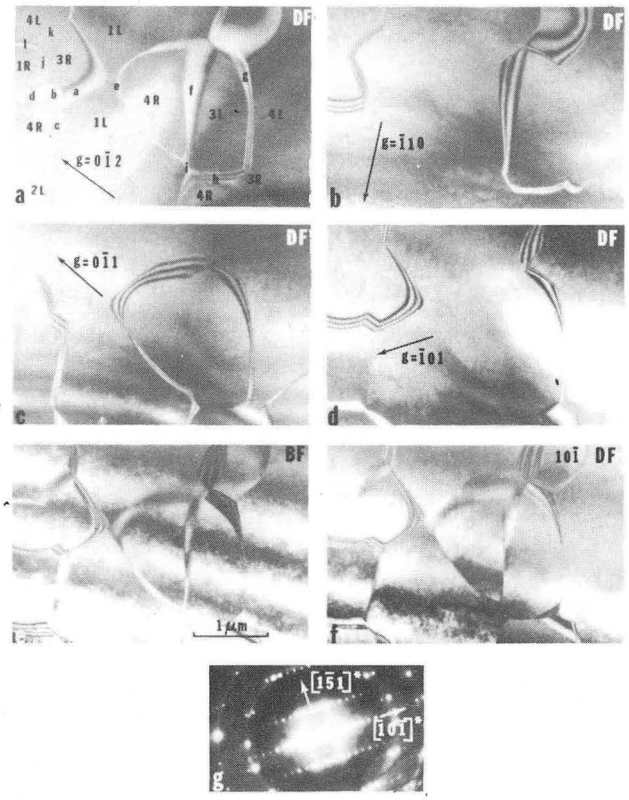

Fig. 3. From the contrast condition in (a), (b), (c) and (d) the nature of the interface between domains can be determined. Following the notation in Fig. 2, the domains can be labeled in a self consistent manner. The diffraction conditions of (e) and (f) are shown in (g). Under these diffraction conditions, Friedel's law does not hold in dark field. This means that when thickness contours are intercepted in (g), an inversion takes place. Hence the general character of the boundary can be quickly determined. The results are consistent with the labeling in (a).
(XBB 743-1710)

*Ph.D. Thesis, LBL-2786

1. O. Van der Biest and G. Thomas, Phys. Stat. Sol. (a) 24, 65 (1974).
2. 1973 Annual Report (LBL-2299).
3. O. Van der Biest and G. Thomas, Identification of Enantiomorphism by Electron Microscopy, Acta Crystl, in press (LBL-2773).

2. PHASE TRANSITIONS IN LITHIUM FERRITE

Raja K. Mishra*

Taking advantage of the ion-thinning machine for preparing ceramic specimens for TEM observation, and the HVEM for examining relatively thick specimens, phase transformations in $LiFe_5O_8$ have been studied. At 1200°C, the formation of lithium ferrate ($LiFeO_2$) phase from lithium ferrite spinel and its subsequent transformation to a lithium deficient spinel has been established by use of electron diffraction and microscopy. Present findings on the phase transition are in contradiction with a portion of the existing phase diagram for Li_2O-Fe_2O_3 system. The main emphasis at present has been to develop suitable microstructures for consequent improvement of magnetic and electronic properties of the ferrimagnetic spinel. Side by side, characterization of slip systems and partial dislocations in the spinel structure are in progress.

*Ph.D. thesis, in progress

3. STRUCTURE OF NON-STOICHIOMETRIC TaC*

D. J. Rowcliffe[1] and Gareth Thomas

A detailed electron microscopy and diffraction analysis of TaC alloys obtained by floating zone melting over the range $TaC_{0.7}$ to $TaC_{0.8}$ shows evidence for intrinsic and extrinsic faulting and short range order. Examples are shown in Figs. 1 and 2. A model is presented which is based on the filling of octahedral sites in {111} planes which can account for the observed faulted structures and the formation of the phases Ta_2C, Ta_4C_3.

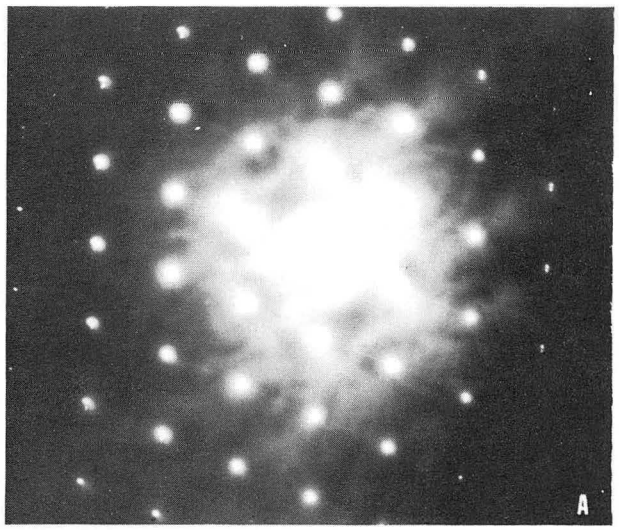

Fig. 1a. Transmission electron diffraction patterns of $TaC_{0.81}$, (211) pole.

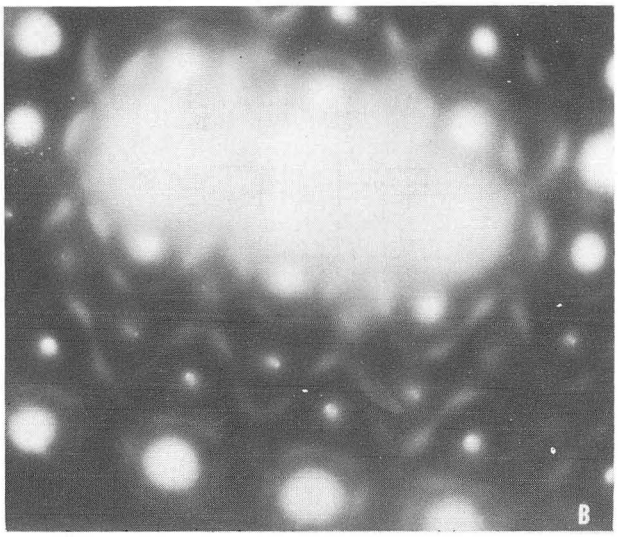

Fig. 1b. $TaC_{0.78}$, (110) pole. Annealed 200 hrs. at 750°C. The streaks in [111] and split spots in (b) are due to {111} stacking faults. (100kv) (XBB 743-1387)

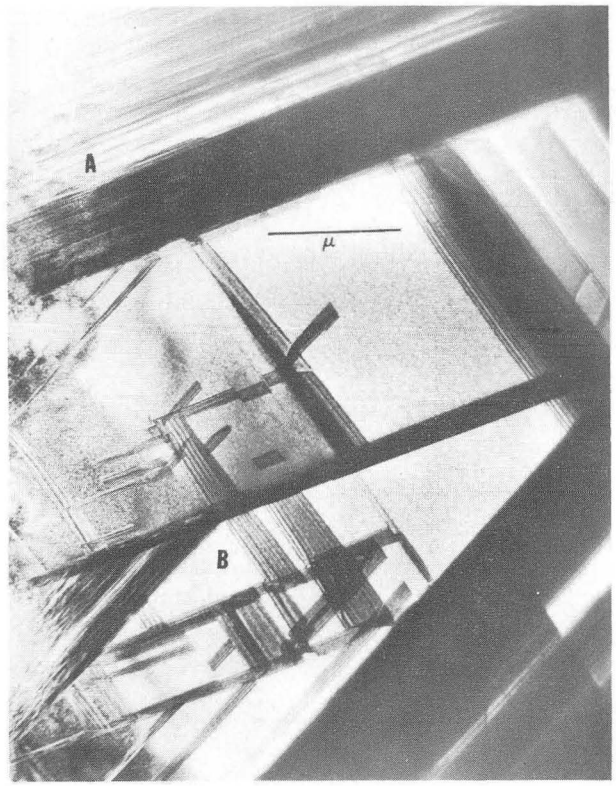

Fig. 2. Coexistence of zeta phase (A), individual stacking faults (B) and fault-free tantalum carbide, in a sample of overall composition $TaC_{0.73}$. (100 kv) (XBB 743-1389)

---

*LBL-2588, Mat. Sci. and Engineering (in press)
1. Brown Boveri Research Centre, Baden, Switzerland.

E. HIGH VOLTAGE, HIGH RESOLUTION ELECTRON MICROSCOPY

Gareth Thomas, Principal Investigator

1. HIGH RESOLUTION STUDIES-ORDERED ALLOYS

Gareth Thomas

With the acquisition of two new high resolution electron microscopes capable of 2Å Fourier line resolution (Philips EM 301 - 100kV and Siemens Elmiskop 102 - 125kV) we are now in a position to make more detailed studies of substructure, especially early stages of phase transformations, than was hitherto possible, (e.g. ref. 1). The main thrust of our work this past year has been towards a better understanding of ordering especially the early stages of the transformation, including short range order. This research is being carried out by Dr. Robert Sinclair (NSF support), Dr. Jan Dutkiewicz (Acadamy of Sciences exchange program with Poland), and graduate students U. Dahmen and R. Gronsky.

The study of short-range ordering in alloys has now progressed beyond the stage of simple approximation involving only pair-wise atom correlation parameters and two-atom pseudopotentials. The more fundamental considerations of many-atom interactions and correlations which will allow a more direct approach to problems of real alloy systems, require more information than can be derived from the customary X-ray diffraction measurements. The most promising method for deriving the relevant data on atom configurations is by high resolution microscopy. Two techniques have so far been applied. The dark-field imaging technique using diffuse scattering peaks gives some information on microstructures but is more complicated than first appears and has definite limitations (refs. 2,8). The alternative of direct imaging of lattice fringes and eventually of direct visualization of atom positions, by ultra-high resolution microscopy is more promising with greater long range potentialities.

a. Theory of Lattice Image Formation

The Fourier lattice image of an alloy is produced in the TEM by allowing the interaction of the transmitted and a particular Bragg diffracted beam in the process of image formation. The resulting fringe image has identical spacing and orientation to the lattice planes giving rise to the chosen Bragg reflection. Kinematically the fringes can be interpreted simply by a one-to-one correspondence between fringe and atomic plane position. Thus, it should be possible to examine the lattice image and determine plane positions and hence atomic configuration in the vicinity of lattice defects. However, it has been recognized that considerable care must be taken in using such a simple interpretation[3,4] since the nature of the image is dependent on many factors, such as foil thickness, proximity to the Bragg condition, defocus of the objective lens and depth of the fault in the specimen. It is important to establish how these variables affect the image before experimental results may be satisfactorily interpreted. In the present study, this has been achieved by simulating fringe images using the dynamical theory of electron diffraction and excellent agreement has been obtained between experimental and theoretical images.[5]

An example of this correlation is shown in Fig. 1, where fringe profiles in partially ordered Cu_3Au are shown. This alloy was chosen as a model test system since its ordering behavior has been widely studied using conventional techniques. Ordering proceeds by growth of ordered domains consuming a predominantly disordered matrix and the theoretical fringe profile of such an ordered domain is shown in Fig. 1a. The fringe periodicity is that of the superlattice (3.8Å) with an intermediate weaker fringe alternating with the strong fringes. An example is shown in Fig. 1(b).

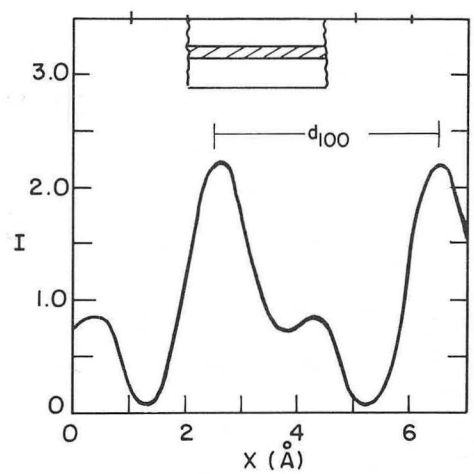

Fig. 1. (a) Theoretical fringe profile of a 50Å fully ordered domain in a disordered Cu_3Au matrix. (XBL 743-5815 lower)

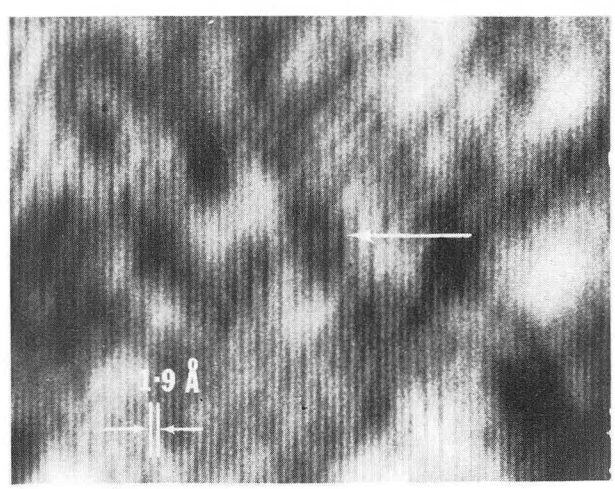

Fig. 1. (b) Lattice image showing domains of order in a disordered matrix in Cu_3Au. (XBB 7412-8988)

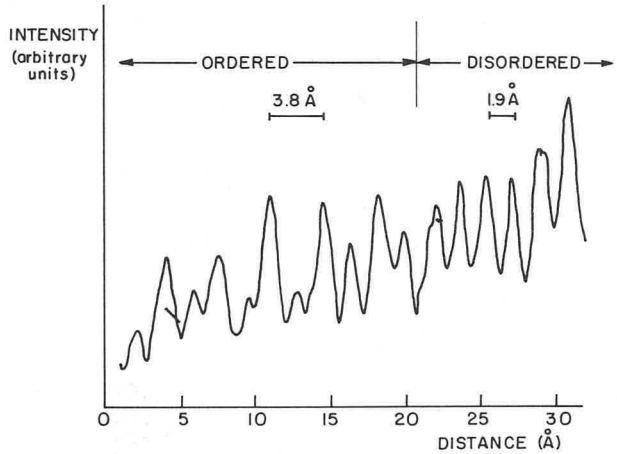

Fig. 1. (c) Microdensitometer trance across the experimental lattice image (Fig. (b) of an ordered domain in partially ordered Cu_3Au, showing good agreement with the theoretical profile. (XBL 7411-7551)

A microdensitometer trace across the lattice image of the domains is illustrated in Fig. 1c. The alternately strong-weak fringes in the ordered region are clearly shown, in excellent agreement with the theoretical profile. The calculations show that the ratio of intensities of alternate fringes depends primarily on two factors:

(i) position of domain in the foil.
(ii) degree of order in the domain.

Since the former can be determined by stereoscopic methods in the conventional dark field micrograph, the degree of order in these small domains (~25Å) may be derived from the nature of the fringe profile of the lattice image. Such information, which cannot be derived in an alternative way for particular domains in Cu_3Au, may be used to understand how the ordering transformation proceeds in the initial stages.[7]

Examples of experimental results and comparison with theory are given in Figs. 2-5.

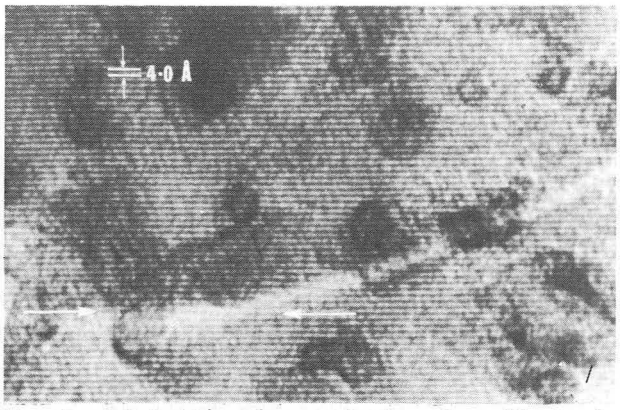

Fig. 2 (a) Lattice image showing the effect of a translational antiphase boundary on superlattice planes (4.0Å spacing) in ordered Ni_4Mo. The upper part of the crystal is translated by two-fifths of the superlattice plane spacing with respect to the lower part. A portion of the boundary (arrowed) is nonconservative. (XBB 7410-7097)

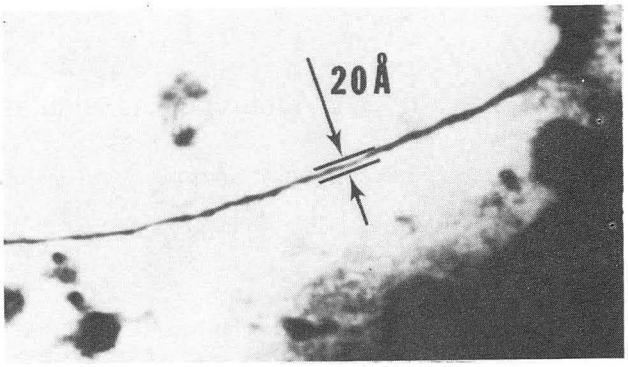

Fig. 2. (b) Superlattice dark field micrograph corresponding to (a). (XBB 7412-8987)

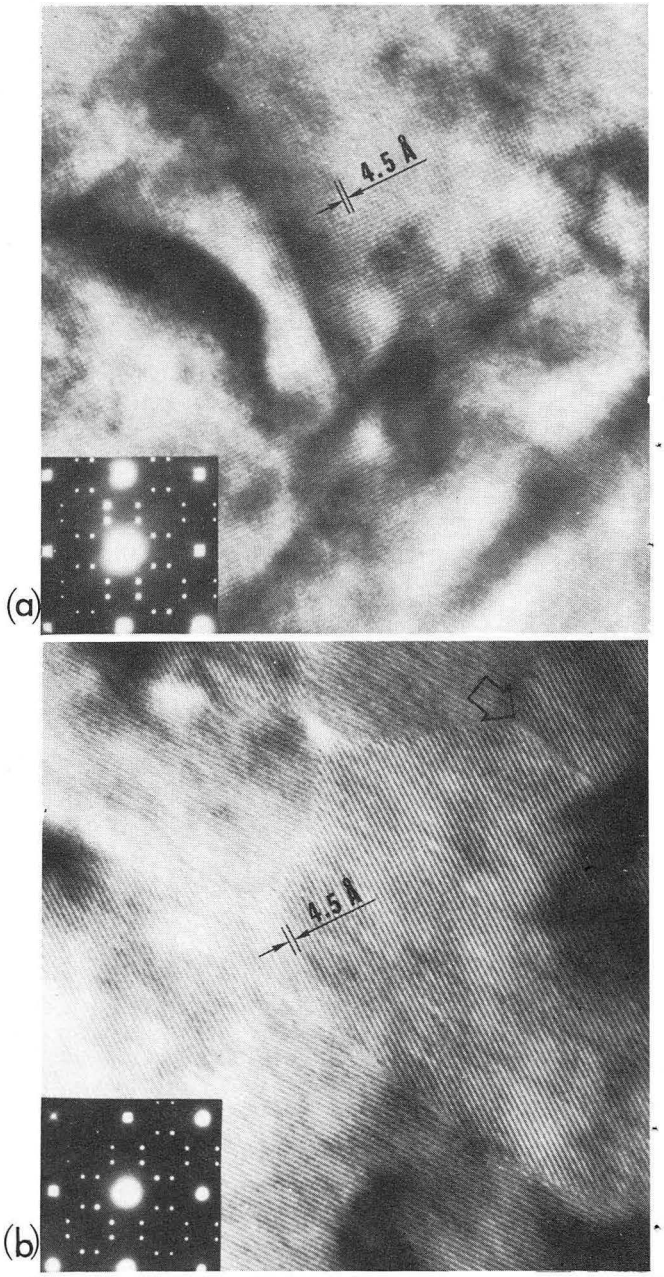

Fig. 3. Lattice image taken from evaporated Au_4Cr alloy after 70h aging at 270°C. a) close to the symmetrical orientation b) foil slightly tilted around the $[1\bar{1}0]$ axis. Two variants of ordered domains showing translational and rotational APB's are shown. (XBB 7412-8991 & XBB 7412-8990)

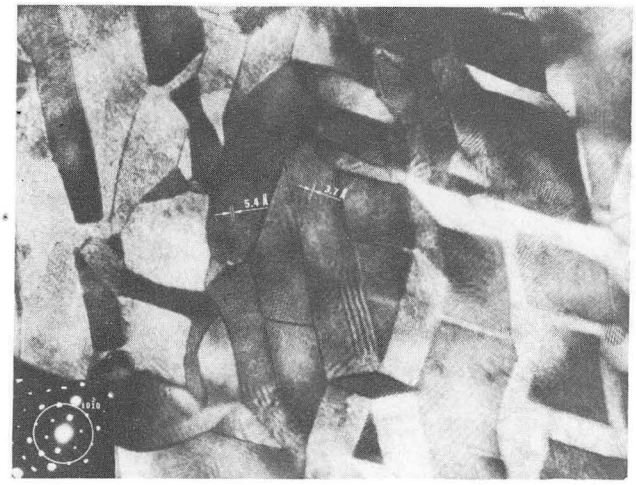

Fig. 4. Lattice image taken in the symmetrical orientation from Mg_3Cd alloy aged for 17 days at room temperature. Three variants of ordered domains showing $\{\frac{1}{2}00\}$ superlattice fringes of spacing 5.4Å, running in three different directions are seen. (XBB 747-5204)

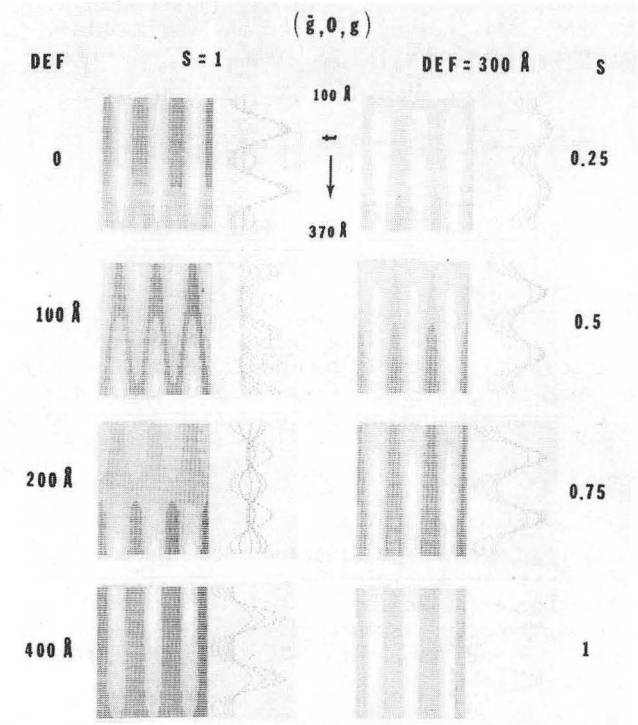

Fig. 5. Computer simulated lattice images and fringe profiles calculated for specimen, with thickness change 100-370Å, symmetrical orientation and (g̃,0,g) beams included in the objective aperture a) calculated for fixed degree of order (S) equal to 1 and various defocus (DEF) equal to: 0,100,200 and 400Å b) calculated for fixed defocus equal 300Å and variable degree of order equal to 0.25, 0.5, 0.75 and 1. (XBB 7412-8505)

b. Spinodal Decomposition in Cu-Mn-Al Alloys

The microstructural changes associated with spinodal decomposition in Cu-Mn-Al alloys have been extensively studied utilizing conventional dark and bright field and electron diffraction methods. However, these techniques are not capable of yielding information about composition changes occurring during the decomposition process. Direct lattice imaging provides a method of studying these changes and allows one to test current theories of the transformation.

A lattice image of the partially transformed alloy is shown in Fig. 6a (courtesy of M. Okada) with a plot of the spacing of successive fringes in Fig. 6b. It can be seen from the latter that regions of alternately higher and lower fringes spacing are present. These correspond to the higher and lower lattice parameter regions in the decomposing alloy caused by variations in manganese content (the equilibrium phases in this system are Mn poor based on the Cu_3Al structure and Mn rich based on the Cu_2MnAl structure). Since the lattice parameter may be related to the Mn content of the alloy, composition variations and changes with aging time can be derived from such experimental images and the decomposition may thus be studied directly.

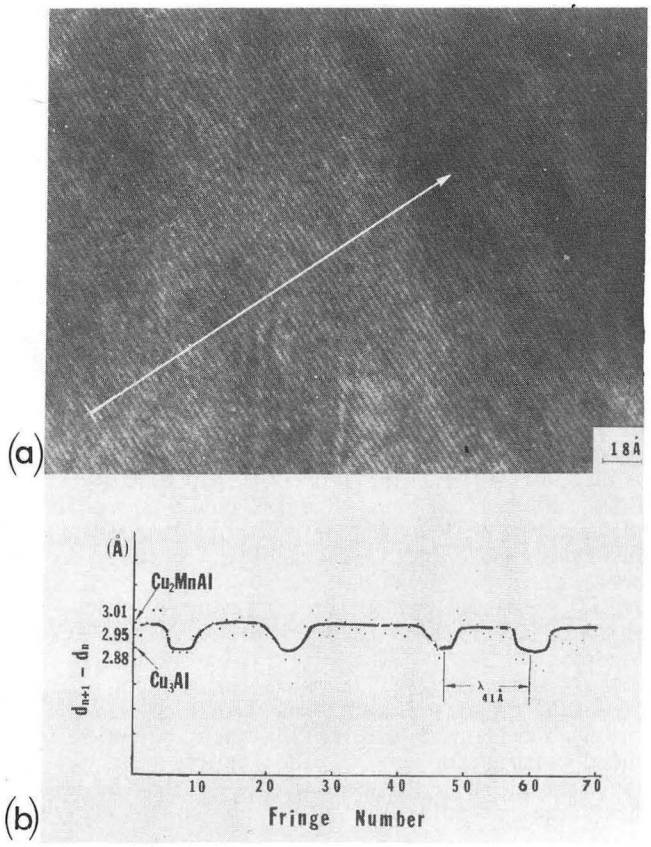

Fig. 6. (a) Lattice image of (200) planes in a Cu-Mn-Al alloy which has undergone partial spinodal decomposition. (b) Plot of successive fringe spacings in this image showing the lattice parameter (and hence manganese composition) variations in the alloy. (Courtesy of M. Okada). (XBB 745-3095)

c. Conclusions

The present work shows that lattice fringe imaging yields considerably more detailed information than conventional methods about lattice defects and the atomic mechanism of transformation processes in alloys.

---

1. V.A. Phillips, Acta Met. 21, 219 (1973); V.A. Phillips and L.E. Tanner, ibid, 411 (1973).
2. J.M. Cowley, The Chemistry of Extended Defects in Nonmetallic Solids, p. 259, ed. L. Eyring and M. O'Keefe, (North Holland) (1970).
3. P.B. Hirsch, A. Howie, R.B. Nicholson, D.W. Pashley and M.J. Whelan, Electron Microscopy of Thin Crystals, (Butterworths, London) (1965), p. 160.
4. D.J.H. Cockayne, J.R. Parsons and C.W. Hoelke Phil. Mag. 24, 139 (1971).
5. R. Sinclair, K. Schneider and G. Thomas, LBL-3194, to be published. K. Schneider, R. Sinclair and G. Thomas, 8th International Congress on Electron Microscopy, Canberra, 520, (1974).
6. S.K. Das and G. Thomas, Order-Disorder Transformations in Alloys, ed. by H. Warlimont (Springer-Verlag, Berlin, p. 332, 1974).
7. R. Sinclair and G. Thomas, J. Appl. Cryst. in press, LBL-2731 (1975).
8. S.K. Das, P.R. Okamoto, P.M.J. Fisher and G. Thomas, Acta. Met. 21, 913 (1973).

2. HIGH VOLTAGE STUDIES

Robert Sinclair, Michael J. Goringe, Jan M. Dutkiewicz, and Andre M. Rocher

a. Critical Voltage Effect: Ordered Alloys

Apart from the well known advantages to be gained from increased penetration and resolution at high voltages,* the high voltage electron microscope can be utilized to obtain quantitative information on structure factor (and hence local chemical composition) utilizing the critical voltage effect arising from multiple diffraction. This past year we have undertaken a theoretical and experimental survey of ordering systems of interest with critical voltage (V_c) effects between 200 and 650 kV, the range available on our HVEM. A multibeam calculation using dynamical electron diffraction theory has been developed for this analysis. The variation of critical voltage with Bragg-Williams degree of long-range order (S) is of prime interest since it was intended to derive information about ordering by the determination of V_c. The results of the theoretical survey, shown in Fig. 1, may be summarized as follows.

i) A variation of V_c with S is shown for those systematic rows which contain superlattice reflections, which means that some important possible reflections cannot be utilized (e.g. for Ni_4Mo and related alloys with the D1a structure no variation of V_c for the (400) reflection will occur).

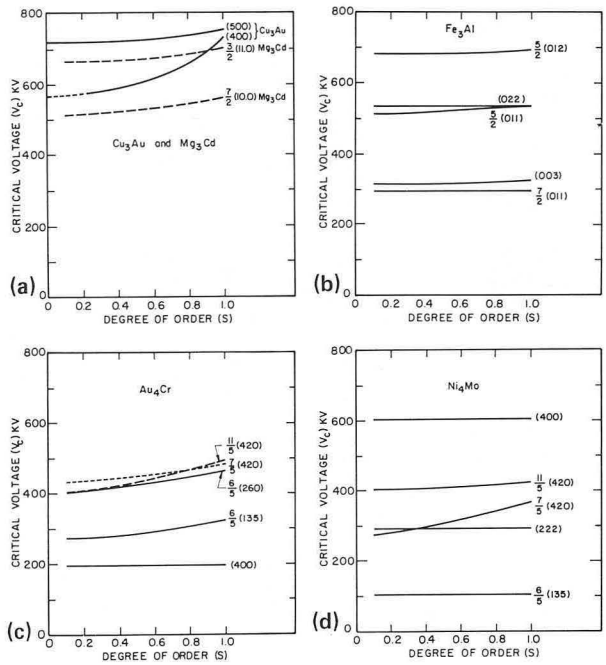

Fig. 1. The variation of the critical voltage (V_c) with degree of order (S) for various reflections in a number of alloy systems, calculated from many beam dynamical electron diffraction theory. All indices refer to the fundamental, disordered lattice.

(a) Cu_3Au and Mg_3Cd
(b) Fe_3Al
(c) Au_4Cr
(d) Ni_4Mo (XBL 748-1351)

ii) In all the alloy systems considered a critical voltage could be found within the range of our microscope. However, in many cases the reflection showing the disappearance effect is a superlattice reflection. Since the intensity of superlattice reflections is considerably smaller than that of fundamental reflections the corresponding Kikuchi lines and bend contours are also very weak. The disappearance of these are often used to determine V_c (e.g. Fig. 2) and hence the exact voltage at which the minimum intensity occurs is more difficult to obtain precisely and the accuracy of the V_c measurement is considerably reduced.

iii) The variation of V_c with S is not marked in many systems. The most promising alloys are those with large differences in atomic scattering factors between the species of the alloy, although this is not always the case (e.g. V_c only increased by ~50kV on ordering Au_4Cr, a small change considering the large scattering factor difference between Au and Cr). Thus Cu_3Au (ΔV_c for (400) ~200kV) is predicted to have the largest variation for the alloy systems considered.

iv) The data shown in Fig. 1 for Cu_3Au confirm the previous calculations of Lally et al.[1] V_c of

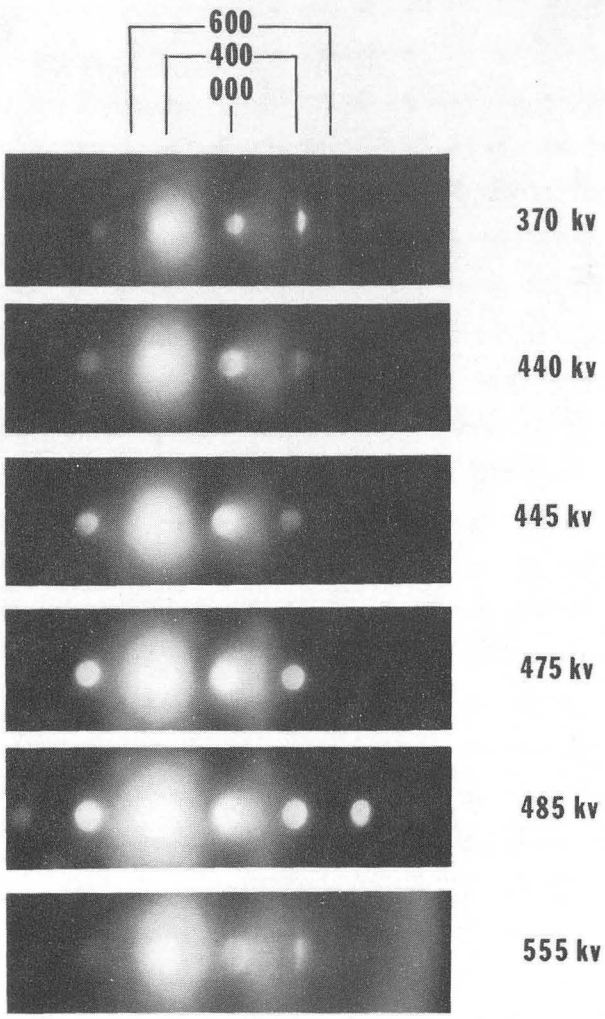

Fig. 2. [001] systematic row of disordered Ni_4Mo at various voltages, indicating that the critical voltage (at which the (400) Kikuchi line disappears) is 460kV. (XBB 743-2049)

(400) (fundamental) and (500) (superlattice) reflections both show a variation with S, the former being the more marked. However, it has more recently been reported[2] that the experimental difference of the (400) critical voltage between disordered and fully ordered specimens of Cu_3Au is only ~45kV and that the calculations are misleading since the effective Debye-Waller factor is different in the two states. This very small difference in V_c reduces considerably the worthwhile information which may be derived from critical voltage measurements on ordering in this system.

b. Experimental Results

Cu_3Au

The recent experimental results of Lally et al.[2] for Cu_3Au have largely been confirmed in the present investigation. Thus the (400) critical voltage increases from 360±10kV in the disordered alloy to 420±10kV in the fully ordered state. The initial variation of V_c with S was also found to be slight (~10kV increase for S up to ~0.7). In practice this indicates that the difference of V_c between a fully ordered region (microdomain) and more disordered material is ~40kV. For a small microdomain this rather small difference is insufficient to detect in a series of dark field micrographs near V_c.

Ni_4Mo

The (400) critical voltage of Ni_4Mo was found to increase from 460±5kV to 490±5kV on ordering. This again is too small a difference to be used in studying the initial stages of the ordering transformation.

Attempts to utilize other critical voltages in this system (e.g. 7/5 (420), 11/5 (420)) were unsuccessful. This arose from the extremely weak Kikuchi lines present for these reflections which were undetectable even on an overexposed photographic plate. No variation of intensity was found throughout the voltage range of our HVEM and thus the critical voltage could not be established.

Mg_3Cd

The 3/2(1$\bar{1}$.0) and 7/2(10.0) critical voltages were found to be outside the range of our HVEM contrary to the expectations of the preliminary calculations.

Whilst the critical voltage effect is an interesting phenomenon which may be useful for certain specialist applications, it is the conclusion of this study that is impractical for investigating ordering reactions in alloys.

One application of the effect which is being pursued[3] is the refinement of the Doyle-Turner atomic scattering factors of the alloy species. Ordering yields reflections which are systematically absent in the pure metal diffraction pattern (e.g. {100}, {110} are present in ordered Cu_3Au but not in the Cu or Au fcc patterns). As the critical voltage is dependent on the values of atomic scattering factor, the absolute values of V_c can be utilized to yield more accurate scattering factor data. The 20% discrepancy between theoretical and experimental values of V_c in Cu_3Au found by Lally et al.[2] can be attributed to these "inaccurate" scattering factors and refined calculations in the present study yield critical voltages in excellent agreement with the experimental results.

---

*See e.g. Annual Report 1973, LBL-2299

1. J. S. Lally, C. J. Humphreys, A. J. Metherell and R. M. Fisher, Phil. Mag. 24, 321 (1974).
2. L. E. Thomas, C. G. Shirley, J. S. Lally and R. M. Fisher, (1974) Proceedings of 3rd International Conference on High Voltage Electron Microscopy, 38.
3. A. Rocher (1975) to be published.

3. RADIATION DAMAGE (200kV - 650kV) IN ORGANIC MATERIALS (AND DEVICES MEASURING ELECTRON BEAM CURRENT DENSITIES)

David G. Howitt*

In this past year investigations have been performed in two specific areas. Firstly the study of the factors which affect the radiosensitivities of various materials and secondly the study of the radiation damage mechanisms in particular materials by direct observation in the electron microscope.

In order to accurately assess the magnitude of the beam current density in an electron microscope a Faraday cup has been constructed which is capable of measuring a sample of the electron intensity distribution in the final image plane with an accuracy of better than 99 percent for currents above $\sim 10^{-15}$ amperes/cm^2/sec. This corresponds to a current of 10^{-25} amperes/cm^2/sec at the specimen when the electron microscope is operated at 100,000 times magnification.

This device has also been used to calibrate the efficiency of a lithium drifted silicon detector, which is commonly used as an electron detector in similar application. The collection efficiency of this detector and its variation with incident intensity is shown in Fig. 1.

In the study of the radiation damage mechanism through direct observation in the electron microscope a study of these effects is being performed upon copper phthalocyanine using conventional minimal exposure techniques. The present experiments indicate the non-uniform degradation of the low resolution structure as typified by Fig. 2 which is an image from the $\{20\bar{1}\}$ lattice planes (11.8Å).

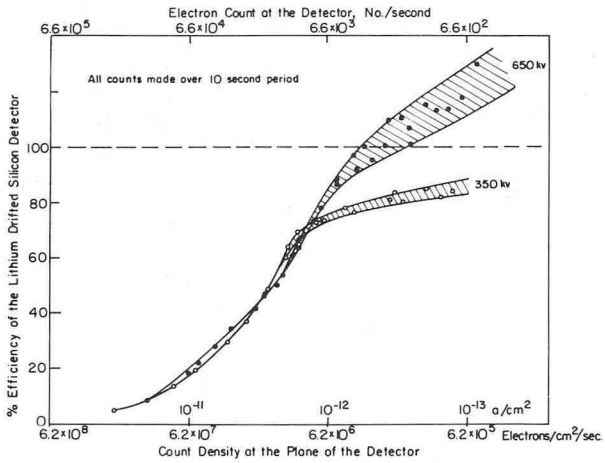

Fig. 1. The relation between the efficiency of the lithium drifted silicon detector and the electron incidence measured by it. The conversion from electron density at the detector to the detectors actual count rate is for the defining aperture used (0.0368 cms diameter).
(XBL 748-7104)

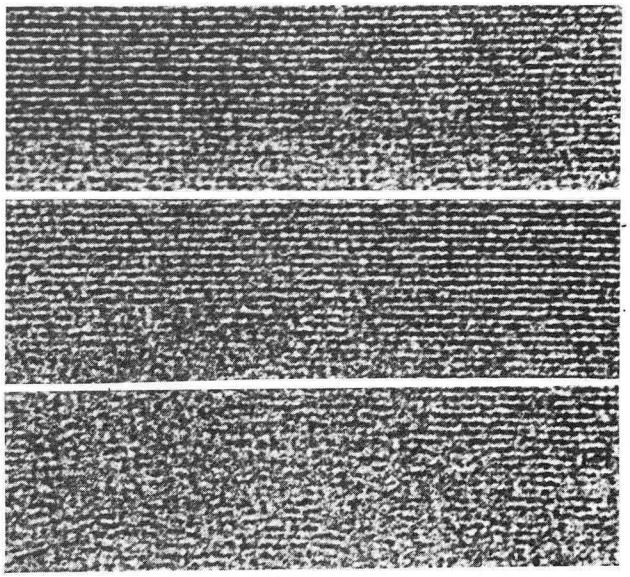

Fig. 2. The effect of continued electron exposure to the lattice images from the $\{20\bar{1}\}$ planes (11.8 Å) of β copper phthalocyanine. The lowest exposure is associated with the topmost picture.
(XBB 743-2157)

At resolutions greater than this we approach the calculated resolution limit of this material (∿3Å)[1] and hence are unable to study the sequential destruction of these images. Lattice images showing the effects of radiation damage at higher resolution have been obtained and are typical of Fig. 3 showing the 5.18Å {102} lattice fringes.

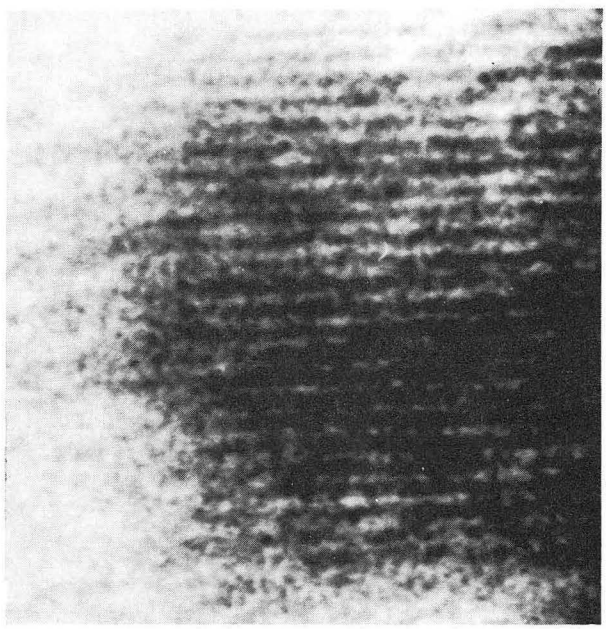

Fig. 3. Lattice images from the {102} planes (5.18Å) of β copper phthalocyanine. (XBB 744-2158)

---

* M.S. thesis LBL-3180

1. R. M. Glaeser, J. Ultrastructure Research, 36, 466 (1971).

4. THEORETICAL AND EXPERIMENTAL ANALYSIS OF CRYSTAL DEFECTS WITH PARTICULAR EMPHASIS TO SILICON

Lih-Juann Chen*

Electron micrographs obtained at high voltages and computed defect image intensity profiles (by solving many-beam dynamical equations of the theory of electron diffraction contrast) have been used to determine the best imaging conditions for small loops and closely spaced dislocation dipoles in systematic reflection conditions. Two practical examples of contrast analysis are described.

In the first, it is shown how the nature of stacking faults (intrinsic or extrinsic) can be found from the contrast of dark field images formed in 1g when the 2g systematic condition is satisfied. The contrast is high if the phase factor $\alpha = -2\pi/3$ and considerably lower when $\alpha = +2\pi/3$. This is a general method and does not have the limitations of current methods of analysis, unless defects are very small ($\ll$ the extinction distance).

In the second example, further exploration is made of the improved resolution that can be obtained for diffraction contrast at defects such as dislocations by lowering the effective extinction distance, e.g. by dark field weak-beam, or bright field high order reflection imaging. The methods have been applied to defects in boron implanted silicon in which, for the first time, dissociated loops have been resolved. From the separation of the partials, the stacking fault energy is estimated to be 45 ± 6 ergs/cm^2 (isotropic elasticity) or 51 ± 7 ergs/cm^2 (anisotropic elasticity theory).

The intrinsic stacking fault energies of four diamond cubic structure elements and eleven zincblende structure compounds have been calculated by the pseudopotential method to second order perturbation approximation. All the calculated stacking fault energies are positive indicating that the method applies better to open structure crystals than close-packed ones, as it gives negative values for some fcc metals. Also from comparison with the available experimental data, the agreement is always to the same order compared to one to two order discrepancy between experimental and theoretical values obtained by hard sphere models.

---

*Ph.D. thesis LBL-3179

5. RESEARCH PLANS FOR CALENDAR YEAR 1975

Gareth Thomas

Long Range Plans - National Center

The major new program is a proposal for the establishment of a National Facility for High Resolution High Voltage Electron Microscopy as has been outlined in detail separately. The Facility will be designed to carry out interdisciplinary research (materials, solid state physics and chemistry, biology; with special emphasis on energy and environment-related problems) and high level training of scientists utilizing the most advanced and sophisticated electron optical instruments and theory so as to push the resolution of structure to the atomic level. It is planned that the facility be available on a national and international basis.

Research Topics

a. Structural Steels: Alloy Design

i) Fe/Cr/C steels: The major emphasis will be on improving the toughness of the Fe/Cr/C type steels by improving the heat treatment processes to control grain size and retained austenite.

ii) Low carbon steels: The interest here is in improving the mechanical properties (strength and ductility) of steels for use in transportation e.g. automobiles. An alloy design program (low alloy, low carbon steels) for improving strength so as to need less material (hence giving fuel savings) for steels in the transportation industry (especially automobiles) is presently being launched.

iii) The program on the effects of boron on the hardenability, strength and fracture characteristics of structural 0.3%C steels should be completed in 1975.

b. Phase Transformations

i) Ceramics - Electronics: Details of the phase transformations possible in lithium ferrites will be worked out so as to obtain two-phase microstructures for potential improvements in magnetic properties (e.g. coercive force). We also intend to study commercial ferrites.

ii) Refractory ceramics: A structure-properties program has been initiated on silicon carbide which has potential applications for turbines. This will involve detailed studies of defects, polytypes and phase transformations using high resolution microscopy and analysis of plastic deformation and fracture characteristics.

iii) Spinodal transformations: A study of the fracture characteristics associated with intergranular embrittlement in coarsened Cu-Ni-Fe alloys and its relationship to the grain boundary precipitate morphology. A new system of commercial interest as a structural alloy viz. Cu-Ni-Cr will be studied to establish structure-property relations. In particular lattice imaging will be utilized to characterize composition amplitude variations.

iv) Lattice imaging of ordered alloys. Structure and irradiation effects.*

This program will be continued and expanded to study in situ in the high voltage electron microscope the effect of radiation damage on several sro and lro alloy systems at various

electron energies and temperatures. Lattice imaging will be utilized to characterize the damage in detail.

c. Irradiation Damage - Organic Crystals†

High resolution lattice imaging will be utilized to investigate the mechanism of decomposition of organic crystals as a result of electron irradiation damage. This damage is a fundamental limiting factor in resolving molecular structure.

---

*(partial support from NSF)

†(partial support from NIH)

6. 1974 PUBLICATIONS AND REPORTS

Gareth Thomas and Associates

Journals

1. W. Wu, L.-J. Chen, J. Washburn and G. Thomas, Indexing of Diffracting Planes Using the Kikuchi Pattern, J. Appl. Phys. 45, 563-566 (1974) (LBL-1811).

2. S. K. Das and G. Thomas, The Metastable Phase Ni_2Mo and the Initial Stages of Ordering in Ni-Mo Alloys, Phys. Stat. Sol. (a) 21, 177 (1974) (LBL-1868).

3. R. J. Livak and G. Thomas, Loss of Coherency in Spinodally Decomposed Cu-Ni-Fe Alloys, Acta Met. 22, 589-599 (1974) (LBL-1842).

4. Glen Stone and Gareth Thomas, Deformation Induced Alpha and Epsilon Martensites in Fe-Ni-Cr Single Crystals, Met. Trans. 5, 2095-2102 (1974) (LBL-1853).

5. K. Schneider, R. Sinclair and G. Thomas, Lattice Imaging of Ordered Alloys, 8th International Congress on Electron Microscopy, Canberra, 1974, Vol. I., 520 (LBL-3173).

6. R. Sinclair and G. Thomas, Lattice Image Contrast of Ordered Domains in Cu_3Au, Proc. 32nd Ann. Electron Microscope Society of America, St. Louis, Missouri (edited by C. J. Arceneaux) Claitors Publishers, Baton Rouge, La., 500 (1974) (LBL-2710).

7. S. K. Das and G. Thomas, On Structural Interpretation of Short Range Order, Proc. International Symposium on Order-Disorder Transformations in Alloys, September 1973, Tubingen, Germany (editor Hans Warlimont), Springer-Verlag, Berlin, 332-343, (1974) (LBL-2285)

8. L.-J. Chen and G. Thomas, Applications of Many Beam Systematic Diffraction Contrast in High Voltage Transmission Electron Microscopy, Phys. Stat. Sol. (a) 25 193-294 (1974) (LBL-2738).

9. G. Thomas, Some Applications of the Berkeley 650 kV High Voltage Electron Microscope in Materials Science, 32nd Annual Proc. Electron Microscope Society of America, St. Louis, (C. J. Arceneaux), Claitors Publishers, Baton Rouge, La., 294-295, (1975) (LBL-2711)

10. G. Thomas, V. Zackay, E. Parker and J. Morris, The Applications of Materials Science to the Design of Engineering Alloys, J. Mat. Science and Engineering 16, 201-221 (1974) (LBL-2261).

11. O. Van der Biest and G. Thomas, Cation Stacking Faults in Lithium Ferrite Spinel, Phys. Stat. Sol. (a) 24, 65-77, (1974) (LBL-2571).

12. G. Thomas, Some Applications of High Voltage Electron Microscopy to Inorganic Materials, High Voltage Electron Microscopy, P. R. Swann, C. J. Humphreys and M. J. Goringe, Eds., Academic Press 223-229 (1974) (LBL-1899).

13. W. Worthington, T. Kosel and R. Sinclair, A New 1000°C Double Tilt Stage for the Hitachi 650 kV Microscope, Proc. 32nd Ann. Electron Microscope Soc. of America, St. Louis, Missouri (edited by C. J. Arceneaux) Claitors Publishers, 442 (1974) (LBL-2587 Rev.).

14. *R. Gronsky, Transmission Electron Microscopy Studies of Grain Boundary Precipitation in Spinodally Decomposed Cu-Ni-Fe Alloys, Proc. 32nd Annual Electron Microscopy Society of America, St. Louis, Missouri, (edited by C. J. Arceneaux) Claitors Publishers, 498 (1974) (LBL-2584).

15. L.-J. Chen and L. M. Falicov, Pseudopotential Calculation of the Stacking Fault Energy in Diamond, Germanium and Gray Tin, Phil. Mag. 29, 5 (1974) (LBL-2594).

16. L.-J. Chen and K. Seshan, High Resolution Imaging in Bright and Dark Field at High Voltages, Proc. 32nd Annual Electron Microscope Society of America, St. Louis, (edited by C. J. Arceneaux) Claitors Publishers, 356-357 (1974) (LBL-2712).

---

*EMSA Student Fellowship Award

LBL reports

1. O. Van der Biest, Lattice Defects in Spinels, (Ph.D. thesis) LBL-2786, July 1974.

2. G. A. Stone, The Crystallography and Structure of Deformation Induced Epsilon and Alpha Martensite in Fe-Ni-Cr Single Crystals, (Ph.D. thesis), LBL-1800, Sept. 1974.

3. L.-J. Chen, Theoretical and Experimental Analysis of Crystal Defects with Particular Emphasis to Silicon, (Ph.D. thesis), LBL-3179, Sept. 1974.

4. R. W. Miller, The Structure and Mechanical Properties of Lower Bainite in Fe/4Cr/0.4C Alloy (M.S. thesis), LBL-3104, Sept. 1974.

5. M. Okada, Phase Transformations in Ordered, Spinodal Cu-Mn-Al Alloys, (M.S. thesis), LBL-3176, Oct. 1974.

6. R. Gronsky, Discontinuous Coarsening During Aging in Spinodally Decomposed Cu-Ni-Fe Alloys, (M.S. thesis), LBL-3134, Oct. 1974.

7. D. J. Howitt, The Measurement of Radiation Damage in Organic Materials in the Range of Electron Energy Between 200 KeV and 650 KeV, (M.S. thesis), LBL-3180, Dec. 1974.

8. F. S. Mirmirani, Structure and Mechanical Properties of Cu-Mn-Al, (M.S. thesis), LBL-2598, April 1974.

9. D. J. Rowcliffe and G. Thomas, Structure of Non-Stoichiometric TaC, (Mat. Sci and Eng. - In Press), LBL-2588, Aug. 1974.

10. O. Van der Biest and G. Thomas, Identification of Enatiomorphism in Crystals by Electron Microscopy, (Acta Cryst. - In Press), LBL-2773, June 1974.

11. P. Rao and G. Thomas, Interstitial Order and Embrittlement in Ta-C Alloys, (Acta Met. - In Press), LBL-2570, Feb. 1974.

12. R. Sinclair and G. Thomas, Antiphase Domains and Superlattice Spot Splitting in Cu_3AuI, (J. Applied Cryst. - In Press), LBL-2731, May 1974.

13. G. Thomas, Some Applications at Berkeley and Possible Future Trends of High Voltage Transmission Microscopy, (Electron Microscopy: Physical Aspects - In Press J. Wiley and Sons), LBL-2274.

14. R. Clark and G. Thomas, Design of Strong Tough Dislocated Martensitic Fe-Mo-C Steels, (Met. Trans. - In Press 1974), LBL-2504, Feb. 1974.

15. K. Seshan, L.-J. Chen, G. Thomas, Contrast and Resolution of Small Dislocation Loops in High Voltage Electron Microscopy, (Phys. State. Sol. - In Press), LBL-1164, Oct. 1974.

16. R. Sinclair, K. Schneider, G. Thomas, Analysis of Ordering in Cu_3Au Utilizing Lattice Imaging Techniques, (Submitted to Acta Met.), LBL-3194, Nov. 1974.

17. O. Van der Biest and G. Thomas, The Order-Disorder Reaction in Lithium Ferrite, (Invited Contribution to Symposium on Mineralogy to be published by Springer-Verlag, 1975), LBL-3510, Nov. 1974.

18. N. B. Rao and G. Thomas, Design of Fe/4Cr/0.4C Martensitic Steels Eliminating Quench Cracking, (Submitted to Nature), LBL-3522, Dec. 1974.

19. R. Gronsky and G. Thomas, Discontinuous Coarsening of Spinodally Decomposed Cu-Ni-Fe Alloys, (Submitted to Acta Met.), LBL-3523, Nov. 1974.

20. W. Worthington, R. Sinclair and G. Thomas A 1000°C Tiltable Specimen Holder for the 650 kV Microscope, LBL-2587, March 1974.

F. HIGH STRENGTH MATERIALS

Victor F. Zackay and Earl R. Parker, Principal Investigators

Introduction. Because this summary is the last one being prepared under AEC sponsorship it is, perhaps, appropriate that some remarks be made regarding our research program in this transition period from AEC to ERDA. In the past dozen years, we have endeavored to discover some of the principles of the quantitative design of alloys. Because of the complexity and size of this task, we have confined our research to certain aspects of the overall problem. These research focal points have been: (1) the elucidation of the detailed relationship between structure (defect, crystal and microstructure) and mechanical properties (strength, ductility and fracture toughness); and (2) the formulation and implementation of a long range program to study the thermodynamics, kinetics, and alloy theory of complex systems. Almost all of our work has been on ferrous systems. The reasons are many; however, two are of overriding importance. These are: (1) iron and its alloys are the most important technological metals; and, (2) virtually all of the phase transformations of importance to alloy design can be readily studied in these systems--from both the theoretical and experimental points of view. Some of the highlights of this work done in the past year are reported below.

In the past six months, considerable thought has been given to the new directions that will be taken relevant to the mission of ERDA. Although at the time of the writing of this report, it was too early to elaborate these new directions in the detail and specificity that is desirable, some tentative goals can nevertheless be indicated. As a direct consequence of our past research, it is felt that some ferrous alloys, when appropriately modified, might prove to be potentially useful in energy-related problem areas. For example, certain Fe-Ni-Ti alloys with improved high temperature properties (700°-800°C range), will be evaluated as candidates for cladding of the fuel elements of the fast breeder reactor. This work is being done in collaboration with personnel of the Pacific Northwest Laboratories of Battelle Institute. Another new program has as its long range purpose, the exploration of the potential of low alloy high strength steels for use in heavy wall nuclear reactor pressure vessels. The immediate objective will be to exploit the unusual combination of strength and toughness in steels containing retained austenite. The unusual mechanical properties demonstrated by high Mn (16 to 20%) ferrous alloys suggest it as a potential substitute, in some applications, for the austenitic Fe-Ni-Cr Alloys now so commonly employed. Studies in the coming year will include efforts to further improve the mechanical properties of ternary Fe-Mn-Cr alloys and to improve the corrosion resistance of ternary and quarterary alloys.

A major research effort, now being planned, has no direct association with the research activities of past years. This program will be concerned with the elevated temperature behavior (above 1000°C) of materials in extremely hostile environments. Basic studies of the erosion and corrosion mechanisms of selected materials will be investigated with emphasis on environments that are of relevance to energy conversion devices and processes. These and other entirely new directions of research will be further developed in the coming year.

1. AN INVESTIGATION OF BAINITE TRANSFORMATION IN MEDIUM CARBON LOW ALLOY STEELS*

B. Naga Prakash Babu

The effects of small additions of common alloying elements (C, Ni, Cr, Mn, Mo and Si) on the kinetics of the bainite reaction in 4340 steel were studied. The 4340 steel was selected as a base because it had the necessary pearlitic hardenability and this enabled studies of the bainite reaction to be made without interference from the proeutectoid or pearlite reactions. A rapid magnetic permeability method was developed to facilitate this investigation. It consisted of quenching the sample from an austenitizing temperature to a subcritical temperature in an isothermal bath which was held within the field of an inductor coil. The increase in permeability accompanying austenite decomposition increased the inductance of the coil, and this changed the resonant period of oscillation of the circuit. An automatic continuous recording of the period provided a convenient and accurate method for following the austenite decomposition. Computer aided methods were used to analyze the isothermal reaction data and to plot the time-temperature-transformation (TTT) diagrams.

An acceleration of the bainite reaction just above the M_s temperature gave an S-shaped curve for the bainite reaction in all the steels studied. In some of the steels, separate C-curves for the upper and lower bainite were observed in the initial stages of transformation, but these overlapped in the later stages. All the alloy additions (wt%) except additions of Mo increased the incubation times for bainite reaction. All the alloying elements except molybdenum shifted the bainite curves to longer times and lowered the kinetic B_s and B_f temperatures. Molybdenum, when added alone, accelerated the bainite reaction and raised the B_s and M_s temperatures, but when added together with Ni or Cr, retarded the bainite reaction. Manganese, up to 2% addition was more effective than Ni or Cr in improving the bainite hardenability. The effect of 2% alloy addition was not equal to 2 times the effect of 1% addition. The ratios of times for 5% transformation for 2%

vs. 1% additions of Ni, Cr and Mn are 1.3, 15.5 and 20 respectively. The effect of combined additions on bainite hardenability was not linear, but mixed additions had an additive effect in lowering the B_s temperature. An equation was derived to calculate the B_s temperature directly from the composition.

In 4340 and 4340 modified with Ni, Cr, Mn and Mo, a distinct change in the experimental activation energy of decomposition occurred around 350°C. This indicates that the initial transformation product may change from upper bainite to lower bainite, or vice versa, at about 350°C. Transmission electron microscopy studies of the morphology of bainite in 4340 + 0.1%C steel showed that mixed bainites formed in the temperature range where the two C-curves of upper bainite and lower bainite overlap. Thus, depending on the transformation temperature, upper bainite may form first followed by lower bainite or vice versa. The classical forms of bainite containing carbides were formed in 4340 + 0.1%C steel. G. Lai (private communication) has shown the upper bainite that formed in silicon modified steels were devoid of carbides.

Partial transformation bainite produced significant amounts of retained austenite in all the steels studied, with Si modified steels showing considerably larger amounts of retained austenite. For the same carbon content, the amount of retained austenite obtained at any particular reaction temperature increased with the increase in silicon content and for the same silicon content, it increased with increasing carbon content.

---

*Abstract from LBL-2772

2. ELEVATED TEMPERATURE PROPERTIES OF NON-CARBON CONTAINING FERRITIC ALLOYS STRENGTHENED BY A LAVES PHASE

M. Shanthidas Bhat, Satbinder Singh and Dilip Bhandarkar

a. Fe-Ta-Cr-Mo Alloys

The effect of different heat treatments on the elevated temperature properties of an Fe-Ta-Cr-Mo alloy (nominal composition Fe-1 at% Ta-7 at% Cr-0.5 at% Mo) was investigated. Preliminary studies[1] had shown that the stress-rupture strength of the above alloy at 1100°F (593°C) was equal to that of greek Ascaloy, but lower than that of 0.3C-1Cr-1Mo-0.25V steel and 422 stainless steel. The particular heat treatment given to the alloy consisted of a solution treatment at 1350°C for one hour followed by a hot water quench. An aging treatment at 700°C for one hour was followed by the spheroidization treatment[1] at 1100°C for two hours. It was, however, shown that the creep strength in terms of stress for a creep rate of 1×10^{-4}%/hr at 1100°F (593°C) was better for the FeTaCrMo alloy as compared to the stress listed above. Further testing at 1200°F (649°C) revealed that the FeTaCrMo alloy had not only better creep strength but also stress rupture strengths equivalent to those of the 422 stainless steel. (See Fig. 1) The results of the study are shown in Table I.

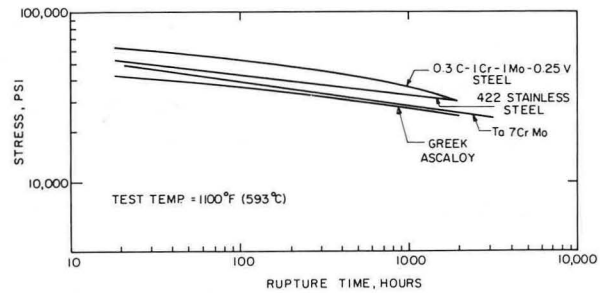

Fig. 1. Plot of stress vs. rupture time for alloy Ta-7Cr-Mo and some commercial ferritic steels. (XBL 751-5544)

The effect of varying the spheroidization treatment by holding for the same time at different temperatures on the stress rupture properties of the FeTaCrMo alloy at 1200°F (649°C) is shown in Table II. It was observed that the higher the temperature of holding in the spheroidization range (for the same time at temperature), the higher was the rupture strength. The results also indicated that at the temperature of the nose of the $\alpha\rightarrow\gamma+Fe_2Ta$ transformation[1] (1020°C) longer times at temperature resulted in lower rupture strengths.

The influence of widely differing microstructures on the stress-rupture properties was also studied. A lamellar structure was obtained by cooling a specimen directly from the solution treatment temperature of 1020°C, the temperature corresponding to the nose of the $\sigma\rightarrow\gamma+Fe_2Ta$ transformation, and then air cooling to room temperature. A spheroidized microstructure was obtained in the usual way[1] by heating to 1020°C. In both treatments, the time of holding at 1020°C was 30 minutes. Table II gives the results of this study. It can be seen that the lamellar structure had a higher rupture strength.

b. Fe-Ta-Cr-W/Fe-Ta-Cr-W-Mo Alloys

The effect of W on improving the high temperature strength in ferritic steels has shown to be similar to that of Mo on an atomic basis.[2] Although some investigators[3] had shown that the combined effect of 0.5% Mo-0.5%W produced greater creep strength than 1.0% Mo or 1.0%W alone, other investigators[2] were not able to confirm this finding. It was of interest to investigate this problem with respect to the high temperature strengthing effects of W and Mo in ferritic alloys strengthened with a Laves phase.

An investigation was initiated with two alloys of nominal composition Fe-1at%Ta-7at%Cr-0.5at%W and Fe-1at%Ta-7at%Cr-0.5at%W-0.5at%Mo. The basic phase transformations involved in these alloys were similar to those in the FeTaCrMo alloy. The solution treatment temperature was found to be 1300°C with an aging treatment of 90 minutes at 700°C resulting in peak hardness. The $\alpha\rightarrow\gamma+Fe_2Ta$

Table I. 1000 hour rupture stress and stress for a creep rate of 1×10^{-4} pct/hour for alloy Ta7CrMo and some commercial ferritic steels.

Alloy	1000 Hour Rupture Stress (psi)		Stress for a Creep rate of 1×10^{-4}pct/hour		Reference
	1100°F(593°C)	1200°F(649°C)	1100°F(593°C)	1200°F(649°C)	
Ta7CrMo	29,000	14,000	26,000	10,000	1
0.3C-1Cr-1Mo-0.25V Steel	36,000	*	**	*	4
Greek Ascaloy 0.15C, 0.40Mn, 0.30Si, 13Cr, 2Ni, 3.0W	27,500	*	**	*	4
422 Stainless Steel 0.2C, 0.65Mn, 0.5Si, 12Cr, 0.75Ni, 1.0Mo, 1W, 0.3V	33,800	15,000	19,000	*	4,5

*No values quoted for 1200°F (649°C)
**No values quoted for 1100°F (593°C)

Table II. The effect of various heat treatments on the rupture time of alloy Ta7CrMo at 1200°F(649°C) and a stress of 17,000 psi.

Heat Treatment	Rupture Time (Hours)
Solution heat 1350°C, 1h(S·T) → Hot Water quench (HWQ) → Age 700°C, 1h(A) → Air Cool (A.C) → Spheroidize (S) 960°C, 2h.	30.0
S·T → HWQ → A → AC → S(1020°C, 30 mins)	39.0
S·T → HWQ → A → AC → S(1020°C, 2L)	68.1
S·T → HWQ → A → AC → S(1100°C, 2L)	326.4
S·T → 1020°C, 30 mins → AC	161.2
S·T → 1020°C, 2h → AC	64.0

transformation, used for the spheroidization treatment, exhibited C-curve kinetics similar to the FeTaCrMo alloy; the nose of the curves for both the W and W-Mo alloy was located at 1000°C.

It was possible to vary the interparticle spacings by holding specimens for different times at the spheroidization temperature. Investigations are underway to study the effect of particle size and spacing on the creep properties of these alloys. The synergestic effect of W-Mo on the creep properties will also be studied.

c. Fe-Nb-Cr-Mo Alloys

The substitution of niobium for tantalum in the FeTaCrMo alloy was considered for two reasons (a) niobium gives a higher volume fraction of precipitate compared to tantalum and (b) niobium is less expensive than tantalum. A ferritic alloy containing Nb, Cr and Mo was designed for an investigation of its stress rupture properties. The solution treatment has been determined to be about 1300°C and aging at 650°C has resulted in a significantly higher hardness compared to the FeTaCrMo alloy. Heat treatments for the Nb alloy are being optimized to impact good stress rupture properties.

---

1. Manjeshwar Shanthidas Bhat, Phase Transformation Characteristics and Creep Properties of a Laves Phase Strengthened Fe-Ta-Cr-Mo Alloy, (M.S. thesis), April 1974, LBL-2277, University of California, Berkeley, California
2. A. E. Powess, Trans. AIME 208, 1373 (1956).
3. E. W. Colbeck and J. R. Rait, Creep Resistant Ferritic Steels, Special Report No. 43, 1951, Iron and Steel Institute, London, p. 107.
4. Metals Handbook, Vol. 1, American Society of Metals, Ohio 1968.
5. F. J. Clauss: Engineers Guide to High Temperature Materials, Addison and Wesley Publishing Co., Inc., Massachusetts, 1971.

3. THE DESIGN OF ALLOYS WITH MINIMAL SWELLING PROPERTIES ON SUBJECTION TO IRRADIATION DAMAGE

Robert A. Clark

The goal of this project is to design alloys with minimal swelling upon irradiation for potential use in the LMFBR and CTR programs. Two approaches are being followed, namely (a) work on a series of Fe-Ni-V, Mo-C alloys has commenced with the intention of duplicating certain beneficial microstructures found in the Fe-Ni-Ti system, and to stabilize these microstructures with either molybdenum and vanadium carbides, and (b) a powder metallurgical approach to the problem of void formation and swelling in austenitic stainless steels. A study is currently underway of 304L and 316L stainless steel prepared using powder metallurgy techniques. The novel approach of adding glass beads to these powder compacts is being attempted, and their effect on microstructure and mechanical properties evaluated. Since glass is supposed to act as a getter for helium, void nucleation in reactors, which is currently thought to be activated by the helium present as a decay product, may be avoided to some extent. Also the use of ultrafine powder allows favoraboe grain size and dislocation microstructures to be developed.

4. DEVELOPMENT OF HIGH STRENGTH/HIGH TOUGHNESS Fe-Cr-Si-(Mo)-C STEELS

Robert A. Clark and Craig Mitchell

Initial work on a series of Fe-Cr-Si-(Mo)-C steels was completed. This program was implemented with the intention of finding a simple, cheap alloy which could serve as a possible substitute for the chemically more complex AISI 4340. Properties of the alloys are expected to be optimized using an isothermal transformation. However, preliminary work involved only a commercially applicable heat treatment consisting of austenitization at 950°C for 1 hr, then quenching into unagitated oil. Mechanical properties examined in this condition were yield and ultimate tensile strength, elongation, K_{IC}, Charpy V-notch impact resistance, and hardness. Standard metallography and scanning electron fractography were also conducted. To date the properties of these alloys seem to be equal or superior to those of 4340, in similarly treated conditions. Preliminary studies indicate that the stress corrosion resistance of the new alloys may be much improved over that of 4340.

In particular the K_{ISCC} of the new alloys, tested in water, was found to be substantially higher than that measured in 4340. Scanning electron micrographs (Figs. 1 and 2) of the

Fig. 1. Mechanism of failure of 4340 steel in water showing area of intergranular cracking. (XBB 751-435)

initiation region of the stress corrosion work indicated that whereas the 4340 steel showed a high proportion of intergranular cracking (Fig. 1) typical of a hydrogen enbrittlement mechanism, such brittle cracking was absent in the Fe-Cr-Si steel (Fig. 2).

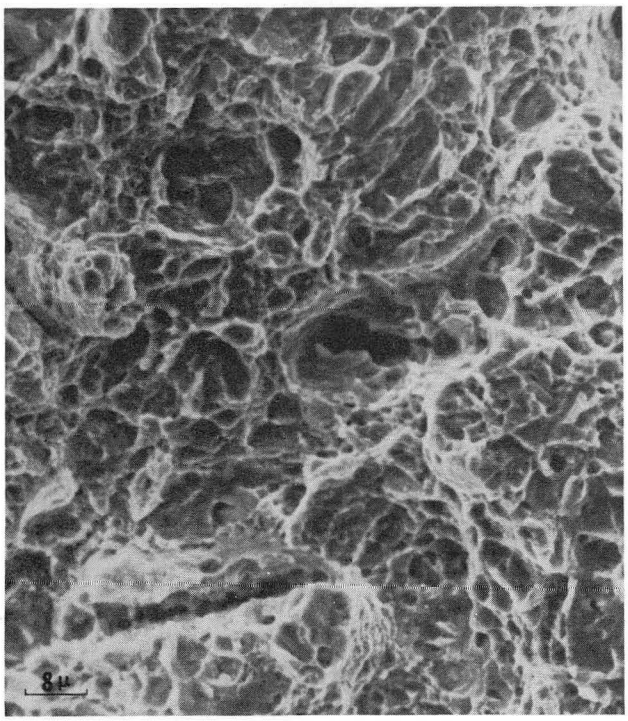

Fig. 2. Mechanism of failure in Fe-Cr-Si steel in water showing microvoid coalescence with no evidence of environmentally induced cracking. (XBB 751-434)

5. FRACTURE TOUGHNESS IN HIGH STRENGTH Fe-Ni-Ti ALLOYS

Benjamin Francis

It is well known that high strength and high fracture toughness (as measured by $K_{IC}/\sigma y$ ratio) rarely occur together. The reason for this is, of course, that at high yield strength levels the tensile stresses at the tip of a sharp crack become very high. At some point these tensile stresses become sufficiently high that fracture occurs by cleavage rather than by ductile tearing. Thus, high fracture toughness in high strength alloys (excluding TRIP steels) may be obtained only by eliminating cleavage initiation sites which can be "activated" at the crack tip stress levels encountered at or near general yield. Essentially, one must eliminate the fracture mechanisms which can cause brittle failure at a crack tip stress level below that obtained at (or somewhat beyond) general yield.

The 18Ni200 (18Ni, 8Co, 3Mo, 0.2Ti, balance Fe) maraging steel is an example of an alloy which has very successfully eliminated such mechanisms. This is clearly demonstrated by the fact that the NDT for this alloy is below -190°C at a yield strength level of ~200 ksi. Other maraging steel systems have been markedly less successful. One such system is the Fe-Ni-Ti alloys. It has been shown[1] that maraging steels in this alloy system exhibit low toughness because of grain boundary precipitation.

If it was possible to eliminate this grain boundary precipitation by a simple heat treatment and/or a variation in the chemical composition of the alloy (i.e. varying the Ni and Ti contents) this alloy would be quite attractive. In the first place it would have an economic advantage over the standard maraging steel because of the elimination of Co and Mo. Secondly, and perhaps more importantly, it would provide a simple system from which it might be possible to learn more about the factors controlling fracture toughness in the maraging type steels, particularly those factors which influence the critical tensile stress for unstable cleavage failure. Ultimately, such information could lead to definition of the maximum fracture toughness obtainable in high strength steels. This would be very useful to know for purposes of alloy design.

There was, in addition, some good evidence that it would be possible to greatly reduce the grain boundary precipitation in the Fe-Ni-Ti system by the proper choice of heat treatment and composition. The evidence for this was that the precipitate formed in this system ($3Ni_3Ti$) did not form in austenite, but only in ferrite. In addition it was known that austenite forms in all the maraging steels in times comparable to the aging times. It therefore seemed that a judicious choice of composition and heat treatment could produce a sufficient amount of austenite at grain boundaries to inhibit or prevent the formation of grain boundary precipitates, and thereby greatly improve the toughness of these alloys. The purpose of this investigation was then to determine whether or not the Fe-Ni-Ti maraging type steels could in fact, when properly processed, attain good fracture toughness at high strength levels.

In the light of the above the Fe-Ni-Ti alloy system has been re-examined and it has been shown that good toughness can be achieved at strength levels up to 200 ksi yield strength, with the proper choice of composition and aging treatment.

The compositions investigated (in wt%'s) were 12Ni-1Ti, 12Ni-2Ti, 16Ni-1Ti, 16Ni-1.5Ti, and 20Ni-1.5Ti. The best properties were obtained in the 16Ni alloys. In the 12Ni alloys it was not possible to eliminate the grain boundary precipitation. In the 20Ni there was considerable retained austenite present (up to ~20%) which reduced the toughness (because of its low yield strength). In the 16Ni-1Ti alloy at a 0.2% offset yield strength (σy) of 180 ksi the best plane strain fracture toughness was estimated to be K_{IC} = 170 ksi$\sqrt{in}$. In the 15Ni-1.5Ti alloy at σy = 200 ksi K_{IC} = 114 ksi$\sqrt{in}$. The Charpy properties for these two alloys were also quite

good and are shown in Fig. 1, along with the Charpy properties of commercial maraging steels.

For these alloys the highest possible aging temperature consistent with achieving the desired strength level was the best aging temperature in terms of fracture toughness. For the 16Ni-1Ti alloy at σy = 180 ksi this temperature was 550°C and for the 16Ni-1.5Ti alloy at σy = 200 ksi it was 600°C. The reason for the improved toughness is that the amount of grain boundary precipitation was greatly reduced at the higher aging temperatures.

Investigations were carried out to establish the relationship between austenite formation at grain boundaries during aging and the amount of grain boundary precipitation. It was found that the austenite, at the higher aging temperatures, was forming at the boundaries at the same rate or faster than the precipitate. This is demonstrated in Fig. 2, which shows the rate of formation of austenite at various temperatures, as determined by a magnetic technique, and compares this rate with the aging response. The presence of the austenite in the grain boundaries during aging definitely inhibits the formation of precipitates on the boundary as evidenced both by the improvement in fracture toughness and by SEM fractography. It is not known whether the austenite is affecting the nucleation or the growth of the boundary precipitate. At the lower aging temperatures the precipitates apparently form on the boundary well before the austenite first appears, and thus the lower aging temperatures have poor fracture toughness.

The relationship between austenite formation on the grain boundary during aging and grain boundary precipitation, that has just been discussed, illustrates a principle which has the potential of being very useful in alloy design. The principle is that it may be possible in some alloys to introduce an "intermediate" phase at a grain boundary which would prevent grain boundary precipitation from occurring. The grain boundary precipitation would be inhibited by the effect of the intermediate phase on either the nucleation or the growth of the boundary precipitate.

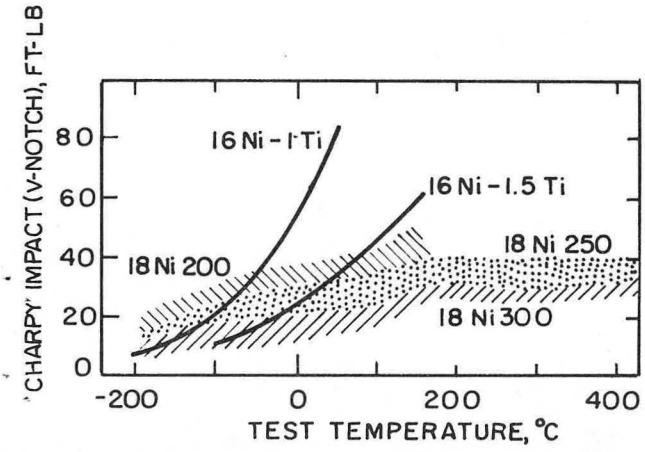

Fig. 1. Charpy V-notch properties of Fe-16Ni-1Ti and Fe-16Ni-1.5Ti alloys compared with three grades of commercial maraging steels. (XBL 7412-7720)

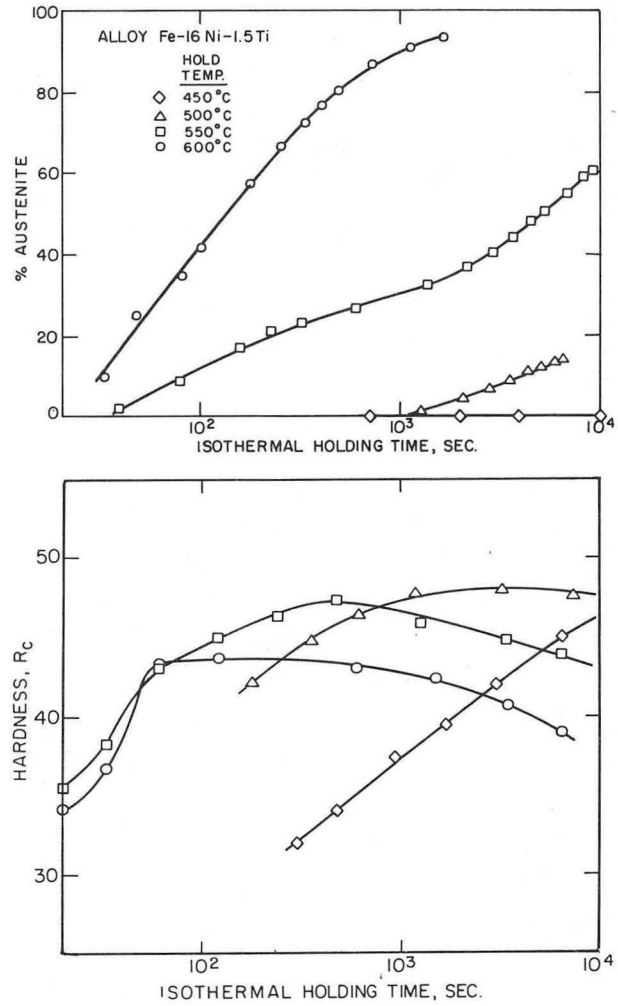

Fig. 2. The isothermal formation of austenite and the aging kinetics at various temperatures. At the higher aging temperatures austenite and Ni_3Ti are forming approximately simultaneously. (XBL 751-5665)

---

1. S. Floreen and G. R. Speich, Trans. ASM 57, 714 (1964).

6. PREPARATION OF METAL-METAL COMPOSITE MATERIALS USING A POWDER METALLURGY

Guy Gettle

A research effort along a different route was initiated with the objective being the development of a material having significantly greater creep strength and thermal conductivity at high service temperatures. The first stage of this undertaking has been the preparation of the component from which the finished material is to be made; this material being a spherical metal substrate particle having a uniform coating of a different metal. Typical metal deposition and "barrel plating"

processes are not suited to the requirements of uniform, nondendritic coatings and controllable deposition rates; thus a different process is being used. We are presently at the point of demonstrating the feasability of using a fluidized bed electrode to bring about the electrodeposition of nickel coatings on copper particles. The fluidized bed electrode consists of a bed of metal particles maintained in a state of agitated suspension by an inward-flowing electrolyte. A "current feeder" (a metal rod or other suitable shape) projects into the bed, through which a current can be passed through the bed and into the electrolyte. If the fluidized bed is made a cathode and a metal salt solution used as the electrolyte, then metal is electroplated from solution onto the particle surfaces.

The substrate used initially in our prototype is a spherical copper particle ranging between roughly 50 to 200 microns in diameter. The nickel coating is plated out of a nickel sulfate-ammonium chloride electrolyte. The optimal system configuration is being studied with respect to flow rate, minimum voltage, cathode-anode placement, electrolyte composition, and the geometry of components in the bed. These parameters relate to obtaining the essential uniform flow and voltage in the bed required for uniform deposition.

Simultaneous to the development of a working prototype of the fluidized bed electrode is the preparation of a mathematical model/computer simulation of phenomena within the particle bed. Development of this model has reached a stage of reasonable and consistent description of current, voltage profiles and deposition within the particle bed.

Operation of the fluidized bed electrode prototype has shown the importance of using a spherical substrate particle and of achieving uniform fluidization properties to obtain good coatings. Selection of a proper electrolyte is important, otherwise dendritic deposition may occur.

The choices of substrate and coating used in the prototype phase were not due to potential engineering application, but instead with regard to favorable electrochemical potential and material availability. For high temperature, high stress conditions, a high melting point, large elastic modulus substrate (not brittle, however) such as nickel or platinum, would be coated with a very ductile, high thermal conductivity layer of a metal whose atoms are of sufficient size to minimize diffusion into the substrate particle.

The preparation of this metal-metal composite involves compacting and sintering the coated particles and then rolling the mass; thus obtaining a continuous matrix of the high thermal-conducting metal with a dispersion of elongated fibers of the high strength metal. Elongation of the fibers would be, desirably, on the order of 100 to 1 to inhibit dislocation movement. The substrate particle would be as small as possible to achieve the maximum concentration of fibers in the matrix. The correct choice of metals for this composite would lead to high fracture toughness and very high directional creep strength. Such a material would also enable the use of simpler cooling systems in many engineering applications, because the thermal conductivity would be much greater than in existing superalloys, or wall materials currently used where liquid metal coolants are used.

7. INFLUENCE OF HEAT TREATMENT AND ENVIRONMENT ON THE FATIGUE CRACK GROWTH RATES IN A SECONDARY HARDENING STEEL

Ronald M. Horn

Investigations of the relationship between microstructure and fatigue crack growth rates in a 0.3C-5Mo secondary hardening steel were concluded. Having established that the fatigue crack growth rates in air vary with microstructure,[1] it was necessary to evaluate the effect of environmental-microstructure interaction. Fatigue tests in a dry argon environment were carried out to do this. Figure 1 shows the fatigue crack growth rates in the dry argon for the as-quenched and 600°C tempering treatments. The broken lines represent the ambient properties. It is clear that moist air environments enhance crack growth rates in the as-quenched steel. This has been repeatedly shown on similar steels. The 600°C tempered material showed less sensitivity to environment, however. The fatigue fracture surface for the specimen tested in dry argon steel showed evidence of intergranular failure modes both in low and high ΔK regions, as had fracture surfaces in an ambient environment.[1] For this microstructure, of unusually poor fracture toughness, the undesirable features dominated environmental effects.

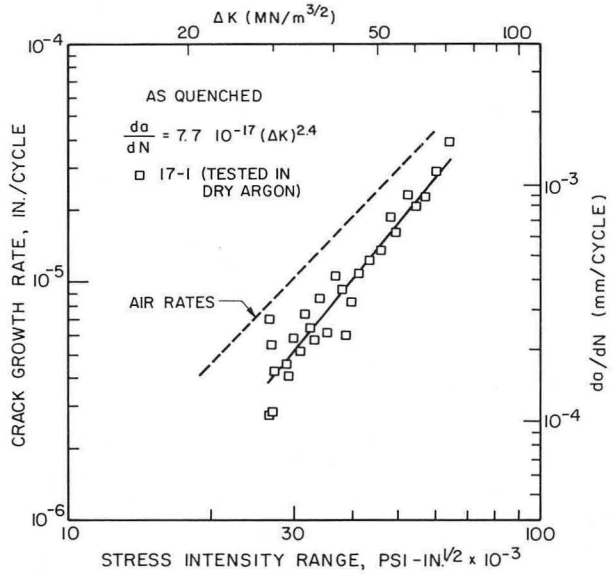

a

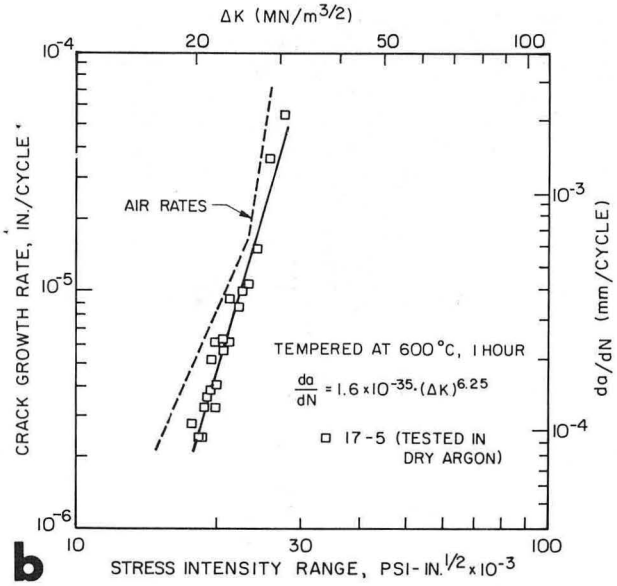

Fig. 1. Fatigue crack propagation rates versus stress intensity range for the 0.3%C-5%Mo steel, carried out in dry argon. (a) Data for as-quenched condition, (b) Data for 600°C tempered condition. (XBL 746-6616, 6617, respectively)

1. IMRD Annual Report, LBL-2299, p. 165-166, April 1974.

8. AN INVESTIGATION OF THE BAINITE REACTION IN Si- AND Al-MODIFIED LOW ALLOY HIGH STRENGTH COMMERCIAL STEELS WITH REGARD TO KINETICS OF THE TRANSFORMATION AND ITS EFFECT ON MECHANICAL PROPERTIES

Gabriel Kohn and M. Shanthidar Bhat

The kinetics of the bainite transformation in modified 4340, 4330 and 300-M steels will be studied with the help of the rapid magnetic permeability technique[1] and dilatometry. In particular the effect of Si, Al and combinations of Al and Si on the extent of austenite retention will be studied.

The correlation between the different microstructures, especially the amount and distribution of carbides and retained austenite, with the mechanical properties (mainly yield strength and fracture toughness) are being investigated.

Test specimen blanks of 4340 steel modified with 1, 2 and 3 wt%Si were subjected to isothermal heat treatments in the bainite range. The heat treatments were similar to those developed by B. N. Babu.[1] Preliminary tests have shown that the fracture toughness versus yield strength band lies in a range that encompasses the maraging steel band.

Although not all the fracture toughness tests yielded valid K_{IC} results in accord with ASTM standards, the deviations from the ASTM requirements were not severe and the tests gave a good indication of the toughness of the isothermally heat treated modified steels.

There was a distinct difference in the mode of crack propagation between the specimens with 1wt%Si and those with 2 and 3wt%Si. In the specimens with 1wt%Si the crack propagation is continuous with increasing load until final fracture. The other specimens exhibit a crack-arrest phenomena where crack propagation is stopped after a short distance and a further increase in load is needed for the crack to propagate. Scanning electron fractography showed that the mode of fracture in both cases was micro-void coalescence and a typical fractograph is shown in Fig. 1. The reasons for the difference in crack propagation is as yet unclear and is being investigated. Some of the test results are shown in Table I (see p. 154).

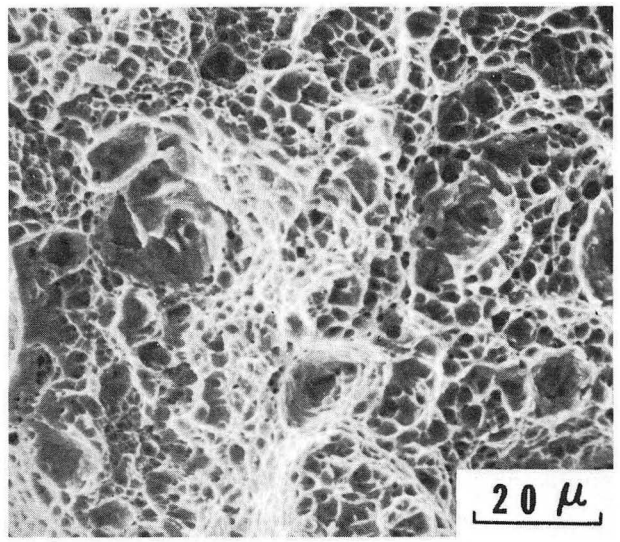

Fig. 1. Fractograph of Specimen No 282 (x1000) showing microvoid coalescence. (XBB 751-705)

1. B. Naga Prakash Babu, An Investigation of Bainite Transformation in Medium Carbon Low Alloy Steels, LBL-2772, Aug. 1974 (D.Eng. thesis).

9. THERMODYNAMICS OF Fe-C-X ALLOYS

Elias Plaza-Meyer

a. Introduction

Accurate knowledge of phase equilibria is a major requirement in the development of new alloys. For ternary or higher order alloys, the conventional metallographic methods of phase diagram determination are too time-consuming and

Table I. Test results of modified 4340 steel specimens.

Si wt%	Spec. No	Aust. Temp. °C	Isothermal Transformation Temp. °C	Time at temperature (min.)	Quench medium	Tempering Temp. for 1 hr. °C	K_{IC} psi-in$^{1/2}$	Y.S. psi .2% offset	U.T.S. psi	$2.5(\frac{K}{\sigma y})^2$	$\frac{P_{max}}{P_Q}$	Valid per ASTM
1	282	900	305	60	air	235	106	196	236	0.7	1.05	✓
1	283	900	314	10	water	235	97.1	194	246	.626	1.07	✓
1	284	900	348	60	air	235	KQ 138	173	213	1.59	1.09	-
2	292	900	305	60	air	235	107.9	184	236	.859	1.02	-
2	293	900	314	10	water	235	87.8	191	258	.528	1.06	✓
3	302	900	305	60	air	235	90.4	172	239	.640	1.15	-
3	303	900	310	10	water	235	79.8	197	258	.410	1.109	✓

expensive. However, experimental information on binary thermodynamics and phase diagrams and phase diagrams and ternary solution thermodynamic data are often available, therefore a thermodynamic model which would allow computation of phase equilibria in ternary and multicomponent alloy systems should be extremely valuable.

b. Thermodynamic Model

For an alloy at atmospheric pressure, the integral free energy of a gram-atom of solution, G_m, can be expressed by

$$G_m = \sum_i x_i \cdot {}^oG_i - T \cdot S^{id} + {}^{\varepsilon}G_m \qquad (1)$$

where x_i represents the atom fraction of component i; ${}^oG_i$ represents the free energy of component i having the same crystal structure as the phase under consideration; S^{id} represents the entropy due to ideal mixing; ${}^{\varepsilon}G_m$ is the excess free energy of solution per gram-atom, and T is the temperature in degrees Kelvin. In what follows all quantities will be expressed in calories per gram-atom.

It has been shown[1] that the certain groups of binary alloys the excess free energy can be accurately expressed by:

$${}^{\varepsilon}G_m^{(binary)} = X_1X_2(A_{12}X_1 + A_{21}X_2) \qquad (2)$$

where the coefficients A_{12}, A_{21} are temperature dependent only. A similar expression can be used to represent the excess free energy in ternary alloys:

$${}^{\varepsilon}G_m^{(ternary)} = X_1X_2(A_{12}X_1 + A_{21}X_2) + X_1X_3(A_{13}X_1 + A_{31}X_3) + X_2X_3(A_{23}X_2 + A_{32}X_3) + X_1X_2X_3 \cdot D \qquad (3)$$

where the term in D takes care of the interactions in the ternary solution.

c. Equilibrium Between Phases

The thermodynamic conditions for equilibrium between two given phases, ϕ_1 and ϕ_2, are given by:

$$\overline{G}_i^{\phi 1} = \overline{G}_i^{\phi 2} \qquad (4)$$

where $\overline{G}_i^{\phi 1}$ represents the partial molar free energy of component i in the phase ϕ_1. Setting

$$S^{id} = -R\sum_i X_i \ln X_i \qquad (5)$$

and using the definition for partial molar quantities we get:

$$\overline{G}_i = {}^oG_i + RT \ln X_i + {}^{\varepsilon}\overline{G}_i \qquad (6)$$

where ${}^{\varepsilon}\overline{G}_i$ is the excess partial molar free energy of component i. The system of Eq. (4) can then be written as:

$$G(i) = RT \ln \frac{X_{i(1)}}{X_{i(2)}} + ({}^{\varepsilon}\overline{G}_i^{\phi 1} - {}^{\varepsilon}\overline{G}_i^{\phi 2}) + ({}^oG_i^{\phi 1} - {}^oG_i^{\phi 2}) = 0 \qquad (7)$$

Here $X_i(j)$ represents the atom fraction of component i in the phase ϕ_1.

The parameters A_{ij} and D can be found by fitting the equations derived from the model to binary phase diagram information and to thermodynamic data, such as activity measurements, for the binary and ternary solutions. The system of Eq. (7) can then be solved by interaction methods using computers.

d. Application to Fe-X and Fe-C-X Alloys

Model parameters have been found for various binary and ternary iron alloys namely (1) the free energy difference between the γ and α phase for pure iron (500 K-1500 K), silicon, aluminum, nickel, cobalt, manganese and carbon; (2) the Aij and D coefficients for the binary systems Fe-C, Fe-Si, Fe-Cr, Fe-Ni, Fe-Co and Fe-Mn; and (3) the Aij and D coefficients for the ternary system Fe-C-Si, Fe-C-Ni, Fe-C-Mn, Fe-C-Cr and Fe-Cr and Fe-C-Co.

e. Para-Equilibrium in Fe-C-X Alloys

In Fe-C-X alloys, if the diffusivity of the component X is very small compared to the diffusivity of carbon, the transformation will proceed under carbon diffusion control only. Local equilibrium of carbon will be maintained across the interface while the ratio of the two substitutional elements (Fe and X) is kept constant across the interface.

The thermodynamic conditions for para-equilibrium in ternary Fe-C-X alloys are given by:

$$\bar{G}_C^{\gamma} = \bar{G}_C^{\alpha}$$

$$\bar{G}_X^{\gamma} - \bar{G}_X^{\alpha} = (\bar{G}_{Fe}^{\gamma} - \bar{G}_{Fe}^{\alpha}) \cdot \frac{X_{Fe}}{X_X}$$

$$\frac{X_{Fe}^{\gamma}}{X_X^{\gamma}} = \frac{X_{Fe}^{\alpha}}{X_X^{\alpha}}$$

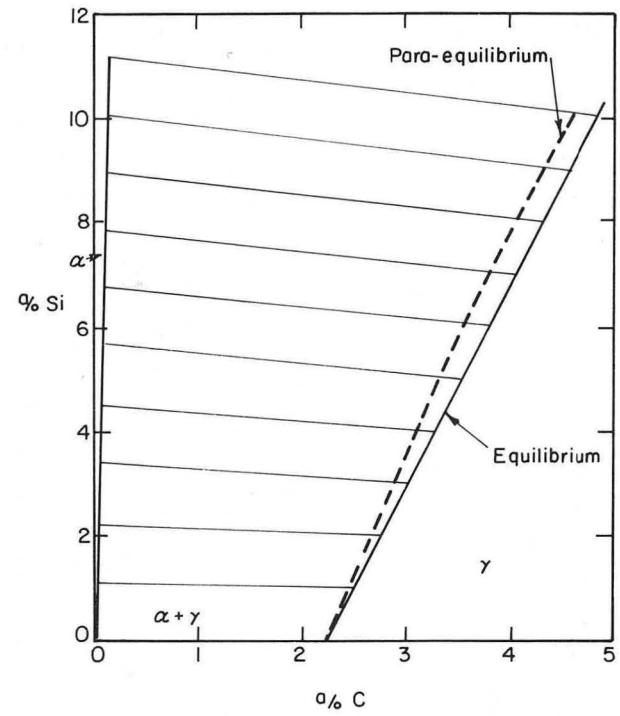

Fig. 2. Computed values of equilibrium and paraequilibrium compositions of α and γ phases in Fe-C-Si alloys at 1030°K. Only tie-lines for equilibrium are shown. Tie-lines for para-equilibrium are nearly horizontal.
(XBL 749-7159)

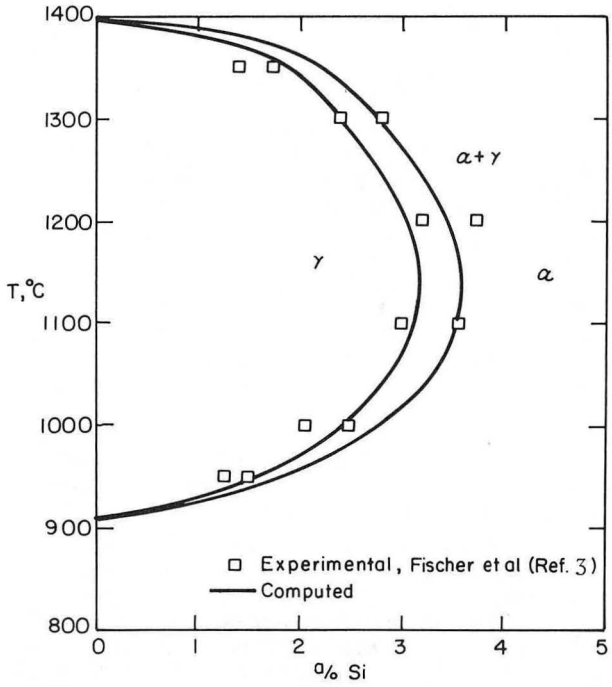

Fig. 1. Experimental and computed values of equilibrium compositions of α and γ phases in Fe-Si alloys at various temperatures.
(XBL 749-7153)

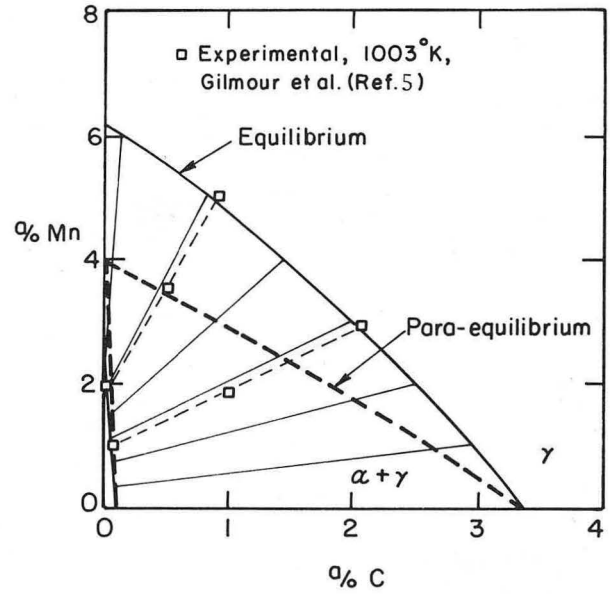

Fig. 3. Computed values of equilibrium and para-equilibrium compositions of α and γ phases in Fe-C-Mn alloys at 1000°K. Only tie-lines for equilibrium are shown. (XBL 749-7170)

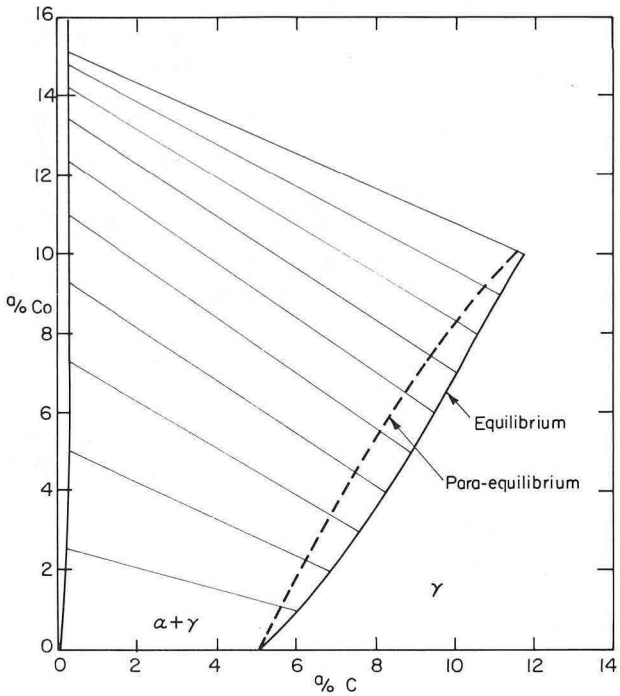

Fig. 4. Computed values of equilibrium and para-equilibrium compositions of α and γ phases in Fe-C-Co alloys at 950°K. Only tie-lines for equilibrium are shown. (XBL 749-7178)

f. Results

Some computed α+γ equilibria in binary and equilibria and paraequilibria in ternary alloys are shown in the following figures. Comparison with experimental values are given.

---

1. L. Kaufman and H. Nesor, Z. Metallkde 64, 249 (1973).
2. R. F. Mehl and C. Wells Trans. AIME 125, 429 (1937).
3. W. A. Fischer, K. Lorenz, H. Fabritius and G. Kalwa, Anch. Eisenhuttenw. 37, 39 (1966).
4. M. Hansen and K. Anderko, Constitution of Binary Alloys (McGraw Hill, N.Y., 1958), 2nd Ed.
5. J. B. Gilmour, G. R. Purdy and J. S. Kirkaldy, Met. Trans. 3, 1455 (1972).

10. CHARACTERIZATION OF BRITTLE CRACK INITIATION IN WELDED A-36 AND A-537 STEELS

Henry Peter Offer

a. Introduction

Numerous brittle fractures of engineering structures fabricated from low yield strength steels have occurred over the past three decades[1-2] and continue to occur despite the existence of several analytical and experimental performance criteria for fracture resistance. A major problem with the existing performance criteria is that engineering structures are often subjected to microstructural, design, fabrication and environmental conditions all of which cannot be accounted for in the performance criteria or in existing test specimens. Some of these conditions which frequently promote brittle fracture are low ductility microstructures, regions of triaxial stress, residual stresses, high strain rates, low temperatures, chemical environments and sharp cracks. Each of these conditions can lead independently to brittle, low energy fracture, and in combination often lead to brittle fracture at average stresses well below material yield strengths.

The purpose of this investigation was to characterize, for use in engineering design, the individual and combined embrittling effects of temperature, microstructure, toughness level and triaxial stress as determined by testing relatively small size sharply cracked fracture toughness specimens of low strength steels. Studies were then made of the fracture toughness of microstructures in the fusion and heat affected zones and in the normalized plate of two welded low strength structural steels. Wedge opening loading (WOL) specimens were machined from 1 in. thick A-36 steel plate and 2 in. thick A-537 steel plate in the transverse direction. These specimens were tungsten-inert gas (TIG) welded in the crack tip area, and were then fatigue cracked to depths corresponding to the three predominate microstructural regions. The effect of temperature was determined by varying the test environment from 23°C to -75°C; the effect of triaxial stress by varying the thickness of smooth faced test specimens and by the use of deep side grooves, and the effect of toughness level by testing steels with different rates of change of toughness with temperature.

b. Fracture Toughness Behavior

i. Normalized plate microstructures--no side grooves. For the A-36 steel normalized plate microstructure, extensive slow crack growth occurred before fast crack propagation for both the 0.750 in. and 1.000 in. thick specimens at 23°C and 0°C. A small amount of slow crack growth occurred for both thicknesses at -40°C, and only crack tip blunting occurred before fast crack propagation for both thicknesses at -75°C, which failed in plane strain conditions. The critical strain energy release rate variation with temperature is plotted in Fig. 1 for these specimens. The very low value of G_c for the 0.750 in. thick specimens tested at 23°C is due to the extensive slow crack growth and corresponding low load at catastrophic failure.

For the A-537 steel normalized plate microstructure, tested at 0.75 in. and 1 in. thicknesses, slow crack growth across the full width of the specimen occurred for both specimen thicknesses at test temperatures of 23°C and 0°C. It was evident that A-537 steel exhibited a higher fracture toughness than the A-36 steel. Further, delamination perpendicular to the fracture surface in the direction of plate rolling was observed in A-537, and this occurred only during

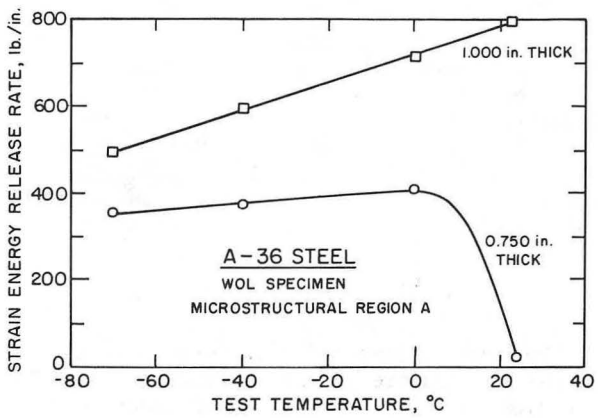

Fig. 1. Variation of critical strain energy release rate with test temperature for 0.75 in. and 1.00 in. thick WOL fracture toughness specimens of A-36 steel in the normalized microstructural condition. (XBL 744-5970)

slow crack growth, being due to the banded microstructure.

ii. Normalized plate microstructures--with side grooves. The amount of slow crack growth before catastrophic fracture was not substantially reduced with the addition of side grooves for A-36 steel, which is evident from a comparison of load-gage displacement records of WOL specimens without and with side grooves having the same ligament thickness.

A-537 steel load-gage displacement records showed the same trends with side grooves in the normalized plate microstructure as the A-36 steel. The use of side grooves did, however, raise the values of G_c at all temperatures tested.

Scanning electron fractographs of A-36 steel in the fatigue crack tip area (Fig. 2) show the

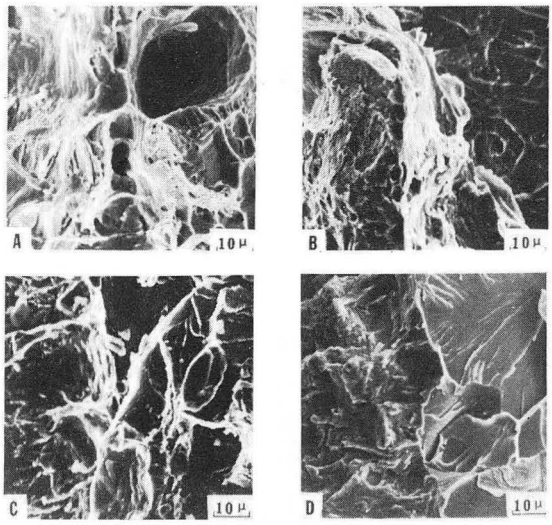

Fig. 2. Scanning electron micrographs of the fatigue crack edge, indicated by arrow, in the normalized plate microstructure of A-36 steel, at temperatures (A) 23°C, (B) 0°C, (C) -40°C and (D) -75°C. (XBB 744-2589)

reduction with temperature in the amount of stretching at the crack tip before crack growth. Essentially, no stretching occurred at -75°C, as evidenced by the abrupt fracture mode change. These fractographs are typical of the four test temperatures for both steels.

iii. Heat affected zone microstructures--with side grooves. The heat affected zone region was found to consist primarily of fine grain size ferrite and pearlite in the A-36 steel and fine grain size ferrite and acicular bainite in the A-537 steel.

The load-gage displacement records for the side grooved A-36 steel WOL specimens tested in this region show a substantial decrease in slow crack growth existed compared to regions further away from H.A.Z. This behavior also existed for A-537 steel except at 23°C, where slow crack growth occurred across the full width of the specimen. Plane strain conditions existed for the side grooved geometries of both steel in region B and -75°C and -40°C. Crack arrest occurred in A-36 steel at 23°C and 0°C and in A-537 steel at 0°C, and was indicated by the darker grey fracture surface typical of ductile tearing.

Tests were also conducted for regions much closer (1mm) from the fusion zone of the weld. The microstructure in this region consisted of large grained proeutectoid ferrite and acicular bainite in the A-36 steel, and large grained feathery bainite in the A-537 steel. In this region, G_c for A-36 steel shows a slight decrease with decreasing temperature, whereas G_c for A-537 steel shows a much larger decrease with decreasing temperature. At 23°C the plastic zone size is large enough relative to the heat affected zone size to prevent fast crack propagation in A-537 steel, but not in A-36 steel.

c. Summary and Conclusions

Conclusions regarding the method of testing for the assessment of the quantitative relationships and the results of the test method are listed below.

1. Slow crack growth is not necessarily reduced in WOL specimens of A-537 steel and A-36 by the addition of deep side grooves, despite the corresponding elimination of large shear tips.

2. A-537 steel shows a higher fracture toughness than A-36 steel as measured by Charpy V-notch and WOL specimens for the temperature range 23°C to -75°C in the normalized plate microstructural condition.

3. Microstructures existing in the HAZ promote brittle crack initiation compared to normalized plate microstructures, if the HAZ size is large relative to the plastic zone size at a crack tip.

4. The use of deep groves improves the resulting value of G_c for specimens of the same ligament thickness by increasing crack tip triaxiality of stress and the corresponding nominal stress required for fast crack initiation.

5. Brittle microstructures at a crack tip are more effective in promoting brittle crack initiation than triaxial stresses produced by deep side grooves in small specimens, especially at low temperatures where the plastic zone size is small.

6. For the ranges of the variables tested, temperature has the strongest effect on brittle crack initiation. At 23°C and 0°C slow crack growth occurred across the full width of several A-537 steel specimens, whereas at -75°C no slow crack growth occurred. At 23°C extensive slow crack growth occurred in A-36 steel specimens, but at -75°C only limited crack tip blunting occurred.

7. Increasing the thickness of WOL specimens without side grooves in the thickness range investigated improves the resulting value of G_c. This effect is attributed to the increase in triaxility of stress at the crack tip and the corresponding average stress at fast crack initiation.

8. Every combination of the variables tested resulted in a mixed state of stress except those combinations including the lowest temperature investigated. Most of the tests at -40°C and all of the tests at -75°C were under plane strain conditions.

9. The amount of slow crack propagation before catastrophic fracture was the most important result associated with altering the variables in the ranges investigated in this study.

---

1. E. R. Parker, Brittle Behavior of Engineering Structures (John Wiley, New York, 1957).
2. W. H. Munse, Brittle Fracture in Weldments in Fracture, H. Liebowitz, ed. (Academic Press, 1969), Vol. 4, p. 371.

11. THE CRYOGENIC PROPERTIES OF Fe-Mn AND Fe-Mn-Cr ALLOYS

Mark J. Schanfein

a. Introduction

Industrial demand for the storage and transportation of cryogenic liquids has brought about research efforts to develop an alloy which exhibits both high strength and toughness at low temperatures. Current alloys in use are either strong with mediocre toughness or tough with low strength. One research effort has been directed towards the development of a strong tough Fe-Ni-Ti alloy.[1] The principal features of this alloy are (1) a low interstitial content and small additions of Ti for gettering the remaining interstitials, (2) small grain size through controlled heat treatments, (3) the presence of noncoherent precipitates (Ni_3Ti) for strengthening, and (4) high nickel contents. This alloy has shown excellent low temperature strength and toughness but the nickel content was approximately 12%. In order to make a lower cost cryogenic alloy, a primary objective of the present investigation was to explore the feasibility of designing Fe-Mn alloys with mixed microstructures for attaining combinations of strength and toughness which approach those of the cryogenic Fe-Ni-Ti alloys.

b. Results and Discussion

The compositions and designations of the alloys studied are listed in Table I. All alloys contained 0.10%Ti and 0.05%Al to inactivate the interstitial, carbon and nitrogen. When these alloys were cooled from the austenite phase a variety of complex microstructures resulted (Fig. 1). The as-quenched structure of low manganese alloys, cooled to -196°C, was entirely bcc, but as the Mn content was increased to about 12% the substructure morphology changes from equiaxed ferrite (α) to lath and plate martensite (α'). Within the 12-20%Mn composition range mixtures of α', ε and austenite (γ) were obtained; the 16%Mn alloy being predominately $\alpha'+\varepsilon$ while that of the 20%Mn alloy being $\varepsilon+\gamma$.

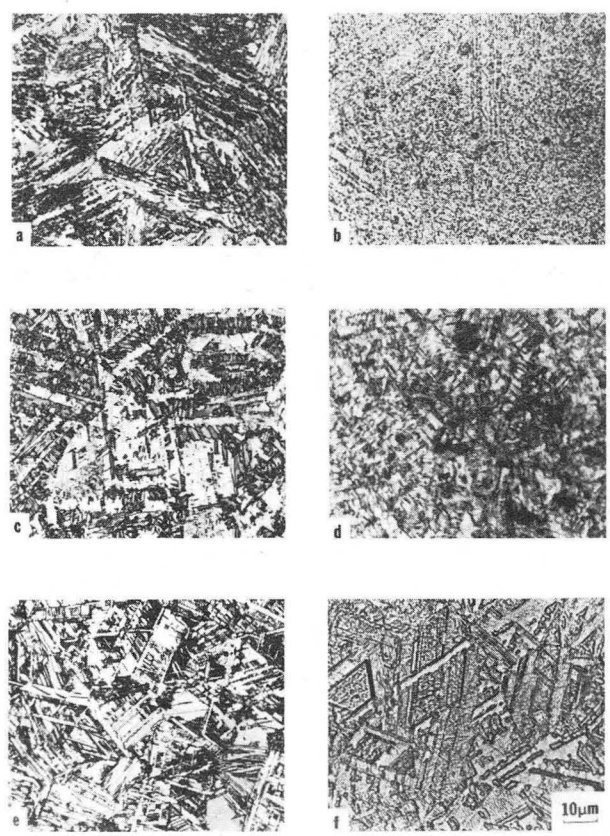

Fig. 1. Optical micrographs of as austenitized 12%Mn (a), 12%Mn-8%Cr (b), 16%Mn (c), 16%Mn-8%Cr (d), 20%Mn (e), and 20%Mn-8%Cr (f) alloys. (XBB 747-4505)

In the alloys containing predominately the bcc α phase manganese additions were observed to raise the ductile-brittle transition temperature (DBTT), but in Fe-Mn alloys without chromium, the formation of both hexagonal ε and fcc γ phases at manganese concentrations exceeding 12% resulted in a decrease in the DBTT. Further increasing amounts of ε in a mixed α-ε microstructure resulted in a decreased yield stress, possibly due to localized flow in the weaker ε phase and a stress induced transformation of ε to α. The yield strength, however, could be raised by increasing the manganese content to 20%, resulting in a mixed ε+γ microstructure (Fig. 2).

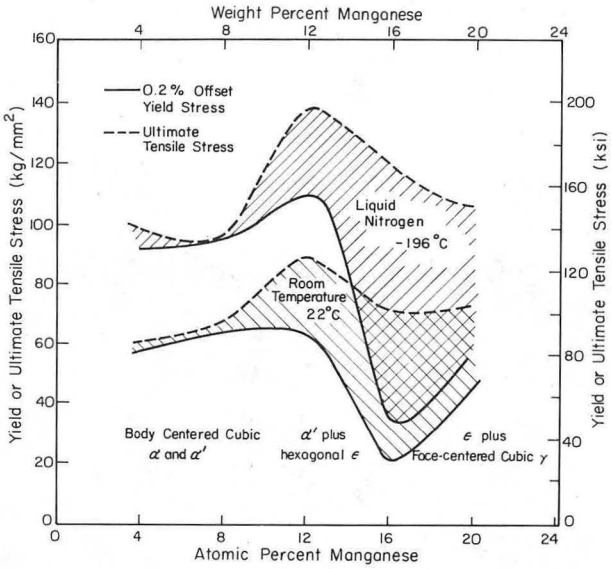

Fig. 2. Yield to ultimate tensile strength at both 22°C and -196°C vs. percent manganese in Fe-Mn alloys. (XBL 745-6257)

Chromium additions of 8% did not cause appreciable changes in the DBTT. In the 12% alloy the chromium addition reduced the yield stress at -196°C by 8%, but increased the fracture toughness by 14%, and shifted the DBTT to a slightly lowered value (Fig. 3). In the case of the 16%Mn alloy, an 8%Cr addition nearly doubled the yield strength at the same DBTT while lowering the CVN shelf energy and reducing the K_{Ic} to less than one half. Chromium additions, however, did not significantly change the yield strength, DBTT or fracture toughness of 20%Mn alloy. The enhanced corrosion resistance that probably would be obtained with such chromium additions is considered desirable for potential cryogenic applications. The results suggested that chromium additions to Fe-Mn alloys favored the transformation of ε and γ to the α phase during deformation.

Further tests were conducted to investigate the interstitial role of carbon on the structure and properties, by obtaining tensile and toughness data an a 16Mn%-0.05%C alloy. The main

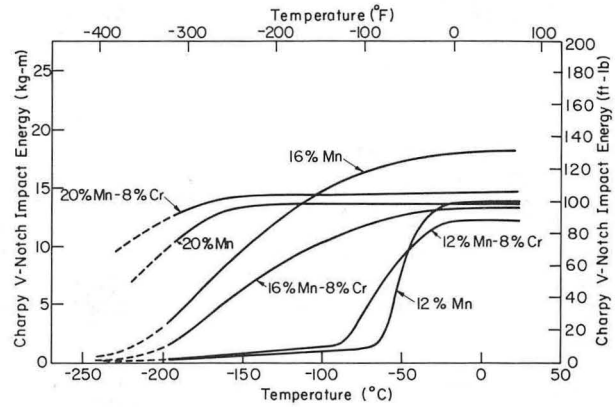

Fig. 3. Charpy V-notch impact toughness vs. testing temperature for the as austenitized 12 and 20%Mn alloys with and without chromium. (XBL 747-6668)

Table I. Chemical compositions of alloys.

	Composition, wt%			
Designation	Mn	Cr	C	Fe
4% Mn	4.1	--	--	Bal.
8% Mn	8.1	--	--	Bal.
12% Mn	12.1	--	--	Bal.
16% Mn	16.0	--	--	Bal.
20% Mn	19.5	--	--	Bal.
12% Mn 8% Cr	12.2	7.7	--	Bal.
16% Mn 8% Cr	15.8	7.9	--	Bal.
20% Mn 8% Cr	20.2	7.9	--	Bal.
16% Mn 0.05% C	16.3	--	0.045	Bal.

effect of the addition of carbon was to favor the formation of the epsilon and gamma phase. This resulted in the beneficial effect of a significant increase in the yield strength (by 75% at room temperature and 36% at -196°C) without changing the Charpy V-notch impact toughness appreciably.

1. V. F. Zackay, Microstructure and Design of Alloys, Institute of Metals, Vol. 1, 591 (1973).

12. FATIGUE CRACK PROPAGATION RATES IN Fe-Ni ALLOYS

Henri Sirot

Investigations were continued on the fatigue crack propagation rates in Fe-Ni alloys. The main objective of this study was to see how the fatigue properties of these cryogenic alloys would change from room temperature to cryogenic temperatures. Crack propagation rates were measured as a function of the stress intensity range ΔK.

Room temperature tests showed that stage II crack propagation rates for cracks propagating faster than 0.2 μm/cycle are relatively insensitive to grain size, yield strength or nickel content, (4 to 16 wt%) and the rates were comparable to those found in a 5Mo 0.3C steel. An equiaxed alpha structure, obtained by a very slow cool, was found to be slightly less resistant to fatigue crack propagation than a structure containing martensite, which was obtained by an iced-brine quench. This slight effect could be due to either the change in substructure or the residual stresses associated with the production of martensite.

Crack growth rates at -77°C, -116°C and -196°C (Figs. 1 and 2) were measured as the interspace between the striations (Fig. 3) seen on the fatigue fracture surface using a scanning electron microscope. No "static" mode of fracture (intergranular cracking or microcleavage) was observed in association with fatigue striations in the 8 wt% and 12 wt% Ni alloys. A programmed loading experiment performed at liquid nitrogen temperature, for the 12 wt% Ni alloy showed that there was uniform growth over the whole crack

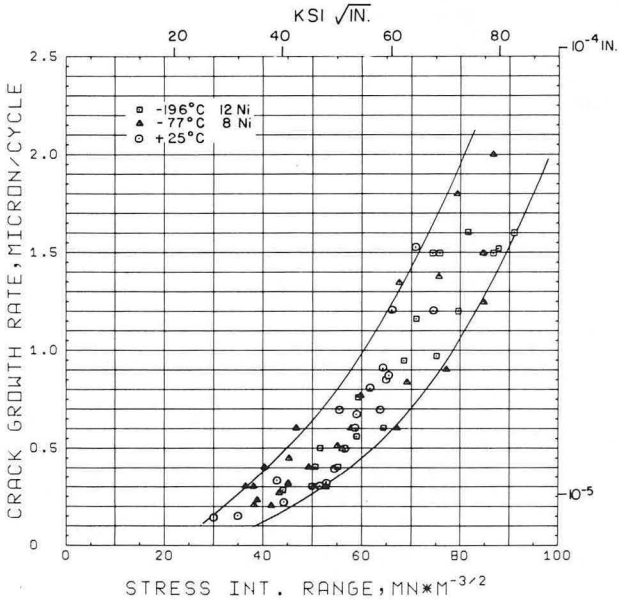

Fig. 1. The results of all tests run at 25°C, -77°C and -196°C in which the striation method was used to derive the fatigue crack growth rate are compared. (XBL 748-6897)

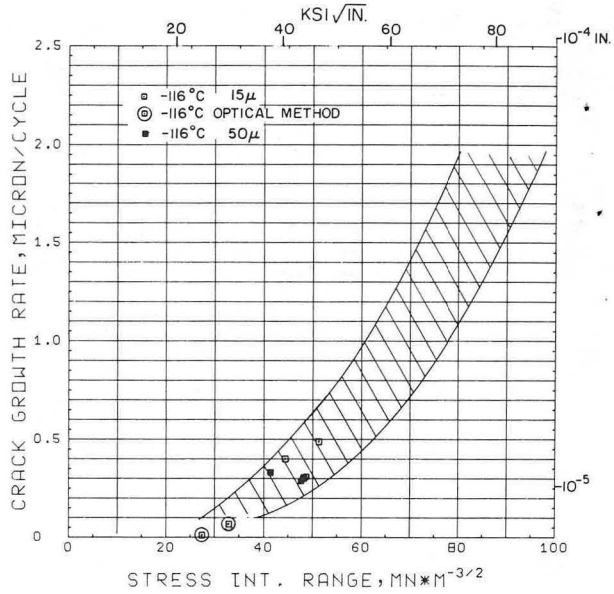

Fig. 2. Fatigue data obtained on testing the 8Ni alloy at -116°C. (XBL 748-6891)

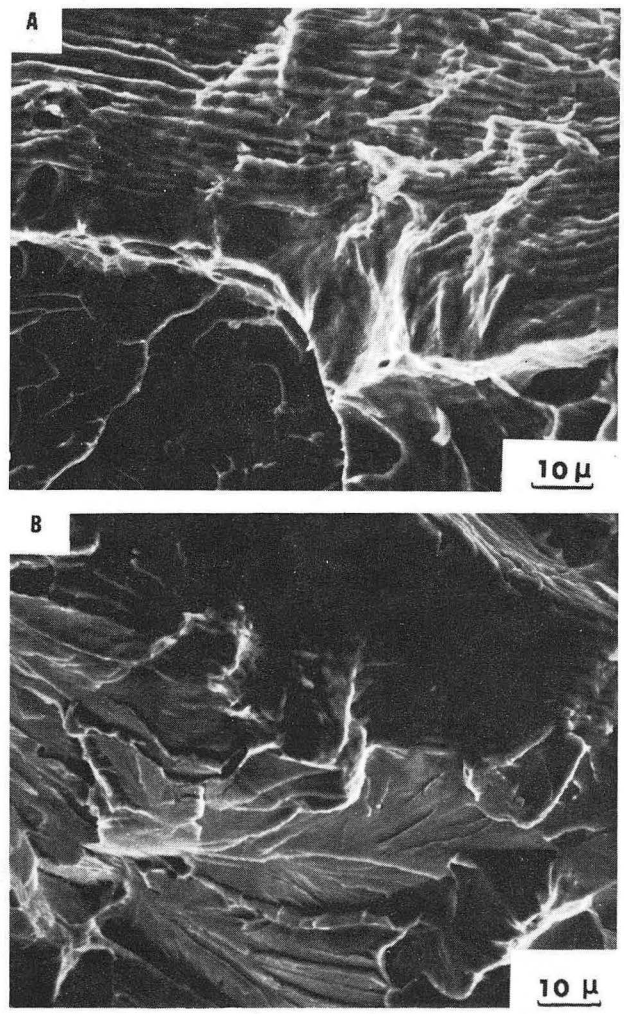

Fig. 3. (A) shows the transition from fatigue striations to quasi cleavage in an 8Ni alloy tested at -77°C. (B) shows the transition from fatigue striations to cleavage facets in an 8Ni alloy tested at -116°C. (XBB 748-5377)

front and one striation per load cycle; therefore microscopic growth rates observed in these alloys are closely related to the macroscopic growth rates. Crack growth rates faster than 0.2 μm per cycle appeared to be insensitive to the temperature of the test, even for the 8Ni alloy fatigued at -116°C which is slightly below its Charpy V-notch transition temperature. The longer fatigue lives of the 8Ni alloy specimens fatigued close to their transition temperature were attributed to slower crack growth rates during the initial stage of the propagation. After the crack had grown to a certain length under fatigue, the specimen fractured in a catastrophic manner by a cleavage mode, the striations being replaced by flat cleavage facets. Since K_{Ic} varies with temperature, the above result showed that striation growth cannot be related to K_{Ic}.

It proved impossible to initiate a fatigue crack at -196°C in the 8Ni alloy nor was it possible to propagate a crack previously initiated at room temperature. The specimen did not crack, or it failed at higher ΔK in a brittle mode. The critical stress intensity values obtained from the final failure under fatigue conditions were lower than K_{Ic} values measured by a conventional test when fracture occurred in a brittle manner, and this was attributed to the differences in strain rates or to the statistical distribution of strength. In the specimens tested in a standard test, the precrack is stopped in an arbitrary position, whereas in a fatigue test the crack keeps advancing until it reaches a low strength region with a corresponding low value of K_{Ic}.

Short periods of high stress cycling were shown to retard subsequent crack propagation under normal stress cycling at room temperature as well as at -196°C in the 12Ni alloy. This effect is probably due to the residual stresses left by the high loads. After the crack had slowly grown beyond the residual stress region, crack propagation was observed to resume normal behavior.

A good correlation between the standard optical crack tip observation technique and the striation measurement technique has been obtained for cracks growing faster than 0.2 μm/cycle. The systematic difference observed in crack growth rates for high values of ΔK has been explained by the curvature of the crack.

13. THE MECHANICAL PROPERTIES AND CORROSION RESISTANCE OF SELECTED Fe-Mn-Cr ALLOYS

Larry D. Thompson

The present investigation is primarily concerned with the improvement of corrosion resistance in Fe-Mn base alloys to be used at ambient temperatures. An initial study of Fe-Mn alloys was made in the author's laboratory by Schanfein.[1] The most encouraging results were found with the Fe-16%Mn and Fe-20%Mn alloys as is evident from Table I.

Table I. Mechanical Properties of Fe-Mn Alloys*†

Alloy	0.2% YS(KSI)	UTS(KSI)	% El.	% R/A	Hardness	DBTT (°C)
Fe-4%Mn	82.1	87.2	11	73	R_c 10.1	- 20
Fe-8%Mn	92.1	96.5	10	68	R_c 17.8	+ 20
Fe-12%Mn	88.2	127.2	17	63	R_c 24.7	- 55
Fe-16%Mn	29.4	101.2	40	71	R_c 10.9	-160
Fe-20%Mn	60.9	101.4	43	70	R_c 15.4	-235
Fe-12%Mn-8%Cr	85.7	131.1	17	66	R_c 26.7	- 55
Fe-16%Mn-8%Cr	44.7	109.1	20	68	R_c 18.8	-110
Fe-20%Mn-8%Cr	57.5	95.0	52	75	R_c 14.6	-220

*The above values are for the "as quenched" condition. The specimens were austenitized two hours at 900°C and ice brine quenched and then cooled to liquid nitrogen temperatures to insure complete transformation. All values are for room temperature testing.

†Mark Jay Schanfein, (M.S. thesis) LBL-2749, Aug. 1974.

Table II. Mechanical Properties of Fe-Mn-Cr Alloys.*

Alloy	0.2% YS(KSI)	UTS(KSI)	% El.	% R/A	Hardness	DBTT (°C)
Fe-16%Mn-13%Cr (26)	55.9	117.0	27	62	R_c 23	-115
Fe-16%Mn-18%Cr (27)	56.4	89.4	35	68	R_c 11	- 60
Fe-20%Mn-13%Cr (28)	58.3	97.0	42	51	R_c 18	---
Fe-20%Mn-18%Cr (29)	93.0	123.0	5	4	R_c 45	---

*All values correspond to specimens in the "as quenched" condition described in Table I. The tests were performed at room temperature.

In the present investigation further chromium additions were made above those tested by Schanfein, and the compositions are listed in Table II.

The mechanical properties of the above mentioned alloys were determined in accordance with ASTM standards and the results are shown in Table II. As one readily notes, the most promising alloys were #26 and #27 which exhibit a ductile-to-brittle transition over the range of testing temperatures (i.e., -196°C to room temperature). Alloys #28 and #29 behaved in a brittle manner over this entire range of temperature.

Mechanical properties have little significance unless they can be successfully correlated with the microstructure and amount of phases present. By use of optical and transmission electron microscopy as well as scanning electron microscopy, the author plans to relate the microstructures present to the mechanical properties displayed. In addition, the author plans to follow the phase transformations, upon heat treatment and upon plastic deformation, by use of dilatometry and well known x-ray techniques. The corrosion behavior of these alloys will be investigated via immersion testing in accordance with ASTM standards.

14. THE STRAIN ENERGY OF A DISK-SHAPED GP ZONE

John Wert

Clusters of solute atoms often formed during the first stage of solid solution decomposition in age hardening alloys are usually referred to as Guinier-Preston (GP) zones. GP zones are coherent with the surrounding matrix phase, thus any difference in atomic spacing between the precipitate and matrix phases will result in coherency strain fields around the clusters. An additional interfacial energy must also be associated with the clusters because of the sharp composition variation at the precipitate-matrix interface. While the strain and additional interfacial energies are dependent on the shape and orientation of the GP zone, the other energy changes accompanying GP zone formation are independent of the configuration assumed by the cluster.

The shape of GP zones may be fairly well understood by considering the relative magnitude of the strain and additional interfacial energies.[1] The orientation of a (non-spherical) GP zone, however, is expected to depend not only on the relative magnitudes but also on the anisotropies of these energies. The purpose of this study is to examine the magnitude and anisotropy of the strain energy of a disk-shaped GP zone in lattices of various elastic anisotropies.

A simplified form of Khachaturyan's solution[2] to the general problem of determining the strain energy of a disk-shaped coherent inclusion has been found for the case of a disk-shaped inclusion. Calculations of the strain energy as a function of orientation of a GP zone in a cubic lattice have been made. The most significant result shows that the orientations associated with the minimum strain energy is dependent uniquely on the anisotropy of the elastic properties of the lattice. In particular, consider the anisotropy parameter A, defined as

$$A = \frac{2c_{44}}{c_{11}-c_{12}}$$

For lattices in which A is greater than one:
- the ⟨100⟩ orientations are strain energy minima
- the ⟨111⟩ orientations are strain energy maxima.

On the other hand, when A is less than one:
- the ⟨100⟩ orientations are strain energy maxima
- the ⟨111⟩ orientations are strain energy minima.

A change in A form less to greater than one clearly reverses the roles of the ⟨100⟩ and ⟨111⟩

orientations. This relationship was first observed by Schwellinger, Leamy and Warlimont.[3]

If the additional interfacial energy is isotropic or if it is small in comparison with the strain energy, then the GP zone will energetically prefer to lie in the orientation for which the strain energy is a minimum. In the two technologically important binary alloys in which disk-shaped GP zones form, Al-Cu and Cu-Be, the disks lie in the ⟨100⟩ matrix planes. For both Al and Cu, A is greater than one so the observed orientations are identical with those for which the calculated strain energy is a minimum.

---

1. A. Kelly and R. B. Nicholson, Prog. Mat. Sci. 10, 149 (1963).
2. A. G. Khachaturyan, Soviet Phys. Solid State 8, 2163 (1967).
3. P. Schwellinger, H. Leamy, H. Warlimont, Acta Met. 19, 421 (1971).

15. THE DEVELOPMENT OF IRON-RICH Fe-Zn SYSTEM

Edward Wylie

Recent improvements in the understanding of the iron rich side of the (Fe-Zn) phase diagram has clarified the relationships in that area. There is a gamma iron loop extending from 800 to 1400°C and out to 10 wt% zinc. But the wide range of solubility of zinc in alpha iron (3% at 400°C to 46% at 783°C) is the portion with which the research is concerned. We believe that iron-zinc alloys in this range will have some interesting mechanical properties coupled with good corrosion resistance.

The main problem is the relatively low boiling point of zinc (high vapor pressures). Previous research workers used small powder samples homogenized over long periods of time at constantly increasing temperatures and using optical and electron microscopy techniques. This study will utilize a new method of making the alloys in less time. The new approach is based on the studies of Pickus, Zackay, Parker and Holthuis in the niobium-tin system. After sintering a powdered iron blank, the blank will be dipped into molten zinc for infiltration. Following deformation to increase the surface contact area between the zinc filaments in the iron matrix the deformed blank will be homogenized.

Variables in the system include: sintering temperatures, times, and atmospheres; infiltration temperatures, times, and pressures; and rolling temperatures and amounts. Also fluxes added to the molten zinc will be tried to change its wetting characteristics. Anticipated problems include the metallography of infiltrated powder samples and the identification of phases present. Preliminary results using static infiltration techniques indicate that for infiltration to be complete the zinc bath must be relatively hot, and the deformation must be done at elevated temperatures. No conclusions about sintering and infiltration atmospheres have been made from the static tests.

Once manufacturing procedures for the alloy are worked out the remainder of the project will involve the interpretation of resulting microstructures on mechanical properties (hardness, tensile, fracture). It is also planned to run a series of basic corrosion tests to compare (the corrosion resistance of) these alloys to galvanized and stainless steels.

16. QUANTITATIVE MEASUREMENTS OF PHASE TRANSFORMATION KINETICS IN LOW ALLOY STEELS DURING PROGRAMMED COOLING

Jim Lum Yuen

Transformation kinetics during programmed cooling of low alloy steels were studied using a magnetic permeability method (MPM). The steel specimens (in wire form) were cooled from the austenitizing temperature along different programmed cooling paths. Resulting data were then used to superimpose transformation curves upon the programmed cooling paths to produce the desired continuous cooling transformation (CCT) diagrams for this investigation. CCT diagrams enable prediction of the influence of different time temperature cooling paths on austenitic decomposition.

Two different alloys were studied; AISI 4340 and AMS 6416 (300-M). Published CCT diagrams for these alloys[1] compare favorably with the experimental diagrams (Figs. 1 and 2), although

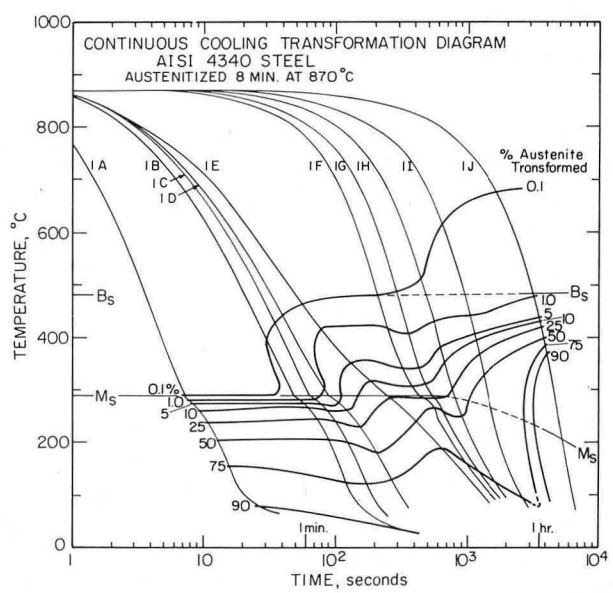

Fig. 1. Continuous cooling transformation diagram for 4340. (XBL 746-6611)

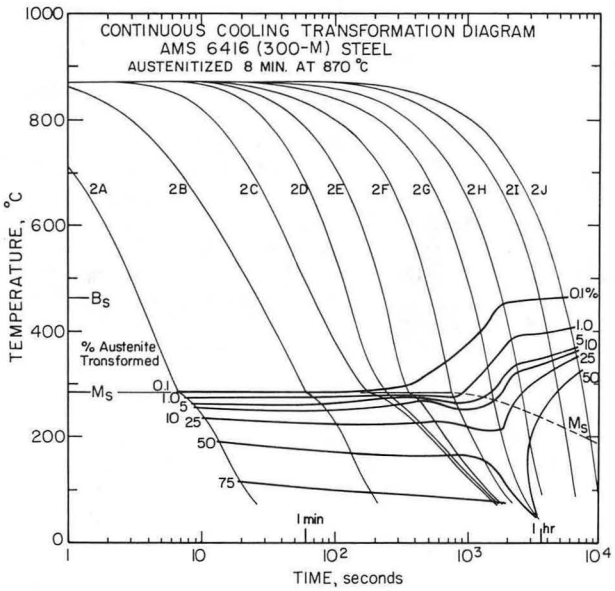

Fig. 2. Continuous cooling transformation diagram for 300-M. (XBL 746-6610)

differing somewhat in detail. The observed spread in reported M_s values using different techniques may be attributed to minor variations in heat treatment and composition. Using the MPM, greater accuracy of definition for M_s is possible because the start of transformation can be measured to within 0.1% martensite. The MPM provides a convenient, rapid, and very sensitive measurement of transformation kinetics.

A large amount of retained austenite was found to exist at room temperature for certain cooling paths. Paths through the bainite nose led to fractions as great as 18%, and up to 40% in 300-M for certain paths. Previously published CCT diagrams have shown that transformations go to completion at any cooling velocity.

Three types of cooling were employed: a gas quench; a partial vacuum cool; and a slow cool. With progressively slow cooling, there is an increasing amount of transformation to bainite, and at sufficiently slow rates the cooling path for 4340 goes through the pearlitic nose. The pearlitic hardenability of 300-M was found to be very high.

The cooling paths that pass through the tip of the bainitic nose show that as the cooling velocity decreases, the amount of retained austenite in bainite increases only slightly. This trend corresponds to curves 1B, 1C and 1D in Fig. 1 for 4340, and for all curves for 300-M (Fig. 2). This suggests that the initial transformation to bainitic stabilizes some of the untransformated austenite as may be seen in Tables I and II. Upper bainite was found to be more effective than lower bainite in retaining austenite at room temperature . The length of time spent in the bainitic transformation temperature range apparently determines how much austenite will be retained. This conclusion, if valid, is pivotal to the selection of critical cooling paths which will result in the maximum amount of retained austenite. This microstructure appears to offer great toughness at ultimate strength levels greater than 200,000 psi.[2]

Table I. Quantitative Measurements for 4340 (volume percent).

Cooling Path	Estimated cooling velocity at 450°C, °C/sec	Ferrite Formed in the Pearlite Range, %	Bainite, %	Martensite, %	Retained Austenite, %	VHN
1A	72	-	-	100	-	616
1B	9.1	-	0.2	91	8.8	-
1C	6.7	-	0.5	90	9.5	-
1D	5.1	-	1	85	14	567
1E	2.2	-	22	60	18	466
1F	1.6	0.1	16	71	12.9	-
1G	1.2	0.2	19	69	11.8	-
1H	0.74	0.2	30	56	13.8	442
1I	0.4	0.5	60	24	15.5	-
1J	0.1	1	89	5	5	301

Table II. Quantitative Measurements for 300-M (volume percent).

Cooling Path	Estimated cooling velocity at 450°C, °C/sec	Ferrite Formed in the Pearlite Range, %	Bainite, %	Martensite, %	Retained Austenite, %	VHN
2A	72	-	-	100	-	654
2B	7.7	-	-	89	11	-
2C	3.1	-	0.1	78	21.9	622
2D	2.8	-	0.3	76	23.7	-
2E	1.9	-	0.5	79	20.5	-
2F	0.8	-	0.4	75	24.6	618
2G	0.4	-	9	65	26	616
2H	0.2	-	33	36	31	-
2I	0.1	-	49	6	45	425
2J	0.09	-	56	1	43	-

1. J. L. Yuen, LBL-3103, July 1974.
2. G. Y. Lai, W. E. Wood, R. A. Clarke, V. F. Zackay and E. R. Parker, Met. Trans. 5, 1663 (1974) (LBL-2250).

17. THE KINETICS OF AUTO-TEMPERING IN SELECTED PLAIN CARBON AND ALLOY STEELS

Paul H. Zajchowski

a. Introduction

Many articles have been written on the tempering of martensite in steels. The tempering process involves the segregation of carbon, the precipitation of carbides, the decomposition of retained austenite, and the recovery and recrystallization of the martensitic structure. Because some of these reactions overlap and occur on such a fine scale, the understanding of them is not complete. Even though the tempering processes of plain carbon steels have been thoroughly studied and are reasonably well understood, much more information is still needed to completely understand the complex effects of alloying elements upon the tempering treatment.[1]

In this investigation two plain carbon steels, AISI 1090 and AISI 1046, and three alloy steels, AISI 4340, AMS 6416 (300-M), and modified 4340+3%Si, were studied to determine the effects of alloying elements in general, and silicon in particular, upon the kinetics of auto-tempering. Specifically, this study was concerned with the first step of the tempering process, the redistribution of carbon to dislocations,[2] and with the so-called first and third stages of tempering, the precipitation of ε-carbide in low carbon martensite and the formation of cementite and ferrite.[3]

To study the kinetics of auto-tempering, it is necessary to suppress any tempering during the quench. This can be accomplished by very rapid quenching. However, the "so-obtained" martensite is often mixed with small amounts of retained austenite, which can be minimized by subsequent cooling to liquid nitrogen temperatures. The fast cooling can be accomplished by using a small diameter wire. With wire specimens, electrical resistance changes provide an excellent means for monitoring the initial kinetics of the tempering process.

This method was chosen because the resistance change, which is a sensitive function of the tempering reaction, can be easily and accurately measured with wire specimens almost immediately because the wire coil attains the tempering bath temperature within 2 secs.

b. Low Temperature Studies

In all five steels the effect of tempering was to cause a progressive decrease in the electrical resistance with tempering time (Fig. 1).

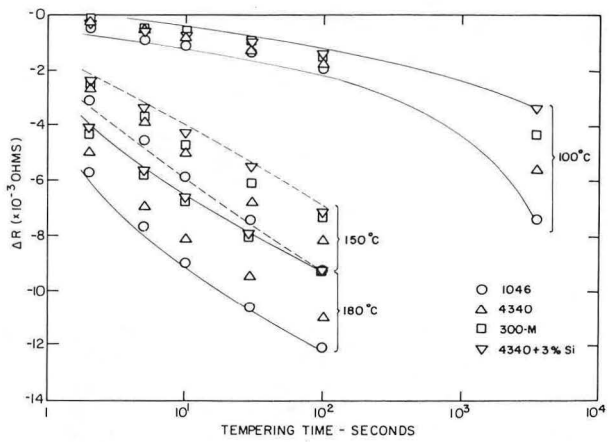

Fig. 1. Absolute resistance change vs. tempering time for 1046, 4340, 300-M, and 4340-3%Si at 100°C, 150°C and 180°C. (XBL 747-6751)

In agreement with the known kinetics of the so-called first stage of tempering, the reaction was observed to start without an incubation period and proceed at a rapidly diminishing rate.[2] The magnitude of the resistance changes in plain carbon steels increased greatly with carbon content, while the magnitude of the changes in the alloy steels increased with decreasing silicon content, as indicated by comparing the 4340, 300-M, and 4340+3%Si curves at all three temperatures.

At 100°C, the steels were tempered for the first 100 secs to observe the auto-tempering rate and then tempered for a total of 1 h to determine the effect of a longer tempering time. It was found that the resistance change initially decreases at a gradual rate during the first 100 sec. During the remaining 1 h of tempering, however, there is a relatively large resistance decrease. This result is different from that obtained for the steels tempered at 150°C and 180°C, where much of the tempering occurs in the first few seconds and then the rate gradually diminishes with time. Presumably, carbide precipitation begins almost immediately upon tempering at these temperatures and the resistance decreases continuously as this precipitation continues. This behavior is consistent with the formation of ε-carbide.[2]

At 100°C, within the first 100 secs of tempering, the absolute resistance changes are practically the same for all four steels. After 100 secs, however, and up to 1 hr. the resistance differences among the steels increase rapidly with time. It appears that within the first 100 secs the alloying elements have very little, if any, effect on the tempering rate. After the first few minutes, however, the alloying elements, particularly silicon, exert sufficient influence to decrease the tempering rate. As a result, after 1 h there is a relative difference among the resistance changes such that 1046 ≫ 4340 > 300-M > 4340 > 4340+3%Si, as indicated in Fig. 1. At 150°C and 180°C, the differences in absolute resistance change among the steels occur almost immediately and become greater with time. The rate changes between the higher silicon steels (300-M and 4340+3%), however, remain relatively the same throughout the first 100 secs of tempering at both temperatures. Thus, at 150°C and 180°C the alloying element effect (particularly silicon) is immediately apparent, whereas, at 100°C the alloying element effect is not really noticeable until after at least 100 secs of tempering. The results found here are in agreement with the results of King and Glover, who found silicon to retard the first stage of tempering in steels.[4]

It appears that in both plain carbon steels the first stage reactions occur relatively quickly, as indicated by the narrow activation energy energy range, and they approach a steady state. In the alloy steels, the process occurs at slower rates so that longer tempering times are necessary to complete the reaction. The differences in activation energies between the plain carbon and alloy steels also indicate the effect of silicon in retarding tempering.

c. High Temperature Studies

The resistance change-time curves of specimens tempered at 240°C, 270°C, and 300°C were similar to those tempered at 150°C and 180°C. The magnitude of the resistance changes, however, was much greater and increased to a greater degree with increases in tempering temperature.

In both of the plain carbon steels, (Fig. 2) a large amount of tempering occurs within the first 5 secs, yet a significant part still occurs within the next 3 h. This trend is probably a result of the so-called third stage of tempering, i.e., the formation of cementite and ferrite which occurs within this tempering range. The magnitude of the resistance changes for the 1090 steel is much greater than the changes for the 1046 steel, as is to be expected.

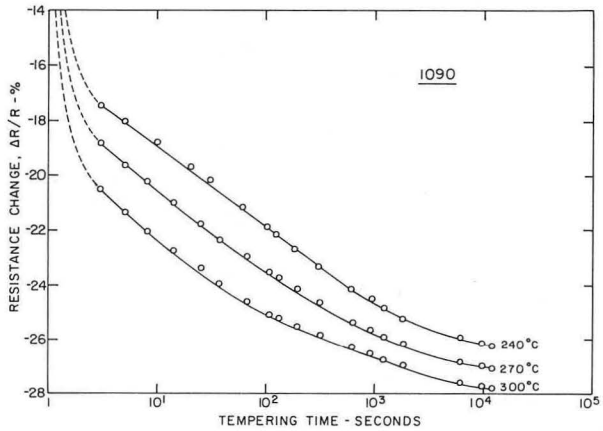

Fig. 2. Percent resistance change vs. tempering time for 1090 steel at 240°C, 270°C and 300°C. (XBL 747-6742)

In the alloy steels, the 4340 steel tempers at a faster rate than the 300-M and the 300-M tempers faster than 4340-3%Si. The data clearly show that the addition of silicon retards the tempering reactions occurring at these temperatures.

The "apparent activation" energies calculated for 1090 and 1046 steels at these high temperatures are somewhat near their calculated values for the first stage of tempering at the lower temperatures. The values calculated for the alloy steels are much higher than those of 1090 and 1046, and are definitely influenced by the silicon content. Increasing the silicon in the steel increases the "apparent" activation energy for the tempering reactions at these temperatures. The general effect of silicon on the kinetics of the tempering process at these temperatures is to retard the precipitation of cementite.

---

1. C. R. Speich and W. C. Leslie, Met. Trans. 3, 1043 (1972).
2. G. R. Speich, Met. Trans. 245, 2553 (1969).
3. B. L. Averbach and M. Cohen, Trans. ASM 41, 1024 (1949).
4. H. W. King and S. G. Glover, J. Iron and Steel Inst. 196, 281 (1960).

18. RESEARCH PLANS FOR CALENDAR YEAR 1975

Victor F. Zackay and Earl R. Parker

A new intensive effort will be directed towards studying the mechanics and mechanisms of "corrosion" fatigue crack propagation in a range of steels, with particular emphasis on the effects of microstructure, mean stress and environment (i.e. air, water and vacuum) on very slow growth rates ($< 10^{-6}$ mm/cycle) near the threshold for crack propagation. This research study will be closely interrelated with presently continuing work on the stress corrosion behavior (under static loading) of 4340, Si-modified 4340 and Fe-Cr-Si steels, and further research effort into improving the fracture toughness of these steels by microstructural control, for example by increasing the amount of retained austenite in continuously cooled structures. It is also planned to make use of Scanning Auger Microscopy in these research programs to examine the influence of any segregated impurity elements (e.g. S, P. Sb, Sn, etc.) on the fracture toughness, stress corrosion properties and fatigue crack growth behavior in these steels. Additional investigations include a research program designed to improve the mechanical properties, particularly impact ductility, of Fe-high Mn-C steels by modifying the complex microstructure of these materials by, say, molybdenum additions; work on identification and control of imperfections and grain growth zones in heat-affected zones adjacent to welds in high carbon quenched and tempered steels; and continuing research on the kinetics of the bainite transformation in low alloy steels using the magnetic permeability technique.

On the thermodynamics of Fe-C-X alloys, continued research is planned to modify the thermodynamic model for calculation of phase equilibria in ternary alloys such that only information on the binary systems involved will be required. In addition calculations of phase equilibria in quaternary and more complex alloy systems will be attempted.

A new area of research will be initiated to study materials-limited energy conservation problems. Experiments will begin to study the problem of void formation and consequent swelling occurring in nuclear reactor components. Ferritic alloys containing small percentages of nickel, aluminum and titanium have been selected for study on the basis of their high austenite and martensite transformation temperatures. Various heat treatments of these alloys will produce microstructures with very high and low dislocation densities whose effect on void formation during nuclear radiation can later be observed by optical and electron microscopy. Another effect will concentrate on trying to optimize microstructure-mechanical properties for use in future alloy design of nuclear materials. A new program of theoretical metallurgical physics has just begun. Pseudopotential techniques will be used to calculate vacancy interaction in metals in order to understand void nucleation and growth from first principles.

19. 1974 PUBLICATIONS AND REPORTS

Victor F. Zackay, Earl R. Parker, and Associates

Journals

1. W. E. Wood and W. W. Gerberich, The Mechanical Nature of Stress-Corrosion Cracking in Al-Zn-Mg Alloys: I. Evaluation of the Ductile Rupture Contribution, Met. Trans. 5, 1285 (1974) (LBL-2229).

2. W. W. Gerberich and W. E. Wood, The Mechanical Nature of Stress-Corrosion Cracking in Al-Zn-Mg Alloys: II. Electrochemical-Mechanical Model, Met. Trans. 5, 1295 (1974) (LBL-2230).

3. G. Y. Lai, W. E. Wood, R. A. Clark, V. F. Zackay and E. R. Parker, The Effect of Austenitizing Temperature on the Microstructure and Mechanical Properties of As-Quenched 4340 Steel, Met. Trans. 5, 1663 (1974) (LBL-2250).

4. V. F. Zackay, E. R. Parker, J. W. Morris, Jr. and G. Thomas, The Application of Materials Science to the Design of Engineering Alloys. A Review, Mat. Sci. and Engr. 16, 201 (1974) (LBL-2261).

5. L. D. Hartsough, Stability of A15 Type Phases, J. Phys. Chem. Solids 35, 1691 (1974) (LBL-119 Rev.).

LBL reports

1. G. Sasaki and M. J. Yokota, Fracture Mode Determinations by SEM, LBL-3120, Aug. 1974.

2. E. R. Parker and V. F. Zackay, Fundamentals of Alloy Design, LBL-2706, May 1974.

3. V. F. Zackay and E. R. Parker, Alloy Design for Fracture Toughness, LBL-2782, July 1974.

4. E. R. Parker, V. F. Zackay, G. Y. Lai and R. M. Horn, Untempered Ultra High Strength Steels of High Fracture Toughness, LBL-2715, April 1974.

5. G. Sasaki and M. J. Yokota, Grain Size Versus Ductile Brittle Transition in an Fe-12% Ni Alloy, LBL-2777, July 1974.

6. Henry Peter Offer, Characterization of Brittle Crack Initiation in Welded A-36 and A-537 Steel, (M.S. thesis) LBL-2251, June 1974.

7. Jim Lum Yuen, Quantitative Measurements of Phase Transformation Kinetics in Low Alloy Steels During Programmed Cooling (M. S. thesis) LBL-3103, July 1974.

8. Henri Albert Sirot, Crack Propagation Rates in Fe-Ni Alloys (M. S. thesis) LBL-2750, August 1974.

9. Paul Henry Zajchowski, The Kinetics of Auto-Tempering in Selected Plain Carbon and Alloy Steels, (M. S. thesis) LBL-3121, Aug. 1974.

10. Mark Jay Schanfein, The Cryogenic Properties of Fe-Mn and Fe-Mn-Cr Alloys (M. S. thesis) LBL-2749, Aug. 1974.

11. Elias Plaza-Meyer, Thermodynamics of Fe-C-X Alloys (Ph. D. thesis) LBL-3161, Sept. 1974.

12. B. Naga Prakash Babu, An Investigation of Bainite Transformation in Medium Carbon Low Alloy Steels, (D. Eng. thesis) LBL-2772, Aug. 1974.

13. Manjeshwar Shanthidas Bhat, Phase Transformation Characteristics and Creep Properties of a Laves Phase Strengthened Fe-Ta-Cr-Mo Alloy (M. S. thesis), LBL-2277, April 1974.

14. John Arthur Wert, The Strain Energy of a Disk-Shaped GP Zone, (M. S. thesis) LBL-3174, Dec. 1974.

15. B. N. P. Babu, D. Ott, E. R. Parker and V. F. Zackay, A Rapid Magnetometric Technique to Plot Isothermal Transformation Diagrams, LBL-2502, Dept. 1974.

16. M. J. Yokota and G. Y. Lai, Toughness of Lath Versus Plate Martensites, LBL-3144, Oct. 1974.

17. M. D. Bhandarkar, M. S. Bhat, E. R. Parker and V. F. Zackay, Creep and Fracture of a Laves Phase Strengthened Ferritic Alloy, LBL-3150, Aug. 1974.

18. M. D. Bhandarkar, M. S. Bhat, V. F. Zackay and E. R. Parker, Structure and Elevated Temperature Properties of Carbon-Free Ferritic Alloys Strengthened by a Laves Phase, LBL-2573, Aug. 1974.

19. R. M. Horn, Influence of Heat Treatment on the Fatigue Crack Growth Rates of a Secondary Hardening Steel, LBL-2239, Oct. 1974.

20. M. J. Yokota, G. Sasaki and W. A. Horwood, Developing High Impact Toughness in Interstitial-Free Fe-Ni Alloys at Liquid Nitrogen Temperature, LBL-2278, Aug. 1974.

21. G. Y. Lai, On High Fracture Toughness of Coarse-Grained AISI 4130 Steel, LBL-2575, Aug. 1974.

22. G. Y. Lai, On the Precipitation of Epsilon-Carbide in Lower Bainite, LBL-2705, July 1974.

23. T. C. Lindley, C. E. Richards and R. O. Ritchie, The Mechanics and Mechanisms of Fatigue Crack Growth in Metals, LBL-3531, Dec. 1974 (presented at the Institute of Physics/ Metals Society Conf. on "Mechanics and Physics of Fracture", Cambridge, U.K., Jan. 6-8, 1975).

Papers presented

1. E. R. Parker and V. F. Zackay, Microstructural Features Affecting Fracture Toughness of High Strength Steels, LBL-2771, June 1974 (invited paper to the International U.S.-Japan Conference on Fracture Mechanics held at Tohoku University of Sendai, Japan, Aug. 12-16, 1974).

2. M. J. Schanfein, M. J. Yokota, V. F. Zackay, E. R. Parker and J. W. Morris, Jr., The Cryogenic Properties of Fe-Mn and Fe-Mn-Cr Alloys, LBL-2764, May 1974 (ASTM Symposium on Properties of Materials for Liquid Natural Gas Tankage, May 21-22, 1974, Boston, Mass.).

3. S. Jin, B. Whitaker, J. W. Morris, Jr. and V. F. Zackay, Cryogenic Toughness Through Microstructural Control in Ferritic Fe-Ni-Ti Alloys, LBL-2756, May 1974 (ASTM Symposium on Properties of Materials for Liquid Natural Gas Tankage, May 21-22, 1974, Boston, Mass.).

4. V. F. Zackay, M. D. Bhandarkar and E. R. Parker, The Role of Deformation Induced Phase Transformations in the Plasticity of Some Iron-Base Alloys, LBL-2775, Aug. 1974 (21st Sagamore Army Materials Research Conference on Advances in Deformation Processing held at Raquette, N. Y., Aug. 13-16, 1974).

G. HIGH FIELD SUPERCONDUCTIVITY

Milton R. Pickus, Principal Investigator

1. FILAMENTARY NIOBIUM-TIN WIRE

Kanithi Hemachalam and Milton R. Pickus

Using as a point of departure the techniques developed for producing a superconducting tape characterized by an array of Nb_3Sn filaments in a ductile niobium matrix, modifications have been made to adapt the main features of the process for making the superconductor in wire form. A wire form provides several advantages: the filament morphology would be superior from the standpoint of the adiabatic stability criterion, and the wire could be used as the basic element of a multicored conductor.

Two variations of the infilration approach were employed to make cylindrical rods of niobium with the required volume fraction of interconnected pores. In one, -400 mesh niobium powder was pressureless sintered for 5 minutes at 1600°C in a mullite tube to provide a self supporting rod, which, after removing the mullite tube, was resintered for 10 minutes at 2300°C. The porous rod thus obtained was infiltrated with tin by immersion for a half minute in a molten tin bath at 800°C. A cross section of the infiltrated rod is shown in Fig. 1. In the second method, -270 mesh niobium powder was isostatically compacted at 30,000 psi to form self supporting rods which were sintered for 10 minutes at 2250°C, and infiltrated with tin in the same manner as described previously. Figure 2 shows a cross section of an infiltrated rod made by isostatic compaction.

To prevent loss of tin and provide support during deformation, infiltrated rods prepared by

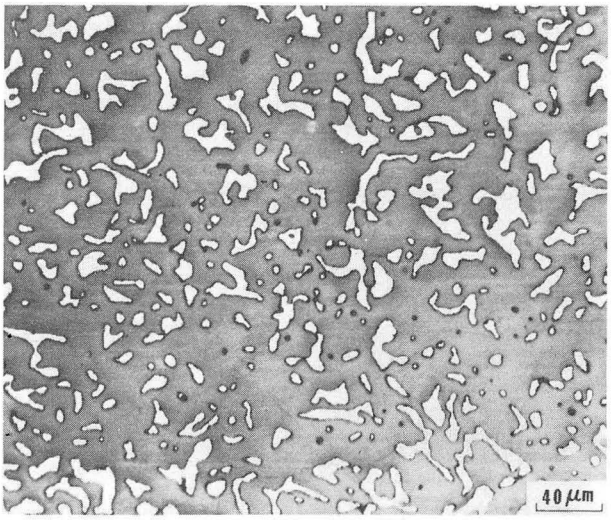

Fig. 1. Cross section of pressureless sintered niobium rod infiltrated with tin. White areas are tin. (XBB 7412-8446)

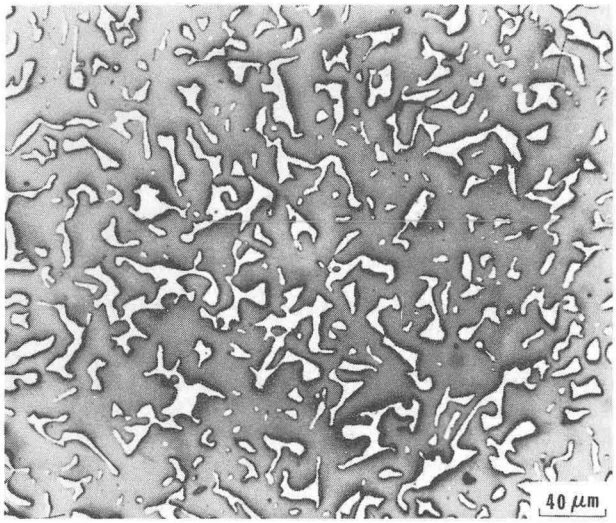

Fig. 2. Cross section of isostatically compacted and sintered niobium rod infiltrated with tin. (XBB 7412-8447)

both methods were ensheathed within a niobium tube. Additionally, because of the susceptibility of niobium to galling, the assemblies were ensheathed in tubing of another metal having a much lower galling tendency. Thus far two metals have been tried for the exterior sheath: copper or monel. From the experience gained it is now believed that cupronickel or bronze would be a better choice and it is planned to evaluate both in comparison with the other two. Assemblies were reduced to wire using one or a combination of the following deformation processes: swaging, form rolling and wire drawing.

A metallographic study of wire sections (Figs. 3 and 4) has indicated that whereas swaging results in the least favorable filament morphology, wire drawing produces the best. Form rolling prior to swaging is better than swaging alone: this has been confirmed by measurements of the respective current carrying capacities, the former

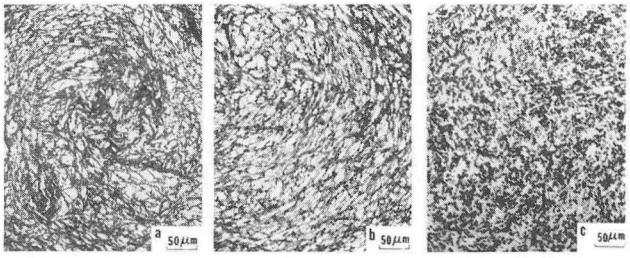

Fig. 3. Cross sections of heat treated wires produced by (a) swaging only; (b) form rolling followed by swaging; (c) wire drawing only. (XBB 7412-8448)

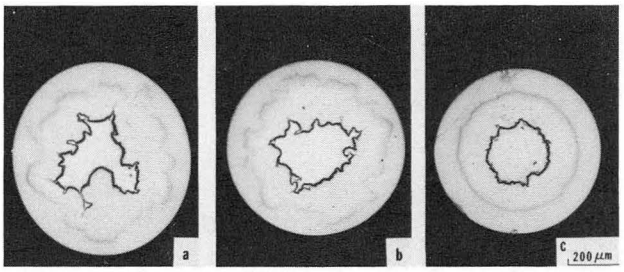

Fig. 4. Longitudinal section of heat treated wire produced by wire drawing only. Dark filaments are Nb_3Sn. (XBB 7412-8449)

exceeding the latter by a factor of 2. Some typical results are shown in Fig. 5 for current carrying capacity as a function of transverse pulsed magnetic field. Curve A was obtained from a sample that was form rolled from 0.205" to 0.100" and then wire drawn to 0.040" O.D. The sample used for curve "B" was wire drawn from 0.205" to 0.30". Figure 4 shows a longitudinal section of the wire used in obtaining curve B. The dark filaments are Nb_3Sn formed by a thermal treatment of 5 minutes at 965°C.

Much remains to be done in resolving the influence of the various process variables. Isostatic compaction is more convenient than pressureless sintering which requires a double sintering. However isostatic compaction results in less than the desired porosities. Several ideas for increasing the porosity will be investigated. Moreover, it has been observed that there is a strong interdependence between the mechanical properties of the core and those of the sheaths. The plastic flow characteristics of each must be properly matched. This can be illustrated by results obtained in still another approach we are exploring to develop multicore conductors. The objective in this case is to produce parallel, non-interconnected superconducting filaments arrayed in a normal matrix. The main features of this approach involve the mechanical reduction of a solid rod of tin contained within a double sheath, the inner one of which is niobium tubing. The wire obtained is cut and an appropriate number of segments are packed within a sheath and again reduced. The result is a multicore wire, which again can be cut, and the whole process repeated as many times as required.

Some preliminary results are shown in Figs. 6 and 7. Figure 6 shows the dramatic influence of the mechanical properties of the tin core, comparing the use of pure tin with tin hardened by various alloy additions. Figure 7 shows the results of a first effort with this approach in which a conductor was prepared containing 25 cores.

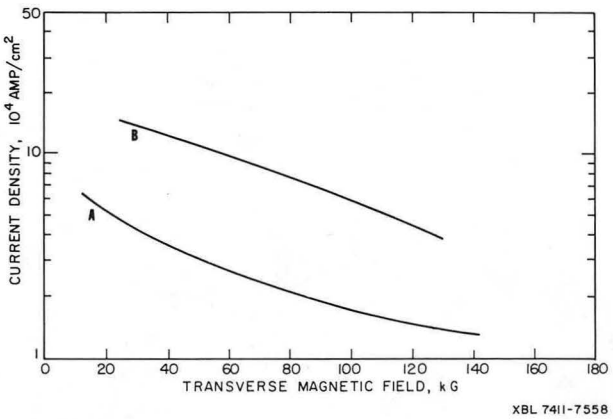

Fig. 5. Current carrying capacity of wires produced by isostatic compaction. Curve A: form rolling plus wire drawing; curve B: wire drawing only (microstructure shown in Fig. 4). (XBL 7411-7558)

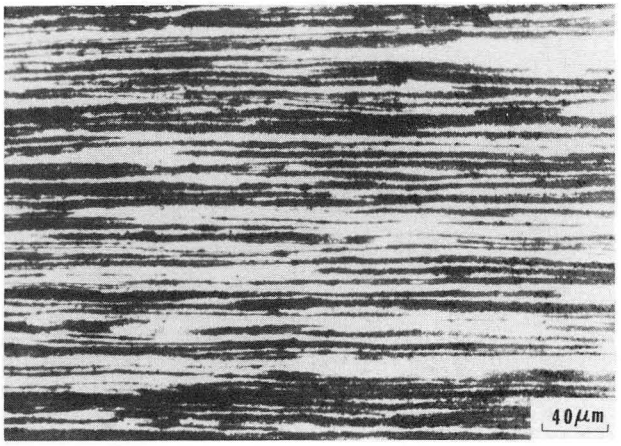

Fig. 6. Cross sections of drawn wires, the cores of which are (a) pure tin; (b) tin plus 2.6 wt.% copper; (c) tin plus 5.3 wt.% copper plus 3.2 wt.% niobium. In each case the inner sheath is niobium and the outer sheath is monel. (XBB 7412-8450)

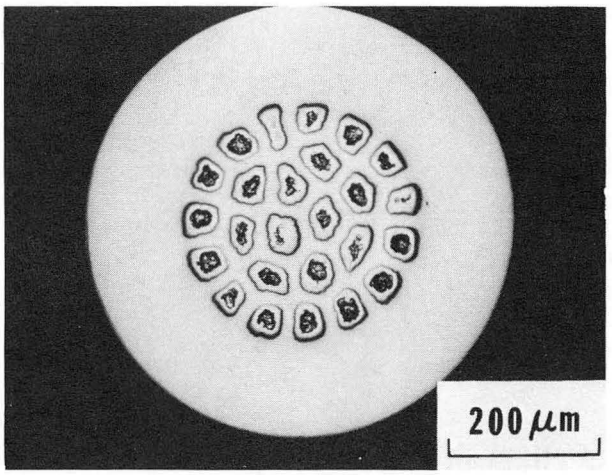

Fig. 7. Cross section of wire containing 25 cores drawn to 0.023" O.D. Each core corresponds with Fig. 6c. The encasing sheath is monel. (XBB 7412-8451)

2. RESEARCH PLANS FOR CALENDAR YEAR 1975

Milton R. Pickus

The program will focus on methodologies for producing both multifilamentary wire and multicore conductors. Preliminary results for the superconducting properties of wire made by the infiltration process have been determined in both steady and pulsed magnetic fields. An effort will be made to optimize the procedures and critically evaluate the technological potential of this type of wire in relation to wire produced by alternative procedures we are now exploring. The most challenging of these alternatives is a new concept which, if the problems associated with it can be successfully surmounted, offers the prospect of a system that combines the advantages of simplicity and versatility in application to a variety of A-15 compounds. All of the methods now being investigated, in this and other laboratories, for producing multifilamentary wire using A-15 compounds as the superconductor have in common the use of a diffusion reaction to form the A-15 compound after the deformation processes have been completed. The conditions for controlling the diffusion reaction are directly related to the phase diagram for the particular system. Consequently, a procedure worked out for one of the A-15 compounds may be completely ineffective for a different compound. For example, the thermal treatment required may be incompatible with the non-superconducting sheath material that forms the matrix. Indeed, this would be the situation for the best superconducting compounds. The new concept we will be investigating involves commencing with precompounded powders--that is to say, the reaction to form the A-15 compound will have been carried out prior to encapsulation within the non-superconducting sheath and hence prior to the mechanical processing. We will study the feasibility of this approach with two different A-15 compounds, Nb_3Sn and $Nb_3(Al,Ge)$, for the latter of which, despite its significantly superior properties, there is at present no viable technological approach at all.

H. POWDER METALLURGY

Milton R. Pickus, Principal Investigator

1. LIQUID PHASE SINTERING OF HIGH CARBON ALLOYS IN THE IRON-CARBON SYSTEM

John R. Klein and Milton R. Pickus

Liquid phase sintering was employed to achieve, by a simple two-stage procedure of compaction and sintering, a virtually fully-dense material. The lowest temperature at which a liquid phase can be obtained in this system is 1155°C, the iron carbon eutectic temperature. It was observed, however, that even rapid heating of compacts of elemental powders to 1175°C did not produce a useful transient liquid phase in compositions containing up to 2 wt.% of graphite. This was attributed to the rapid homogenization resulting from the high diffusion rate of carbon in iron. To achieve a liquid phase in compacts containing less than 2 wt.% graphite it would be necessary to heat to increasingly higher temperatures, as the carbon content decreased, temperatures far in excess of those used in commercial practice, and therefore impractical. Consequently a two stage approach was adopted: (1) the use of carbon contents in the range of 2 to 2.5 w/o to investigate the potential of liquid phase sintering at moderate temperatures, and (2) an effort to control the microstructure by thermal treatments and alloy additions so that materials with useful properties could be obtained. This is a report of the work done on the first stage.

Parameters such as powder characteristics, uniformity of blending, compacting pressure, heating program and the volume fraction of liquid phase at the sintering temperature were all found to influence the sintered density. Using atomized iron powder and Dixon "microfine" graphite, a number of mixing techniques were investigated; all resulted in a mix that segregated during handling. The addition of 3×10^{-4} cc of mineral oil per gram contributed sufficient interparticle cohesion for a stable blend to result from standard mixing procedures. Samples compacted at 20,000 psi in a steel die were heated in a vacuum (10^{-6} mm Hg) at a rate of 30°C/min. Two minutes after the temperature had exceeded 1155°C, distortion of the compacts by outgassing was visually observed. To circumvent this, the temperature was maintained for 30 min. at 1130°C before being increased to the super solidus temperature of 1175°C. Compacts containing 2.2, 2.3 and 2.5 wt.% carbon were heated in this manner and sintered for 30 minutes at 1175°C. It was found that the sintered density increased with increasing carbon content, reaching a maximum of 95% theoretical density for compacts with 2.5 wt.% carbon. According to the iron-carbon phase diagram a volume fraction of 25% liquid phase was present for this carbon content. Large isolated pores were observed in the microstructure, as shown in Fig. 1. From a consideration of equilibrium conditions at the sintering temperature, it was concluded that these large pores could be a result of graphite segregation which caused localized melting. The liquid thus formed would flow by capillary action into the pore network leaving in its place the observed large pores. This hypothesis was confirmed by several experiments.

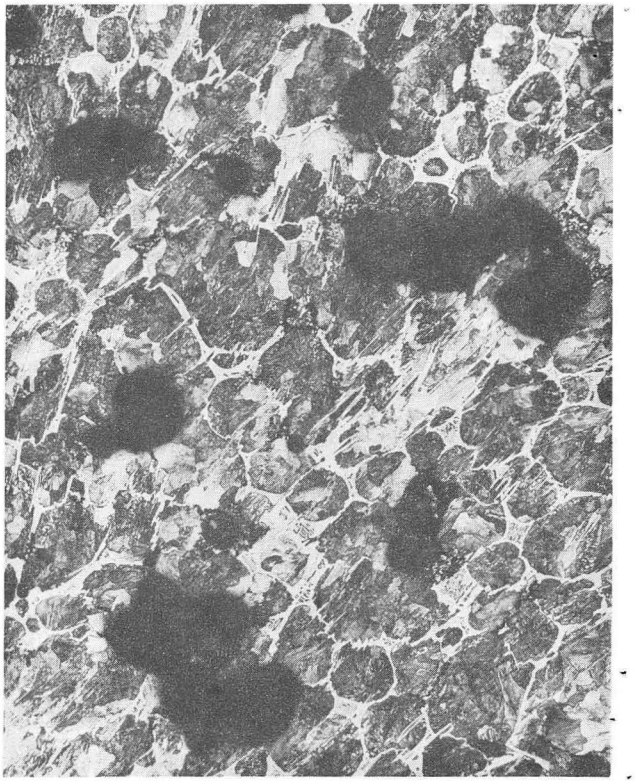

Fig. 1. Microstructure of compact containing 2.5 wt.% carbon, liquid phase sintered for 30 min at 1175°C, showing large isolated pores. (XBB 752-1521)

One experiment was designed to exclude the possibility of graphite segregation by eliminating the need for an extremely intimate blend of constituents. The same powders and mixing techniques were employed to prepare samples containing 2 wt.% carbon. Compacts were heated for one hour at 1140°C to allow for outgassing, and complete homogenization, since gamma iron can dissolve 2 wt.% carbon at this temperature. To maintain a 25% volume fraction of liquid phase for this composition, the sintering temperature had to be raised to 1250°C. Virtually full density (~ 99%) was obtained after sintering for 30 min at this temperature.

A second experiment was designed to achieve full density at the lower temperature of 1175°C, by ensuring a more intimate powder blend and thus

avoiding graphite segregation. In this case the iron particles were coated with graphite, using DAG 154, a colloidal suspension of graphite. Compacts containing 2.4 wt.% carbon prepared in this manner were 99% dense after a 30 min sinter at 1175°C. Another successful technique for avoiding graphite segregation was found. Nearly full density at 1175°C was also obtained when the carbon was added as a white cast iron powder rather than as free graphite.

In order to determine the volume fraction of liquid phase necessary for complete and rapid densification, samples containing 2.2, 2.3 and 2.4 wt.% graphite (corresponding to 11, 16 and 21 volume percent liquid phase at 1175°C) were prepared by coating atomized iron powder with colloidal graphite. After sintering for 1/2 h at 1175°C the respective densities were 92, 95 and 99% of the theoretical. To get an indication of how rapidly densification was proceeding in the presence of a liquid phase, a sample containing 2.4 wt.% graphite was heated for 10 min. at 1175°C. The density achieved was 98% of theoretical.

The reason for the need of an extensive heating at 1130°C prior to the super solidus sintering was investigated. It was found to be the result of a characteristic of the atomized iron powder. Isolated pores presumably containing entrapped gas, and unidentified inclusions were observed in the microstructure of the powder particles. Carbonyl iron powder, in contrast, was found to be free of these sources for outgassing. Figure 2 shows the microstructure of a compact made from carbonyl powder with 2.4 wt.% graphite as a colloidal coating. The compact was heated from 500 to 1175°C in one min. and held at 1175°C for 10 min. The density was 99% of theoretical.

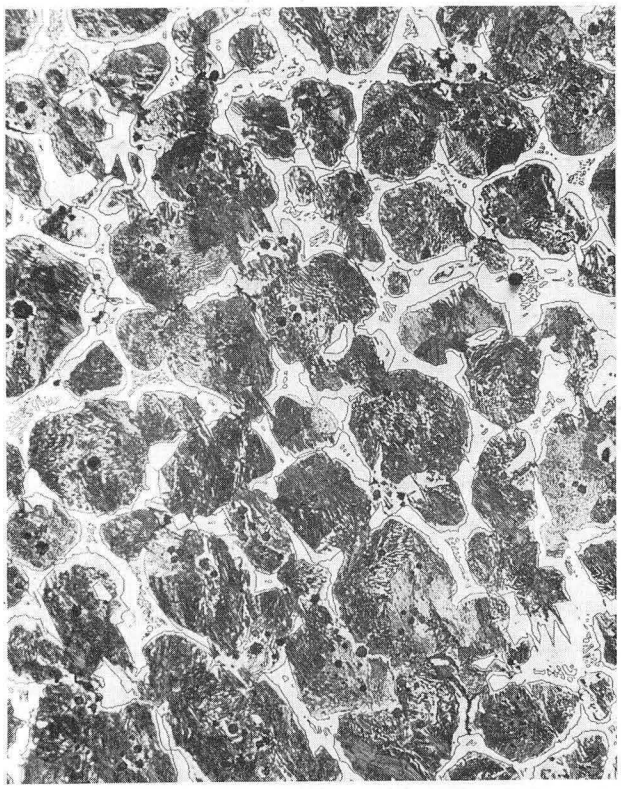

Fig. 2. Microstructure of compact containing 2.4 wt.% carbon, liquid phase sintered for 10 min at 1175°C. Nearly theoretical density (~99%) (XBB 752-1522)

Work on stage 2, control of microstructures, is just beginning. Preliminary results suggest interesting developments.

2. PRELIMINARY STUDIES OF THE RARE-EARTH IRON LAVES PHASES PREPARED BY POWDER METALLURGY TECHNIQUES

Moshe P. Dariel and Milton R. Pickus

Outstanding among the remarkable properties of the rare-earth (R)-iron, RFe_2 Laves phases is the recently reported huge magnetostriction, larger by nearly two orders of magnitude than that of previously known materials. Noteworthy also is the large "ΔE" effect, i.e., the significant increase of the sound velocity upon the application of an external magnetic field. These compounds appear therefore to be potentially valuable materials for a variety of practical applications.

The Laves phases, like most intermetallic compounds, are extremely brittle and cannot be formed or machined by conventional methods. A powder metallurgical approach to prepare these materials in useful shapes and sizes seemed therefore appropriate. The immediate objective is to determine the variables and optimize the conditions associated with powder metallurgical processing methods.

The first experiments were carried out on the Gd-Fe and Tb-Fe systems. The initial effort is to achieve control of the micro- and macro-structural characteristics of the material prepared from powder. The results indicate that a significant excess of the rare earth component (38 a/o instead of the stoichiometric 33.3 a/o) is required. The gases absorbed on the surface of the powder particles in the course of the various stages of their preparation react preferentially with the rare earth metal during sintering at elevated temperatures. This results in radial concentration gradients within each particle and the formation of iron-rich intermetallic phases such as $TbFe_3$ and Tb_6Fe_{23}.

The presence of a large excess of the rare-earth metal causes the appearance of a liquid phase above the R-RFe_2 eutectic temperature. It was observed that liquid phase sintering as compared with solid state sintering gives rise to a greatly increased grain size of the RFe_2 phase.

As work continues in seeking solutions to these problems, studies are being made of various compaction methods to obtain the desired geometrical configurations. Figure 1 shows a 3/4 in.-diameter ring made by uniaxial compaction of $TbFe_2$. Preliminary results indicate that for

this configuration isostatic compaction would be preferable.

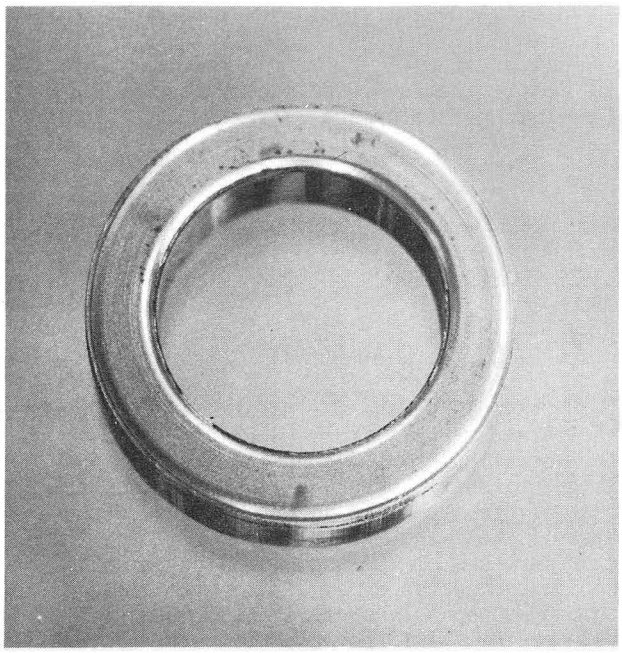

Fig. 1. A 3/4 in. diameter ring made by uniaxial compaction of terbium-iron Laves phase powder. (LBB 752-1530)

3. MORPHOLOGY CONTROL OF TITANIUM CARBIDE AS A DISPERSED PHASE IN A TYPE 410 STAINLESS STEEL MATRIX

Federico J. Reinel and Milton R. Pickus

A class of materials needed in advanced systems, and for which a powder approach is especially suited, is that characterized by a dispersion, in an appropriate matrix, of fine particles of thermally stable, hard compounds such as the oxides, carbides, borides and nitrides of the reactive and refractory metals. Such materials can provide the important properties of low friction, resistance to abrasion and corrosion, and increased strength at ambient and elevated temperatures. As part of an effort in this direction a study was initiated on the titanium carbide-stainless steel system. To provide a wide range of properties type 410 stainless was chosen as a heat treatable matrix.

Elemental powders in proportions corresponding to type 410 stainless steel were blended with titanium carbide powder. The compositions studied ranged from 20 to 45 volume percent titanium carbide. Process variables investigated included milling procedures, sintering time, temperature and atmosphere; and the influence of varying proportions of titanium carbide.

It was found that ball milling the component powders for 24 h under a protective cover of hexane produced a uniform blend that was reflected in good compaction and final microstructure. Sintering in vacuum or in an atmosphere of helium produced similar results. Sintering time and temperatures were the critical parameters. The influence of varying the proportions of matrix and titanium carbide was negligible. Good bonding between the matrix and the titanium carbide was obtained by sintering for 2 h at a temperature of 1450°C. Under these conditions a liquid phase was present, and this appears to be the most significant factor in obtaining a uniform dispersion of well-rounded particles of titanium carbide. Lower temperatures and shorter times tended to result in a continuous network of the titanium carbide. An indication of the progress made thus far is shown in Fig. 1. A few isolated residual pores are evident.

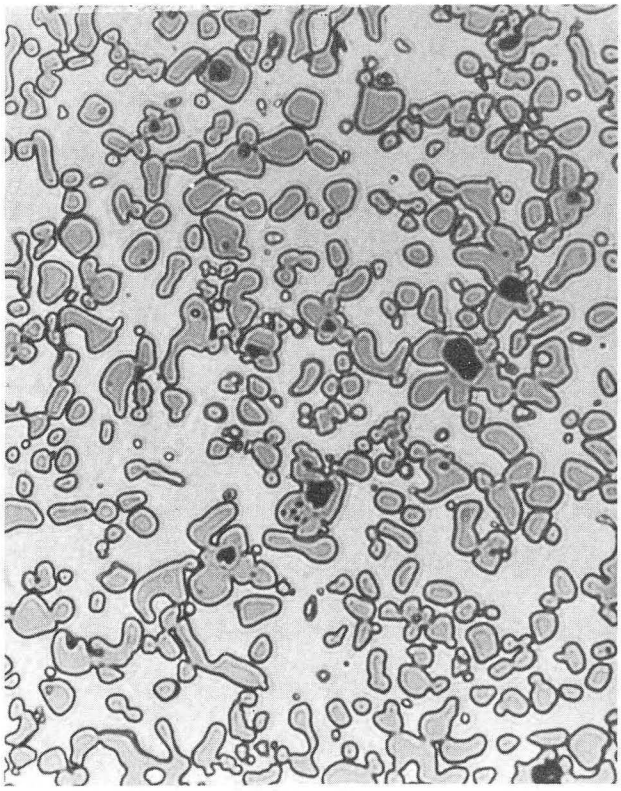

Fig. 1. Microstructure of compact containing 42 volume percent titanium carbide dispersed in a type 410 stainless steel matrix. Sintered 2 h at 1450°C. (XBB 752-1520)

4. A SURVEY OF METHODS FOR COATING POWDER PARTICLES, WITH RESULTS OF SOME EXPLORATORY EXPERIMENTS

Marija H. Fukarova

Engineers concerned with nuclear reactors, gas turbines and aerospace applications have been confronted with design demands which led to a new technology. This is the field of coated powders in which a core particle is sheathed

within another material. Coated powders have potential in powder metallurgy because they protect the substrate particles from each other, which is important in producing magnetic materials; they permit improvements in compaction by providing lubrication and binding; and they modify the interaction properties of the base particles. A literature survey has been conducted to assess the current state of the art. From the available methods described, a few have been selected for experimental investigation of their suitability for laboratory scale operation. The results of these preliminary experiments are discussed with particular reference to particle size and shape.

Because of the limited time available, the major part of the effort was concentrated on two variations of electro-deposition: the use of a fluidized bed and the use of simple mechanical agitation. The fluidized-bed approach was found to be suitable for a variety of substrate powders provided the particle size was larger than approximately 44 microns. With smaller particle sizes the results were unsatisfactory. Fine powder was carried by the flowing electrolyte out of the fluidizing tube even at low flow velocities. Modifications of the apparatus to keep the powder in a constant volume of electrolyte were unsuccessful due to clogging of the upper porous plate.

Simple agitation of the powder by means of a variable speed stirrer gave better results with two of the powder size ranges attempted: +325 mesh (> 44 microns) and -400 mesh (< 37 microns). For powders in the submicron range, the method employed was not very satisfactory. Figure 1 shows a cross section of -200 + 325 mesh copper powder electrolytically coated with tin. While the coating appears uniform on each copper particle, it was noted that the thickness of the coat appeared to vary inversely with particle size.

It is now believed that vapor plating in conjunction with a fluidized bed would be the most versatile approach for smooth and continuous deposits on powders varying in size even down to the submicron range.

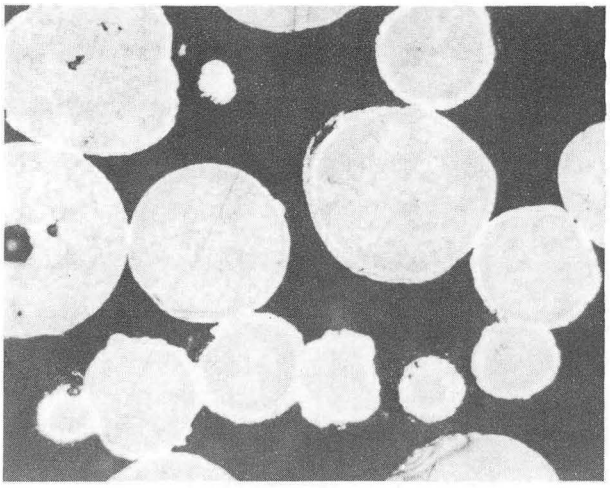

Fig. 1. Cross section of -200+325 mesh atomized copper powder electrolytically coated with tin. (XBB 747-4705)

5. RESEARCH PLANS FOR CALENDAR YEAR 1975

Milton R. Pickus,

The research program on the rare earth-iron Laves phases will concentrate on the terbium-iron system. The compound $TbFe_2$ is one of the most promising from a technological standpoint. Since the properties on which this potential is based--for example, its very large magnetostriction--have become known only recently, the system has received little attention. In fact, there is no published phase diagram, and we may well find it necessary to determine at least its principal features in order to achieve our objective of developing procedures to produce this compound in technologically useful forms. A powder approach appears most appropriate in view of the extreme brittleness of the compound. It is planned to determine the influence of the following process variables: mode of compaction, sintering time, temperature and atmosphere, and the effect of additives.

In order to achieve nearly theoretical density in the iron carbon system by means of liquid phase sintering at moderate temperatures, it was found necessary to use carbon contents in the range of 2 to 2.5 wt%. The resulting microstructure is characterized by a carbide network that is detrimental to mechanical properties. An immediate objective is to investigate procedures to develop controlled microstructures and to correlate them with mechanical properties. A further aim is to apply these results to other ferrous systems.

For the program concerned with cermets containing carbides, borides, oxides, and nitrides in a variety of matrices, both ferrous and nonferrous, test equipment is being designed and constructed so that measurements can be made of relevant properties such as coefficient of friction and resistance to wear. Furthermore, composites involving intermetallic compounds will also be considered.

To fill a recurring need in designing new alloy systems a powder making facility will be designed and fabricated that will make possible the preparation of prealloyed powders under controlled conditions of atmosphere and rate of solidification. Two of the important applications may be mentioned: the preparation of master alloy powders to facilitate the addition of specified amounts of special alloying elements, and secondly, the preparation of alloy powders in a metastable state.

Depending on the progress made in certain ongoing programs a more intensive involvement in powder coating procedures may become necessary. These are programs which require a very homogeneous blend of elemental powders. At the present time conventional mixing techniques are being used, and they may prove inadequate.

6. 1974 PUBLICATIONS AND REPORTS

Milton R. Pickus and Associates

Journals

1. M. R. Pickus, K. Hemachalam and B. N. P. Babu, Superconducting Properties of a Powder Rolled Composite Tape Containing Nb_3Sn Filaments, Materials Science and Eng. 14, 265 (1974) (LBL-1838).

2. Milton R. Pickus, Earl R. Parker and Victor F. Zackay, Method of Manufacturing A Ductile Superconductive Material, U.S. Patent 3,815,224 June 11, 1974.

LBL Reports

1. Milton R. Pickus, A Powder Approach to the Design of High Field Superconducting Materials, LBL-2563 Abstract; Jan. 1974 (Invited lecture presented at the Metallurgical Society Meeting, Pittsburgh, Pa., May 19-23, 1974.

2. Marija H. Fukarova, A Survey of Methods for Coating Powder Particles with Results of Some Exploratory Experiments, LBL-3506, Dec. 1975.

3. John R. Klein, Liquid Phase Sintering in the Iron Carbon System LBL-3549, Dec. 1974.

4. Kanithi Hemachalam and Milton R. Pickus, Filamentary Superconducting Wire Made by a Powder Metallurgy Approach, LBL-3552, Dec. 1974.

5. Federico Reinel, Morphology Control of Titanium Carbide As a Dispersed Phase In a Type 410 Stainless Steel Matrix, LBL-3561, Dec. 1974.

6. M. P. Dariel and U. Atzmony, Unusual Easy Directions of Magnetization in Some Rare-Earth Iron Cubic Laves Compounds, LBL-3555, Dec. 1974.

I. ADVANCED MATERIALS

Robert H. Bragg, Principal Investigator

Introduction. Recent developments in the synthesis of materials have stimulated interest in the physical properties of vitreous or Glassy Carbon (GC), and directionally solidified eutectics. Glassy Carbon is of interest because it is the hardest, least chemically reactive, and the most impermeable known form of carbon (exclusive of diamond). These properties have already found many commercial applications as refractories such as thermocouple tubes and ceramic boats, dental implants, and heart valves, as well as classified military applications. Glassy Carbon is of fundamental interest because it is the best available representative of the general class of "hard" (nongraphitizing) carbons. It does not undergo appreciable grain growth or ordering in layer stacking even when heated to temperatures near 3000°C. While a reasonably fundamental understanding of soft carbons has been reached in the last 10 years, much less is known about hard carbons. This research addresses the problem of determining if the physical properties of hard carbons can be understood from a unified viewpoint. Our immediate objective is to determine if the heat-induced changes in lattice disorder, microstructure, and physical properties of GC can be described as a unique function of temperature and time. To do this we are studying the structure of heat treated GC using X-ray diffraction; small angle X-ray scattering; and measurements of the electrical conductivity (σ); Hall effect, R_H; and magnetoresistance, $\Delta\rho/\rho$.

Directionally solidified eutectics are composite materials which have emerged from the laboratory as a result of fundamental studies of solidification. They are of interest and importance because eutectic alloy systems have been found that demonstrate great improvements in critical physical properties such as fatigue, creep and corrosion. Because of the thermodynamic properties of eutectics, improvements in microstructural stability at elevated temperatures compared to wrought or conventionally cast materials is obtained. There are three basic types of eutectics: (1) metal-metal, in which at least one phase is an intermetallic and regular microstructures are relatively easy to obtain; (2) metal-nonmetal in which coupled growth (planar liquid-solid interface) is difficult to obtain; and (3) nonmetal-nonmetal eutectics. While many of the principles applicable to the prediction of mechanical and thermophysical composite properties are understood, little is known about electrical properties. We are studying the growth, characterization and electrical properties of the Al-Cu and Al-Si eutectics to provide a basis for predicting these properties. Where applicable the basic mechanical properties, e.g. elastic modulus, and strength, are studied.

1. X-RAY STUDIES OF GLASSY CARBON

Ram R. Saxena and Robert H. Bragg

X-ray diffraction characterization of Glassy Carbon (GC) is difficult because only a few extremely broad, low-intensity interference maxima are observable unless the material has been heated to a very high temperature. Figure 1 shows typical data obtained with CuK_α radiation. The apparent crystallite sizes for the 1000°C material is of the order of 10 A, and even after heating at 2800°C grain growth has only progressed to about 50 A. There is a strong diffuse scattering at low angles (especially for low-temperature heat treatments) which heretofore has been interpreted as "disordered" carbon. It is necessary to determine both the line widths and peak positions, and to characterize the "disordered" carbon in order to measure crystallite size and carbon interlayer spacings as these parameters are changed by heat treatment. A possible explanation of the origin of the scattering due to "disordered" carbon is that it is an artifact due to multiple diffraction from the small randomly oriented crystallites. Following Warren,[1] approximate calculations have been made which predict the qualitative features of the observed "disordered" scattering as a function of crystallite size, and furthermore explain a heretofore puzzling diffuseness and overlapping of the (10) and (004) maxima. Theory indicates that the effect should decrease as the depth of irradiated material decreases. Data from a GC plate polished to 0.014 in. thick are also shown in Fig. 1. The magnitude of the "disordered" component is decreased by thinning the specimen. Further evidence that the "disordered" component is an artifact is gained by comparing the shapes of line profiles obtained by subtracting the rising background from the two 1000°C curves. As

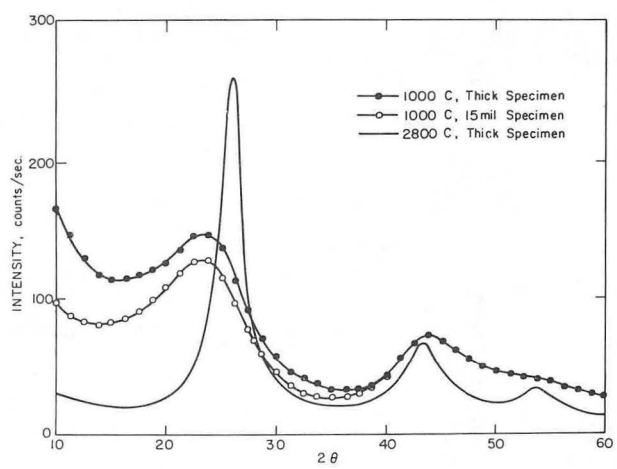

Fig. 1. X-ray studies of GC. (XBL 751-5424)

shown in Fig. 2, the derived curves superimpose when normalized. The indications are clear that the interpretation of line profiles can be simplified by a suitable choice of experimental conditions. An asymmetry in the line profile derived in this way has been found to be removed (and the line width is decreased) when account is taken of the variation in the Lorentz polarization factor and atomic scattering factor, f^2, of carbon over the range of the broad (002) interference maximum. The broadening due to this source causes an overestimate of line width and hence an underestimate of crystallite size. When this is considered along with the additional broadening due to strain[2] in carbons, it is clear that the X-ray studies of crystallite size of this material must be far more thorough than is the case for metallic materials. It also appears that it will be possible to determine both crystallite size parameters L_a and L_c, by separating the overlapping (10) and (004) maxima, even in cases where previously, only an estimate of L_c was considered possible. This is vital to our characterization of temperature-induced crystallite growth in GC.

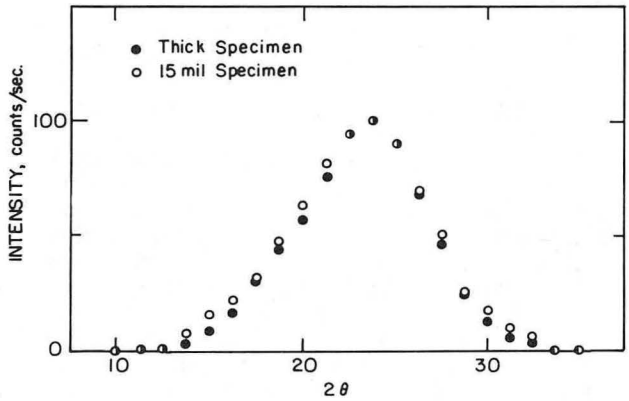

Fig. 2. Normalized (002) line profiles.
(XBL 751-5423)

1. B.E. Warren, X-Ray Diffraction (Addison-Wesley, Menlo Park, 1969), pp. 116-149.
2. P. Thrower and T. Nagle, Carbon 11, 663 (1973).

2. KINETIC STUDIES OF ORDERING IN GC

Ram R. Saxena and Robert H. Bragg

The (002) maxima X-ray diffraction were obtained for a series of GC samples heat treated at various temperatures. The results were corrected according to procedures described in section 1 and are shown in Fig. 1. If a translation along the time axis can bring the curves for all temperatures into superposition, it will be demonstrated that structural changes in GC follow one path in (T,t) space, just as in the case of soft carbons.[1] A curve derived from a plot of the ln t translations vs 1/T will have one or more linear portions, an indication that the

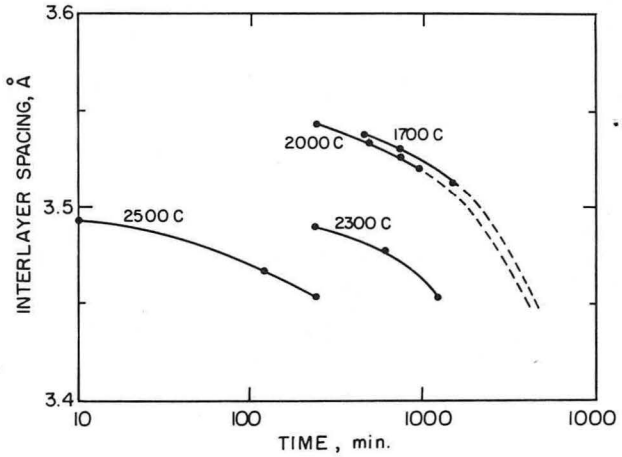

Fig. 1. Kinetic studies of ordering in GC.
(XBL 751-5422)

structural changes in GC can be represented by first-order processes. The data obtained thus far show that kinetic data for GC can be derived, just as was found for the changes in pore size by small-angle scattering, but are not extensive enough to permit the analysis indicated. However, they indicate a strong likelihood that an activation energy for at least one process can be obtained. Our results also serve as a guide to planning the experiments necessary to complete the analysis. One of the implications is that at the lower temperatures, runs of the order of 50 hours at ~1700°C will be required, but fortunately much shorter times will suffice at the higher temperatures where the heating element life is short. These kinetic data are believed to be the first obtained for any characteristic of GC.

1. D. B. Fishbach, JPL Technical Report, 32-532, 1969.

3. ELECTRICAL PROPERTIES OF GLASSY CARBON

Ram R. Saxena

In previous work[1] it was found that the electrical conductivity of GC indicates a small, 0.0015 eV, band gap semiconductor and at sufficiently low temperatures has features analogous to amorphous semiconductivity. Measurements have also been made of the Hall effect and magnetoresistance, $\Delta\rho/\rho$, in GC samples. The variation of $\Delta\rho/\rho$ with magnetic field H from one sample is shown in Fig. 1. Both positive and negative magnetoresistance is observed. As yet there is no accepted theory to explain both negative and positive values of $\Delta\rho/\rho$ in one material. The data are shown replotted versus log H in Fig. 2. In each case the theoretical H^2 dependence of $\Delta\rho/\rho$ is not obtained. Also, it appears that the magnetoresistance always contains both positive and negative components with the positive component dominant at low temperatures, but more data are needed to establish the generality of this phenomenon. Hall

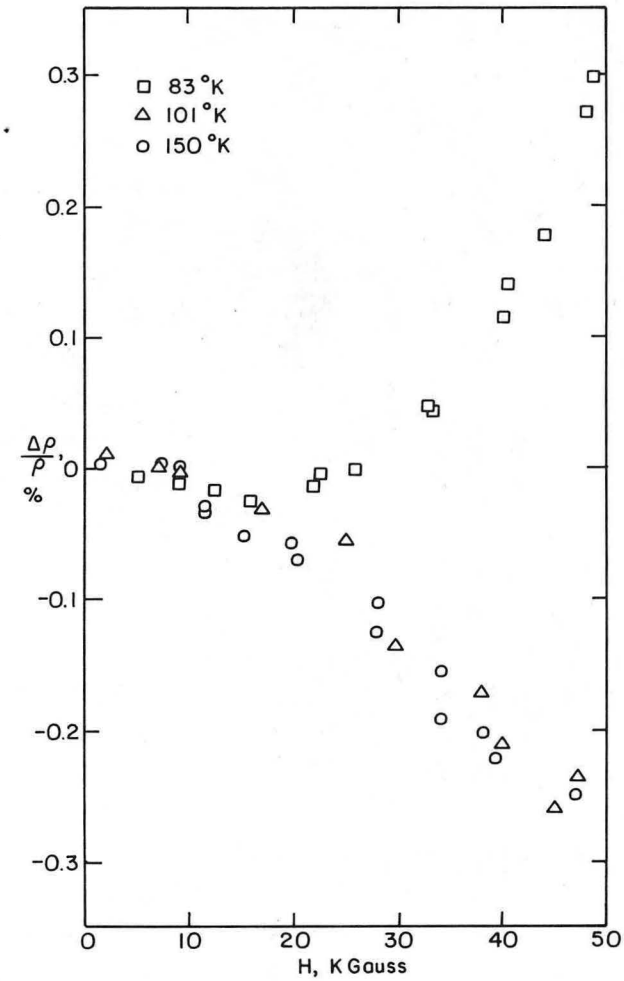

Fig. 1. Variation of $\Delta\rho/\rho$ with temperature. (XBL 751-5420)

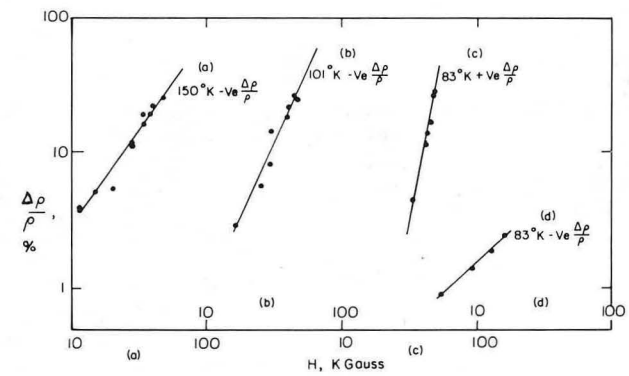

Fig. 2. Variation of $\Delta\rho/\rho$ vs T. (XBL 751-5421)

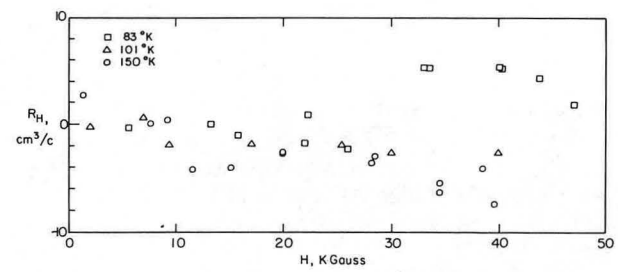

Fig. 3. Hall effect in GC. (XBL 751-5419)

effect data on the same sample are shown in Fig. 3. The scatter of these data is still considerable, but it appears that the number of charge carriers is ~$10^{18}/cm^3$, the same order of magnitude as in soft carbons and oriented pyrolytic graphite. When this fact is combined with the results of conductivity and magnetoresistance measurements, both most sensitive to mobility changes, it seems that an explanation must be sought in the microstructure of GC. Thus a strong correlation and coordination must be maintained between the X-ray studies and the electrical-property investigation.

---

1. R. Saxena and R. H. Bragg, IMRD Annual Report for 1973 (LBL-2299), pp. 180.

4. ELECTRICAL RESISTIVITY OF Cu-Al_2 EUTECTIC

Kwaku Danso and Robert H. Bragg

Electrical resistivity measurements have been made on in situ composite materials grown by unidirectional solidification of the Al-Cu eutectic. The objective of this work was to determine if the simple rule of mixtures, applicable to the mechanical properties of ideal lamellar composites having a microstructure such as that shown in Fig. 1, also applies to the electrical resistivity. Al-Cu eutectic composites and an Al-5.7Cu alloy were grown at various rates, R, cm/sec, in a horizontal furnace in which the temperature gradient, G, at the liquid-solid interface was 29°C/cm. Typical microstructures are shown in Fig. 2(a), (b), and (c). It was found that the interlamellar spacing λ obeyed the expected relationship $\lambda^2 R$ = constant. Electron micrographs of the eutectic, Fig. 3, showed that whereas the composite is essentially a duplex single crystal, the θ phase precipitates in the K (Al-5.7Cu) matrix are not oriented. The effect of directional solidification on the longitudinal resistivity of the eutectic and the

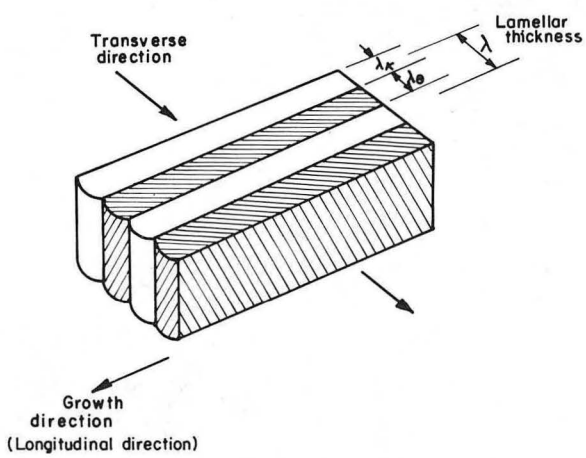

Fig. 1. Ideal microstructure of a two-phase lamellar composite. (XBL 7412-7678)

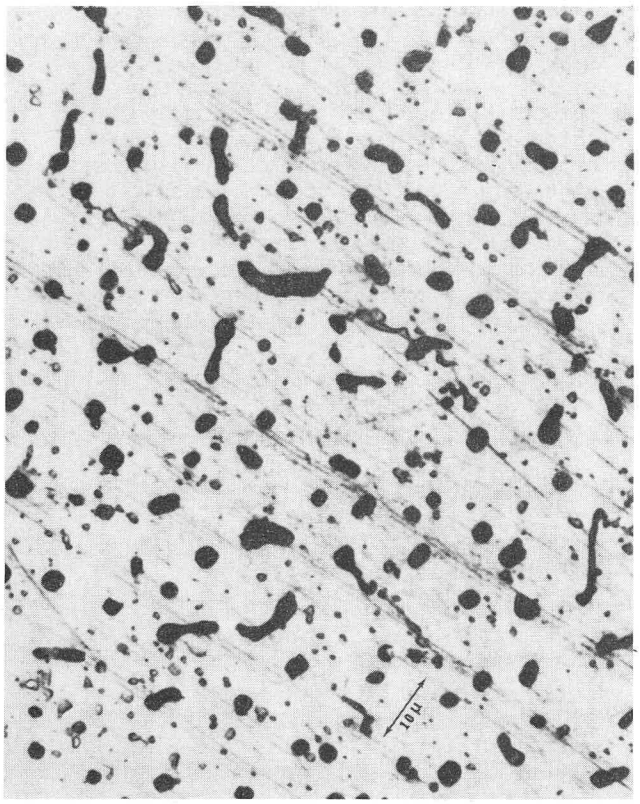

Fig. 2a. Structure of as-cast polycrystalline Al-5.7 wt% Cu showing formation of $CuAl_2(\theta)$ precipitates in the Al-rich (κ) phase. Magnification 2000×. (XBB 7412-8870)

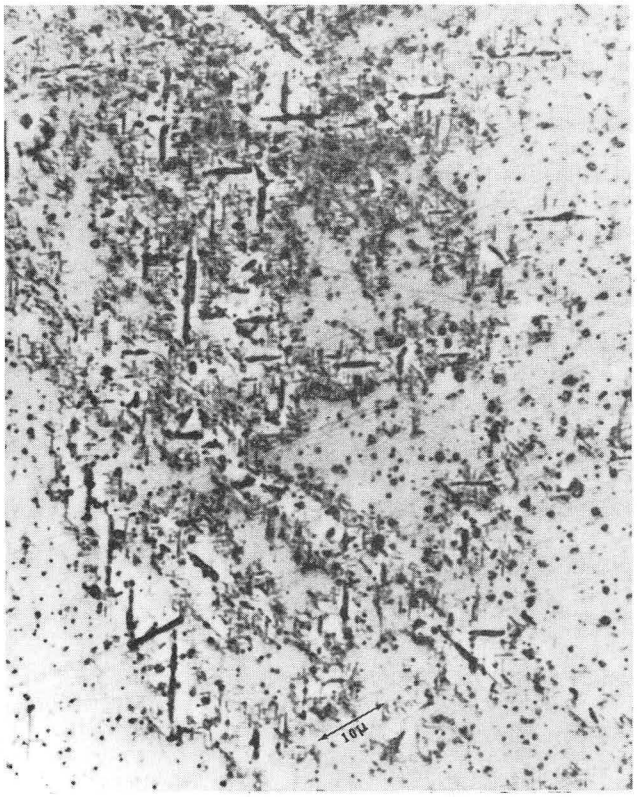

Fig. 2b. Longitudinal view of unidirectionally solidified Al-5.7 wt% Cu. Growth direction left to right. Magnification 2000×. (XBB 7412-8869)

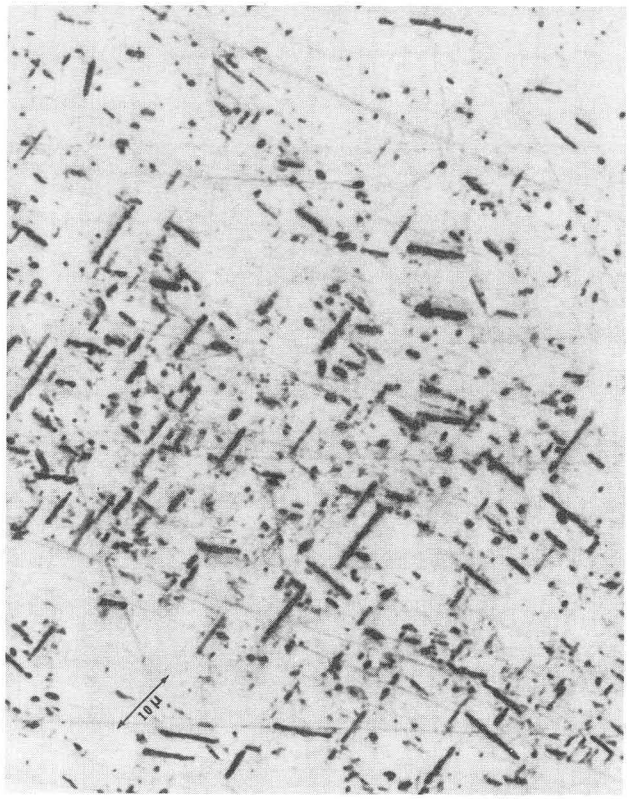

Fig. 2c. Transverse view of same alloy as (b). Growth direction perpendicular to picture. Magnification 2000×. (XBB 7412-8868)

Al-5.7Cu alloy are shown in Fig. 4. The resistivity of both is reduced by directional solidification, but the reduction of resistivity for the Al-5.7Cu alloy was contrary to expectations. Resistivity data for the eutectic alloy and the K phase are shown in Fig. 5, in which both have been solution heat treated, aged at 315°C, and quenched to 25°C for electrical measurements. Calculations of the resistivity of the θ phase assuming the simple rule of mixtures (upper curve in Fig. 5), showed that the inferred values are not reliable, even if the assumption is correct. The value derived for the resistivity of $CuAl_2$, θ, from these data is 9.9±0.1 μΩ cm, whereas in experiments where the aging was done at 25 and 150°C, resistivities of 8.2 and 8.3 μΩ cm respectively were estimated. No transverse measurements have been made to date, and as yet no attempts have been made to grow the θ phase separately. It appears that the assumption that the simple rule of mixtures is not justified in in situ composites where one or both phases has properties sensitive to microscopic phase geometry. One definitive result of the work was the finding that the room temperature resistivity of the Al-5.7Cu alloy is 4.65±0.05 μΩ cm. As shown in Fig. 6 this result extends Mathiessen's rule across the whole range of solid solubility in the Al-rich end of the Al-Cu phase diagram. This work was the M.S. thesis of K. Danso, LBL-3547, Dec. 1974.

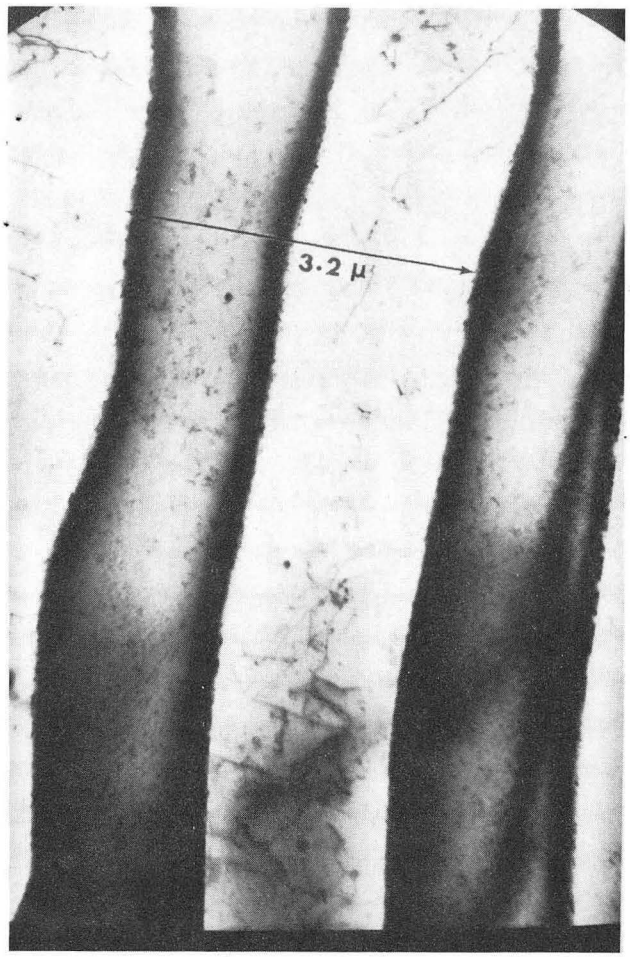

Fig. 3. Bright field transmission electron microscope picture of Al-$CuAl_2$ lamellar eutectic. Transverse view-growth direction normal to picture. (XBB 7412-8875)

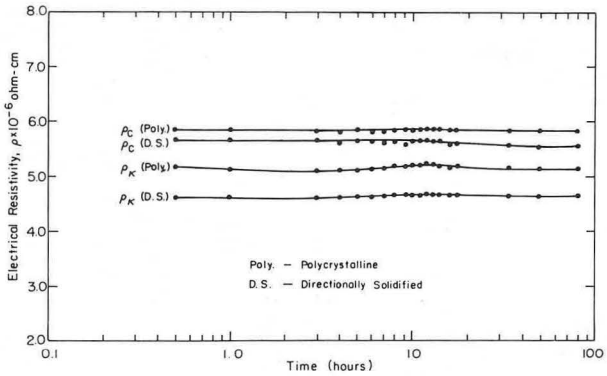

Fig. 4. Electrical resistivity vs aging curves at 25°C showing effect of unidirectional solidification on ρ for Al-5.7 wt% Cu (κ) and Al-33.3 wt% Cu. (XBL 7412-7677)

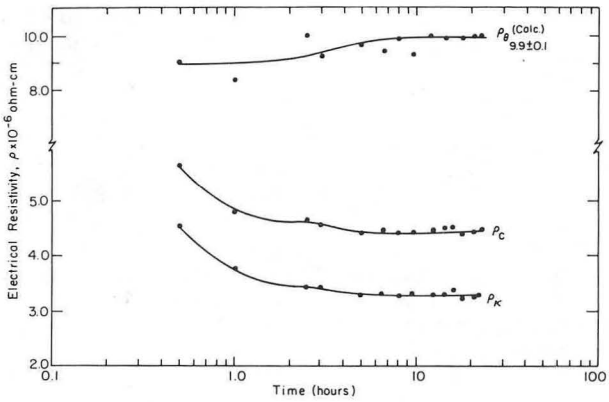

Fig. 5. Electrical resistivity vs aging curve at 315°C. (XBL 7412-7682)

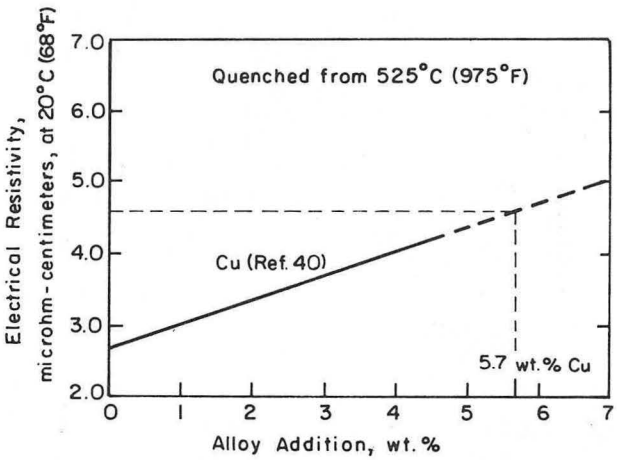

Fig. 6. Effect of Cu additions on the electrical resistivity of Al. (XBL 7412-7676)

5. UNIDIRECTIONAL SOLIDIFICATION OF Al-Si EUTECTIC

Stefan Justi* and Danny G. Morrow

Well-aligned unidirectionally solidified eutectics can be obtained if the conditions during growth satisfy the relationship

$$\frac{G}{R} \geqslant \frac{mC_s(1-k_0)}{Dk_0} ,$$

where G is the temperature gradient at the solid/liquid interface; R is the growth rate; m is the slope of the liquidus line; k_0 is the distribution coefficient defined by $k_0=C_s/C_\ell$, where C_s and C_ℓ are the compositions of the solid and liquid phases respectively; and D is the diffusion coefficient in the liquid ahead of the solid/liquid interface. Thus best results are expected with high-temperature gradients, low growth rates, and high-purity materials. Alloys of Al-Si eutectic composition have been prepared from 99.999 purity

Al and Si. The apparatus used successfully in the solidification of Al-Cu eutectic could only attain gradients G of 29°C/cm, which is not sufficient for the Al-Si system. The furnace has been redesigned with improved chilling so that temperature gradients of 60···100°C/cm can be attained, high enough to prevent constitutional supercooling. Also, a ceramic boat has been substituted for graphite to improve unidirectional (longitudinal) heat flow conditions. Tests of the redesigned apparatus in growing the Al-$CuAl_2$ eutectic showed that even in this case, improved lamellar microstructures are always obtained. In the Al-Si eutectic, silicon is the leading phase during solidification. Thus, in order to prevent independent growth of this phase, and hence irregular dedritic growth into the melt, an optimum G/R must be used. Figure 1(a) shows the microstructure of as-cast Al-Si eutectic alloy, and Fig. 1(b) shows the microstructure obtained after directional solidification. It can be seen in Fig. 1(b) that growth is mostly noncoupled, although there is a preferential orientation of silicon rods parallel to the growth direction. However, in some areas [Fig. 1(c)] coupled growth is observed. Since coupled growth is favored at lower growth rates a series of runs in the range 0.1 to 47.0 cm/h have been made but the specimens have not been analyzed.

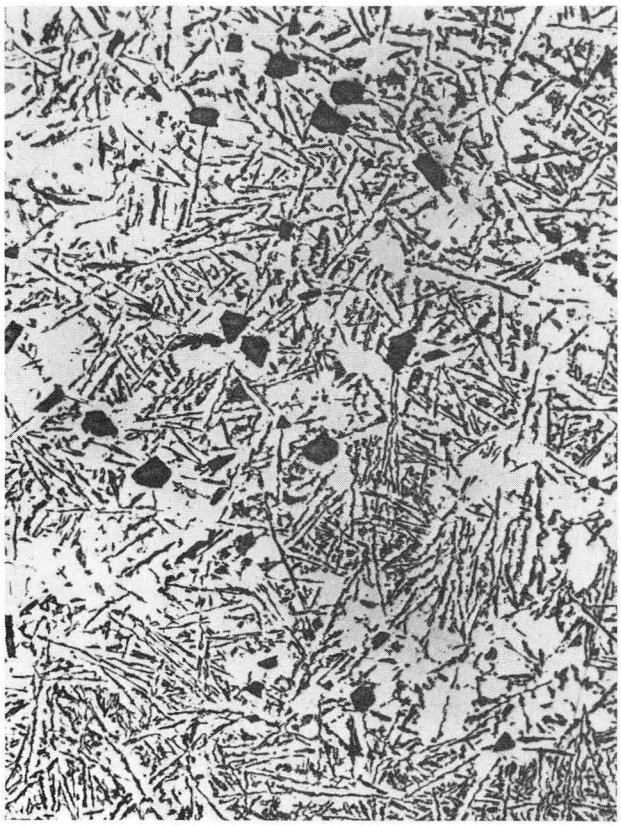

Fig. 1(a) Al-Si eutectic (as cast) mag. 80x. Dark spots are porosity. XBB 751-202

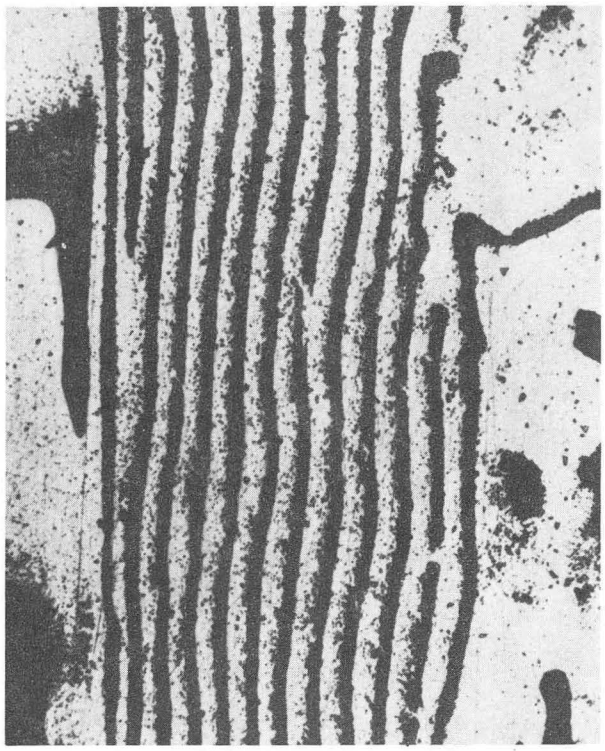

Fig. 1(b) Unidirectionally solidified Al-Si eutectic. R=4.6 cm/hr, G=66°C/cm, mag. 80x, Growth direction from bottom to top. XBB 751-200

Fig. 1(c) Unidirectionally solidified Al-Si eutectic showing an area of coupled growth. R=4.6 cm/hr, G=66°C/cm, mag 1000x. Growth direction from bottom to top. XBB 751-201

---

*Dr. S. Justi is a Max Kade Postdoctoral Fellow from the Technical University of West Berlin.

6. SMALL-ANGLE SCATTERING BY GLASSY CARBON AND PYROLYTIC GRAPHITE

Sundkangshu Bose and Robert H. Bragg

This work is a continuation of that begun by M. M. Biswal. Considerable time has been spent reviewing the previous work and recalibrating the small-angle scattering apparatus. A fixture to simplify studies of oriented materials has been designed. Specimens of heat treated Glassy Carbon (see work of R. Saxena) have been prepared for small-angle scattering measurements, along with specimens of pyrolytic graphite necessary to complete the experimental confirmation of the theory of Hamzeh and Bragg.[1] In this work it is shown that a dilute suspension of oriented ellipsoids of revolution of axes 2a, 2a, 2b and a fixed orientation ϕ scatter as a Rayleigh sphere whose radius is $[a^2\sin^2\phi + b^2\cos\phi]^{1/2}$. The theory has been tested for ϕ=0 and $\pi/2$, but not intermediate values. Also no account was taken of the distortion of the intensity data introduced by the slit systems of the apparatus. "Unfolding" computational techniques must be used to eliminate this distortion. It has become apparent in reviewing data obtained by M. M. Biswal on Glassy Carbon, that the previously ignored component of scattering by local electron density fluctuations changes significantly with heat treatments, becoming smaller as the heat treatment progresses. There is mounting evidence that the pores in Glassy Carbon are really slit shaped and the electron density fluctuations are associated with the edges of slits. Thus it is necessary to construct a model to improve the interpretation of parameters which can be derived from the small-angle scattering data.

---

1. F. Hamzeh and R. H. Bragg, J. Appl. Phys. 45, 3189 (1974).

7. RESEARCH PLANS FOR CALENDAR YEAR 1975

Robert H. Bragg

Work on the lattice structure, void structure, microstructure, and electrical properties of Glassy Carbon will be continued. Additional data points at longer times at temperatures already used, plus runs in the range between 2000 and 2800°C will be obtained to complete the analysis necessary to determine if the structural changes are first order, and if more than one activation energy is involved. Concurrently the small-angle and wide-range diffraction studies will be continued. Computer programs for these studies will be written, because a large amount of raw data must be accumulated and analyzed. In the wide-range diffraction experiments better line profile analyses of layer spacings and crystallite sizes will be developed, because the quality of the raw data are greatly improved as specimen thickness is decreased. Concurrently, attempts will be made to determine to what extent the scattering in the raw data from thick samples previously regarded as due to "disordered" material can be explained quantitatively in terms of multiple diffraction. The negative magnetoresistance and amorphous semiconducting electrical properties require an as yet unavailable theory or model, and attempts will be made to fabricate, or at least simulate, a microstructure of ribbons of graphite to determine if at least a qualitative explanation is possible. The work on directionally solidified Al-$CuAl_2$ eutectics will be extended to include measurements of transverse (perpendicular to lamellae) resistivity and the variation of resistivity with interlamellar spacing, and independent measurements of the resistivity of the θ phase. It appears that single crystals of the θ phase have not been grown, but this seems feasible using the traveling solvent method. Direct quantitative determinations of the texture and orientation relationships between K and θ, in the eutectic as well as the submicrostructure of the θ precipitates in the K phase, will be made. A fixture will be designed, which can also be used for the Al-Si eutectic, to measure preferred orientation for near-single crystalline duplex material. Also, the resistivity apparatus will be redesigned to allow more accurate measurements with smaller specimens.

The elastic modulus, tensile strength, and electrical resistivity of Al-Si eutectic composites grown at rates in the range 0.1 to 47.0 cm/h will be measured and their microstructures characterized. It is known that the interdendritic spacing obeys a $\lambda^2 R$ = constant law, and in other in situ composite systems a tensile strength versus $\lambda^{-1/2}$ relationship (Petch) has been found. Careful experiments will be conducted to ascertain if the relationship holds for both rod-like Al-Si and plate-like Al-$CuAl_2$ eutectic composites. Some recent work has shown that the morphology of θ precipitates in the K phase can be controlled by application of stress during precipitation. Attempts will be made to prepare oriented θ platelets in the K phase and measure their electrical properties.

8. 1974 PUBLICATIONS AND REPORTS

Robert H. Bragg and Associates

Journals

1. R. R. Saxena and R. H. Bragg, K-Emission from Glassy Carbon, Carbon 12, 210 (1974) (LBL-1860).

2. F. M. Hamzeh and R. H. Bragg, Small-Angle Scattering of X-Rays from Groups of Nonrandomly Oriented Ellipsoids of Revolution of Low Concentration, J. Appl. Phys. 45, 3189 (1974) (LBL-1874).

0 0 0 0 4 2 0 / 2 5 5

III. Ceramic Science

A. HIGH TEMPERATURE REACTIONS

Alan W. Searcy, Principal Investigator

1. TRANSITION STATE THEORY FOR VAPORIZATION AND CONDENSATION*

Alan W. Searcy and Dario Beruto

A theory of Langmuir exactly predicts the rates of many vaporization reactions as functions of temperature. For these reactions his theory is shown to be superior to absolute reaction rate theory, which can be made to yield the same rate equation in requiring hypotheses which are less dependent on the detailed mechanism and fewer of them, and in utilizing a kinetic factor that has been directly verified by experiment. Langmuir's theory is extended to provide an exact description of the kinetics of some dissociative vaporization reactions. It is pointed out that Langmuir's gas-like kinetic factor has been experimentally verified for the desorption step of two substances that undergo retarded vaporization. It is argued that the transition state particles for desorption are free gas molecules and for surface diffusion in the self-adsorption layer are particles with gas-like velocities parallel to the surface. Rate equations which utilize gas-translation kinetic factors are derived for substances that vaporize with nonequilibrium distributions of electronic states and for substances with vaporization rates limited by separation of self-adsorbed particles from catalytic surface sites or particles. The equations for dissociative vaporization reactions require that transition state particles consist sometimes of a coupled flux of particles of two or more different kinds.

*Abstracted from J. Phys. Chem. 78, 1298-1304 (1974).

2. THE KINETICS OF ENDOTHERMIC DECOMPOSITION REACTIONS: I. STEADY STATE CHEMICAL STEPS

Alan W. Searcy and Dario Beruto

When the solid product of an endothermic decomposition reaction is porous, the rate limiting chemical step is usually assumed to be a surface step of the gaseous product or of a precursor of that product. It is shown in this paper, however, that the rate of an endothermic decomposition reaction of the general form

$$AB(s) \rightarrow A(s) + B(g) \qquad (1)$$

may be limited by a diffusion step for the ultimate gaseous product, which can be written and symbolized as

$$B \text{ (at AB-A solid interface)} \rightleftharpoons B \text{ (at AB surface)} \quad [B_i \rightleftharpoons B_s] \qquad (2)$$

instead of a surface step of that reaction component,

$$B \text{ (at AB surface)} \rightarrow B \text{ (gas)} \quad [B_s \rightarrow B_g] \qquad (3)$$

or, if component A does not readily equilibrate with component B, by either

$$A \text{ (at AB surface)} \rightleftharpoons A \text{ (at AB-A solid interface)} \quad [A_s \rightleftharpoons A_i] \qquad (4)$$

$$A \text{ (at AB-A interface)} \rightleftharpoons A \text{ (solid product phase)} \quad [A_i \rightleftharpoons A_p] \qquad (5)$$

coupled with either substep 2 or 3.

A general rate equation for steady state decomposition in vacuum is derived in terms of the rate constants for the four substeps of the overall reaction and of the thermodynamic activity of the solid product. Solutions are given for the two limiting cases when a single substep is rate limiting and for the four cases when a coupled pair of the substeps limit the reaction rate:

$$J = k_3 a_{Bp}$$

$$J = k_2 a_{Bp}$$

$$J = (k_3 k_5 K_i)^{1/2}$$

$$J = (k_2 k_5 K_i)^{1/2}$$

$$J = (k_4 k_3 K_s)^{1/2}$$

and

$$J = \frac{k_3 k_4 a_{Ap}}{k_2}$$

where J is the flux of A and of B per unit time per unit area of AB surface plus interface, the k's are rate constants for the substeps indicated by the subscript numbers, a_{Ap} is the activity of component A in the solid product phase and the K's are equilibrium constants equal to the products of activities of component A and component B at the interface i or surface s (with a_B defined as unity when the pressure of B is the equilibrium dissociation pressure). The first of these limiting solutions, with a_{Ap} assumed always equal to unity, is the only one of these solutions that has been used to interpret decomposition reactions in previous studies. The dependence of the apparent activation enthalpy for decomposition on activation enthalpies for individual reaction steps and the enthalpy of formation of the solid reaction product are found for the limiting cases, and it is shown that the rate limiting process(es) cannot be deduced from the temperature dependence of a decomposition reaction in vacuum except in the special case that all reaction steps except

desorption of the gaseous reaction product are at equilibrium.

The rate equations are compared with recent measurements of the rate of decomposition of calcite single crystals.[1] It is shown that the rate data are consistent with the interpretation that the reaction is unretarded with respect to formation of a metastable modification of calcium oxide, which was shown in the experimental study to be present as a 30 micron thick layer at the reaction interface.

---

1. D. Beruto and Alan W. Searcy, Trans. Far. Soc. I. Phys. Chem. 1974, 2145.

3. THE KINETICS OF ENDOTHERMIC DECOMPOSITION REACTIONS: II. THE EFFECTS OF PRESSURES OF THE GASEOUS PRODUCT

Alan W. Searcy and Dario Beruto

It is shown that the steady state flux J measured in an endothermic reaction

$$AB(s) \rightarrow A(s) + B(g)$$

is given by $J = J_o(1 - P_B/P_B^o)$, where J_o is the flux in vacuum, P_B is the background pressure of B gas and P_B^o is the equilibrium dissociation pressure of the reaction, if component A of the decomposition reaction is sufficiently mobile to remain at equilibrium with component B throughout the AB phase and at the solid reactant-solid product interface. If, however, a reaction step involving A is slower than any of the steps involving component B, then the steady state flux is given by

$$J = J_o \left(\frac{P_B^o}{P_B} - 1\right)$$

The difference in predicted pressure dependence between these two equations should provide a means for testing the importance of reaction steps involving the solid product of the decomposition reactions. The second equation may well provide an explanation of previously unexplained effect for decomposition reactions, an apparent approach to zero rate when the background pressure is significantly lower than the equilibrium decomposition pressure.

4. EFFECT OF POROUS BARRIERS ON THE MOLECULAR COMPOSITIONS OF REACTIVE GAS MIXTURES*

Pirooz Mohazzabi and Alan W. Searcy

Molecular effusion of chemically reactive gas mixtures through porous barriers has been studied. Our theoretical analysis indicates that when surface diffusion is negligible compared to Knudsen flow and a pressure dependent chemical reaction can take place between species of the gas mixture, then the ratio of the total mass flux of the species at the outlet side of the porous barrier to that at the inlet side of the barrier, defined as the transmission coefficient of the barrier, should be independent of any particular reaction, and should vary inversely with the thickness of the barrier. Furthermore, when equilibration of the species throughout the porous barrier is assumed and the theory is applied to a monomer-dimer reaction it turns out that the ratio of the gas flux of the dimer to that of the monomer must also vary inversely with the thickness of the barrier, i.e.

$$\frac{J_d}{J_m} = \frac{C}{\ell}$$

where J_d and J_m are exit fluxes of the dimer and monomer, respectively. C is a constant and ℓ is the thickness of the porous barrier. This result could prove useful whenever enrichment is desired in the simpler species of a reactive gas mixture. It is also shown that for Knudsen flow the total mass flux of a chemically reactive mixture, through a porous barrier should be independent of the extent to which reaction proceeds in the porous barrier and should be reduced by the same fraction for any gas that passes by Knudsen flow through the given barrier. The predications of the theory were confirmed experimentally using sodium chloride vapor and alumina disks. Figure 1 shows that monomer/dimer ion intensities, which are proportional to the monomer/dimer pressure ratio, vary

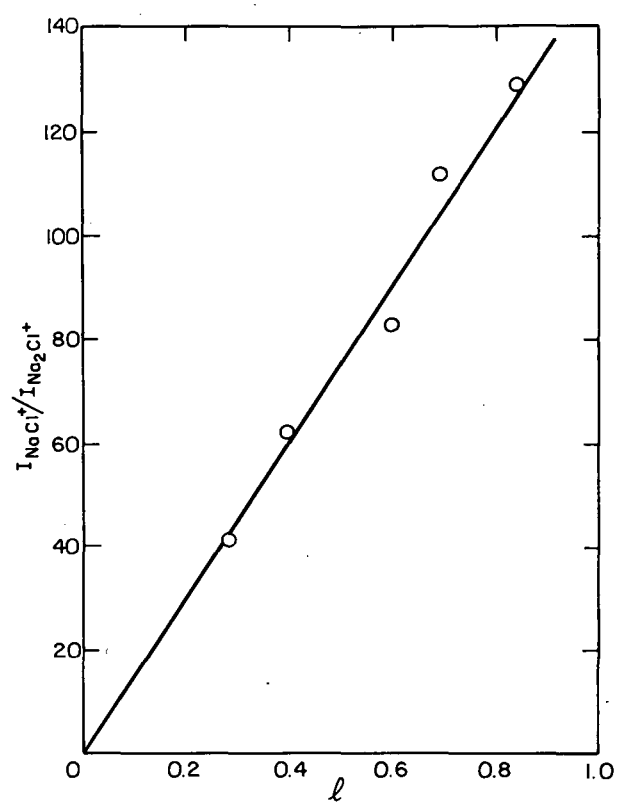

Fig. 1. Variation of the monomer/dimer intensity ratio with the thickness of the porous alumina disks (in mm) at 1025°K. (XBL 7412-7735)

as predicted. The fact that the outlet flux is an equilibrium mixture of dimers and monomers despite a decrease of dimer intensities by a factor of the order of 10,000 is confirmed by experiments in which the monomer weight losses were determined in order to obtain absolute values of pressures. The theoretical prediction that total mass transport through a porous barrier is independent of changes in molecular composition in the barrier is partially confirmed by the experimental demonstration that fractional reductions in fluxes of zinc and sodium chloride vapors through two different barriers are nearly equal. Full confirmation requires proof that surface diffusion was a negligible source of transport for both zinc and sodium chloride. Projected experiments with helium gas should settle this question.

*Part of this material has been reported in J. Chem. Phys. 61, 4358 (1974).

5. APPLICATION OF THE EFFECT OF POROUS BARRIERS ON MOLECULAR COMPOSITIONS TO DETERMINATION OF MASS SPECTROMETER CROSS SECTIONS

Pirooz Mohazzabi and Alan W. Searcy

In the determination of thermodynamic data for high temperature systems from mass spectrometer intensity measurements, it is customary to assume that when an ion is formed in the ion source of a mass spectrometer as a result of electron bombardment of a neutral species orginated in the Knudsen cell then the ratio I_i^+T/P_i is a constant of temperature, where I_i^+ is the measured intensity of the species i originated in Knudsen cell in which it has partial pressure P_i at absolute temperature T. This is the so called specificity rule in mass spectrometry. The only inorganic molecule so far reported to disobey this rule is the monomer of lithium fluoride[1], LiF(g).

Because the specificity rule is of crucial importance in thermodynamic studies made with mass spectrometers, we have applied the barrier effect described in the previous research summary to reexamine the influence of temperature on the mass spectrometer fragmentation pattern of lithium fluoride at reduced intensities of the dimer. Lithium fluoride was found to pass through porous alumina readily by surface diffusion so that a barrier which reduced the total mass flux of sodium chloride vapor by more than a factor of 100 reduced the flux of lithium fluoride vapor by less than a factor of 10. However, nickel powder proved a better barrier in that larger reductions in total flux and in the dimer/monomer intensity ratios were achieved. These results plus those obtained from Knudsen effusion experiments with lithium fluoride indicate that the deviation of the monomer from the specificity rule is at most a few percent in a temperature range over which the previous study indicated a variation of a factor of two.

1. J. Berkowitz, H. A. Tasman, and W. A. Chupka, J. Chem. Phys. 36, 2170 (1962).

6. THE EFFECT OF POROUS ALUMINA BARRIERS ON THE RATE OF DECOMPOSITION OF CALCIUM CARBONATE

Sheldon Lim, David J. Meschi and Alan W. Searcy

The rate of decomposition of calcite single crystals has previously been found by Beruto and Searcy to be independent of the thickness of the porous calcium oxide product layer for thicknesses up to 1 mm. The reaction may be independent of CaO product layer thickness either because the surface step of the overall reaction

$$CaCO_3\ (s) \rightarrow CaO\ (s) + CO_2\ (g)$$

is highly irreversible or because surface diffusion of CO_2 through the CaO layer is sufficiently efficient that the CO_2 activity gradient through the layer is negligible.

Weight loss and mass spectrometer measurements have been used to compare the effect of porous alumina barriers on the flux of CO_2 from calcite single crystals and powdered calcite to the effect on sodium chloride vapor. The porous alumina barriers reduce the NaCl vapor flux by more than a factor of 100. The flux from calcite single crystal is reduced by at most a factor of 6. The possibility that the irreversibility of the reaction is responsible for the high efficiency of transport of CO_2 through porous alumina was eliminated by heating the calcite powder in effusion cells, which provided an equilibrium vapor source to the porous barriers. The flux reduction was at most a factor of two.

It can then be concluded that surface diffusion must be a very efficient means of transport of CO_2 through porous alumina. Surface diffusion is also the probable mechanism for the efficient CO_2 transport through the CaO product layer in calcite decomposition. While surface diffusion is a well known mode of transport in porous solids, existing theory appears inadequate to explain these results.

7. THE COMPOSITION OF ALKALI CHLORATES VAPORS

Alfred Büchler, Pirooz Mohazzabi, David J. Meschi and Alan W. Searcy

Smyrl and Davlin[1] have studied the infrared spectra of alkali chlorates by means of the matrix isolation technique, but they could not be sure of the vapor composition. We have since determined the composition of sodium and potassium chlorate vapors mass-spectrometrically with, for sodium chlorate, use of the porous barrier technique.[2]

In the case of the potassium chlorate the different temperature dependences of the K^+ and

$K_2ClO_3^+$ ions show that K^+ comes from the monomer $KClO_3$, while the $K_2ClO_3^+$ results from the dimer $(KClO_3)_2$. The absence of the monomer parent ion $KClO_3^+$ in the mass spectrum suggests that potassium chlorate is the most ionic alkali pseudo-halide so far studied.

For sodium chlorate the Na^+ and $Na_2ClO_3^+$ ions have nearly the same temperature dependence. However, experiments using a crucible with a porous alumina lid, in the manner described by Mohazzabi and Searcy elsewhere in this report, showed that the Na^+ results from the monomer $NaClO_3$, while the $Na_2ClO_3^+$ ion arises from the dimer. The intensity of the $Na_2ClO_3^+$ ion was reduced approximately ten times as much as that of the Na^+ by the porous lid.

The presence of the $Na_2ClO_4^+$ ion in the mass spectrum of sodium chlorate indicates the presence of the dimer $(NaClO_4)_2$ in the vapor. This species probably arises from $NaClO_4$ formed via the disproportionation reaction $4NaClO_3 = 3NaClO_4 + NaCl$.

From the variation of ion intensities with temperature it was possible to determine approximate second-low enthalpies for the reactions

$$NaClO_3(s) = NaClO_3(g),$$

and

$$2NaClO_3(s) = (NaClO_3)_2(g)$$

These are, respectively, - 41(±3)kcal and - 39(±3) kcal., which gives a value of - 43(±7)kcal for the dissociation reaction

$$(NaClO_3)_2(g) = 2NaClO_3(g)$$

---

1. N. Smyrl and J. P. Davlin, J. Chem. Phys. 60, 2540 (1974).
2. P. Mohazzabi and Alan W. Searcy, J. Chem. Phys. 61, 4358 (1974).

8. KINETICS OF DECOMPOSITION OF STRONTIUM SULFATE

Tushar Basu and Alan W. Searcy

Equilibrium vapor pressures were determined as a function of temperature over the temperature range 1400°K - 1600°K for the reaction

$$SrSO_4(s) = SrO(s) + SO_2(g) + 1/2\ O_2(g)$$

by the torsion-effusion technique. Measurements with two different orifice diameters yielded for the enthalpy ΔH^o and entropy ΔS^o 133.06 ± 0.8 kcal/mole of $SrSO_4$ and 64.0±0.5 e.u. respectively.

The rate of decomposition in vacuum from the (001) face of celestite ($SrSO_4$) single crystals was measured by the torsion-Langmuir method over the same temperature range. The rate was independent of time from the start of the reaction until the product layers reached at least 0.5 mm thickness. The activation enthalpy ΔH^* and enthalpy ΔS^* were calculated to be 163.5±1.8 kcal/mole of $SrSO_4$ and 63.5±1.0 e.u. The decomposition coefficient of the material (α_a) was found to be 8×10^{-3} at 1500°K.

The X-ray pattern of the porous product layer was that of the stable modification of strontium oxide.

The fact that the rate of the reaction is independent of time, that the apparent activation enthalpy is greater than the enthalpy of the equilibrium reaction, and that the apparent activation entropy is approximately equal to the entropy of the equilibrium reaction leads to a simple interpretation in the terms of the model under development by Searcy and Beruto.

The reaction steps involving diffusion and desorption of the gaseous products, or their precursor particles, and the gases in the porous layer are maintained at equilibrium with the local activity of strontium oxide in the strontium sulfate phase, but diffusion of strontium oxide in the strontium sulfate or transfer of strontium oxide across the strontium sulfate-strontium oxide phase boundary is irreversible.

If this interpretation is correct, an SO_2 plus oxygen flux generated from an equilibrium source may, like carbon dioxide from an equilibrium source, be little affected by a porous alumina barrier at high temperatures. This possibility will be tested experimentally.

9. THE MAGNETIC MOMENT OF Se_2

David J. Meschi, Alfred Büchler and Jon T. Hougen*

Previous measurements in this laboratory of the magnetic moment of Se_2[1] set an upper limit of a tenth of a Bohr magneton. The aparatus has been improved and another attempt has been made to determine the moment. Measurement by Barrow and co-workers[2,3] indicate that Se_2 has a magnetic moment governed by Hunds case (c). Calculations of moments for Hund's case (c) have apparently never been reported. Concurrently with the experimental work, such calculations were carried out by the method outlined by Hougen[4] for comparison with the experimental data. The basis functions were those for Hund's case (a). By means of a perturbation technique the wave functions and energies were found for the three components of the $^3\Sigma_g^-$ state. These are given in Table I, where the states are labelled 1, 2 and 3. State 1 is the 0_g^+ state and states 2 and 3 comprise the degenerate 1_g state.

The magnetic field was then introduced as a further perturbation and the magnetic moments were calculated. Because of their degeneracy states 2 and 3 also make appreciable second order contributions to the magnetic moments. These contributions were also calculated.

TABLE I. Wave Functions and Energy Levels of Se_2

State	Wave Function	Energy
1 (0_g^+)	$\lvert 010;0JM\rangle + \frac{E(J)}{\sqrt{2}}\left(\lvert 011;1JM\rangle + \lvert 01\text{-}1;\text{-}1JM\rangle\right)$	$E_1 = B[J(J+1)+1]+\lambda-[(\lambda-B)^2+4B^2J(J+1)]^{1/2}$
2 (1_g)	$\frac{1}{\sqrt{2}}\left(\lvert 011;1JM\rangle - \lvert 01\text{-}1;\text{-}1JM\rangle\right)$	$E_2 = BJ(J+1)+2\lambda$
3 (1_g)	$\frac{1}{\sqrt{2}}\left(\lvert 011;1JM\rangle + \lvert 01\text{-}1;\text{-}1JM\rangle\right)-E(J)\lvert 0J0;0JM\rangle$	$E_3 = B[J(J+1)+\lambda+[(\lambda-B)^2+4B^2J(J+1)]^{1/2}$

$\lambda \equiv$ Splitting constant = 183.3 cm^{-1}; $B \equiv$ rotational constant = 0.08997 for 1_g; 0.08977 for 0_g^+, in cm^{-1}

$E(J) \equiv \frac{2BJ(J+1)}{\lambda-B}$ These values are from Barrow, reference 2 and 3.

The relative distribution of moments were calculated by means of a computer for fields of 14 kgauss and a temperature of 1000°K (Fig. 1). The mean absolute values of the moments for the three states are $7.7 \times 10^{-2}\mu_B$, $2.3 \times 10^{-2}\mu_B$ and 6.7×10^{-2} for states 1, 2 and 3 respectively. The mean absolute moment overall is $6.0 \times 10^{-2}\mu_B$.

A beam chopper was introduced into the apparatus described earlier[1]. The raw measurements resulting from ten scans were normalized and centered by means of a computer. The data were then averaged using a graphical method with the result shown in Fig. 2. These data are for a field of 14 kgauss and a field gradient of 55 kgauss per cm. The decrease of intensity at the beam center with magnet on, relative to that with the magnet off, is 10%, which is in good agreement with a calculated value of 11% obtained by means of a computer assuming the moment distribution of Fig. 1.

*J. T. Hougen is with the National Bureau of Standards.

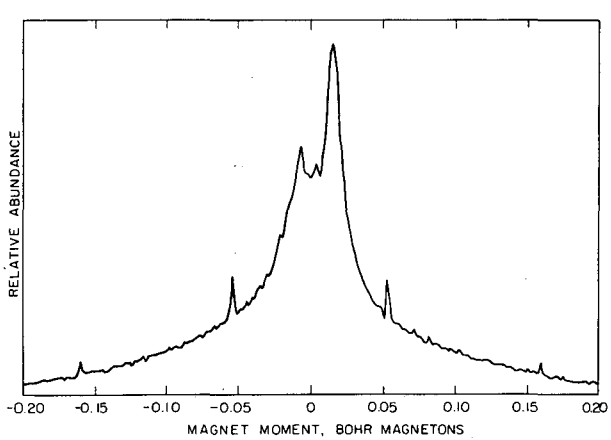

Fig. 1. Distribution of magnetic moments among Se_2 molecules at 1000°K, and a field of 14 kgauss. (XBL 751-5625)

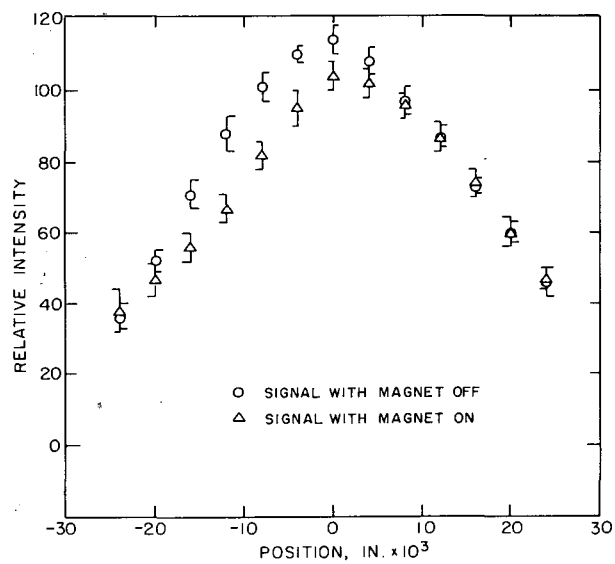

Fig. 2. Beam profile with magnet oH, and with H = 14 kgauss, ∇H = 55 kgauss/cm. (XBL 751-5626)

1. D. J. Meschi and A. W. Searcy, J. Chem. Phys. 51, 5134 (1969).

2. R. F. Barrow, G. G. Chandler and C. B. Meyer, Phil. Trans. Roy. Soc. (London) A260, 395 (1966).

3. R. F. Barrow, W. G. Burton and J. H. Callomon, Trans. Faraday Soc. 66, 2685 (1970).

4. J. T. Hougen, NBS Monograph 115, (National Bureau of Standards, Washington, D. C., 1970).

10. RESEARCH PLANS FOR CALENDAR YEAR 1975

Alan W. Searcy

Theoretical and experimental studies of the thermodynamics of solutions and surfaces will be continued. The experimental studies will center on tests and exploitation of an apparatus now under construction for static measurements of the partial pressure of a volatile component of a solid of very narrow composition limits. For the exploratory studies, the partial pressure of carbon dioxide above calcium carbonate will be measured as a function of temperature and mole ratio of CaO to CO_2 in the calcium carbonate phase. Partial molal thermodynamic quantities will be calculated from these pressures. Because partial molal thermodynamic quantities have not been measured by phases that show as large variations of activities with composition as expected for calcium carbonate, the data obtained should be valuable in providing a greater range of tests of thermodynamic solution theory. The possibility that the carbon dioxide partial pressures in seas of historic and prehistoric times can be determined from the carbon dioxide partial pressures of shells formed in those seas will be explored.

Theoretical and experimental studies of the kinetics of decomposition reactions will be continued. Emphasis of the theoretical work will be on completion of an analysis of the influence of porous product layers on the rate of decomposition reactions both in vacuum and in the presence of non-negligible pressures of the gaseous product. The effect of porous alumina barriers on a flux of SO_2 and oxygen from decomposition of strontium sulfate under equilibrium and non-equilibrium conditions will be measured experimentally to provide new evidence on the nature of the rate limitation step of the decomposition reaction. If a new student becomes available we should undertake an experimental study of the kinetics of decomposition of an intermetallic solid to yield one volatile product and a porous solid phase. The vapor flux from such a reaction may be very much closer to the maximum possible flux (which can be calculated from thermodynamic data and from kinetic theory) than has been the case for any of the four decomposition reactions--all for complex inorganic salts--that we have so far studied. The alloy data, therefore, may provide a significantly different range of data for testing our theories of decomposition reaction kinetics.

Theoretical and experimental studies of the kinetics of transport of gases and vapors through porous barriers will complement the studies of the kinetics of decomposition reactions. Particular emphasis will be placed on attempts to develop a theoretical explanation for the anomalously high transport found experimentally for carbon dioxide through porous barriers at high temperatures which was demonstrated during the 1974 program. Our nuclide high temperature mass spectrometer is being modified to permit studies of the effect of porous barriers on single component gases and gas mixtures of known compositions in the range of room temperature to 1500°C. The apparatus will provide a much longer temperature range for study of gas transport through porous barriers than has previously been studied. Permeabilities will be measured for barriers formed from a variety of materials, such as alumina, zeolites, nickel metal, and carbons, to gases and vapors that are prototypes for substances that would be encountered in coal gasification, in particular, aliphatic and aromatic hydrocarbons, sulfur dioxide, hydrogen sulfide, carbon dioxide, and water. Helium permeability will be measured as a reference base because helium is known to undergo negligible surface diffusion in the temperature range of the projected study. It is hoped that selective surface diffusion through solids with pores with much larger diameters than found in conventional molecular sieves will provide a practical means for separating relatively polar molecules such as sulfur dioxide and hydrogen sulfide from less polar and non-polar gas molecules.

The apparatus that has been used for studies of the deflection of gas molecules which have unpaired electrons by an inhomogeneous magnetic field will be modified, if funds are available, for studies of the non-steady state transport of gases and vapors through porous barriers. For these studies a beam from the present high temperature source chamber will be directed against one face of a porous barrier that is heated in a second chamber and the escape flux of the barrier will be monitored as a function of time by means of a quadrupole mass filter. A shutter and a beam chopper which are located between the two high temperature chambers will make possible precise determination of the time delay imposed on the molecules of the beam by the porous barrier.

11. 1974 PUBLICATIONS AND REPORTS

Alan W. Searcy and Associates

Journals and books

1. Alan W. Searcy, Alfred Büchler and Dario Beruto, The Relationship Between Forward and Reverse Reaction Rates Under Nonequilibrium Conditions, High Temp. Sci. 6, 64 (1974) (LBL-1460 Rev.).

2. David J. Meschi and Alan W. Searcy, The Kinetics of Dissociative Vaporization Reactions, High Temp. Sci. 6, 221 (1974) (LBL-1852).

3. Alan W. Searcy and Dario Beruto, Transition State Theory for Vaporization and Condensation, J. Phys. Chem. 78, 1298 (1974) (LBL-2215).

*4. Z. A. Munir, M. E. Benavides and D. J. Meschi, Thermodynamic Stabilities of the Arsenides of Zinc, High Temp. Sci. 6, 73 (1974).

5. Pirooz Mohazzabi and Alan W. Searcy, The Effect of Porous Barriers on the Molecular Compositions of Reactive Gas Mixtures, J. Chem. Phys. 61, 4358 (1974) (LBL-3108).

6. Dario Beruto and Alan W. Searcy, Use of the Langmuir Method for Kinetic Studies of Decomposition Reactions: Calcite, Faraday Society Transactions I. Phys. Chem. 70, 2145 (1974) (LBL-2552).

LBL reports

1. Alan W. Searcy and Dario Beruto, The Kinetics of Endothermic Decomposition Reactions: I. Steady State Chemical Steps, LBL-3137, Nov. 1974.

2. Pirooz Mohazzabi, Application of the Temperature-Jump Relaxation Technique to Verification of the Onsager Reciprocal Relations, LBL-3515, Nov. 1974.

3. James A. Roberts, Jr., High Temperature Mass Spectrometry, (Ph. D. thesis) LBL-2507, Feb. 1974.

4. Tushar Kanti Basu, The Kinetics of Decomposition of Barium Carbonate, (M.S. thesis) LBL-2580, April 1974.

---

*Funded by Dept. of Mech. Engr., UC-Davis.

B. MICROSTRUCTURE AND BEHAVIOR OF CERAMIC MATERIALS: GLASS AND CERAMIC-METAL SYSTEMS

Joseph A. Pask, Principal Investigator

A continuing overall objective of the research program is to contribute to the development of a fundamental understanding of the factors involved in obtaining ceramic materials with controlled character (which includes microstructure with emphasis on grain boundaries), and of the relationship of character to mechanical behavior at room and high temperatures. This objective involves studies on the kinetics and mechanisms of solid state reactions, sintering, and distribution of phases which in general play a part in the development of microstructure. It also involves studies on the mechanisms responsible for the mechanical behavior of single crystals, and on the application of such knowledge to the understanding of the behavior of polycrystalline ceramic materials.

The compositions under study--mullite, alumina, forsterite, spinel, magnesia--are basic materials of industrial ceramics and refractories, and sintering is the basic method for their manufacture. The fundamental approach in these studies in terms of physical chemistry, solid state chemistry, and dislocation theory also makes the work relevant in that the determined principles should be applicable to other polycrystalline metal and ceramic materials, and composites.

A second objective of this program is concerned with structural, thermodynamic, and electrochemical studies of glass-metal and ceramic-metal systems. It involves studies related to wetting, bonding, and the nature of the interfaces between dissimilar phases; to the thermodynamics and kinetics of chemical reactions at such interfaces; and to the kinetics and mechanisms of dissolution and diffusion in glasses. A basic understanding of the nature of interfaces and the mechanisms of reactions at interfaces is critical in all materials.

1. THERMODYNAMIC CONSIDERATIONS OF SOLID STATE SINTERING*

Carl E. Hoge and Joseph A. Pask

Sintering is the important metallurgical and ceramic process of densification of a powder compact with the application of thermal energy. Most of the experimental and theoretical work on sintering has been performed from a kinetic standpoint. This study deals with thermodynamic considerations.

In a sintering powder compact the change in free energy of the system at constant temperature, pressure and phase composition can be expressed as

$$\delta(G_{syst}) = \delta\int \gamma_{sv} dA_{sv} + \delta\int \gamma_{ss} dA_{ss} \qquad (1)$$

where γ_{sv} = solid/vapor interfacial energy, γ_{ss} = solid/solid interfacial energy, dA_{sv} = decreasing differential solid/vapor interfacial area, and dA_{ss} = increasing differential solid/solid interfacial area. As long as $\delta(G)$ remains negative, sintering will continue. When $\delta(G)$ becomes zero for a given packing, the critical γ_{ss}/γ_{sv} ratio can be determined for that packing from Eq. (1). This ratio then determines the equilibrium dihedral angle Φ from

$$\gamma_{ss} = 2\gamma_{sv} \cos\frac{\Phi}{2} \qquad (2)$$

The densification model used is based on the concept that the cap material removed at every contact, or grain boundary, between spheres is uniformly distributed on the free surfaces with the radii of the spheres increasing to keep the total solid volume constant. This model differs from that normally employed for predicting kinetics in which the material removed at a contact forms a bridging neck of increasing diameter. Although neck formation is associated with a decrease in free energy, such a geometry does not correspond to the minimum free energy configuration for the system and is thus an intermediate stage favored by kinetic considerations.

To illustrate: when two spheres are just in contact, Fig. 1A, the experimental $\Phi = 0$. Now,

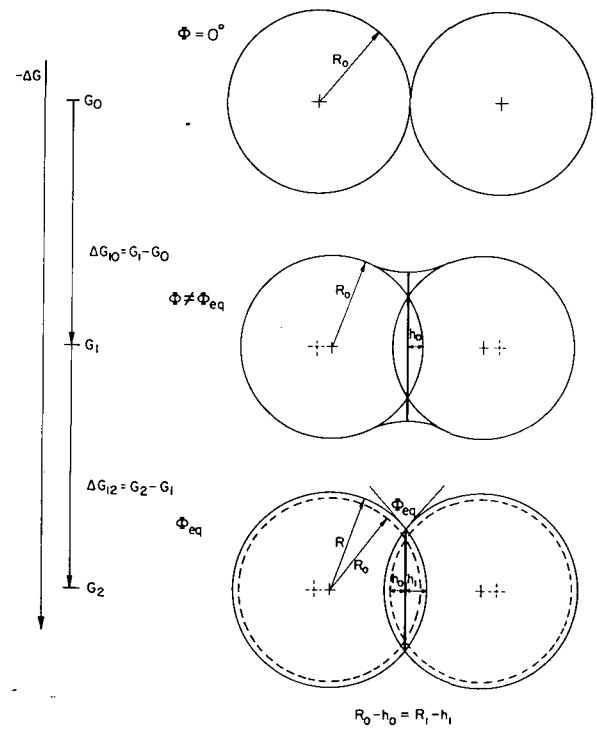

Fig. 1. Sintering models. (XBL 749-7297)

if the spheres interpenetrate until a certain cap height, h_o, is removed and deposited in the neck region, Fig. 1B, the radius of each sphere is unchanged. At this point, if no further densification or change in h_o occurs but the solid/solid and solid/vapor interfaces equilibrate as shown in Fig. 1C, material from the neck region is deposited uniformly on the surfaces of the spheres causing R_o to increase to R and h_o to h_1 so that $R_o - h_o = R - h_1$. The latter geometry, which corresponds to the minimum free energy configuration for that particular degree of densification, becomes the model used in this analysis. It becomes the equilibrium geometry when δG in Eq. (1) is numerically equal to zero. The γ_{ss}/γ_{sv} critical, and the corresponding Φ can then be determined for this equilibrium configuration. Four particle packings based on uniform sized spherical particles with isotropic interfacial energies were analyzed: diamond cubic (DC), simple cubic (SC), body-centered cubic (BCC), and face-centered cubic (FCC) (corresponding to a particle coordination of 4, 6, 8, and 12). For a given packing by using Eq. (1) it becomes possible to determine the relationship between critical values of γ_{ss}/γ_{sv} and h_o/R_o which is equivalent to $\Delta L/L_o$ (where L_o is the particle radius. Figure 2 shows such curves for uniform size spherical particles in DC, SC, BCC and FCC packings. These curves are based on the minimum free energy densification model which corresponds to a starting value of 2 for γ_{ss}/γ_{sv} (0° dihedral angle) and a decrease of γ_{ss}/γ_{sv} (increase of dihedral angle) as shrinkage or h_o/R_o increases. The increasing dispersion of the curves with decrease of γ_{ss}/γ_{sv} is due to the fact that R increases more rapidly than h_1 for an equivalent amount of shrinkage when the coordination number of nearest neighbors increases.

The analysis of the four sintering geometries indicates that the densification pattern is the same for any kind of packing, regular or irregular, until second neighbor contacts are made or until densification is reached along some crystallographic plane when closed pores develop. This stage is represented by the a-b segments in Fig. 2. Further densification requires lateral transport of material from these planes; this condition could lead to kinetic barriers. In any case, there would be no thermodynamic barriers to densification if the γ_{ss}/γ_{sv} ratio for the system is smaller than the critical value for a particular packing represented by the lowest value for γ_{ss}/γ_{sv} for a given packing in Fig. 2.

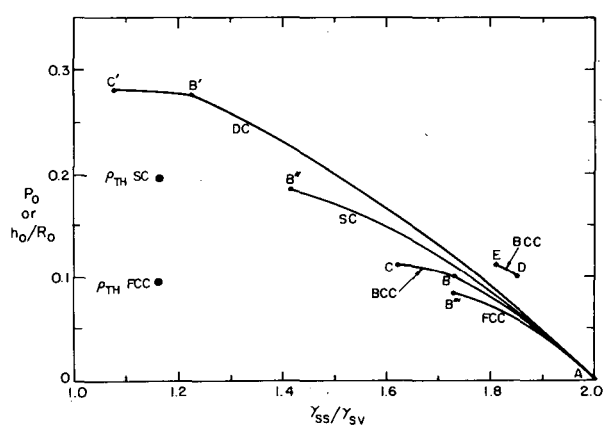

Fig. 2. Shrinkage versus critical γ_{ss}/γ_{sv} ratios for four arrays of uniform size particles.
(XBL 749-7198)

In any instance during sintering, if the experimental or dynamic dihedral angle is less than the equilibrium value determined by γ_{ss}/γ_{sv} for the system, a thermodynamic driving force exists for continued mass transport from the grain boundary to the adjoining free surfaces. The overall driving force for sintering may thus be expressed as

$$\Delta\Phi = \Phi_{eq} - \Phi_{dyn} \qquad (3)$$

where Φ_{eq} is the value based on γ_{ss} for a planar grain boundary and on γ_{sv} for surfaces in equilibrium with their own vapor; and Φ_{dyn} is the instantaneous value in a sintering compact which is dependent on geometry, chemical effects, and atmospheric conditions. When Φ_{dyn} becomes equal to Φ_{eq} sintering ceases with an endpoint density unless Φ_{crit} for the packing is less than Φ_{eq} for the system in which case there is no thermodynamic barrier for sintering.

Several experiments were performed to verify the theoretical model. Compacts of MgO powder were sintered at 1510°C for different times in static air, flowing air, and flowing water vapor. Density values of the sintered specimens are plotted versus time in Fig. 3. This behavior correlated well with dihedral angle measurements in flowing water vapor - 32°, in flowing air - 56°, and in static air - 96°. A considerably faster densification rate was observed in flowing water vapor in which the grooved grain boundaries showed the greatest corrosive effect as represented by the smallest experimental dihedral angle of 32° which resulted in the largest driving force for sintering according to Eq. (3).

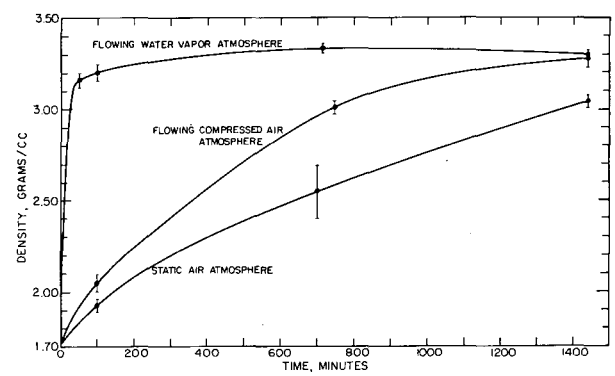

Fig. 3. Density versus time for compacts sintered at 1510°C in several ambient atmospheres.
(XBL 749-7341)

*Abstracted from LBL-3546.

2. KINETICS OF INTERMEDIATE AND FINAL STAGES OF SINTERING

Boon Wong and Joseph A. Pask

A continuing overall objective of this research program is to develop a fundamental understanding of the kinetics and mechanisms of the solid state sintering processes. The approach to this objective is twofold: (1) to derive more realistic and general theoretical models for the process and verify them by experimental results; (2) to develop better techniques for the process so that materials can be fabricated with a given microstructure.

By associating Skorokhod's sintering viscous flow models with Nabarro-Herring type creep models and assuming suitable geometries, kinetic equations have been derived for sintering of a polycrystalline refractory for several conditions. During the past year experimental verification of proposed theoretical models for the intermediate stage of sintering (below ~95% of theoretical density) has been undertaken.

Mallinckrodt MgO powder, after ball milling and subsequently calcining at 1200°C in air, was cold pressed into compacts with a green density of ~46% of theoretical. The compacts were then sintered isothermally at six different temperatures (1280°C, 1330°C, 1380°C, 1430°C, 1500°C and 1600°C) for various times. The bulk density of the sintered specimens was measured by the displacement technique with mercury. Analysis of the kinetic data indicated that a porosity function as determined by the derived kinetic equations is linearly related to the sintering time for each of the isothermal runs up to ≈85% relative density.

The scanning electron microscope was used to examine the "fractured" and "as fired" surfaces of the specimens. A qualitative analysis indicated that grain growth was significant only above 85% relative density for all isothermal runs. The linear relationship of the porosity function with time should thus hold at all sintering temperatures up to ≈85% relative density for powder compacts of this starting structure. An appropriate Arrhenius plot indicated that the activation energy calculated for the process is equal to 106 Kcal/mole, which agrees well with the activation energy for oxygen intrinsic diffusion in MgO (110 ± 4 Kcal/mole) reported by Narayan and Washburn.[1]

Sintering experiments have been initiated on MgO powders doped with 0.2 wt% CaO and 0.2 wt% TiO_2. Preliminary kinetic data on CaO doped MgO compacts indicate that sintering has been enhanced. An isothermal sintering series in a flowing water vapor atmosphere will also be made. Studies will be undertaken to correlate the kinetic data with the thermodynamic concepts on sintering developed within the group.

1. J. Narayan and J. Washburn, Acta Met. 21, 533 (1973).

3. POLYCRYSTALLINE SPINEL FROM POWDERS PREPARED BY FREEZE DRYING TECHNIQUE

Chi-Shine Tao and Joseph A. Pask

To process polycrystalline ceramics of desired microstructure is a long-standing technological objective. In many applications, fine grain polycrystalline ceramics completely free from pore and secondary phases is required. The most important steps in attaining this objective are the powder preparation, characterization and correlation with the densification process. Ultrafine powders are needed that are uniform in size and homogeneous in chemical composition. However, large aggregates of strong structure frequently form in the preparation of ultrafine powder. Grinding has been used as a physical means to achieve uniformity of powder size, but it has the disadvantages of introducing impurities and being uneconomical. Work has continued on the preparation, characterization and densification of stoichiometric spinel ($MgAl_2O_4$) powders. Spinel powder is being prepared by calcining freeze dried powders formed from an aqueous solution of magnesium sulfate hydrate and aluminum sulfate hydrate in a one to one molar ratio.

When droplets of the mixed sulfate aqueous solution are sprayed into a freezing media, water segregates out as ice crystals. Upon sublimation of the ice crystals in the subsequent drying step, the freeze dried powders form a framework of a web-like structure. The fineness of the framework is determined by the ice crystal size and thus the freezing rate of the aqueous solution. On calcination, the drastic decomposition reaction causes the freeze dried particles to break down into sizes equivalent to the web of the framework. Ultrafine (0.5-3 μm) spinel powder has thus been made without grinding. The success of reproducing such a powder free from aggregates, however, depends on several factors: the concentration and acidity of the aqueous solution, the size distribution of the freeze dried powder, the freezing rate, the drying condition, and the calcination condition. These factors have to be properly controlled so that the framework of the freeze dried powder completely breaks down by the decomposition reaction during calcination. The reproducibility of the powder as a function of these factors is now being studied.

An alternative way of producing a uniform ultrafine powder has consisted of breaking down the framework of the freeze dried powder mechanically before the calcination step. Short time (about 10 min) grinding of the freeze dried powder in a planetary alumina ball mill has been shown to serve the purpose. With this reproducible uniform ultrafine powder, homogeneous particle packing can be achieved in the powder compact before firing which will enable the study of the relationship between other powder characterizations and their densification process.

For chemically derived oxide powders, anion impurities are a major concern in the realization of a fully densified microstructure. For sulfate derived oxides, a minor residue usually stays in the structure up to elevated temperatures.

This residue, although small in quantity, will be present as entrapped gas in the final stage of sintering and prevent complete densification. A hydrogen anneal is being used to reduce the residue sulfate of the low temperature calcined spinel powders. Thermodynamics and kinetics of this reaction are being studied. Experimental results have indicated that both sulfates can be reduced at a fast rate at about 750°C in flowing hydrogen at a positive pressure of 1/3 psi. The effect of such treatments on sintering kinetics and the nature of the microstructure will be studied.

4. THE SILICA-ALUMINA SYSTEM: STABLE AND METASTABLE EQUILIBRIA AT 1.0 ATMOSPHERE*

İlhan A. Aksay[†] and Joseph A. Pask

Sapphire-fused silica diffusion couples, which were annealed in the temperature range of 1678° to 2003°C and analyzed by electron beam microprobe, provided data on the stable phase equilibrium of the SiO_2-Al_2O_3 system. Under stable equilibrium conditions, the intermediate compound of this system, mullite ($3Al_2O_3 \cdot 2SiO_2$) melts incongruently at 1828±10°C, and its solid solution field extends from 70.5 to 74.0 wt% Al_2O_3. The stable phase diagram is a composite of the two binary eutectic diagrams: silica-mullite in the absence of alumina and silica-alumina in the absence of mullite. Under metastable conditions, mullite melts congruently at ≈1890±10°C, and its solid solution field extends to ≈83.2 wt% Al_2O_3.

[†]Present address: Xerox Corp., Wilson Research Center, Webster, N.Y.

5. IMMISCIBILITY AND CRYSTALLIZATION STUDIES IN THE SILICA-ALUMINA SYSTEM

Subhash Risbud and Joseph A. Pask

Following the recent revision of the alumina-silica stable phase diagram,[1] the evidence in favor of the metastable immiscibility gap reported in literature[2] must be considered with reservation. Data necessary to obtain immiscibility regions on the diagram are normally obtained from experimental studies on quenched glasses. In the silica-alumina system, however, such data are virtually impossible to obtain in view of the difficulty in quenching from the high temperatures involved (higher than 2000°C) and because the liquids devitrify quite readily even with the fastest possible cooling rates especially for compositions with alumina contents greater than about 25 mole%. For example, a TEM study on splat cooled glasses in this system[3] was unable to point to the location of any immiscibility regions on the phase diagram.

Mindful of these experimental difficulties, an approach involving calculations of activities of reacting components has been used in this study to generate isothermal free energy composition curves in the silica-alumina system. This approach is an adaptation of the technique suggested by Charles[4] for assessing metastable equilibria in glass forming ceramic systems. The data on activities of alumina and silica that has been obtained so far from the liquidus curve of the phase diagram,[1] is rather definite in pointing to the existence of a hitherto unreported metastable two liquid region on the phase diagram with a consolute temperature of about 1120°C and at a critical composition of 0.78 mole fraction of alumina. The work on estimating the exact compositional limits of the immiscibility dome is in the final stages. It is of interest to note that this metastable gap is partially submerged beneath a curve representing the upper limit of metastability of glasses in this system.[3] Although one would expect glass transition temperatures to be lower than the limit of metastability, it is likely that only portions of the predicted gap above the glass transition are expected to be observed in practice. Portions lying below the glass transition are however predictable on a theoretical basis. The somewhat low temperature associated with the top of the immiscibility gap predicted here may well be the reason why immiscibility has been difficult to observe in high alumina compositions in this system.

Experimental work is also in progress on studying the crystallization rates of various compositions in the silica-alumina system. It will be particularly useful to assess what effect phase separation would have on the crystal growth rate at the high alumina compositions, in view of the differing nucleation behavior one would expect for glasses that are in the two liquid region as compared to glasses in the homogeneous regions.

1. İ. A. Aksay and J. A. Pask, Science, 183, 69 (1974).
2. J. F. MacDowell and G. H. Beall, J. Am. Ceram. Soc. 52 (1) 17 (1969).
3. T. Takamori and R. Roy, ibid, 56,(9) 639 (1973).
4. R. J. Charles, ibid 50, (12) 631 (1967).

6. IMPACT FRACTURE BEHAVIOR OF GLASS

William E. Snowden and Joseph A. Pask

During the past year, study of crack growth in glass plates subjected to impact has continued. The principal objective of the program, to determine the relationship between pulse characteristics and crack growth, has been reached. Critical impact velocities required to cause extension of pre-cracks have been determined for flyers giving initial pulse durations from 0.10 μsec to 0.71 μsec, and for plates of two different widths. Behavior is consistent with a least-action concept for failure prediction. However, calculation of stress vs time histories at the crack location remain to be completed.

A number of problems have been encountered which will be discussed below.

The experimental apparatus for producing impacts was described in detail in a recent LLL report (UCRL-51496). Aluminum flyers were accelerated to some constant velocity using a magnetic hammer system capable of producing impact stresses of up to 50 kbar. The glass (Pyrex) target plates used for most shots were approximately 5 cm × 10 cm × 0.6 cm. Each plate contained a pre-crack of ~1 cm in length introduced using a hot wire technique. The test plate configuration is shown in Fig. 1, and the area of impact is indicated by the dark shaded region. Relative values for the normal stresses, neglecting geometric attenuation due to finite flyer width, are also indicated in the figure for cases of plane strain and plane stress. K represents the bulk modulus, μ is the shear modulus, and ν is Poisson's ratio.

The impact event during testing was recorded using a high-speed streaking and framing camera. The streaking slit was aligned parallel to the crack plane and along the axis of impact. Crack growth was observed to occur in small increments, and both acceleration and deceleration were recorded. Good agreement was noted between crack growth increments recorded on film and those clearly visible on the fracture after impact. At the critical impact velocity, defined as that velocity required to cause the pre-crack to extend some small fraction of the characteristic pulse length, a single growth step was observed. In most instances the maximum velocity reached by this step was < 500 m/sec. At higher velocities of impact, the size and number of crack growth steps increased due to the influence of reflected and superimposed waves. The maximum recorded crack velocity under these conditions was ~2200 m/sec. This is approximately 0.6 times the shear wave velocity in the glass, a theoretical maximum value.

The critical impact stresses (σ_{11} in Fig. 1) were much lower than the maximum possible value given above. The critical impact velocities ranged from 0.065 mm/μsec for an initial pulse duration of 0.10 μsec to 0.018 mm/μsec for an initial pulse duration of 0.71 μsec. These velocities correspond to maximum stresses σ_{11} of approximately 4.3 kbar and 1.2 kbar, respectively, when geometric attentuation is neglected. However, the stress σ_{22} normal to the crack plane is responsible for growth, and the respective values for σ_{22} are 1.1 kbar and 0.3 kbar for conditions of plane strain. Critical impact velocity as a function of initial pulse duration is shown in Fig. 2.

According to several recent theoretical papers related to crack growth caused by stress pulses, a least action law of the form

$$\left(\frac{\sigma^2\tau}{E}\right) \geq K\left(\frac{\gamma_f}{C_L}\right) \qquad (1)$$

should give the conditions necessary for fracture. That is, a pulse of amplitude σ and duration τ will cause an existing crack to extend if the

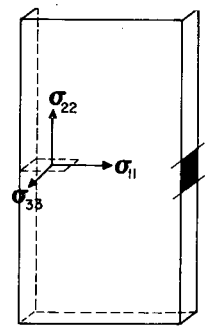

Al Flyer
Glass Target

$$\sigma_{ij} = \lambda\,\delta_{ij}\,\epsilon_{kk} + 2\mu\,\epsilon_{ij}$$

Case I: $\epsilon_{22} = \epsilon_{33} = 0$ (thick plate)

$$\sigma_{22} = \sigma_{33} = \left(\frac{K - \frac{2}{3}\mu}{K + \frac{4}{3}\mu}\right)\sigma_{11}$$

Case 2: $\sigma_{33} = 0$ (thin plate)

$$\sigma_{22} = \nu\,\sigma_{11}$$

Fig. 1. Precracked impact specimen.
(XBL 751-5478)

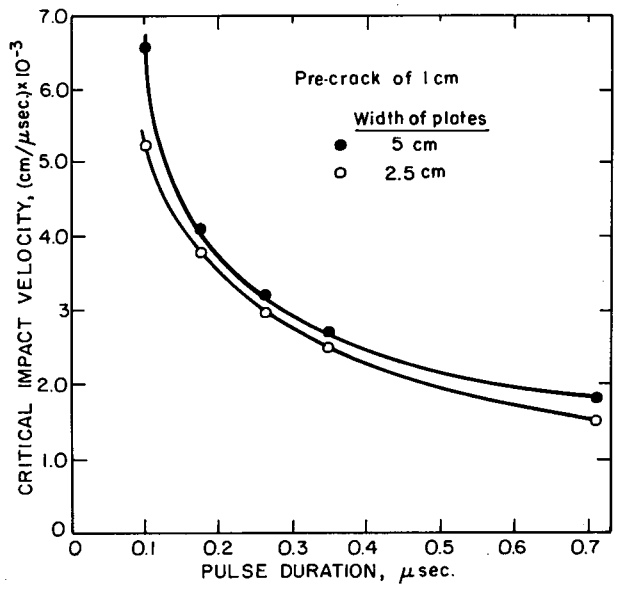

Fig. 2. Critical impact velocity required for crack growth as a function of pulse duration.
(XBL 751-5477)

above condition is fulfilled. E is the elastic modulus, γ_f is the fracture surface energy, C_L is the characteristic pulse velocity (in this work C_L is the longitudinal sound speed), and K is a constant. For idealized waveforms, σ and τ are easily defined. In real materials, however, these parameters are constantly changing, so an integrated stress vs time profile must be obtained; i.e., crack growth might be expected to occur when

$$\int_{t_0}^{t_c} \frac{\sigma^2 dt}{E} \geq K\left(\frac{\gamma_f}{C_L}\right) \qquad (2)$$

Such a determination of the action integral requires an accurate means of calculating stresses in the target plate. This is most difficult, and will be discussed below.

Stress vs. time histories are being calculated using one and two-dimensional finite-difference computer codes. These codes solve the equations of motion directly, and together with suitable relations between stress and strain and an accurate formulation of the material equation-of-state, can give the desired information. However, for the very short pulse durations being considered in this work, the computing time becomes very great since a minimum number of zones must be used to describe the pulse regions, leading to a very small zone size. In addition, the problem is decidedly three-dimensional, so several solutions must be combined using the principle of superposition to adequately describe the problem. At the present time, a single one-dimensional solution is being coupled with two two-dimensional solutions. Results are as yet inconclusive.

7. HIGH-TEMPERATURE DEFORMATION OF MgO

Chung P. Dokko and Joseph A. Pask

This investigation is directed toward understanding of the nature and the role of dynamic recovery in high-temperature deformation of both single crystal and polycrystalline MgO. Among several possible mechanisms, the deformation by dislocation motion has been of primary concern.

Since recovery could affect deformation by altering the dislocation structure, it seemed necessary to first determine whether the change of structure could be followed in terms of stress. According to the literature, the structural contribution (internal stress) can be separated from total applied stress, while the remainder (effective stress) corresponds to the driving force available for dislocation glide. Using the technique of sudden interruption followed by incremental unloading, the magnitudes of internal/effective stress have been determined during stress-strain tests. The present data show that effective stress increases with internal and hence applied stress for a given strain rate. It thus suggests that effective stress should be another structure term. By the same token, effective stress cannot be uniquely related to strain-rate as implied in the literature.

Rates of recovery taking place during and after the measurement of internal effective stress were measured in the same test. It was revealed that thus-measured rate agrees well with that determined dynamically with a change in strain-rate. The stress and temperature dependence of recovery rate tended to approach those of steady creep rate. Precise correlation could not be anticipated in view that the transient stage representing most of the stress-strain curves is not defined by stress alone as is steady state. For instance, the recovery rate at a given stress and temperature was found to increase with strain-rate, indicating the reciprocal effect of structure on recovery. Because of such additional dependency, the recovery rate for steady creep cannot be predicted from those for stress-strain curves.

Effect of initial condition on the stress-strain curves and transient creep was shown by the effect of annealing. Prior annealing resulted in strengthening of both single and polycrystals; the latter exhibited yield drops on stress-strain curves and sigmoidal creep.

Additional correlation might be expected between stress-strain curves and transient creep, and it was found that the length of transient period reflected the difference in recovery rate; i.e., primary strain was larger for the material showing a higher recovery rate at a given stress. Also the primary strain increased with stress and temperature as did the recovery rate. This behavior illustrated the role of recovery in delaying the achievement of steady state against strain-hardening.

8. MICROSTRUCTURE ANALYSIS AND STRESS-STRAIN BEHAVIOR OF A MODEL REFRACTORY SYSTEM MgO - $CaO \cdot MgO \cdot SiO_2$*

William E. Snowden and Joseph A. Pask

The effects of the presence of a silicate boundary phase on the high-temperature stress-strain behavior of MgO materials has been studied using a model system $MgO-CaO \cdot MgO \cdot SiO_2$ (monticellite). Specimens for testing were fabricated by hot pressing, or by hot pressing and annealing, and contained up to 15% silicate phase. The boundary phase consisted primarily of CMS, but small amounts of a glassy phase were also present. The stress-strain behavior of these specimens was found to be strongly dependent on the degree of continuity of the boundary phase, and on the temperature in the range 1200-1400°C. At 1200°C deformation was concluded to be the result of dislocation motion within the MgO framework. At higher temperatures deformation was controlled by viscous flow of the boundary regions.

*Abstract from LBL-3507.

9. HIGH-TEMPERATURE DEFORMATION OF POLYCRYSTALLINE MAGNESIUM OXIDE*

William E. Snowden and Joseph A. Pask

The mechanical behavior of two types of polycrystalline MgO was studied in compression over the temperature range 1200-1400°C. Differences in behavior between hot-pressed specimens and specimens which were hot pressed, then annealed, were attributed to differences in the structure of the grain boundary regions. Results indicate that creep in the hot-pressed specimens was controlled by a grain boundary sliding mechanism

characterized by the movement of dislocations along grain boundaries, with a stress exponent n = 1.8 and an apparent activation energy for the process of ~70 kcal/mol. Creep in the specimens which were also annealed was found to be controlled by a dislocation climb mechanism within the grains, with a stress exponent n=7 and an apparent activation energy of ~110 kcal/mol.

*Abstract from LBL-1120.

10. EFFECT OF PROCESSING ON MICROSTRUCTURE AND MECHANICAL BEHAVIOR OF MAGNESIUM OXIDE*

Truett B. Sweeting† and Joseph A. Pask

Specimens of polycrystalline MgO were fabricated from two different MgO powders by hot pressing in graphite and alumina dies, followed by annealing in air, vacuum, or within the graphite die in vacuum. The two powders were prepared by dispersing in isopropanol, drying, and milling in a rubber-lined mill with alumina balls. The relatively high cation content, particularly Ca and Si, in Type II MgO was the most significant difference in the two powders as it led to the formation of a small amount of liquid phase along the grain boundaries during the annealing step at 1550°C.

Impurities introduced and modified throughout the entire processing procedure of powder preparation, pressing in a graphite die, and annealing in different ambient atmospheres resulted in microstructures with varying grain size and grain boundary structure in the specimens produced from Type I MgO. The formation of a small amount of liquid phase occurred during the annealing step at 1550°C in Type II MgO specimens.

Impurities introduced and modified throughout the entire processing procedure of powder preparation, pressing in a graphite die, and annealing in different ambient atmospheres resulted in microstructures with varying grain size and grain boundary structure in the specimens produced from Type I MgO. The formation of a liquid phase in the Type II MgO specimens tended to eliminate the effect of these processing variables but led to the development of grain sizes two or three times larger in size.

Correlations of the microstructures of the specimens were made with their mechanical behavior in compression at a constant strain rate at 1200°C. The Type I specimens had considerably higher yield and maximum stresses than the Type II. Also, the specimens annealed in air had the largest strain at failure, and the ones annealed in the graphite die had the smallest; this behavior was attributed to a more perfect grain boundary for the former. The Type II specimens failed at considerably lower stresses and failures with little differences in value with different annealing atmospheres which was attributed to the presence of the brittle phase along the grain boundaries. Stress-strain curves are shown in Fig. 1.

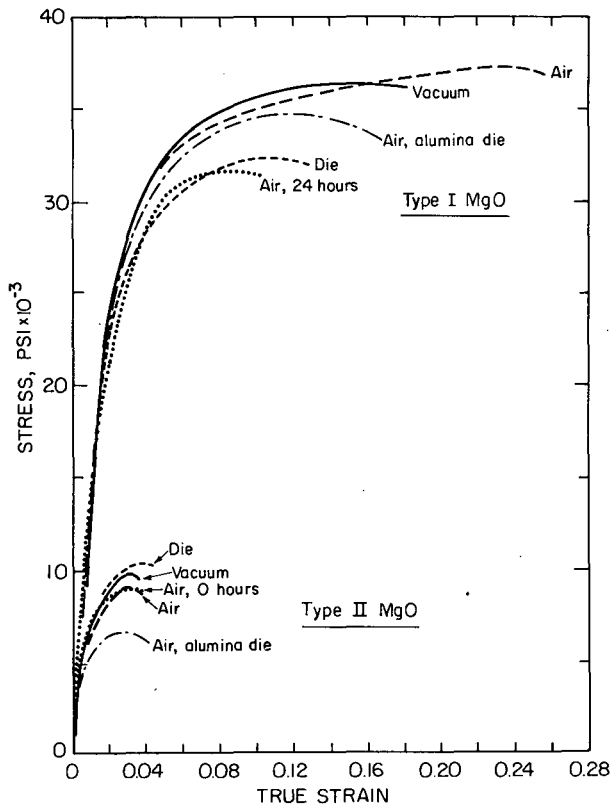

Fig. 1. Stress-strain curves in compression at 1200°C obtained at a constant strain rate of 0.025/min. (XBL 749-7120)

*Abstracted from LBL-3107

†Present address: New York State College of Ceramics at Alfred University, Alfred, N.Y.

11. WETTING AND REACTION BETWEEN ALUMINUM AND VITREOUS SILICA

Chisato Marumo and Joseph A. Pask

The objective of this study is to understand the wetting behavior of vitreous silica by molten aluminum. Since the wetting behavior is affected by interfacial reactions, the determination of the nature of the reactions and reaction mechanisms is also an objective. A number of studies on reactions between these components have been reported in the literature, but the reactions are not yet understood completely.

Sessile drop experiments of a spherical drop of aluminum on silica have been performed at 800 and

900°C versus time (Fig. 1) and up to 1200°C at heating rates of 10°C/min. (Fig. 2) and 40°C/min. at a pressure of 10^{-5} torr. The use of a cubic specimen of aluminum resulted in modifications of the curves because of a larger initial contact area. Cross-sections of the sessile drop specimens have indicated several reaction products between the aluminum and vitreous silica. The surface energies of the reaction products and the interfacial energies between the products and liquid aluminum, with and without saturation with silicon are different. These values plus the contribution of the free energies of reaction all play a role in determining the nature of the curves shown in the figures.

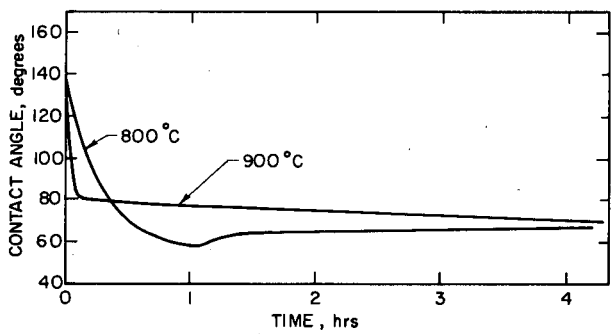

Fig. 1. Contact angle versus time at 800 and 900°C for a starting spherical drop of aluminum on vitreous silica. (XBL 751-5480)

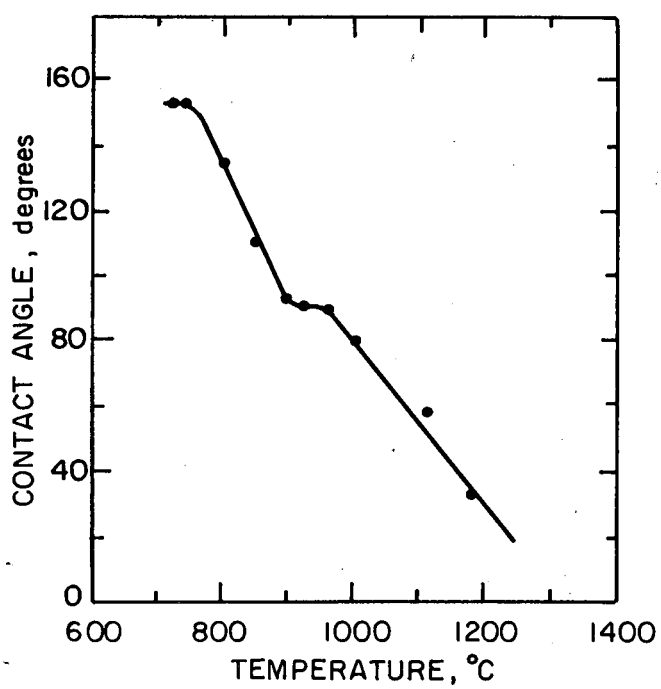

Fig. 2. Contact angle versus temperature at a heating rate of 10°C/min. for a starting spherical drop of aluminum on vitreous silica. (XBL 751-5479)

The reactions are complex since they are redox reactions and involve the appearance of the suboxides of aluminum and silicon at the experimental temperatures. Studies are now in progress in an effort to determine the reaction products and the reaction mechanisms in this system.

12. METAL-GLASS INTERFACES

Glenn A. Holmquist and Joseph A. Pask

Studies on the factors that affect the wetting of metals by molten glasses and the nature of the glass-metal interfaces are continuing. Systems being investigated are platinum and gold with molten B_2O_3 and B_2O_3 with small amounts of soda. Sessile drop experiments of the molten glasses on platinum and gold with increasing air pressure from 10^{-5} torr to atmospheric pressure have indicated a decrease in contact angle from about 60° to 10° at a pressure of about 10^{-2} torr. This phenomenon has been attributed to a change in the surface energy of the metal. The nature of the changes in the surface and interfacial energies are under study.

13. RESEARCH PLANS FOR CALENDAR YEAR 1975

Joseph A. Pask

(a) Development of Microstructures

Studies on the thermodynamic aspects of solid state sintering, grain growth, and microstructure development will be continued. These studies will also be extended to liquid phase sintering.

Experimental studies designed to verify equations developed to follow the kinetics of solid state sintering will be continued. These studies will also undertake to correlate kinetic data with the thermodynamic aspects.

Studies are being continued on the utilization of freeze drying techniques for the preparation of spinel powders for purposes of ultimately attaining polycrystalline specimens with controlled microstructures. The factors that play a role in the formation of aggregates during the preparation of the powders are being determined. The resulting characterization parameters will be correlated with the development of microstructure during sintering.

Studies are being carried on on the factors that play a role in the development of microstructure in mullite compacts. A desirable microstructure for strength and toughness is one with acicular instead of equiaxed crystals.

(b) Solid State Reactions

Studies on phase separation within the silica-alumina system are continuing. Nucleation and growth phenomena within this system of α-Al_2O_3 and mullite will also be explored. The effect of

additives on the solid solution range of and diffusion kinetics in mullite will also be determined. These studies should provide information as to the possibility of other metastable relationships within the system that have not as yet been identified. Within the oxide realm the silica-alumina system is one of the most promising because of the abundance of the component oxides in the earth's crust and because of their potentially favorable properties.

(c) Mechanical Behavior

Correlation of compressive stress-strain behavior with compression creep behavior is continuing. The objective is the development of a capability of predicting mechanical behavior on the basis of limited available data. Single crystals of MgO in ⟨100⟩, ⟨110⟩, and ⟨111⟩ orientations and polycrystalline MgO are being used for development of data at high temperatures. Such studies contribute to the general understanding of mechanical behavior of polycrystalline materials.

Studies of crack growth in glass plates subjected to high velocity impact are continuing. Stress versus time histories at the crack location in precracked specimens are being determined.

One of the least known factors in determining the mechanical behavior of polycrystalline specimens is the effect of the nature of the grain boundaries. Studies are continuing on determining the nature of grain boundary structures and their effect on mechanical behavior.

(d) Ceramic-Metal Interfaces

Interfaces between ceramics (glass or crystalline) and metals are critical in determining the behavior of composites, protective coatings, thin and thick films in electronic devices, and electrical lead-throughs. It is thus important to understand the interfacial structures and the reactions that may occur at interfaces because of lack of chemical equilibrium between the phases. Studies are continuing on SiO_2-Al, SiO_2-AlSi, Si-Al, Si-Al_2O_3, Pt-glass, and Au-glass systems.

14. 1974 PUBLICATIONS AND REPORTS

Joseph A. Pask and Associates

Journals and books

1. Carl E. Hoge and Joseph A. Pask, Thermodynamics of Solid State Sintering, in Physics of Sintering, edited by M. M. Ristic (Boris Kidric Institute of Nuclear Sciences, Belgrad, Yugoslavia, 5, 109-142 (1974) (LBL-1495).

2. İlhan A. Aksay and Joseph A. Pask, The Silica-Alumina System: Stable and Metastable Equilibria at 1.0 Atmosphere, Science 183, 69 (1974) (LBL-1835).

3. William E. Snowden and Joseph A. Pask, High-Temperature Deformation of Polycrystalline Magnesium Oxide, Philosophical Mag. 29, 441 (1974) (LBL-1120).

4. İ. A. Aksay, C. E. Hoge, and J. A. Pask, Wetting under Chemical Equilibrium and Non-equilibrium Conditions, J. Phys. Chem. 78, 1178 (1974) (LBL-1870-Rev.).

5. İlhan A. Aksay, Carl E. Hoge, and Joseph A. Pask, Phase Distribution in Solid-Liquid-Vapor Systems, in Surfaces and Interfaces of Glass and Ceramics, Materials Science Research, Vol. 7, edited by V. D. Frechette, W. C. LaCourse and V. L. Burdick, Plenum Publishing Corp., N. Y., 299-321 (1974) (LBL-2205).

Invited talks

1. Joseph A. Pask and İlhan A. Aksay, Determination of Phase Diagrams Using Diffusion Techniques, LBL-2599 Abs., March 1974. Talk given at Case Western Reserve University, Cleveland, Ohio, June 2-5, 1974.

2. "Ceramic-Metal Bonding," Pacific Coast Meeting of American Ceramic Society, Los Angeles, Calif., October 23-26, 1974.

LBL reports

1. İlhan A. Aksay and Joseph A. Pask, Stable and Metastable Equilibria in the SiO_2-Al_2O_3 System, LBL-2747, July 1974.

2. Joseph A. Pask and İlhan A. Aksay, Determination of Phase Diagrams Using Diffusion Techniques, Chapter in the Proceedings of the 1974 University Conference on Ceramic Science--Transport Phenomena in Ceramics, Case Western Reserve Univ., Cleveland, Ohio, June 3-5, 1974. (LBL-2599, Aug. 1974).

3. Truett Belin Sweeting, Effect of Processing on Microstructure and Mechanical Behavior of Magnesium Oxide, LBL-3107, Aug. 1974 (M.S. Thesis).

4. William E. Snowden, Microstructure Analysis and Stress-Strain Behavior of a Model Refractory System MgO-CaO·MgO·SiO_2, LBL-3507, Dec. 1974.

5. Carl E. Hoge and Joseph A. Pask, Thermodynamic Considerations of Solid Phase Sintering, LBL-3546, Dec. 1974.

6. William E. Snowden, Magnetically Accelerated Flyer Plates for Use in Impact Fracture Studies, UCRL-51496 (Livermore), Dec. 1973 (not previously listed).

C. RELATION OF MICROSTRUCTURE TO PROPERTIES IN CERAMICS

Richard M. Fulrath, Principal Investigator

Introduction. The mechanical, electrical, and magnetic properties of ceramic materials are essentially determined during the processing of the ceramic composition. Unlike metals (where cast alloys may be treated mechanically, thermally, or combinations of both to significantly change their properties) polycrystalline ceramic materials are brittle at low temperatures eliminating mechanical treatments and during processing have been subjected to such high temperatures that further heat treatment cannot make significant changes in properties.

Structural properties of polycrystalline ceramics, especially fracture strength at low temperatures where the ceramic is brittle, are primarily controlled by grain size and porosity. These two parameters are determined by the composition and densification process used to produce a dense polycrystalline ceramic from a powder compact. The densification process (sintering) may take place by complete solid state reaction or may have a liquid phase developed at high temperatures to assist the mass transport process. This important area of ceramic research is under investigation in this research effort employing the IMRD developed capabilities in high temperature scanning electron microscopy. Many ceramic and metallic compositions have compatible properties with the vacuum environment of the scanning microscope and offer a wide range of systems for study.

The electrical and magnetic properties of polycrystalline ceramic materials involve a more complex set of parameters than encountered in the structural ceramics. Here not only grain size and porosity influence the properties but significant property changes may be made by changes in both the intrinsic and extrinsic defect structure. Here processing and characterization of the processed ceramic must be included in any study of electrical or magnetic properties. The primary research effort in this group on the electrical and magnetic properties of ceramic materials is to process ceramics of controlled composition under known processing conditions and then relate the properties to the grain size, porosity and defect structure produced during processing.

These two research areas are essential to the development of a basic understanding of the science of processing and the development of ceramic materials with controlled properties for application and material substitution in the many new technological areas generated by the raw material and energy shortages presently facing the nation.

1. SOLID STATE SINTERING STUDIES

David N. K. Wang and Richard M. Fulrath

The densification (sintering) of refractory powder compacts without the aid of liquid phases is an important processing step in the production of refractory ceramic materials. In spite of the extensive research activity on the mechanisms involved in the sintering process, we are still severely limited in predicting the sintering behavior of a refractory powder compact. The reason is because the complexities associated with the sintering of a real powder compact cannot be represented realistically by an oversimplified theory based on ideal spherical particles. Therefore, a thorough phenomenological study of the evolution of the structure, the change of density, and the densification rate as a function of temperature and time from the start to the completion of the sintering process is important.

Previous sintering studies have concentrated on the use of isothermal techniques. A complete analysis of densification kinetics is unattainable due to uncertainties in the change of density of the compact with temperature and time in the initial heating period. The present work is to use a nonisothermal constant heating rate technique to monitor the complete densification kinetics.

Powder compacts made by cold pressing high purity submicron Al_2O_3 and MgO doped compacts containing binders and lubricants are heated in air to low temperatures relative to the sintering temperature to remove the organic materials. These compacts are then heated in the hot stage of the scanning electron microscope under programmed heating rates to various temperatures to determine the sintering characteristics. The linear shrinkage of the compact is determined by placing W microsphere markers on the surface of the sample and recording the marker's movement continuously on 16 mm film during the sintering run.

Three constant heating rates, 2.5, 4.6 and 9.4° C/min have been used. In each run the specimen was first heated to 800°C then the temperature was increased to 1700°C at a controlled rate. The change in relative density was calculated from linear shrinkage data and plotted in Fig. 1. As indicated, the slower the heating rate, the higher the density at any given temperature. Independent of heating rate, the densification rate is the same at a given temperature as long as the sample has a density below 73% of the theoretical density. This can be seen in Fig. 2. For example, at 1380°C a sample heated at 2.5° C/min has achieved a density of 75%, while the other two samples with identical densification rates were heated at 4.6° C/min and 9.4° C/min and

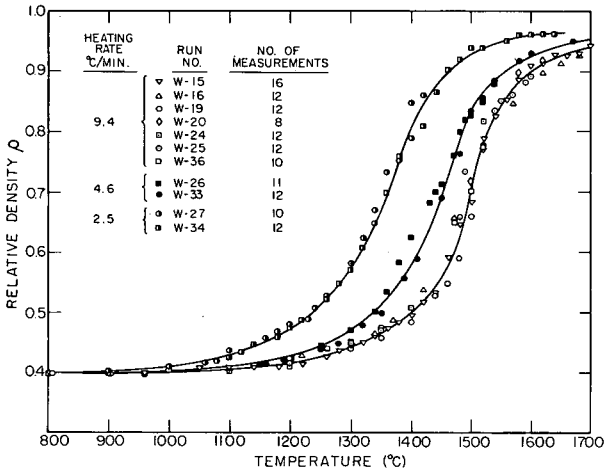

Fig. 1. The relative density of a MgO doped (0.1 wt.%) Al_2O_3 powder compacts as a function of temperature for various constant heating rates. (XBL 746-6551)

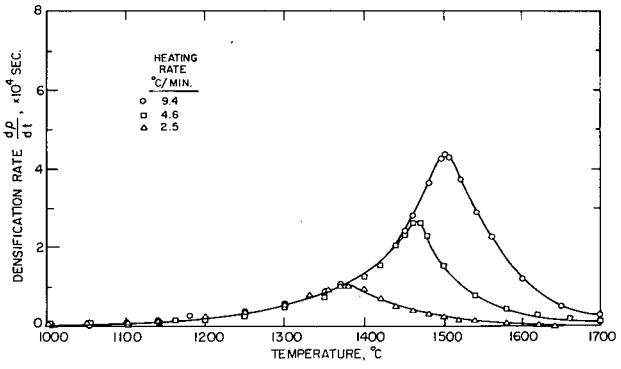

Fig. 2. The densification rate of 0.1 wt.% MgO doped Al_2O_3 powder compacts as a function of temperature. The maximum densification rate in each case corresponds to a relative density of 0.73 of the theoretical density. (XBL 746-6546)

have densities of only 55% and 49% of theoretical density, respectively, at the same temperature. This indicates that the densification rate below a given critical density of about 73% is not a function of porosity or heating rate but a function of temperature only.

Figure 3 is a plot of the temperature-compensated densification rate against 1/T for three heating rates. The sintering process covered a temperature range from 1200°C to 1500°C. An activation energy of 57 Kcal/mole was calculated. This value is remarkably close to the 57.6 Kcal/mole activation energy experimentally determined by Kingery and Oishi for oxygen bulk diffusion in crushed Al_2O_3 single crystal grains between 1200°C and 1620°C. This is much lower than the activation energy for sintering calculated by previous investigators using model equations and differs from the experimental activation energy obtained in the final stage of the sintering process. The low activation energy in the

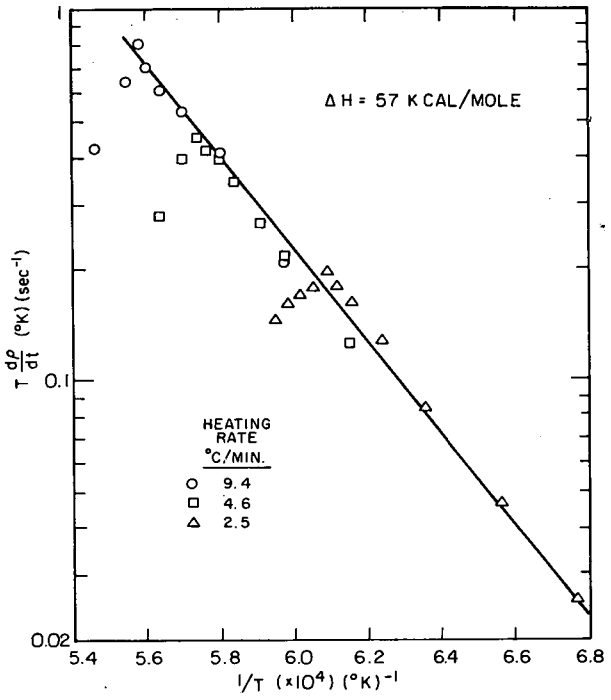

Fig. 3. The temperature compensated densification rate as a function of 1/T for 0.1 wt.% MgO doped Al_2O_3 powder compacts. (XBL 746-6550)

present study could be caused by the existence of a nonequilibrium defect structure in the crystalline lattice. This is possible if the powder is produced by the decomposition of a salt at low temperature.

In order to understand the effect of MgO on the kinetics of the sintering of Al_2O_3 powder compacts undoped Al_2O_3 powder compacts were studied. Figure 4 shows the densification curves for both doped and undoped samples at a constant heating rate. There is no effect of MgO on the densification kinetics before the maximum densification rate. Others have reported that addition of MgO

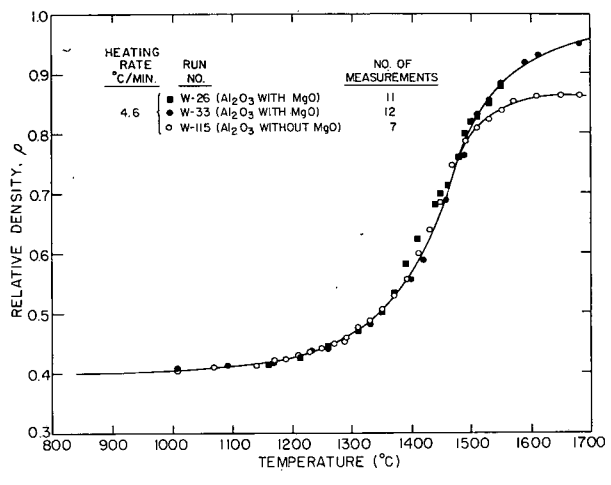

Fig. 4. The relative density as a function of temperature for undoped and 0.1 wt.% MgO doped Al_2O_3 powder compacts. (XBL 749-7322)

would change the densification rate. After the attainment of the critical density, 73% of theoretical density, a deviation in the rate of densification occurs for doped and undoped compacts. The deviation is attributed to the difference in grain boundary mobility between doped and undoped Al_2O_3. The lower grain boundary mobility in Al_2O_3 after the addition of MgO results in a smaller pore-pore distance and, hence, a smaller pore-grain boundary sink distance. This difference in diffusion path gives a different rate of densification for doped and undoped Al_2O_3.

In order to study the microstructures of porous compacts a sulfur impregnation technique is used. A study on the changes of microstructures during densification will be the major work in the next year.

2. UNIAXIAL BEND STRENGTH AND FRACTURE INITIATION ENERGY IN GLASS-MATRIX COMPOSITES

Dipak R. Biswas and Richard M. Fulrath

For a glass-matrix composite system a fracture theory was proposed by Hasselman and Fulrath[1] using the well known Griffith equation:

$$\sigma = \left(\frac{2\gamma E}{\pi c}\right)^{1/2}$$

where σ is the fracture stress, γ is the surface energy per unit area, E is the Young's modulus and c is the flaw size. The composite system used was a sodium borosilicate glass matrix and dispersed spherical alumina particles. The volume fraction and particle size was varied. They proposed that the second phase dispersed particle would limit the size of the Griffith flows in glass matrix and replaced c in above equation as the mean free path, d, between spherical particles. When the strength of the composite was plotted against $(E/d)^{1/2}$, it showed two distinctly different regions as shown in Fig. 1. In region I, the average distance between the particles was greater than the induced flaw size and the strength was independent of the second phase. In region II, the flaw size was governed by the mean free path between the particles and the strength was a function of volume fraction and particle size of alumina particles. The slope of the straight line in region II should give the dynamic surface energy when it is a constant.

Using glass-nonspherical alumina composites Lange[2] showed that the fracture surface energy of the composite was increased by the second phase alumina particles. This increase in fracture surface energy was given as the reason for strengthening of glass matrix composites. The present investigation was to measure the uniaxial bend strength and fracture initiation energy of glass-nonspherical alumina and glass-spherical tungsten composites. The experimental results were analyzed to see the validity of the strengthening model[1,2] of glass-matrix composites.

Glass matrix composites were fabricated by

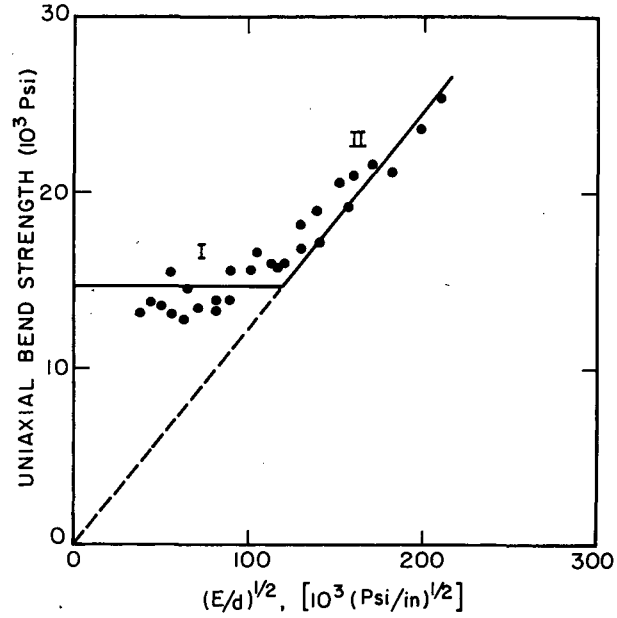

Fig. 1. Uniaxial bend strength vs. $(E/d)^{1/2}$ for glass matrix composites containing spherical Al_2O_3 particles as the dispersed phase.
(XBL 7410-7489)

intimately mixing the powders in a ball mill and then vacuum hot-pressing at 725°C and 1000 to 2000 psi pressure for 10 to 40 minutes. Uniaxial bend strength was measured by using a 4-point bending. A diamond sawed surface was stressed to failure. Fracture initiation energy was measured by the double Cantilever beam technique. The load was recovered at the point of catastrophic failure. This load P was used to calculate the fracture energy from the equation:

$$\gamma = \frac{6P^2L^2}{Ew^2t^3}\left[1 + 1.32\,(t/L) + 0.542\,(t/L)^2\right]$$

where E is Young's modulus, and L, w and t were the geometric constants. The plot of uniaxial bend strength and fracture initiation energy of glass-nonspherical alumina composites is shown in Fig. 2. The above equation was derived by Gilman[3] and modified by Wiederhorn et al.[4] The equation was applied to an isotropic-homogeneous material with a slow moving crack. When a second phase material is introduced into the glass matrix. The system is non-homogeneous as observed from the microstructure and the specimen failed catastrophically during the test. So the applicability of the above equation to calculate the fracture energy of the composites can be questioned. In a specimen, like glass or glass matrix composite with a machined slot, numerous microflaws are left along the root of the notch. Fracture can initiate at any of these microcracks in the double cantilever beam test. The load necessary to break the specimen is dependent on these microflaws. In the 4-point bending test, the load is recorded at the time of fracture. At the surface of the specimen, there are a number of microflaws that are produced during diamond

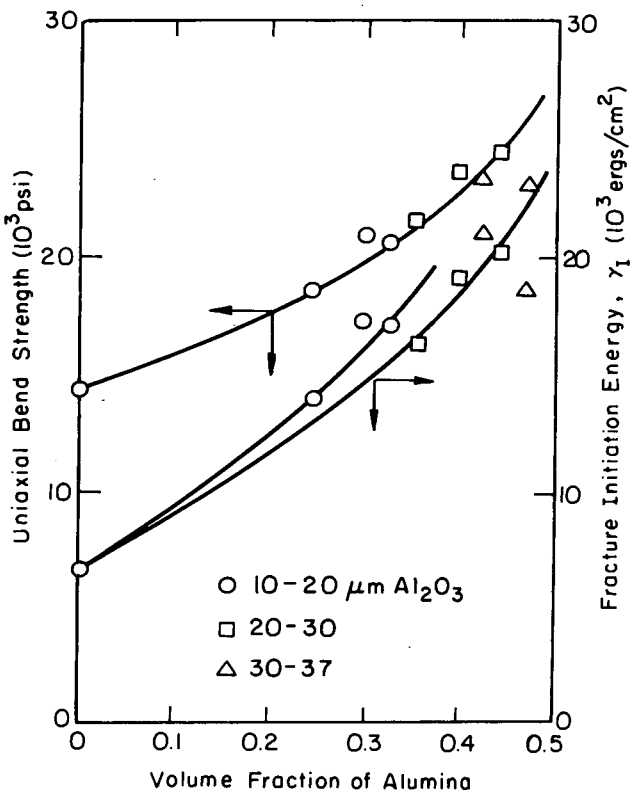

Fig. 2. Uniaxial bend strength and fracture initiation energy for glass matrix composites as a function of the volume fraction of dispersed phase non-spherical Al_2O_3 particles. (XBL 742-5575A)

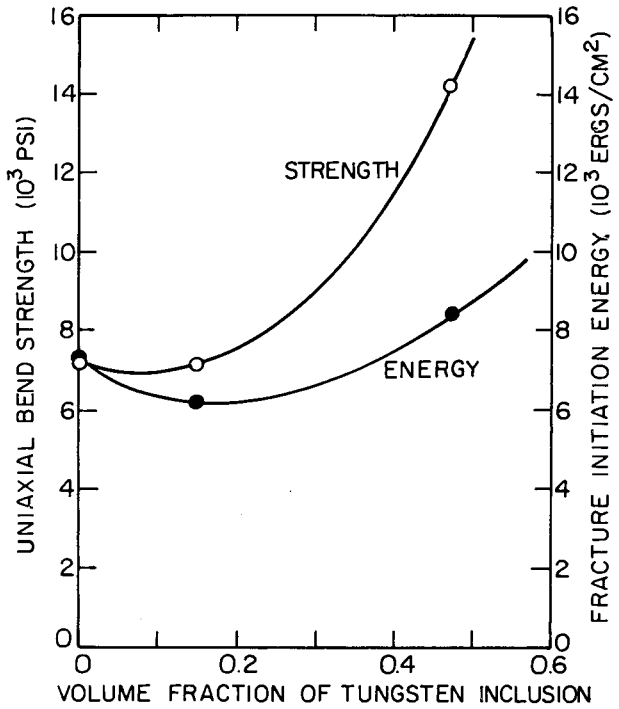

Fig. 3. Uniaxial bend strength and fracture initiation energy for glass matrix composites as a function of the volume fraction of dispersed phase spherical W particles. (XBL 7410-7381)

sawing. When the load reaches to a certain critical value at the tip of a microflaw, failure occurs. In both tests the load necessary to fracture the specimen is controlled by the same microflaws. From Fig. 2, it is shown that the strength and the fracture initiation energy of glass-nonspherical alumina composites increased with increase in volume fraction of alumina--almost identical to the data reported by Lange.[2] But from the proposed fracture theory,[1] the surface energy should be constant as evident from the slope of region II in Fig. 1.

Using spherical tungsten particles as the second phase, glass-tungsten composites were fabricated and measured both by the uniaxial bend test and double cantilever beam test exactly as were the glass-alumina composites. The results are plotted in Fig. 3--which showed that the strength increased with increase in volume fraction of tungsten inclusions but the fracture initiation energy was more or less the same as that of the glass. This was expected from the proposed fracture theory[1] of glass-matrix composites. The fracture surfaces were examined by Scanning Electron Microscopy and it showed that the fracture always remained in the glass matrix.

These results suggest that the strengthening of glass-matrix composite can be well explained by the proposed fracture theory[1] with the second phase spherical particles limiting the flaw size in glass matrix. The effect of non-spherical particles in the glass matrix is more complex due to particle shape. The fracture behavior in glass matrix composites is dependent on the microflaws that are produced during diamond sawing.

---

1. D.P.H. Hasselman and R.M. Fulrath, J. Am. Ceram. Soc. 49(2), 68 (1966).
2. F.F. Lange, ibid, 54(12), 614 (1970).
3. J.J. Gilman, J. Appl. Phys. 31(12) 2208 (1960).
4. S.M. Widerhorn, A.M. Shorb and R.L. Moses, ibid, 39(3) 1569 (1968).

3. ELECTRICAL CONDUCTIVITY IN $LiFe_5O_8$ CERAMICS

Juinn-Jye Dih and Richard M. Fulrath

Lithium ferrite ($LiFe_5O_8$) is a very promising magnetic material for applications such as computor memories. It is ferrimagnetic and has an inverse spinel structure. Electrical conductivity which is directly related to the power loss of the system during use is one of the most important parameters. The electrical conduction behavior of lithium ferrite has not been fully investigated. Reported resistivity data vary from a few ohm-cm to values many orders of magnitude higher. The origin of the activation energy of resistivity is still not understood. For other inverse spinel ferrites (e.g., $CoFe_2O_4$), it is established that

their electrical conduction is satisfactorily described by a "hopping mechanism" charge transport among the octahedrally coordinated metal ions by electron or hole conduction. The mobility of the charge carrier transported along like ions is given by a diffusion type expression:

$$\mu = \frac{ed^2\nu}{kT} \exp\left(-\frac{Q}{kT}\right)$$

where

μ = the mobility of the charge carrier

d = the distance between octahedral sites

ν = the effective lattice vibration frequency

Q = the activation energy

The primary problem in studying the electrical properties of lithium ferrite is the lack of information concerning the fabrication of the samples and the sample composition. Most ferrites have a tendency to lose oxygen at high temperature. Lithium ferrite loses both oxygen and lithium during the heat treatment necessary for densification and thus adds to the problem of processing. In this laboratory a packing powder technique used extensively for the processing of lead zirconate titanate ceramics was employed to control the material loss from lithium ferrite during sintering. The purpose of the present study was to investigate the dc resistivity behavior of polycrystalline lithium ferrite with well defined composition and the dependence of the resistivity on temperature and stoichiometry.

In order to make a series of samples* with known deviation from the stoichiometric composition, $LiFe_5O_8$ powder was mixed with proper proportions of $LiFeO_2$ and Fe_2O_3 powder, ball milled and dried. The powder was then pressed into disks and sintered at 1150°C for two hours in 1 atmosphere O_2 using $LiFe_5O_8$ as stoichiometric packing powder. Specimens were always buried deeply into the packing powder. The material loss from the system was controlled by using the packing powder technique and controlled O_2 pressure. Densities of all specimens were above 98% theoretical density.

DC bulk resistivity was measured by using a guard ring method. The ends of the sample were sputtered with gold to ensure intimate contacts. The contact resistance was negligible. Thermoelectric measurements were made to determine the type of charge carrier contributing to the conduction process in $LiFe_5O_8$. Measurements were made from room temperature to 300°C. The surface of all the samples was ground to a depth sufficient to eliminate any inhomogeneity due to surface reactions.

The influence of composition on the resistivity of $LiFe_5O_8$ at different temperatures is shown in Fig. 1. Resistivity always drops while moving from the $LiFeO_2$ doped region into the Fe_2O_3 doped region. This is due to the increasing Fe^{+2} content on the octahedral sites. As both Fe^{+2} and Fe^{+3} locate on the octahedral sites, electron hopping from Fe^{+2} to Fe^{+3} acts as the primary charge transfer process. While moving from the

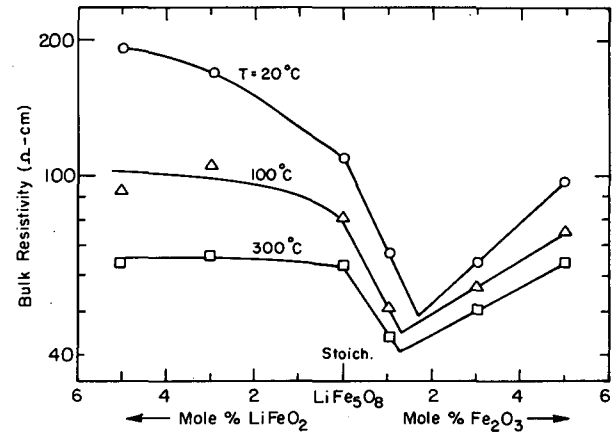

Fig. 1. The influence of composition on the resistivity of $LiFe_5O_8$ at different temperatures. (XBL 749-7216)

Fe deficient region ($LiFeO_2$ doped) into the Fe excess region (Fe_2O_3 doped), more and more Fe^{+2} would be active in charge transport. The resistivity value decreases with increasing Fe_2O_3 in the composition. Measurements of the thermoelectric voltage showed that electron conduction dominated in all samples. This is consistent with the picture of n-type charge carriers due to the Fe^{+2} ions. The resistivity value increases while moving away from the near stoichiometric region for Fe_2O_3 doped samples. This is probably due to a second phase developing or disordering. Fe^{+2} on the octahedral site tends to introduce disorder into the system. This disorder may decrease the mobility of the charge carrier and thus increase resistivity.

In Fig. 2 all the resistivity data at the same temperatures were normalized with that of the stoichiometric composition. For a single type of charge carrier the conductivity is proportional to the product of concentration of the charge carrier and the mobility of the charge carrier. The concentration of the charge carrier (Fe^{+2}) for a particular composition should remain constant in the temperature range where the measurements were made. The shift of the curve

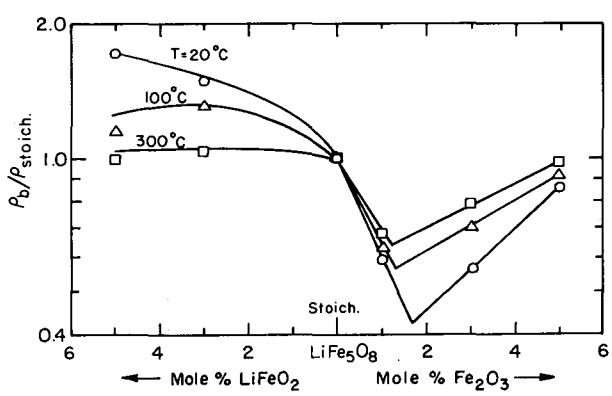

Fig. 2. Normalized value of the resistivity of $LiFe_5O_8$ vs. composition. (XBL 749-7217)

with temperature as shown in the figure is clearly an influence of the mobility term.

The temperature dependence of the resistivity for various compositions is shown in Fig. 3. The resistivity decreases with increasing temperature. Normalization of all the resistivity data of a fixed composition with that at room temperature should indicate only the mobility effect. As shown in Fig. 3, mobility divided by temperature follows an exponential relation with temperature which is similiar to the mobility expression proposed for other inverse spinel ferrites. The activation energy of mobility for each composition (as shown in Fig. 4) can be calculated from the slope of the straight line in Fig. 4. It is found that the activation energy does not change significantly through the stoichiometry region, which clearly indicates that the conductivity change through the same region is primarily due to the change in carrier concentration. In fact, the conductivity increases linearly with the amount of dopent in that near stoichiometric region as shown in Fig. 5.

In summary, data have been presented to show the influence of stoichiometry (which affects the carrier concentration) and temperature (which

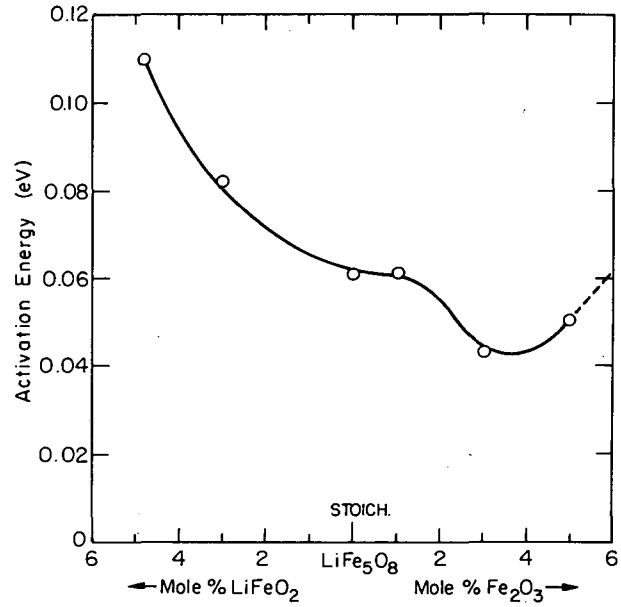

Fig. 4. Activation energy for the mobility vs. composition. (XBL 7410-7443)

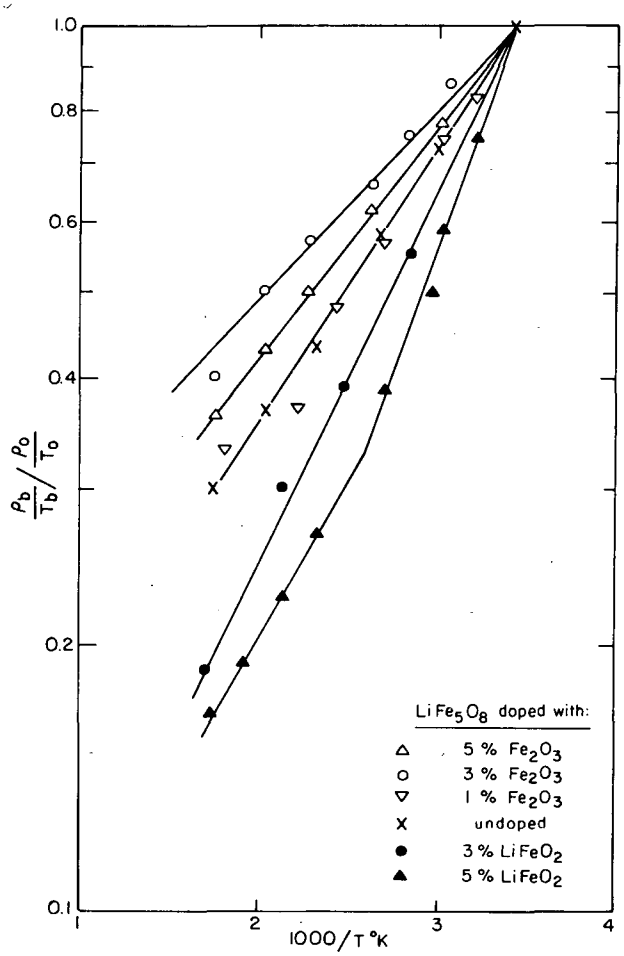

Fig. 3. Normalized resistivity for various compositions of $LiFe_5O_8$ vs. temperature. ρ_b is the resistivity at temperature T_b. ρ_o is the resistivity at room temperature T_o. (XBL 749-7218)

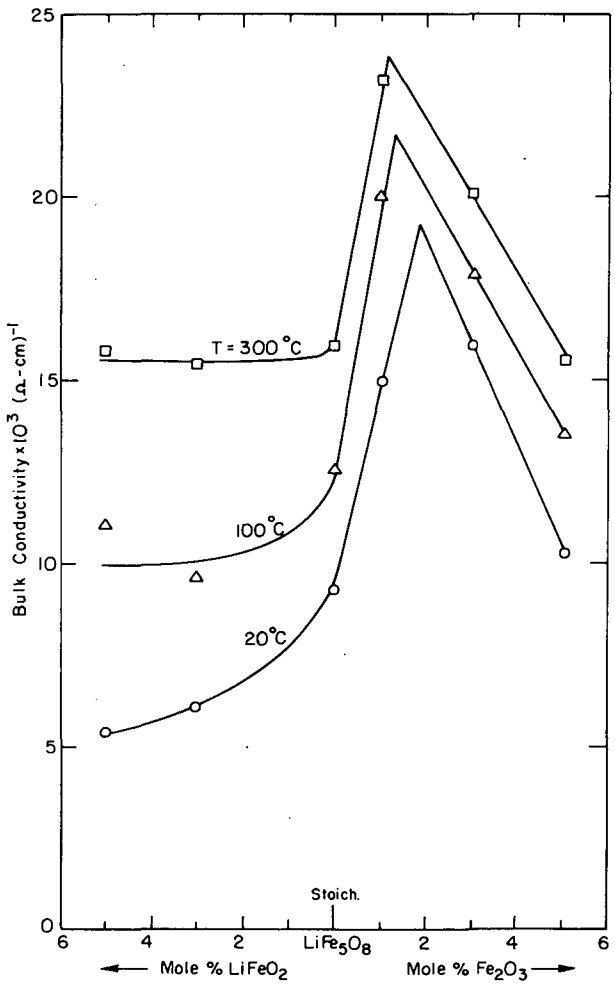

Fig. 5. The influence of composition of $LiFe_5O_8$ on the conductivity on a linear scale. (XBL 749-7215)

affects the carrier mobility) on the dc resistivity value of lithium ferrites. The exponential temperature dependence of the electrical resistivity is in good agreement with the electron hopping model. The electrical conduction occurs by thermally activated electron hopping between the octahedral Fe^{+2} and Fe^{+3}.

*All the samples used in this study were fabricated by Dr. Bandyopadhyay, a former graduate student.

4. PHYSICAL AND ELECTRICAL PROPERTIES OF CONTROLLED STOICHIOMETRY PZT

Kenneth E. Crabtree and Richard M. Fulrath

Outstanding ferroelectric and piezoelectric properties[1] have created considerable interest in ceramics of the pseudobinary solid solution series $PbZrO_3$-$PbTiO_3$ (PZT). Volatilization of the PbO constituent during high temperature processing makes reproducibility of electrical properties difficult to achieve.[3] This vaporization has been suppressed using a "packing powder" to surround specimens with a PbO atmosphere during sintering.[1,2,3] It became feasible to manipulate PbO defect concentration by employing this packing powder technique when the PbO vapor pressure equilibria and non-stoichiometry[4] in the $PbZrO_3$-$PbTiO_3$ system were determined. The purpose of this study was to relate effects of microstructure and composition on electrical properties by employing this equilibration technique.

Compositions chosen for this study are listed in Table I.

Table I. Compositions of Samples

$A^{2+}\ [B^{4+}]\ O_3$
$Pb\ [Zr_{.5}Ti_{.5}]\ O_3$
$Pb_{.99}\square_{.01}[Zr_{.49}Ti_{.49}Nb^{5+}_{.02}]\ O_3$
$Pb_{.99}\square_{.01}[Zr_{.495}Ti_{.495}W^{6+}_{.01}]\ O_3$

□ denotes a vacancy

Mixing and milling were done in plastic jars with Al_2O_3 balls to facilitate particle size reduction. This process introduced an amount (0.7±0.4 a/o) of Al_2O_3 which significantly influenced properties of the undoped composition.

Powders were calcined twice for 4 hours at 1000°C to produce a more homogeneous starting material and obtain higher fired densities. Samples were isostatically pressed into cylinders (7/16 " diameter × 1 1/2 " length) which were completely surrounded during sintering by a packing powder chosen from compositions in Table II.

Table II. Packing Powders

Powder	$a_{PbO}^{1200°C}$	X_{PbO}
$PZ_{.5}T_{.5}$ + 5 w/o PbO	.25	0
PZ + 5 w/o Z	.08	.020
$PZ_{.5}T_{.5}$ + 5 w/o Z,T	<.035	>.025

Sample discs were cut with a diamond saw after appropriate sintering times. The remaining slug was surrounded with fresh packing powder and sintered for longer times.

By X-ray analysis, a small amount of ZrO_2 impurity was detected in all specimens fired 30 hours or longer in the low PbO activity packing powder indicating that the PbO atmosphere surrounding the sample was not at the single phase boundary. The composition of this packing powder actually lay well within the PT/PZ + Z primary field. Thus the $PZ_{0.5}T_{0.5}$ phase actually became enriched at high temperatures with some of the excess Ti phase. Since PbO activity decreases as the Zr/Ti ratio decreases,[4] the activity created by this powder is slightly lower than that at the single phase boundary of $PbZr_{0.5}Ti_{0.5}O_3$. The effect of the low PbO atmosphere

$$(a_{PbO}^{1200°C} < 0.034)$$

on electrical properties after short sintering times was negligible.

Improved properties were observed for higher PbO activity atmospheres. Reduced porosity [i.e. increased density (Fig. 1)] and improved electrical properties (Fig. 2) reinforce Webster's[5] observation that porosity is the most significant factor effecting electrical properties. Lower remnant polarization, higher coercive fields, and higher dielectric constants (Fig. 2) were observed with lower PbO defect concentrations. Dielectric losses were lowest for the undoped composition.

Contrary to the observations of Takahashi,[6] tungsten was found to be an ineffective grain growth inhibitor. It is postulated that the multivalence (2, 3, 4, 5, 6) of the tungsten atom validates the observations of this study. The principle valence states of tungsten are +4 and +6. The equilibrium vapor pressure of oxygen, calculated from JANAF data, for the reaction

$$WO_{2.72} \xrightarrow{1200°C} WO_2 + 0.36\ O_2$$

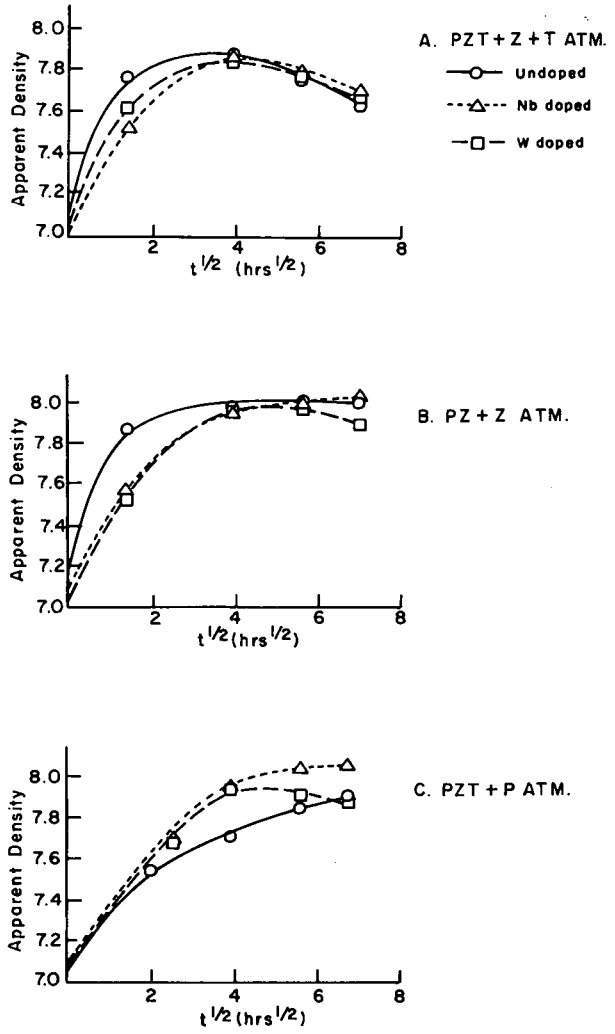

Fig. 1. Density achieved during sintering in various packing powder controlled PbO atmospheres as a function of the square root of the sintering time. (XBL 7411-7596)

is 26.3 atmospheres. The rules of crystal chemistry would also favor substitution of W^{4+}(0.70Å) rather than W^{6+}(0.62Å) which is actually at the limits of compatibility with the perovskite structure. Apparently, the energy required to reduce tungsten is less than that necessary to create charged vacancies in the PZT structure.

Sufficient amounts of W^{6+} substitute into the structure to compensate for the presence of charged oxygen vacancies (created by Al^{3+}), making electrical behavior essentially intrinsic (Fig. 3). This is also evidenced in similarities between lattice constants and ferroelectric properties of this material and intrinsic material of other studies. Quantities of W^{6+} in excess of the amount necessary to compensate for the presence of charged oxygen vacancies substitute as W^{4+} which would not be expected to significantly effect physical or electrical properties.

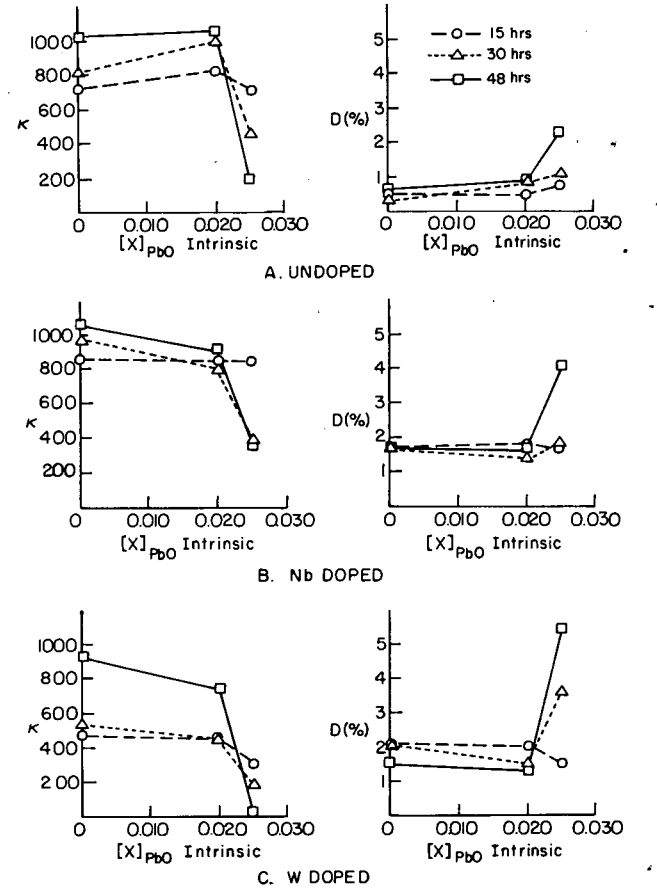

Fig. 2. Dielectric constant and dissipation factor as a function of intrinsic defect structure, $[X]_{PbO}$ and sintering time. (XBL 7411-7599)

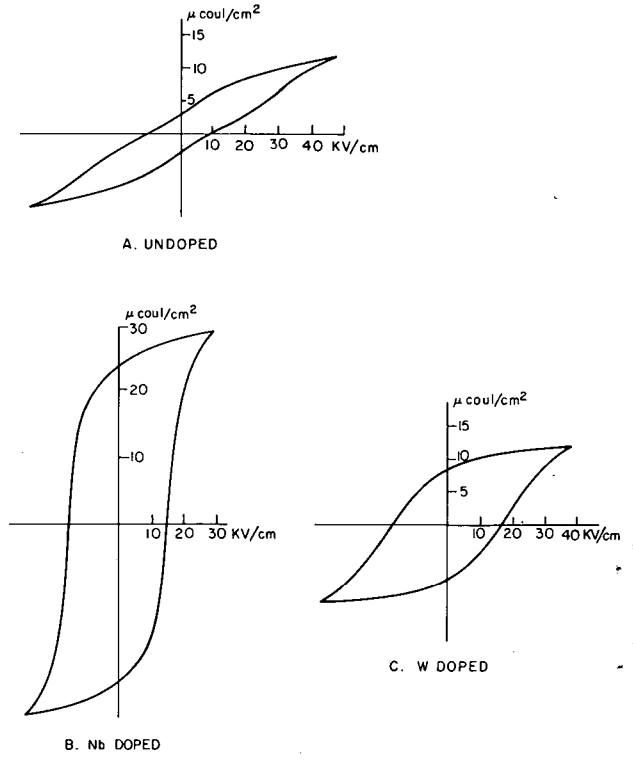

Fig. 3. Ferroelectric loops for undoped, Nb and W doped sintered ceramic PZT. (XBL 7411-7600)

*Abstracted from K.E. Crabtree, Physical and Electrical Properties of Controlled Stoichiometry PZT, M.S. Thesis, LBL-3543, Dec. 1974.

1. B. Jaffe, R. S. Roth and S. Marzullo, J. Appl. Phys. 25(6), 809 (1954).
2. P. D. Levett, Bull. Am. Ceram. Soc. 42(6), 348 (1963).
3. T. B. Weston, Canada Dept. of Mines & Tech. Surveys Rept. MPI 63-7 (1963).
4. R. L. Holman and R. M. Fulrath, J. Appl. Phys. 44(12), 5227 (1973).
5. A. H. Webster, T. B. Weston and N. F. H. Bright, J. Am. Ceram. Soc. 50(9), 490 (1967).
6. M. Takahashi and S. Takahashi, Japan J. A. P. 11(1), 31 (1972).

5. A LIQUID PHASE DENSIFICATION TECHNIQUE FOR THE LEAD ZIRCONATE TITANATE SYSTEM*

John W. Sherohman† and Richard M. Fulrath

The lead zirconate titanate (PZT) system has been utilized for many years in the fabrication of piezoelectric devices because of its large piezoelectric constants, high Curie temperature, and high permittivity. With the addition of lanthanum, modified PZT (PLZT) has also been used in the development of electro-optic devices. Yet at the temperatures required for densifying PZT powder compacts, intrinsic nonstoichiometry can occur due to the high vapor pressure of lead oxide (PbO).[1] If the evaporation of PbO from the PZT ceramic is not controlled, loss of PbO can develop second phases that can affect both its electrical and physical properties. A processing procedure is therefore necessary to improve the densification and quality of PZT ceramics.

A unique liquid phase densification technique has been developed to produce a highly dense unmodified single phase PZT material with fixed stoichiometry. The procedure for this technique is essentially a two-step process. The first step makes use of a low temperature liquid phase that can optimize, with the aid of external applied pressure, the rearrangement of particles after the formation of the liquid. The second step involves a subsequent heat treatment without applied pressure to allow liquid phase sintering to occur. During this heat treatment, a fixed PbO atmosphere is established that permits the liquid to be removed in a controlled manner and maintain the PZT material within its single phase region.

The densification technique was investigated using a $PZ_{0.5}T_{0.5}$ composition, i.e. $Pb(Zr_{0.5}Ti_{0.5})O_3$. The $PZ_{0.5}T_{0.5}$ material was prepared from both mixed oxides and chemical compounds. The low temperature liquid phase added to both powder preparations after forming $PZ_{0.5}T_{0.5}$ was lead oxyfluoride ($PbO \cdot PbF_2$) that has a melting temperature of approximately 500°C. A flow chart outlining the procedure in the preparation of the mixed oxides, the chemically prepared, and the lead oxyfluoride powders is shown in Fig. 1.

To determine the proper liquid content to obtain maximum density in the first step of the process, various weight percents of $PbO \cdot PbF_2$ were mixed in both the mixed oxides and chemically prepared $PZ_{0.5}T_{0.5}$ powder. Each sample was hot pressed at 600°C for 3.5 hours in helium. The liquid was then removed from the samples using a thermogravimetry method, after which their densities were determined. From the highest measured density after removal of the liquid phase, the optimum $PbO \cdot PbF_2$ content was established. As shown in Fig. 2, the liquid content necessary to achieve maximum density for the mixed oxides was an initial 22 w/o as compared to an initial 18 w/o for the chemically prepared material. Samples containing the optimum liquid content were then hot pressed hence completing the first step of the process.

The second step of the liquid phase densification technique involves a heat treatment after hot pressing that allows removal of the liquid phase from the PZT compact in a controlled manner while liquid phase sintering. A study using three different multi-phase powder compositions was performed on the mixed oxide prepared $PZ_{0.5}T_{0.5}$ sample of optimum liquid content as determined in the first step of the process. The multi-phase packing powder compositions were chosen to

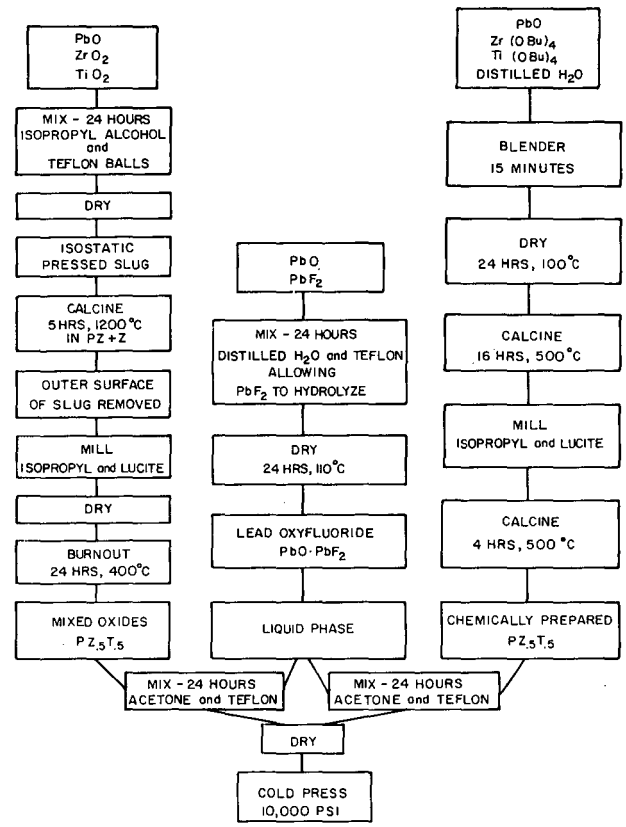

Fig. 1. Powder preparation flow chart for the mixed oxides, the chemically prepared, and the liquid phase materials. (XBL 7310-5494)

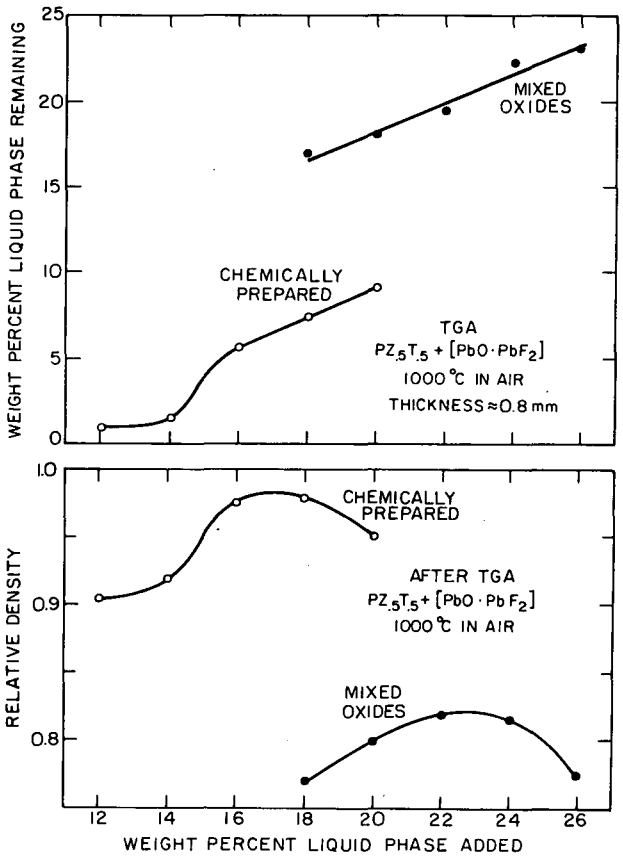

Fig. 2. Amount of liquid phase remaining in samples after hot pressing and a comparison of resultant densities after liquid removal. (XBL 7310-5495)

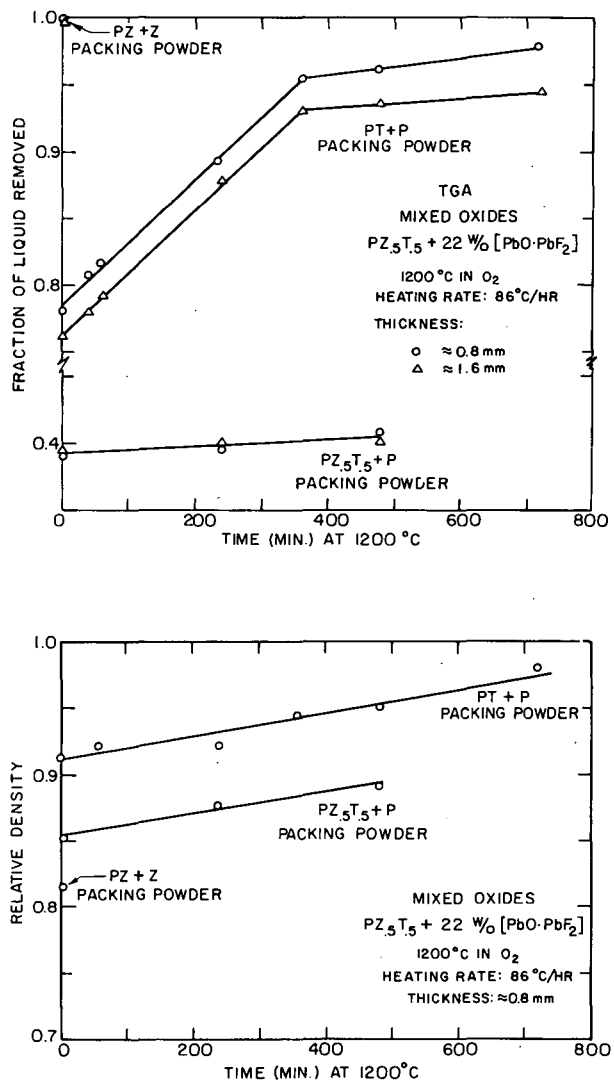

Fig. 3. Rate of removal of the liquid phase from $PZ_{0.5}T_{0.5}$ in various multi-phase packing powder compositions and a comparison of density after removal of the liquid phase. (XBL 7310-5497)

establish atmospheres of various PbO activities that would allow the sample to attempt to equilibrate by losing PbO, but maintain the sample in its single phase region. The results of the study are shown in Fig. 3.

A "control experiment" packing powder ($PZ_{0.5}T_{0.5}$ + P) of the same PbO activity as that of the sample was used to prevent PbO loss and insure that only the PbF_2 portion of the liquid evaporates. In the case of the lead zirconate plus excess zirconia (PZ + Z) where the PbO activity difference from the sample is large, all the liquid was removed before reaching temperature. Comparison of the density with that in Fig. 1 indicates very little liquid phase sintering had occurred. For the lead titanate plus excess lead oxide (PT + P) packing powder where the PbO activity difference is small, it is seen that the rate of PbO loss is thickness independent until a density of approximately 94% is reached. Above this value closed pores develop and the loss of PbO becomes thickness dependent. With respect to density, there tends to be a steady increase with the mixed oxides prepared $PZ_{0.5}T_{0.5}$ sample reaching 98% in 12 hours.

The PbO vapor pressure of the $PZ_{0.5}T_{0.5}$ material containing the PbO rich liquid was calculated using the Langmuir equation from the rate of evaporation in a PT + P packing powder. By comparing the Langmuir PbO vapor pressure at different temperatures with the equilibrium PbO vapor pressure from Knudsen effusion data, the evaporation coefficient was determined as shown in Fig. 4. In the temperature range from 1150° to 1250°C the evaporation coefficient appears to be constant having a value of approximately 1.8×10^{-6}

The chemically prepared $PZ_{0.5}T_{0.5}$ material containing the optimum $PbO{\cdot}PbF_2$ content was liquid phase sintered in a PT + P packing powder composition to investigate the effect of temperature on removal of the liquid. Figure 5 shows the fraction of liquid removed determined by the TG method versus temperature. Because of the lower weight percent of liquid remaining in the chemically prepared $PZ_{0.5}T_{0.5}$ after hot pressing, as shown in Fig. 2, most of the liquid was removed from the specimen by heating up to a temperature

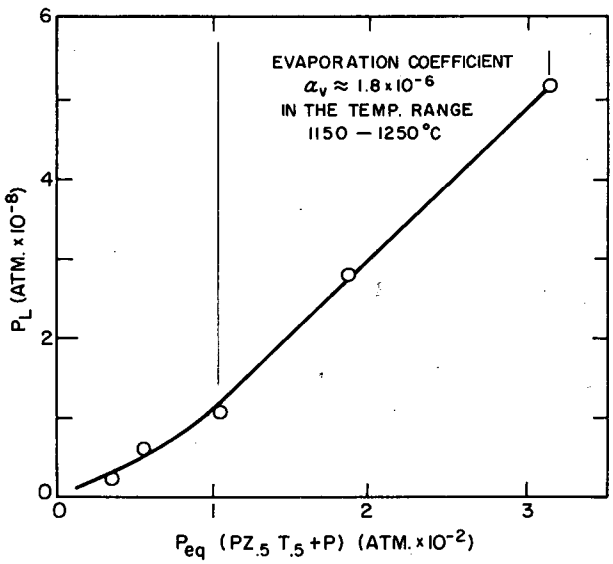

Fig. 4. Determination of α_V for the evaporation of liquid PbO from $PZ_{0.5}T_{0.5}$ in an atmosphere of PbO activity fixed by a PT + P packing powder. (XBL 746-6623)

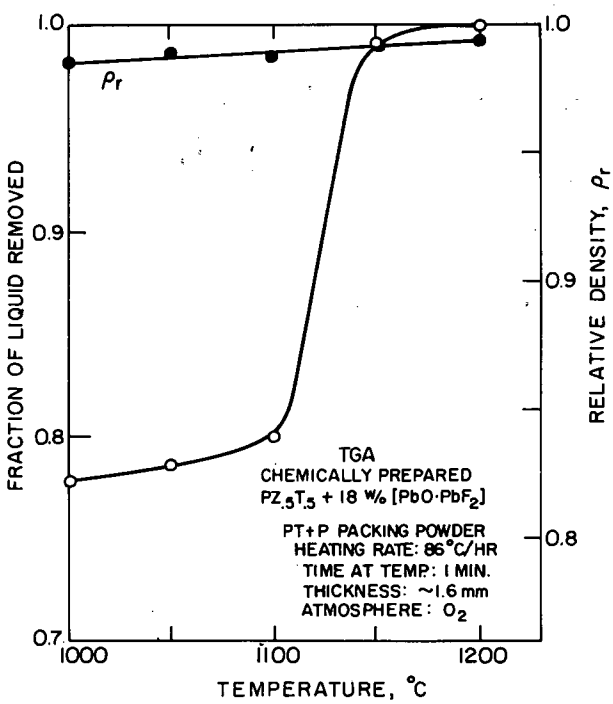

Fig. 5. Fraction of liquid removed and resultant density as a function of temperature. (XBL 746-6626)

above 1100°C. The relative density continuously increases with temperature showing that by heating up to a temperature of 1200°C, the relative density of the chemically prepared specimen can reach a value of 99.5%. This represents the highest density for an unmodified PZT material that has been reported.

*Abstracted from J.W. Sherohman, A Liquid Phase Densification Technique for the Lead Zirconate Titanate System (Ph.D. thesis), LBL-2767, Oct. 1974.

†Present address: Lawrence Livermore Laboratory, University of California, Livermore, Calif. 94550

1. D.A. Northrop, J. Am. Ceram. Soc., I 50 (9) 441 (1967); II 51(7) 357 (1968).

6. RESEARCH PLANS FOR CALENDAR YEAR 1975

Richard M. Fulrath

The increased demands placed on ceramic materials for use in energy systems has reinforced the need for better processing methods to provide controlled properties. The sintering process for powder compacts, one part of the processing scheme, is still relatively little understood. During 1974 the studies on sintering Al_2O_3 concentrated on one very sinterable powder. This work will be expanded to study less expensive alumina powders. The work on sintering UO_2 initiated in 1974 will be continued.

The activity in electronic ceramics is being expanded to include electrical conduction in multi-phase ceramic-metal systems and the reaction kinetics in forming perovskite structures (ABO_3 compounds) from single oxides of the AO and BO_2 type. A project on the mechanical properties of piezoelectric ceramics has been initiated to attempt to determine the affect of pore size on strength. This work will use previous theories developed in this laboratory for the effect of pore volume and size on the strength of brittle materials. The investigation of controlled extrinsic defect structure and its relation to the ferroelectric, piezoelectric and conduction properties of Pb(Zr, Ti) O_3 will be continued.

7. 1974 PUBLICATIONS AND REPORTS

Richard M. Fulrath and Associates

Journals

1. G. Bandyopadhyay and R. M. Fulrath, Processing Parameters and Properties of Lithium Ferrite Spinel, J. Am. Ceram. Soc. 57, 182 (1974) (LBL-1875).

2. G. Bandyopadhyay, A. M. Lacy and R. M. Fulrath, Densification and Grain Growth in Doped $LiFe_5O_8$ Spinel, J. Am. Ceram. Soc. 57, 460 (1974) (LBL-2245).

3. G. Bandyopadhyay and R. M. Fulrath, Thermogravimetry of Lithium Spinel Ferrites, J. Am. Ceram. Soc. 57, 483 (1974) (LBL-2204).

LBL reports

1. R. M. Fulrath, L. Froschauer and D. N. K. Wang, Hot Stage Scanning Electron Microscopy Applied to Sintering Refractory Ceramics, presented at the Royal Microscopical Society on "High Performance Ceramic Materials" held in London, England, July 8-12, 1974 (LBL-2572 Abs., Jan. 1974).

2. Dipak Ranjan Biswas, Uniaxial Bend Strength and Fracture Initiation Energy in Glass-Alumina Composites (M.S. thesis), LBL-2566, April 1974.

3. John William Sherohman, Jr., A Liquid Phase Densification Technique for the Lead Zirconate Titanate System (Ph.D. thesis), LBL-2767, Nov. 1974.

4. L. Froschauer and R. M. Fulrath, Direct Observation of Liquid-Phase Sintering in the System Iron-Copper, LBL-2770, June 1974.

5. Leonard Froschauer and R. M. Fulrath, Direct Observation of Liquid-Phase Sintering in the System Tungsten Carbide-Cobalt, LBL-3189, Oct. 1974.

6. R. M. Fulrath, Basic Ceramic Processing Techniques, presented at Japanese Electronic Ceramic Seminar held in Kamakura, Japan, LBL-3100, March 22-23, 1974.

7. R. M. Fulrath, Sintering Mechanisms in PZT, ibid LBL-3101.

8. Kenneth Edward Crabtree, Densification and Electrical Properties of Controlled Stoichiometry PZT (M.S. thesis) LBL-3543, Dec. 1974.

0 0 0 0 4 2 0 7 2 7 0

IV. Solid State Physics

A. THEORETICAL SOLID STATE PHYSICS

Marvin L. Cohen, Principal Investigator

Introduction. Research in our group centered around the electronic structure of solids. The empirical pseudopotential method (EPM) was extended and used to calculate the electronic properties of a variety of materials. Bulk properties; surface states; properties of amorphous materials; chain, layer, ternary and narrow-gap semiconductors; metals; superconductivity; dielectric functions; and lattice vibrations were characteristic subjects of investigation. Many new developments resulted from these investigations. (All work jointly funded with NSF).

1. ELECTRONIC STRUCTURE OF DIAMOND, ZINCBLENDE AND CHALCOPYRITE SEMICONDUCTORS*

Marvin L. Cohen

A nonlocal pseudopotential scheme was used in the EPM to calculate the electronic structure of diamond and zincblende semiconductors to very high precision. Although local pseudopotential calculations are able to accurately reproduce the major optical gaps and cyclotron masses, deviations from the experimental measurements are manifest in photoemission and X-ray charge density results when calculations are extended to lower valence bands. For silicon a nonlocal s-potential corrects the deviations and calculations of optical, photoemission, X-ray, cyclotron resonance, and charge density properties are all consistent with the measurements. The temperature dependence of the forbidden (222) reflection is also calculated and found to be in excellent agreement with experiment.

The calculated pseudocharge density for Si was displayed and compared with recent measurements; this was the first such comparison ever made for a solid (Fig. 1). Pressure coefficients for the Si band gaps were also calculated.

Optical reflectivity, modulated reflectivity and photoemission measurements were analyzed for the series Ge, GaAs and ZnSe using the nonlocal pseudopotential scheme. In this series the properties of the d-nonlocal potential were critical. Structure in the measured spectra which were previously unidentified or misinterpreted were explained in terms of interband transitions at specific points in the Brillouin zone.

The tight-binding method was used to calculate the valence band structures and densities of states for C, Si, Ge, GaAs and ZnSe. Good agreement with other calculations is obtained when all nearest neighbor and one second nearest neighbor interactions are included. The effects of the various interactions on the density of states are determined.

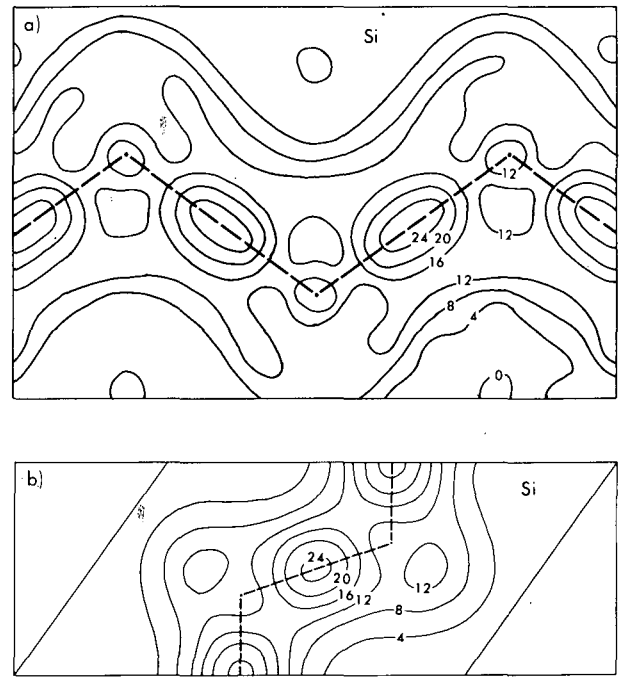

Fig. 1. The top figure (a) shows the valence charge density for silicon as determined by experiment (in the plane of the bonds). The bottom figure (b) shows the valence charge density as calculated by a nonlocal pseudopotential in a section of the same plane. (XBL 751-5507)

Chalcopyrite semiconductors like $ZnGeP_2$ are interesting optically nonlinear materials. These complex ternary compounds can be treated using the EPM scheme. Using $ZnGeP_2$ as a prototype, density of states calculations were analyzed in terms of bonding properties. Spectral peaks were assigned to specific bonds using charge density plots. The density of states spectra were compared with measured XPS spectra. Reflectivity spectra were also computed and detailed comparison was made with experimental measurements.

Many of the charge density calculations used the "special point" scheme developed by our group to significantly reduce the number of Brillouin zone k-states needed to compute the charge density. Analytic expressions for the charge density in group IV materials were derived and used to study the electronic properties of these materials.

---

*Journals 1,3,5,6,7,9,13,14 and reports 4,5,6.

2. CHAIN AND LAYER MATERIALS*

Marvin L. Cohen

The electronic properties of chain (Se and Te), and layer (SnS_2, $SnSe_2$, and $NbSe_2$) materials were investigated. For Se and Te charge density and density of states calculations revealed that two easily resolved peaks in the photoemission spectra are directly related to interchain and intrachain bonding. The EPM band structures and densities of states were in excellent agreement with recent photoemission measurements. Tight binding models were used to obtain analytic expressions for the energy bands and to interpret the EPM band structures in terms of real space orbital-orbital interactions. In studying the bonding structure of these materials, a new method was introduced for determining bonding charges by extracting short-wavelength components of the electronic charge density.

Electronic charge densities of the layer compounds SnS_2 and $SnSe_2$ were computed and compared with hexagonal ZnS. This calculation yielded new information about the bonding nature of these materials. For 2H-$NbSe_2$, the EPM was augmented with a nonlocal d-potential to account for the Nb d-states and a band structure and charge density calculation was performed. The charge density calculations revealed interesting features of the bonding structure of this type of material and various bonding models were investigated.

*Journals 4,8,12,21 and reports 2,7.

3. NARROW GAP IV-VI SEMICONDUCTORS*

Marvin L. Cohen

We have continued our calculations on narrow gap semiconductors. These materials have interesting physical properties and are useful in device applications. Most of our recent work involved a new investigation of the electronic properties of PbSe and PbTe using nonlocal corrections to the EPM. The calculations resulted in extremely accurate band structures which were used to explore a variety of properties of these materials. It was possible using one band structure model to compute electronic features related to effective masses, Knight shift measurements, photoemission measurements and optical properties in an energy range from 0 to 20 eV (e.g. reflectivity, modulated reflectivity, synchrotron radiation studies, etc.). Using the synchrotron radiation studies (18-26 eV) and the EPM calculation, it was possible to determine the angular momentum character of the final conduction band states. Detailed analysis of photoemission and reflectivity studies revealed a 0.8 eV shift between the two experiments for the reflectivity threshold, and electron-hole interactions were suggested as a possible explanation for the shift.

The pressure and temperature coefficients for the states near the fundamental gap in PbSe and PbTe were investigated using both Brook-Yu and Fan formulations of the temperature dependent band theory. Inconsistencies between experiment and theory were attributed to intravalley and intervalley Fan scattering and these were estimated. Charge densities for PbSe and PbTe were also computed and related to bonding properties and the ionicity of these compounds.

*Reports 1,12,13,14,18,19

4. METALS, BONDING AND SUPERCONDUCTIVITY*

Marvin L. Cohen

Charge density calculations, which were used to determine bonding properties in semiconductors and insulators, were extended to analyze metals. In some cases the relation between the building up of bonding charge and superconductivity was investigated.

In addition to the studies of bonding charges and photoemission experiments in chain and chalcopyrite materials (discussed above), bonding effects in general and the correlation between ionicity parameters, and pseudopotentials was explored. In addition by changing crystal structures (zincblende and rocksalt) for a specific choice of pseudopotential, it was possible to explore the dependence of the crystal structure on the form of the pseudopotential.

The electronic charge distributions for the noble metals Cu and Ag were calculated for the first time. These calculations were done for individual bands and the total charge density was computed. The two metals were compared with each other and with experiments via density of states calculations and photoemission measurements.

Our theoretical investigations which suggested that high temperature superconductivity in PbTe was unlikely, appear to be substantiated by new experiments which contradict older, less precise experiments claiming to observe superconductivity in the 22 K range.

The role of phonon softening in superconductivity was investigated. New sum rules and expressions for the electron-phonon interaction parameter were derived. Using these expressions, the observed transition temperatures were related to phonon softening in some materials, and predictions were made about materials not yet found to be superconducting.

Using nonlocal EPM studies of the electronic structure of NbC and NbN (charge density, band structure, density of states and Fermi surface) some speculations were made relating the electronic properties with the superconductivity of these materials. An analysis of $NbSe_2$ was also made in an effort to examine the role of bonding in superconductivity.

Cesium metal is a superconductor under pressure. It is the only monovalent metal which exhibits a

superconducting transition. We have computed the energy bands of Cs under pressure and we find that the d-bands in this material are occupied at high pressures, i.e. when Cs is a superconductor, it is also a transition metal. We have explored the charge density in this material with interesting results. When the metal is at pressures such that it is superconducting, charge builds up along the Cs-Cs direction and forms a bond-like structure. This appears to be consistent with some of our earlier results for NbC and NbN. Superconductivity appears to be related to the covalent-like bonding component of the charge.

*Journals 2,8,10,13,19,25 and reports 1,11,16.

5. ELECTRONIC STRUCTURE OF POLYTYPES AND AMORPHOUS PHASES OF GROUP IV AND III-V MATERIALS*

Marvin L. Cohen

Using tight-binding models and the EPM, the effects of two types of disorder on the density of states of III-V compounds was investigated. The first type involved stoichiometric systems with fourfold coordination (all bonds satisfied). Variations in bond lengths and angles, and only unlike-atom bonds were considered. The second type of disorder includes the properties of the first with the addition of like-atom bonds. GaAs was used as a prototype and the effects of both types of disorder were described. Models of amorphous III-V materials were constructed based on short-range disorder. Features in the density of states were suggested as potential indicators of the existence of III-III and V-V bonds (i.e. "like" bonds).

A new method was introduced to calculate local densities of states of arbitrary tetrahedrally coordinated solids. It involves the selection of a finite cluster of atoms connected to an infinite Bethe lattice of coordination four. The method is accurate, easily handled numerically, and converges fast. Low-order approximations yield sufficient information which is susceptible to consistent physical interpretation. Computations have been made for the diamond, BC-8 and ST-12 structures in terms of the ring topology around a given atom. Comparison with exact calculations is very good and the ring interpretation is physical and conceptually appealing. The method was also applied to heteropolar systems and model structures of amorphous systems.

Photoemission data on amorphous and crystalline Se and Te together with EPM and tight-binding models of the density of states provided new information and insight about the structural properties of the amorphous phase of these materials. The effects of bond angle variations on chains and the presence of eight and six-fold rings of bonds were used to interpret the changes observed in the experimental amorphous spectra. A new model of amorphous Se was proposed.

*Journals 15-18, 20,21 and reports 2,3,7,17,20.

6. SURFACE STATES ON SEMICONDUCTORS*

Marvin L. Cohen

Surface states on diamond and zincblende semiconductors were investigated using tight-binding models. For the (110) surface an unrelaxed model yielded several new surface states near the bottom of the valence bands. The origin, localization and character of the surface states were examined. For the (111) surface, calculations were done for unreconstructed Ge, GaAs and ZnSe. Relaxation effects were considered for Ge. The observed surface states were examined and described in detail.

*Journal 24 and reports 8,9,10.

7. LOCAL FIELDS, DIELECTRIC FUNCTIONS, LATTICE VIBRATIONS*

Marvin L. Cohen

In principle the total dielectric function including local field effects (i.e. Umklapp contributions) can be calculated and used to compute many properties of solids like the phonon spectrum. In practice this is a difficult calculation and the diagonal elements of the dielectric tensor are calculated. For grey tin this latter calculation, together with an approximate method of calculating the inverse of the dielectric function matrix, was used to compute the phonon dispersion curves. Fairly good overall agreement with the experimental dispersion curves was obtained.

A more complete calculation of the dielectric function was performed for silicon. The full matrix for zero wavevector was computed. This frequency dependent function was used to evaluate the effects of local fields on the optical spectrum of silicon. The results were different from previous calculations on diamond which were not as accurate. The dielectric matrix was also used to compute the electron energy loss spectrum and the results were considerably closer to experiment than results which ignore the effects of local fields.

A useful correlation was found between the minimum energy gap, the volume per valence electron and the static dielectric function for $A^N B^{8-N}$ type crystals.

*Journals 11, 23 and report 15.

8. RESEARCH PLANS FOR CALENDAR YEAR 1975

Marvin L. Cohen

We have just developed a method to explore local configurations using the pseudopotential scheme. This should prove to be a significant breakthrough since this allows the use of a highly accurate method for a new class of problems.

We will attempt to treat (self-consistently) molecules, semiconductor and metal surfaces, interfaces, vacancies, impurities, etc. Preliminary calculations have been extremely encouraging. We have calculated surface states on Si and have even included the effects of relaxation and reconstruction. This is the first such calculation and we expect the results to be important to experimentalists and device physicists exploring or using the properties of semiconductor surfaces. If we can extend our method to interfaces, this should prove valuable in device physics.

Although we will concentrate on the development of the above new method, we also plan to explore the electronic properties of semiconductors, attempt to calculate phonon dispersion curves in silicon, compute a full wavevector and frequency dependent local field dielectric function, and explore some new developments in superconductivity theory.

9. 1974 PUBLICATIONS AND REPORTS

Marvin L. Cohen and Associates

Journals

1. J. R. Chelikowsky and M. L. Cohen, High Resolution Band Structure and the E_2 Peak in Ge, Phys. Rev. Lett. 31, 1582 (1973) (not previously listed) (LBL-2267).

*2. D. J. Chadi, M. L. Cohen, and W. D. Grobman, Atomic Pseudopotentials and the Ionicity Parameter of Phillips and Van Vechten, Phys. Rev. B8, 5587 (1973) (not previously listed).

*3. D. J. Chadi and M. L. Cohen, Special Points in the Brillouin Zone, Phys. Rev. B8, 5747 (1973) (not previously listed).

4. C. Y. Fong and M. L. Cohen, Electronic Charge Densities for Two Layer Semiconductors--SnS_2 and $SnSe_2$, J. Phys. Chem. 7, 107 (1974) (LBL-2556).

5. C. Varea de Alvarez and M. L. Cohen, Pressure Coefficients for Band Gaps in Silicon, Solid State Comm. 14, 317 (1974) (LBL-2268).

6. J. R. Chelikowsky and M. L. Cohen, Electronic Structure of GaAs, Phys. Rev. Letters 32, 674 (1974) (LBL-2560).

7. J. R. Chelikowsky and M. L. Cohen, Calculated Valence Band Density of States and Reflectivity for ZnSe, Phys. Letters 47A, 7 (1974) (LBL-2555).

8. C. Y. Fong and M. L. Cohen, Band Structure and Charge Density of 2H-$NbSe_2$, Phys. Rev. Letters 32, 720 (1974) (LBL-2554).

*9. D. J. Chadi and M. L. Cohen, Analytic Expression for the Electronic Charge Density Distribution in Diamond Structure Crystals, Phys. Stat. Sol. (b) 62, 235 (1974).

10. Y. W. Tsang and M. L. Cohen, Pseudopotential Study of Bonding in the Zincblende and Rocksalt Structures, Phys. Rev. B9, 3541 (1974) (LBL-2558).

11. R. P. Gupta, S. K. Sinha, J. P. Walter and M. L. Cohen, Dielectric Function and Phonon Spectrum of Grey Tin, Solid State Comm. 14, 1313 (1974) (LBL-3725).

12. M. Schlüter, J. D. Joannopoulos and M. L. Cohen, New Interpretation of Photoemission Measurements on Trigonal Se and Te, Phys. Rev. Letters 33, 89 (1974); Erratum Phys. Rev. Letters 33, 337 (1974) (LBL-2791).

13. D. J. Chadi and M. L. Cohen, Electronic Band Structures and Charge Densities of NbC and NbN, Phys. Rev. B10, 496 (1974) (LBL-2557).

14. C. Varea de Alvarez, M. L. Cohen, L. Ley, S. P. Kowalczyk, F. R. McFeely, D. A. Shirley and R. W. Grant, Electronic Density of States and Bonding in Chalcopyrite-type Semiconductors, Phys. Rev. B10, 596 (1974) (LBL-2330).

15. J. D. Joannopoulos and M. L. Cohen, Electronic Density of States of Amorphous III-V Semiconductors, Solid State Comm. 15, 105 (1974) (LBL-2266).

*16. F. Yndurain, J. D. Joannopoulos, M. L. Cohen and L. M. Falicov, New Theoretical Method to Study Densities of States of Tetrahedrally Coordinated Solids, Solid State Comm. 15, 617 (1974).

*17. J. D. Joannopoulos and M. L. Cohen, Disorder and the Electronic Density of States of Amorphous Binary Compounds, Tetrahedrally Bonded Amorphous Semiconductors, ed. M. H. Brodsky, S. Kirkpatrick and D. Weaire, (American Institute of Physics, N. Y., 1974) p. 85.

*18. J. D. Joannopoulos, F. Yndurain, L. M. Falicov and M. L. Cohen, Characterization of Amorphous Systems using Local Configurations, ibid., p. 167.

*19. P. B. Allen and M. L. Cohen, Superconductivity and Anomalous Phonon Dispersion in TaC, in Proceedings of the 13th International Conference on Low Temperature Physics, Vol. 3, ed. by K. D. Timmerhaus and W. O'Sullivan (Plenum Press, N. Y., 1974) p. 619.

20. J. D. Joannopoulos and M. L. Cohen, Effects of Disorder on the Electronic Density of States of III-V Compounds, Phys. Rev. B10, 1545 (1974) (LBL-2769).

21. M. Schlüter, J. D. Joannopoulos, M. L. Cohen, L. Ley, S. P. Kowalczyk, R. A. Pollak and D. A. Shirley, The Structural Nature of Amorphous Se and Te, Solid State Comm. 15, 1007 (1974) (LBL-2792).

22. J. R. Chelikowsky and M. L. Cohen, Electronic Charge Densities and the Temperature Dependence of the Forbidden (222) Reflection in Silicon and Germanium, Phys. Rev. Letters 33, 1339 (1974) (LBL-3109).

23. D. J. Chadi and M. L. Cohen, Correlation Between the Static Dielectric Constant and the Minimum Energy Gap, Phys. Letters 49A, 381 (1974) (LBL-3190).

24. J. D. Joannopoulos and M. L. Cohen, New Surface States of an Unrelaxed (110) Surface, Phys. Letters 49A, 391 (1974) (LBL-3129).

25. S. G. Louie and M. L. Cohen, Electronic Structure of Cesium Under Pressure, Phys. Rev. B10, 3237 (1974) (LBL-2793).

26. E. Mooser, I. C. Schlüter and M. Schlüter, The Electronic Charge Densities in Semiconducting Layer and Chain Structures, J. Phys. Chem. Solids 35, 1269 (1974) (LBL-3724).

27. C. Varea de Alvarez, M. L. Cohen, S. E. Kohn, Y. Petroff and Y. R. Shen, Calculated and Measured Reflectivity of $ZnGeP_2$, Phys. Rev. B10, 5175 (1974) (LBL-3110).

28. J. D. Joannopoulos and F. Yndurain, "Cluster-Bethe-Lattice" Method: Electronic Density of States of Amorphous and Crystalline Homopolar Solids, Phys, Rev. B10, 5164 (1974) (LBL-3181).

29. J. R. Chelikowsky and M. L. Cohen, Electronic Structure of Silicon, Phys. Rev. B10, 5095 (1974) (LBL-3127).

30. J. D. Joannopoulos and M. L. Cohen, Intrinsic Surface States of (110) Surfaces of Group IV and III-V Semiconductors, Phys. Rev. B10, 5075 (1974) (LBL-3131).

*Not supported by IMRD funds.

LBL reports

1. M. L. Cohen, Electronic Structure of Narrow Gap Semiconductors, Proceedings of the International Conference on Narrow Gap Semiconductors, Nice, France, 1973 (in press) (LBL-2268).

2. J. D. Joannopoulos and M. Schlüter and M. L. Cohen, Electronic Densities of States of Amorphous and Trigonal Se and Te, Proceedings of the 12th International Conference on the Physics of Semiconductors, Stuttgart, Fed. Rep. Germany July 1974 (in press) LBL-2790).

3. D. J. Chadi and M. L. Cohen, Tight-Binding Calculations of the Valence Bands of Diamond and Zincblende Crystals, Phys. Stat. Solidi (in press) (LBL-3128).

4. J. D. Joannopoulos, M. Schlüter and M. L. Cohen, The Electronic Structure of Trigonal and Amorphous Se and Te, Phys. Rev. (in press) (LBL-3130).

5. D. J. Chadi and M. L. Cohen, Tight-Binding Calculations of (111) Surface Densities of States of Ge and GaAs, Solid State Comm. (in press) (LBL-3132).

6. D. J. Chadi and M. L. Cohen, Intrinsic (111) Surface States of Ge, GaAs and ZnSe, Phys, Rev. (in press) (LBL-3534).

7. C. Y. Fong, J. P. Walter and M. L. Cohen, Comparison of Band Structures and Charge Distributions of Copper and Silver, LBL-3535, Nov.1974.

8. G. Martinez, M. Schlüter, M. L. Cohen, R. Pinchaux, P. Thiry, D. Dagneaux and Y. Petroff, Synchrotron Radiation Measurements and Calculation of Core- to Conduction-Level Transitions in Lead Chalcogenides, LBL-3538, Nov. 1974.

9. G. Martinez, M. Schlüter and M. L. Cohen, The Electronic Structure of PbSe and PbTe, I. Band Structure, Densities of States and Effective Masses, Phys. Rev. (in press) (LBL-3536).

10. G. Martinez, M. Schlüter and M. L. Cohen, The Electronic Structure of PbSe and PbTe, II. Optical Properties, Phys. Rev. (in press) (LBL-3537).

11. S. G. Louie, J. R. Chelikowsky and M. L. Cohen, Local Field Effects in the Optical Spectrum of Silicon, Phys. Rev. Letters (in press) (LBL-3539).

12. C. Y. Fong, D. J. Chadi and M. L. Cohen, An Alternate Form of the Non-Local p-Potential in the Empirical Pseudopotential Method, LBL-3540, Nov. 1974.

13. F. Yndurain and J. D. Joannopoulos, The "Cluster-Bethe-Lattice" Method: The Electronic Density of States of Heteropolar Systems, LBL-3567, Oct. 1974.

14. M. Schlüter, G. Martinez and M. L. Cohen, Pressure- and Temperature Dependence of Electronic Energy Levels in PbSe and PbTe, LBL-3568, Oct. 1974.

15. M. Schlüter, G. Martinez and M. L. Cohen, Electronic Charge Densities in PbSe and PbTe, LBL-3569, Dec. 1974.

16. J. D. Joannopoulos and F. Yndurain, Moments and Averages of the Electronic Density of States of Amorphous and Crystalline Homopolar Solids, Phys. Letters (in press) (LBL-3570).

17. J. D. Joannopoulos, Electronic Structure of Complex Crystalline and Amorphous Semiconductors, (Ph.D. thesis) LBL-2724, May 1974.

18. D. J. Chadi, Pseudopotential and Tight-Binding Calculations of the Bulk and Surface Electronic Structure of Solids, (Ph.D. thesis) LBL-3138, Aug. 1974.

B. FAR INFRARED PROPERTIES OF SOLIDS

Paul L. Richards, Principal Investigator

1. A BALLOON-BASED MEASUREMENT OF THE COSMIC BACKGROUND RADIATION

David P. Woody, John C. Mather, Norman S. Nishioka and Paul L. Richards

Big bang cosmology theory, and measurements in the microwave and optical region, support the idea that the universe is filled with isotropic blackbody radiation with a characteristic temperature of ~3°K. The emission from the atmosphere limits direct ground-based measurements of this cosmic background radiation to frequencies below the peak in the 3°K blackbody spectrum, which occurs at 5.9 cm^{-1}. The first accurate direct measurement of the cosmic background radiation in the 3 to 30 cm^{-1} region has been made using a balloon-base liquid-helium-cooled spectrometer.

The instrument features a cooled conical antenna, a polarizing interferometer for Fourier transform spectroscopy, and a germanium bolometer detector. The development and characterization of the instrument are described in the 1973 IMRD Annual report.

The apparatus was flown successfully from Palestine, Texas on July 24, 1974. The flight was terminated near Pecos, Texas after measuring the sky emission for 6 h at an altitude of 39 km. The gondola and payload were recovered in good condition. During the flight the apparatus performed very well and excellent sky emission spectra were obtained.

Both the detector noise and responsibity were the same as measured in the laboratory before the flight. Another noteworthy success was the operation of the instrument without any warm window in the optical path. After reaching a float altitude of 39 km the protective window over the antenna was removed and the helium boil-off gas was vented through the antenna. Pictures taken during the flight verified that the flow of vented gas was sufficient to prevent condensation of solid air into the cooled optics.

Samples of the sky emission spectra obtained during the flight are shown in Fig. 1(a). Since the expected cosmic background signal is a small part of the sky emission at frequencies above 15 cm^{-1}, the major burden on the data analysis is to determine these contributions to the observed spectrum. The dominant signal is the emission from H_2O, O_3 and O_2 in the atmosphere. A model of the atmospheric emission has been constructed from tabulated molecular line strengths and fitted to the observed spectra with only three free parameters. The calculated atmospheric

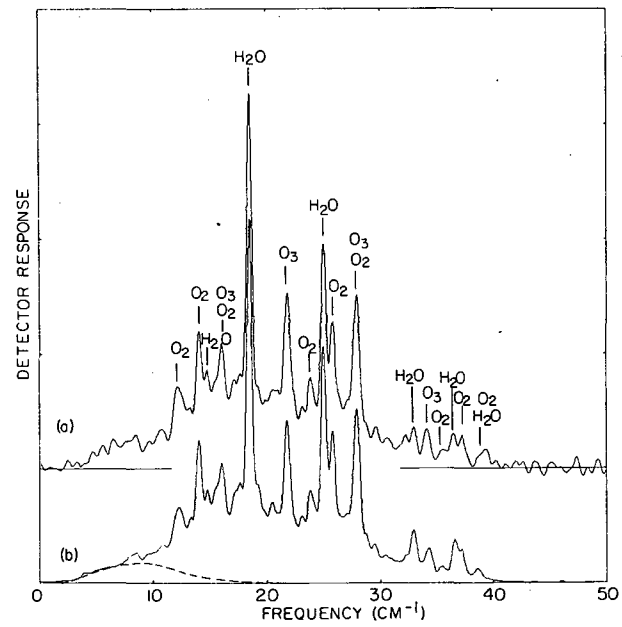

Fig. 1. (a) High resolution sky spectrum. (b) Theoretical atmospheric emission spectrum and 2.97°K blackbody curve. (XBL 7412-7744)

emission plus that of a 3°K blackbody is shown in Fig. 1(b).

Other sources of extraneous radiation are the emission from the instrument itself and radiation from the earth diffracted or scattered into the spectrometer. During the flight the temperature of the radiation collecting antenna was changed from ≈4°K to ≈10°K. This gave a measure of the instrumental emission. In addition, measurements were made at two different zenith angles (24° and 45° from vertical). These measurements combined with the atmospheric model determine the contribution of earthshine to the observed signal. The antenna emission contribution was shown to be negligible and a small correction for the diffraction was computed.

The final data analysis was accomplished by fitting the atmospheric model with adjustable amounts of the three gases, a diffraction correction, and a blackbody curve with adjustable temperature to our most precise low-resolution spectra. The rms residual was minimized by a blackbody temperature of 2.97°K. Our measurement of the cosmic background radiation is thus the sum of the residual plus the 2.97°K blackbody curve. These results are shown in Fig. 2.

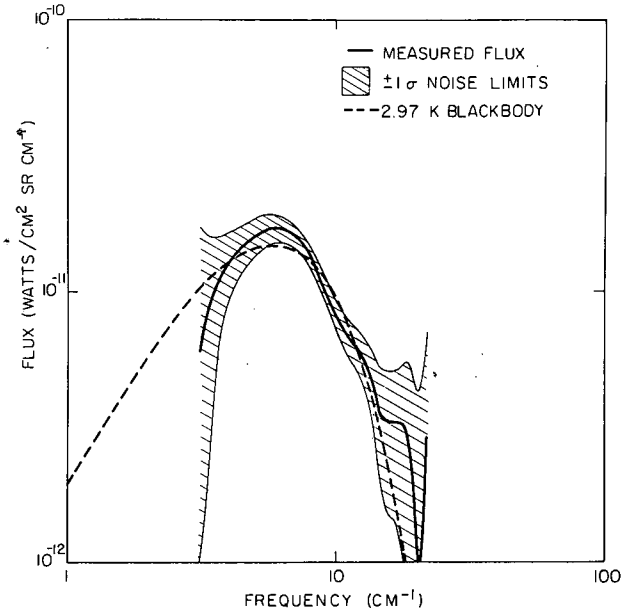

Fig. 2. Measured cosmic background radiation (solid line) compared with a 2.97°K blackbody curve. The limits of probable error are given by dashed lines at ±σ. (XBL 7412-7745)

2. FAR INFRARED EPR OF $Al_2O_3:Mn^{3+}$

Richard L. Aurbach and Paul L. Richards

Fourier transform spectroscopy has been used to study the spectrum of Mn^{3+} ions in Al_2O_3 in the frequency range from 4 to 30 cm^{-1} in applied magnetic fields up to 55 kG. Spectra were measured for applied fields oriented both parallel and perpendicular to the crystallographic $\underset{\sim}{c}$ axis and for incident radiation polarized both parallel and perpendicular to $\underset{\sim}{c}$. The observed absorption lines were identified as being due to electric dipole transitions. Ground state transitions were identified by varying the sample temperature from 1.4 to 20°K. Detailed analysis of the temperature-dependence data permitted verification of a level diagram for the low lying states. The ground state transition intensities depend on the applied magnetic field. Several of the transitions have zero intensity in zero-applied field. The observed ground and excited state transitions are shown in Figs. 1a and 1b respectively.

A simple model was developed which explains many of the features observed. It is based on a purely electronic Hamiltonian and includes crystal field, spin-orbit, spin-spin and Zeeman interactions. The solid lines in Figs. 1a and 1b are results from this model. The model gives good quantitative agreement with experiment for the observed ground state transitions but fails to properly account for the excited state transitions. The strengths and weaknesses of this model give interesting clues as to the role played by the Jahn-Teller interaction, which is known to be present in this ion.

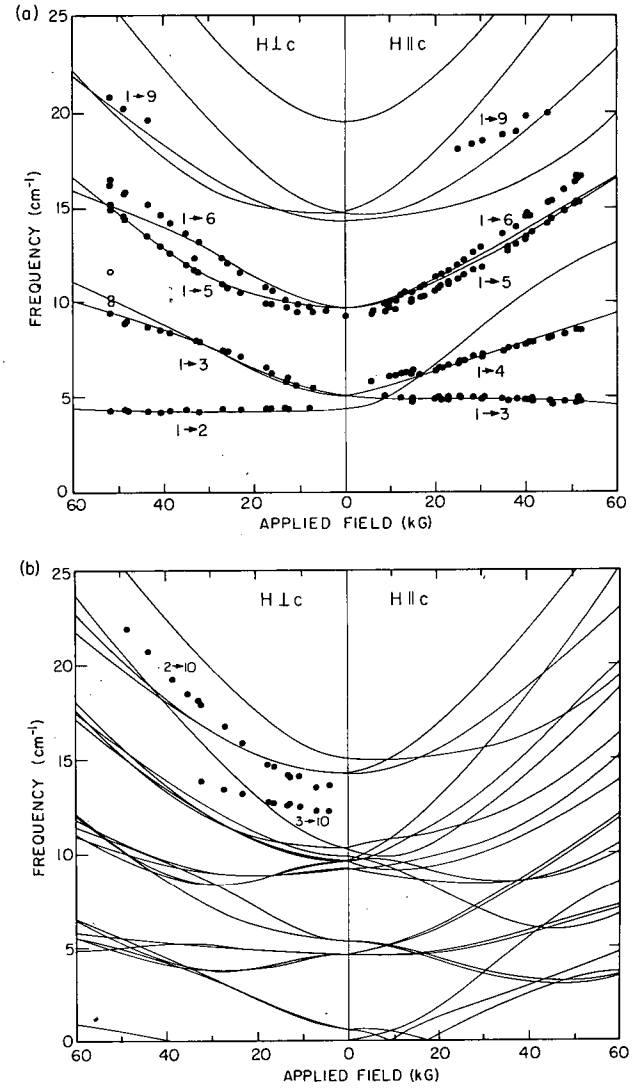

Fig. 1. Positions of observed absorption lines as a function of applied field (points), compared to transitions (lines) predicted from a simple electronic Hamiltonian for ground state transitions (a) and excited state transitions (b). (XBL 751-5438)

3. SURFACE MAGNETIC RESONANCE IN MnF_2

Robert B. Bailey and Paul L. Richards

Far-infrared transmission spectra of MnF_2 powders show a series of weak absorption lines whose behavior suggests the presence of surface magnetic effects. We are continuing to investigate these absorptions using a variety of spectroscopic techniques. If they prove to be surface spin wave resonance this will be the first experimental observation of such an effect in any material.

Manganese fluoride is a widely studied example of a simple, uniaxial antiferromagnet. Its antiferromagnetic resonance (AFMR) at 8.7 cm^{-1} has been observed in both optical and microwave

resonance spectra. Our data, obtained using fourier transform spectroscopy techniques, show additional lines between 7.4 cm^{-1} and 8.3 cm^{-1}. These lines increase in intensity as the particle size in the powders is reduced, and they are not present in single crystals from which the powders were prepared. Figure 1 shows the spectrum of our finest powder sample with an average particle dimension of one micron. Neither impurities, grinding strains, nor conventional magnetostatic effects can account for the detailed behavior of these extra absorptions.

Surface spin wave modes have been predicted below the AFMR frequency. A sharp resonance should be associated with each different crystallographic plane. Such modes could account for the magnetic field splittings of the strongest extra mode at 8.3 cm^{-1}. However, the measured dependence on surface area of the 8.3 cm^{-1} mode intensity is not as rapid as that expected for a simple surface effect. Our spectra were not sensitive enough to study the magnetic splittings or surface area dependence of the weaker lines appearing below 8.3 cm^{-1} in Fig. 1. Their intensities do fall within the range predicted for surface magnon modes.

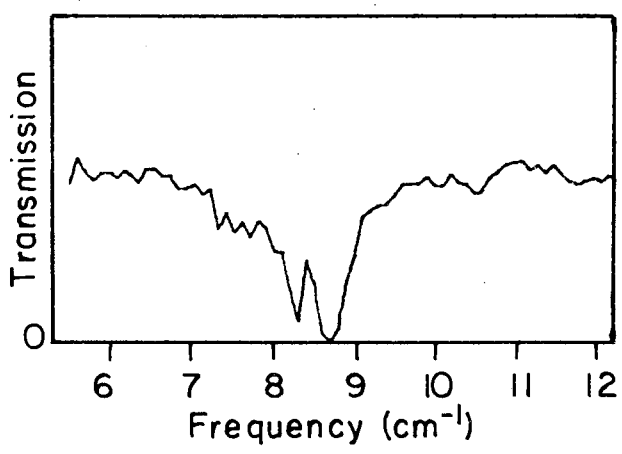

Fig. 1. Transmission spectrum of a 293 mg MnF_2 powder sample. (XBL 7411-8602)

Surface absorptions seen in powder samples with very large effective areas should also be present in the spectra of single crystals if the correct surface is present in the sample and if sufficient sensitivity is available. To search for extra absorptions in single crystals, a series of field swept transmission measurements were made using a 5 cm^{-1} microwave source. This technique improved upon our infrared data but not enough to detect surface modes. For powder samples the microwave apparatus matched the sensitivity of our optical measurements yet failed to detect even the strong 8.3 cm^{-1} absorption. This provides evidence that the linear splitting observed at low magnetic fields in the infrared spectra does not persist to the 50 kG field values used to observe the microwave resonance.

Further improvement in both single crystal and powder spectra is being sought using conventional electron spin resonance techniques at X-band microwave frequencies. A spectrometer which is under construction employs a 100 kG superconducting solenoid and should be sensitive enough to detect surface modes in small single crystal samples.

4. HIGH RESOLUTION FOURIER TRANSFORM SPECTROSCOPY OF IMPURITIES AND DEFECTS IN HIGH-PURITY GERMANIUM

Eugene E. Haller, William L. Hansen, Fred S. Goulding and Paul L. Richards

The investigation of high-purity germanium ($|N_A-N_D| \leq 10^{10}$ cm^{-3}) with far-infrared photothermal ionization spectroscopy yields a large amount of information. In such high-purity material line broadening due to the overlapping of bound excited states of shallow, hydrogenic impurities is negligible. Making full use of the high resolution provided by Fourier Transform Spectroscopy it is possible to identify unambiguously all known shallow, hydrogenic acceptors and donors down to concentrations of less than 10^6 cm^{-3} (1 part in 10^{16}!). This was demonstrated with germanium produced at LBL. The dominant residual impurities listed in order of their importance are aluminum (Al), phosphorous (P) and boron (B). The ratios of the strength of corresponding lines in the impurity spectra is equal to the ratio of their concentrations. This allows the study of the segregation of impurities along the crystal growth axis. It was found that aluminum segregates much more slowly than expected if the crystals are grown from quartz crucibles. Several independent experiments revealed that an aluminum-oxygen complex in the germanium is the cause for the unusual behavior.

Illumination of the Ge-sample with band-edge light ($h\nu \geq E_{gap}$) makes it possible to observe acceptors and donors simultaneously as can be seen in Fig. 1

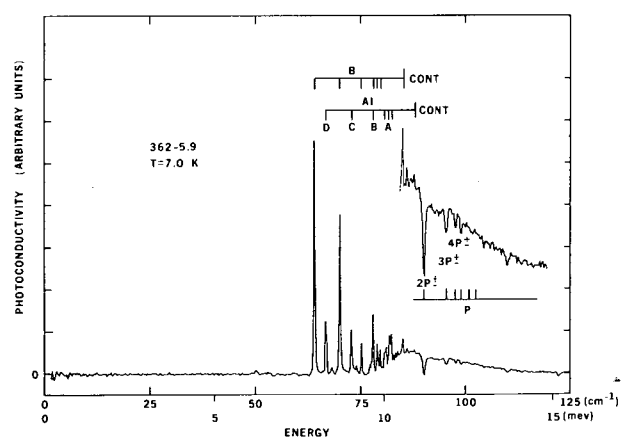

Fig. 1. Spectrum obtained with sample 362-5.9 containing the acceptors boron (B) and aluminum (Al). Band-edge light ($h\nu > E_{gap}$) makes the detection of the minority impurity phosphorous (P) possible. Sample volume ≈ 0.4 cm^3; temperature T = 7.0°K. The region above 85 cm^{-1} is magnified by a factor of four. (XBL 7411-8633)

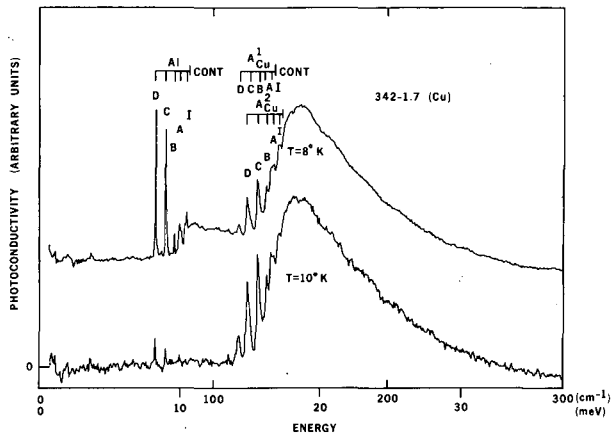

Fig. 2. Spectrum of sample 342-1.7. Copper was plated and then diffused for 24 hrs at 450°C under argon. The two acceptors A_{Cu} and A^2_{Cu} are due to complexes containing copper. The upper spectrum recorded at T = 8°K shows also the lines of aluminum. At 10°K most of the Al acceptors are ionized as can be seen in the lower spectrum. Sample volume 0.15 cm^3, N_A-N_D ≃ 2×10^{12} cm^{-3}. (XBL 7411-8632)

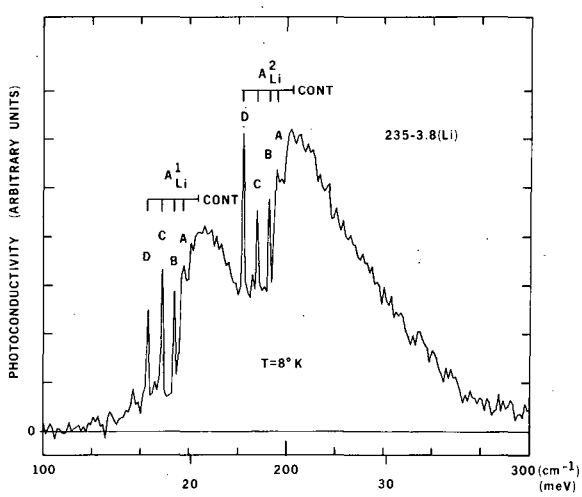

Fig. 3. Spectrum of sample 235-3.8 recorded at 8°K. A limited amount of lithium was diffused at 400°C for 4 hrs under argon. The two acceptors spectra A^1_{Li} and A^2_{Li} are due to complexes containing lithium. Sample volume: 0.14 cm^3; N_A-N_D ~ 10^{10} cm^{-3}. (XBL 7411-8631)

Besides the known group III acceptors and group I and V donors several series of lines of unknown origin were found. The concentrations of one of the unknown donors is extremely sensitive to heat treatment of the sample. It is believed that many of the unknown acceptors and donor spectra are due to complexes between impurities and/or between impurities and lattice defects. We purposely created such complexes by diffusing copper or lithium into high-purity samples. In the first case, two closely spaced acceptor series appeared as can be seen in Fig. 2. The ground states are located at 17.1 and 17.5 MeV above the valence band. In the case of lithium (Fig. 3) we found again two acceptors with ground states at 20.2 and 25.0 MeV above the valence band. Further investigations are necessary before a detailed description of the involved complexes can be given.

5. INSTRUMENTATION FOR INFRARED SPECTROSCOPY

Richard L. Aurbach, Robert B. Bailey, Stephen E. McBride and Paul L. Richards

In order to provide for expansion and improvement of the IMRD Fourier spectroscopy facility, a new data acquisition system has been designed and constructed. The analog section is capable of handling up to eight single-ended or four differential inputs and performs 15-bit analog-to-digital conversions at a maximum throughput of 65 kHz. A stepping motor controller, display, and real-time clock are included in the system. A PDP-11 computer interface has been designed and constructed which permits the computer to perform and control a wide variety of sophisticated measurements. Software has been developed to implement the data acquisition requirements of the Fourier spectroscopy.

The success of the cosmic background experiment described above has demonstrated that the polarization interferometer is the best instrument for Fourier spectroscopy in the frequency range from 1-100 cm^{-1}. Construction has started on a polarization interferometer intended for general laboratory use over this frequency range with a resolution of 0.03 cm^{-1}. No instrument of this type is commercially available.

The IMRD Fourier spectroscopy facility has been limited to far-infrared frequencies because of the lack of an interferometer with adequate accuracy for operation in the near infrared. Such near-infrared interferometers are available commercially, but adequate capital equipment money has not been available to purchase one. A high resolution (0.03 cm^{-1}) rapid scan interferometer is under construction for the chemical infrared-frequency range (700-3000 cm^{-1}). When completed, this instrument will have performance specifications which improve on those of the Fourier spectrometer sold by the Digitlab Corporation for $90,000. This instrument is expected to be useful for a wide variety of problems including low temperature solid state physics, catalysis and high-temperature chemistry.

During the last few years, a large number of far-infrared laser transitions have been observed in gases pumped with CO_2 lasers. An optically pumped molecular laser has been constructed and a CO_2 laser purchased to provide fixed frequency sources for spectroscopy in the far infrared.

6. INFRARED BOLOMETER DETECTORS

John Clarke, Gary I. Hoffer, Norman S. Nishioka, Paul L. Richards and Nan-Hsiung Yeh

The far-infrared bolometer detectors in use in our laboratory are 1-2 orders of magnitude less sensitive than the theoretical limits. The situation is even worse in most other far-infrared laboratories. A program to improve these detectors is being carried out in collaboration with the Clarke group.

The conventional semiconducting bolometers suffer from the problems of low absorptivity and excess noise. We have demonstrated that a film of bismuth with a resistance of 100 Ω/□ on a thin Al_2O_3 substrate provides broad band far-infrared absorption close to the theoretical value of 0.75 in a structure with very low heat capacity at low temperatures. A variety of superconducting evaporated film thermometers has been explored to provide the temperature sensing without excess noise. These include superconductor-normal-superconductor (SNS) Josephson junctions, arrays of proximity effect Josephson junctions, and films operated at the superconducting transition.

A theoretical computer optimization of bolometer parameters has been carried out by Monte-Carlo methods. The properties of actual superconducting thermometers and a full noise theory are included in the calculations. The results show a complicated dependence of the optimum bolometer type on the amount of background infrared radiation present in the experiment.

Experimental results for the SNS bolometer include a specific detectivity $D^* \approx 10^{14}$ cm$\sqrt{\text{Hz}}$/W. This is the best ever reported for a far-infrared bolometer and is very close to theoretical limits for bolometer performance. The SNS bolometer is rather inconvenient to use because it requires a superconducting quantum interference device (SQUID) amplifier. Experimental development is in progress on other superconducting bolometers which are expected to combine high sensitivity with simplicity of construction and operation.

This program represents a very fruitful application of the fundamental noise studies of the Clarke group to the practical problem of improving infrared detectors.

7. INFRARED SKY SURVEY

Stephen E. McBride, Norman S. Nishioka and Paul L. Richards

In order for the improvements in bolometer detectors to be accepted by the infrared community it will be necessary to demonstrate their usefulness under actual experimental conditions. This can best be done by carrying out an experiment of high scientific visibility which could not be done with the old technology.

There exists no survey of the sky for sources of astronomical interest at any far-infrared frequency. The reason for this lack is the poor performance of far infrared bolometer detectors. The new detectors under construction permit such a survey to be made at low cost with sensitivity comparable to that achieved in existing near infrared surveys.

Plans are well advanced for the construction of any array of superconducting bolometer detectors to be used with a low background infrared balloon telescope. The computed performance of the system suggests that three balloon flights would be required for a survey for all of the northern hemisphere in five frequency bands from 10-1000 cm^{-1} with a flux sensitivity of 2-30 flux units (1 fu = 10^{-26} $Wm^{-2}Hz^{-1}$), at an angular resolution of 10 arc min.

This project is planned with the collaboration of the Berkeley Space Sciences Laboratory.

8. FAR INFRARED SPECTROSCOPY OF EXCITON DROPLETS

Laurence Eaves, Carson D. Jeffreys and Paul L. Richards

New developments in far infrared sensitivity make possible a variety of experiments on excitons in semiconductors. Among the most interesting of these is the search for geometrical resonances in exciton droplets in Ge. Other experiments include studies of the plasma effects in exciton droplets and the low lying excitation states of free excitons.

The group in the Berkeley Physics Department headed by Professor C. D. Jeffreys has succeeded in making the largest exciton droplets yet observed in Ge. An optical dewar has been constructed with provisions for laser pumping to create excitons as well as ports for far infrared transmission measurements and for monitoring the near infrared fluorescence from exciton decay.

A program of measurements of the far-infrared properties of excitons in Ge is planned in collaboration with the Jeffreys group.

9. MILLIMETERS WAVE COHERENT DETECTORS

John C. Claassen, Paul L. Richards and Yuan Taur

Development of low noise millimeter microwave receivers for coherent radiation is being carried out under the sponsorship of the Office of Naval Research. This program is mentioned here only to provide a complete picture of the research activities of P. L. Richards. Under this program, the usefulness of superconducting Josephson effect point contact junctions for low noise millimeter wave devices is being explored. Results of the program to date include construction of the lowest noise millimeter wave heterodyne mixer yet achieved (T_m = 54°K at 36 GHz). Both the noise and the conversion efficiency of this device have

been shown to be in agreement with theory. Present experimental projects include the construction of a Josephson effect heterodyne mixer at 140 GHz and a parametric amplifier at 36 GHz.

10. RESEARCH PLANS FOR CALENDAR YEAR 1975

Paul L. Richards

It is anticipated that the cosmic background experiments will yield valuable information about the spectra of gases in the stratosphere, including trace pollutants. It is hoped that the study of magnetic surface modes will have progressed to the point of providing an important new tool for the study of surfaces. It is probable that the program of development of superconducting infrared bolometers will have developed to the point that an order of magnitude increase in far infrared sensitivity will be available in the laboratory. The detectors will also have valuable applications to infrared astrophysics. The new program on the far infrared properties of semiconductors should develop into a major study of the properties of excitons.

The continuation of the cosmic background experiments will require the support of one postdoctoral fellow. It will also require about $25,000 to pay for two balloon flights per year.

The establishment of new programs will depend on the availability of funds. Projects under consideration are: (1) The fabrication of far infrared heterodyne mixer receivers for diagnostic work on Tokomac plasmas, and (2) near infrared Fourier emission arc spectroscopy to test theories of high temperature chemistry.

11. 1974 PUBLICATIONS AND REPORTS

Paul L. Richards and Associates

Journals and Conference Proceedings

1. J. Clarke, G. I. Hoffer and P. L. Richards, Superconducting Tunnel Junction Bolometers, Rev. Phys. Appliquee 9, 69 (1974) (LBL-2222).

2. E. E. Haller and W. L. Hansen, High Resolution Fourier Transform Spectroscopy of Shallow Acceptors in Ultrapure Germanium, Solid State Comm. 15, 687 (1974) (LBL-2487).

3. E. E. Haller and W. L. Hansen, Impurities in High-Purity Germanium as Determined by Fourier Transform Spectroscopy, IEEE Trans. Nucl. Sci. 21, 279 (1974) (LBL-2436).

*4. Y. Taur, J. H. Claassen and P. L. Richards, Conversion Gain and Noise in a Josephson Mixer, Rev. Phys. Appliquee 9, 263 (1974).

*5. Y. Taur, J. H. Claassen and P. L. Richards, Appl. Phys. Letters 24, 101 (1974).

6. Y. Taur, P. L. Richards and F. Auracher, Application of the Shunted Junction Model to Point-Contact Josephson Junctions, Low Temperature Physics-LT 13, Vol. 3, edited by K. D. Timmerhaus, W. J. O'Sullivan and E. F. Hammel (Plenum Press, 1974) p. 276 (LBL-1136).

7. John C. Mather, Paul L. Richards and David P. Woody, Balloon-Based Measurements of the Cosmic Background Radiation, IEEE Trans. on Microwave Theory and Techniques, MTT-22, 1046 (1974) (LBL-2726).

LBL and other reports

1. P. W. Anderson and P. L. Richards, Comment on Search for the AC Josephson Effect in Liquid He, LBL-2569, Jan. 1974.

2. R. L. Aurbach and P. L. Richards, Dynamic Jahn-Teller Quenching of the ^5E State in $Mn^{3+}:Al_2O_3$, LBL-3146 Abs., Aug. 1974.

3. R. B. Bailey, P. L. Richards and W. E. Tennant, New Resonance Effects in Antiferromagnetic MnF_2, LBL-3152 Abs. and LBL-2566, Aug. 1974 (paper presented at the 20th Annual Conference on Magnetism and Magnetic Materials, San Francisco, Dec. 3-6, 1974.

4. John Cromwell Mather, Far Infrared Spectrometry of the Cosmic Background Radiation, LBL-2258, (Ph. D. thesis) Jan. 1974.

†5. Yuan Taur, Josephson Junctions as Microwave Heterodyne Detectors, (Ph. D. thesis) LBL-2597, April 1974.

‡6. P. L. Richards, Improvement of Diamond Machining Techniques, 1974 Materials Research Council Report.

7. D. P. Woody, J. C. Mather, N. Nishioka and P. L. Richards, A Balloon-Based Measurement of the Cosmic Background Radiation, LBL-3519 Abs., Nov. 1974.

*8. Y. Taur, J. H. Claassen and P. L. Richards, Josephson Junctions as Heterodyne Detectors, June 1974 (to be published in IEEE Trans. Microwave Theory and Techniques).

*9. J. H. Claassen, Y. Taur and P. L. Richards, Noise in Josephson Effect mm-Wave Mixers, Oct. 1974 (to be published in Proceedings of the 1972 Applied Superconductivity Conference, Oakbrook, Illinois).

*10. J. H. Claassen, Y. Taur and P. L. Richards, Noise in Josephson Point Contacts with and without RF Bias, Aug. 1974 (to be published in Appl. Phys. Letters).

*11. Y. Taur and P. L. Richards, Relaxation Oscillations in Point Contact Josephson Junctions, Sept. 1974.

12. E. E. Haller, W. L. Hansen and F. S. Goulding, Photothermal Ionization Spectroscopy, LBL-3629, December 1974 (to be published in IEEE Trans. Nucl. Sci. 22).

13. W. E. Tennant, R. B. Bailey and P. L. Richards, New Resonance Effects in Antiferromagnetic MnF_2, LBL-3566, Dec. 1974 (to be published in the Proceedings of the 20th Annual Conference on Magnetism and Magnetic Materials, San Francisco, Dec. 3-6, 1974).

*14. P. L. Richards, The Josephson Junction as a Detector of Microwave and Far Infrared Radiation, Dec. 1974 (to be published in Semiconductors and Semimetals, Vol. 11 - Infrared Detectors (II), Willardson and Beer, eds.)

15. D. P. Woody, J. C. Mather, N. Nishioka and P. L. Richards, A Comment on "Spectrum of the Cosmic Background Radiation between 3 mm and 800 μm", LBL-3572, Dec. 1974.

---

*Sponsored by the Office of Naval Research (ONR).

†Partly sponsored by the ONR.

‡Sponsored by the Advanced Research Projects Agency (ARPA).

C. SUPERCONDUCTIVITY

John Clarke, Principal Investigator

1. A LOW NOISE RELIABLE SQUID MADE FROM JOSEPHSON TUNNEL JUNCTIONS

John Clarke, Wolfgang M. Goubau and Mark B. Ketchen

Superconducting quantum interference devices (SQUIDs) have proven valuable in the physics laboratory for detecting extremely small changes in magnetic fields. Recently, interest in using SQUIDs has spread to geophysical and medical research. For field use, SQUIDs must have low noise and good stability over periods of hours. In addition the electronics used with the SQUID must be reliable and easy to operate. At present all commercially available SQUIDs are rf biased weak link Josephson devices requiring high-frequency electronics that are often difficult to tune. The output of the rf SQUIDs tends to drift with time, and occasionally has abrupt jumps. These features limit the usefulness of rf SQUIDs for long term measurements.

We have developed reliable thin film dc SQUIDs using two shunted Nb-NbO_x-Pb tunnel junctions (Fig. 1). These SQUIDs have excellent magnetic field resolution and long term stability. They can be used at any temperature below 7 K. The SQUIDs operate at the Josephson frequency (typically 250 MHz) determined by a dc bias voltage across the tunnel junctions and therefore require no external high-frequency (rf) signal generators.

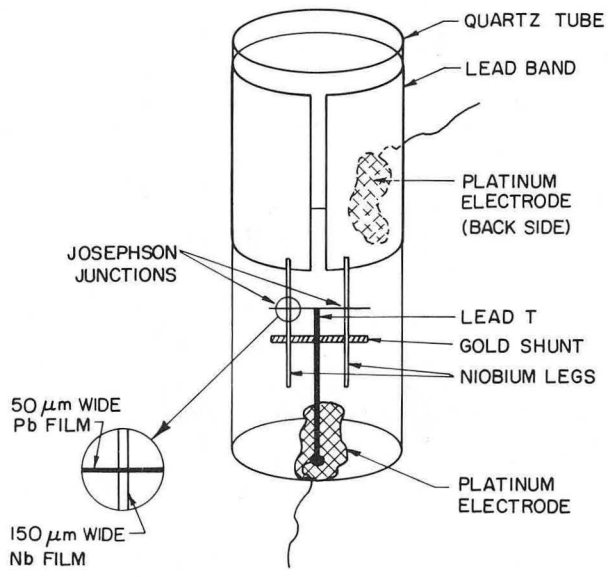

Fig. 1. Schematic of a Nb-NbO_x-Pb tunnel junction SQUID. The substrate for the metal films is a 3 mm o.d. quartz tube. All films with the exception of the Nb are deposited by evaporation. The Nb is dc sputtered. The tunneling barrier for the junctions is produced by thermally oxidizing the Nb. (XBL 749-7211)

We detect time varying magnetic fields using the standard technique of modulating them with an audio-frequency field, amplifying the resulting SQUID signal, and then demodulating the amplified signal at the audio frequency. However, we have improved the electronics design to the point where magnetic field resolution becomes limited by 4 K Johnson noise in the SQUID itself. The major improvement is the use of a resonant tank circuit operating at 4 K to amplify the SQUID signal and to optimally match the output impedance of the SQUID to a low noise amplifier at room temperature. We have achieved a magnetic field resolution as high as 10^{-10} gauss at frequencies above 1 Hz. This resolution is an order of magnitude better than that claimed for commercially available rf SQUIDs.

We have investigated the problems of low-frequency noise and drift common to all SQUIDs. We found that changes in the temperature of the He^4 bath in which the SQUIDs are immersed are the major cause of these problems. Variations in bath temperature result from fluctuations in atmospheric pressure, and from the decrease in hydrostatic pressure with the decrease in the level of the liquid He^4. We have constructed a simple temperature stabilizer which operates by controlling the rate of He^4 gas blowoff from the cryostat and have reduced the drift over a period of three hours to less than 2×10^{-10} gauss/h. The SQUID signal as a function of time is shown in Fig. 2.

We have built a single axis magnetometer using one of our SQUIDs and have successfully tested it

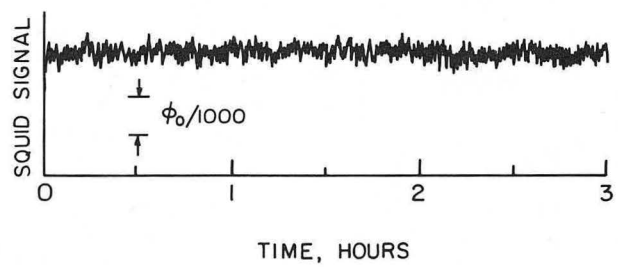

Fig. 2. SQUID signal as a function of time. There is no measurable drift over the three hour period. An upper limit for drift is set by the width of the trace which sets the drift at less than 2×10^{-10} gauss/h. (XBL 749-7239A)

in the Nevada desert. Figure 3 shows the field version of our system. We are currently constructing gradiometers and a three-axis magnetometer using tunnel junction SQUIDs.

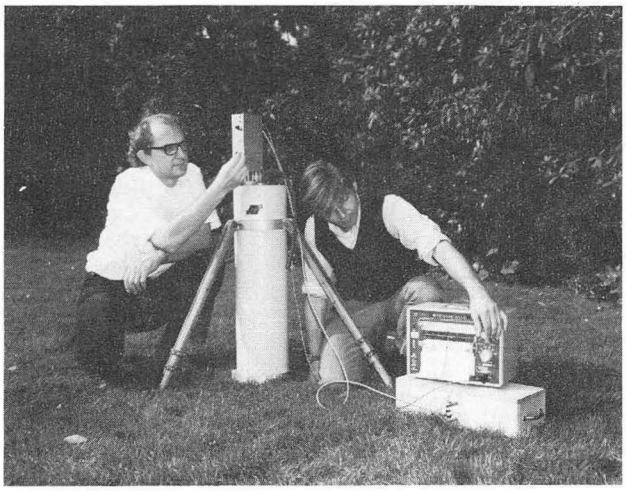

Fig. 3. Field version of SQUID magnetometer, showing cryostat, battery box, and chart recorder. (XBB 7410-7303)

2. JOSEPHSON JUNCTION MAGNETOMETER FOR USE IN GEOPHYSICS

John Clarke, Thomas Gamble, and Wolfgang M. Goubau

A number of magnetic measurements in geophysics are limited by the noise of the magnetic sensors. It is therefore highly desirable to develop new techniques for measuring magnetic fields with higher sensitivity. The Josephson junction magnetometer (SQUID) has a sensitivity two to three orders of magnitude higher than instruments currently used. After successfully testing a single-axis magnetometer in the field, we are now assembling a three-axis magnetometer that makes use of three of our thin film dc SQUIDs mounted at right angles to each other. We expect to achieve a noise of 2×10^{-10} gauss/$\sqrt{\text{Hz}}$, a frequency response of 200 Hz, and a dynamic range of 10^6.

The intended application of this instrument is for mineralogical and geological surveying, in collaboration with Professor Morrison of the geoscience department. The presence of minerals or geothermal energy sources causes a change in the electrical conductivity of the earth. Also there are indications that the conductivity across a fault line changes before an earthquake. The conductivity by itself however is not a very discriminating probe. It cannot determine the depth or distribution of the current between two points. The application of this instrument would then be to map the current distribution from its magnetic field. The natural fluctuations of the earth's magnetic field are a source of random noise which interferes with this experiment. This noise can be discriminated against by using a current at a frequency where there is a minimum of natural noise (about 3 Hz), and by making the instrument sensitive to only a narrow band of frequencies, thus using the great sensitivity available.

3. A THIN FILM GRADIOMETER

John Clarke and Claudia D. Tesche

Thin film magnetometers (SQUIDs) recently have been developed utilizing Josephson tunnel junctions. The low noise and drift of these magnetometers make them sensitive detectors of time varying magnetic fields. To fully utilize the sensitivity of these devices, however, it is necessary to operate them in carefully screened environments. Such screening is impossible for many geophysical and biological applications such as mineral surveying and magnetocardiography.

This problem may be partly overcome by using a gradiometer instead of a magnetometer to measure the gradient of the magnetic field. The gradiometer samples the field at two different locations, and responds to the difference of the two values. Since most noise sources are much further away from the detector than the signal source, the magnetic gradient of the noise will be considerably less than the magnetic gradient of the signal, even though the average fields may be comparable. Hence a suitably balanced gradiometer could be used in an unscreened environment to detect very small fields. Such a gradiometer is now being developed.

The two Josephson junctions that form the SQUID are connected to two field sensors (Fig. 1). Two superconducting lead bands are evaporated 5 cm apart on a 3 mm diameter quartz tube. The bands are connected to the junctions so that the net flux measured by the SQUID is the difference of the fluxes threading the loops. Our magnetometer noise measurements suggest a gradiometer sensitivity of 2×10^{-11} gauss/cm$\sqrt{\text{Hz}}$. The gradiometer will be mounted in a non-magnetic fiberglass cryostat to form a compact and robust system for use in the field.

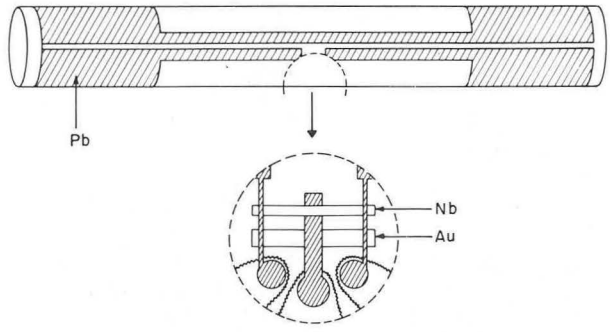

Fig. 1. Configuration of thin film gradiometer. (XBL 7412-7618)

4. Nb-Nb THIN FILM JOSEPHSON TUNNEL JUNCTIONS

Gilbert Hawkins and John Clarke

Since the first experimental observations of Josephson tunneling in 1963, the study of weakly-linked superconductors has played a fundamental role in basic research and has been widely applied to the construction of practical devices, for example, SQUID magnetometers and gradiometers, and far-infrared detectors. Because of the extremely rapid switching characteristics of the unshunted thin film Josephson tunnel junctions, much experimental effort has also been devoted to their potential use as ultrahigh-speed computer memory elements. For such applications, the reproducibility and reliability of the thin film junctions themselves is of critical importance. While the early tunnel junctions were not considered reliable, several authors have recently prepared Nb-NbO_x-Pb junctions which exhibit greater reproducibility and improved storage and cycling characteristics. However, because of the low mechanical strength and rapid oxidation-deterioration properties of the lead films, the Nb-NbO_x-Pb junctions still require special precautions in handling and must, in particular, be protected from excessive thermal shock and from exposure to water vapor.

We have developed a new type of Josephson thin film tunnel junction which does not appear to suffer from these defects. The new junctions employ Nb for both thin film strips. We have observed no deterioration in these junctions from rapid thermal shocks or from contact with water or water vapor. The junctions display much greater mechanical durability than those employing lead films and demand only minimal care in handling. Their characteristics are at least as predictable as those of the Nb-NbO_x-Pb junctions and their cycling and storage properties appear to be excellent. Fabrication techniques are comparably straightforward.

The new junctions are constructed by sputter deposition of Nb strips, 150μ wide and 1500Å thick, on soda glass substrates followed by thermal oxidation of the strips for times of from 1 to 20 min at temperatures between 25°C and 150°C. A disk of Cu 10-15Å thick is then evaporated at a rate of 1 Å/sec over a region of the oxidized Nb strip. To complete the junction, a cross strip of Nb of dimensions similar to the first Nb strip is sputtered across the region of the Cu disk. The thin Cu layer applied to the oxidized Nb strip is crucial in preventing the second Nb strip from penetrating the oxide barrier and forming a superconducting short.

The resistance and critical current of the new junctions depends upon the extent of thermal oxidation of the first Nb strip and upon the amount of Cu evaporated. We have observed critical currents in the range 0.2 μA to 1.5 mA with resistances from 40Ω to 0.5Ω for the range of parameters studied so far. A typical current-voltage characteristic is shown in Fig. 1. The appropriate value of magnetic field applied parallel to one of the strips reduces the critical current almost to zero as expected, indicating that the barrier is more or less uniform. However, the higher order maxima that should occur as the magnetic field is further increased are not usually observed.

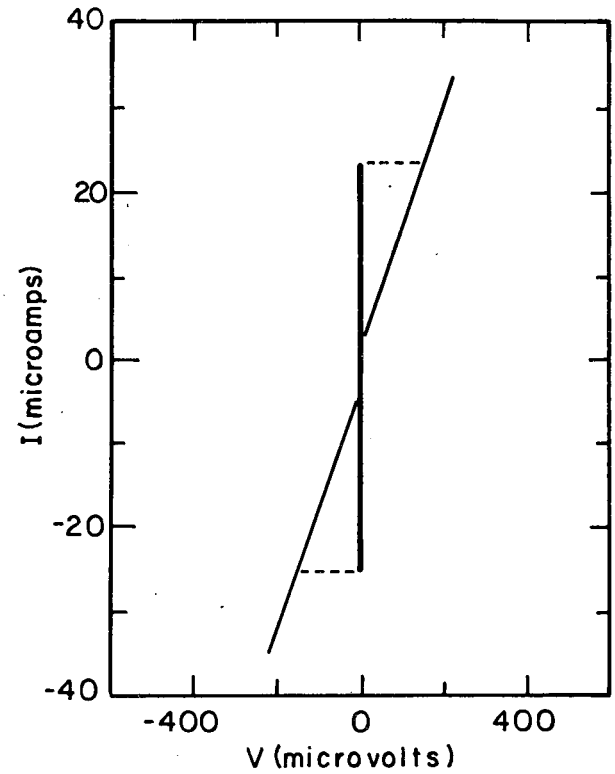

Fig. 1. Current-voltage characteristic of Nb-Nb tunnel junction. (XBL 751-5425)

We plan to continue our studies of the dependence of the junction characteristics upon the degree of thermal oxidation and upon the extent of Cu deposition as well as to investigate more fully the reproducibility and recycling characteristics. In addition, we plan to construct reliable SQUID devices from the junctions. An attempt will also be made to develop a physical model of the junction characteristics.

5. 1/f NOISE

John Clarke and Richard F. Voss

"Flicker noise" or 1/f noise limits the accuracy of many measurements. Consequently, an understanding of the physical origins of the noise is of great theoretical and practical importance.

We have been able to show that 1/f noise in thin metal films is due to temperature fluctuations modulating the resistance. A region of heat capacity C undergoes temperature fluctuations $(\Delta T)^2 = kT^2/C$ when coupled to a heat bath independent of the manner of coupling. The spectrum of the

fluctuations, $S_T(f)$, does, however, depend in a detailed way on the heat flow to the bath. If the region of interest is part of a uniform medium, simple diffusion theory predicts the spectrum, which, although 1/f-like shows no extensive 1/f region. The theory also predicts a frequency dependent spatial correlation to the noise which we have been able to observe, as shown in Fig. 1. The metal films on glass substrates, however, are not uniform for heat conduction. Making the ad hoc assumption that this nonuniformity gives the spectrum an explicit 1/f region, we are able to make a prediction for the voltage noise spectrum:

$$S_V(f) = \frac{\bar{V}^2\beta^2kT^2}{C[3+2\ \ln(l_{max}/l_{min})]\,f} \qquad (1)$$

In Eq. (1), $\bar{V}$ is the mean voltage across the sample, β is the temperature coefficient of resistance, and l_{max} and l_{min} are the longest and shortest dimensive of the sample. The predictions of Eq. (1) are in excellent agreement with experiment, as indicated in Table I.

Work on InSb films shows that semiconductors do not fit this model. The 1/f noise is much greater than predicted by Eq. (1) as well as lacking in spatial correlation. We have, however, been able to show that the noise is due to equilibrium resistance fluctuations by showing that the amplitude fluctuations of Johnson noise have a 1/f spectrum at low frequencies.

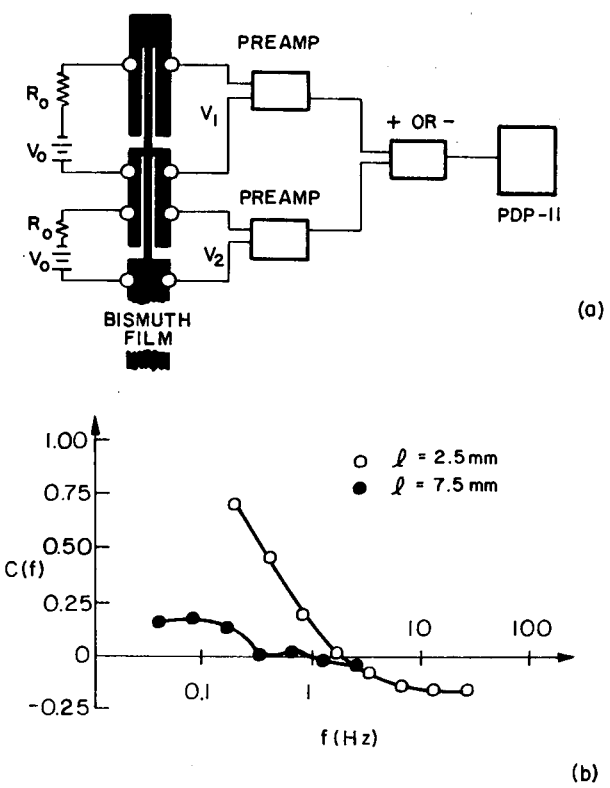

Fig. 1 (a) Experimental configuration for correlation experiment. (b) Correlation function.
(XBL 7312-6762)

Table I. The measured and calculated noise power at 10 Hz and the measured temperature coefficient of resistance for seven materials.

Material	$S_V(f)/V^2$ measured at 10 Hz (10^{-16} Hz^{-1})	$S_V(f)/V^2$ calculated at 10 Hz (10^{-16} Hz^{-1})	Measured β (K^{-1})
Cu	10	16	0.0038
Ag	10	2	0.0035
Au	1	0.76	0.0012
Sn	12	7.7	0.0036
Bi	20	9.3	- 0.0029
Manganin	$< 10^{-2}$	$< 3.5\times10^{-3}$	$\lvert\beta\rvert < 10^{-4}$
InSb	3×10^4	20	- 0.0054

It is now apparent that the simple diffusion model is not entirely adequate, and that it needs modification. For example, T. Hsiang has shown that if the film is strongly coupled thermally to a second diffusive medium, the spectrum is drastically modified. Work on theoretical models that takes into account these additional effects shows great promise. We believe these models may also apply to semiconductors in which the carriers are in diffusive motion, and surface traps play the role of substrate.

The noise spectra are taken on-line with an interfaced PDP-11 computer. The softwave for this computer has been greatly improved with the introduction of machine language Fast Fourier Transform algorithms compatible with the BASIC language. The computer now provides simple, efficient, real time measurement, analysis, and plotting of noise spectra in the frequency range of 0-10 kHz. It is also able to function as a digital lock-in detector, measuring the spectrum of amplitude fluctuations of an ac signal; as well as serve as a useful tool for computer modeling of diffusive systems.

6. LOW FREQUENCY NOISE IN SUPERCONDUCTING THIN FILMS

John Clarke and Thomas Y. Hsiang

We have measured the low frequency voltage noise in current-biased tin films at the superconducting transition temperature. These experiments were performed to test the validity of the Clarke-Voss theory of 1/f noise. The results also enable us to optimize the performance of superconducting bolometers.

Tin films were evaporated onto glass or sapphire substrates. Each substrate was mounted in a vacuum can immersed in liquid helium, and the substrate temperature adjusted to the transition temperature

the sensitivity of far-infrared bolometers. Our sensor is shown in Fig. 1. Two nylon threads attached to a mount (not shown) are coated with a thin film of indium. A superconductor-normal metal-superconductor (SNS) Josephson junction and a heater are evaporated on a 8×4×0.12 mm sapphire substrate that has strips of indium evaporated along the sides. The indium-coated nylon threads are cold welded to the indium films. The threads thus provide mechanical support for the substrate, and separate electrical contact to the SNS junction and to the heater. The whole assembly is mounted in a vacuum can. When radiation falls on the substrate, which is coated with a thin bismuth film to give a high absorption coefficient, the critical current at the junction falls. This change in critical current is detected by means of a SQUID voltmeter.

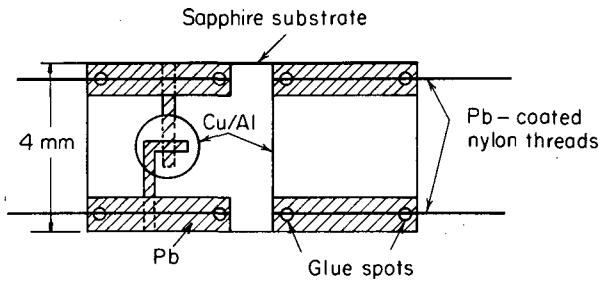

Fig. 1. Configuration of SNS bolometer.
(XBL 7112-4927A)

We have recently investigated an alternative detection scheme. The SNS junction is replaced by an evaporated strip of aluminum, which has a superconducting transition temperature of about 1.5 K. The bolometer is temperature-biased at the mid-point of the transition with a constant current flowing through the film. A change in temperature produces a change in the resistance of the film, and hence a change in the voltage developed across it. This voltage change can be detected using conventional room temperature electronics.

For both types of detector, it should be possible to achieve an NEP approaching 10^{-15} W/$\sqrt{\text{Hz}}$. The best NEP obtained so far with the SNS bolometer is 5×10^{-15} W/$\sqrt{\text{Hz}}$. However, the area of the bolometer, 32 mm^2, is a factor of at least 30 greater than the area of semiconductor bolometers. The response time of our bolometer is about 0.1 sec at 1.5 K. Development of both types of bolometer is continuing.

9. DETERMINATION OF BCS PARAMETER N(0)V IN "NORMAL METALS"

John Clarke and Michael L. Rappaport

A large number of metals do not become superconducting at the lowest achievable temperature ($\lesssim$ 1 mK). However, we have developed a technique to estimate these transition temperatures T_c even though they may be far below the working temperature of the experiment. These estimates can then be compared with theoretical predictions in order to test the reliability of the theory. Our experiment in fact measures the parameter N(0)V [N(0) is the density of states at the Fermi surface for one spin, and V is the electron-electron interaction parameter], which is related to the Debye temperature and T_c by $T_c = 1.14\ \theta_D \exp(-1/N(0)V)$.

When a superconductor, S, is in intimate contact with a normal metal, N, an exponentially decaying energy gap, Δ_N, is induced in N. If one can measure the position and temperature dependence of Δ_N, one can deduce $[N(0)V]_N$, and hence the transition temperature. We measure Δ_N by measuring the resistance of SNS sandwiches as a function of temperature with a superconducting voltmeter (SQUID). In order to obtain maximum resolution, the samples are cooled in a dilution refrigerator down to temperatures of order 20 mK.

Measurements of the resistance of Sn-Ir-Sn samples, in which the Ir becomes superconducting at 57 mK, are in good accord with a semi-empirical theory. The resistances of Pb-Cu-Pb and Pb-Rh-Pb samples dropped by about 5% and 8% when they were cooled from 4.2 K to 20 mK. This result indicates that the T_c of copper is significantly lower than that of rhodium. The resistance of a Pb-Ni-Pb was constant over the same temperature interval. This result was expected, as nickel is ferromagnetic, and confirms that the resistance changes of the copper and rhodium samples were not experimental artifacts.

We hope to make further measurements on magnesium and silver, and to make estimates of the transition temperatures of all the metals studied.

10. RESEARCH PLANS FOR CALENDAR YEAR 1975

John Clarke

We will further investigate the noise limitations and long term drift of dc SQUIDs. We will study several batches of SQUIDs to determine the spread in their characteristics. We hope to control our fabrication technique sufficiently well that all of our SQUIDs have near-optimum characteristics. We will build a three-axis magnetometer for use in geophysical measurements. The system will be thoroughly field tested and calibrated. We plan to use the instrument in collaboration with Professor Morrison. The presence of minerals or geothermal sources causes a change in the conductivity of the earth. This change can be detected by applying a low frequency current between two terminals buried in the earth's surface, and measuring the magnetic response. We shall also investigate the use of the instrument to monitor changes in the earth's magnetic field near an earthquake fault line.

Several of the thin film gradiometers will be built and studied. We will determine the noise

limitations of the gradiometer, and the degree of imbalance between the two pick-up loops. If the device works successfully, it should be extremely reliable and mechanically stable. Its applications will be in geophysics, for example, to monitor gradient fluctuations in the earth's magnetic field, and in medicine, for example, to take magnetocardiograms.

The work on the Nb-Nb tunnel junctions will be continued. We will make a systematic study of the dependence of junction characteristics on niobium oxidation time and on copper thickness.

We hope thereby to be able to accurately predetermine the junction characteristics. The junctions can then be used in a number of different applications, for example, our dc SQUIDs. The junction also has potential as computer elements.

Further theoretical work is being undertaken on 1/f noise. Our semi-empirical theory accounts quantitatively for the noise in metal films, superconducting films, and Josephson junctions. In particular, the model explains the flattening of the noise spectrum observed when the sample is strongly thermally coupled to the substrate. However, we feel that the present theory involving a diffusion mechanism is not complete, and that an additional term is needed in the diffusion equation. This term has to explain why the observed spectrum has a 1/f dependence down to rather low frequencies. A preliminary model has successfully explained this observation, and we hope to develop it further. We are particularly interested in accounting for the 1/f noise in semiconductors. A more comprehensive theory would enable us to design devices with low 1/f noise.

The measurements of 1/f noise in superconducting films will be extended. Of particular interest is the noise developed by a magnetic field large enough to significantly suppress the transition temperature. The phase transition will then involve a latent heat, and one might expect the noise spectrum to be modified, and the noise at a given frequency to be lowered. Apart from the fundamental aspects of this effect, a lowering of the noise could have considerable impact on the operation of superconducting bolometers.

There are several remaining aspects to the noise measurements on Josephson junctions. We plan to look for correlation in the noise developed by two junctions in close proximity, and to investigate the effect of replacing the glass substrate by a sapphire substrate. We will also measure the noise with the junction immersed directly in liquid helium.

We will continue to work on superconducting far-infrared bolometers, in collaboration with Professor Richards. We will investigate, in detail, the far-infrared absorptivity of bismuth films on the sapphire substrates. The superconducting transition edge bolometer will be developed into a routinely-available laboratory instrument. We will improve upon the necessary electronics, and develop a field-hardened version.

We hope to complete our work to measure the BCS parameter N(0)V in Cu, Ag, Rh, and Mg. We also plan to further develop the theory of the resistance of SNS sandwiches.

11. 1974 PUBLICATIONS AND REPORTS

John Clarke and Associates

Journals

1. J. Clarke, G. I. Hoffer and P. L. Richards, Superconducting Tunnel Junction Bolometers, Revue de Physique Appliquee 9, 69 (1974) (LBL-2222).

2. J. Clarke, Josephson Junction Detectors, Science 184, 1235 (1974) (LBL-2283).

3. Richard Dalven, Proposed Search for Superconductivity in the Semiconductor SiTe, Phys. Rev. B 10, 870 (1974); Errata, Phys. Rev. B 10, 4812 (LBL-2525).

4. John Clarke and Richard F. Voss, 1/f Noise from Thermal Fluctuations in Metal Films, Phys. Rev. Lett. 33, 24 (1974) (LBL-2536).

5. Richard Dalven, Comments on the Probable Electronic Structure of the Group II Polonides, Phys. Stat. Sol. (b) 62, K5 (1974) (LBL-2526).

6. John Clarke and James L. Paterson, Measurements of the Relaxation of Quasiparticle Branch Imbalance in Superconductors, J. Low Temp. Phys. 15, 491 (1974) (LBL-2289).

7. John Clarke, Observation of Pair-Quasiparticle Potential Difference in Non-Equilibrium Superconductors, Low Temperature Physics-LT 13, Vol 3, edited by K.D. Timmerhaus, W.J. O'Sullivan, and E.F. Hammel (Plenum, 1974) p. 798 (LBL-855 Abs.).

8. J. Clarke, Macroscopic Quantum Devices, ibid. Vol. 4, p. 483 (LBL-1144 Abs.).

9. John Clarke and Louis A. Schwartzkopf, Magnetic Focusing of Electrons and Holes in Bismuth, J. Low Temp. Phys. 16, 317 (1974) (LBL-2567).

Reports

1. Richard Dalven, A Course in Applied Solid State Physics (Notes and Discussion), Am. J. Phys., LBL-2784, June 1974.

2. John Clarke, W. M. Goubau and M. B. Ketchen, A Reliable DC Squid Made with Tunnel Junctions, IEEE Trans. on Magnetics, LBL-3191, Oct. 1974.

3. John Clarke and Thomas Y. Hsiang, Low Frequency Noise in Superconducting Sn Films at the Transition, LBL-3188, October 1974 (IEEE Transactions on Magnetics).

4. John Clarke and Gilbert Hawkins, Low Frequency Noise in Josephson Junctions, LBL-3182, Oct. 1974 (ibid).

5. Richard Dalven, Recent Studies of Lead Polonide (PbPo), LBL-2524, January 1974,

6. John Clarke, Josephson Junction Devices, LBL-3528, December 1974.

7. Michael L. Rappaport, Superconducting Pb to Nb Unions, LBL-3513, Oct. 1974.

D. EXPERIMENTAL SOLID STATE PHYSICS AND QUANTUM ELECTRONICS

Y. Ron Shen, Principal Investigator

1. STUDY OF PRETRANSITIONAL BEHAVIOR OF LASER-FIELD INDUCED ORDERING IN ISOTROPIC LIQUID CRYSTALLINE MATERIALS

Eric Hanson, Y. Ron Shen, and George K. L. Wong

We have measured the optical Kerr effect and the intensity-dependent ellipse rotation in order to study the pretransitional behavior of field-induced molecular alignment in the isotropic nematic substances p-methoxy-benzylidene p-n-butylaniline (MBBA) and p-ethoxy-benzylidene-p-butylaniline (EBBA). The results agree well with predictions of the Landau-de Gennes model. Both the order-parameter relaxation time and the steady-state field-induced birefringence show critical divergence towards the isotropic → nematic transition with a $(T-T^*)^{-1}$ temperature dependence. (See Figs. 1 and 2) In the case of MBBA, our results are also consistent with the results from light scattering, but the method we use is perhaps more straightforward and accurate. The nonlinear refractive indices and other relevant parameters of the materials are derived from the experiment.

Such a pretransitional behavior is common in all liquid crystalline materials. We have studied the same effects in other nematic compounds, in some smectic compounds, and in some cholestine compounds. Using different materials with adjustable temperature, we can now have a Kerr cell with a relaxation time variable from 1 μ to less than 1 μsec. Applications of such a Kerr cell are currently under investigation.

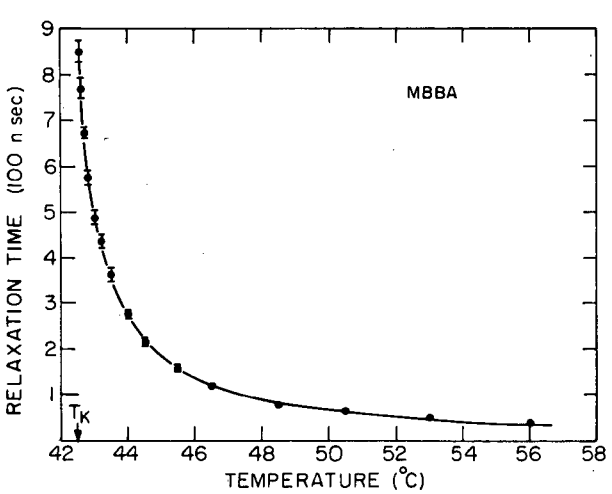

Fig. 1. Relaxation time τ of the order parameter as a function of temperature for MBBA. The solid curve is the theoretical curve described in the test. The dots are the experimental data points.
(XBL 7212-7358A)

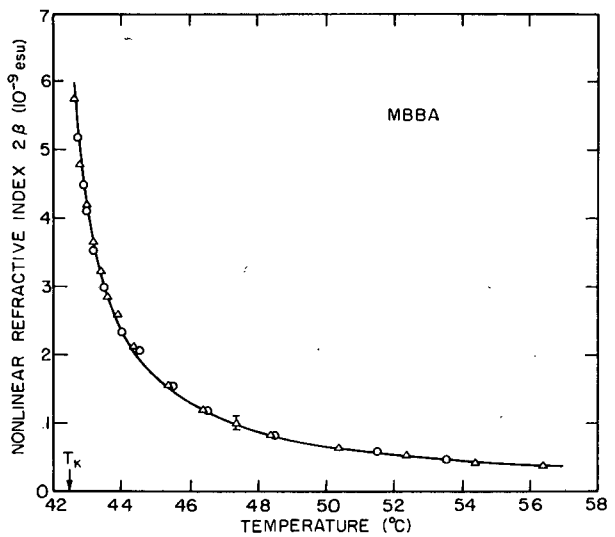

Fig. 2. Nonlinear refractive index 2β as a function of temperature for MBBA. Δ(open triangles) are experimental data obtained from measurements of optical Kerr effect, ○ (open circles) are experimental data obtained from measurements of ellipse-rotation effect. The solid curve is the theoretical curve given by $(5.4\times10^{-9})/(T-T^*)$ esu with $T^*=314.7°K$.
(XBL 743-5721)

2. STUDY OF TRANSIENT SELF-FOCUSING

Eric Hanson, Y. Ron Shen, and George K. L. Wong

Self-focusing of light in a Kerr liquid has been a subject of extensive investigation. It gives rise to the observed intense streaks and many other related phenomena. Quasi-steady-state self-focusing is now well understood. Most of the observed results can be explained satisfactorily by the picture of moving foci.[1] Transient self-focusing is however still in a state of confusion. There already exist a number of detailed numerical calculations on the subject, but no quantitative experimental results are yet available to check these calculations. The reason is obvious. Transient self-focusing occurs when the laser pulse width W is shorter than or comparable to the relaxation time τ of the field-induced refractive index Δn. Since in ordinary Kerr liquids τ is in the picosecond range, picosecond pulses must be used in the transient studies. Unfortunately, picosecond pulse technology is still in such a primitive stage that quantitative measurements are extremely difficult and expensive. Experiments on transient self-focusing would be so much easier if nanosecond pulses could be used, but then the medium should have a relaxation time τ in the 50-nsec range. This happens to be the case for liquid crystalline material in the isotropic phase.

We have made the first quantitative experimental study of transient self-focusing in a Kerr liquid by propagating Q-switched laser pulses in isotropic nematic MBBA. Our results show good qualitative agreement with the theoretical prediction on the deformation of the laser pulse shown in Fig. 1 and good quantitative agreement with the numerical estimates of the self-focused beam radius shown in Fig. 2.

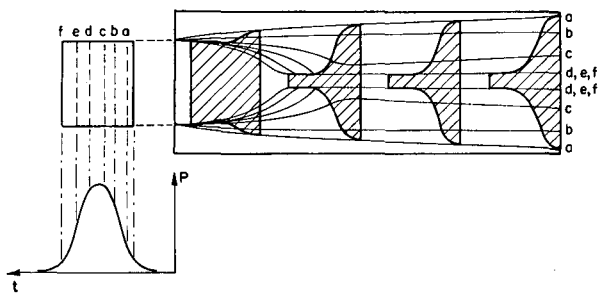

Fig. 1. Schematic drawing showing how an input pulse gets deformed through self-focusing into a horn-shaped pulse which then propagates on with little change in shape. (XBL 7312-7163)

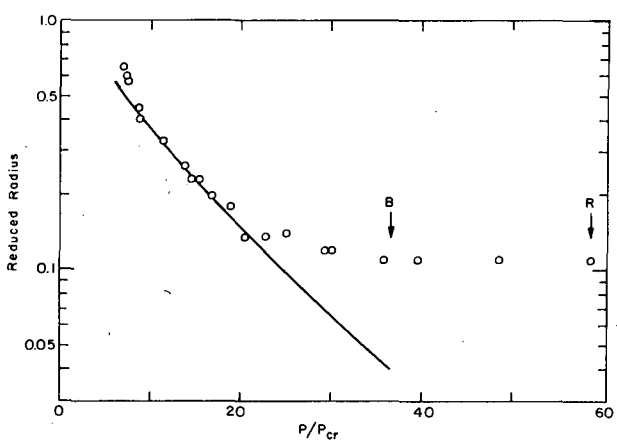

Fig. 2. Radius of the self-focused beam at the end of a 9.5-cm MBBA cell at 50°C as a function of the incoming peak power. The reduced radius is normalized against the radius of the incoming beam, and P_{cr}=0.12 kW. The solid curve is a theoretical curve. The arrows B and R indicate where stimulated Brillouin and Raman scattering set in. (XBL 7312-7166)

1. M. M. T. Loy and Y. R. Shen, Phys. Rev. Lett. 22, 994 (1969); 25, 1333 (1970).

3. MOLECULAR THEORY OF ORIENTATIONAL FLUCTUATIONS AND OPTICAL KERR EFFECT IN THE ISOTROPIC PHASE OF A LIQUID CRYSTAL

Y. Ron Shen

The spectrum of light scattering from an isotropic nematic substance has a narrow central component presumably arising from fluctuations of the order parameter.[1] The order parameter here describes the orientational order of the long molecules in the medium. On the other hand, a much broader central component was also observed in the spectrum.[2] Such a component always exists in ordinary liquids and is often called the Rayleigh-wing component. It is well known that the Rayleigh-wing component comes from orientational fluctuations of molecules. Thus, from the microscopic point of view, both components appear to be due to orientational fluctuations of molecules. It is then interesting to see how the orientational fluctuations can give rise to two very different components in the spectrum and how they are related. Using Kubo's statistical formalism, we show that orientational fluctuations of molecules are responsible for both the narrow central component and the broad Rayleigh-wing component. The narrow component appears because of large mean-field modification on the orientational motion near a phase transition. We have also derived expressions for the optical Kerr response due to molecular reorientation and the equation of motion for the macroscopic order parameter. The theory is general. In particular, it also applies to solids such as the plastic crystals. Observations of light scattering by orientational fluctuations and the corresponding optical Kerr effect in a plastic crystal have recently been reported.

1. T. W. Stinson and J. D. Litster, Phys. Rev. Lett. 25, 503 (1970).
2. N. M. Amer, Y. S. Lin, and Y. R. Shen, in Proceedings of the Fourth International Liquid Crystal Conference, Kent, Ohio, August 1972 (to be published).

4. STUDY OF DISPERSIVE RAMAN MODES IN Cu_2O BY RESONANT RAMAN SCATTERING

Y. Ron Shen and Peter Y. Yu

It is generally accepted that one-phonon Raman modes are characterized by zone-center phonons while multiphonon Raman modes reflect the phonon density of states near critical points. In either case for a given crystal orientation, the Raman frequency shift is independent of the exciting photon energy. We report for the first time the observation of some Raman modes in Cu_2O whose frequencies vary with the exciting laser frequency. We explain such energy shifts as due to dispersion in the phonons involved and obtain quantitative agreement between theory and experiment as shown

in Fig. 1. From our data we have also determined the effective mass of the 1s yellow exciton in Cu_2O to be $(3.0\pm0.2)m_0$.

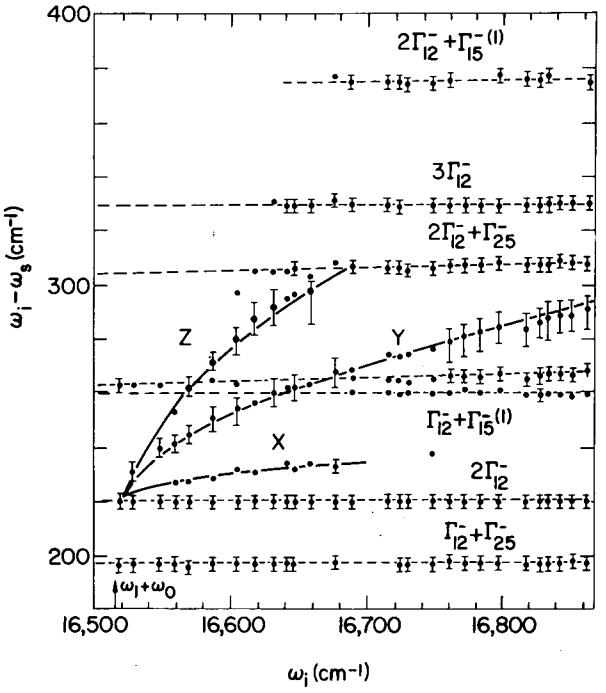

Fig. 1. The position of all the observed Raman modes of Cu_2O between 190 and 400 cm^{-1} as a function of incident photon energy. The broken curves are drawn for clarity. The solid curves are theoretical curves. The vertical bars over the experimental points indicate the half-widths of the corresponding Raman peaks. The position of the absorption edge $(\omega_1+\omega_0)$ is indicated by an arrow. (XBL 744-5959)

5. EFFECT OF DOPING ON THE RESONANCE RAMAN SCATTERING IN InSb NEAR THE E_1 TRANSITION

Y. Ron Shen and Peter Y. Yu

Resonant Raman scattering (RRS) of highly doped InSb at the E_1 transition has been measured. Increase in impurity concentration broadens and shifts the RRS peaks towards lower energies and changes the peak light of the surface-field-induced LO phonon and 2LO phonon curves, as shown in Figs. 1 and 2. The observed shift and broadening of the RRS curves in InSb with increased doping can be attributed to the corresponding shift and broadening of the E_1 transition. We have also studied RRS in InSb at different temperatures. Our results support the contention that the effect of impurities in broadening structures in optical spectra by decreasing carrier lifetime and by breaking down momentum conservation is comparable to raising the sample temperature. Increased doping changes the peak heights of the three Raman modes in InSb differently (note that the same unit for Raman cross-section is used in both figures). With increase in doping, the peak height of the TO phonon curves decreases by less than a factor of 2 while the 2LO phonon curves decrease by an order of magnitude for both n- and p-type samples. The height of the SFI LO phonon curve, however, depends on the sign of the free carrier. It increases in the n-type sample and decreases in the p-type sample.

The drop in the height of the TO phonon and the 2LO phonon RRS curves is due to broadening of the peaks. The different behavior of the SFI LO phonon curves suggest that they are induced by surface electric field and not due to wave vector dependence.

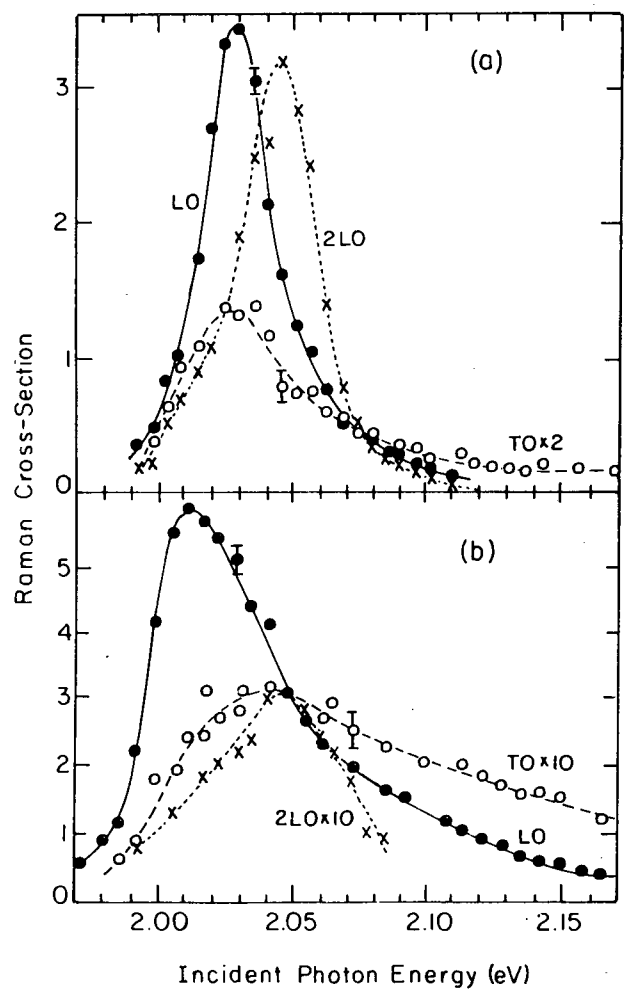

Fig. 1. Raman cross-section of two n-type InSb samples with carrier concentrations (a) 2×10^{14}cm^{-3} and (b) 1×10^{18} cm^{-3} as a function of incident phonon energy. The incident radiation is parallel to the [111] axis in both cases. TO×2 means the cross-section of the TO mode has been multiplied by a factor of 2. (XBL 753-5911)

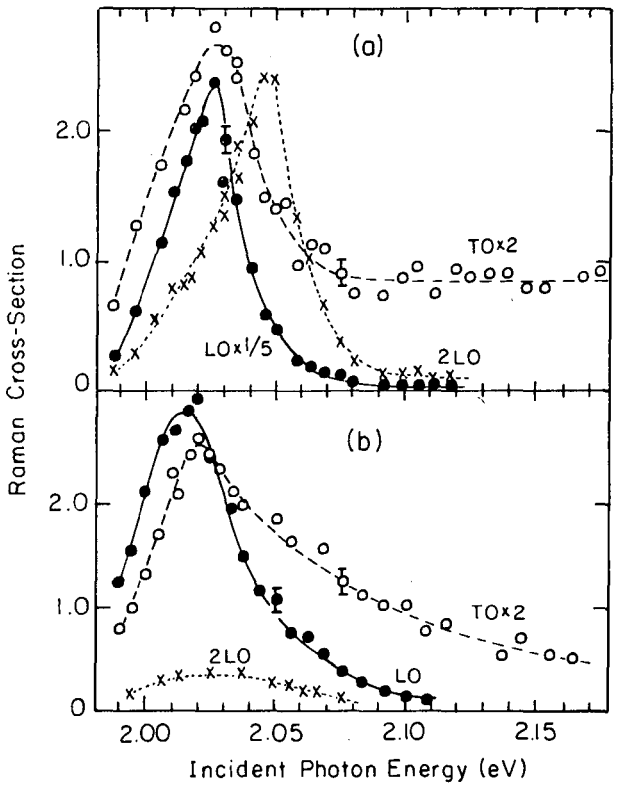

Fig. 2. Raman cross-section of two p-type InSb samples with carrier concentrations (a) 1.6×10^{16} cm^{-3} and (b) 4.8×10^{18} cm^{-3} as a function of incident photon energy. The incident radiation is parallel to the [110] axis in both cases. Notations are same as in Fig. 1. (XBL 753-5912)

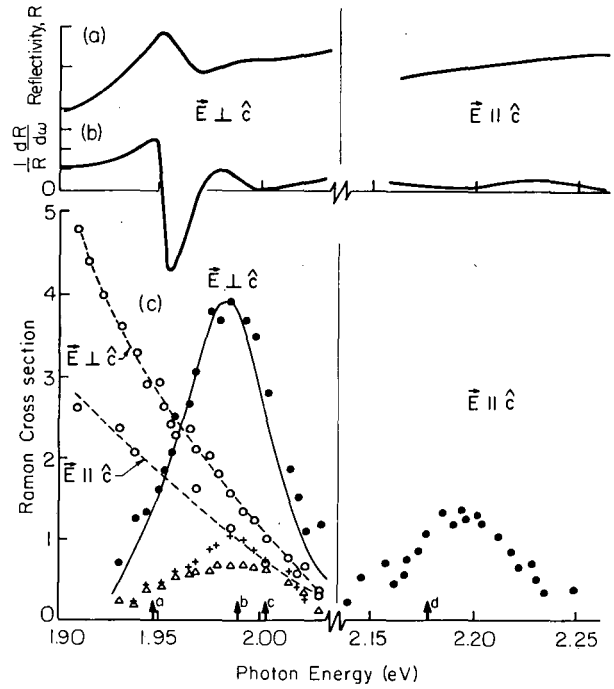

Fig. 1. (a) Reflectivity at 4.2°K; (b) logarithmic derivative of reflectivity at 4.2°K; (c) resonant Raman curves at 1.6°K for trigonal Se. The results for the various Raman modes are + for 114 cm^{-1}, ● for 151 cm^{-1}, ○ for 232 cm^{-1}, and Δ for 303 cm^{-1}. The solid curve is the theoretical curve. (XBL 746-6451)

6. RESONANT RAMAN SCATTERING IN Se

Nabil M. Amer, Yves P. Petroff, Y. Ron Shen, and Peter Y. Yu

Resonance enhancement in the Raman cross-section of longitudinal optical phonons in trigonal Se have been measured around its excitonic absorption edge at low temperatures. We present in Fig. 1 the variation of the Raman cross-sections of some of the stronger Raman modes of Se with ω_i. The resonant peak around 2.0 eV was observed only for polarizations of incident and scattered radiation both perpendicular to the c-axis, while the peak around 2.2 eV was observed only for both polarizations parallel to the c-axis. For the 232 cm^{-1} $A_1+E^{(2)}$ mode, we observed a resonant peak only for $\vec{E} \perp \hat{c}$ at the 1.95 eV exciton transition. We assign the 114, 151, and 303 (± 1) cm^{-1} lines respectively as the LO components of the modes A_2, $E^{(1)}$, and the overtone of $E^{(1)}$. Their resonant behavior is very different from the $A_1 + E^{(2)}$ mode. It can be explained by the strong electric field associated with these LO phonons which couple strongly to the excitons via the Fröhlich interaction. The frequencies of A_2 and $E^{(1)}$ we observed are respectively 2 and 4 cm^{-1} higher than those reported by Mooradian.[1] It could be that Mooradian's off-resonance measurements detected only the TO components. The LO-TO splittings of A_2 and $E^{(1)}$ deduced from infrared measurements are 4 and 6 cm^{-1} respectively.[2]

---

1. A. Mooradian, The Physics of Selenium and Tellurium, ed. by W. C. Cooper, Pergamon Press (1969). p.266.
2. G. Lucovsky, R. C. Keezer, E. Burstein, Solid State Communications 5, 439 (1967).

7. WAVELENGTH-MODULATION SPECTROSCOPY OF SOLIDS

Stanley E. Kohn, Yves P. Petroff, and Y. Ron Shen

A. $ZnGeP_2$

Reflectivity spectra of the chalcopyrite ternary compound $ZnGeP_2$ are studied experimentally and theoretically. The measurements of the reflectivity in both the complete parallel and perpendicular polarizations are made at 5°K. A full zone energy band structure, the reflectivity and imaginary part of the frequency dependent dielectric function are calculated using the empirical pseudopotential method.

Comparison of the calculated and measured reflectivity spectra (Fig. 1) shows that our model gives most of the prominent optical structure but the calculated structure is shifted by about 0.3 eV to higher energies. Better agreement can be expected if the form factors are slightly adjusted. This comparison also allows us to identify the interband transitions responsible for the prominent structure in the reflectivity, thus making it possible to extract all the pertinent information that the experimental reflectivity gives on the direct interband transitions.

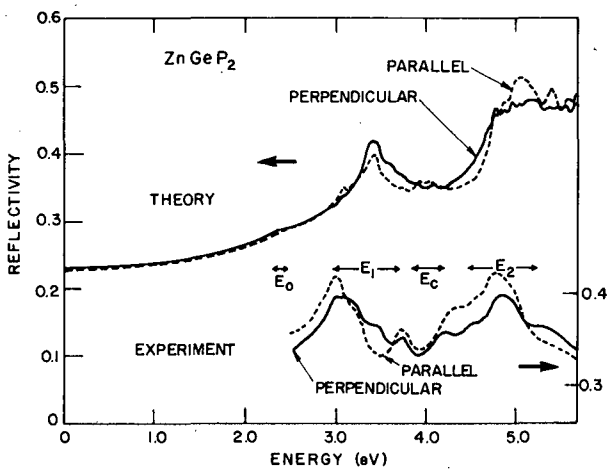

Fig. 1. Comparison of the theoretical and experimental $R(\omega)$ for $ZnGeP_2$ in the parallel and perpendicular polarizations. (XBL 738-1762)

B. SbSI

The semiconducting crystal SbSI has unusual properties. (a) In cooling down from room temperature, the crystal undergoes several phase transitions, the high-temperature phase above 19°C being paraelectric. (b) It shows very strongly anisotropic properties. (c) It has the largest known piezoelectric constant, and strongly nonlinear optical properties. Since the phase transitions involve changes in crystal structure and symmetry, it is possible that they are manifested by changes in the optical spectra, especially affecting the logarithmic derivative of the reflectivity, $(1/R)(dR/d\omega)$. We have measured the reflectivities of SbSI and their logarithmic derivatives at different temperatures. We then compare and identify the observed structures in the optical spectra with those obtained from an independent pseudopotential calculation for SbSI in the paraelectric phase (Fig. 2).

The experimental optical spectra of SbSI show no new structure caused by the paraferroelectric phase transition. We believe that the small change (<8.0%) of the relative distances among the atoms during the phase transition does not significantly alter the potential energy of the electrons. The reasonable agreement between theory and experiment for $\hbar\omega \leq 3.0$ eV, obtained without adjustment of the form factors, is remarkable. This indicates that the method of scaling the

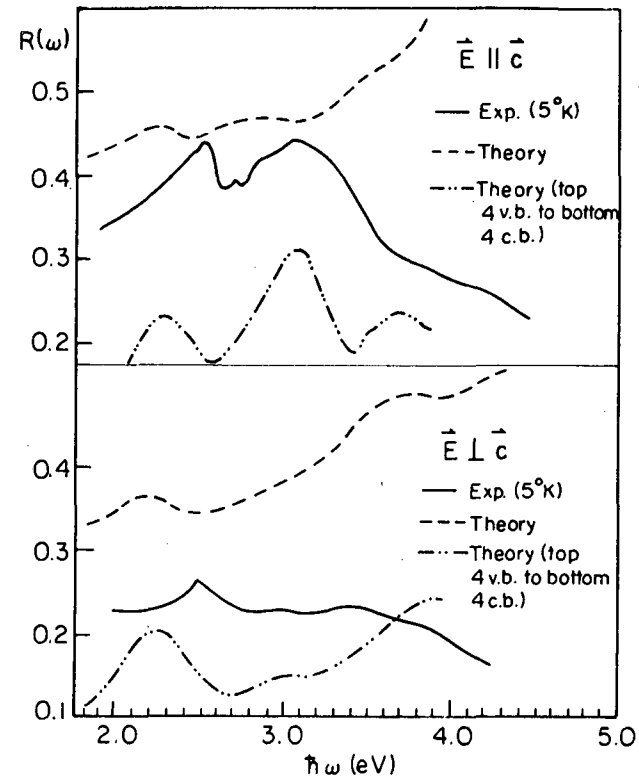

Fig. 2. Comparison between the experimental and calculated reflectivities. (XBL 752-5873)

atomic form factors in the calculations can be applied to strongly anisotropic crystals, and is comparatively simpler than other methods for crystals with many atoms per unit cell. It should prove to be a valuable tool in attempts to gain an understanding of the main features near the absorption edge in the optical spectra of more exotic semiconductors.

8. LUMINESCENCE OF CdS UNDER HIGH-INTENSITY EXCITATIONS

André Mysyrowicz, Arnold J. Schmidt, and Y. Ron Shen

In recent years, photoluminescence under high-intensity excitation has been investigated in a large number of semiconductors. In particular, the case of CdS has been studied by several research groups using laser excitation with photon energies larger than the band gap. Several new features in the luminescence spectrum were observed. The observed spectra and their intensity dependence are in good qualitative agreement among various groups, although the interpretations vary to a considerable extent. Most people, however, believe that the new features in the spectrum are due to a high exciton concentration and the existence of exciton molecules. It is conceivable that by studying the luminescence with tunable laser excitations around the exciton lines and the band edge, one might obtain some clarifying information about these new features.

We have used a N_2-laser-pumped tunable dye laser as the excitation source. At all laser frequencies, with or without linear absorption, the luminescence spectra show the same characteristic variation with laser intensity shown in Fig. 1 for two excitation frequencies, one close to the A_L exciton absorption peak and the other away from any absorption structure. In both cases the lowest intensity (Fig. 1a), we obtained the usual low-excitation luminescence spectrum. At higher excitation intensity (Fig. 1b), a broad line (called M) appeared on the low energy side of the bound exciton line I_2 and started to dominate the spectrum. With even higher excitation intensity (Fig. 1c), another broad line (called P) centered around 2.53 eV appeared and grew nonlinearly with the excitation intensity. As shown in Fig. 2a, with low excitation intensity ($\leqslant$ 1 μJ per pulse), the excitation spectrum of the I_2 luminescence line shows clear resonant enhancement at the three exciton lines A_L (2.5542 eV), A (2.5534 eV), and A_F (2.5519 eV). But with high excitation intensity, the excitation spectrum of the M line showed no sharp structure but only a general decline towards the low frequency side.

We therefore suggest that the high-excitation luminescence of CdS in our case came from direct two-photon excitations of carriers via interband transitions. The lack of fine structure in the excitation spectrum might be due to appreciable saturation in the absorption process since otherwise we should have found sharp and strong resonant enhancement around the various exciton lines.

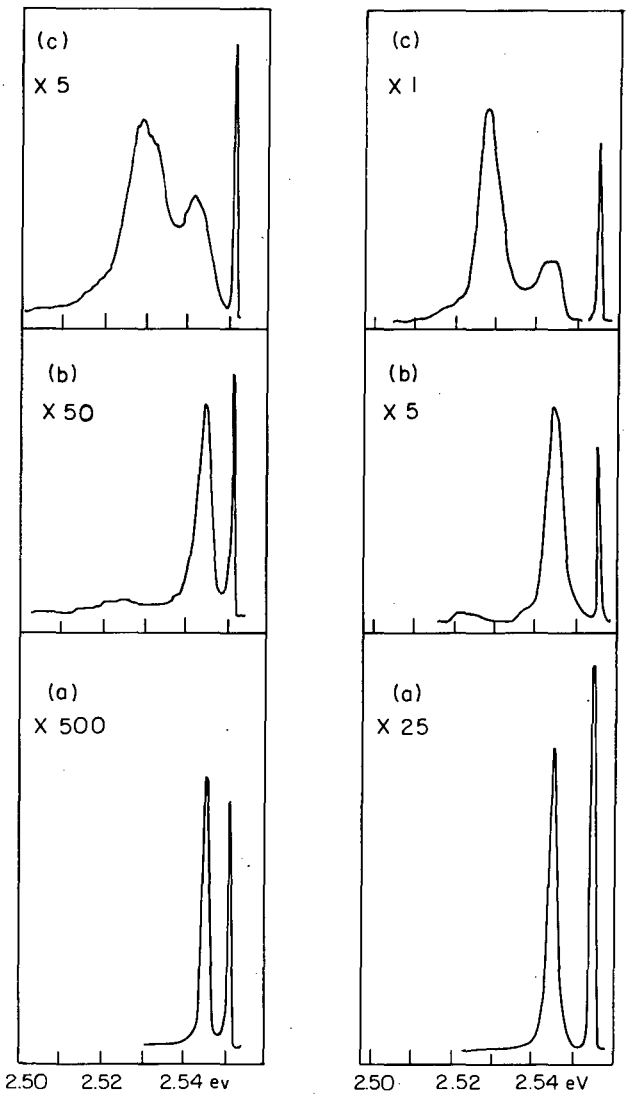

Fig. 1. Intensity dependence of the luminescence of CdS for two selected excitation frequencies; hν = 2.5511 eV (left) and hν = 2.5542 eV (right). The spectra were taken in the backward geometry. The exciting light is polarized ∥ to the c-axis of the sample. The luminescence is predominantly polarized ⊥ to c. The excitation laser intensities are: (a) 0.01 MW/cm^2; (b) 0.1 MW/cm^2; (c) 1 MW/cm^2. The luminescence spectra are magnified by the amount shown in the figure. (XBL 7411-7601)

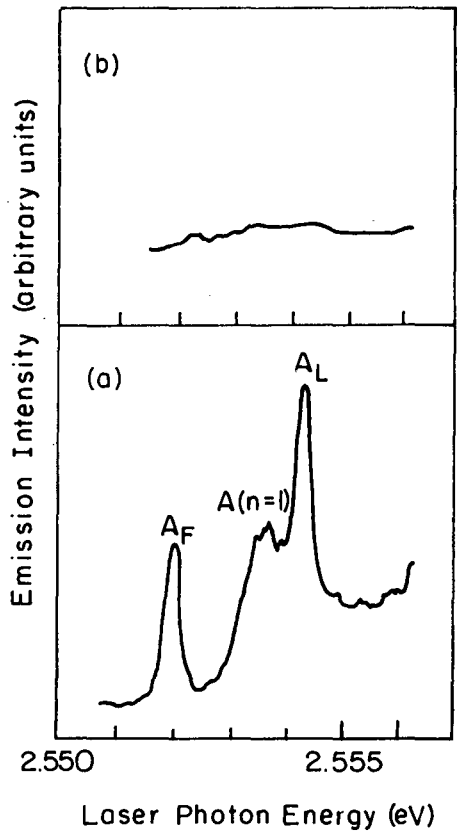

Fig. 2 (a) Excitation spectrum of the I_2 emission line (backward geometry). The spectrometer bandpass (1.5 meV) was centered at the peak of the I_2 line and the excitation frequency was scanned over a region near the A(n=1) exciton line with a laser intensity of ~ .03 MW/cm^2. The input polarization was parallel to c and the output polarization perpendicular to c.

(b) Excitation spectrum of the M line taken under similar conditions but with a laser intensity of 1 MW/cm^2. Note that the emission intensity in (b) is much larger than in (a). (XBL 7411-7603)

9. DISPERSION OF NONLINEAR OPTICAL SUSCEPTIBILITIES $\chi^{(2)}(2\omega)$ of GaAs, InAs, and InSb

Don S. Bethune, Arnold J. Schmidt, and Y. Ron Shen

The dispersion of optical nonlinear susceptibilities has always been a subject of great importance in nonlinear optics. It not only predicts how the nonlinear optical effects vary with frequencies but also yields information about the optical properties of the materials. In most semiconductors, because of the increasing number of critical points with increasing frequency, we expect to find more structure in $\chi^{(2)}(2\omega)$ at large ω. This is particularly true when both ω and 2ω are above the band gap. The measurements of $\chi^{(2)}(2\omega)$ of zincblende semiconductors have so far been limited to $\hbar\omega < 1.8$ eV. We have measured $\chi^{(2)}(2\omega)$ for GaAs, InAs, and InSb with $\hbar\omega$ extended from 2.0 to 2.7 eV. The experimental results show fair agreement with prediction from simple critical point argument. They are also in fair agreement with the theoretical calculations obtained by the empirical pseudopotential method.

10. NONLINEAR OPTICAL EFFECTS IN ALKALI VAPOR

Alexander G. Jacobson, Robert A. Smith and Y. Ron Shen

Nonlinear optical effects in atomic vapor, leading to the generation of tunable infrared and uv radiation, have recently received much attention. The mechanisms involved in these nonlinear optical phenomena are however still not well understood. A number of other possible nonlinear effects have not yet been studied. We are now planning to look into this class of problems more closely. Our aim is to achieve a better understanding of the physics involved in the nonlinear optical wave propagation in atomic vapor. We are presently in the process of building a N_2 laser which will then be used to pump a tunable dye laser necessary for such experiments.

11. RESONANT RAMAN SCATTERING IN MAGNETIC CRYSTALS

Nabil M. Amer, Tai C. Chiang, and Y. Ron Shen

Work has just been started on resonant Raman scattering and luminescence in magnetic crystals. Such problems have never been studied before. We expect to see strong resonant enhancement of not only the phonon modes, but also the magnon modes in Raman scattering from these crystals. A cw dye laser necessary for such experiments has been constructed.

12. RESEARCH PLANS FOR CALENDAR YEAR 1975

Y. Ron Shen

We plan to continue our investigation on nonlinear optical effects in liquid crystals, in particular, on transient self-focusing and optical-field-induced orientation in various kinds of liquid crystalline materials and mixtures. We shall try to extend the tunable range of our cw dye laser and use it to do resonant Raman scattering and luminescence in a variety of crystals. We are also setting up N_2-laser-pumped dye lasers to do nonlinear optical effects in atomic vapor, multiphoton photoemission, and tunable high excitations in solids. We shall also continue our wavelength modulation spectroscopy work on alloys and on layer compounds and extend the spectral range into vacuum uv.

13. 1974 PUBLICATIONS AND REPORTS

Y. Ron Shen and Associates

Journals

1. Y. Petroff, P. Y. Yu and Y. R. Shen, Absorption, Photoluminescence, and Resonant Raman Scattering in BiI_3, phys. stat. sol. (b) 61, 419 (1974) (LBL-1890).

2. Peter Y. Yu and Y. R. Shen, Multiple Resonance Effects on Raman Scattering at the Yellow-Exciton Series of Cu_2O, Phys. Rev. Letters 32, 373 (1974) (LBL-2290).

3. George K. L. Wong and Y. R. Shen, Transient Self-Focusing in a Nematic Liquid Crystal in the Isotropic Phase, Phys. Rev. Letters 32, 527 (1974) (LBL-2540).

4. C. Flytzanis and Y. R. Shen, Molecular Theory of Orientational Fluctuations and Optical Kerr Effect in the Isotropic Phase of a Liquid Crystal, Phys. Rev. Letters 33, 14 (1974) (LBL-2579).

5. P. Y. Yu and Y. R. Shen, Resonant Raman Scattering by Two LO Phonons in InSb at the E_1 Transition, Sol. State Commun. 15, 161 (1974) (LBL-2576).

6. George K. L. Wong and Y. R. Shen, Study of Pretransitional Behavior of Laser-Field-Induced Molecular Alignment in Isotropic Nematic Substances, Phys. Rev. A 10, 1277 (1974) (LBL-2723).

7. P. Y. Yu and Y. R. Shen, Effect of Doping on the Resonance Raman Scattering InSb Near the E_1 Transition, Proceeding of the XII International Conf. on Physics of Semiconductors (Stuttgart, 1974) p. 453 (LBL-2765).

8. N. Amer, Y. Petroff, Y. R. Shen and P. Y. Yu, Exciton Enhanced Raman Scattering of LO Phonons in Trigonal Se, ibid, p. 473 (LBL-2781).

9. P. Y. Yu and Y. R. Shen, Study of Dispersive Raman Modes in Cu_2O by Resonant Raman Scattering, Phys. Rev. Letters 32, 939 (1974) (LBL-2577).

10. C. Y. Fong, Y. Petroff, S. Kohn and Y. R. Shen, Wavelength-Modulation Spectra of SbSI and Its Electronic Band Structure, Sol. State Commun. 14, 681 (1974) (LBL-2225).

*11. Y. R. Shen, Distinction Between Resonance Raman Scattering and Hot Luminescence, Phys. Rev. B9, 622 (1974).

*Work done while on sabbatical leave at Laboratory of Quantum Optics, University of Paris.

Conferences

1. E. G. Hanson, George K. L. Wong and Y. R. Shen Third-Order Nonlinearity in Liquid Crystalline Materials, VIII International Quantum Electronic Conference, June 10-13, 1974, San Francisco, Paper F. LBL-2549 Abs. San Francisco.

2. George K. L. Wong and Y. R. Shen, A Quantitative Experimental Study of Transient Self-Focusing, VIII International Quantum Electronic Conference, June 10-13, 1974, Paper H.2, LBL-2543 Abs.

3. George K. L. Wong and Y. R. Shen, Optical Kerr Effect and Related Phenomena in the Isotropic Phase of a Nematic Liquid Crystal, International Conference on Liquid Crystals in Commemoration of the 25th Anniversary of the Raman Research Institute (India, Dec. 1973), Paper 22.

4. P. Y. Yu and Y. R. Shen, Phonon Dispersion Curves of Cu_2O from Resonant Raman Scattering, Bull. Am. Phys. Soc. 19, 225 (1974).

5. Y. R. Shen, Resonant Raman Scattering in Cu_2O at the Yellow Exciton Series, Bull. Am. Phys. Soc. 19, 225 (1974).

6. Y. R. Shen, Dispersion of Nonlinear Susceptibilities of GaAs, InAs and InSb, Bull. Am. Phys. Soc. 19, 313 (1974).

7. G, K. L. Wong and Y. R. Shen, Nonlinear Wave Propagation in Liquid Crystalline Materials, Vth International Liquid Crystal Conference, (June 1974, Stockholm).

8. E. G. Hanson, G. K. L. Wong and Y. R. Shen, Third-Order Nonlinearity of Liquid Crystalline Materials, Vth International Liquid Crystal Conference (June 1974, Stockholm).

LBL reports

1. E. G. Hanson, G. K. L. Wong and Y. R. Shen, Third-Order Nonlinearity in Liquid Crystalline Materials, presented at the 8th International Quantum Electronics Conference, June 10-13, 1974, San Francisco, California (LBL-2549 Abs., Jan. 1974).

2. G. K. L. Wong and Y. R. Shen, Nonlinear Wave Propagation in Liquid Crystalline Materials, presented at the Vth International Liquid Crystal Conference, June 17-21, 1974, Stockholm, Sweden (LBL-2581 Abs.).

3. Y. R. Shen and C. Flytzanis, Theory of Light Scattering and Optical Kerr Effect, ibid. (LBL-2582 Abs.).

4. E. G. Hanson, G. K. L. Wong and Y. R. Shen, Third-Order Nonlinearity in Liquid Crystalline Materials, ibid. (LBL-2583 Abs.).

5. Y. R. Shen, Stimulated Raman Scattering, LBL-2709, March 1974.

6. Y. R. Shen, Self-Focusing of Light: Review on Experimental Results and Physical Interpretations, LBL-2703, March 1974.

7. Y. R. Shen, Far-Infrared Generation by Optical Mixing, LBL-3114, July 1974.

8. Ke-Lun Wong, Self-Focusing and Optical-Field-Induced Effects in Liquids and Liquid Crystals, (Ph.D. thesis) LBL-2592, May 1974.

9. Y. Petroff, Nabil Amer and Y. R. Shen, Resonant Luminescence in Cu_2O, paper presented at the 12th International Conference on Physics of Semiconductors, Stuttgart, Germany, July 15-19, 1974, LBL-2704 Abs.

10. A. Mysyrowicz, A. J. Schmidt, Y. R. Shen, P. Robrish and H. Rosen, Luminescence of CdS Generated by High-Intensity Excitation Below the Bandgap, LBL-3544, Dec. 1974.

IMRD STAFF FOR 1974

Principal Investigators	Postdoctoral Fellows and Other Scientists	Graduate Students
Neil Bartlett	R. Peacock *K. Seppelt	L. Graham K. Leary T. Richardson
Robert Bragg	*S. Justi	*K. Ankra S. Bose K. Danso R. Mishra D. Morrow R. Saxena
Leo Brewer	L. Andrews J. Wang	G. Bullard J. Stiga
John Clarke	*R. Dalven M. Frommer W. Goubau *G. Hawkins	T. Gamble G. Hoffer T. Hsiang *M. Ketchen J. Orthel M. Rappaport R. Voss N. Yeh
Marvin Cohen	L. Falicov *J. Joannopoulos G. Martinez *M. Schluter *J. Wang	*D. Chadi *J. Chelikowski *J. Joannopoulos S. Louie
Robert Connick	*T. Norris	W. Earl K. Klotter T. Rowland
Lee Donaghey	*R. Agnihotri A. Lin	T. Anderson R. Bissinger C. Figueroa K. Geraghty C. Manke P. Mundkur *R. Pong S. Styer
Richard Fulrath	*L. Froschauer	D. Biswas S. Chandratreya K. Crabtree J. Dih J. Dullea D. Miller V. Nagesh P. Ruf J. Sherohman D. Wang
Charles Harris	H. Brenner M. Fayer *M. Glasbeek F. Ochs *R. Schlupp A. Zewail	W. Breiland J. Brock A. Burns M. Fayer M. Lewellyn *R. Shelby M. Tarrasch

Principal Investigators	Postdoctoral Fellows and Other Scientists	Graduate Students
Ronald Herm		R. Behrens A. Freedman *L. Gundel T. Parr C. Sholeen
†Ralph Hultgren		
Harold Johnston	D. Martin R. Watson	J. Birks P. Connell J. Girman R. Graham B. Nordstrom *J. Podolske G. Streit
William Jolly	M. Lazarus *R. Rietz *T. Schaaf	S. Avanzino T. Briggs J. Illige W. Perry J. Reed D. Yang
George Jura		*T. Chen R. Glienna B. Jurado
Bruce Mahan	J. Farrar	R. Davis J. Fair W. Ruska P. Schubert R. Terkowitz
William Miller	*S. Chapman *A. Hickman *R. Preston *O. Weres	*J. Adams *S. Augustin B. Garrett B. Garrison *S. Hornstein *A. Isaacson A. Raczkowski *G. Zahr
J. W. Morris, Jr.	*D. Huang *S. Jin *Y. Ohtakara C. Syn	M. Alavi S. Altintas K. Chang D. Grivas F. Hamzeh K. Hanson S. Hwang S. Jin C. Krause M. Lee J. Sanchez S. Wen B. Whitaker
Rolf Muller		C. Chew J. Cooper F. McLarnon M. Sand C. Smith
Rollie Myers		D. Lindner M. St. John R. Wilson

Principal Investigator	Postdoctoral Fellows and Other Scientists	Graduate Students
John Newman		*R. Homsy J. Miksis C. Mohr P. Pierini D. Ullman R. White
Donald Olander	M. Balooch	R. Acharya R. De Paula J. Doshi S. Guarro A. Machiels *F. Nuh R. Yang
Earl Parker Victor Zackay	D. Bhandarkar *S. Bush J. Evans *K. Htun B. Francis G. Lai *A. Mukhopadhyay E. Plaza *F. Ravitz *R. Ritchie J. Shively M. Yokota	B. Babu M. Bhat M. Castro-Cedeño R. Clark *T. Darroudi B. Francis W. Garrison G. Gettle G. Haddick R. Horn J. Huang S. Ivy P. Joukoff N. Kar R. Kar G. Kohn T. Lechtenberg *A. Llopis C. Mitchell H. Offer R. Omer E. Plaza P. Ruf M. Schanfein S. Singh H. Sirot L. Thompson J. Wert E. Wylie J. Yuen P. Zajchowski
Joseph Pask	R. Langston	P. Dokko C. Hoge G. Holmquist *C. Kramer *C. Marumo S. Risbud W. Snowden T. Sweeting C. Tao B. Wong
Norman Phillips	G. Brodale E. Hornung	W. Fogle B. Krusor M. Wun
Milton Pickus	M. Dariel M. Fukarova	R. Ciardella J. Granda K. Hemachalam J. Klein M. Malekzadeh F. Reinel G. Shiflett

Principal Investigators	Postdoctoral Fellows and Other Scientists	Graduate Students
Alexander Pines	J. Chang *D. Ruben	S. Allison M. Hoza T. Shattuck D. Wemmer
Kenneth Pitzer	L. Bernstein *L. Silvester	*L. Bernstein J. Kim Y. Lee G. Vogt
†Otto Redlich		
Paul Richards	*J. Claassen *Y. Taur	R. Aurbach R. Bailey *J. Mather S. McBride N. Nishioka Y. Taur D. Woody
Gene Rochlin		
Alan Searcy	*A. Büchler D. Meschi	T. Basu C. Chen S. Lim P. Mohazzabi J. Roberts R. Shukla
Y. Ron Shen	*J. Camassel *K. Miyano A. Mysyrowicz *Y. Petroff A. Schmidt *J. Voitchovsky K. Wong	D. Bethune T. Chiang E. Hanson A. Jacobson S. Kohn *Y. Lin S. Longcor R. Smith K. Wong
Garbor Somorjai	S. Brumbach J. Buchholz *C. Chang M. Chesters D. Hagen *T. Kaminska *L. Kesmodel *W. Siekhaus C. Steinbruchel *T. Taylor *Y. Tsang	S. Bernasek *D. Blakely *R. Brewington *S. Ceyer J. Crump L. Firment R. Johnson C. Megerle S. Overbury *C. Smith P. Stair
Gareth Thomas	D. Clarke *J. Dutkiewicz M. Goringe *A. Rocher *K. Schneider R. Sinclair G. Stone O. Van der Biest	L. Chen *Y. Chen *U. Dahmen F. Dizon G. Goeser R. Gronsky D. Howitt D. Huang M. Kao J. Koo K. Kubarych R. Miller F. Mirmirani R. Mishra B. Narasimha Rao M. Okada C. Wu O. Van der Biest

Principal Investigators	Postdoctoral Fellows and Other Scientists	Graduate Students
Charles Tobias	*R. Atanasoski *T. Lengas *C. Vass	*R. Acosta E. Carlson *O. Chacon U. Landau H. Law R. Putt J. Riggs C. Smith
Jack Washburn	J. Lira-Olivares *J. Grilhe K. Stolt	S. Alavi B. Chin R. Drosd T. Huo *T. Kosel C. Lampert *J. Lira-Olivares H. Mohamed T. Peterson K. Seshan A. Srivastava W. Wu

SUPPORT STAFF

C. Peterson - Business Officer

Administrative Staff

S. Ashley - Staff Assistant - Technical Reports
M. Janzen - Staff Assistant - Administration
E. Skrydlinski - Staff Assistant - Personnel/Travel
S. Stewart - Staff Assistant - Purchasing

Clerical and Secretarial Staff

‡P. Acuña	K. Hoffer	A. Ramirez
‡C. Adams	K. Janes	B. Rancatore
L. Betters	D. Kaufman	M. Saarni
G. Brazil	K. Krushwitz	‡A. Thompson
‡I. Chan	J. Lowrie	J. Wolslegel
L. Fernander	D. Martin	‡E. Wright
C. Hacker	M. Ossa	C. Yoder
L. Hesleph	E. Radmilovic	

Technical Staff

E. Edwards - Mechanical Coordinator
D. Curtis - Electronics Coordinator

G. Baum	H. Harrell	J. Liu	‡D. Sawyer
H. Brendel	J. Holthuis	G. Mikkelsen	J. Severns
M. Brown	C. Ivy	‡T. Mowles	P. Stagnaro
C. Davis	J. Jacobsen	D. Newhart	B. Stuart
P. Eggers	L. Johnson	F. Park	W. Toutolmin
J. Frease	D. Jurica	J. Patenaude	C. Vandouris
L. Galovich	E. Kozak	G. Pelatowski	P. Witherell
‡G. Georgakopoulos	D. Kreitz	D. Peterson	J. Wodei
W. Giba	K. Krieger	B. Pope	W. Wong
G. Gordon	R. Lindberg	M. Robson	A. Yuan

*Participant Status †Emeritus ‡No longer with IMRD Support Staff

DEGREES AWARDED IN 1974

Ph.D. Degrees

1. Raul Edmundo Acosta, Transport Processing in High Rate Electrolysis (LBL-2242, May).
2. Thorvald Astrup, On the Annealing of Stacking-Fault Tetrahedra and Frank Dislocation Loops in Silver (LBL-1172, May).
3. Stuart Dudley Augustin, Semiclassical Methods and Their Application to Problems in Collision Theory (LBL-3143, Sept.).
4. Samuel David Bader, Some Calorimetric Investigations of the Role of f-electrons in Superconductivity and Magnetism (LBL-2297, Jan.).
5. Lawrence Steven Bernstein, Large Amplitude Motion in Molecules (LBL-2701, May).
6. John William Birks, Theory of the Dissociation of Diatomic Molecules and a Study of the Emission Spectra of IF (LBL-2743, Nov.).
7. Djamshid Chadi, Pseudopotential and Tight-Binding Calculations of the Bulk and Surface Electronic Structure of Solids (LBL-3138, Sept.).
8. Lih-Juann Chen, Theoretical and Experimental Analysis of Crystal Defects with Particular Emphasis to Silicon (LBL-3179, Sept.).
9. Tang-Hua Chen, Microsecond Pulse Technique for Heat Capacity Measurement (LBL-2574, May).
10. James Alan Fair, An apparatus for Investigating Low Energy Ion-Molecule Reactions and Its Application to the Reactive Scattering of N^+ by H_2 (LBL-3178, Nov.).
11. Michael David Fayer, Coherence in Excited Triplet States of Molecular Crystals (LBL-2708, May).
12. Raymond Fredric Glienna, Infrared Properties of Solids Under High Pressure: Chlorinated Benzenes and Inorganic Carbonates (LBL-3169, Sept.).
13. Robert Victor Homsy, Mass Transfer to a Plane Below a Rotating Disk (LBL-2291, March).
14. Thomas Michael Hynes, Proton and Electron Spin Relaxation in Aqueous Solutions of Nickel (II) and Cobalt (II) Ions (LBL-2248, May).
15. Sunho Jin, Enhancement of Cryogenic Fracture Toughness Through Microstructural Control in a Ferritic Fe-12 Ni-0.25 Ti Alloy System (LBL-2789, June).
16. John Joannopoulos, Electronic Structure of Complex Crystalline and Amorphous Semiconductors (LBL-2724, May).
17. Berado Jurado, The Heat Capacity of Bismuth as a Function of Pressure and Temperature (LBL-3162, Sept.).
18. Charles William Krause, The Effect of a Long Range Interatomic Potential on the Stability of Crystal Lattices (LBL-3151, Sept.).
19. Valerie Ruth Petersen Kruger, The Kinetics of Radiolytic Gas Phase Reactions by Modulated Molecular Beam Mass Spectrometry (LBL-2727, Nov.).
20. Joaquin Lira-Olivares, A Study of Electron Current Intensities Emitted From the Superlattice Planes of an Ordered Alloy (LBL-2265, May).
21. Lambert Ching-Hon Loh, Molecular Beam Studies of Electronic Energy Transfer Processes with Metastable Mercury Atoms (LBL-2253, Jan.).
22. John Cromwell Mather, Far Infrared Spectrometry of the Cosmic Background Radiation (LBL-2258, Jan.).
23. Frank Raymond McLarnon, Interferometry of Electrochemical Mass Transfer Boundary Layers (LBL-3500, Dec.).
24. Winfield Blount Perry, Electronic Structure in Small Inorganic Molecules: Some Results Obtained From X-Ray Photoelectron Spectroscopy (LBL-3133, Oct.).
25. Thomas Jay Richardson, Perfluoroaromatic Cations and Related Studies (LBL-3183, Dec.).
26. James Adams Roberts, Jr., High Temperature Mass Spectrometry (LBL-2507, Feb.).
27. Elias Plaza-Meyer, Thermodynamics of Fe-C-X Alloys (LBL-3161, Sept.).
28. Peter J. Schubart, Ion Molecule Reactions: Correlation Time-of-Flight Ion Spectroscopy and the CO_2^+ - H_2 System (LBL-3154, Oct.).
29. Louis A. Schwartzkopf, Electron Focusing in Bi: A New Size Effect Measurement of a Fermi Surface (LBL-1877), May).
30. John William Sherohman, Jr., A Liquid Phase Densification Technique for the Lead Zirconate Titanate System (LBL-2767, Nov.).
31. Glen Andrew Stone, The Crystallography and Structure of Deformation Induced Epsilon and Alpha Martensite in Fe-Ni-Cr Single Crystals (LBL-1800, Sept.).
32. Gerald Edward Streit, Hydroxyl Radical Kinetics: Reaction with Ozone and Vibrational Quenching (LBL-2795, Aug.).
33. Yuan Taur, Josephson Junctions as Microwave Heterodyne Detectors (LBL-2597, April).
34. William Emerson Tennant, Low Temperature Studies. I. New Antiferromagnetic Resonance Effects in the Iron-Group Flourides. II. Impedance Matching a Josephson-Effect Galvanometer by Means of a Superconducting Transformer (LBL-1844, May).
35. Omer Oscar Van der Biest, Lattice Defects in Spinels (LBL-2786, July).
36. Ke-Lun Wong, Self-Focusing and Optical-Field-Induced Effects in Liquids and Liquid Crystals (LBL-2592. May).

37. Kei-Hsiung Yang, I. Generation of Far-Infrared Radiation by Optical Rectification of Picosecond Light Pulses and by Mixing of Two Tunable Dye Lasers. II. Theoretical Study of Coherent Phonon Generation by Optical Means in a One-Dimensional Superlattice (LBL-1876, Dec.).

D.Eng. Degrees

1. B. Naga Prakash Babu, An Investigation of Bainite Transformation in Medium Carbon Low Alloy Steels (LBL-2772, Aug.).

M.S. Degrees

1. Tushar Kanti Basu, Kinetics of Decomposition of Barium Carbonate (LBL-2580, April).
2. Manjeshwar Shanthidas Bhat, Phase Transformation Characteristics and Creep Properties of a Laves Phase Strengthened Fe-Ta-Cr-Mo Alloy (LBL-2277, April).
3. Ronald Henry Bissinger, Vapor Phase Etching Kinetics of GaAs (LBL-2783, June).
4. Dipak Ranjan Biswas, Uniaxial Bend Strength and Fracture Initiation Energy in Glass-Alumina Composites (LBL-2566, Feb.).
5. Oscar Antonio Chacon, Cathodic Reduction of Potassium in Propylene Carbonate Electrolytes (LBL-3542, Nov.).
6. Pei-shiun Chen, Flow Patterns and Solvent Selection for Liquid Phase Epitaxial Crystal Growth on Rotating Crystals (LBL-2284, Dec.).
7. Kenneth Edward Crabtree, Densification and Electrical Properties of Controlled Stoichiometry PZT (LBL-3543, Dec.).
8. Kenneth George Geraghty, Reactive Sputtering of Titanium Oxides: Target Oxidation Phenomena and Thin Film Characterization (LBL-2788, Sept.).
9. Dionysios Ioannis Grivas, Steady State Creep in Pb-Sn Eutectic Alloys (LBL-2547, May).
10. Ronald Gronsky, Discontinuous Coarsening During Aging in Spinodally Decomposed Cu-Ni-Fe Alloys (LBL-3134, Oct.).
11. David George Howitt, The Measurement of Radiation Damage in Organic Crystals in the Range of Electron Energy Between 200 keV and 650 keV (LBL-3180, Dec.).
12. Sun-Keun Hwang, The Effect of Retained Austenite on the Cryogenic Mechanical Properties in Fine-Grained Fe-12Ni-0.25 Ti Alloys (LBL-3503, Dec.).
13. Robert Walter Miller, Structure and Mechanical Properties of Bainitic Fe/4Cr/0.4C Steel (LBL-3104, Sept.).
14. Fereshteh Samimi Mirmirani, Structure and Mechanical Properties of Cu-Mn-Al Alloy (LBL-2598, April).
15. Pravin Vasudeva Mundkur, Computer Simulation of Sputtering (LBL-3172, Dec.).
16. Henry Peter Offer, Characterization of Brittle Crack Initiation in Welded A-36 and A-537 Steels (LBL-2251, June).
17. Masuo Okada, Phase Transformation in Ordered, Spinodal Cu-Mn-Al Alloys (LBL-3176, Oct.).
18. Jon Allan Roberts, Memory Filaments in Amorphous As-Te-I Semiconductors (LBL-1463, Dec.).
19. Mark Jay Schanfein, The Cryogenic Properties of Fe-Mn and Fe-Mn-Cr Alloys (LBL-2749, Aug.).
20. Henri Albert Sirot, Crack Propagation Rates in Fe-Ni Alloys (LBL-2750, Aug.).
21. Truett Belin Sweeting, Effect of Processing on Microstructure and Mechanical Behavior of Magnesium Oxide (LBL-3107, Aug.).
22. John Arthur Wert, The Strain Energy of a Disk-Shaped GP Zone (LBL-3174, Dec.).
23. Marilyn Wun, Calorimetric Studies of Singlet Ground State Systems (LBL-3177, Sept.).
24. Jim Lum Yuen, Quantitative Measurements of Phase Transformation Kinetics in Low Alloy Steels During Programmed Cooling (LBL-3103, July).
25. Paul Henry Zajchowski, The Kinetics of Auto-tempering in Selected Plain Carbon and Alloy Steels (LBL-3121, Aug.).

VISITING SCIENTISTS/SEMINAR SPEAKERS

Professor Philip B. Allen,* Department of Physics, State University of New York at Stony Brook, N.Y.

Professor George Ansell,* Rensselaer Polytechnic Institute, Troy, New York.

Dr. Stephen Antolovich, University of Cincinnati, Ohio.

Professor J. Bargon, International Business Machines, Incorporated, San Jose, California.

Professor Morrel H. Cohen,* James Franck Institute, University of Chicago, Illinois.

Dr. H. M. Crosswhite, Physics Department, Johns Hopkins University, Baltimore, Maryland.

Glen K. Ellis, U. S. Energy Research and Development Administration Headquarters, Washington, D. C.

Professor M. A. El-Sayed, Department of Chemistry, University of California at Los Angeles, Calif.

Dr. Volker Heine, Department of Physics, Cavendish Laboratory, Cambridge, England.

Professor P. Krishna, Physics Department of the University of Banares, India.

Professor Reiner Labusch,* Institüt fur Metallphysik der Universitat Göttingen, West Germany.

Dr. U. Landman,* Xerox Corporation, Webster Research Center, Webster, New York.

Professor M. Mehring, Department of Physics, University of Dortmung, West Germany.

Milton F. Moore, Information Services, U. S. Energy Research and Development Administration, San Francisco Operations Office, Oakland, California.

Professor J. Oudar,* Institute of Chemical Physics, University of Paris, France.

Professor P. Pershan,* Department of Applied Physics, Harvard University, Cambridge, Massachusetts.

David R. Picasso, Program Management and University Contracts, U. S. Energy Research and Development Administration, San Francisco Operations Office, Oakland, California.

J. A. Rabo,* Union Carbide Corporation, Tarrytown Technical Center, Old Saw Mill River Road, Tarrytown, New York.

Dr. Henry Resing, Naval Research Laboratory, Washington, D. C.

Mr. Sakogawa and study team, Japan Industrial Development, Inc., Tokyo, Japan.

Anthony W. Thompson,* Science Center, Rockwell International, Thousand Oaks, California.

Dr. William E. Tucker, Assistant General Manager for Administration, U. S. Energy Research and Development Administration Headquarters, Washington, D. C.

Professor C. H. Wang, Department of Chemistry, University of Utah, Salt Lake City, Utah.

Professor Peter Wilkes,* Department of Metallurgy, University of Manchester, England.

---

*Speaker

1974 RESEARCH SEMINARS

Date	Title	Speaker
1/16	Ductility Losses in Austenitic Stainless Steels Caused by Hydrogen	A. W. Thompson Rockwell International Thousand Oaks, Calif.
1/23	Crystals, Liquid Crystals and Super Fluids	P. Pershan Dept. of Applied Physics Harvard University Cambridge, Mass.
2/1	Heterogeneously Catalyzed Vapor-Phase Oxidation of Ethylene to Acetaldehyde	J. A. Rabo Union Carbide Corp. Tarrytown, New York
3/7	Phase Transformation Research at Rensselaer Polytechnic Institute	G. B. Ansell Rensselaer Polytechnic Institute, Troy, N. Y.
5/6	Systematic Atomic Parameters for Lanthanide and Actinide Ions	H. M. Crosswhite Johns Hopkins University Baltimore, Maryland
7/11	Pseudorotation in XeF_6	L. Bernstein*
	High Strength-High Toughness Cryogenic Alloy for Use Down to Liquid Helium Temperature	S. Jin*
	Study of Pretransitional Behavior of Laser-Field-Induced Molecular Alignment in Isotropic Nematic Substances	K-L. Wong*
8/1	Adsorption of Sulfur and Oxygen on Metal Surfaces. Thermodynamic and Structural Aspects	J. Oudar University of Paris Paris, France
8/8	Temperature Dependence of Energy States in Solids	P. B. Allen State University of N.Y. Stony Brook, New York
8/12	TTF-TCNQ "and all that"	M. H. Cohen James Franck Institute University of Chicago Chicago, Illinois
8/14	Fracture Toughness of High Strength Fe-Ni-Ti	B. Francis*
	Molecular Beam Study of H_2-D_2 Exchange on Platinum Single Crystal Surfaces	S. Bernasek*
	A Liquid Phase Densification Technique for the Lead Zirconate Titanate System	J. Sherohman*
8/27	The Modulus Defect in Solid Solutions and the Initial Susceptibility of Ferromagnets	R. Labusch University of Göttingen West Germany
9/12	Interplanar Interactions in Metallic Alloys	C. Krause*
	Interferometry of Electrochemical Mass Transfer Boundary Layers	F. McLarnon*
10/10	Thermodynamics of Fe-C-X Alloys	E. Plaza-Meyer*
	Lattice Defects in Spinels	O. Van der Biest*
	Periodic Phenomena in the High Current Density Anodic Dissolution of Copper	J. Cooper*

Date	Title	Speaker
10/14	Surface Structure Determination. Results and Expectations	U. Landman Zerox Corporation Webster Research Center Webster, N. Y.
10/22	Magnetic Anisotropy and Magnetoelasticity in the Rare-Earth Iron Laves Phase Compounds	M. P. Dariel Ben-Gurion University of the Negev, Beer-Sheva, Israel
11/7	Dislocation Glide Through a Random Array of Point Obstacles	K. Hanson*
	Perfluoroaromatic Cations, $C_6F_6^+$ and $C_{10}F_8^+$	T. Richardson*
	Techniques of Measuring Electron Beam Currents	D. Howitt*
11/14	Modulated Microstructures	P. Wilkes University of Manchester Manchester, England
12/5	The Effect of Retained Austenite on the Cryogenic Mechanical Properties in Fine-Grained Fe-12Ni-0.25Ti Alloy	S-K. Hwang*
	Gallium-Antimony Negative Deviations from Ideality	R. Pong*
	LEED and AES Studies of Iron Single Crystal Surfaces	C. Megerle*
12/10	Thermodynamic Approaches to Sintering	C. Hoge*
	Characterization and Origin of Defects in Ion Implanted Silicon	K. Seshan*
	A Chemisorption Study on Thorium	T. N. Taylor†

*Graduate Student

†Postdoctoral Fellow

☆ GPO 693-074

LEGAL NOTICE

This report was prepared as an account of work sponsored by the United States Government. Neither the United States nor the United States Energy Research and Development Administration, nor any of their contractors, subcontractors, or their employees, makes any warranty, express or implied, nor assumes any legal liability or responsibility for the accuracy, completeness or usefulness of any information, apparatus, product or process disclosed, or represents that its use would not infringe privately owned rights.